Courants de spin ultra-rapides assistés par interactions spin-orbite : vers de nouveaux concepts pour les émetteurs THz

Enzo Rongione

▶ **To cite this version:**

Enzo Rongione. Courants de spin ultra-rapides assistés par interactions spin-orbite : vers de nouveaux concepts pour les émetteurs THz. Condensed Matter [cond-mat]. Université Paris-Saclay, 2022. English. NNT : 2022UPASP159 . tel-04009699

HAL Id: tel-04009699

https://theses.hal.science/tel-04009699

Submitted on 1 Mar 2023

HAL is a multi-disciplinary open access archive for the deposit and dissemination of scientific research documents, whether they are published or not. The documents may come from teaching and research institutions in France or abroad, or from public or private research centers.

L'archive ouverte pluridisciplinaire **HAL**, est destinée au dépôt et à la diffusion de documents scientifiques de niveau recherche, publiés ou non, émanant des établissements d'enseignement et de recherche français ou étrangers, des laboratoires publics ou privés.

université
PARIS-SACLAY

Ultrafast spin-currents mediated by spin-orbit coupling: towards new concepts for THz emitters

Courants de spin ultra-rapides assistés par interactions spin-orbite : vers de nouveaux concepts pour les émetteurs THz

Thèse de doctorat de l'Université Paris-Saclay

École doctorale n°564 : Physique en Île-de-France (PIF)
Spécialité de doctorat : Physique
Graduate School : Physique
Référent : Faculté des sciences d'Orsay

Thèse préparée au sein de l'**Unité Mixte de Physique** (Université Paris-Saclay, CNRS, Thales), et du **Laboratoire de Physique de l'École Normale Supérieure** (ENS, PSL, CNRS, Sorbonne Université, Université Paris-Cité), sous la direction de **Henri JAFFRÈS**, Directeur de Recherche (CNRS), la co-direction de **Sukhdeep DHILLON**, Directeur de Recherche (CNRS), le co-encadrement de **Romain LEBRUN**, Ingénieur de Recherche (THALES).

Thèse soutenue à Paris-Saclay, le 16 décembre 2022, par

Enzo RONGIONE

Composition du jury

Membres du jury avec voix délibérative

Laura THEVENARD Directrice de Recherche (CNRS) Institut des Nanosciences de Paris	Présidente
Alexey KIMEL Professeur Université Radboud de Nimègue	Rapporteur & Examinateur
Nicolas TIERCELIN Directeur de Recherche (CNRS) Institut d'Électronique, de Microélectronique et de Nanotechnologie	Rapporteur & Examinateur
Chiara CICCARELLI Professeure associée Université de Cambridge	Examinatrice

THÈSE DE DOCTORAT
NNT : 2022UPASP159

Remerciements

Je me dois de remercier en premier lieu mon trio de thèse: Henri, Sukhy et Romain, merci à tous les trois pour m'avoir accompagné durant ces trois années passionantes. Vous avez toujours été très complémentaires dans vos expertises et c'est sans doute la raison pour laquelle j'ai pu apprendre autant grâce à vous. J'ai toujours pu trouver quelqu'un avec qui discuter et je vous remercie sincièrement pour la thèse et ses à-côtés! Je recommencerais avec plaisir si c'était à refaire... mais heureusement je ne fais qu'une thèse !

Merci à Paolo Bortolotti et Vincent Cros pour m'avoir accueilli à l'UMPhy, ainsi qu'aux deux Frédéric avant eux et également à Daniel Dolfi. Merci pour votre soutien sur ce sujet peu abordé à l'UMPhy et à TRT avant. Merci à Agnès Barthélémy de m'avoir présenté en premier lieu à Henri !

Je remercie chaleureusement les membres de mon jury, Laura Thevenard et Chiara Ciccarelli pour nos discussions lors de la soutenance, et en particulier mes deux rapporteurs, Alexey Kimel et Nicolas Tiercelin, pour leurs suggestions sur le manuscrit.

Je voudrais remercier particulièrement l'équipe *Isolants topologiques* à l'UMPhy: Laëtitia Baringthon, Diana She, Nicolas Reyren et Jean-Marie George. Une grosse partie de ce travail a été réalisé avec vous et vous avez su parfaitement maitriser la croissance des isolants topologiques et les mesures (S)ARPES à SOLEIL. Merci également à Huong, Nicholas, Sachin, Sajid, Marius et Marwan. Merci et bon courage à toi Sylvain pour continuer le travail sur la spintronique THz à l'UMPhy.

Je remercie également l'équipe *nano-THz* du LPENS pour m'avoir accueilli pendant ces trois ans: Juliette, Jérôme et Louis-Anne, mais aussi Niloufar, Thibault, Thomas, Minoosh, Pavel, Simon, Romaine, Martin, Hadrien, et Jacques. Je vous souhaite bonne continuation dans vos projects respectifs. Bon courage aux nouveaux pour vos thèses: Adrien, Anna, Solen et Aurélie.

Je vais passer un peu de temps à remercier les collègues de l'UMPhy. Même si j'ai été souvent délocalisé entre l'UMPhy et le LPENS, j'ai toujours été content de vous retrouver en rentrant de mes runs de manips. Il fait vraiment bon travailler à l'UMPhy, qui ressemble à une grande famille bien animée (c'est surtout parce qu'on apprécie les ragots qui courent, non ?). Merci d'abord à Jéremie, Simon, Kévin, Sarah et Vincent H pour avoir égayé mes années au labo. On a passé de bons moments ensemble, et bravo à vous pour m'avoir supporté lorsque ça allait moins bien! Merci à Pierre pour avoir été un super parrain de thèse. Merci énormément à Mafalda et à Dédalo et bonne

continuation à tous les deux. Merci à Fayçal, Denis, Isabella et Madjid. Un petit clin d'oeil également à la team *Supra* qui m'a souvent accueilli le midi pour déjeuner, et en particulier à Aurélien et Santiago. Merci à Julien K, Sougata, aux deux Javier et à Sophie mes voisins de bureau. Merci à Diane, Laurette, Victor Z, Aymeric, Aya, Victor H, Matthieu, Marie, Gabriel, Julian, Hugo, Julien, Pauline, Ralph, Vincent G, Florian, Bruno et Karim. Merci et bon courage à Benjamin, Nicolas et Quentin pour vos thèses ! J'ai sûrement oublié du monde, mais un grand merci à vous tous pour ces trois ans.

Je pense également au soutien administratif et technique, merci à Anne pour ton infinie patience avec nous, merci à Florence, à Clémence pour ton accompagnement sur la thèse, à Véronique et à Coralie pour avoir supporté nos nombreux devis lorsque nous avons décidé de monter un setup THz à l'UMPhy, merci aussi à Hasan et à Christophe pour leur aide de tous les jours.

Je passe maintenant aux collaborateurs, avec qui j'ai eu la chance de travailler. Cette thèse est vraiment le fruit d'échanges avec plusieurs équipes de recherche, et je voudrais commencer par nos collaborateurs côté croissance et caractérisation de couches fines, car il s'agit d'un immense travail en soi pour produire des échantillons de très bonne qualité: P. Le Fèvre (SOLEIL), A. Lemaître (C2N), l'équipe d'A. Dimoulas (INN, S. Fragkos, E. Xenogiannopoulou, P. Tsipas), l'équipe de C. Felser et A. Markou (Max Planck Institute), l'équipe de M. Jamet (Spintec, M. Ribeiro Oliviera, F. Bonell), l'équipe de M. Kläui (JGU, C. Schmitt, H. Meer) et à l'équipe de E. Saitoh (Tokyo University, R. Ramos, T. Kikkawa), à I. Sagnes (C2N), à S. T. B. Goennenwein (University of Konstanz) et à S. Geprägs (Walther-Meißner- Institut). Merci également à M. Mattern et M. Bargheer (University of Potsdam) pour la diffraction par rayons X ultra-rapides et nos discussions à Nancy. Je remercie particulièrement O. Gomonay (JGU) pour nos discussions sur la dynamique THz du vecteur de Néel dans NiO. Côté THz, merci à T. Kampfrath et à son équipe (FUB), T. Seifert, O. Gueckstock, G. Bierhance, R. Rouzegar pour m'avoir accueilli à Berlin pour une session de mesures (et pour nos études communes!). Merci également à P. Kolejak, G. Lezier, J.-F. Lampin et M. Vanvolleghem (IEMN), à R. Grasset, L. Perfetti (LSI), à P. Oppeneer (Uppsala University) pour nos discussions sur NiO/Pt, M. Vergès, J. Gorchon, G. Malinowski (IJL) et C. Rinaldi (Politechnico di Milano).

Un peu plus loin de la science (mais pas trop quand même), un immense merci à Pierre et Arthur. Vous avez toujours su m'inonder de memes extrêmement pertinents sur la thèse. Merci d'avoir été des oreilles attentives pendant ces trois ans, j'ai de la chance de vous avoir. Merci également à Mathilde et Annia et à nos moments ragots autour de trop nombreuses pizzas à midi place du Panthéon. Bon courage pour ta nouvelle vie au Canada Mathilde, et à toi Annia pour la fin de ta thèse, tu es presque au bout ! Merci à Abel et félicitations pour ta thèse également! Des directs Lyon-Barcelone vont être lancés cet été, coïncidence ? Je pense pas ! Merci à Adrien et Rami. Merci également à Léo et à Mathieu. Merci pour notre rencontre Andrea, j'espère réussir à parler italien avec toi à un moment! Un clin d'oeil également à Marie du LSI, rencontrée par hasard à Berlin !

Et enfin, merci à mes parents, à Alex et à ma grand-mère. Bien qu'étrangers à la science, vous avez toujours eu une confiance aveugle dans mes choix. J'imagine que ça n'a sans doute pas été facile de vous projeter sur des spins et des ondes THz, mais au fond si j'ai pu le faire c'est grâce à vous, alors merci infiniment. En résumé, ça n'est pas utile de polir un morceau de charbon, mais il faut le faire soi-même pour le comprendre...

Serment doctoral

Ce travail de thèse est le fruit d'une démarche de recherche originale et indépendente, effectué dans le respect des règles d'éthique et d'intégrité scientique. Les sources d'information utilisées dans ce travail ont été dûement citées, référencées et remerciées.

Prestation de serment (à l'oral, le jour de la soutenance):

En présence de mes pairs, parvenu à l'issue de mon doctorat en Physique, et ayant ainsi pratiqué, dans ma quête du savoir, l'exercice d'une recherche scientifique exigeante, en cultivant la rigueur intellectuelle, la réflexivité éthique et dans le respect des principes de l'intégrité scientifique, je m'engage, pour ce qui dépendra de moi, dans la suite de ma carrière professionnelle quel qu'en soit le secteur ou le domaine d'activité, à maintenir une conduite intègre dans mon rapport au savoir, mes méthodes et mes résultats.

This thesis work comes as a result of an original and independent research approach, realized in agreement with ethic and scientific integrity rules. All information sources used in this work have been properly cited, referenced and acknowledged.

Doctoral oath (orally, the day of the defense):

In the presence of my peers, with the completion of my doctorate in Physics, in my quest for knowledge, I have carried out demanding research, demonstrated intellectual rigour, ethical reflection, and respect for the principles of research integrity. As I pursue my professional career, whatever my chosen field, I pledge, to the greatest of my ability, to continue to maintain integrity in my relationship to knowledge, in my methods and in my results.

Palaiseau, le 16 décembre 2022,

Enzo Rongione

Preface

This work has been carried out between October 2019 and October 2022 in close collaboration between Unité Mixte de Physique CNRS/Thales, Laboratoire de Physique de l'École Normale Supérieure and Thales Research and Technology. It took place in the framework on national and European collaborations which aim to develop novel THz emitters based on spintronic phenomena in nanometer-thin structures and on topological insulators to increase the spin-charge conversion efficiency. This project also aims to envision THz detectors using antiferromagnetic materials.

In particular, this work has received support from grant ANRT CIFRE n°2019/0924 and funding from Horizon 2020 Framework Programme of the European Commission FET-Open grant agreement No. 863155 (s-Nebula). A close collaboration in the framework of Horizon 2020 FETPROAC via Project No. SKYTOP-824123 "Skyrmion–Topological Insulator and Weyl Semimetal Technology" has also been carried out.

In this thesis, several perspectives are highlighted for the reader in colored boxes. Yellow boxes are scientific transitions and necessary scientific background to understand the described effects. Blue boxes are key messages and perspectives to other domains of research while red boxes stand for important conclusions.

Contents

Remerciements *iii*

Serment doctoral *v*

Preface *vii*

Introduction **1**

I From conventional to ultrafast spintronics and spin-orbitronics. **5**
1 Theoretical description of nanomagnetism. . . . 6
1.1 Transition metals : band ferromagnetism. . . . 6
1.2 Involvement of the spin-orbit interactions in bulk and at interfaces. . . . 7
2 Emergence of spintronics. . . . 8
2.1 The discovery of giant magnetoresistance. . . . 9
2.2 Concepts and manipulation of spin accumulation and spin current. . . . 10
2.3 Magneto-transport and the Stoner-Wohlfarth model. . . . 11
2.4 The spin Hall trio. . . . 12
3 Spin-orbit coupling and spin-charge conversion mechanisms. . . . 13
3.1 (Inverse) spin Hall effect. . . . 13
3.2 (Inverse) Rashba-Edelstein effect. . . . 16
4 Spin transport in the steady-state regime. . . . 18
4.1 Focus on length- and time-scales in bulk (magnetic) systems. . . . 18
4.2 Spin waves and magnons. . . . 21
4.3 Spin-transmission at spintronic interfaces and spin memory loss. . . . 22
5 Spin dynamics. . . . 24
5.1 Radiofrequency magnetization dynamics. . . . 24
5.1.1 Landau-Liftschitz-Gilbert phenomenology. . . . 24
5.1.2 Spin pumping. . . . 24
5.2 Investigating a description of ultrafast spin phenomena. . . . 25
5.2.1 Emergence of ultrafast magnetism. . . . 25
5.2.2 Introduction to the three temperature model (3TM). . . . 26
5.2.3 Focus on typical magnetization timescales. . . . 27
5.2.4 Towards THz spintronics. . . . 27

II THz technologies and the emergence of spintronic THz devices. **29**
1 Conventional THz technologies: applications and challenges. . . . 30
2 Introduction to THz free-space emitters. . . . 32
2.1 Electric field derivation: near-field and far-field range. . . . 32
2.2 Ultrafast light-matter interactions in semiconductors and non-linear medias. . . . 34
2.3 Actual THz free-space sources, antennas and detectors. . . . 38
3 Concepts of metallic THz spintronic emitters. . . . 43
3.1 First developments and scientific context. . . . 43
3.2 Properties of spintronic THz devices. . . . 43
3.3 Emission performances. . . . 45
3.4 Wavelength and pump dependence. . . . 45
3.5 Impact of material composition and spin Hall effect-based alloys. . . . 46

3.6 Spectroscopy tool to probe the interface transmission. . . . 48
4 Novel spintronic THz emitters based on enhanced pure interfacial systems. . . . 49
4.1 Rashba 2D electron gas and topological surface states of topological insulators. . . . 49
4.2 Towards 2D materials THz heterostructures. . . . 50
5 Alternatives research paths for higher THz dynamics. . . . 51
5.1 Probing high spin-polarization materials. . . . 51
5.2 Antiferromagnetic based structures explored by THz probes. . . . 52
6 Enhanced spin-based THz functionalities. . . . 53
6.1 Near-infrared cavities. . . . 53
6.2 Antenna-enhanced spintronic emitters. . . . 54
6.3 High-speed THz modulation rate and polarization control. . . . 56
7 Envisioned THz applications using spintronic heterostructures. . . . 58
7.1 Near-field free-space imaging. . . . 58

III Metallic spintronic THz emitters: modelling and spectroscopy of spin-orbit multilayers. 61
1 Modelling of optically-induced spin currents and THz transients. . . . 62
1.1 Numerical implementation: the wave-modelling. . . . 63
1.2 Simulation results and trends. . . . 66
1.2.1 Steady-state regime in the confined geometry. . . . 66
1.2.2 Dynamical spin-current injection: role of the spin Hall angle and the thicknesses. . . . 67
1.2.3 Impact of the interfacial spin transmission and the spin-relaxation time. . . . 69
1.2.4 THz response on the pump time duration. . . . 71
1.3 Perspectives: the generalized spin voltage model. . . . 74
2 THz emission spectroscopy in the time-domain. . . . 76
2.1 Experimental spectroscopy protocol. . . . 76
2.2 Extraction of THz efficiency by removing absorption contributions. . . . 79
2.3 Extraction of the magnetic and non-magnetic components. . . . 81
2.4 Ultrafast spin current dynamics spectroscopy. . . . 81
3 $3d/5d$ metallic THz spintronic emitters: material engineering. . . . 84
3.1 Role of the spin-charge conversion efficiency with spin Hall alloys. . . . 85
3.2 Repetition layers strategy. . . . 86
3.3 Spin-sink layers. . . . 88
3.4 Comparative study with extracted spin-orbit torques. . . . 93
3.5 Probing of interfacial spin-current and spin-charge conversion properties. . . . 94
4 Take-home message and future developments. . . . 98
4.1 Spin-orbitronics. . . . 99
4.2 Towards larger spin-polarization for ultrafast injection using Weyl semi-metals. . . . 100

IV Topological surface states based spin-charge conversion mapped via THz spectroscopy. 103
1 Bi-based topological insulators: a novel platform for efficient spin-charge conversion. . . . 104
1.1 Topological order. . . . 104
1.2 Interfacial spin-charge interconversion via inverse Rashba-Edelstein effect. . . . 106
1.3 Topological protection, surface states hybridization, surface exchange and charge transfer: the effect of a magnetic contact. . . . 107
1.4 Optical non-linearities in topological insulators: towards spin-related phenomena. . . . 109
2 Bi_2Te_3 and stoichiometric $SnBi_2Te_4$ family. . . . 111
2.1 An engineered topological insulator with Fermi level pinning. . . . 111
2.2 Topological surfaces states of $SnBi_2Te_4$. . . . 111
2.3 THz emission features from $SnBi_2Te_4$/Co bilayers. . . . 113
2.4 Spin THz efficiency. . . . 114
2.5 Separation of the non-magnetic contributions to the THz emission. . . . 115
2.6 $SnBi_2Te_4$ thickness dependence and azimuthal angular profile. . . . 116
3 $Bi_{1-x}Sb_x$ alloy. . . . 119
3.1 Crystallographic structure of $Bi_{1-x}Sb_x$. . . . 119
3.2 Topological band structure and ARPES characterization. . . . 120
3.3 Spin-polarized density of states: spin-resolved ARPES and tight-binding calculations of $Bi_{1-x}Sb_x$. . . . 121
3.4 THz interfacial spin-charge conversion in $Bi_{1-x}Sb_x$/Co: experiments. . . . 130

3.5 Identifying the spin-charge conversion nature via THz angular mapping, thickness dependence and spin-current relaxation dynamics. . . . 135
3.6 Comparison with the literature and summary. . . . 137
4 Future prospects for interfacial interconversion. . . . 139
4.1 Bi_2Se_3 and 2D transition metal dichalcogenide WSe_2 inset. . . . 140
4.1.1 Growth and material characterization. . . . 140
4.1.2 THz emission features from Bi_2Se_3/Co multilayer. . . . 141
4.1.3 Thickness dependence of the emission symmetries in Bi_2Se_3/WSe_2/Co. . . . 142
4.2 Control of the Fermi level and fully-implemented interfacial systems. . . . 147

V Antiferromagnetic order based THz emission. 149
1 Motivations for antiferromagnetic spin-based THz devices. . . . 150
2 Spin arrangement and dynamics in antiferromagnets. . . . 152
2.1 Modelling the dynamics of the antiferromagnetic order. . . . 153
2.2 NiO: a model easy-plane insulating antiferromagnet. . . . 154
3 Combined emission of coherent and broadband THz magnons in NiO/Pt bilayers. . . . 154
3.1 Observation of THz magnons by inverse spin Hall effect in NiO thin films. . . . 155
3.2 Magneto-optical torque: inverse Faraday and Cotton-Mouton effects. . . . 159
3.3 THz dynamics driven by ultrafast thermal excitations. . . . 164
3.3.1 Ultrafast lattice response upon optical pumping. . . . 164
3.3.2 Thermo-magneto-elastic coherent response of NiO/Pt bilayers. . . . 165
3.3.3 Uncoherent phonon propagation and thermal effects. . . . 168
4 Perspectives for antiferromagnetic-based pulsed THz emitters. . . . 172
4.1 Narrowband emission tunability by electrical control. . . . 172
4.2 THz emission from canted easy-plane antiferromagnet α-Fe_2O_3/Pt through the Morin transition. . . . 173

VI Engineering spintronic THz emitters: from device integration to continuous THz waveform. 175
1 Challenges for high power spintronic THz emitters. . . . 176
2 Confinement and amplification of the THz wave. . . . 176
2.1 Wave impedance matching. . . . 176
2.2 Quarter-wavelength resonant THz cavities. . . . 177
3 Quasi-index matching structures. . . . 183
3.1 Parylene polymer as a top anti-reflective coating. . . . 183
4 Continuous THz wave emission by means of spintronic-based structures. . . . 186
4.1 Current state-of-the-art of CW THz. . . . 186
4.2 Optical photomixing pump profile and pulsed-to-CW efficiency ratio. . . . 186
4.3 THz CW modelling by the wave-diffusion model. . . . 187
5 Conclusions and projected implementations. . . . 189
5.1 Role of the substrate: thermal management and THz refractive index. . . . 189
5.2 Spintronic coupled THz antennas and resonators. . . . 191
5.3 Experimental integrations of THz spintronics-based functionalities. . . . 191

Conclusions and perspectives 193

Bibliography 216

Résumé de la thèse 217

Appendix 223
A1 Physical constants, usual conversions and list of acronyms. . . . 224
A2 Calculations of the spin-charge conversion in the linear response theory. . . . 225
A2.1 Derivation of the interconversion tensors from the Kubo formula. . . . 225
A2.2 Interfacial conversion angular profile *vs.* crystalline orientation. . . . 225
A3 Derivation of the spin current profile in spin-sink layers from the Valet-Fert model. . . . 227
A4 THz emission mechanisms in free-space. . . . 228
A4.1 Case of the classical dipolar oscillator. . . . 228
A4.2 Quantum equivalence: the Fermi golden rule for emission. . . . 229
A4.3 Comparing electric and magnetic dipolar radiations. . . . 229
A5 Continuity equations for the wave-diffusion model. . . . 230

A6 Derivation of the Tinkham formula. . . . 232
A7 Modelling of the electronic transfer involving spin-orbit interactions. . . . 233
A8 Equivalence to the inverse Rashba-Edelstein length in $Bi_{1-x}Sb_x$/Co interfacial conversion. . . . 235
A9 Properties of the ultrafast pulsed sources. . . . 235
A10 Electro-optic sampling and phase-matching in non-linear crystals. . . . 237
A11 Optical and electrical properties of materials. . . . 240
A12 Spin-orbit torque and spin-transfer torque. . . . 242
A13 Ultrafast X-ray diffraction on NiO/Pt bilayers. . . . 243
A13.1 Extraction of the out-of-plane transient strain in NiO/Pt bilayers. . . . 243
A13.2 Simulation of the phonon propagation: coherent strain wave and incoherent heat. . . . 244
A14 THz emission in canted rare-earth antiferromagnet $TmFeO_3$/Pt. . . . 245
A15 Finite elements methods to simulate the structure response. . . . 247
A16 THz reflector by buried metallic plane. . . . 248

Introduction

The study of the dynamical response of a magnetic material upon an intense pulsed light excitation has challenged both the ultrafast optics and magnetism communities since the pioneering work of Beaurepaire *et al.* in 1996. On the other hand, the electronics community turned towards a novel research area called spintronics, which aims to use the electron spin to store, carry and manipulate information. The transversal work of joining the two communities of ultrafast optics and spintronics, now called ultrafast spintronics, aims to understand and control spin populations and spin currents at sub-picosecond (ps, 10^{12} s) timescales to built efficient dynamical devices. Through this ultrafast spintronic field, it is only since 2016 that a breakthrough was realized, resulting in a novel spin-based high frequency terahertz (THz, 10^{12} Hz) emitter that can help fill the so-called THz gap between 0.1 and 30 THz. Spintronics THz emitters are an innovative type of THz emitters based on the ultrafast spin-charge conversion of a transient spin current generated using an ultrafast optical pulse pumping. Compared to the available THz technologies that have reached a certain technological maturity (semiconductor-based or non-linear crystal technologies), spintronic THz emitters offer unique properties, such as a gapless broadband generation up to 30 THz owing to the absence of phonon absorption in thin metallic layers, or the manipulation of the output THz polarization by means of an externally applied magnetic field, which both tackle the functionalities currently offered by well-established THz sources in the community.

Since their first experimental demonstration in 2016, concurrently by Huisman *et al.* and Seifert *et al.*, spintronics THz emitters have been focused on metallic multilayers. Such structures typically consist of a nanometer-thin optically-excited $3d$ ferromagnetic reservoir in contact with a high spin-orbit coupling material, $5d$ heavy metal in the first generation of THz spintronic emitters (*e.g.* Co/Pt, W/CoFeB/Pt). An ultrafast femtosecond (fs, 10^{-15} s) optical pump launches an ultrafast spin-current from the ferromagnetic unbalanced spin reservoir. The injected spin-current is converted in the high spin-orbit coupling material via so-called spin-to-charge conversion mechanisms (inverse spin Hall effect in $5d$ materials) which leads to the generation of a transverse THz charge current burst radiating a THz free-space single-cycle pulse. Various enhancement paths have been already explored in metallic $3d/5d$ heterostructures, for instance by designing the heterostructure thicknesses, the choice of the composing materials, *etc.* to account for spin-current relaxation processes. However, the non-negligible THz absorption in metallic layers hampers the expected performances enhancement, and the derived THz performances obtained from such spintronic emitters still require significant improvements to transpose the novel properties offered by spintronic THz emitters to everyday applications (medical imaging, high data-rate telecommunications, *etc.*).

In the perspective of improving the resulting emission from those novel THz emitters, a fundamental understanding of the physics of photo-excited spins and spin-charge conversion in nanometer-thin spintronic heterostructures is required. This thesis addresses a broad spectrum of the ultrafast spintronic processes: the dynamical spin-related excitation, injection, conversion and relaxation mechanisms on THz frequencies in high spin-orbit coupling heterostructures.

We will demonstrate the realization of a novel class of spintronic THz emitters relying on an interfacial interconversion mechanism, the so-called inverse Rashba-Edelstein effect, such as those based on topological insulators. We then propose the integration of antiferromagnetic materials to offer additional functionalities (*e.g.* narrowband emission) to the already-established spintronic THz technology. This work addresses the full "THz chain" with the generation of THz transients in free-space. We will finish by proposing prospects for the future generation of emitters, with novel functionalities such as the theoretical prediction of spintronic THz photomixing, and THz detection using antiferromagnetic materials. This thesis is organized as follows:

Chapter I will be devoted to the presentation of spintronics, a recently developed domain which uses the electron spin, rather than the electron charge, as the elemental brick for manipulating information at the nanoscale. We will present the spin-orbit interactions leading to the presence of so-called spin-charge conversion mechanisms which allow to efficiently convert a spin current generated from a thin ferromagnetic layer into a transverse charge current in strong spin-orbit coupling material. We will describe the transport properties of spins in complex heterostructures and provide insights regarding the domain of ultrafast light-matter interactions to control the magnetization of thin films.

Chapter II will first discuss the established and optimized THz technologies currently in use and derived from both electronic and photonic communities. We will describe the ultrafast contributions that can participate to single-cycle THz pulse generation (*e.g.* non-linear optics, transient charge oscillatons or magnetization dynamics). Thereafter, we will propose an actualized state-of-the-art of spintronics THz emitters and the leading research trends in the community in which this thesis contributes: optimization of metallic spintronic THz emitters, spin-interfaces, topological THz spintronics, insulating antiferromagnets, emitter functionalization, *etc.*

In Chapter III, we present a model of the spin-dependent processes leading to the THz pulse generation for metallic spintronic THz emitters. We will extract a figure of merit of the THz emission as a function of the interface, the spin-relaxation processes (spin diffusion length, *etc.*) as well as the spin-injection relevant properties. Using this updated understanding of spintronic THz emitters, we present several experimental studies derived from THz emission spectroscopy whose principle will be detailed. First, from a material perspective to serve as optimization routes, we will study the emitter repetition strategy, the optimization of the spin-charge conversion in spin Hall alloys (*e.g.* Au:Ta, Au:W) or the use of high-spin polarization ferromagnetic reservoirs with Weyl semi-metals (*e.g.* Co_2MnGa). A second step will focus more closely on the interface and spin-current tailoring properties via the use of spin-sink layers (*e.g.* Au:W alloys) to avoid detrimental spin reflections, and the evidence of Rashba scattering potentials at interfaces that are shown to reduce the spin-injection rather than enhancing the THz emission via interfacially-mediated interconversion.

Chapter IV will be dedicated to the study of a new type of structures based on topological insulators which present a stronger spin-orbit coupling at interfaces than in $5d$ heavy metals bulk. In such quantum materials, due to the presence of spin-textured topological surface states at their interfaces, a novel interfacial spin-charge conversion mechanism is predicted via the inverse Rashba-Edelstein effect that is expected to generate a charge current of higher amplitude. After a short introduction about topological physics, we will focus on three topological insulator systems which represent three different strategies to isolate the pure interfacial contribution of surface states to the spin-charge conversion process: *i*) in $SnBi_2Te_4$/Co, an efficient Fermi level pinning is realized to set free from the bulk conduction bands compared to its parent material Bi_2Te_3, *ii*) in $Bi_{1-x}Sb_x$/Co, the electronic gap can be controlled by stoichiometry and strain engineering, and *iii*) in the system Bi_2Se_3/Co where a two-dimensional semiconductor transition

metal dichalcogenide WSe_2 is inserted between the topological insulator and the ferromagnetic layer to control the spin-injection properties. Such topological heterostructures provide both interesting non-linear optics effects as well as an efficient platform for spintronics. In particular, we will address via THz emission spectroscopy the exact role of the interface and consequent ultrafast interfacial spin-charge conversion.

In Chapter V, we take a different approach where one can replace the ferromagnetic layer with an insulating antiferromagnetic layer where the two sub-lattice magnetizations are coupled in an antiparallel way. Such materials are anticipated to provide THz dynamics owing to their high exchange field, exchange interactions and very low magnetic damping, even though one drawback of relying on compensated antiferromagnetic textures is the weak net magnetic moment they provide once excited. Alongside THz pulsed emitters, antiferromagnets also hold the potential to host THz detection owing to the interaction between the driving electric field and the antiferromagnetic order (called the Néel vector) as well as the electrical control of such THz modes. We will focus on insulating antiferromagnetic materials to generate high-frequency dynamics in an antiferromagnet/5d heavy metal structure, and in particular in promising NiO/Pt easy-plane antiferromagnet. We show the generation of coherent magnons that results in a narrowband THz emission centered at 1.1 THz, reported for the first time in such spintronic THz structures, and in contrast with broadband emission previously reported. Moreover, our extensive study demonstrates two distinct spin current generation mechanisms depending on NiO orientation, either by an instantaneous optical Raman-type torque for (111) oriented NiO samples, or via ultrafast spin-phonon interactions for (001) oriented NiO thin films. In the latter mechanism, unreported in the literature until now, we will evidence the strong role played by ultrafast magneto-strictions in NiO induced by a strain wave launched from Pt as a heat-to-strain transducer, as well as thermal spin-related contributions. We then offer insights about the use of canted antiferromagnets (*e.g.* α-Fe_2O_3, $TmFeO_3$) to manipulate both the antiferromagnetic order and weak canted magnetic moment in those materials.

Finally, Chapter VI will conclude on new engineering perspectives to further optimize the emission from spintronic THz emitters and to provide interesting functionalities for such THz emitters. Up to now in the literature, various methods to optimize the optical pump interaction with the spintronic THz emitter have been proposed, such as the application of photonic crystals or Bragg reflectors. Here, we propose and realize methods to enhance the THz radiation by means of photonic strategies applied at THz frequencies, such as cavity-based THz emitters using GaAs/AlGaAs semiconductors or THz anti-reflective coatings by capping the spintronic THz emitter with a carefully designed polymer. As a future perspective, we also theoretically predict the operation of spintronic THz photomixing to generate narrowband continuous-waveform (CW) THz radiation.

I

From conventional to ultrafast spintronics and spin-orbitronics.

This first chapter introduces the main physical concepts and description of magnetism at the nanometric scale. We introduce the band ferromagnetism picture and the properties of ferromagnetic transition metals from the $3d$ family that are needed to build spin-based devices. We will then get into spin electronics - or spintronics - emerging from the giant magneto-resistance independently discovered in 1988 by A. Fert and P. Grünberg, awarding them jointly of the Nobel prize in 2007. Originating from the spin-orbit interactions, the spin-to-charge conversion mechanism - or how to convert efficiently a spin current into a transverse charge current - is the elementary brick of this novel electronics. We will describe the spin Hall and Rashba-Edelstein effects before discussing today's spintronics research problematics. The reciprocal (inverse) spin-charge conversion mechanisms will be detailed via the description of the inverse spin Hall and inverse Rashba-Edelstein tensors. We then present the spin transport properties in metals, semiconductors and insulators. In particular, we will present the role of the interface in the spin-transmission which will appear as a key parameter in multilayers elaborated in the frame of THz emitter proof of concepts. We then describe the spin-pumping and spin-orbit torque mechanisms, as ways to provide spin-current and magnetization switching in the steady-state regime. We will then move to the dynamics of the magnetization and in particular, we will finish this chapter with an emergent research area of spintronics, namely ultrafast (THz) spintronics which is at the heart of this thesis.

Especially, ultrafast and THz spintronics lack of a global theoretical framework owing to the strongly out-of-equilibrium processes involved (frontier with non-adiabatic transitions). Therefore, we separately first present in this chapter spintronics and later on THz physics in a second introductory chapter, before endeavoring to present a common framework with the ultrafast wave-diffusion model in the third chapter, in which we have contributed in this thesis.

1 Theoretical description of nanomagnetism.

1.1 Transition metals : band ferromagnetism.

From all the natural elements available in the universe, it only exists three pure ferromagnetic elements from the $3d$ transition metals family: iron (Fe, $Z = 26$), cobalt (Co, $Z = 27$) and nickel (Ni, $Z = 28$) where Z refers to the atomic number. Ferromagnetic materials present a net magnetization in their ground state. They have been studied and characterized from the late nineteenth century and the emergence of quantum mechanics helped to answer the simple question: why some elements are presenting magnetization properties, unlike main materials?

Electronic structure of ferromagnetic materials.

Fe: [Ar] $3d^6\ 4s^2$ Co: [Ar] $3d^7\ 4s^2$ Ni: [Ar] $3d^8\ 4s^2$

Let us take the example of Co. If one opens back its solid-state physics notebook [1], we obtain the electronic structure of Co atom in the valence shell as [Ar] $3d^7\ 4s^2$. All the electronic bands are here full except the $3d$ outer band occupied by seven (over ten) electrons. Following the Hund's rules for filling the electronic band structure, it comes $S = 3/2$ and $L = 3$. For more than half-filled d band, it comes in the ground state $J = L + S$ and a magnetization following $L + gS$ where g is the Landé factor (note that in the case of less than half-filled band, we would have $J = |L - S|$). In such systems, the Coulomb repulsion is different for parallel and antiparallel spins due to exchange interaction, so that it overcomes the kinetic energy. This is called the Stoner criterion, also formulated $J_{\text{ex}}\mathcal{N}(\varepsilon_{\text{F}}) > 1$ where $\mathcal{N}$ is the density of states at the Fermi level and J_{ex} is the exchange interaction. The metal becomes magnetic in the ground state, with an energy splitting $\Delta\varepsilon$ of the $3d$ bands between up and down spins as represented in Fig. 1.1.

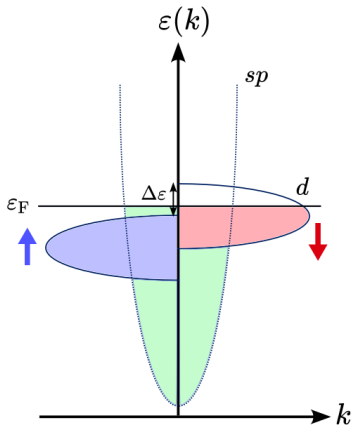

Figure 1.1: Band ferromagnetism. Spin-polarized density of states for a ferromagnet from the $3d$ family (Fe, Co, Ni) with a spin-splitting $\Delta\varepsilon$ of the $3d$ bands due to the Stoner criterion.

Considering now a set of atoms arranged in a crystallographic structure (for instance the hexagonal close-packed - or hcp - for Co), it exists a direct exchange interaction J_{ex} between the neighbouring spins $\mathbf{s}_i$ and $\mathbf{s}_j$ defining the energy of the system:

$$\mathcal{H}_{ij} = J_{\text{ex}}^{(0)} \sum_i \mathbf{s}_i \cdot \mathbf{s}_i - \sum_{i \neq j} J_{\text{ex}}^{(ij)} \mathbf{s}_i \cdot \mathbf{s}_j \tag{E1.1}$$

In the case of ferromagnetism, the exchange interaction J_{ex} can be decomposed with an intra-site exchange $J_{\text{ex}}^{(0)}$ and a neighbouring inter-site exchange $J_{\text{ex}}^{(n)}$ which are both positive (n refers to the n-th neighbour index). This leads for ferromagnets to fully aligned magnetic moments, all pointing in the same direction so that the total magnetization is $\mathbf{M} = \sum_i \mathbf{m}_i$. On the contrary,

if the first neighbouring inter-site exchange $J_{ex}^{(1)}$ is negative, the neighbouring spins are coupled antiferromagnetically which is an opposite spin ordering between two respective neighbourings spins. In this case, the net magnetization is zero, as represented in Fig. 1.2. An intermediate state, where the second sublattice magnetization is opposed to the first one but with a smaller magnetization, is called the ferrimagnetic state, and thus present a small non-zero magnetization. This behaviour is encountered mostly in magnetic garnets such as $Y_3Fe_2(FeO_4)_3$ or Gd-based rare-earth ($4f$) itinerant ferromagnetism.

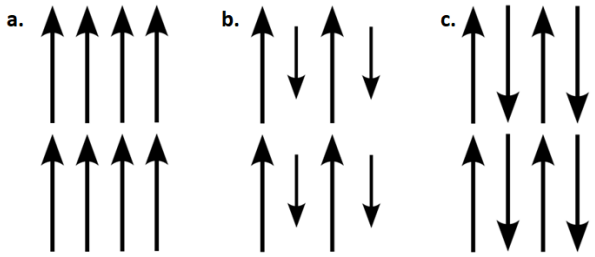

Figure 1.2: Common magnetic ordering in solids. (a) Ferromagnetic, (b) ferrimagnetic and (c) antiferromagnetic orderings.

Spin polarization and influence of the temperature. The magnetic ordering depends on various material parameters like its crystallinicity, its temperature, *etc.* The net magnetization decreases with temperature due to the thermal activation energy $k_B T$, where k_B is the Boltzmann constant. We call Curie temperature T_C the critical temperature over which a ferromagnetic state ($T < T_C$) is transformed into paramagnetic state for $T > T_C$ with the absence of a macroscopic magnetization. Similarly, for an antiferromagnet, the transition temperature between an antiferromagnetic ordering to a paramagnetic state is called the Néel temperature T_N. We present in Table I.1 the Curie temperature T_C and the spin-polarization P of some magnetic materials. Due to a difference of filling of the d (magnetic) outer shell depending on the material, the spin-polarization is different. The spin-polarization P is defined as the spin asymmetry of the spin density of states $\mathcal{N}_\sigma$ at the Fermi level (ε_F):

$$P = \frac{\mathcal{N}_\uparrow(\varepsilon_F) - \mathcal{N}_\downarrow(\varepsilon_F)}{\mathcal{N}_\uparrow(\varepsilon_F) + \mathcal{N}_\downarrow(\varepsilon_F)} \tag{E1.2}$$

Material	Co [2, 3]	CoFeB [4, 5, 6]	Ni [2, 3]	Fe [2, 3]
Curie temperature T_C (K)	1388	1100	631	1043
Spin polarization P (%)	42	65	46	45
Resistivity ρ_{FM} (μΩ.cm)	20-30	190	20-25	20-25

Table I.1: Experimental Curie temperature T_C, spin polarization P and resistivities ρ_{FM} for selected ferromagnetic materials: Co, CoFeB, Ni, Fe and NiFe.

1.2 Involvement of the spin-orbit interactions in bulk and at interfaces.

The spin-orbit interaction arises from the coupling between the spin-relativistic movement in the lattice (orbital) potential $\mathcal{V}$, leading to the occurrence of an effective electric field $\mathbf{E} = -(1/e)\nabla\mathcal{V} - \partial\mathbf{A}/\partial t$ where $\mathbf{A}$ is the potential vector. The general form of the spin-orbit Hamiltonian [7] can be written as:

$$\mathcal{H}_{SO} = -\frac{e\hbar}{4(m^*)^2c^2}(\mathbf{E} \times (\hat{\mathbf{p}} - e\mathbf{A})) \cdot \hat{\sigma} \tag{E1.3}$$

where $\hat{\mathbf{p}} = -i\hbar\nabla$ is the impulsion, m^* and e are respectively the electron mass and charge, $\hbar$ is the Planck constant and c the speed of light. The spin operator $\hat{S} = (\hbar/2)\hat{\sigma}$ has been defined with respect to the three-component Pauli matrices:

$$\sigma_x = \begin{bmatrix} 0 & 1 \\ 1 & 0 \end{bmatrix}, \quad \sigma_y = \begin{bmatrix} 0 & -i \\ i & 0 \end{bmatrix}, \quad \sigma_z = \begin{bmatrix} 1 & 0 \\ 0 & -1 \end{bmatrix} \tag{E1.4}$$

which represents the eigenvalues and eigenvectors of the spin for the three-dimensional cartesian basis $\{\vec{e}_x, \vec{e}_y, \vec{e}_z\}$. As the set of the Pauli matrices forms a basis of the special unitary group SU(2), it is more convenient to define a spinor σ which allows to generate rotations while respecting the spin invariance under 4π-rotation. If one assumes that the vector potential does not depend on time, the spin-orbit term can be reformulated more conveniently as:

$$\mathcal{H}_{\text{SO}} = \frac{\hbar}{4m^2c^2}(\nabla\mathcal{V} \times \hat{\mathbf{p}}) \cdot \hat{\sigma} \tag{E1.5}$$

Demonstration.

We consider that we have $\partial\mathbf{A}/\partial t = 0$, thus:

$$\mathcal{H}_{\text{SO}} = -\frac{e\hbar}{4m^2c^2}(\mathbf{E} \times (\hat{\mathbf{p}} - e\mathbf{A})) \cdot \hat{\sigma} \tag{E1.6}$$

$$= \frac{\hbar}{4m^2c^2}(\nabla\mathcal{V} \times \hat{\mathbf{p}} - e\nabla\mathcal{V} \times \mathbf{A}) \cdot \hat{\sigma} \quad \text{in the static case } \partial\mathbf{A}/\partial t = 0 \tag{E1.7}$$

$$\mathcal{H}_{\text{SO}} = \frac{\hbar}{4m^2c^2}(\nabla\mathcal{V} \times \hat{\mathbf{p}}) \cdot \hat{\sigma} \quad \text{as the product } \nabla\mathcal{V} \times \mathbf{A} \text{ is negligible} \tag{E1.8}$$

The spin-orbit coupling thus represents a contribution of the relativistic electron movement depending on its spin orientation, that we will call the atomic spin-orbit coupling $\mathcal{V}_{\text{at}} \propto \lambda_{\text{SO}}\hat{\mathbf{L}} \cdot \hat{\mathbf{S}}$. The spin-orbit interaction strength λ_{SO} (often labelled λ_{nl}) has been empirically found to increase with the atomic number Z [8], as represented in Fig. 1.3. For atomic hydrogene-like systems, the spin-orbit coupling λ_{SO} evolves as Z^4. We now look at the trend for the strong spin-orbit coupling material from the $5d$ transition metal family (Ta, W, Ir, Pt) that evolves more closely to a Z^2 dependence due to the valence shell electron screening. One of the important assertion induced by the spin-orbit interaction is that a generated spin current j_s (that will be defined in the next section) cannot be endlessly conserved during propagation, because of its interaction with the lattice [9, 10, 11].

Towards interfacially-related spin-orbit interactions. In the case of interfacial symmetry-breaking leading to the generation of a normal electric field (or by application of an external electric field $\mathbf{E}_{\text{ext}} = -\nabla\mathcal{V}_{\text{ext}}$), an additional term $\mathcal{V}_{\text{ext}}$ contributes to the total spin-orbit coupling which can be rewritten $\mathcal{V} = \mathcal{V}_{\text{at}} + \mathcal{V}_{\text{ext}} = \lambda_{\text{SO}}\mathbf{L} \cdot \mathbf{S} - e\mathbf{E}_{\text{ext}} \cdot \mathbf{r}$. The so-called Rashba term in the spin-orbit Hamiltonian, that will be extended to the physics of topological insulators in Chap. IV, becomes:

$$\mathcal{H}_{\text{SO}} = -\frac{\hbar}{4m^2c^2}(\mathbf{E}_{\text{ext}} \times \hat{\mathbf{p}}) \cdot \hat{\sigma} \tag{E1.9}$$

2 Emergence of spintronics.

Spin electronics, or spintronics, aims to integrate efficient spin-information manipulation down to the nanometric scale [15]. In conventional devices, the transport of the information is ensured by the electronic charge e whose limitations are many-fold: heat dissipation due to Joule heating, high power consumption, limits of the miniaturization challenging the Moore's law, *etc.* In spintronic based devices, the information is carried by the electron spin $\hat{S} = (\hbar/2)\hat{\sigma}$ and is

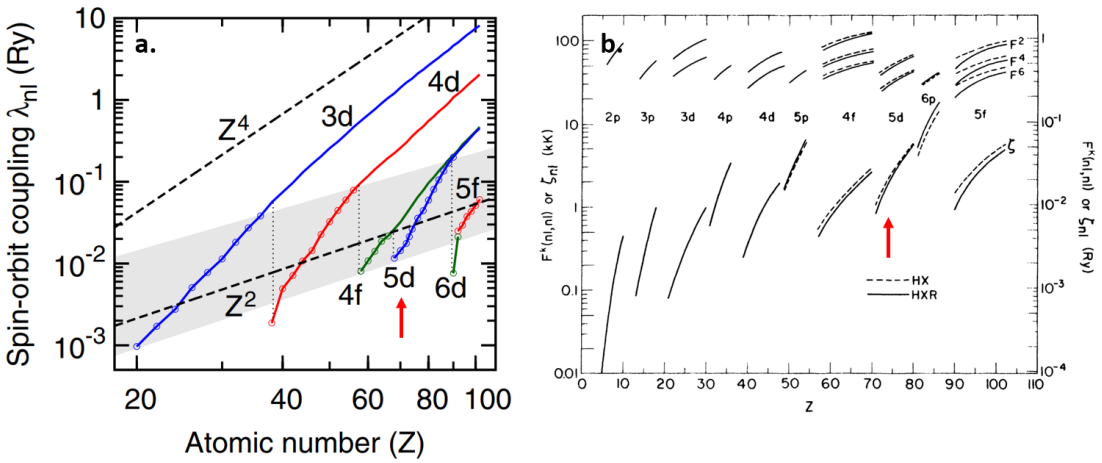

Figure 1.3: Spin-orbit coupling strength. (a) Spin-orbit coupling λ_{SO} (or λ_{nl}) for the $3d$, $4d$, $4f$, $5d$, $6d$, $5f$ series as a function of the atomic number Z (logscale). (b) Values of the spin-orbit parameter λ_{SO} as a function of Z for a more detailed atomic series in linear scale of Z. The $5d$ strong spin-orbit coupling series is highlighted with a red arrow. Left and right panels are respectively adapted from Refs. [12, 13, 8] and Ref. [14].

encoded on the two projections of the spin state (↑ or ↓ in its eigenstates). The spin-information transport answers the issues raised by conventional electronics: it can be heat dissipation-less and more compact. Besides, the challenges of the global warming pushes the development of low-consumption electronics as the planned electrical consumption (data centers, used devices, *etc.*) is expected to exponentially rise in the future decades [16].

Spintronics, and nowadays spin-orbitronics, is envisioned as a novel field of modern electronics for building faster dynamics, energy-saving devices with high-integrability [17]. The implementation started with compact magnetic data storage [18] and now looks forward to the next generation of magnetic random access memory (MRAM) with the development of STT-MRAM (spin-transfer torque). Spintronics is also prospecting beyond-CMOS (complementary metal-oxide semiconductor) transistors with the example of the magneto-electric spin-orbit (MESO) devices offering high-switchability [19, 20]. High-scale dynamics devices are also currently developed such as the spin–torque nano-oscillators (STNO), radio-frequency (RF) spin-wave based logical devices, and recently very high frequency devices with the research on the spintronic THz emitter (STE) which will be widely developed and discussed in the scope of this thesis.

2.1 The discovery of giant magnetoresistance.

Spintronics finds its origin with the discovery of the giant magnetoresistance in Fe/Cr magnetic heterostructures, independently discovered in 1988 by A. Fert [21] and P. Grünberg [22] whose results are reproduced in Fig. 1.4. In this experiment, an electric current is passing through Fe/Cr/Fe spin-valves of controlled thicknesses and the longitudinal resistance is measured. The magnetization of one Fe layer is fixed by exchange bias with Cr (antiferromagnetic coupling) while the second magnetization is free and can be tuned by application of a magnetic field. It is found that for situations where the magnetization of the free layer is parallel to the one of the fixed layer (parallel situation), the electrical resistance R_{P} is decreased while it is increased for the antiparallel configuration R_{AP}. This strongly evidences that the electrical resistance is dependent on the layer magnetization: this is the birth of spintronics where the manipulation of electrical current admits an alternative degree of freedom: the electron spin σ. In other terms, the giant magnetoresistance can be viewed as a static probe of the resistance of a so-called quantity called spin-current, where the electrical signature is linked to the current polarization P_{P} and P_{AP} according to:

$$\frac{R_{\mathrm{AP}} - R_{\mathrm{P}}}{R_{\mathrm{P}}} = P_{\mathrm{P}}^2 - P_{\mathrm{AP}}^2 \tag{E1.10}$$

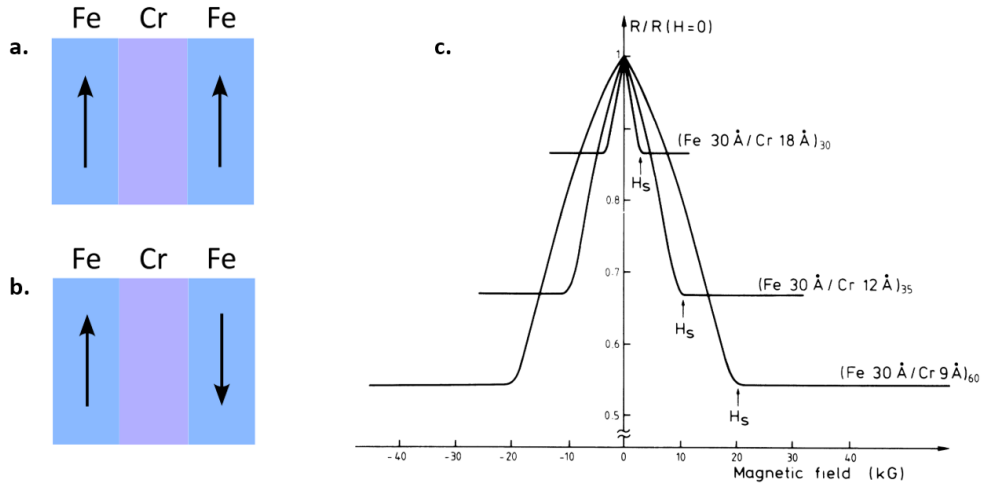

Figure 1.4: Giant magnetoresistance. Schematic representation of (a) the parallel and (b) antiparallel configuration in a Fe/Cr/Fe spin-valve. (c) Resistance as a function of applied magnetic field for different thicknesses of the Cr inset. Right panel is reproduced from Baibich *et al.* [21].

2.2 Concepts and manipulation of spin accumulation and spin current.

In this novel electronics [9], the conventional electric potential V is generalized to a spin potential (reservoir) called spin accumulation n_σ. It is defined by counting the number of spins σ following $\delta n_\sigma = \mathcal{N}_\sigma \delta\mu_\sigma$ with μ_σ the chemical potential. By considering the two spin populations imbalance, we denote as $m = n_\uparrow - n_\downarrow$ the so-called out-of-equilibrium spin accumulation which can been seen macroscopically as the magnetization $\mathbf{m}$. Note that for a metal, the charges cannot accumulate like the spin, thus offering novel perspectives for spintronic devices.

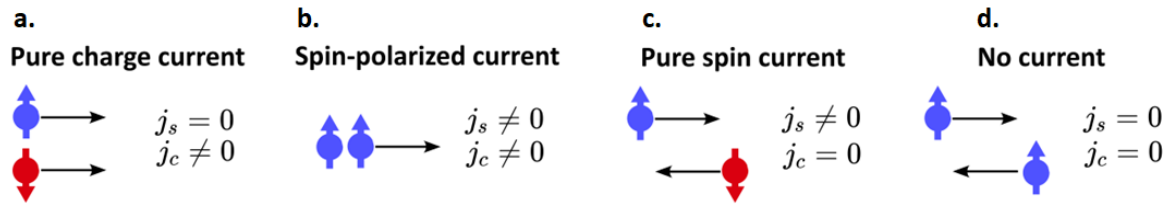

Figure 1.5: Spin-polarized electronic transport. Spin and charge transport in the case of (a) pure charge current, (b) spin-polarized current, (c) pure spin current and (d) no current of any type.

For transporting the spin-information, spintronics rely on the displacement of spins via the creation of so-called spin currents. To avoid any misunderstanding in the future, we define here the differences between a charge and a spin current, as represented in Fig. 1.5. Considering a set of mobile conduction s-electrons of charge $-e$, a net charge current j_c is only the collective displacement of electrons in one direction. If the two charges flow in reversed direction compared to each other, the net charge current is zero. In spintronics, the spins carried by the electrons play also their parts. If two electrons of opposite spins travel in the same direction, the net spin current is zero ($P = 0$). However, if the electrons share the same spins, the net spin current is non-zero. An interesting situation can occur where two electrons carrying an opposite spin travel in opposite directions. Here, the net charge current is zero but the net spin-current is non-zero:

this is called a net spin current ($P = 1$). Therefore, we can generalize all the cases by defining the charge current j_c as the sum of the spin-up and spin-down electron currents whereas the spin current j_s is defined as the difference between both quantities:

$$\mathbf{j}_c = \mathbf{j}_\uparrow + \mathbf{j}_\downarrow \qquad \mathbf{j}_s = \mathbf{j}_\uparrow - \mathbf{j}_\downarrow \tag{E1.11}$$

2.3 Magneto-transport and the Stoner-Wohlfarth model.

Anisotropy of the magneto-resistance. Magnetic field magnetoresistance is initially discovered by Lord Kelvin (W. Thomson) [23] in 1857 where he experimented variations of the electrical resistance of iron pieces while applying an external magnetic field in the same direction (or normal direction) of applied current. Several decades later in 1975, McGuire and Potter [24] explained this effect by introducing the role of the layer magnetization. As a strong enough magnetic field is applied to force the magnetization to point along the direction of the magnetic field, two cases occur. If the magnetization points in the same direction of the electrical current, the resistance possesses maxima values while, if the magnetization points in the direction orthogonal to the current, the electrical resistance experiences minima. The resistance change is of the order of 5% for ferromagnetic alloys at room temperature [24]. The magneto-transport characterization provides thus an experimental probe of the steady-state magnetization switching and spin-torque efficiency.

The Stoner-Wohlfarth model. In the general configuration, the electrical resistance $R(H, \theta, \phi)$ is dependent on a full parameter set which includes the magnitude of the applied magnetic field H, and its relative orientation with respect to the magnetization $M(\theta, \phi)$. In the general case of non-collinearity between the magnetization and magnetic field, the Stoner-Wohlfarth model [25] captures the evolution of a single-domain ferromagnetic state. The energy ε of the magnetic system can be written as:

$$\varepsilon = K_u V \sin(\phi - \theta) - \mu_0 M_s V H \cos\phi \tag{E1.12}$$

where V is the magnetic volume, M_s is the saturation magnetization, K_u is the uniaxial anisotropy constant and ϕ and θ are respectively the out-of-plane and in-plane angle. With the help of the Stoner-Wohlfarth model, one can derive the minima of energy of the system and it is thus possible to predict the response of the magnetization as a function of the magnetic field and to follow the hysteresis loops of a magnetic system *vs.* the magnetic field.

Anisotropy in magnetic systems.

In some magnetic systems called anisotropic systems, the magnetization tends to orient along particular directions. These are called easy-axis, compared to hard-axis along which an external magnetic field is necessary to force the magnetization to lie in this direction. In the most simple case, the magnetic layer possesses an uniaxial anisotropy of energy $\varepsilon_u = K_u \sin^2(\theta)$ where K_u is the uniaxial anisotropy constant (given in J.m^{-3}) and θ is the angle between the magnetization and the easy-axis.

One of the other anisotropy term is the perpendicular magnetocrystalline anisotropy, which is a competition between the in-plane uniaxial anisotropy and the out-of-plane magnetocrystalline anisotropy, expressed via the effective field $H_{\text{eff}} = 2K_{\text{eff}}/M_s$ with $K_{\text{eff}} = K_u - \mu_0/2M_s^2$ with μ_0 is the vacuum permeability and M_s is the saturation magnetization.

In very thin films, an additional shape anisotropy has to be included, represented via a demagnetization field $H_s = -M_s$ of anistropy constant $K_s = -NM := -\mu_0/2M_s$.

2.4 The spin Hall trio.

Non-conventional transport results in the presence of a transverse component of the current linked to the deflection of injected carriers, whether depending on their charge (conventional Hall effect) or on their spin orientation (anomalous and spin Hall effects) [26]. The contributions to the transverse component, called the Hall conductivity σ_{xy}, can be multiple and we will focus on the ordinary Hall effect, anomalous Hall effect and spin Hall effect as illustrated in Fig. 1.6. This list is non-exhaustive as one could also mention several Hall effects like the quantum Hall effect or the orbital Hall effect which are not included in the scope of this thesis.

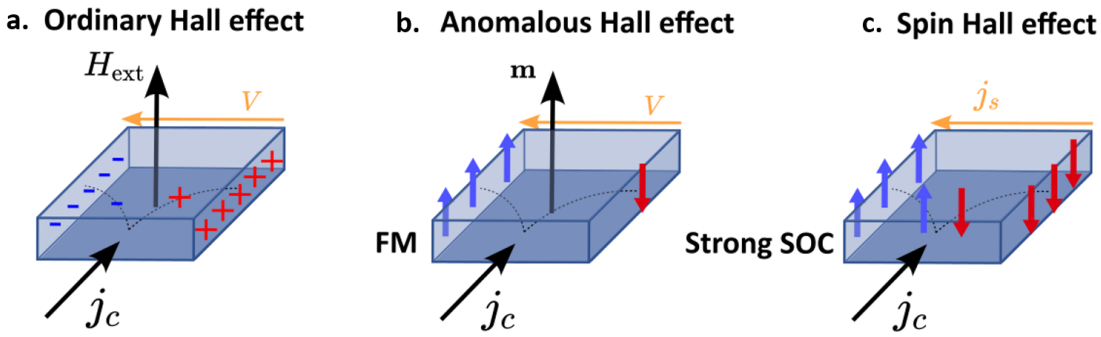

Figure 1.6: The Hall trio. Schematic representation of the (a) ordinary Hall effect, (b) anomalous Hall effect and (c) spin Hall effect. The input charge current j_c lead to the presence of a electric potential V (respectively spin current j_s) for the Hall effect and anomalous Hall effect (respectively the spin Hall effect).

Ordinary Hall effect. Among the Hall effects [26], the first one discovered in 1879 by E. Hall is the ordinary Hall effect and reports the deflection of carriers, as a charge current is injected in a conductive sample in a magnetic field $\mathbf{H}_{\text{ext}}$ perpendicular to the conduction plane. It is explained by the Lorentz force where the charges experience a force transverse to both their velocities and to the applied magnetic field. The force also depends on the charges of the carriers and thus is opposite for electrons and holes. This results in the generation of a transverse voltage V linked to a transverse electric resistance R_{xy} associated with the Hall conductivity σ_{xy}. In spintronics, such transverse contributions to the conductivity σ_{xy} are based on the spin degree of freedom and we will describe two of these effects: the anomalous Hall effect and the spin Hall effect.

Anomalous Hall effect. In a ferromagnetic material, a second contribution to the transverse component has been evidenced in 1881: the anomalous Hall effect [27]. As one applies an electrical current through a ferromagnetic metal, it is possible to measure a transverse electric potential V. Similarly, this effect is associated to the presence of a so-called transverse anomalous Hall conductivity σ_{xy}. To explain such effect, one has to introduce the deflection angle $\theta_{\mathrm{AHE}} = (\sigma_{xy}^{\uparrow} + \sigma_{xy}^{\downarrow})/(\sigma_{xx}^{\uparrow} + \sigma_{xx}^{\downarrow})$ that depends on the spin-splitted longitudinal (σ_{xx}) and transverse (σ_{xy}) conductivities. The different contributions entering in the physical explanation of the anomalous Hall effect are called the intrinsic and extrinsic contributions to the transverse (anomalous) Hall conductivity and will be developed in the next section.

3 Spin-orbit coupling and spin-charge conversion mechanisms.

3.1 (Inverse) spin Hall effect.

One of the charge-to-spin current conversion mechanisms which arises from the spin-orbit interactions is the spin Hall effect (SHE). The spin Hall effect has first been theoretically proposed by Dyakonov and Perel in 1971 [28] and reworded by Hirsch [29] in 1999. This effect takes place in the bulk of a high spin-orbit coupling material of identical spin-polarization $n_{\uparrow} = n_{\downarrow}$ and converts a charge current j_c into a transverse spin current j_s.

Here, the spin-orbit coupling takes the form of three effects: *i*) the intrinsic contribution and *ii*) the extrinsic contributions in which we develop the respective skew-scattering and the side-jump mechanisms. The extrinsic contribution, represented in Fig. 1.7 will be seen as the effect of impurities in a material, as opposed to the ideal case of a pure material relying only on the intrinsic contribution (Fig. 1.8). A common theoretical frame has been proposed [30] to explain the origin of both anomalous (magnetic system) and spin Hall (large spin-orbit system) effects. Indeed, we can represent the system Hamiltonian by introducing *i*) the impurities scattering potential $\mathcal{V}(r)$ as well as *ii*) the spin-orbit terms possibly involving the correction term from impurities as:

$$\mathcal{H} = \mathcal{H}_0 + \mathcal{H}_{\mathrm{SO}} = \frac{\hat{\mathbf{p}}^2}{2m} + \mathcal{V}(r) + \frac{\lambda_{\mathrm{SO}}}{\hbar}(\nabla\mathcal{V}(\mathbf{r}) \times \hat{\mathbf{p}}) \cdot \hat{\sigma} \tag{E1.13}$$

Extrinsic contribution: the skew scattering. The skew-scattering mechanism is historically the first explanation of the spin Hall effect given by Smit in 1950 [31, 32, 33]. It consists in a spin-dependent elastic electron-scattering of Coulombic type with the impurities. This type of scattering is sometimes referred to as the Mott scattering, and is dependent on the spin-orbit coupling which scales with the impurity central potential $\mathcal{V}$ seen by the electrons. After multiple scattering events of this nature, the electrons will be spatially oriented separately to $\mathbf{k}'$ by a certain angle $\alpha_{\mathrm{scatter}}$ with respect to the injection direction ($\mathbf{k}$), depending on their spins and thus creates a spin accumulation at the two lateral edges [34]. Such scattering process can be written following the Fermi golden rule:

$$W_{\mathbf{k}\mathbf{k}'}^{(3)} = -\frac{(2\pi)^2}{\hbar}\lambda_{\mathrm{SO}}\mathcal{N}(\varepsilon_{\mathrm{F}})(\mathcal{V}^3(\mathbf{k}' \times \mathbf{k}) \cdot \hat{\sigma})\ \delta(\varepsilon_{\mathbf{k}} - \varepsilon_{\mathbf{k}'})\delta_{\sigma\sigma'} \tag{E1.14}$$

where $\mathcal{N}(\varepsilon_{\mathrm{F}})$ is the density of states at the Fermi level and $\delta(\varepsilon_{\mathbf{k}} - \varepsilon_{\mathbf{k}'})$ and $\delta_{\sigma\sigma'}$ ensure that the scattering conserves both the spin and the energy.

Extrinsic contribution: the side-jump mechanism. The side-jump mechanism, proposed by Berger [35] in 1970, comes as a second approach in the understanding of the anomalous and spin Hall effects. It consists of the scattering between the incoming electron wave-packet and the spin-orbit potential $\mathcal{V}_{\mathrm{SO}}$ of the impurities or of the phonons. The injected electrons

(displacement along $-\mathbf{E}$) are moving at a relativistic speed (Fermi velocity), which leads to a distortion of the electronic wave-packet while entering the spin-orbit potential interaction region of impurities, including relativistic corrections as shown in Eq. (E1.13). This loss of energy is converted as *i*) a deflection of the electron trajectory by a certain angle depending on the energy ("classical" inelastic scattering) and as *ii*) a non-zero charge current density due to the wave-packet distortion, which moves laterally the electron trajectory by a distance Δy. The second point is specifically called the side-jump mechanism and is arising directly from spin-orbit coupling between the local impurity and the angular momentum carried by the scattered electron. Berger [35] estimated the side-jump Δy to be around $10^{-10} - 10^{-11}$ m per collision. The side-jump mechanism contribution to the anomalous and spin Hall effects is rather important for ferromagnetic Fe and Ni (and their alloys) compared to heavy metals, which explains only in part the progressive deflection of the two opposite spin accumulation trajectory leading to SHE as one finds more interesting values of θ_{SHE} for heavy metal systems. The transverse spin current generated via the side-jump mechanism can thus be written according to (n is the density of carriers):

$$\mathbf{j}_{\text{sj}} = \frac{ne^2\lambda_{\text{SO}}}{\hbar}(\mathbf{E} \times \sigma) \tag{E1.15}$$

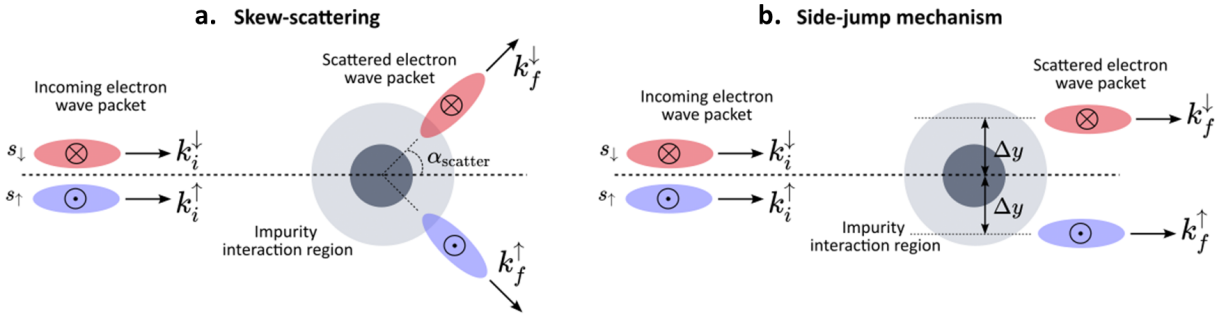

Figure 1.7: Extrinsic contributions to the anomalous and spin Hall effects. Representation of (a) the skew-scattering and of (b) the side-jump mechanism.

Intrinsic contribution. To explain the anomalous and spin Hall effects, we have to describe the intrinsic contribution and anomalous velocity participating to the lateral displacement, both arising from the Berry phase [36]. First, the Berry curvature can be seen as closed currents loops in the reciprocal space (k-space), defined from occupied and unoccupied surrounding bands (the so-called Fermi sea). Upon the application of an electric field allowing the $|nk\rangle \rightarrow |mk\rangle$ transition(s), we can assume the effect of the Berry curvature as an effective path to be followed by the excited electrons (of velocities $\hat{v}_x$ and $\hat{v}_y$) in the corresponding electronic bands. After electronic relaxation processes, the electrons will come back to their initial state with a certain phase $\Omega_z \neq 0 \mod 2\pi$ depending on the trip followed. Thus, we can relate the phase acquired by integrating the curl of the Berry curvature: this is called the Berry phase Ω_z. This formalism looks like the effect of a magnetic field in k-space. The intrinsic transverse conductivity can be written as:

$$\sigma_{xy}^{\text{int}} = 2\frac{e^2\hbar}{V}\,\text{Im}\sum_{n,m}(f_{\text{FD}}(\varepsilon_n) - f_{\text{FD}}(\varepsilon_m))\underbrace{\frac{\langle nk|\,\hat{v}_x\,|mk\rangle\,\langle mk|\,\hat{\mathcal{O}}_z\hat{v}_y\,|nk\rangle}{(\varepsilon_{nk} - \varepsilon_{mk})^2}}_{\text{Berry phase }\Omega_z} \tag{E1.16}$$

where V is the volume, f_{FD} is the Fermi-Dirac occupation function and $|nk\rangle$ and $|mk\rangle$ are respectively the unoccupied and occupied states of energies ε_{nk} and ε_{mk}. This formula represents the contribution of the Berry phase Ω_z integrated over the Fermi sea. In case of the anomalous

Hall effect, the spin $\hat{\mathcal{O}}_z$ is assimilated to the identity $\hat{\mathcal{O}}_z = \mathrm{Id}_2$ while for the spin Hall effect, the spin is assimilated to the Pauli matrix $\hat{\mathcal{O}}_z = \sigma_z$.

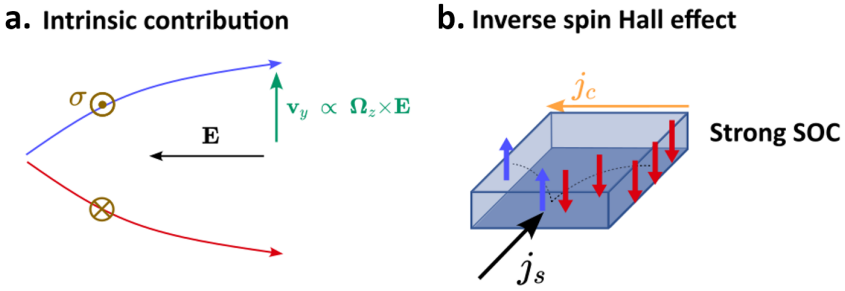

Figure 1.8: Intrinsic contribution to the anomalous and spin Hall effects. (a) Schematic representation of the intrinsic contribution. (b) The reciprocal (inverse) spin Hall effect spin-to-charge conversion mechanism is represented.

Spin Hall angle and inverse spin Hall effect. The role of impurities composing heavy metals, and in particular heavy alloys, is therefore crucial for the observation of the extrinsic part of the spin-charge conversion and can be for instance experimentally performed in alloys of Au:W, Au:Ta [37, 38, 39]. As the created spin accumulation n_σ on each edge is opposite to the other, a spin current j_s will flow in between the two lateral surfaces to balance the spin population. In that way, a transverse spin current is generated via the conversion of an incoming charge current by the spin Hall effect. We can then expressed the obtained spin current as:

$$\mathbf{j}_s = \left(\frac{\hbar}{2e}\right)\theta_{\mathrm{SHE}}\,(\mathbf{j}_c \times \hat{\sigma}) \quad \text{with} \quad \theta_{\mathrm{SHE}} = \left(\frac{\hbar}{2e}\right)\frac{j_c}{j_s} \tag{E1.17}$$

where the factor of merit of this conversion is given by the spin Hall angle $\theta_{\mathrm{SHE}} \equiv j_c/j_s$. In the same spirit as the conventional Hall effect, the spin-charge conversion creates a transverse spin current. It can be thus associated a specific transverse conductivity, called the spin Hall conductivity σ_{SHE} [30]:

$$\theta^*_{\mathrm{SHE}} = \left(\frac{2e}{\hbar}\right)\frac{\sigma_{\mathrm{SHE}}}{\sigma_{\mathrm{HM}}} = \left(\frac{2e}{\hbar}\right)\sigma_{\mathrm{SHE}}\rho_{\mathrm{HM}} \tag{E1.18}$$

where ρ_{HM} is the resistivity of the HM layer. Summing all the extrinsic ($\sigma^{\mathrm{sj}}_{xy}$ and $\sigma^{\mathrm{sk}}_{xy} = \theta^{\mathrm{sk}}\sigma_{xx}$) and intrinsic ($\sigma^{\mathrm{int}}_{xy}$) contributions participating in the spin Hall effect, the effective spin Hall conductivity can be written in the following form:

$$\sigma^*_{\mathrm{SHE}} = \sigma_{xy} = \sigma^{\mathrm{ext}}_{xy} + \theta^{\mathrm{sk}}\sigma_{xx} + \sigma^{\mathrm{sj}}_{xy} \tag{E1.19}$$

Reciprocally, the inverse spin Hall effect (ISHE) allows a conversion from a spin current into a transverse charge current via:

$$\mathbf{j}_c = \left(\frac{2e}{\hbar}\right)\theta_{\mathrm{SHE}}\,(\mathbf{j}_s \times \hat{\sigma}) \tag{E1.20}$$

Experimentally, the spin Hall effect has first been reported semiconductors concurrently by Kato *et al.* [40] and Wunderlich *et al.* [41] in 2005 and in metals in 2006 by Valenzuela *et al.* [42]. Table I.2 gives several example of θ_{SHE} for different heavy metals [43]. We derive in Annex A2 the spin Hall conductivity tensor to determine that the interconversion profile is isotropic as a function of the crystallographic angle ϕ, which will be compared with THz spectroscopy during experiments. This effect is at the core of metallic spintronic THz emitters (Chap. III).

Material	Pt [44]	β-W [45, 46]	β-Ta [5, 47]	Au:W [38, 37, 39]	Au:Ta [38, 37, 39]	V [48]
θ_{SHE}	+0.06 – +0.07	+0.3 – +0.4	-0.12 – -0.15	+0.10 – +0.15	+0.25 – +0.50	-0.07 – -0.1
σ_{SHE} ($k\Omega^{-1}.cm^{-1}$)	3.5	1.75	0.7	1.6	5	0.4
ρ_{HM} ($\mu\Omega$.cm)	30	100–300	190	90	50	200
l_{sf} (nm)	2-3	3.5	5.1	2 – 3	1 – 2	15-16

Table I.2: Review table of spin Hall angle θ_{SHE}, the spin Hall conductivity σ_{SHE}, the resistivity ρ_{HM} and the spin diffusion length l_{sf} for heavy metals.

Onsager reciprocal relations.

The transition between the direct and inverse spin Hall effect can be made by use of the Onsager reciprocal relations [49], valid for extensive physical quantities, even for out-of-equilibrium thermodynamics. We directly note that only the sign of the cross product changes while the amplitude of the conversion is identical in both effects and proportional to the spin Hall angle θ_{SHE}. On a similar perspective, this reciprocity can be applied on the direct and inverse Rashba-Edelstein effects developed further below. Indeed, the magnetization m and the spin current j_s depends on the number of spins, and so on the volume V considered. Following this idea, we will come back to the Onsager relations in correlated experiments of spin-sink efficiency via reciprocal spin-torque and THz emission measurements (Chap. III).

3.2 (Inverse) Rashba-Edelstein effect.

More recently, another charge-to-spin mechanism focusing on the conversion from a charge current j_c into a transverse spin accumulation n_σ has been unveiled by taking into account the interfacial spin-orbit interactions mediated by the previously defined Rashba term. This effect is presently called the Rashba-Edelstein effect and has been theoretically proposed by Rashba [50] and Edelstein [51] in the beginning of the 90s. It involves an additional interfacial spin-orbit Hamiltonian, namely the Rashba Hamiltonian $\mathcal{H}_R$, introducing a spin-degeneracy lifting owing to the symmetry-breaking interfacial electric field:

$$\mathcal{H}_R = \alpha_R \left(\mathbf{k} \times \mathbf{e}_z\right) \cdot \hat{\sigma} = \hbar v_{SO}(k_y \sigma_x - k_x \sigma_y) \tag{E1.21}$$

where $\mathbf{k}$ is the momentum of the charge carriers, $\mathbf{e}_z$ the orientation normal to the interface and σ the injected spin-polarization. The Rashba Hamiltonian strength is given by $\alpha_R = \hbar v_{SO}$ called the Rashba coefficient often given in eV.Å, linked to the built-in internal electric field leading to a symmetry reduction (space-inversion symmetry breaking). It is possible to associate such Rashba coefficient to the spin-orbit velocity v_{SO}. One can define thus a certain conversion figure-of-merit with the Rashba-Edelstein length λ_{REE} linked to the interfacial relaxation time τ_{int} according to:

$$\lambda_{REE} = \frac{\mathbf{j}_c^{2D}}{\mathbf{j}_s^{2D}} = \frac{\alpha_R \tau_{int}}{\hbar} = v_{SO}\tau_{int} \equiv \theta_{SHE} l_{sf} \tag{E1.22}$$

In this picture, one can compare the quality of the interconversion on one side in spin Hall systems with the spin Hall angle θ_{SHE} and equivalent spin diffusion length $\theta_{SHE} l_{sf}$, and on the other hand for interfacial Rashba-Edelstein systems: *i*) via the Rashba splitting with $\lambda_{REE} = \alpha_R \tau_{int}/\hbar$ for Rashba-like systems, and *ii*) via the spin-orbit velocity v_{SO} and with $\lambda_{REE} = v_{SO}\tau_{int}$ in topological insulators (Chap. IV).

We now focus on the description of the reciprocal effect, the inverse Rashba-Edelstein effect. Fig. 1.9 presents the two-dimensional electron gas (2DEG) dispersion relation and interfacial interconversion. The energy of the 2D free electron gas can therefore be corrected by the spin-orbit strength α_R:

$$\varepsilon(\mathbf{k}) = \frac{\hbar^2\mathbf{k}^2}{2m^*} \pm \alpha_\mathrm{R}|\mathbf{k}| \tag{E1.23}$$

Free-electron relation dispersion.

For the free-electron Hamiltonian without Rashba splitting, we have:

$$\mathcal{H}_0 = \frac{\hbar^2\mathbf{k}^2}{2m^*} \Rightarrow v_g = \frac{1}{\hbar}\frac{\partial\varepsilon}{\partial|\mathbf{k}|} = \frac{\hbar\mathbf{k}}{m^*} \quad \text{and} \quad \mathcal{N}_\mathrm{2D} = \frac{m^*}{2\pi^2\hbar^2} \tag{E1.24}$$

where v_g is the group velocity and $\mathcal{N}_\mathrm{2D}$ is the 2D density of states.

At the Fermi level, considering an additional Rashba interaction, we have:

$$v_g = \frac{\hbar\tilde{k}_g}{m^*} \quad \text{and} \quad \mathcal{N}_\mathrm{2D}^\pm = \frac{m^*}{2\pi^2\hbar^2}\left(\frac{k_\mathrm{F}^\pm}{\tilde{k}_g}\right) \quad \text{with} \quad \tilde{k}_g = \frac{k_\mathrm{F}^+ + k_\mathrm{F}^-}{2} \tag{E1.25}$$

where $\tilde{k}_g$ is the group (average) wavevector (with velocity $v_g = \hbar\tilde{k}_g/m^*$ equivalent for the two Fermi surfaces) and $k_\mathrm{F}^\pm$ is the Fermi wavevector for the spin-up (down) band. The Fermi golden rule links the scattering rate $\Gamma_\mathrm{REE} = 1/\tau_{\pm\to\mp}$ (with $\tau_{\pm\to\mp}$ the interfacial scattering time) to the spin-orbit energy and the two-dimensional density of states at the Fermi level $\mathcal{N}_\mathrm{2D}(\varepsilon_\mathrm{F})$:

$$\Gamma_\mathrm{REE} = \frac{1}{\tau_{\pm\to\mp}} = \frac{2\pi}{\hbar}\langle\mathcal{H}_\mathrm{SO}\rangle^2\mathcal{N}_\mathrm{2D}(\varepsilon_\mathrm{F}) \quad \text{giving} \quad \frac{\Delta m_+}{\tau_{+\to-}} = \frac{\Delta m_-}{\tau_{-\to+}} \tag{E1.26}$$

From this, we thus know that a total fixed incoming spin-accumulation $\Delta m = \Delta m^+ - \Delta m^- \neq 0$ injected from a certain reservoir will shift the Fermi contours respectively by:

$$\Delta m^+ = \frac{\mathcal{N}_\mathrm{2D}^+}{\mathcal{N}_\mathrm{2D}^+ + \mathcal{N}_\mathrm{2D}^-}\Delta m \quad \text{and} \quad \Delta m^- = \frac{\mathcal{N}_\mathrm{2D}^-}{\mathcal{N}_\mathrm{2D}^+ + \mathcal{N}_\mathrm{2D}^-}\Delta m \tag{E1.27}$$

As a Fermi contour shift by $\Delta\mathbf{k}$ will happen, this can be understood in the direct space as an electronic displacement and thus the creation of a charge current. The transverse generated charge current can thus be expressed as:

$$\mathbf{j}_c = e(\Delta m^+ - \Delta m^-)\, v_g = e\left(\frac{k_\mathrm{F}^+ - k_\mathrm{F}^-}{k_\mathrm{F}^+ + k_\mathrm{F}^-}\right)\Delta m\, v_g = \frac{e\hbar}{m^*}\Delta k\Delta m = e\Delta m\, v_\mathrm{SO} \tag{E1.28}$$

with $\Delta k = k_+ - k_- = 2v_\mathrm{SO}m^*/\hbar$. The injection of a spin-population onto this spin-textured Fermi contour will shift the Fermi surface towards a certain direction $\Delta\mathbf{k} = -e\mathbf{E}\tau_\mathrm{int}/\hbar$. Thus, a charge current will be generated having the property to be transverse to both spin population injection direction and spin polarization. The figure-of-merit of the interconversion is given by $\lambda_\mathrm{REE} = v_\mathrm{SO}\tau_\mathrm{int}$.

This effect has been experimentally reported in Bi/Ag system by Rojas-Sanchez *et al.* [52]. We propose in Table I.3 a review of some interfacial conversion efficiencies for interfacial systems, like Bi/Ag 2DEG system. Moreover, a novel type of quantum materials in the example of topological insulator, also possessing such spin-polarized surface states, will be extensively studied in the scope of Chap. IV to host inverse Rashba-Edelstein effect. One can see that the equivalent of the spin Hall angle in such systems is very high and above 100%. This motives thus the study of such interfacial systems for efficient spintronic devices. We derive in Annex A2 the inverse Rashba-Edelstein tensor to determine that the interconversion profile is isotropic as a function of the crystallographic angle ϕ, and even in presence of six-fold topological surface states warping, which will be compared with THz spectroscopy during experiments.

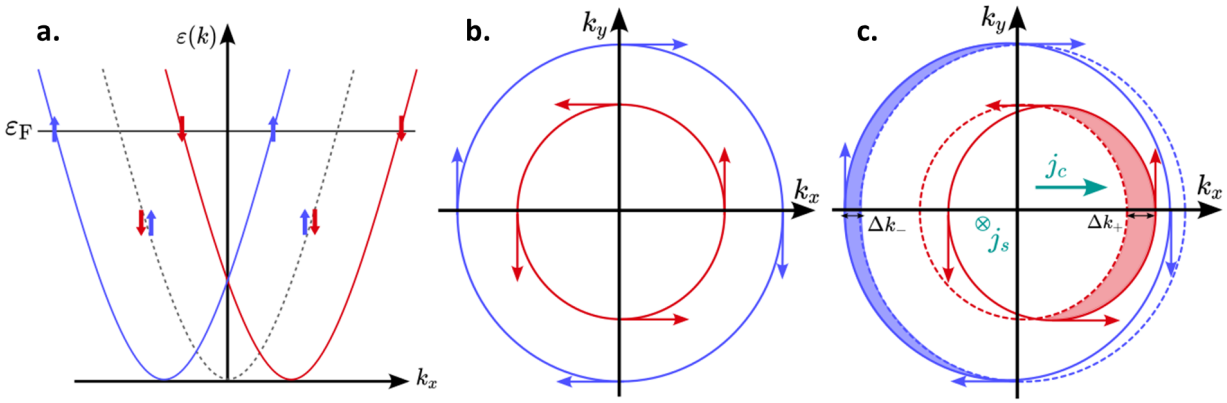

Figure 1.9: Inverse Rashba-Edelstein conversion for a 2DEG system. (a) Degenerated (dotted line) and lifted degeneracy for the free electron dispersion relation, with the Fermi level noted as ε_F. (b) Fermi contour presented in k_x, k_y space with textured opposed bands. (c) Under the application of a spin-current propagating along e_z and polarized along e_y, the Fermi contour shifts from $\Delta\mathbf{k}_x$.

System	Bi/Ag [52]	α-Sn [53]	Bi_2Se_3 [54, 55]	$Bi_{1-x}Sb_x$ [54, 56]
α_R (eV.m)	7.6	-	-	-
v_F ($\times 10^5$ m.s^{-1})	-	7.3	2.9	10
$\hbar v_F$ (eV.m)	-	4.8	1.9	6.6
Equiv. θ_{SHE}	+1.5	+0.62	+2.5-3.5	+52

Table I.3: Review table of interfacial spin-charge conversion parameters for Bi/Ag 2DEG and several topological insulator systems.

4 Spin transport in the steady-state regime.

An efficient spin-transport in thin multilayers is a cornerstone for spintronics applications and information manipulation. To present the different issues of spin-injection and spin-transport, we will address two main concerns: the bulk region and the interfacial properties. It is important to dissociate, at first, the spin transport in metals, semi-conductors (*e.g.* topological insulators) and insulators. We will see finally that a common framework can be derived for the spin-transport contrary to the electronic transport (differences between metals and insulators for instance).

Spin transport in metals. We first remind to the reader that electrons are fermions with a spin one-half, thus following the Fermi-Dirac distribution:

$$f_{FD}(\varepsilon) = \frac{1}{\exp\left(\frac{\varepsilon-\mu}{k_B T}\right)+1} \tag{E1.29}$$

where μ is the chemical potential (Fermi level for non-zero temperature), k_B is the Boltzmann constant, ε is the energy and T is the temperature. In a material, electron collision events occur with other particles or defects in the system. These collisions can be of two types: elastic (which conserves the energy) and inelastic (leading to an electron energy loss), particularly true for an optically excited electron population. It is thus necessary to discriminate ballistic from diffusive spin-transport by introducing the different spin-dependent length and timescales.

4.1 Focus on length- and time-scales in bulk (magnetic) systems.

Due to the existence of an additional degree of freedom through the spin quantity, one should reconsider length- and time-scales regarding spin quantity. The diffusion of the spin can be regarded as a random displacement with typical lengthscales detailed below, and represented in

Fig. 1.10. We consider to the diffusion process several ingredients [57, 58]:

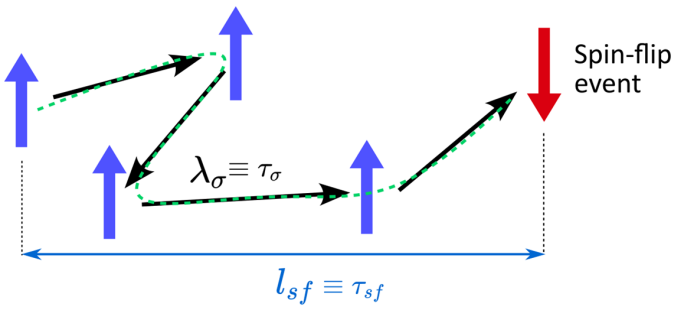

Figure 1.10: Spin transport and elastic and inelastic scatterings. A diffusive spin encounters several elastic scatterings (keeping the spin orientation) until an inelastic scattering event occurs, leading to spin-flip. From this, we define the spin diffusion length l_{sf} and the spin-dependent mean free path λ_σ, corresponding respectively to the spin scattering time τ_{sf} and to the spin-dependent carrier lifetime τ_σ.

- **Carrier velocity** v_σ
  At the Fermi level $\varepsilon = \varepsilon_\mathrm{F}$, the electrons move with a certain Fermi velocity v_F. Below the Fermi level $\varepsilon < \varepsilon_\mathrm{F}$, the electrons are rather slow and move only via hole excitations (localized d band). Above the Fermi level $\varepsilon > \varepsilon_\mathrm{F}$, the hot sp-electrons are more mobile. Notably in ferromagnets, due to the Stoner criterion, the conduction band is now slightly dependent of the spin-channel, leading to a spin-dependent diffusion. The carrier velocity is then spin-dependent and expressed as fractions of the Fermi velocity v_F.

- **Spin-dependent carrier lifetime (or spin-flip time)** τ_σ
  The momentum relaxation time τ_σ is the spin-dependent timescale between two consecutive collisions. At the Fermi level, the collisions are elastic. For energies different that the Fermi level, the transport is inelastic for electrons (sp band) and holes (d band). From Zhukov *et al.* [58], the carrier lifetime evolves as $\tau_\sigma \propto (\varepsilon - \varepsilon_\mathrm{F})^{-2}$.

- **Mean-free path** λ
  The mean free path represents the (spin-dependent) mean distance traveled by the electron between two consecutive collisions.

$$\lambda_\sigma(\varepsilon) = v_\sigma(\varepsilon)\tau_\sigma(\varepsilon) \tag{E1.30}$$

- **Diffusion coefficient** D_σ
  From the carrier velocity and the carrier lifetime, we can establish a diffusion coefficient which is spin-dependent in a ferromagnet. Note that the prefactor $1/3$ simply comes from the energy equipartition theorem.

$$D_\sigma = \frac{1}{3}\tau_\sigma v_\sigma^2 \tag{E1.31}$$

- **Spin scattering time** τ_{sf} **and spin diffusion length** l_{sf}
  The spin scattering time is defined as the characteristic timescale for which one can expect a spin-flip. It is related to the spin diffusion length l_{sf} which is the length travelled by the spin before spin-flip occurring after a scattering event and to the mean-free path λ which is the distance between two collisions.

$$\tau_{sf} = \frac{6l_{sf}^2}{v_F \lambda (1-\beta^2)} \quad \text{and} \quad \frac{1}{\tau_{sf}} = \frac{1}{\tau_{sf}^{\uparrow}} + \frac{1}{\tau_{sf}^{\downarrow}} \quad \text{with} \quad \beta = \frac{\rho_\uparrow - \rho_\downarrow}{\rho_\uparrow + \rho_\downarrow} \tag{E1.32}$$

Here, we have included the spin asymmetry β which is the relative difference between the spin up and spin down resistivity channels ρ_σ in the bulk of the material. We can from this define the spin-orbit parameter $\gamma_{SO} = \sqrt{\tau_\sigma / \tau_{sf}}$ which we will widely used in Chap. III when performing wave-modelling simulations for artificially changing the spin-orbit influence of metallic spintronic THz emitters.

- **Spin diffusion length** l_{sf}
  It represents the typical evanescence length of the spin accumulation due to spin-flip events as previously defined.

$$l_{sf} = \sqrt{\tilde{D}\tau_{sf}} \quad \text{with} \quad \tilde{D} = \frac{D_\uparrow D_\downarrow}{D_\uparrow + D_\downarrow} \tag{E1.33}$$

- **Ferromagnetic decoherence length** λ_{sc}
  It describes the typical evanescent dissipation of a transverse spin-current (or spin accumulation) absorbed at the interface of a ferromagnetic layer due to spin precession and subsequent dephasing. This originates from the penetration of different Bloch waves characterized by different wavevectors $k_F^{\uparrow\downarrow}$ owing to different electronic incidences [11].

$$\lambda_{sc} = \frac{\pi}{\left| k_F^{\uparrow} - k_F^{\downarrow} \right|} \tag{E1.34}$$

  where $k_F^{\downarrow}$ and $k_F^{\downarrow}$ represents the Fermi wavevector respectively for spin-up and spin-down.

- **Remagnetization time** τ_r
  It can be seen as the time for which the magnetic system fully remagnetize, typically expected around 1-10 ps for ferromagnetic systems after ultrafast demagnetisation.

Spin transport in semiconductors. In semiconductors, although the electronic properties are different than in metallic layers, the spin-transport is hampered in gapped materials below the bandgap while it is similar to the spin-transport carried by the conduction electrons above the bandgap [59]. Besides, the spin-injection from a metallic layer into a semiconductor can be made difficult due to the presence of Schottky barriers that could hampered the injection, and this topic will be widely discussed in Chap. IV for topological insulators. In particular, the spin-scattering processes in semiconductors are similar than the ones in metals and can be described by the Elliott-Yafet scattering [60, 61], which states that the spin-orbit parameter γ_{SO} scales with the spin-orbit coupling strength λ_{SO} and the characteristic spin-splitting of the band $\Delta\varepsilon_{SO}$ according to:

$$\gamma_{SO} = \sqrt{\frac{\tau_\sigma}{\tau_{sf}}} \propto \left(\frac{\lambda_{SO}}{\Delta\varepsilon_{SO}} \right) \tag{E1.35}$$

Spin-current, spin-resistance and spin accumulation in the steady-state regime. From the Valet-Fert model, one can relate the diffusion of the spin current with the spin accumulation. In Chap. III, we will extend those steady-state transport equations to the dynamical (sub-picosecond timescale, or THz dynamics) regime. More details are given to the reader in Annex A3. We have:

$$j_s = \frac{\sigma}{e}\frac{\partial \Delta m}{\partial t} \quad \text{and} \quad \nabla j_s = \pm\frac{em}{\tau_{sf}} = \pm\frac{1}{\rho_{xx} l_{sf}^2}\frac{\Delta m}{e} \tag{E1.36}$$

where we have introduced the spin resistance r_s, which prevents spin-flip events (high spin-resistance case) such as:

$$r^s(t) = r^s_\infty \coth\left(\frac{t}{l_{sf}}\right) \quad \text{with} \quad r^s_\infty = \rho_{xx} l_{sf} = \frac{m^*}{ne^2\tau_\sigma}\frac{\hbar k_\mathrm{F}}{m^*}\sqrt{\tau_\sigma \tau_{sf}} = \frac{\hbar}{e^2}\frac{1}{N_\mathrm{ch}}\sqrt{\frac{\tau_{sf}}{\tau_\sigma}} \tag{E1.37}$$

We observe that in the case of $t \ll l_{sf}$, the expression of the spin resistance can be reduced to $r^s = r^s_\infty l_{sf}/t = \rho_{xx} l_{sf}^2/t$. Besides, we note that the ratio between the spin-resistance r_s and the Sharvin resistance R_Sh is equal to $T^*\sqrt{\tau_{sf}/\tau_\sigma} = T^*/\gamma_\mathrm{SO}$.

Sharvin resistance.

In the ballistic regime, following the Landauer-Büttiker model (that will be defined shortly), one can assign to the interface a resistance, called the Sharvin resistance R_Sh:

$$R_\mathrm{Sh} = \frac{\hbar}{e^2}\frac{1}{N_\mathrm{ch}}\frac{1}{T^*} \tag{E1.38}$$

where N_ch is the number of channels participating in the conduction and T^* is the transmission coefficient of the interface. The Sharvin resistance is close to 0.2 fΩ.m^2 in our case.

4.2 Spin waves and magnons.

Before addressing the properties of the spin transport in magnetic insulators, it is essential to understand the role of spin excitations in a magnetic layer. In a microscopic view of the ferromagnetic resonance, each magnetic moment precesses coherently in phase at the frequency ω_FMR. Launching a small perturbation onto one magnetic moment propagates to neighbouring moments by exchange interaction. It creates a small dephasing between neighbouring spins which induces the propagation of a magnetic wave called spin-wave [1]. A parallel can be made with a particle, called magnon, which can be assigned a wavelength λ and an energy $\hbar\omega$ [1]. A magnon is a boson of spin one and thus obeys the Bose-Einstein occupation distribution function [1]:

$$f_\mathrm{BE}(\varepsilon) = \frac{1}{\exp\left(\frac{\varepsilon-\mu}{k_\mathrm{B}T}\right) - 1} \tag{E1.39}$$

where μ is the (boson) chemical potential, k_B is the Boltzmann constant, ε is the energy and T is the temperature.

Spin transport in insulators. Compared to metallic ferromagnetic materials where the spin-transport is ensured by the conduction electrons, insulating magnetic materials involves the spin waves (magnons) carrying the spin angular momentum. The spin-transport is therefore defined in insulators and can be associated to characteristic relaxation lengthscales and timescales, with no equivalence in magnetic metallic layers (hundreds of microns for the spin diffusion length l_{sf} in insulators for instance [62]) as ensured by the group velocity of spin waves. Such framework is essential as we will study the magnonic transport in insulating antiferromagnets in Chap. V. We remind that the ferromagnetic resonance mode can be written according to the Kittel formula, valid for an in-plane magnetization, according to:

$$\omega_\mathrm{FMR} = \frac{\gamma\mu_0}{2\pi}\sqrt{H(H + M_\mathrm{eff})} \tag{E1.40}$$

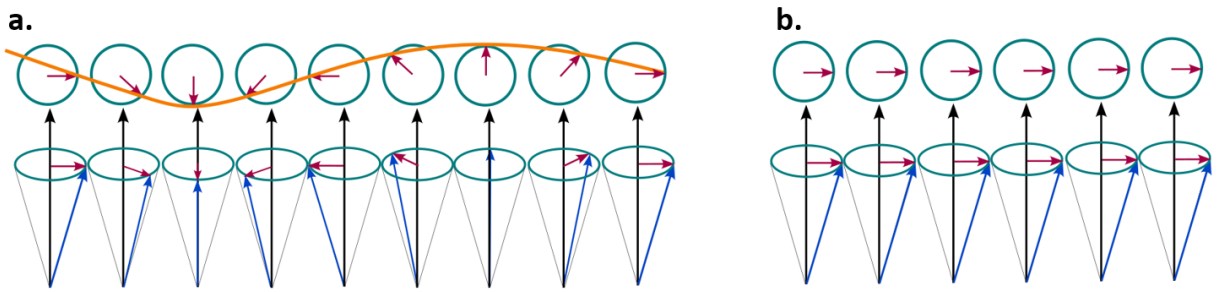

Figure 1.11: Spin-wave and magnons. (a) Spin-wave propagation (magnon) and (b) ferromagnetic resonance (FMR) mode ω_{FMR}.

4.3 Spin-transmission at spintronic interfaces and spin memory loss.

We now come to an important issue which is the properties of the spin-transmission at a given interface, typically between a ferromagnet and a heavy metal. Such processes are of prime important in many experiments described in this thesis (THz emission, spin-pumping and spin-torque in particular). For that goal, we address several features by considering spin-polarized electrons as quantum particles described by characteristic Bloch wavefunctions possessing specific orbital and spin symmetries. The specific form of the interfacial Hamiltonian involves for instance localized Rashba and/or exchange and potential steps introduced from the contact itself. Chemically, the interface region will be illustrated by a abrupt change of material characterized by different electronic potentials and transport properties. However in a realistic picture, one have to keep in mind that the interfacial region could be more spread in thickness.

Concepts of the spin-mixing conductance. Interfacial physics play a fundamental role regarding spin-orbit effects and interconversion efficiency. In the absence of spin-orbit coupling at the interface, the electronic transmission is parameterized by the Landauer-Büttiker model [63] which accounts for the quantization of the different conduction modes:

$$G = G_0 \sum_{i \in k_{\parallel}}^{N} T_i \quad \text{with} \quad G_0 = \frac{2e^2}{h} \tag{E1.41}$$

where G_0 is the quantum of conductance (the factor 2 in G_0 expression stands for the spin-degeneracy) and T_i is the interfacial transmission for the i-th conduction channel (for $k_{\parallel}$ in-plane wavevectors). In the presence of exchange interactions and in the non-collinear geometry configuration between conduction spins and local magnetization, one can introduce the spin-mixing conductance $G_{\sigma\sigma'}$ which can be seen as the spin-generalization [9] of the Landauer-Büttiker electronic formalism. Typically expressed in m^{-2}, the spin-mixing conductance accounts for the interfacial scattering matrix and thus allows to describe the effective spin conduction and spin transparency at the interface depending on the spin channel σ:

$$G_{\sigma\sigma'} = \frac{e^2}{h} \sum_{n,m} \left\{ \delta_{nm} - r^{\sigma}_{nm} (r^{\sigma'}_{nm})^* \right\} \tag{E1.42}$$

where r^{σ}_{nm} accounts for the σ-spin transmission, summed over the all possible orbital $n \leftrightarrow m$ state transitions (n belongs to the FM layer and m to the HM layer). We also define the effective spin-mixing conductance such as:

$$g_{\sigma\sigma'} = \frac{e^2}{2\pi} \mathcal{N}(\varepsilon) v_{\text{F}} T_{\sigma\sigma'} \quad \text{and} \quad g^{\uparrow\downarrow}_{\text{eff}} = \frac{h}{e^2} G_{\uparrow\downarrow} \tag{E1.43}$$

In most of the models, we can approach the spin-mixing conductance by considering only its real component as $\text{Re}\,(g) \gg \text{Im}\,(g)$ (the imaginary component is however non-zero). For

simplicity, the notation $g_\uparrow = g_{\uparrow\uparrow}$ and $g_\downarrow = g_{\downarrow\downarrow}$ can be encountered. We can therefore give to the interface a transmission coefficient $T^\star$ leading to a splitting of the transmission (conductance) depending on the spin channel T_σ. The spin interfacial asymmetry γ is defined as the change of the interfacial resistance r_σ of the two-spin system:

$$T_\sigma = \frac{T^\star}{1 \mp \gamma} \Rightarrow T^\star = \frac{1-\gamma^2}{2}(T_\uparrow + T_\downarrow) \quad \text{with} \quad \gamma = \frac{r_\uparrow - r_\downarrow}{r_\uparrow + r_\downarrow} \tag{E1.44}$$

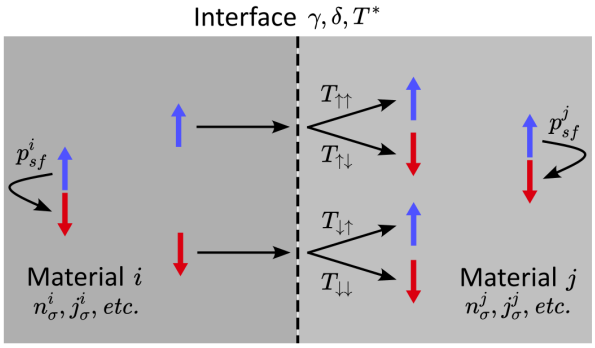

Figure 1.12: Interfacial spin transmission. Schematic representation of the spin-transmission at the interface characterized by an interfacial spin-asymmetry γ, an interfacial transmission coefficient T^* and potentially spin-memory loss δ. The border spin-flip probability is represented via p_{sf} and is developed in Annex A5.

Interfacial spin-orbit interaction and spin memory loss. Interfacial transmission discussed above is not truly realistic regarding the quality of the interface, as one does not take into account possible spin-flip events during the transmission. We introduce now imperfections at the interface due to the existence of a certain interfacial resistance r^s_{I} linked to surface potentials modelled via an empirical parameter: the spin memory loss parameter δ. We define the probability of spin-flip events at the interface as $p_{sf} = 1 - \exp(-\delta)$ [30]. We can therefore include spin information loss at the interface using the transmission coefficients related to the spin-flip probability:

$$T = \begin{bmatrix} T_{\uparrow\uparrow} & T_{\uparrow\downarrow} \\ T_{\downarrow\uparrow} & T_{\downarrow\downarrow} \end{bmatrix} = \begin{bmatrix} \left(1-\frac{p_{sf}}{2}\right)^2 T_\uparrow + \left(\frac{p_{sf}}{2}\right)^2 T_\downarrow & \left(1-\frac{p_{sf}}{2}\right)\left(\frac{p_{sf}}{2}\right)(T_\uparrow + T_\downarrow) \\ \left(1-\frac{p_{sf}}{2}\right)\left(\frac{p_{sf}}{2}\right)(T_\uparrow + T_\downarrow) & \left(\frac{p_{sf}}{2}\right)^2 T_\uparrow + \left(1-\frac{p_{sf}}{2}\right)^2 T_\downarrow \end{bmatrix} \tag{E1.45}$$

The spin memory loss [44] can therefore be assimilated as a loss of the longitudinal spin polarization component from the heavy metal to the ferromagnet due to spin precession around interfacially-located spin-orbit exchange field. Empirically, the spin memory loss can be seen as $\delta = t_{\mathrm{I}}/l^{\mathrm{I}}_{sf}$ where t_{I} is the spreading of the interface potential region and l^{I}_{sf} the corresponding spin-scattering length on surface potentials. We illustrate several interfaces by experimental values for the spin-mixing conductance $g_{\uparrow\downarrow}$ and spin-memory loss δ in Table I.4. This concept of spin memory loss will be largely used in Chap. III when dealing with the comparison of THz and spin-pumping experiments.

System	Co/Pt [44]	Co/Cu/Pt [44]
$g_{\uparrow\downarrow}$	80 nm^{-2}	20 nm^{-2}
δ	0.9	1.2

Table I.4: Interfacial parameters illustrated with the spin-mixing conductance $g_{\uparrow\downarrow}$ and the spin-memory loss δ for different interfaces such as Co/Pt and Co/Cu/Pt.

5 Spin dynamics.

5.1 Radiofrequency magnetization dynamics.

All those effects has been well studied in the static regime (DC) and we will move in this part to the description on spin dynamics and in the transient regime at ultrafast timescales towards the description down to the sub-picosecond.

5.1.1 Landau-Liftschitz-Gilbert phenomenology.

We first start with the description of the spin precession under an external perturbation at radiofrequencies (GHz) as schematically pictured in Fig. 1.13. To that extend, we introduce the phenomenological approach of the Landau-Liftschitz equation, arising from the exchange interaction between the system magnetization and an external magnetic field:

$$\frac{\partial \mathbf{m}}{\partial t} = -\gamma\mu_0 \left(\mathbf{m} \times \mathbf{H}_{\text{eff}}\right) \tag{E1.46}$$

where μ_0 is the vacuum permeability and γ is the gyromagnetic ratio of the electron defined as $\gamma = 2\mu_{\text{B}}/\hbar$ with μ_{B} the Bohr magneton. In this formula, we have considered an effective magnetic field $\mathbf{H}_{\text{eff}}$ which is the summation of all contributions to the free energy $\mathbf{F}$ which includes for example the external magnetic field, the exchange interaction field, crystal anisotropy, demagnetizing field, *etc.* This idea could be written more formally, defining $\mathbf{H}_{\text{eff}} = \partial\mathbf{F}/\partial\mathbf{m}$.

Intuitively, Eq. (E1.46) leads to a dampingless precession of the magnetization $\mathbf{m}$ around the effective magnetic field $\mathbf{H}_{\text{eff}}$ at the Larmor frequency $\omega = \gamma\mu_0|\mathbf{H}_{\text{eff}}|$. Without any damping contribution, the torque is always tangent to the circular trajectory of the precession. However, this is a lacking picture of the reality as relaxation is not included. In order to include magnetic energy dissipation during the rotation of the magnetization, Gilbert [64] included a damping factor α called the Gilbert damping:

$$\frac{\partial \mathbf{m}}{\partial t} = -\gamma\mu_0 \left(\mathbf{m} \times \mathbf{H}_{\text{eff}}\right) + \alpha \left(\mathbf{m} \times \frac{\partial \mathbf{m}}{\partial t}\right) \tag{E1.47}$$

We give in Table I.5 several values of the damping coefficient α for several ferromagnetic materials.

System	NiFe [39]	Co [44]	Co/Cu/Pt [44]	Co/Pt [44]
α	7×10^{-3}	7.6×10^{-3}	10.5×10^{-3}	14×10^{-3}

Table I.5: Values of the damping α for selected ferromagnetic materials: NiFe, Co, Co/Cu/Pt and Co/Pt.

5.1.2 Spin pumping.

The spin-pumping effect in the ferromagnetic resonance regime (FMR) [9] describes the generation of a spin-current along the direction normal to the layer with the spin direction oriented along the local magnetization direction fixed by an external magnetic field $\mathbf{H}_{\text{eff}}$. It can be understood as the transfer of angular momentum from the FM layer to the adjacent layer as illustrated in Fig. 1.13. Indeed by conservation of the angular momentum, launching a precession of the magnetization $\partial\mathbf{m}/\partial t \neq 0$ (by means of an external modulated RF magnetic field for instance) is similar as introducing a second Slonczewski torque produced between the injected spin current $\mathbf{j}_s^{\text{pumped}}$ on the dynamical magnetization $\mathbf{m}(t)$. The pumped spin-current $\mathbf{j}_s^{\text{pumped}}$ can be written from Tserkovnyak *et al.* [65, 66]:

$$\mathbf{j}_s^{\text{pumped}} = \frac{\hbar}{4\pi}\left(A_r \mathbf{m} \times \frac{\partial \mathbf{m}}{\partial t} - A_i \frac{\partial \mathbf{m}}{\partial t}\right) \tag{E1.48}$$

where A_r and A_i are the real and imaginary spin-pumping conductance in the general case of a HM/FM/HM trilayer. In the case of a FM/HM bilayer or for a HM/FM/HM trilayer with the ferromagnetic thickness larger than the ferromagnetic spin-coherence length λ_{sc}, the spin-pumping conductance A reduces to the spin-mixing conductance $g_{\uparrow\downarrow}$. Due to the transfer of the angular momentum carried by the pumped spin-current into the HM layer, the magnetization undergoes a change in its precession motion. Note that in presence of spin-orbit coupling at interfaces and in the bulk of heavy metals, the injected DC spin-current at resonance is transformed into a lateral charge current: this is called a voltage rectification effect. Following the Landau-Lifshitz-Gilbert equation, one can thus describes the dynamics of the magnetization precessing and transferring as [65, 66]:

$$\frac{\partial \mathbf{m}}{\partial t} = \gamma\mu_0 \mathbf{m} \times \mathbf{H}_{\text{eff}} + \alpha \mathbf{m} \times \frac{\partial \mathbf{m}}{\partial t} + \frac{\gamma}{M_s t_{\text{FM}}} \mathbf{j}_s^{\text{pumped}} \tag{E1.49}$$

$$\left(1 + g_i^{\uparrow\downarrow} \frac{\hbar\gamma}{4\pi M_s t_{\text{FM}}}\right) \frac{\partial \mathbf{m}}{\partial t} = \gamma\mu_0 \mathbf{m} \times \mathbf{H}_{\text{eff}} + \left(\alpha + g_r^{\uparrow\downarrow} \frac{\hbar\gamma}{4\pi M_s t_{\text{FM}}}\right) \mathbf{m} \times \frac{\partial \mathbf{m}}{\partial t} \tag{E1.50}$$

where $\gamma = g\mu_{\text{B}}/\hbar$ is the gyromagnetic ratio. By neglecting the imaginary part of the spin-mixing conductance $g_{\text{eff}}^{\uparrow\downarrow} \simeq g_r^{\uparrow\downarrow}$, we can identify that the damping term is now an effective damping term α_{eff}:

$$\alpha_{\text{eff}} = \alpha + \Delta\alpha = \alpha + g_{\text{eff}}^{\uparrow\downarrow} \frac{g\mu_{\text{B}}}{4\pi M_s t_{\text{FM}}} \tag{E1.51}$$

where α is the Gilbert damping constant in the absence of the spin current escape term and $\Delta\alpha$ is the additional damping contribution due to the spin-pumping. Importantly, the introduction of the deviation from the standard damping is linked to the interfacial spin-mixing conductance $g_{\uparrow\downarrow}^{\text{eff}}$ and consequently, a measure of the damping via ferromagnetic resonance (FMR) experiments allows to access the spin-mixing conductance $g_{\uparrow\downarrow}^{\text{eff}}$.

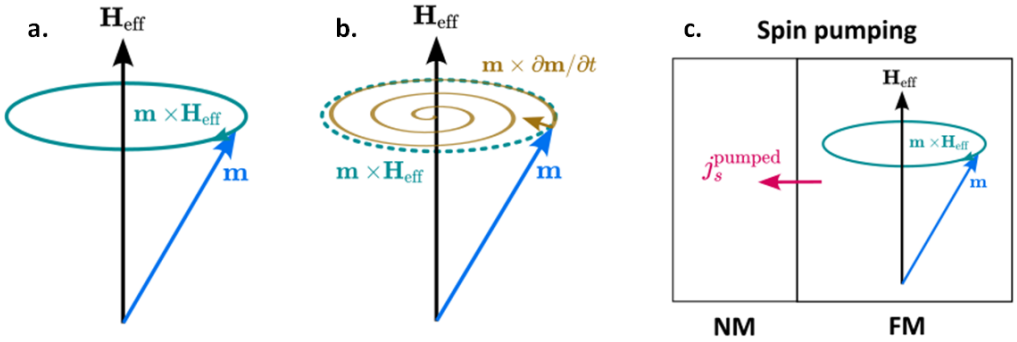

Figure 1.13: Magnetization dynamics and spin-pumping. (a) Undamped magnetization precession given by the term $\mathbf{m} \times \mathbf{H}_{\text{eff}}$. (b) Damped magnetization precession due to the term $\alpha\mathbf{m} \times \partial\mathbf{m}/\partial t$. (c) Illustration of the spin-pumping process, where a DC spin current j_s^{pumped} is pumped from the FM into the adjacent NM by transfer of angular momentum.

5.2 Investigating a description of ultrafast spin phenomena.

5.2.1 Emergence of ultrafast magnetism.

Initially, the spintronics research focused on electronics (charge current, *etc.*) interacting with the spin degree of freedom, as reported above with spin-transfer torque operated devices, *etc.* A lot of the spin-operation were actually performed in the stationary regime or at very low dynamics. Yet, the light-matter interactions (and especially ultrafast dynamics) were not explored to control

the magnetic system until recently. The pioneer work of E. Beaurepaire and J.-Y. Bigot in 1996 [67] opened the way towards light control of the magnetic order and by extension to ultrafast spintronics, by means of ultrashort optical pulses. They reported (results reproduced in Fig. 1.14) the study of the ultrafast demagnetization of a 20 nm-thick Ni film by ultrashort laser pulses with a pump fluence of 7 mJ.cm^{-2}. The measurements evidenced a very rapid drop of the Ni magnetization in the first picosecond with a remagnetization process operating at longer timescales. This was the first demonstration of the transient magnetization loss and dynamics $\partial \mathbf{M}/\partial t$ using ultrafast light pulses, and paved the way to efficient spin-photon interactions. The physics involved here is radically different from what has been used in the past years of spintronics. At that time, no ultrafast spin-current were investigated, and then a very recent domain emerged, first centered on the ultrafast control of magnetization to go today up to THz spintronics.

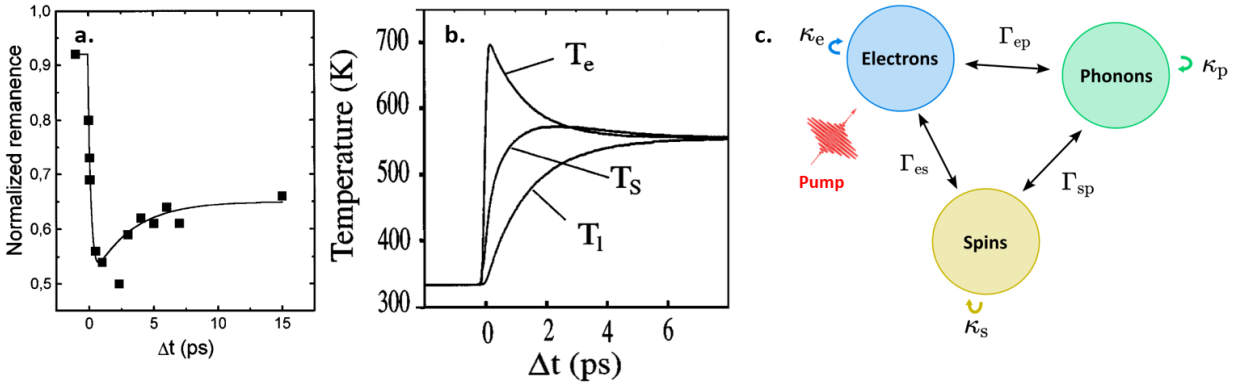

Figure 1.14: Experimental discovery of the ultrafast demagnetization process upon femtosecond pulses. (a) Normalized remanence of Ni(20nm) (capped with MgF_2(100nm)) as a function of time. (b) Evolution of the electronic temperature, spin temperature and lattice temperature as a function of time delay. (c) Three-temperature model scheme. Left and middle panels adapted from Ref. [67].

Then, in 2005, Kimel *et al.* [68] reported the non-thermal spin excitations by means of circularly-polarized light from $DyFeO_3$ rare-earth orthoferrite, and detected with the help of the magneto-optical Faraday effect. This was the starting point of the non-thermal control of the magnetic state by light pulses to achieve faster dynamics on the magnetic control (as the laser-induced demagnetization is limited by the typical remagnetization time). Indeed, the interaction time is expected to be instantaneous as stated by the optical process rules.

Inverse Faraday effect.

The inverse Faraday effect arises from the Raman-like coherent optical scattering between magnetic moments and circularly polarized light. It is proportional to the susceptibility χ of the material following:

$$\mathbf{M}_{\mathrm{DC}} \propto \chi[\mathbf{E}(\omega) \times \mathbf{E}^*(\omega)]$$

5.2.2 Introduction to the three temperature model (3TM).

To account for these effects, the three temperature model (or 3TM) has been proposed and is now widely used to describe the interactions between three interacting reservoirs: the electrons, the spins and the phonons (lattice) [69, 70, 71]. Each of these macroscopic reservoirs are characterized by a subsystem temperature T_i, a specific heat C_p^i and are interacting with each other via coupling constants G_{ij}. These interactions are described by the differential equation Eq. (E1.52), coupled with the two other equations on j, k indices. It is to be noted that the coupling indices G_{ij} encodes directly the sign of the coupling between two successive reservoirs, we have:

$$C_p^i \frac{\partial T_i}{\partial t} = \kappa_i \nabla^2 T_i + G_{ij}(T_j - T_i) + G_{ik}(T_k - T_i) \quad \text{(E1.52)}$$

where κ_i is the thermal conductivity (following the Fourier law). The increase of the temperature induced by the ultrashort pump (considering NIR fluences around few mJ.cm^{-2}) in insulators is typically about several tens of K due to their low pump absorption (large bandgap), still well below the Curie temperature [72]. Therefore, only a part of the sample is demagnetized and recovers on fast timescales the full magnetization. In metals, the typical temperature elevation is about several hundreds of K and the demagnetization can reach up to 40% of the total magnetization (at few mJ.cm^{-2}) [67].

5.2.3 Focus on typical magnetization timescales.

As an alternative to the three-temperature model, several theories have been proposed to describe the ultrafast demagnetization mechanisms, from a pure electronic point of view. First, a widely used description of the ultrafast spin transport mechanisms in stacked heterostructures emerged via the so-called superdiffusion model developed by Oppeneer *et al.* [73, 74]. Alternatively, an electronic diffusive to ballistic *d-sp* model has been developed by Koopmans *et al.* [75, 70]. Although the two models provide similar results, they both rely on the modelling of electronic scattering events within integrated magnetization timescales.

We present in Fig. 1.15 the typical magnetization timescales [76]. The exchange interactions are the fastest timescale, with a typical response in the 1-10 fs window. It comes after the spin-orbit coupling and spin-flip events, which includes the spin-transfer torque and spin-charge conversion mechanisms, from few tens of fs to the picosecond timescale, unlike the laser-induced ultrafast demagnetization ranging around few hundreds of femtoseconds to picoseconds. Typically, the remagnetization timescale ranges around several picoseconds. All those sub-picosecond timescales corresponds to THz dynamics of the magnetization.

We now come to longer magnetization dynamics, starting with the precession in the scope of the Landau-Lifzschitz-Gilbert framework, typically ranging above 1 ps up to several hundreds of ps. It is followed by the Gilbert damping term which leads to a realignment of the magnetization on few hundreds of picoseconds to several nanoseconds. In the meantime, this timescale corresponds to the magnetic writing process in magnetic memories or even vortex core switching and spin wave dynamics. Above tens of nanoseconds and beyond to the microsecond, we have the typical timescale of domain wall motion. It is thus evident that the dynamical properties of the magnetization are multiple and very complex depending on the systems investigated. From now on, we will focus on the sub-picosecond timescale of the magnetization dynamics like played by the transient time of the ultrafast spin current on THz frequencies window, well shorter than the damping and spin precession times, having then a small influence on the THz dynamics.

5.2.4 Towards THz spintronics.

All-optical switching. From this point, two examples of applications are envisioned using ultrafast demagnetization processes: all-optical switching and THz spintronics. All-optical switching, or the local efficient magnetic switching, can be envisioned in opto-electronics devices where the writing/reading of the stored information is accessed via optical pulses as evidenced in 2007 by Stanciu *et al.* [77]. The current research in this field focuses on helicity-dependent pumping for instance in GdFeCo systems, to allow switching without local heating.

Following the study of ultrafast demagnetization leading to the generation of transient spin current, it has been proposed [78] to efficiently probe the dynamical magneto-transport in spin-valves [79], or the spin-current dynamics by capping on top of the FM layer a strong SOC

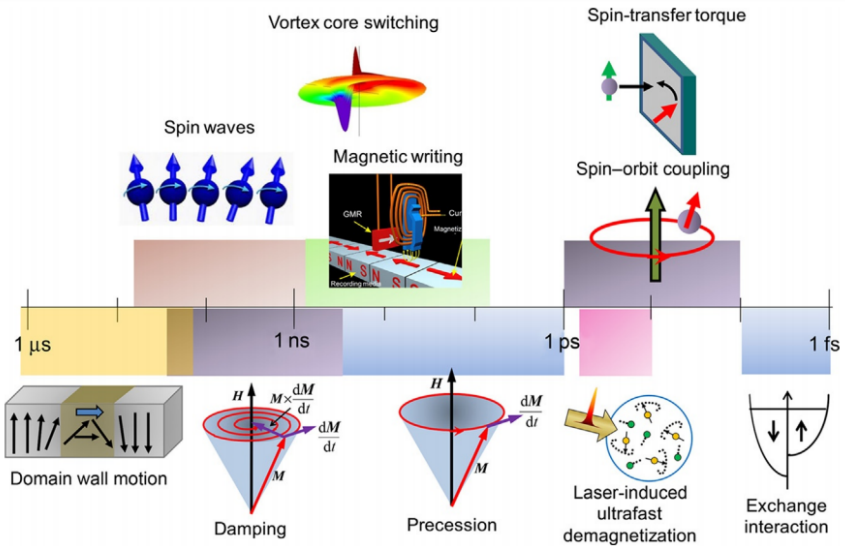

Figure 1.15: Typical timescales in magnetism. The covers timescale from the femtosecond (exchange interaction, spin-orbit coupling, spin-transfer torque and optically-induced demagnetization) to spin precession, magnetic writing, magnetic damping, spin waves and domain wall motion. Adapted from Ref. [76].

HM material in the latter case. Indeed, relying on the spin-charge conversion mechanism (THz spin current generation) in the HM layer would result in a larger signal compared to the weak term $\partial\mathbf{m}/\partial t$ (see Appendix A4.3 for order of magnitude).

Surprisingly, this also launched a new research area with THz spintronics where a THz emission is generated from the transient sub-picosecond spin-current converted in a non-magnetic strong spin-orbit coupling material. Following the theoretical prediction of a very intense spin current generation under femtosecond light illumination by Battiato *et al.* [80], Melnikov *et al.* [81] claimed the experimental observation of this effect in Fe/Au structure. The next step has been to perform heterostructures of a ferromagnet with a 5*d* heavy metal, as done by Kampfrath *et al.* [78] to obtain a free-space THz emission. Then, the optimization of this 5*d* heavy metal to a strong spin-orbit coupling material was concurrently demonstrated in 2016 by A. Kimel's team in Huisman *et al.* [82] and few months after by T. Kampfrath's team in Seifert *et al.* [83]. This promising, sizeable, broadband, polarization-controlled THz emitter opens perspectives for THz on-chip high data transmission rate and for increasing computation speed, currently with clock-rate about few GHz. It has been quickly followed by integration attempts in repetitions [84] or flexible PET substrates [85], and we will present in Chap. II a detailed state-of-the-art of spintronic THz emitters.

Combining spintronics and ultrafast spin-related phenomena.

All the presented concepts of spintronics will be at the basis of the implementation of several strategies for spintronic THz emitters: interfacial spin-charge conversion using inverse Rashba-Edelstein effect, interfacial scattering properties, magnonic current in insulating antiferromagnets, *etc.* We propose now a dedicated framework of the THz radiation in free-space and a review of the THz research domain, and THz spintronics.

II

THz technologies and the emergence of spintronic THz devices.

This chapter presents an overview of the THz research field in sources, from the various physical generation mechanisms arising from non-linear light-matter interactions, to the current widespread THz technologies. After a short presentation of the THz domain, trapped between the conventional electronics and optics, we develop briefly the non-linear light-matter interactions in solids before reviewing current emission and detection technologies.

The second part of this chapter is dedicated to the presentation of the recent research on spintronic THz emitters. The discovery of spintronic THz emitters is relatively recent, becoming in a few years a hot topic in the community. We present an actualized state-of-the-art (as of 2022) from the realization of spintronic THz emitters in 2016 to recent findings and give perspectives about the future of this highly active research field, with a special care on interfacial effects and high-scale dynamics, which will be developed in the scope of this thesis.

1 Conventional THz technologies: applications and challenges.

Historically, the terahertz radiation (1 THz = 10^{12} Hz, sometimes called T-waves, far-infrared or sub-millimeter waves) has been poorly studied in the past owing to the lack of convenient technologies compared to the possibilities offered in the two neighbouring electromagnetic domains: the high frequency electronics up to hundreds of GHz on one side, and the optics and photonics with well-studied far infrared light on the other side [86, 87]. Yet, this THz domain, conventionally defined between 0.3 THz (300 GHz) and 30 THz as shown in Fig. 2.1, has recently attracted attention due to its novel physics, opening interesting application perspectives as well as academic research. Indeed, THz radiation intrinsically represents very fast oscillations of the electric field (typically the picosecond and sub-picosecond timescale) and carries energies close to few meV. THz radiation allows to probe spin excitations and magnons dynamics, the superconducting gap, the optical phonons and even plasmons, whose energies lies in the THz band [88].

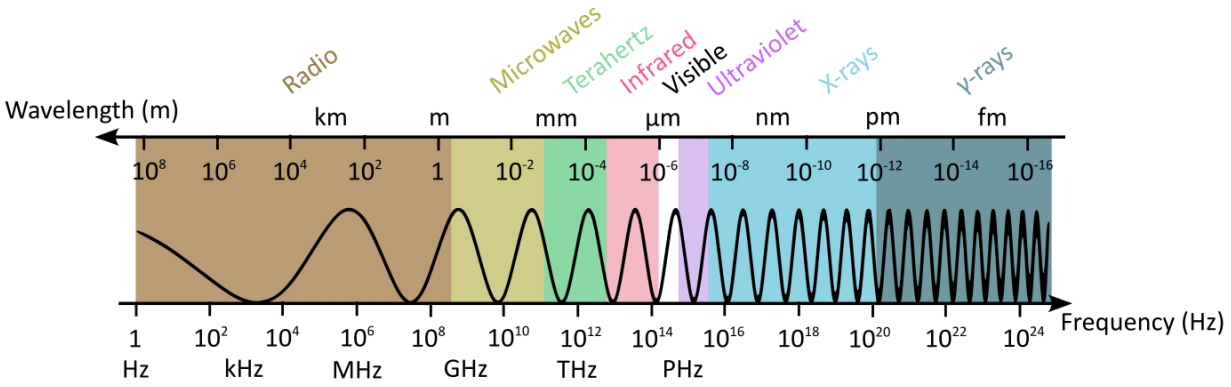

Figure 2.1: Electromagnetic spectrum. The THz range (in green) is typically included between 0.1 THz and 30-50 THz.

Order of magnitude of the THz radiation.

Frequency ν THz	**Pulse duration** τ ps	**Free-space wavelength** λ μm	**Wave-number** σ cm^{-1}	**Energy** ε meV	**Temperature** T K
1	1	300	33	4.1	48
2	0.5	150	67	8.3	96
5	0.2	60	167	20.6	240
10	0.1	30	333	41.3	480

Applications of the THz radiation. While the mode energies of the intramolecular vibrational and rotational modes of molecules range in the infrared regime, the intermolecular vibrational modes of polar molecules are typically in the THz range, as for instance the textbook example of polar molecules: H_2O (water). The THz radiation is therefore strongly absorbed by water, which makes difficult the THz transmission in air. This property of the THz radiation is at the basis of developed applications related to spectroscopy of real systems such as the advances in THz tomography techniques [89].

Medical. THz spectroscopy starts to emerge as a new tool in medical research against cancer with a clinical development of early-stage tumor diagnosis. Research showed previously [90, 91] that tumor cells present a higher composition rate of water compared to normal cells. Using this property, one is able to set a THz absorption map of ex-vivo sampled tissues, presenting locally the area corresponding to cancerous cells. It would then be envisioned to use this technique

in complement to already established tumor detection techniques to detect breast cancers [92], cell carcinoma (skin cancers) [93], colon cancers [94], *etc.* THz radiation has the property to be non-ionizing and the integration of such spectroscopy procedure would be possibly employed after a biopsy. This way, THz cancer spectroscopy would be far less costly than tumor imagery performed via magnetic resonance imaging in some cases [91]. The integration of future THz devices for medical imaging would thus be highly valuable [95].

High-rate telecommunications. The second widely known application of THz is novel telecommunication channels with the recent (and future) development of the fifth and sixth generation of wireless telecommunications (5G and 6G). This unexplored (and yet unregulated) frequency band between 0.2 and 10 THz attracts a lot of industrial potential with high data transmission rate, from 10 Gbit.s^{-1} at 9 µm ($\simeq$ 33 THz) [96] to several Tbit.s^{-1}, especially pertinent for near-range communications.

Security, imaging and non-destructive testing. THz radiation are also starting to be widely used in security applications, for non-destructive testing of drugs and reactive chemicals [97]. Due to its weak penetration in human skin (because of water absorption) and its reflections from metallic surfaces, THz radiation can be used as a powerful body scanner to uncover hidden weapons in airports, as widely spread nowadays in North America [88]. The detection of chemicals and drugs is also an interesting application as many chemical fingerprints lay in the THz range, as well as for quality control (for instance with car paints, *etc.*) [97]. We can also think about ellipsometry to measure with precision the thickness of metals and optically-opaque materials (non-destructive testing operations).

Astronomy. THz spectroscopy is also essential in scientific field of research such as astronomy [88]. Due to the absorption of THz radiation by intermolecular vibrational modes of polar molecules, THz detectors are ideal tools to characterize the composition of planetary atmospheres as developed with Schottky diodes by the Observatoire de Paris and the European Space Agency (ESA) [98].

Following these applications, there is a strong need of high power, polarization controlled THz emitters. We present in the next part the current THz sources and detectors and give further perspectives about the future of THz devices with a particular focus on the recent advances in spintronics THz sources.

2 Introduction to THz free-space emitters.

2.1 Electric field derivation: near-field and far-field range.

The concepts and foundations of THz free-space emitters based on charges (electrons and holes in a semiconductor) or spin dynamics (in spintronic THz emitters) obey the Maxwell equations:

Recall of the Maxwell's equations.

Maxwell-Gauss	$\nabla \cdot \mathbf{E} = \rho/\epsilon_0$	Maxwell-Faraday	$\nabla \times \mathbf{E} = -\partial \mathbf{B}/\partial t$
Maxwell-Thomson	$\nabla \cdot \mathbf{B} = 0$	Maxwell-Ampère	$\nabla \times \mathbf{B} = \mu_0 j_c + \mu_0 \epsilon_0 \partial \mathbf{E}/\partial t$

where one can also define the polarizability $\mathbf{D} = \epsilon \mathbf{E}$ and magnetic induction as $\mathbf{B} = \mu_0(\mathbf{H} + \mathbf{M})$ with $\epsilon = \epsilon_0 \epsilon_r$ the dielectric permittivity and μ_0 the vacuum permeability. The output THz electromagnetic wave $\mathbf{E}(t)$ and $\mathbf{B}(t)$ may then have different origin:

- the appearance of a charge current $\mathbf{j}_c(t)$ in the sub-picosecond timescale acting as a source (dipolar radiation). This term is called the electric dipolar radiation.
- a change of the magnetization $\mathbf{M}(t)$ at the sub-picosecond timescale. This is the magnetic dipolar radiation.
- a change of the polarizability $\mathbf{P}(t)$ at the origin of the emission from non-linear crystals (strong electric susceptibility $\chi^{(2)}$ inducing a dynamical polarizability change)

In the scope of this thesis, we will focus on the first case including dynamical charge currents. This case is totally equivalent to the picture of an electromagnetic wave emitted from a classical charge dipole oscillator, centered close to a certain origin, and able to radiate an electric (magnetic) field away from the center and described by a spherical electromagnetic wave.

One can then discriminate the charge-induced process between (photo-excited) electron-hole dynamics in a semiconductor (photoconductive switches, surge currents like the photo-Dember effect, surface-field contributions, *etc.*) from the photo-excited spin-polarized carriers giving rise to a transient spin-current converted into the charge current, source of the spin-based THz emission. In order to model the resulting THz wave, one have to perfectly describe the time dynamics of the different constituents and carriers at stake.

Near-field and far-field expressions. Considering THz emitters, one often has to consider respectively the near-field (NF) and the far-field (FF) emission. The interested reader is referred to a detailed development of a dipolar emission from Cohen-Tannoudji *et al.* [99] addressed in Appendix A4.1. The two quantities are characterized in that the near-field electric field $\mathbf{E}^{\mathrm{NF}}$ corresponds to the region very close to the nanometer-thick structure, whereas the far-field electric field $\mathbf{E}^{\mathrm{FF}}$ corresponds to the radiated electric field at the level of the detector (typically several tens of cm of distance). Of course, it exists a certain proportionality relationship $\mathbf{E}^{\mathrm{NF}} \propto \mathbf{E}^{\mathrm{FF}}$ between the two quantities which makes it possible to study either one of the two quantities.

- In the near-field region, the electric field derived from the charge current source can be written as:

$$E^{\mathrm{NF}}_{\mathrm{THz}}(\omega) \propto eZ(\omega)\theta_{\mathrm{SHE}} l_{sf} j_s^{\mathrm{2D}}(\omega) \text{ or in the time-domain } E^{\mathrm{NF}}_{\mathrm{THz}}(t) \propto j_c(t) \qquad \text{(E2.1)}$$

  and is directly proportional to the THz charge current. We have considered a spin-based emission with e the electron charge, $Z(\omega)$ the THz impedance, θ_{SHE} the spin Hall angle,

l_{sf} the spin diffusion length and j_s^{2D} the spin current density source. Alternatively, the magnetic dipolar radiation term (see Annex A4.3) can be written as:

$$E_{\text{THz}}^{\text{NF}}(\omega) \propto -\frac{i\omega n_{\text{THz}} d_{\text{FM}}}{c} Z(\omega) M(\omega) \text{ or in the time-domain } E_{\text{THz}}^{\text{NF}}(t) \propto \frac{\partial M(t)}{\partial t} \tag{E2.2}$$

with n_{THz} the THz refractive index, d_{FM} the magnetic layer thickness, meaning that one can relate the measured near-field THz electric field to the time-derivative of the magnetization dynamics $M(t)$, originating as an inductive term. In spintronic THz heterostructures, we can show that the term induced by the spin-injection and transient charge current is dominating the term describing the time-dynamics of the magnetization (Annex A4.3).

- For describing the far-field emission, one has to consider the integrated output power in free-space according to:

$$P_{\text{THz}} = \int_{\Omega} \epsilon E_{\text{THz}}^2(r,t) c dS \tag{E2.3}$$

where $\Omega = 4\pi R_0^2$ is the integrated surface where R_0 is the distance to the detector. The THz output power is thus expressed as:

$$P_{\text{THz}} \simeq \frac{T n_{\text{NIR}} \lambda_{\text{rel}}^2 S_{\text{NIR}}^2}{4\pi\epsilon_0 c^3} \left(\frac{\partial j_c(t)}{\partial t} \right)^2 = \frac{T n_{\text{NIR}} \lambda_{\text{rel}}^2 S_{\text{NIR}}^2 \omega^2}{4\pi\epsilon_0 c^3} j_c^2 \tag{E2.4}$$

where $T = t^2$ is the effective transmission coefficient, n_{NIR} is the optical refractive index, S_{NIR} is the pump spot with the current $I_c = j_c S_{\text{NIR}}$, ω is the oscillation frequency and λ_{rel} is the typical relaxation length in the active material (for instance l_{sf} for ISHE-type emitter or λ_{REE} for IREE-type emitter). One can thus show, by considering the integrated power $P_{\text{THz}} = \epsilon E_{\text{THz}}^2 \Omega c$, that the far-field electric is related to the time-derivative of the charge current with a certain prefactor assimilated to an effective THz impedance Z_{eff}:

$$E_{\text{THz}}^{\text{FF}}(t) \propto Z_{\text{eff}} \frac{\partial j_c(t)}{\partial t} \text{ or in the frequency-domain } E_{\text{THz}}^{\text{FF}}(\omega) \propto -i\omega Z_{\text{eff}}(\omega) j_c(\omega) \tag{E2.5}$$

The far-field regime is often considered for distances above 3λ. In particular, in the case of spintronic THz structures, the frontier between the near and far-field regimes differs depending on the thickness of the layer and the considered frequency. It has been calculated by Nenno *et al.* [100] that the approximation $E_{\text{THz}} \propto j_c$ is valid at low frequencies and in the thin film approximation, which is the case mostly encountered. However, as one drives away from those two conditions either in thicker films (compared to the wavelength) or at higher frequencies, the consideration of $E_{\text{THz}} \propto \partial j_c / \partial t$ is justified.

Interaction with the pump. To evidence the relation between the generated THz power and NIR pump power, we adapted the approach of Preu *et al.* [101] for a photo-excited density of electrons n_e in an emitter:

$$\nabla \cdot j_c = -e\theta_{\text{SHE}} \lambda_{\text{rel}} \frac{\partial n_e}{\partial t} \quad \text{with} \quad \frac{\partial n_e}{\partial t} = \frac{P_{\text{NIR}}}{l_{\text{NIR}} \hbar \omega_{\text{NIR}} S_{\text{NIR}}} \tag{E2.6}$$

where P_{NIR} is the average pump power with S_{NIR} the pump surface, l_{NIR} is the typical absorption length of the heterostructure at NIR frequencies ω_{NIR} and λ_{rel} is the typical spin current relaxation length with θ_{SCC} the spin-charge conversion efficiency. It comes the expression of the THz output power as a function of the pump input power:

$$P_{\mathrm{THz}} \propto \underbrace{\frac{T^* e^2 \lambda_{\mathrm{rel}}^4}{4\pi\epsilon_0 c^3 l_{\mathrm{NIR}} \hbar^2} \left(\frac{\omega_{\mathrm{THz}}^2}{\omega_{\mathrm{NIR}}^2}\right)}_{:=A} P_{\mathrm{NIR}}^2 \tag{E2.7}$$

2.2 Ultrafast light-matter interactions in semiconductors and non-linear medias.

We have presented a global picture, where the THz free-space radiation owns to the very short variations (timescales shorter than the picosecond) of a generated charge current $\mathbf{j}_c$, a change of the polarizability $\mathbf{P}$ or of the magnetization $\mathbf{M}$ [102, 103]:

$$\mathbf{E}_{\mathrm{THz}} = \frac{\partial^2 \mathbf{P}}{\partial t^2} + \frac{\partial \mathbf{j}_c}{\partial t} + \frac{\partial}{\partial t}(\nabla \times \mathbf{M}) \tag{E2.8}$$

One of the wealth of THz physics is the numerous effects that can combinedly generate free-space THz emission. Among those effects, we focus now on the charge current-induced $\mathbf{j}_c$ and polarization-induced $\mathbf{P}$ effects. Afterwards, we will separate in our studies (Chap. IV in topological insulators) the magnetic-based component S_- of the THz emission (the weak-magnetic dipolar field presented before, or spin-based emission in spintronic THz emitters) and the non-magnetic-based THz emission S_+ (non-linear optics) according to:

$$S_+ = \frac{S_{+\mathbf{M}} + S_{-\mathbf{M}}}{2} \quad \text{and} \quad S_- = \frac{S_{+\mathbf{M}} - S_{-\mathbf{M}}}{2} \tag{E2.9}$$

The branch of physics that refers to the propagation properties of light and to the light-matter interactions in non-linear materials is called non-linear optics. In this regime, the light electric field is conventionally considered to be above 10^8 V.m^{-1} that is a fraction of the atomic electric field (around 10^{11} V.m^{-1}). At this stage, to consider the non-linear interactions between the intense incoming radiation $\mathbf{E}$ and the non-linear media, we introduce the polarizability connected to the electrical susceptibility tensor χ and can be now expressed as different orders of the electric field according to:

$$\mathbf{P} = \epsilon_0 \chi \mathbf{E} \rightarrow \mathbf{P} = \epsilon_0 \left(\chi^{(1)}\mathbf{E} + \chi^{(2)}\mathbf{E}^2 + ...\right) = \mathbf{P}_0 + \mathbf{P}_{\mathrm{NL}} \tag{E2.10}$$

As an example which will be useful for the future descriptions non-linear optics in crystals such as the optical rectification process, let us consider the expression of the second-order polarizability of a bichromatic radiation [104]:

$$E(\omega_1, \omega_2) = E_1(\omega_1) + E_2(\omega_2) \tag{E2.11}$$

$$P^{(2)} = \epsilon_0 \chi^{(2)} E^2 \tag{E2.12}$$

$$P^{(2)} = \epsilon_0 [\chi_{\mathrm{SHG}}^{(2)}(E_1(2\omega_1) + E_2(2\omega_2)) + 2\chi_{\mathrm{SFG}}^{(2)} E_{12}(\omega_1 + \omega_2) + 2\chi_{\mathrm{DFG}}^{(2)} E_{12}(\omega_1 - \omega_2) \tag{E2.13}$$

$$+ 2\chi_{\mathrm{OR}}^{(2)}(|E_1|^2 + |E_2|^2)] \tag{E2.14}$$

Interestingly, the propagation of an intense beam generates second-order electric fields, respectively via frequency-doubling (also called second harmonic generation), sum and difference frequency generation and a DC component called optical rectification (rectification can here be understood as the conversion of an AC signal into a DC signal proportional to the magnitude of the electric field). These effects are directly dependent on the electric susceptibility tensor χ and therefore to the symmetries of the crystal. We will describe some of those non-linear phenomena further on in this chapter.

Ultrafast optical effects in crystals. Illuminating non-linear materials with high power optical sources allow the generation of ultrafast transient in the THz range via a large number of physical non-linear effects illustrating the intense light-matter interactions [103]. In this part, we provide the key comprehension elements of ultrafast optical effects in semi-conductors following the classification of Sipe *et al.* [105] into three type of photo-excited currents: injection currents, shift currents and surge currents, as well as the optical rectification process.

Injection current. Circular photogalvanic effect.

Among photogalvanic effects, it is important to distinguish between the linear photogalvanic effect (LPGE) which can be associated with the shift current class, and the circular photogalvanic effect (CPGE) which can be associated to injection-type of THz current [106, 107]. The THz injection current can be seen, for a pump energy above the bandgap of semiconductors and circularly polarized pump (Fig. 2.2a), as:

$$j_{\text{inj}} = \sigma_{\text{inj}} \Delta v \Theta(t) \exp\left(-\frac{t}{\tau_{\text{inj}}}\right) * |\mathbf{E}(t)|^2 \tag{E2.15}$$

which includes the first derivative of the electronic displacement $\Delta v = \partial x/dt$ and the sheet charge density $\sigma_{\text{inj}} = eN\Delta z_{\text{inj}}$. τ_{inj} is the typical relaxation time of injection currents, $\Theta(t)$ is the Heaviside function and $\mathbf{E}(t)$ is the pump intensity envelope. For time-reversal invariant systems, those injection currents are proscribed in space inversion-symmetry semiconductors and in semiconductor of point group $\bar{6}m2$, $\bar{6}$ and $\bar{4}3m$ which thus exclude the GaAs and zinc-blende structure semiconductors (the interested reader can look at the classification drawn by Sipe *et al.* [105] for more details). From Kinoshita *et al.* [108], it comes:

$$j_{\text{CPGE}} \propto \xi \mathbf{e}_{\text{pump}} \sigma_{\pm} * |\mathbf{E}(t)|^2 \tag{E2.16}$$

where ξ represents a second-rank tensor linked to the Rashba-Dresselhaus spin-orbit coupling, $\sigma_{\pm}$ is the helicity of the pump (circular left-handed or right-handed) and $\mathbf{E}(t)$ is the pump intensity envelope. We will focus on the example of topological insulators and their spin-polarized surface and bulk states as represented in Fig. 2.2a. Experimentally, the helicity-dependent (C), helicity-independent (L_1 and L_2) and thermal contributions (D) of generated photocurrents can be addressed in parts to circular photogalvanic effect and have been characterized in topological insulators with the work of McIver *et al.* [107, 109] such as (α is the quarter-wave plate ($\lambda/4$) angle):

$$S_{\text{PGE}}(t, \alpha) = C(t)\sin(2\alpha) + L_1(t)\sin(4\alpha) + L_2(t)\cos(4\alpha) + D(t) \tag{E2.17}$$

Shift currents. Linear photogalvanic effect.

We now focus on the second class of current that are called shift currents and are sensitive to the crystalline orientation. The shift currents arise from the electronic cloud displacement Δx upon excitation above the bandgap as shown in Fig. 2.2b [107]. In this class of THz currents accessible for instance in zinc-blende structure semiconductor (GaAs), we can include the linear photogalvanic effect following the form:

$$j_{\text{shift}} \propto \sigma_{\text{shift}} \Delta x \frac{\partial}{\partial t}\left(\Theta(t)\exp\left(-\frac{t}{\tau_{\text{shift}}}\right)\right) * |\mathbf{E}(t)|^2 \tag{E2.18}$$

where τ_{shift} is the shift current relaxation time, σ_{shift} is the conductivity integrated on the effective thickness Δz_{shift} participating to the sheet conduction. It can be theoretically expressed via the use of a third-rank tensor ν_{ijk} introduced by Bas *et al.* [110], which follows the symmetry of the semiconductor lattice. The shift current can be expressed as:

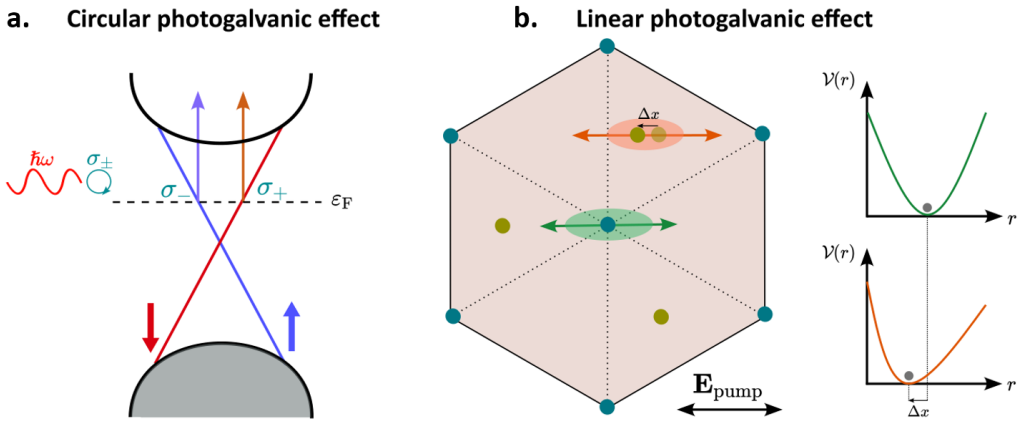

Figure 2.2: Photogalvanic effects. Scheme of the (a) circular photogalvanic effect (CPGE) which generates an injection-type current, and (b) linear photogalvanic effect (LPGE) which generates a shift-type current.

$$j_{\text{shift}} = \nu_{ijk} E^{j}_{-\omega} E^{k}_{\omega} + c.c. \tag{E2.19}$$

where $c.c.$ denotes the complex conjugate. The symmetry of the tensor imposes the symmetries of the generated charge current. In the case of topological insulators from the Bi-family that we will study in the scope of Chap. IV, we follow the example of centrosymmetric Bi_2Se_3 given by Bas *et al.* [110] and see that the tensor shrinks to its ν_{xxx} component due to the inversion-symmetry breaking at the interface. This leads to the following expression of the linear photogalvanic effect as:

$$j_{\text{shift}} = \nu_{xxx}(\cos(3\phi)\mathbf{e}_{\parallel} - \sin(3\phi)\mathbf{e}_{\perp})|E_{\omega}|^2 \tag{E2.20}$$

where ϕ is the azimuthal crystalline orientation. While fixing the detector orientation to $\mathbf{e}_{\perp}$ for instance, it is thus expected a $\cos(3\phi)$ dependence of the THz shift currents in topological insulators.

We now focus on so-called surge currents which do not depend on the crystalline orientation and are mediated for pump energy above the bandgap (interband transition).

Surge currents. Photo-Dember effect.

The photo-Dember [111, 112] results from the difference of mobility $\Delta\mu = \mu_e - \mu_h$ between the photoexcited holes and the electrons in a semiconductor (pump energy above the bandgap) of respective mobilities μ_h and μ_e (Fig. 2.3a). This creates an electric dipole arising from the different spatial distribution of electrons and holes in the vicinity of the top surface of the semiconductor. It radiates a charge current normal to the semiconductor surface and thus, this effect should be independent on the pump polarization α but strongly depends on the tilt orientation β. It is in theory independent on the crystallographic azimuthal orientation ϕ except in case of slight tilt misorientation β due to the small in-plane projection of the normal charge current.

Surge currents. Surface-depletion field.

A second effect [112] involving semiconductor surface is the surface-depletion field effect (Fig. 2.3b), which is the acceleration of the photoexcited electrons and holes by the surface electric field E_z^{surf} in the vicinity of the semiconductor interface with a metallic material, due to the formation of a Schottky barrier. This effect should be independent on the pump polarization α and azimuthal crystalline orientation ϕ, but could depend on the tilt β of the pumping to

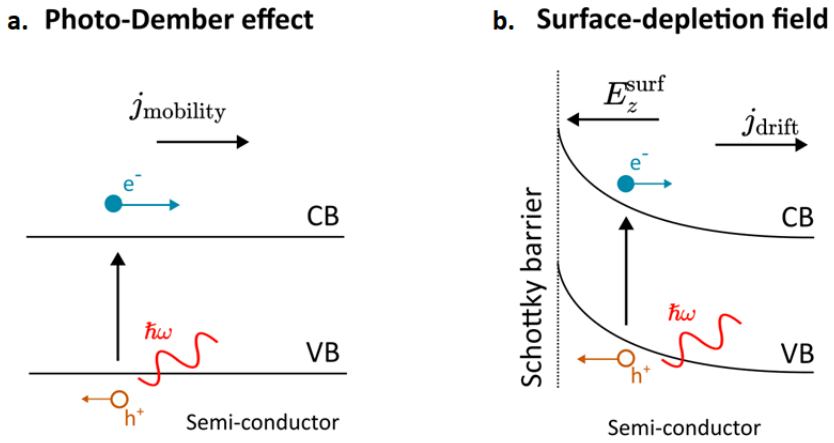

Figure 2.3: Surge currents. (a) Photo-Dember effect and (b) surface-depletion field effect in semiconductors.

efficiently photo-excite indirect gap semiconductors (β is the angle between the pump incidence and the sample plane).

Surge currents. Surface electric-field contributions

Surface-field effects are associated in centrosymmetric and non-centrosymmetric materials to the presence of a normal surface electric field E_z^{surf}. An effective second-order electrical susceptibility is enhanced by the surface electric field following:

$$\chi_{ijk}^{(2)\ \text{eff}} = \chi_{ijk}^{(2)\ \text{bulk}} + 3\chi_{ijkz}^{(3)\ \text{bulk}} E_z^{\text{surf}} \tag{E2.21}$$

where $\chi_{ijk}^{(2)\ \text{bulk}}$ and $\chi_{ijkz}^{(3)\ \text{bulk}}$ are respectively the second and third-order susceptibility. Particularly, in the case of centrosymmetric materials, where the second-order susceptibility is not allowed, a second-order signal (with the electric field) can be measured by this effect while applying an normal surface electric field E_z^{surf}. This effect is for instance at stake in graphene [113].

Optical rectification.

Optical rectification can be seen as the reciprocal effect of the electro-optic sampling (that will be widely used for THz detection in Section III.2.1 and Annex A10), both happening in an inversion-symmetry breaking non-linear media of strong second-order susceptibility $\chi^{(2)}$. Pumping below the bandgap creates a DC-polarization $P^{(2)}(0)$ that scales with the pump intensity:

$$P_i^{(2)}(\Omega) = \sum_{j,k} \varepsilon_0 \chi_{ijk}^{(2)}(\Omega, \omega+\Omega, -\omega) E_j(\omega+\Omega) E_k^*(\omega) \tag{E2.22}$$

where $\chi_{ijk}^{(2)}$ is the so-called second-order non-linear susceptibility tensor. The pump time profile shapes the dynamics of the non-linear polarization. The generated electric field can be simply expressed in case of $\langle 110 \rangle$ orientation of a ZnTe crystal (following a derivation available in Ref. [114]) as:

$$E_{\text{THz}} = r_{41} E_0^2 \sqrt{\sin^2\phi\ (1+3\cos^2\phi)} \tag{E2.23}$$

where E_0 is the pump electric field and r_{41} is the electro-optic coefficient and ϕ is the azimuthal crystalline orientation.

Summary. In brief, the non-linear THz generation effects are various and are possible sources of parasitic contributions to spin-related effects that we address in the scope of this thesis. To decorrelate these effects from our spin-injection and spin-charge conversion signals, we will address the symmetries of the measured THz transients as summarized in Table II.1, that will help us afterwards to separate the non-magnetic and magnetic contributions in our heterostructures.

Class	Effect	Crystal (ϕ)	Tilt (β)	Pump polarization	Energy
Injection	Circular photo-galvanic	Independent	Independent	Circular ($\sigma_{\pm}$)	$> \varepsilon_g$
Shift current	Linear photo-galvanic	Dependent	Dependent	Linear (α)	$> \varepsilon_g$
Surge current	Photo-Dember	Independent	$\sin(\beta)$	Independent	$> \varepsilon_g$
Surge current	Surface-depletion field	Independent	$\sin(\beta)$	Independent	$> \varepsilon_g$
Surge current	Surface electric-field	Dependent	Dependent	Dependent	$> \varepsilon_g$
Optical rectification	Optical rectification	Dependent	Independent	-	$< \varepsilon_g$

Table II.1: Classification of the non-linear THz photocurrents. The azimuthal crystallographic orientation is noted as ϕ, the out-of-plane tilt is noted as β and the linear (circular) pump polarization angle is noted α ($\sigma_{\pm}$). The pump energy needed is also marked with respect to the bandgap energy ε_g.

2.3 Actual THz free-space sources, antennas and detectors.

THz sources and antennas.

This part presents the state-of-the-art of THz emitters and detectors, from the beginning of the research in the domain to the challenges and roadmaps of this very dynamic research field. Historically, the first reported THz emission in 1911 owns to an illumination of a quartz mercury lamp [115]. The reader interested in historical details of the THz radiation can further read the brief history review proposed by Sizov [116]. It is only recently, in the 80s-90s, that more direct and powerful ways to generate THz emission emerged, starting with the development of quantum cascade lasers [117]. Although we will focus mostly on the pulsed emission derived from spintronic THz emitters in this thesis, we present quickly the current THz emission and detection devices for CW and pulsed operation/detection. The challenges of the THz research and technological developments are addressed in the 2017 recent review [88].

Quantum cascade lasers - CW operation. Quantum cascade lasers (QCL) were first developed by J. Faist *et al.* in 1994 in the mid-infrared regime [117]. They are composed of a multistacking (up to hundreds of repetitions) of semiconductor heterostructures engineered to realize quantum wells (QW) via three adjacent semiconductors. The central one presents a slightly different value of the bandgap to confine the electrons in the central conduction band, for instance in the well-studied AlGaAs/GaAs/AlGaAs QW system. The band structure for the electrons of a THz QCL is schematically shown in Fig. 2.4. By application of an external bias, the band structure is bent and allows the electrons to tunnel from one QW to another QW, of potentially different quantized energy. In each QW, the electrons will undergo relaxation (intersubband transitions) while emitting a photon corresponding to the difference of energy of the QCL. Their emission performances reach up to few W of peak power, centered around given wavelengths, with a noticeable constraint being the operation at cryogenic temperatures only, although recent work has shown Peltier operation (250 K) [118]. Besides, the careful choice of the semiconductors and their thicknesses allows to finely tune the emission in energy (wavelength). The first demonstration in the THz range has been performed in 2002 by Köhler *et al.* [119] at 4.4 THz as shown in Fig. 2.4b with a THz output power of 2 mW at 50 K. Note that the strong narrowing of the emission spectrum above the threshold current (above 1240 mA in the case of Ref. [119], corresponding to current densities about few hundreds of A.cm^{-2}) demonstrates the laser operation at THz frequencies, which corresponds to an efficient population inversion in the system driven by the applied electric field. The applied electric field permits to align the sub-bands such that the tunneling barrier

rate is tuned. At a threshold electric field, the tunneling time becomes shorter than the relaxation rate of the electrons in the QW, allowing an efficient population inversion. The carriers are injected into the upper laser state via resonant tunneling. The strength of those devices is the low current density needed to operate if one compares with spintronic devices where current densities of the order of 10^{11} A.m^{-2} ($= 10^{7}$ A.cm^{-2}) are needed to modulate the magnetic properties. QCLs are also developed to envision THz frequency combs [120] but remain very complex in terms of realization and need to be cryo-cooled for an efficient lasing (77 K).

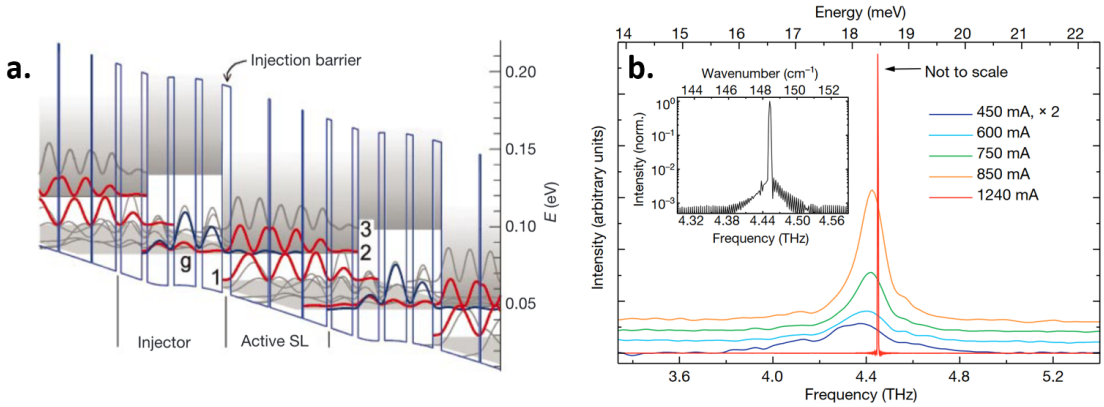

Figure 2.4: Quantum cascade laser. (a) Energy diagram of the THz-QCL as a function of the position. An applied electric field bends the band diagram allowing inversion population (shaded areas). (b). Spectrum of a QCL as a function of applied current. The THz lasing is demonstrated above 1240 mA (red curve). Adapted from [119].

Photoconductive antennas - pulsed operation. Another way to generate THz radiation is to use photoconductive antennas based on optical bandgap semiconductors (GaAs, AlGaAs, *etc.*). They are also known as photoconductive switches or Auston switches and represent today widely commercialized THz sources. An ultrafast optical pump excites photocarriers in the semiconductor, living up to their recombination time $1/\nu_{\text{rec}}$. During this time, an external bias applied on the antenna accelerates the photo-excited charges which creates a THz dynamical charge current radiating in free-space. The applied bias can also be modulated up to several tens of kHz for heterodyne detection purposes. This is represented in Fig. 2.5. To generate high frequency THz pulses, it is preferable to use a semiconductor with small recombination times τ_{rec} such as in LT-GaAs (low-temperature grown GaAs) due to the more efficient carrier trapping. However, the PCAs are limited generally around 5 to 10 THz at maximum bandwidth owing to the recombination time (which depends on the semiconductor materials), and the emitted power drops above these frequencies. Besides, even for short recombination times, it is reported the presence of a transverse optical (TO) phonon mode in GaAs at 8 THz, which severely prevents the ultrabroadband emission [121].

THz photomixers - CW operation. The powerful and tunable generation of narrowband CW THz radiation is also at the heart of the research interests in the THz community. The THz gap, as illustrated in Fig. 2.6 shrinks from both sides of the spectrum. The use of CW THz QCLs [124] from the 'optics' side is also reinforced from the 'electronics' side with the use of THz photomixing [101]. They typically consist of a material with fast current dynamics pumped using detuned narrowband laser sources ν_1, ν_2 (with $\nu = \omega/2\pi$), thus generating a continuous waveform (CW) pump beating at a so-called beatnote frequency $\nu_{\text{THz}} = \nu_1 - \nu_2$, either with photoconductive antennas (as described above for a femtosecond excitation) or with uni-traveling-carrier photodiodes (UTC-PD) [101]. The latter, shown in Fig. 2.5c, is composed of a photo-active absorber that generates electrons which are accelerated towards a drain (whereas the hole mobility is low) [123].

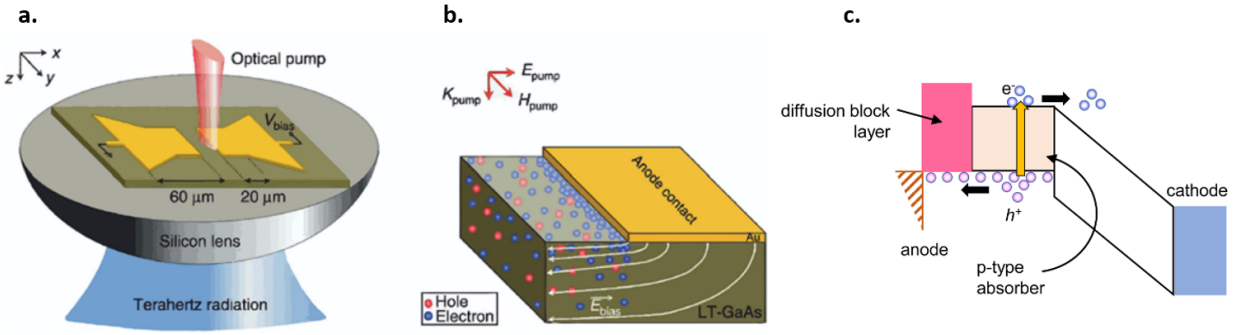

Figure 2.5: Photoconductive antennas. (a) A bow-tie photoconductive antenna on optical gap semiconductor (here LT-GaAs) drives a THz radiation in free-space. (b) The application of a bias V_{bias} accelerates the photocarriers. (c) Band diagram for the uni-traveling-carrier photodiode (UTC-PD). Left, middle and right panels are respectively adapted from Refs. [122, 123]

In both cases, this generates a photocurrent beating at the beatnote frequency ν_{THz}. We will propose in Chapter VI to transpose the concept of photomixing for CW-operation of spintronic THz emitters.

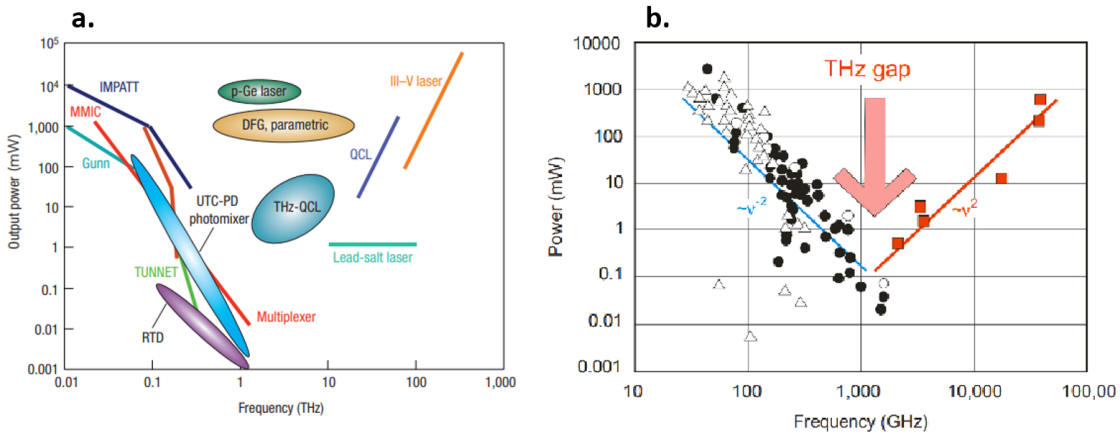

Figure 2.6: CW THz gap. (a-b) Illustration of the THz gap presented from different solid state CW technology sources. The region covered by THz spintronic emitters is displayed in blue. Adapted from [125, 126, 127, 86].

THz free electron lasers - CW and pulsed operations. THz free electrons lasers [128] (or THz-FEL) follow the procedure of synchrotron-like radiation, where accelerated unbounded electrons are launched into a series of ondulators (strong magnets of opposite polarities) to be curbed repeatedly while propagating. During their deceleration due to their periodic change of direction, it creates a breaking radiation that is amplified as it travels in a cavity tuned for the THz wavelengths. Typically, the tunable emission range obtained by such THz-FEL can be from few hundreds of GHz to 4-5 THz with powers about the kW. However, as it is supported by synchrotron-like dedicated structures, this type of high-brightness THz sources are only accessible for scientific uses.

Femtosecond laser plasma filaments - pulsed operation. An interesting source for broadband THz radiation and detection is the laser plasma filamentation [129], initially evidenced by Hamster *et al.* [130]. While strongly focusing femtosecond pulses to obtain optical intensities above 10^{14} W.cm^{-2}, the gas molecules start to ionize, which creates at the position of the pump focal point an intense air-plasma. Several schemes of THz generation has been evidenced as shown in Fig. 2.7a, whether via the ponderomotive force (acceleration of the ionized electrons due to

the electric field gradient induced by the pump), plasma biasing (acceleration of the ionized electrons by the electric field induced by the external gradient), two-color pumpings, *etc.* Recently, Liu *et al.* [131] demonstrated the use of STE-derived THz electric field as a second acceleration source for the ionized electrons to control the THz polarization of such air-plasma laser filamentation processes.

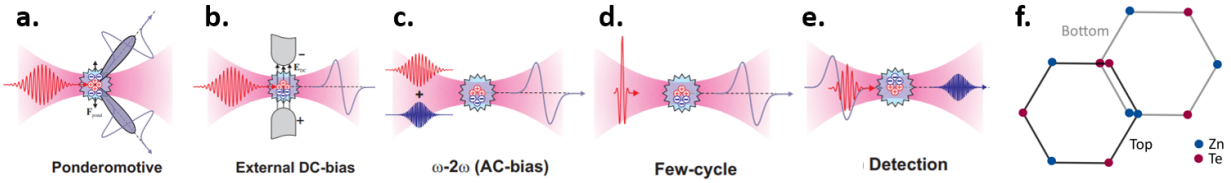

Figure 2.7: Air-plasma and non-linear crystal THz emission. (a-e) Representation of the different THz generation and detection schemes using femtosecond laser plasma filaments. (f) Surface of a zinc-blende non-linear crystal (*e.g.* ZnTe) who presents a distortion of the top unit cell which reinforces the bulk optical rectification upon ultrashort pumping. Left panels adapted from Ref. [129].

Non-linear crystals - pulsed operation. A widely used THz source relies on organic or non-organic non-linear crystals, in particular ZnTe, GaP, GaSe or $LiNbO_3$ as pictured in Fig. 2.7b. Their second-order susceptibility $\chi^{(2)}$, owing to the bulk inversion-symmetry breaking, is very high and allow to generate intense THz radiation via the so-called optical rectification effect presented before. However, the radiation bandwidth is strongly restricted by phonon absorptions in such crystals. In particular, for ZnTe$\langle 110 \rangle$ and GaP$\langle 110 \rangle$ surface, a slight misorientation of the last atomic plane helps in providing higher interfacial non-linear susceptibility due to the interfacial inversion-symmetry breaking.

Use of third-order THz generation in graphene - pulsed operation. In centrosymmetric materials, the second order contribution (and all even-order) vanishes due to symmetry arguments. To generate transients properties in those materials, one can imagine using third-order process as it has been reported in graphene via photon drag effect [113] which induced a second order non-linearity via surface electric-field contributions, as we have discuss in the previous section. It allowed to generate THz transients with a theoretically predicted radiation bandwidth up to 60 THz [113].

Photon drag effect.

The photon drag effect results in the generation of an oriented shift current by means of an oblique pumping on a non-centrosymmetric material, so that both energy and photon momentum $\hbar\mathbf{k}$ are transferred from incident light to the material.

THz detectors.

We briefly discuss now the different technologies for THz detection. The interested reader can refer to the review of Sizov [132] for a complete picture.

Non-linear crystals. Reciprocally to the THz generation via second-order rectification, non-linear crystals (organic or non-organic, like ZnTe or GaP) can be used to sample incoming THz fields. This effect is called electro-optic sampling and will be widely used in the scope of this thesis in THz time-domain spectroscopy. A detailed derivation is proposed in Annex A10.

Photoconductive switches. Photoconductive switches (or Auston switches) can also be used as a detector by the following process. A NIR pulse pumps an unbiased PCA which generates photocarriers. When the THz pulse electric field hits the PCA, it modulates the excited photocarriers and this modulation can transcribe the detected THz electric field. This detection technique can be used for bandwidth up to 5 to 10 THz, matching both the relaxation dynamics in the photoconductive antenna and more importantly the THz phonon absorption.

Bolometers and pyroelectric detectors. THz bolometers maps the (very small) change of temperature induced by the incoming THz radiation (typically around 40-400 K in the 1-10 THz range). However, owing to the thermally-induced detection effect, their response is extremely slow even if their detection sensitivity is high. Thus, they are strongly disturbed by parasitic radiations. Therefore, to reduce the measurement noise, THz bolometers operate at cryogenic temperatures (4 K) [88].

Towards a new type of THz emitter: spintronic THz emitters.

After developing the current challenges in the conventional THz sources and technology, we will now develop the research trends on a novel broadband THz emitter explored widely in the scope of this thesis: the spintronic THz emitter.

3 Concepts of metallic THz spintronic emitters.

3.1 First developments and scientific context.

In 2016, a novel and efficient broadband THz source has been developed based on metallic spintronic heterostructures (Chap. III), following the concurrent publications of Huisman *et al.* [82] and Seifert *et al.* [83]. They typically consist of a nanometer-thin heterostructure composed of a ferromagnetic (FM) layer from the $3d$ family, and a non-magnetic (NM) strong spin-orbit element, mostly heavy metals (HM) from the $5d$ family. In this way, the structure is often called a $3d/5d$-based bilayer, as schematically represented in Fig. 2.8a. The principle is as follows: *i*) shining an ultrashort femtosecond NIR pulse leads to the partial demagnetization of the ferromagnetic unbalanced spin reservoir from the d band, which thus creates a spin current j_s due to diffusive photo-excited s-electrons, of different diffusion velocities due to spin-dependent scatterings. A non-zero spin-current thus *ii*) enters the NM layer where a spin-charge conversion process occurs, in a first picture via the so-called inverse spin Hall effect (ISHE), with θ_{SHE} the spin Hall angle being the conversion figure of merit. This creates *iii*) a transverse charge current j_c which radiates a THz transient in the free-space and detected in our case by electro-optic sampling (EOS, see Annex A10).

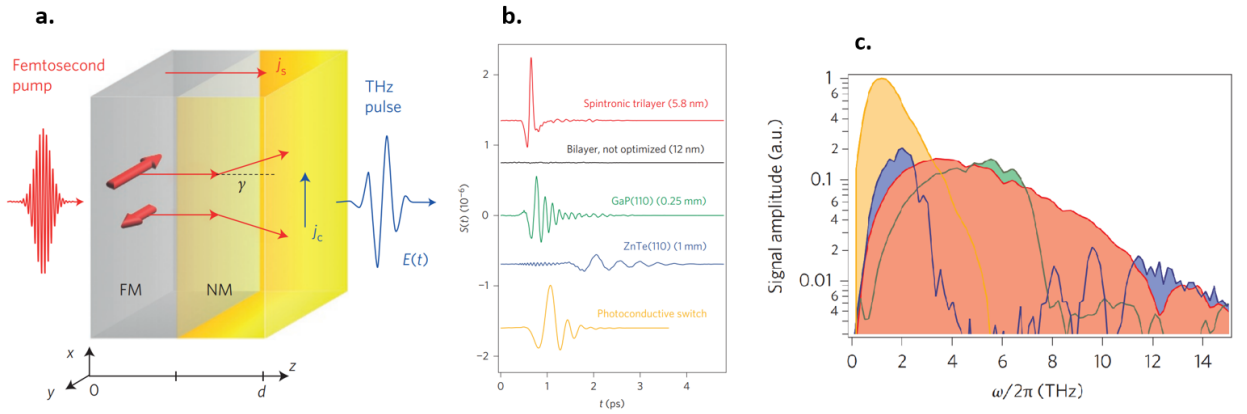

Figure 2.8: Spintronic THz emitters. (a) Scheme of the emitter. (b) Comparison of the THz time traces between an optimized 5.8nm-thick W/CoFeB/Pt STE, a not-optimized spintronic 12 nm-thick STE, GaP⟨110⟩(250µm), ZnTe⟨110⟩(1mm) and a photoconductive switch. (c) Comparison of the obtained spectrum from previous emitters. Adapted from Ref. [83].

Contrary to their semi-conductor based THz emitters counterparts, the resulting emission (derived from pump femtosecond pulses) is broadband and totally gapless due to the absence of phonon absorption. The bandwidth of the electric field has been reported to reach up to 30 THz [133], as shown in Fig. 2.8b-c. Moreover, we will see that performances of nanometer-thin unbiased metallic structures compete with the performances offered by micrometer-thick nonlinear crystals. Spintronic THz emitters have now gained a strong interest in the community for the interesting properties they offer and that we will present in the rest of this chapter. After introducing the key elements governing a spintronic THz emitter, we will give insights on the research axes in this very recent domain. The reader seeking for advanced details can also browse recent reviews [134, 135, 136, 137, 138, 139].

3.2 Properties of spintronic THz devices.

Spin current escape, spin Hall angle, pumping order, polarization control and modulation.

We now address the properties of spintronic THz devices and in particular the out-coming polarization of the THz pulse ruled by the following spin-charge conversion rule:

$$\mathbf{j}_c = \frac{2e}{\hbar}\theta_{\mathrm{SHE}}(\mathbf{j}_s \times \mathbf{m}) \tag{E2.24}$$

where one considers a pure interfacial injection of the spin current $\mathbf{j}_s = j_s\mathbf{e}_z$. At this level, one has considered that the direction of the conduction spin σ strictly follows adiabatically the direction of the magnetization $\mathbf{m} = \mathbf{M}/|\mathbf{M}|$. The maximum of the spin-charge conversion is then obtained for an in-plane magnetization and becomes null if the magnetization lies out-of-plane. We consider thus an in-plane magnetization $\mathbf{m} = m\cos(\theta)\sin(\beta)\mathbf{e}_x + m\sin(\theta)\sin(\beta)\mathbf{e}_y + m\cos(\beta)\mathbf{e}_z$ by fixing the out-of-plane angle $\beta = 0$ and with θ the in-plane orientation of the magnetization determined by an applied magnetic field. The generated charge current can be written as:

$$\mathbf{E}_{\mathrm{THz}}^{\mathrm{gen}} \propto \mathbf{j}_c = \mathbf{j}_x + \mathbf{j}_y \propto \theta_{\mathrm{SHE}} m j_s \sin(\beta)(\cos(\theta)\mathbf{e}_y - \sin(\theta)\mathbf{e}_x) \tag{E2.25}$$

It thus shows that for every configuration of the in-plane magnetization, the THz charge current is always perpendicular to the magnetization. The generated electric field is by definition polarized along the charge current direction. The THz detection $\mathcal{D}$ is not isotropic as it is dependent on the orientation of the crystal (calling γ the angle between the main detection axis and $\mathbf{e}_x$) so that we consider the convolution between the detector orientation and the generated THz electric field:

$$\mathbf{E}_{\mathrm{THz}}^{\mathrm{mes}} = \mathbf{E}_{\mathrm{THz}}^{\mathrm{gen}}(\theta) \cdot \mathcal{D}(\gamma) \propto \mathbf{E}_x\cos(\gamma) + \mathbf{E}_y\sin(\gamma) \tag{E2.26}$$

In the most used practical case, we fix the detector orientation along $\mathbf{e}_y$ ($\gamma = 90°$) so that we are only sensitive to the x-component of the THz polarization $\mathbf{E}_x$.

It is to be noted via Eq. E2.24 that for an opposite spin current flow/escape ($j_s \rightarrow -j_s$), the THz polarization reverses. This situation can be experimentally controlled by either *i*) a reversed stacking order of a structure (the FM layer position is interchanged with the conversion layer) or with *ii*) a flipping of the heterostructure with respect to the pump (the pump first hits the substrate rather than the initial case where the pump first hits the STE capping). In particular, the THz polarization would reversed under those two situations. This demonstrates that the THz electric field arises in this case from an electric dipole radiation, in opposition to a magnetic dipole radiation where the generated polarization would have remained unchanged. This will allow us to distinguish spin-charge conversion profile compared to pure magnetic dipole radiation or AHE in FMs [140]. Generally, when pumping for a double-side polished substrate, the emission is found to be larger as the pump hits the substrate first in transmission configuration, measured about a factor $\times 3$ on sapphire substrate, mostly due to the better wave impedance matching with free-space. At last, if we replace the conversion layer of spin Hall angle θ_{SHE} like Pt with a conversion layer having an opposite sign of conversion $-\theta_{\mathrm{SHE}}$, the THz polarization also reverses.

In summary, we can establish the following THz polarization rules for spintronic emitters, that will help us in the next studies to disentangle spin-charge conversion contributions among alternative THz radiation processes in more complex multilayers.

THz polarization rules for spintronic emitters.

$$\mathbf{E}_{\mathrm{THz}} \parallel \mathbf{j}_c \perp (\mathbf{j}_s \perp \mathbf{m})$$

Magnetization reversal: $m \rightarrow -m \Longrightarrow \mathbf{E}_{\mathrm{THz}} \rightarrow -\mathbf{E}_{\mathrm{THz}}$

Spin Hall angle reversal: $\theta_{\mathrm{SHE}} \rightarrow -\theta_{\mathrm{SHE}} \Longrightarrow \mathbf{E}_{\mathrm{THz}} \rightarrow -\mathbf{E}_{\mathrm{THz}}$

Spin current reversal: $\mathbf{j}_s \rightarrow -\mathbf{j}_s \Longrightarrow \mathbf{E}_{\mathrm{THz}} \rightarrow -\mathbf{E}_{\mathrm{THz}}$

Sample reversal ($\beta = 180°$ and $-\,j_s$) $\equiv$ Electric dipole radiation $\Longrightarrow \mathbf{E}_{\mathrm{THz}} \rightarrow -\mathbf{E}_{\mathrm{THz}}$

A reversal of two of the previous parameters will give $\mathbf{E}_{\mathrm{THz}}$

3.3 Emission performances.

With oscillators sources, the output electric field of STEs is sizeable compared to the THz emission of non-linear crystals such as ZnTe [83], with electric field about several tens to hundreds of V.cm^{-1}. The reported electric field obtained from amplified sources can reach single-cycle peak electric field around 300 kV.cm^{-1} [133]. STEs therefore give the ability to investigate non-linear effects [131] induced by THz intense pulses, where typically electric fields above 100 kV.cm^{-1} are needed. The THz power is estimated around several tens of µW (amplified source) for a conversion efficiency (ratio between the generated THz and the NIR pump brought to the system) about 2 to 5×10^{-6} [141]. However, STEs lacks of emission power compared to already-established photoconductive antennas technology, both for amplified and oscillators sources. In particular for oscillator sources, the obtained field amplitude difference is roughly about $\times 10$ in amplitude (about $\times 100$ in power). However, STEs are promising candidates for high power THz emitters compared to already optimized PCA. Indeed, with amplified sources, PCAs can saturate quickly owing to the saturation of the photoexcited carriers (good pump absorption). On the contrary, STEs still posses margins to increase the pump absorption at higher fluences. Besides, owing to the fact STEs are ultrathin optically excited passive structures (no need of bias application to accelerate the carriers to obtain a sizeable THz emission), the possibilities of optimization of STEs are numerous.

The THz emission from spintronic structures interestingly present a gapless broadband response up to 30 THz, reaching higher frequencies components compared to non-linear crystals and their low phonon frequency absorption cutoff [83] (also called the Reststrahlen band). STEs are also better than photoconductive switches where the bandwidth is limited by the relatively large electron lifetimes in semiconductors, about several nanoseconds like in Si [101]. The polarization of the generated THz radiation can be efficiently tuned by applying an external magnetic field, opening applications to ellipsometry. However, the THz performances are weaker than expected from this type of structure owing to *i*) the weaker optical (NIR) absorption compared to semiconductors (where practically all the pump is absorbed in the material bulk with typical absorption lengths about the micron), leading to an absorption difference typically about factor $\times 3$, and also owing to *ii*) the strong THz absorption losses in metals due to the multiple reflections of the generated wave owing to strong refractive indices $n = \sqrt{i\sigma/\epsilon_0\omega}$ with σ the conductivity, ω the pulsation and ϵ_0 the vacuum permittivity.

3.4 Wavelength and pump dependence.

Behind the THz radiation process, the wavelength dependence of the spintronic emitter has been studied in the near-infrared range up to 2 µm [142, 143, 144] and down to the ultraviolet wavelengths [145]. Several references reported the invariance of the THz emission as a function of

the pump wavelength as shown in Fig. 2.9d. This is rather in line with the hot electron generation scenario on which highly mobile electrons in the *sp*-bands are generated to transport the spin momentum, followed by a rapid relaxation process. In the near-infrared region above 1 µm, the reports indicate a slight effect of the radiation absorption by metallic capping composing the STE, which can influence the THz emission. On the other side of the spectrum, Ilyakov *et al.* [145] have demonstrated the use of STE in the UV region, opening an interesting perspective to probe in the future, high-energy and sub-femtosecond dynamics resolution of spin-based effects (down to attosecond owing to the reduction of the optical cycle).

Interaction with the pump. In metallic spintronic elements, it has been widely reported that a major part (90%) of the THz emission does not depend on the pump polarization and in particular the pump helicity. The pump polarization-independent contribution arises from the spin-excitation, injection and conversion. The remaining pump polarization-dependent contribution (10%) would be due to the injection process owing to circular photogalvanic effects [109] mediated by Rashba-splitted interfacial states due to interface potentials between the two metals, as in the work of Huisman *et al.* [82] where circular pump has been employed. We therefore focus in future on the thermal generation of hot spin-polarized electrons in the FM layer, a process unselective with respect to the pump polarization. Besides, the THz emission is linear with the pump fluence up to the damage threshold which is quite high for fully metallic spintronic THz emitters, of the order of 5 mJ.cm^{-1} [146]. Typically in metallic STEs, the part of induced-demagnetization is negligible compared to the net magnetization of FM layers (some tens of % at high fluences about few mJ.cm^{-2} and few % for low fluences about few hundreds of µJ.cm^{-2} [67]), thus a more efficient pump capture would likely give higher emission amplitude. Note that in order to avoid radiation losses because of the impedance mismatch between free-space and the STE, a hyper-hemispherical Si lens are sometimes mounted on the back (substrate side) in the transmission configuration. This strategy can be seen as a premise for THz anti-reflective coatings which will be presented in Chap. VI.

We will present in the following sections approaches to increase THz radiation efficiency of STEs and propose a review of the novel physics following the discovery of STEs.

3.5 Impact of material composition and spin Hall effect-based alloys.

A considerable advantage of STEs is that they can be typically grown by sputtering deposition method, at least for metallic STEs, which is an industrial-compatible deposition technique widely spread today and offering high scalability. We focus on this part on the layer composing the spintronic heterostructure as imaged in Fig. 2.9.

Bilayers and trilayers configuration. Wu *et al.* [85] from National University of Singapore have studied the radiation obtained from STE bilayer NM/Co in various non-magnetic material NM={Pt, Ir, Gd, Ru, Ta, W}. The authors reported that the Pt NM layer is the most efficient converter for THz emission and the two signals obtained with Ta and W show a phase reversal owing to the opposite spin Hall angle sign. Notably, they reported a zero-signal configuration in the case of single NM (Pt) or single FM (Co), illustrating the strong importance of the bilayer (or trilayer) stacks and the spin-charge conversion (SCC) process as the main origin in the emission mechanism. A similar study has been presented by Seifert *et al.* [83] as displayed in Fig. 2.9c.

Trilayers composed of two NM layers in which a FM layer is inserted in between is afterwards proposed. In this type of STE, a dual conversion occurs owing to *i*) the spin current escape from both interfaces of the FM layer and to *ii*) the ISHE conversion in both NM layers of opposite spin Hall angle. This generates two THz transients that oscillate in phase in the thin layer limit. The layer happens in the optimized W/CoFeB/Pt trilayers, demonstrating about a factor $\times 3 - 4$

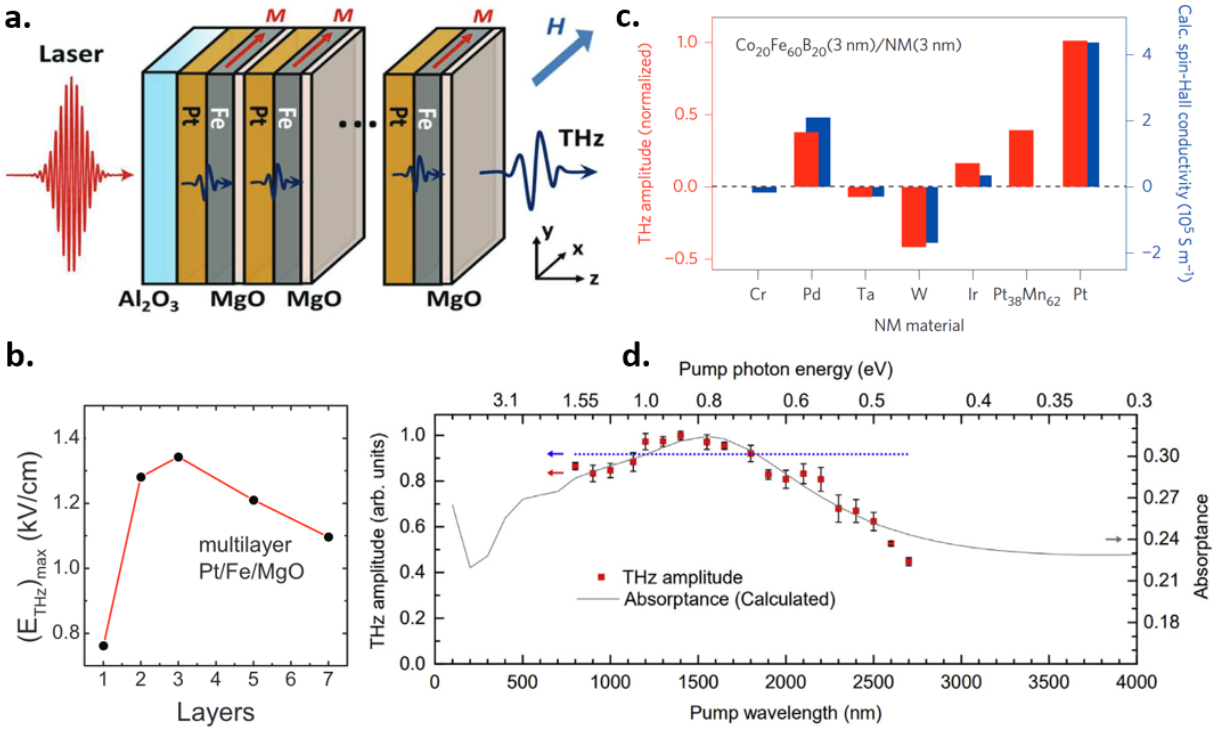

Figure 2.9: Beyond single STE bilayer. (a) Repetition strategy by stacking multiple Fe/Pt bilayers. (b) Result of the multilayer $[Pt/Fe/MgO]_N$ strategy demonstrating an optimal repetition around $N = 3$. (c) Review of the THz amplitude for various NM materials: Cr, Pd, Ta, W, Ir, PtMn alloy and Pt. (d) Dependence on the THz emission as a function of the pump wavelength. The dotted blue line represents the level of signal from the THz efficiency, independent on the pump wavelength. Adapted respectively from Refs. [84, 83, 144].

in THz amplitude compared to Co/Pt bilayer reference. Although those optimized structures are efficient for THz generation, they are not recommended of use in the case of THz spintronic spectroscopy as it would lead to uncertainties on the extraction of the relaxation timescales in complex multilayers [147]. Alternatives routes on the use of compensated magnets has been studied for efficient spintronic THz emitters [148].

Optimization of the thickness. In all structures, it is important to consider the optimization of the layer thickness in order *i*) to prevent a strong absorption of the generated radiation and *ii*) to efficiently manipulate the spin current conversion. Indeed in the latter case, it is assumed that the dynamical spin current is fully converted in the NM layer up to a thickness equivalent to the spin diffusion length l_{sf}, making useless extra NM material for thicknesses above the spin diffusion length [85].

Role of the interface. The peculiar role of the interface, whether it is for the spin-injection efficiency or for the interfacial spin-orbit coupling, is of crucial importance for STE. Wahada *et al.* [149] have studied the role of an insulating MgO inset between a ferromagnetic reservoir and a heavy metal from the $5d$ family and discussed the importance of such inset to avoid a loss of the spin transmission by interfacial spin memory loss in less than half-filed $5d$ material such as in Ta ($5d^3$). Alternatively, it has been shown by Gueckstock *et al.* [150] the role of the interfacial scattering by playing with various growth deposition like the pressure, annealing, the reverse growth (on the FM layer or on the NM layer first), *etc.* They reported that the skew-scattering mechanism is enhanced in those engineered interfaces and in particular in light elements (Al) which interdiffuses much more in the structure. This defect engineering is similar in the spirit to the previous work of Nenno *et al.* [151] and Li *et al.* [152]. Liu *et al.* [153] have

recently demonstrated the THz generation in prototypical Co/Si bilayers for the integration of STE in semiconductor optoelectronics THz devices. A metallic silicide layer seems to form at the interface, leading to a THz emission about 16% of Co/Pt bilayer reference. Contrary to the weak SOC of Si, the silicide interfacial layer would lead to a spin Hall angle about 1.6%. We will develop the more specific role of the interface in Chap. III.

Patterning and repetition layers An approach to optimize the THz emission of STE is to combine several repetitions of them in a serial structure. This has been firstly implemented by Yang *et al.* [84] in a Fe/Pt N repetition separated by a thin MgO barrier as shown in Fig. 2.9a-b. The purpose of the insulating barrier is to avoid *i*) the shunting of the generated current in the multistack and *ii*) the cancellation of the spin currents from both interfaces (destructive interferences in the THz electric field), while allowing radiation crossing in the interlayer. One expects the THz emission to scale with the number of repetitions N but the authors have reported a maximum enhancement around N=2 repetitions owing to the radiation absorption in the heterostructure. This trend has also been unveiled separately by Feng *et al.* [154]. We will see in more details in Chap. III that the repetition structure is also not ideal for the optimized STE W/CoFeB/Pt trilayer samples although we map a THz efficiency enhancement scaling linearly with N.

Impact of the substrate. Another advantage of STEs is that they can be deposited on a wide range of substrates: dielectrics, semi-conductors, *etc.* An important element to consider is the THz absorption which evolves with the THz refractive index n_s^{THz} of the substrate. Semiconductor substrates can also have an impact on the radiated THz with additional contributions owing to photo-Dember or surface-field effects. Also, they would possibly lead to an absorption of the NIR pump, depending on the bandgap value, which would prevent using designed STE in transmission configuration. In that regard, the NIR refractive index n_s^{NIR} is a key parameter to engineer. Some values of the THz and NIR refractive indices are reported in Annex A11. Alternatively, the role of the substrate is also important regarding the heat diffusion while working in the saturation limit of STEs and to that regard, it has been proposed by Vogel *et al.* [141] the use of Peltier-mounted heat dissipater substrates and we will propose a similar exploration path in Chap. VI.

3.6 Spectroscopy tool to probe the interface transmission.

Conversely, THz emission spectroscopy of magnetic multilayers recently revealed to be a technique of choice to probe the dynamical spin-injection and spin-conversion properties due to its many advantages: contact-free measurements, rapidity of the data acquisition, high averaging, efficient characterization, *etc.* with only few drawbacks.

Recently, THz emission arising from FM/HM multistacks has found an interesting research-oriented application in a dynamical spectroscopy of spin-related properties. For instance, Neeraj *et al.* [155] proposed to use THz spectroscopy to quantify the role of magnetic and crystalline ordering in the spin-injection and spin-scattering processes. Zhang *et al.* [156] and Agrawal *et al.* [157] proposed the use of the STE related phenomena to realize THz spintronic magnetometry to measure the in-plane anisotropy of a CoFeB layer by following the THz peak amplitude as a function of the applied magnetic field. In that way, they have been able to reconstruct the hysteresis loop and access the magnetic coercivity as one would have obtained concurrently using conventional vibrating-sample magnetometry (VSM). Similarly, Bulgarevich *et al.* [158] proposed a compact THz magneto-optic on-chip sensor using STEs.

However, the use of THz spectroscopy in magnetic multilayers is not free of limitations. Recently, Gorchon *et al.* [147] reminded that extracting spin-transport properties using THz emission spectroscopy can be a delicate task due to the THz optical absorption and that a careful

treatment of the signals and calculations of the absorption as a function of the conductivity are needed, especially in thick metallic multilayers.

Besides, one could legitimately ask if the comparison with conventional DC measurements is reasonable since the steady-state and transient transport can be different [159]. Indeed, the ultrafast pulse pump would result in an out-of-equilibrium regime where the adiabatic approximations can difficultly be made. Up to now, it is difficult to disentangle experimentally this effect and it is therefore commonly assumed that the dynamical properties are similar to the static properties (conversion at high frequencies, *etc.*). To tackle this, an actualized theoretical description would be valuable. However, it is to be noted that the interfacial transmission, which depends on the energy, evolves as the spin-mixing conductance near the Fermi level whereas it tends to evolve as the interfacial conductance $g_{\uparrow\uparrow} + g_{\downarrow\downarrow}$ for energies well above the Fermi level [160].

4 Novel spintronic THz emitters based on enhanced pure interfacial systems.

The search of novel STEs also includes to take advantage of novel interconversion properties in quantum materials. Topological insulators and 2D materials are predicted to exhibit a strong interfacial spin-charge conversion, possibly owing to the inverse Rashba-Edelstein effect as derived in Chap. I. Although several reports demonstrated the strong gain obtained via such interfacial systems for THz spintronics, the exact origin of the spin-charge conversion remains elusive. Indeed, the community opened a large number of debates about the inclusion of inverse Rashba-Edelstein effect as the conversion mechanism. Several hypothesis would discard the pure contribution of topological surface states, via for example the conversion on spin-polarized Rashba-like states or even in the bulk states of topological insulators. We will see in Chap. IV how we can try to answer this particular point on various topological insulator systems.

4.1 Rashba 2D electron gas and topological surface states of topological insulators.

Following the strong interest in Rashba 2DEG interfacial systems in conventional spintronics to achieve magnetization reversal via interfacial torques, Jungfleisch *et al.* [161] and Zhou *et al.* [162] concurrently started to look at the interfacial THz emission in Bi/Ag system and Fe/Bi/Ag. This is shown in Fig. 2.10a-b. They have reported that the Rashba-active interface owns a THz conversion efficiency about 20% of Pt ISHE. They also attribute circularly pump polarization dependence of the THz emission to two hypothesis: either the presence of interfacial surface potential that could lead to circular photogalvanic effects, or from inverse Faraday effect component $\mathbf{j}_{\text{IFE}} \propto \mathbf{m} \times (\mathbf{m} \times \sigma)$.

Following the idea of interfacially-mediated spin-charge conversion, researchers have also investigated additional interfacial systems carrying strong Rashba-Edelstein spin-charge conversion in the example of topological insulators based topological surface states. This has been performed starting in 2018 on Bi_2Se_3/Co [163], Bi_2Te_3/(Bi)/Co [164], Bi_2Te_3/Fe [165] or in $Bi_{1-x}Sb_x$ alloy [166, 167], well known in spintronics for the report of a large magnetic torque [54]. Alongside the search of more efficient THz emitters, THz spectroscopy of topological spintronic structures reveals also to be interesting to map the study the dynamical spin-injection and interconversion of semiconducting TI/FM structures [168]. As shown in Fig. 2.10c, the obtained THz emission in a Bi_2Se_3/Co [163] system due to spin-excitation, injection and conversion is an order of magnitude larger than non-linear effects in TIs (surge currents mostly) and even larger than the self-emission from a ferromagnet. Stepping forward topological insulators-based emitters is also of interest not only for the strong interfacial conversion expected but also to the reduced conductivity of the multilayer which allows a higher gain in the emission due to a

lowered wave absorption.

Alternatively, it has been reported the prototypical implementation of fully-interfacial system based on the combination of a 2D material and topological insulator Fe_3GeTe_2/Bi_2Te_3 [169] which makes the bridge with the last part of the interfacially-mediated THz systems. In those type of structures (shown in Fig. 2.10d-e), the THz absorption would even be reduced compared to the previous case of topological insulators. The conversion would be made on a ultimate layer thus leading a very small absorption and it can be envisioned to use 2D ferromagnetic layers to avoid additional absorptions.

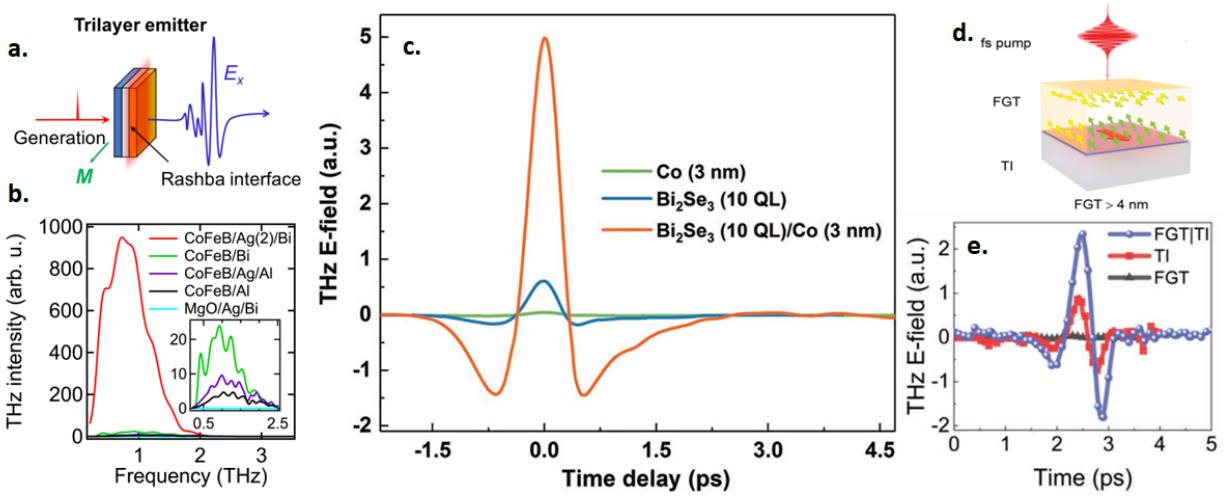

Figure 2.10: Interfacially-based spintronic THz emitters.. (a) Schematics of interfacial THz emitter based on Rashba interface. (b) THz emission from CoFeB/Ag/Bi compared to CoFeB/Bi, CoFeB/Ag/Al, CoFeB/Al and Ag/Bi control samples. A strong amplification by a factor $\times 50$ is measured experimentally. (c) THz emission based on topological insulator Bi_2Se_3/Co compared to Bi_2Se_3 and Co control samples. (d) Schematics of topological insulator/2D ferromagnet THz structure. (e) THz emission from Fe_3GeTe_2/Bi_2Te_3 compared to THz emission from pure Bi_2Te_3 and Fe_3GeTe_2. Left, middle and left panels are respectively adapted from Refs. [161, 163, 169].

4.2 Towards 2D materials THz heterostructures.

Indeed, 2D materials have recently attracted strong attention owing to their unique properties foreseeking them as ultimate spin-charge conversion layers [170]. One of their advantages is that they can be envisioned in an easily stackable and modulable Van der Waals component [171] to build efficient 2D interfacial systems. In particular, the family of transition metal dichalcogenides (TMDC) follows the formula MX_2 where M is the metallic compound (for instance W or Mo) while X_2 represents the dichalcogenide (ex: S, Se, Te). Compared to graphene, TMDCs present an opened bandgap in the eV range, which can be tuned depending on the TMDC flexible composition, opening up new perspectives for opto-electronics and opto-spintronics [172]. Research has firstly focused on their strong non-linearities, comparable to bulk semiconductors [173] allowing efficient second harmonic generation for instance in WSe_2 [174]. Due to their non-linear optical properties, investigators are also starting to envisioned TMDCs as efficient broadband THz detectors, here with the example of $PtTe_2$ material [175].

For these perspectives, transition metal dichalcogenides (TMDC) has been reported to present Rashba spin-splitting in monolayers [176] opening efficient interfacial spin-charge conversion in those layers. For instance, band spin-splitting induced by the spin-orbit coupling ranges about hundreds of meV in the valence band to few meV in the conduction band of several

TMDCs [177]. It is thus only recently that 2D materials and in particular TMDC has entered into the domain of spintronic for building efficient interfacial spin-charge conversion systems [170] and already found various applications in spintronic devices such as in tunnel junctions with an efficient spin-filtering [178].

On the other hand, Van der Waals heterostructures with a FM reservoir study by use of THz emission spectroscopy only started, for instance in MoS_2/Co [179], Co/WSe_2 [180], Fe/$NbSe_2$ [181] or using 2D hybrid metal halides [182]. Those materials are particularly appealing for seeking inverse Rashba-Edelstein effect. This type of conversion is highly debated in the community. For instance, Cheng *et al.* [179] efficiently injected spin through the semi-conducting interfacial $MoSe_2$ TMDC. Recently, Nadvornik *et al.* [181] concluded that the main spin-charge conversion occurs in the bulk of $NbSe_2$, with a negative spin Hall angle θ_{SHE} ranging between -0.2% and -1.1%. TMDCs thus offer and interesting platforms for studying interfacial spin-charge as a function of their various properties which depends on their phase: 2H is the semi-conducting phase and 1T is the (semi-)metallic phase and will be studied in the scope of this thesis with WSe_2 material (Chap. IV).

5 Alternatives research paths for higher THz dynamics.

5.1 Probing high spin-polarization materials.

Weyl semi-metals: spin-polarization and strong spin-orbit coupling. Due to the requirement of the direct magnetization M in the THz figure-of-merit, the search of higher spin-polarization materials is highly desirable to increase the net THz emission. For a Weyl semi-metal, the Fermi level ideally cuts one spin reservoir making thus the spin-polarization $P = 1$ as shown in Fig. 2.11. In practical cases, small contributions of the majoritary spin reservoir can reduced the total spin-polarization but the reported spin-polarization are still consequent compared to ferromagnets, as reported in Table 2.11. Research focused on Heusler alloys for which the spin properties depend strongly on the crystalline structure. The structural properties of Heusler alloys for the Co_2XY material family can be dissociated in three phases: the L2 fully ordered ($Fm\bar{3}m$), the B2 partially-ordered and the disorder A2 phase, respectively with the loss of the semi-metallicity and the decrease of the spin-polarization [183]. Besides, due to the strong orbit-coupling in Weyl semi-metals (absence of bandgap), a high anomalous Hall effect is expected intrinsically from this class of materials, opening interesting perspectives for high spin-polarization and spin-charge conversion materials [184].

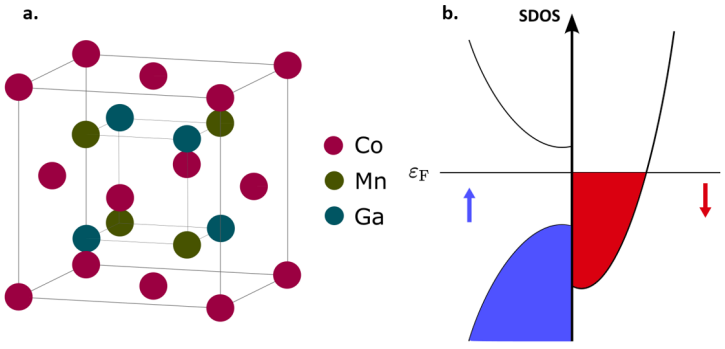

Figure 2.11: Heusler materials. (a) Phase structure of Heusler materials from the $Fm\bar{3}m$ point group, and (b) high spin-polarization at the Fermi level. The example of Co_2MnGa is presented.

STE-based Weyl semi-metals. FM/HM heterostructures have started to be investigated in the literature where the ferromagnetic layer is switched by a Weyl semi-metal. Heidtfelt *et al.* [185]

reported the THz emission owing to $Co_2Fe_{0.4}Mn_{0.6}Si$/HM for various HM cappings (Ta, Al) although the more efficient case is reported for the optimized Pt. It seems admitted that the spin-charge conversion arises via the ISHE mechanism. Gupta *et al.* [183] presented the THz emission from Heulser-based STE Co_2FeAl/Pt with a bandwidth going from 0.2 to 4 THz. The THz amplitude is sizeable compared to Fe/Pt reference and even above for optimized Pt(4.5nm)/Co_2FeAl(3nm). They however warn that the semi-metallic behaviour can be lost in the ultralow thickness limit due to the phase growth issues (ordering loss). The self spin-charge conversion in Weyl semi-metals is not yet addressed in THz Weyl-based STEs. We will propose a similar study with Co_2MnGa in a dedicated part of Chap. III.

System	Co_2MnGa [186]	Co_2FeAl [187, 183]	Co_2MnSi [187, 183]	Co_2MnGe [187, 183]
Spin polarization P (%)	55	86	59-66	70

Table II.2: Spin-polarization of selected Heusler materials: Co_2MnGa, Co_2FeAl, Co_2MnSi and Co_2MnGe.

5.2 Antiferromagnetic based structures explored by THz probes.

We discuss now the more specific role of antiferromagnetic materials explored by THz probes [188]. In antiferromagnets, the induced $\partial\mathbf{m}/\partial t$ is weak leading to a low THz amplitude. However, antiferromagnets present higher spin dynamics lying in the THz range compared to ferromagnets (GHz), thus presenting a strong interest for narrowband THz STEs and resonant THz manipulation [189]. Although we explore this topic in a dedicated chapter (Chap. V), we offer in this part recent explorations about THz antiferromagnets.

Metallic antiferromagnets. In metallic antiferromagnets, the interfacial conductance $g_{\uparrow\uparrow}$, $g_{\downarrow\downarrow}$ (as the pump excites far above the Fermi level) with metallic layers is sizeable, allowing to probe the spin-charge conversion generated by the injection of an ultrafast spin current from a ferromagnetic reservoir pumped via optical excitation. The converted THz spin current has been studied in various AFM/FM systems such as in Mn_2Au/Co [190], IrMn/NiFe [191], $IrMn_3$/NiFe [192] and $IrMn_3$/CoFeB [193]. Interestingly, Gueckstock *et al.* [191] reported shorter propagation distances for the spin current on THz frequencies, compared to the GHz range (typically a factor $\times 4$). The obtained THz response is shown in Fig. 2.12. Interestingly, one can obtained the ultrafast spin-current time profile from THz transient extraction (method described in Section III.2.4). Recently, Wu *et al.* [193] proposed a magnetic field-free THz emitter where the direction of the FM magnetization is pinned via exchange bias with an adjacent $IrMn_3$ antiferromagnet. They successfully demonstrated a quadri-layers sample CoFeB/$IrMn_3$/CoFeB/W where the obtained triple interconversion (two times by ISHE in $IrMn_3$ and one time by ISHE in W) emits a THz signal about a factor $\times 1.6$ compared to the W/CoFeB/Pt reference trilayer.

Exchange bias.

In a ferromagnet/antiferromagnet bilayer, the exchange bias is the pinning of the ferromagnet interfacial magnetization due to the strong exchange interaction with the antiferromagnetic layer.

Insulating antiferromagnets. In insulating antiferromagnets, the spin-mixing conductance $g_{\uparrow\downarrow}$ (as the pump cannot pumps the electronic subsystem but the magnon chemical potential instead) is smaller with metallic reservoir compared to ideal metal/metal interfaces. However, due to a lower damping, the THz modes of antiferromagnets are expected to live longer in the system and the magnons to travel on longer distances, making insulating antiferromagnets promising THz narrowband devices. Very recently, Qiu *et al.* [194] demonstrated the ultrafast generation of THz spin current from insulating antiferromagnetic NiO and detected via the ISHE in NiO/Pt (or

W) bilayer, as reproduced in Fig. 2.12c-f. They linked the emission to the excitation of the Néel order via optically-induced effect (inverse Faraday effect) following the obtained dependence presented in Fig. 2.12e-f as a function of the sample azimuth and pump polarization. Alternatively, Qiu *et al.* [195] reported the THz spin current dynamics in α-Fe_2O_3/Pt. In the class of canted antiferromagnets, one could expect larger spin-pumping signals at GHz frequencies due to the presence of a small canted magnetic moment [196]. Both systems will be widely discussed in the scope of our studies presented in Chap. V. To finish, it has been envisioned to use antiferromagnets as narrowband THz emitters by the fine control of magneto-striction interactions [197].

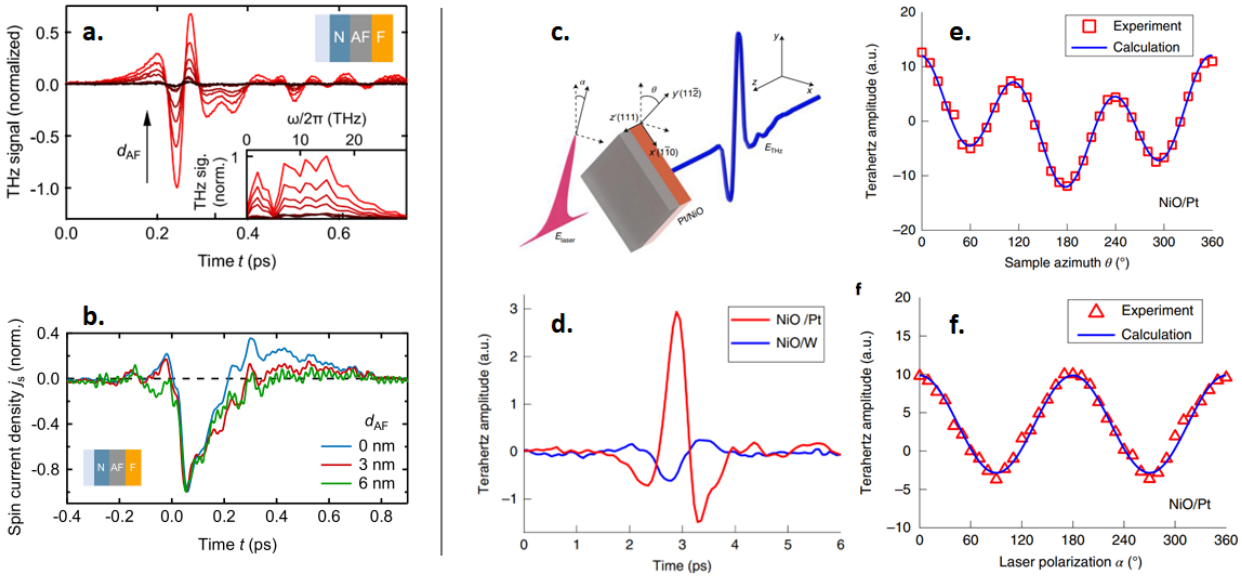

Figure 2.12: Antiferromagnetic-based THz heterostructures. (a). THz signal from Pt/IrMn(d_{AF})/NiFe structures with d_{AF} ranging from 0 to 12 nm, and (b) derived ultrafast spin current for $d_{AF} = \{0, 3, 6\}$ nm. (c) THz emission spectroscopy of NiO/Pt bilayers in transmission geometry. (d) THz signals from NiO/Pt and NiO/W. (e) THz amplitude as a function of the sample azimuthal angle and (f) pump polarization angle from NiO/Pt bilayers. Left and right panels are respectively adapted from Refs. [191, 194].

6 Enhanced spin-based THz functionalities.

As the proof-of-concept of efficient THz emitters by spintronic means has been given in 2016, research also focused on ways to efficiently functionalize the emitters looking forward for strong industrial perspectives. Several enhancement paths have been explored: the NIR pump collection enhancement, the THz enhancement from the charge current using antenna, cavities and polarization-control. We will provide in Chap. VI perspectives about THz amplitude enhancement transposed from the photonic strategies on THz frequencies (anti-reflective coating and THz cavities) to the theoretical prediction of a novel functionality hosted by spintronic THz emitters: the narrowband emission via spintronic photomixing.

6.1 Near-infrared cavities.

Current spintronic THz emitters only weakly couples with the pump radiation, in such way that a lot of NIR pumping energy is lost. Many strategies have be envisioned to have a more efficient pump catching, starting with the use of Bragg mirror as reported by Herapath *et al.* [142]. In this strategy shown in Fig. 2.13a-b, TiO_2/SiO_2 layers of hundreds of nm, repeatedly multistacked, are optimized for a pump wavelength around 1030 nm. The authors reported a THz electric field enhancement about a factor $\times 2$, corresponding to a power enhancement of $\times 4$. A similar idea is

also proposed by use of NIR photonic crystal by Kolejak *et al.* [198].

Another strategy developed by Jin *et al.* [199] is the use of similar NIR and THz refractive indices of the substrate to efficiently build cascaded STE. In that way, the group velocity of the pump in the structure would be similar compared to the THz group velocity and reduce the destructive interference between two consecutive STEs. The experimental implementation is performed on polyethylene terephthalate (PET) plastic substrate of NIR and THz refractive indices respectively of n_{NIR}=1.6 and n_{THz}=1.75. It leads to a THz field enhancement about +55% ($\times 2.4$ in power) and the authors also report the use of a resonator metasurface to control the THz polarization derived from flexible STEs.

6.2 Antenna-enhanced spintronic emitters.

The starting point: the charge current. Enhancing the THz radiation has been proposed before by the improvement of the SCC process, the spin-polarization reservoir, the NIR pump capture rate, *etc.* However, the final step generating the THz radiation in free-space is the charge current j_c and a lot of research has focused into this point that is explored in this part.

First, Chen *et al.* [200] proposed to combine the SCC-related THz emission with a biased antenna-based semi-conductor radiation similar to PCAs deposited on top of Co/Pt. Interestingly in this configuration, the advantage of longer electron-hole recombination dynamics to selectively enhance the low frequency profile of the overall THz radiation. An enhancement of two orders of magnitude of the spintronic radiation is reported in the 0.1-0.5 THz range using this method.

Generated THz charge current and confinement effects.

It is important to also discuss the role of the charge current confinement. First, the current is generated only on the NIR pump spot. The obtained THz power is thus proportional to the pump power density P_{pump}/d^2, where d is the pump diameter [201]. Secondly, as one can envision patterning of the STE into separated STE plots (by lithography for instance), the THz power would be integrated as a function of *i*) the number of plots under the pump beam and *ii*) for spot size greater or equal than the plot size. Lastly, considering the report of Yang *et al.* [84] who proposed the use of etched grating stripes of STE, followed by Jin *et al.* [202] as shown in Fig. 2.13d. It is found that charge current confinement effects allow to tune the peak THz frequency. This is explained in particular for thin stripes, where the THz electric field creates an additional sign-opposed electric field $E_b(t) = U(t)/\varepsilon l_{\text{eff}}$ arising from charge accumulation $U(t)$ at the stripe lateral edges. Note that ε is the dielectric constant and l_{eff} is the effective length of charge oscillations. It is thus important to consider not too thin STE stripes to avoid such detrimental effects on the amplitude despite the ability to tune the spectrum peak frequency [203].

THz antenna-coupled STE, resonators and micropatterning. Around 2019, researchers have started to transpose THz antenna and emitter design to STEs, which are inspired from the previous THz technologies (semi-conductors).

Nandi *et al.* [201] first reported in 2019 the use of a H-dipole antenna coupled with a W/CoFeB/Pt STE. The typical dimensions of the implemented H-dipole antenna are the length l_a = 200 µm and the width w_a = 10 µm. The authors report a more efficient coupling in the far-field regime of the STE-coupled antenna via an effective THz impedance that we briefly discuss. First, the generated charge current is proportional to $j_c \propto P_{\text{pump}}/d^2$ where d is the pump spot

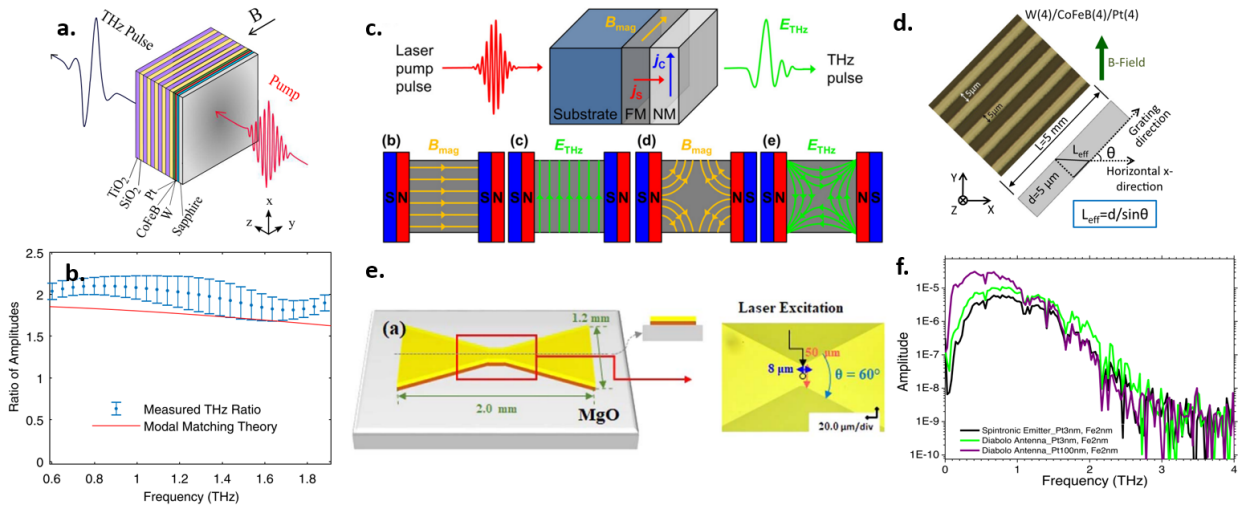

Figure 2.13: Enhancing spintronic THz emitter functionalities. (a) Illustration of NIR Bragg mirror for STE. (b) Field enhancement obtained on the Bragg mirror-based STE, as a function of frequency. (c) THz polarization by magnetic-field space profile tailoring. (d) Grating of spintronic THz emitter for polarization control, charge confinement and field enhancement. (e) Bow-tie antenna-coupled spintronic THz emitters. (f) Experimental enhancement of bow-tie STE antenna shifted towards lower frequencies. Left, top and bottom panels are adapted respectively from Refs. [142, 204, 202, 205].

diameter. To account for the distribution of the charge current in the arms of the antenna, we call $Z_\mathrm{a} = R_\mathrm{a} + iX_\mathrm{a}$ the complex impedance of the antenna composed of the resistance R_a and reactance X_a, the authors proposed the following figure of merit:

$$\frac{P_\mathrm{AC\text{-}STE}}{P_\mathrm{STE}} \propto \frac{\eta_\mathrm{prop}\eta_\mathrm{circ}R_a}{(789\ \Omega)\ n_s}\left(\frac{2\pi c}{\omega w_a}\right)^2 \quad \text{with} \quad \eta_\mathrm{circ} = \frac{R_s^2}{(R_s+R_a)^2+X_a^2} \tag{E2.27}$$

between the antenna-coupled (AC) and no-antenna derived powers, with n_s is the substrate refractive index, c is the light velocity in vacuum and $\eta_\mathrm{prop}(\omega)$ is the frequency-dependent term accounting for the propagation of the THz pulse from the emitter to the detector. In this framework, it has been neglected the term accounting for the large-scale illumination case. Experimentally, the authors reported an enhancement factor in field about $\times 2.4$ (about $\times 5.8$ in power) for the H-dipole antenna. The reported field enhancement for the slotline antenna is about $\times 1.5$ ($\times 2.25$ in power), with a slight bandwidth change towards lower frequencies. For a detailed derivation, the interested reader have to refer to Ref. [201]. The authors also reported the use of a slotline antenna (two separated by a width w_a = 25 µm following Ref. [201]).

Talara *et al.* [205] reported in 2021 a diabolo-shaped spintronic THz antenna from Fe(2nm)/Pt(3nm) bilayer as shown in Fig. 2.13e-f. In this realization, the bow-tie central design is 50 µm wide at the center with a half-angle of 30° from the longitudinal axis, extending over millimeter wide antenna. The authors reported a field enhancement by a factor up to +50% ($\times 2.25$ in power) for thin Pt flares (3 nm) and up to +100% ($\times 4$ in power) for thick Pt flares (100 nm). The authors linked the THz enhancement by *i*) the optimized outcoupling of the THz radiated by the STE with free-space and *ii*) the change of the THz impedance offered by the antenna. Connecting an antenna of impedance Z_a on top of a STE of characteristic impedance Z_s would likely give an impedance $Z = Z_\mathrm{STE} + Z_\mathrm{antenna}$ which would have the effect to offer an alternative escape to the electronic current out of the pumped area and thus optimize the coupling of the THz radiation with free-space. The same group reported very recently a field enhancement of $\times 4.2$ (power enhancement $\times 17.6$) using a rectangular antenna [206]. It has also been reported the use of horn-antenna to control the directivity of the THz emission, thus increasing the collected THz amplitude by a factor $\times 38$ (amplitude enhancement about $\times 6$) centered around 2 THz [207].

Micropatterning and plasmonics. An alternative approach to tune the emission properties is the development of micropatterned STEs. Rahje *et al.* [208] reported the use of plasmonic structures to enhance the radiation of STEs by used of U-shaped split-ring resonators in a large-scale array. The targeted objective is here to tailor the obtained THz frequencies depending on the shape of the resonator. The combination of STE and plasmonics via gold-structured nanorods has also been proposed in 2022 by Liu *et al.* [209], demonstrating a field enhancement up to +140%.

In the same spirit, Song *et al.* [210] patterned a STE following a subwavelength-dimensioned grating pattern: aligned STEs blocks of length $l \simeq 20 - 180$ µm, width w=20 µm and separation Δw = 10 µm. The grating pattern allowed to tune the THz amplitude, bandwidth and center frequency by use of a better charge confinement but the authors did not report a emission enhancement, mostly likely due to a weak coupling with free-space due to the sub-wavelength patterning. It is an interesting tool to select the emission properties by affecting the generated charge current, independently of the spin dynamics ruled by the FM and HM layers composing the STE. It has also been reported the microfabrication of STEs to tailor the polarization properties of STEs [203]. This makes the transition with the polarization control and high-rate modulation of the THz emission obtained from STEs.

On-chip THz devices. One strong application objective of THz spintronic emitter will be the integration with on-chip devices. Due to the limitation of the actual electronic, no measurement device can currently measure ultrafast dynamical electrical current at THz scale (the cutoff is rather about several GHz in some vector network analyzer (VNA) or oscilloscopes even if some low THz solutions exist, at a certain cost and rarity). In 2021, Hoppe *et al.* [211] demonstrated that an on-chip waveguide-based device can launched a THz wave derived from a spintronic THz emitter, where the THz pulse is concurrently measured by electronic detection (<40 GHz) and optical detection (EOS). It opens perspectives for on-chip integration of spintronic THz devices.

6.3 High-speed THz modulation rate and polarization control.

We now focus on recent research about polarization control of STEs and towards high frequency modulation of the obtained THz radiation. These functionalities, yet lacking for STEs, are of particular relevance for non-destructive applications like ellipsometry. For instance in PCAs, an applied electrical bias accelerates the photoexcited carriers and this bias can be modulated, typically at frequencies of the order of tens of kHz. In STEs however, this electrical approach is not yet fully implemented and one directly thinks of the inner sample magnetization to dynamically tune the THz electric field.

Quick words about ellipsometry.

Ellipsometry is a widely used in material research and industry for thickness and quality control. A THz signal of controlled polarization is sent onto the studied sample. The interaction with the THz beam and the sample changes the reflected THz polarization properties of the THz and are thus detected by used of crossed-configured wire grid polarizers. Interestingly, no reference samples are needed in ellipsometry techniques. Having a THz source of tunable polarization is of great interest to increase ellipsometry measurements sensitivity [97].

Modulating by applying an external magnetic field. The first explored path in the community is the external control of the polarization using the applied magnetic field. The initial demonstration has been reported by Hibberd *et al.* [204] followed by Niwa *et al.* [212], where a particularly shaped magnetic field profile allows to generate the targeted THz polarization of the

STE, up to a quadrupole-like polarization profile as shown in Fig. 2.13c. THz electric fields about 15 V.cm^{-1} are reported, and the authors predict that the focusing of the quadrupole-like magnetic field profile would increase the longitudinal component of the THz polarization even further, allowing a theoretical prediction approaching the order of 1 MV.cm^{-1} in such configurations.

Recently, Gueckstock *et al.* [213] demonstrated experimentally the feasibility of high-speed modulation of THz generated by STEs with a modulation contrast above 99% for all the spectral bandwidth of STEs (up to 30 THz) and a modulation rate up to 10 kHz. In details, they applied a time-dependent external magnetic field $\mathbf{B}(t)$ which is no more stationary as preferentially set in spectroscopy experiments. This method is well-suited for magnetic systems without magnetic anisotropies. A particular tailoring of the THz polarization by applying an extra stationary magnetic field $\mathbf{B} = \mathbf{B}_0 + \mathbf{B}(t)$ is also reported, as we always have $\mathbf{E}_{\text{THz}} \perp \mathbf{B} \perp \mathbf{e}_z$ (THz polarization rules).

Magneto-electric voltage for modulating the magnetic anisotropy. An innovative approach very recent emerged where the application of a twisted external magnetic field is not needed. Instead, in the approaches reported concurrently by Lezier *et al.* [214] and Chaurasiya *et al.* [215], an electrical bias serves as a control of the magnetic anisotropy and in particular by the use of magneto-striction. The applied electrical bias shrinks or expands the PMN-PT substrate ($(1-x)$Pb($Mg_{0.33}Nb_{0.66}$)O_3 $-$ xPbTiO_3) by strain piezoelectricity which launches efficient magneto-striction in the magnetic layer and thus changes the magnetic anisotropy. This approach would potentially enable the THz modulation at even higher frequency rates owing to the large frequency range accessible by electrical control (compared to magnetic field switching timescale). The electric control of STE polarization by magneto-striction induced by PMN-PT has also been evidenced by Agrawal *et al.* [216].

This approach followed the study of Kolejak *et al.* [217] in which the authors reported a full rotation of the THz polarization by adapting the magnetic isotropic layer in STEs by an engineered FeCo/$TbCo_2$/FeCo uniaxial anisotropy buffer. This creates an in-plane easy-axis for the magnetization that can vary from 360°only by applying a variable magnetic field perpendicular to the small anisotropic axis. In a similar spirit, Hewett *et al.* [218] recently demonstrated the polarization control of a STE by only controlling the magnetic field strength and not with the magnetic field direction. This is done by maximizing the uniaxial magnetic anisotropy of the FM layer during deposition and afterwards by applying a magnetic field in the direction perpendicular to the easy axis.

New routes for polarization control. Another approach uses the spatial distribution of the magnetization in micrometer-wide plots shaped from a magnetic layer. Indeed, Wu *et al.* [219] reported the polarization control of the THz plot emitters as the magnetic texture changes at the edges (border effects). Moreover, the application of a bias magnetic field allows to tune from on-to-off state the THz emission leading to the possibility of high modulation rate of STEs by tuning only the field strength. The same path has also been explored numerically by Schulz *et al.* [220]. Alternatively, the use of synthetic antiferromagnets [221, 222] by interlayer exchange coupling has been reported by several groups to control the THz emission of synthetic structures via thermal control [223] or magnetic control [224] of the THz polarization of STEs.

Chiral THz spintronics.

It has been recently envisioned the use of STE to generate chiral THz radiation, where the THz polarization varies as a function of time which makes the output pulse to carry an angular momentum, to probe for instance several chiral materials or molecules. Typically, it is done by carefully engineering the magnetization of the STE as a function of time and the interested reader can look at several references listed here [165, 225, 226, 220].

7 Envisioned THz applications using spintronic heterostructures.

7.1 Near-field free-space imaging.

The ease of depositing metallic STE allow to envision high resolution near-field free-space imaging with STEs in close contact with the patterns to image. For instance, Stiewe *et al.* [227] proposed to image a 100 nm thick Au plane deposited in a close contact with the STE separated by an insulating layer, as shown in Fig. 2.14a-b, thus alloying to go below the diffraction limit. Similarly, Chen *et al.* [228] proposed the near-field imaging of reconfigurable arrays (ghost imaging) below the sub-diffraction limit and Li *et al.* [229] proposed the microscopy of nanostructured gold nanorods deposited on a THz spintronic emitter. Complementary to the imaging of near-field structure geometry, an important step in biological imaging (biodetection) has been realized with the terahertz spectroscopy of cancerous cells with W/CoFeB/Pt STE by Bai *et al.* [230] (Fig. 2.14c) or on beetle exoskeletons presenting chiral surface microstructures using topological-based STE [165].

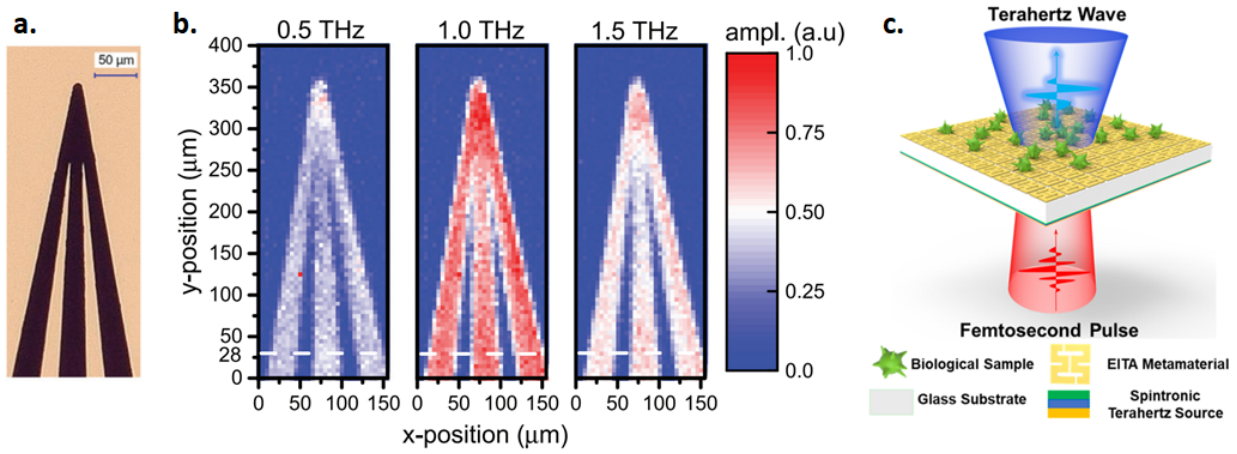

Figure 2.14: THz imaging using spintronic THz emitters. (a) Optical image of the metallic inverted pattern to image. (b) THz near-field imaging of the same metallic structure at 0.5, 1 and 1.5 THz. (c) Proof-of-concept of THz near-field bio-sensing of cancerous cells using a spintronic THz emitter. Adapted respectively from Refs. [227, 230].

Towards THz detection using spintronic heterostructures. In a perspective, the use of THz spintronic structures shall not only be limited to the emission operation but also for detection purposes. Owing to the bandwidth advantages of magnetic heterostructures, one could expect to measure signals from the hard THz range to above 20 THz due to the absence of phonon absorption in thin metallic layers, unlike in non-linear crystals which limits the detection bandwidth of electro-optic sampling. The detection performances should however need to be compared with PCA-based detection (sensitivity down to equivalent measurable electric field about 100

mV.cm^{-1}) or non-linear crystal based detection to be envisioned as a promising THz detection method [88].

Insertion of this thesis work with the state-of-the-art.

In summary, THz spintronics offer a wide possibility of novel physics (interfacial conversion, topological materials, antiferromagnetic, *etc.*) and applications. This motivates the deep study of THz spintronics in the context of this thesis work. In particular, we will dedicate each chapter to a specific research area, to know:

- in Chapter III, we will provide a fundamental understanding of the THz radiation via the so-called wave-diffusion model. We will be able to propose a emission figure-of-merit and from this updated understanding, we will provide different studies about enhancing the extrinsic contribution of the spin-charge conversion in spin Hall alloys (Au:W), using repetition of STEs multilayers and the strategy of spin-sink (Au:W). We will also propose to study high spin-polarization material with Heusler alloy Co_2MnGa.
- in Chapter IV, we will develop spintronic THz emitters based on topological insulators. Owing to the strong interfacial spin-orbit coupling of such materials, the spin-charge conversion is enhanced and expected to happen on topologically-protected surface states via the inverse Rashba-Edelstein effect. We will shed light on both emission understanding and high performance potential in $SnBi_2Te_4$/Co, $Bi_{1-x}Sb_x$/Co and Bi_2Se_2/WSe_2/Co topological insulators based emitters.
- in Chapter V, we will evidence the THz narrowband emission features from antiferromagnetic-based NiO/Pt (001) bilayers. We will discuss the origin of this contribution that has not been evidenced by the literature before in (111) oriented thin films. For that, we will consider the role of ultrafast spin-phonon interactions, and in particular magneto-strictions and incoherent phonon propagation.
- in Chapter VI, we will present perspectives about the optical and THz engineering of STEs. In particular, we will implement THz anti-reflective coatings and THz cavities. We will also demonstrate the theoretical working of spintronic THz photomixing.

III

Metallic spintronic THz emitters: modelling and spectroscopy of spin-orbit multilayers.

This chapter reviews a dual aspect of metallic spintronic THz structures: their emission power enhancement and the use of dedicated metallic structures acting as active spectroscopy tool to reveal information about the dynamical properties of the injected spin-current and spin-charge conversion.

In a first part, we discuss the main trends of THz emission from SCC within metallic bilayers or trilayers, with SCC relying on the ISHE and/or IREE mechanisms. For that goal, after having introduced the main concepts of the electronic diffusion and relaxation (Boltzmann transport, spin relaxation and spin diffusive regime) together with the ability to use them at sub-picosecond timescales, we present in more details a simplified picture, the so-called *wave-diffusion* model able to explain in a simple way the main features of the spin-charge related THz transient generation. We then check the validity of our numerical approach from continuous (steady-state) regime, continuous wave and pulsed optical pump regime by solving numerically the constitutive coupled equations in bilayers.

We then address in a second step different experimental situations that we will try to correlate to the electron dynamics or diffusion in the corresponding metallic multilayers. For that goal, we will use the THz emission spectroscopy technique that we will introduce in a second part. This will explicitly also show the power of THz emission spectroscopy technique for evaluating the efficiency of the spin-injection and spin-charge conversion in active spintronic interfaces.

In particular, we propose, in a first part, experimental investigations on transition metal-based structures by *i*) varying the heavy metal layer and thickness and by stacking multiple repetition of the standard spintronic THz structure in bilayer Co/Pt and trilayer W/Co/Pt. We will then propose *ii*) the use of an additional layer playing the role of a so-called spin-sink to avoid detrimental back-scattering at the converter interface. We finally study *iii*) the role of the ferromagnetic reservoir on the injected spin-polarization and obtained THz signal enhancement.

We acknowledge the collaboration with T. H. Dang and J. Boust for participating in the wave-diffusion model development. We acknowledge the collaboration with L. Perfetti's group for the study probing the interfacial spin-current properties. We acknowledge the collaboration with S. Krishnia who performed the harmonic Hall voltage measurement on the spin-sink samples. We acknowledge the collaboration with C. Felser's group for the epitaxial growth of higher spin-polarization Co_2MnGa material.

1 Modelling of optically-induced spin currents and THz transients.

We developed in this part the wave-diffusion model applied to spintronic THz emitters via a numerical finite difference time domain model deriving the THz response from the ultrafast near-infrared pumping. This work has been published in Appl. Phys. Rev. [231].

Motivations. To account for the ultrafast spin current generation by short optical pulses, several models have been proposed such as the injection of hot (photo-excited) electrons or the spin-pumping in $sp-d$ interactions picture [232, 233]. However, those models lack the role of the spin-orbit interaction in the electronic transmission and a full-integration with spin-charge conversion (SCC) mechanism to account for the THz generation. For that goal, we thus propose in this first part to account for a simple picture of the THz radiation mechanism by integrating the ultrafast demagnetization model to a dynamical spin-charge conversion and free-space radiation of the generated charge current. This simple picture will give us the possibility to propose the design of more efficient THz spintronic emitters: we will first study numerically the role of several parameters as the interface parameters or the choice of the material for instance. From this study, we will establish a theoretical ideal profile and we will propose, in the second part of this chapter, their experimental implementations.

Accounting for the optically-induced spin-current generation: spin pumping and superdiffusive models. The employed models are various and are including rich but complex physics such as secondary-source generation and multiple reflections derived in the superdiffusive model [80, 74], the electron-magnon interactions [233] and supporting tools such as the transfer-matrix techniques [151, 234]. In the superdiffusive transport regime, we have $j_s \propto -\partial\mathbf{m}/\partial t$ and consider initially high velocities after pumping (order of $v \simeq 1$ nm.fs^{-1}) with relaxation processes exciting low-energy carriers. The superdiffusive transport thus acts numerically as a second-order pumping $\mathcal{P}^{(2)}$. Although this model successfully reproduce the hot-electron spin current, it lacks of interfacial transmission and loss description, thus motivating our algorithm development on the basis of the spin-orbit generalized wave-diffusion model. It is however quite shared now that, whether superdiffusion is included or not, the same physical origin drives the demagnetization process and the spin current generation, according to:

$$\mathbf{j}_s(t) \propto \Delta\mathbf{m}(t) \propto -\frac{\partial\mathbf{m}(t)}{\partial t} \tag{E3.1}$$

The starting point: the Boltzmann transport. We start with the Boltzmann equation which account for the dynamics of a system put out of its equilibrium state by an external source term $\mathcal{P}_\sigma(\mathbf{r},\mathbf{k},t)$ which depends on the spin σ. Boltzmann transport equations are often solved in a single-particle (or particle-in-cell) model [235] and can be written as:

$$\left[\frac{\partial}{\partial t} + \frac{\hbar}{m^*}\mathbf{k}\cdot\nabla_\mathbf{r} + \frac{1}{\hbar}\mathbf{E}_\sigma(\mathbf{r},t)\cdot\nabla_\mathbf{k}\right] f_\sigma(\mathbf{r},\mathbf{k},t) = \underbrace{\mathcal{P}_\sigma(\mathbf{r},\mathbf{k},t)}_{\text{source term}} - \underbrace{\frac{f_\sigma(\mathbf{r},\mathbf{k},t)}{\tau_\sigma(\mathbf{r},\varepsilon)}}_{\text{in-scattering}} + \underbrace{\sum_{\sigma,\sigma'}\int d^3k' w(\mathbf{r},k',\sigma';\mathbf{k}) f_\sigma(\mathbf{r},k',t)}_{\text{out-scattering}}$$

where $\mathbf{E}$ is the possibly present electric field and $f_\sigma = f_\sigma^0 + \phi_\sigma$ is the distribution function which can be separated by an equilibrium part $f_\sigma^0(\varepsilon)$ and a non-equilibrium part ϕ_σ. It represents the spin and time-dependent distribution function in space ($\mathbf{r}$) and in the reciprocal space ($\mathbf{k}$). $\mathcal{P}_\sigma(\mathbf{r},\mathbf{k},t)$ is the pump term addressing the $d \rightarrow sp$ optical transitions and $\hbar$, m^* are respectively the reduced Planck constant and the effective electron mass. The system returns to its equilibrium following two scattering event types as identified in Eq. (E3.2). First, an in-scattering

term describes the spin-dependent scattering between hot photoexcited electrons with a spin-dependent diffusion time $\tau_\sigma(\mathbf{r}, \varepsilon)$ which is dependent of the energy ε. The second term describes the out-scattering term which accounts for the probability $w(\mathbf{r}, k', \sigma'; \mathbf{k})$ of diffusion in $\mathbf{k}$ per unit volume. We will use the Boltzmann scattering formalism to determine the dynamical transport of hot spin-polarized electrons in multilayers after an external ultrafast pulse pump of duration τ_p. In this picture, we treat both elastic and inelastic scattering times on a equal footing.

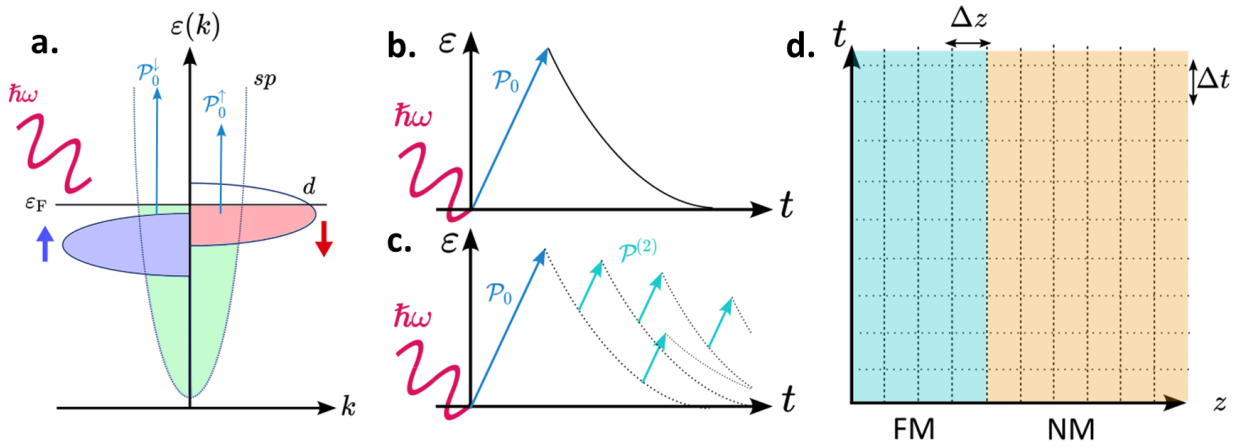

Figure 3.1: Illustration of the excitation and relaxation mechanisms. (a) Representation of the photo-excitation of hot spin electrons via the $d \rightarrow sp$ transition. Scheme of the electronic energy *vs.* time for (b) the diffusive relaxation processes and (d) the superdiffusive relaxation processes. (d) Representation of the finite difference time domain resolution principle.

1.1 Numerical implementation: the wave-modelling.

Laser-induced ultrafast demagnetization as the pumping source. To reproduce the $d \rightarrow sp$ transition shown in Fig. 3.1, we assume the femtosecond pump profile to follow a Gaussian shape:

$$\mathcal{P}_0(\sigma, \mathbf{r}, t) = s_\sigma \frac{A}{\sqrt{2\pi\tau_p^2}} \exp\left(-\frac{(t-4\tau_p)^2}{2\tau_p^2}\right) \tag{E3.2}$$

where τ_p is the pump duration typically around 100 fs, s_σ is the spin-pumping selectivity of the spin channel $\sigma = \{\uparrow, \downarrow\}$ and A is a renormalization factor. In details, the list of parameters used in the modelling will be available in Table III.1. Different pumping profiles are tabulated in the model to account for several temporalities: the steady-state regime, the dynamical regime and for future implementation of the continuous-wave (CW) THz photomixing using spintronic THz emitters (proposed in Chap. VI). Therefore, to compare the results between them, the presented pumping profiles are normalized *i.e.* $\int_0^T \mathcal{P}(\sigma, \mathbf{r}, t) = 1$.

Wave-diffusion modelling. We focus on the wave-diffusion model [151, 236, 100] which accounts for the diffusion of a distributed spin populations $n_\sigma(z,t)$ and spin currents $j_\sigma(z,t)$ following a finite difference time domain derivation in one dimension (1D-FDTD). The time and space are discretized in space and time following $dz = (z_{\max} - z_{\min})/N_z$ and $dt = (t_{\max} - t_{\min})/N_t$ where N_z and N_t are the total number of points in the space (time) dimension. The wave-diffusion model accounts for the following set of two differential evolution equations:

$$\begin{cases} \dfrac{\partial n_\sigma^i}{\partial t} = \underbrace{-\dfrac{n_\sigma^i - n_{-\sigma}^i}{\tau_{sf}^i}}_{\text{spin-flip}} - \underbrace{\nabla j_\sigma^i}_{\text{flux term}} + \left(\underbrace{\mathcal{P}(\sigma, \mathbf{r}, t)}_{\text{source term}} - \underbrace{\dfrac{n_\sigma^i}{\tau_r^i}}_{\text{remag}} \right) \delta_{i,\text{FM}} \\ \dfrac{\partial j_\sigma^i}{\partial t} = \underbrace{-\dfrac{j_\sigma^i}{\tau_\sigma^i}}_{\text{spin-flip}} \underbrace{-\dfrac{D_\sigma^i}{\tau_\sigma^i} \nabla n_\sigma^i}_{\text{flux term}} \end{cases} \tag{E3.3}$$

where, for the i-th layer, τ_{sf} is the carrier scattering time, τ_σ is the spin lifetime, τ_r is the remagnetization time (only valid in ferromagnets) and $D_\sigma = v_\sigma^2 \tau_\sigma / 3$ is the diffusion coefficient. From this set of differential equations, we identify three elements: the first term is the spin-flip term linked to a spin-flip probability in the bulk of the material being linked to its spin scattering time τ_{sf}. The second term is the current flux term and the last term is the pump term $\mathcal{P}(\sigma, \mathbf{r}, t)$ that we assume only on the FM region. A spontaneous remagnetization time is included in the model to account for the relaxation (loss of energy) of the excited s-electrons returning to the d band in the FM layer. It is to be noted that spin-flip events are reaction factors which are independent of the n-th scattering step as it does not depend on the history of the collisions. By introducing the dynamical magnetization $m = n_\uparrow - n_\downarrow$ and the total spin current $j_s = j_\uparrow - j_\downarrow$, the previous system of equations can be rewritten as:

$$\begin{cases} \dfrac{\partial^2 m}{\partial t^2} + \left[\dfrac{1}{\tilde{\tau}} + \dfrac{1}{\tau_{sf}} \right] \dfrac{\partial m}{\partial t} + \dfrac{m}{\tilde{\tau} \tau_{sf}} - \dfrac{\tilde{D}}{\tilde{\tau}} \dfrac{\partial^2 m}{\partial z^2} = \dfrac{\partial \mathcal{P}}{\partial t} \\ \dfrac{\partial^2 j_s}{\partial t^2} + \left[\dfrac{1}{\tilde{\tau}} + \dfrac{1}{\tau_{sf}} \right] \dfrac{\partial j_s}{\partial t} + \dfrac{j_s}{\tilde{\tau} \tau_{sf}} - \dfrac{\tilde{D}}{\tilde{\tau}} \dfrac{\partial^2 j_s}{\partial z^2} = -\dfrac{\tilde{D}}{\tilde{\tau}} \dfrac{\partial \mathcal{P}}{\partial z} \end{cases} \tag{E3.4}$$

where we have introduced the $\tilde{D} = 2D_\uparrow D_\downarrow / (D_\uparrow + D_\downarrow)$ the average diffusion constant, $\tilde{\tau} = 2\tau_\uparrow \tau_\downarrow / (\tau_\uparrow + \tau_\downarrow)$ the average scattering time and $\mathcal{P} = \mathcal{P}_0(\uparrow, \mathbf{r}, t) - \mathcal{P}_0(\downarrow, \mathbf{r}, t)$. We detail the continuity equations at the interface and borders in Appendix A5. In particular, we state the charge current at the interface, as well as a vanishing charge and spin current at the external borders. The interfacial spin transport conditions follow the scope of the interfacial spin-memory loss as described in Chap. I.

Classification of the diffusion regimes.

We define the mean displacement as $\langle x(t) \rangle = \int n(x,t) x dx$. From this, one can extract the diffusion regime depending on the trend of $\langle x(t) \rangle$: *i*) if $\langle x(t) \rangle = vt$ is linear, the regime is called ballistic and the number of collisions are minimized (reduced to zero). In the case where *ii*) $\langle x(t) \rangle = \sqrt{Dt} \propto t^{1/2}$, the regime is called diffusive contrary to the last case *iii*) where $\langle x(t) \rangle \propto t^{\alpha + 1/2}$ is called the superdiffusive regime in which relaxation induces a certain probability of second-order pumping that contributes again to a certain probability of pumping after their relaxation. This superdiffusive modelling is particularly developed by P. Oppeneer and coworkers [74, 80].

Notably, our wave-diffusion approach [100, 236] allows to simplify the transport equations of the superdiffusive model (secondary emission sources) by using a unique carrier (τ_σ) and spin (τ_{sf}) relaxation times, whereas those relaxation rates highly depend on the energy as $\tau_\sigma(\varepsilon), \tau_{sf}(\varepsilon)$ in the superdiffusive image. This idea is widely discussed in the scope of Zhukov *et al.* [57, 58] in which we expect the following dependence for the two relaxation times with $\tau_\sigma(\varepsilon) \propto (\varepsilon - \varepsilon_\text{F})^{-2}$ and $\gamma_\text{SO} = \sqrt{\tau_\sigma(\varepsilon)/\tau_{sf}}$, called the spin-orbit parameter, and generally relating in the literature the $3d$ band widths $\Delta\varepsilon_\text{SO}$ via $\gamma_\text{SO} = (\lambda_\text{SO}/\Delta\varepsilon_\text{SO})^2$. This owns to the fact that the relaxation of photo-excited hot carriers is limited by available states for relaxation at lower energies (the

Parameter	Use	Material	Value	Reference
Ferromagnetic layer thickness t_{FM}	Variable	Co	2-10 nm	-
Carrier lifetime (majority spins) $\tau_\uparrow$	Input	Co	22 fs	[237]
Carrier lifetime (minority spins) $\tau_\downarrow$	Input	Co	20 fs	[237]
Velocity of the majority spins $v_\uparrow$	Input	Co	0.6 nm.fs^{-1}	[237]
Velocity of the minority spins $v_\downarrow$	Input	Co	0.2 nm.fs^{-1}	[237]
Fermi velocity v_{F}	Input	Co	0.3 nm.fs^{-1}	[238]
Diffusion of the majority spins $D_\uparrow$	$\frac{1}{3}\tau_\uparrow v_\uparrow^2$	Co	2.64 nm^2.fs^{-1}	-
Diffusion of the minority spins $D_\downarrow$	$\frac{1}{3}\tau_\downarrow v_\downarrow^2$	Co	0.27 nm^2.fs^{-1}	-
Spin asymmetry β	Input	Co	0.36	[239]
Mean free path λ	Input	Co	8.6 nm	[238]
Spin diffusion length l_{sf}	Input	Co	10 nm	[239]
Spin scattering time τ_{sf}	$\frac{6l_{sf}}{v_{\mathsf{F}}\lambda(1-\beta)^2}$	Co	267.2 fs	-
Remagnetization time τ_r	Fixed	Co	10 ps	-
Non magnetic layer thickness t_{NM}	Input	Pt	4 nm	-
Carrier lifetime $\tau = \tau_\uparrow = \tau_\downarrow$	Input	Pt	10 fs	[100]
Carrier velocity $v = v_\uparrow = v_\downarrow$	Input	Pt	0.2 nm.fs^{-1}	[74]
Diffusion coefficient $D = D_\uparrow = D_\downarrow$	$\frac{1}{3}\tau v^2$	Pt	0.53 nm^2.fs^{-1}	-
Spin diffusion length l_{sf}	Input	Pt	2 nm	[44]
Spin scattering time τ_{sf}	$\frac{6l_{sf}}{v_{\mathsf{F}}\lambda}$	Pt	20 fs	[240]
Spin Hall angle θ_{SHE}	Input	Pt	5%	[44]
Interfacial spin asymmetry γ	Variable	Co/Pt	+0.5	[241]
Interfacial spin resistance r_{B}^*	Input	Co/Pt	0.83 $\times 10^{-15}$ Ω.m^2	[241]
Interfacial transmission coefficient $T^\star$	Variable	Co/Pt	$\{10^{-4} - 10^{-1}, 0.25, 0.5\}$	-
Spin memory loss δ	Variable	Co/Pt	0.9	[44]
Pump pulse duration τ_p	Variable	-	10-200 fs	-
Spin-up channel source term $s_\uparrow$	Variable	-	$\{0.5, 1\}$	-
Spin-down channel source term $s_\downarrow$	Variable	-	$\{0.5, 1\}$	-
Pump repetition rate f_r	Variable	-	80 MHz	-

Table III.1: Parameters used in the FDTD simulations for FM ≡ Co, NM ≡ Pt and the interface I ≡ Co/Pt.

energy dispersion evolves as ε^2 for 3D systems).

However, several ingredients are necessary to integrate the superdiffusive model, which complexifies the implementation. First, we will employ an energetic-free representation of the system where both the pumping energy and the system chemical potential are not defined, due to the indefinition of the number of available electrons in our system. Thus the energetic interaction with the pump is not including. This would allow to simulate the response at different pump energies (wavelengths). From this, the superdiffusive model could be written according to Refs. [80, 74] via a second-order pumping (as illustrated in Fig. 3.1c):

$$\mathcal{P}^{(2)}(\sigma, \mathbf{r}, t) = \Gamma_{sd} \frac{n_\sigma + n_{\sigma'}}{2N_d} \left(N_{d,\sigma} - n_\sigma\right) \tag{E3.5}$$

where N_d is the number of total electrons in the d-band (*e.g.* 7 for Co on a total of 10 available states) and Γ_{sd} is the $sp-d$ collision rate. This secondary pumping represents the secondly excited d-electrons due to the relaxation of firstly pumped sp-electrons. The computation is challenging as this secondary pump is highly non-linear. From energetic considerations, future implementations of the model could include the three-temperature model to consider non-magnetic materials and the interactions between the excited electrons, spin and phonons.

Dynamical spin-charge conversion, THz charge current and radiation. As we compute $n_\sigma(z,t)$ and $j_\sigma(z,t)$, we can derive [100] a charge current and subsequent far-field electric field by considering the spin current flowing in the HM layer(s):

$$\mathbf{E}_{\mathrm{THz}} \propto \frac{\partial j_c(t)}{\partial t} \quad \text{with} \quad j_c(t) \propto \int_{z\in \mathrm{HM}} \theta_{\mathrm{SHE}}(z') j_s(z',t) dz' \tag{E3.6}$$

This last equation already includes the spin diffusion length dependence as the integral of the spin current varies as $\tanh(z/2l_{sf})$. As in THz emission spectroscopy, we can focus on both the amplitude and the phase of the THz signal. A fast Fourier transform (FFT) allows to compute the spectrum of the THz electric field $\mathcal{F}[E_{\mathrm{THz}}(t)]$.

Compared to the superdiffusive model [80, 74, 242], our simulations include *i*) the potential specular/non-specular reflections at the external interfaces (Annex A5) and *ii*) the possibility of spin-flip events on internal and external interfaces, which are very relevant processes in the case of spintronic THz emitters. Taking into account those effects in our model represent, in the current vision of ultrafast spin-current diffusion models, improvements compared to existing models.

1.2 Simulation results and trends.

1.2.1 Steady-state regime in the confined geometry.

In this first part, we will consider a steady-state regime of spin-injection, either optical or electrical, to check the validity of the spin-accumulation and spin current profiles derived from our model compared to the analytical equations are well-known in metallic bilayers for electrons of energy close to the Fermi level (standard Valet-Fert model [241]). Indeed, in the steady-state ($\partial/\partial t \to 0$), the magnetization and the spin current read from Eqs. (E3.4):

$$\begin{cases} m(z,t) = m(z) = -\tilde{D}\tau_{sf} \dfrac{\partial^2 m}{\partial z^2} \\ j_s(z,t) = j_s(z) = -\tilde{D}\tau_{sf} \dfrac{\partial^2 j_s}{\partial z^2} \end{cases} \tag{E3.7}$$

admitting for solutions an exponential decay for $m(z)$ and $j_s(z)$ as $\propto \exp(-z/l_{sf})$ with $l_{sf} = \sqrt{\tilde{D}\tau_{sf}}$. To model the steady-state regime in our model, we used a continuous and constant pumping:

$$\mathcal{P}_0(\sigma, \mathbf{r}, t) = s_\sigma \frac{A}{T_{\mathrm{max}}} \tag{E3.8}$$

where T_{max} is the total time window calculated and A is a normalization coefficient. In the following example, we will take $T_{\mathrm{max}} = 30$ ps. For simplicity, we set a spin-up pumping only (*i.e.* $s_\uparrow = 1$ and $s_\downarrow = 0$) corresponding to injected majority spins only, for a Co(10nm)/Pt(4nm) structure. We also set a confined case regime where the transmission coefficient $T^* \to 0$, approximately to 10^{-3} and a spin-symmetrical interface $\gamma = 0$ to simplify. It will allow us to check the validity of the electronic transmission at the interface at the same time.

We display in Fig. 3.2 the spatial profile of the total spin accumulation $m(z)$ and spin current $j_s(z)$ at long times (> 30 ps) in Co(10nm)/Pt(4nm) where we vary the relaxation times in both FM and HM layer, by tuning the spin and electron-electron scattering times by a respective factor $\alpha_{\mathrm{FM}} = \sqrt{\tau_{sf}^{\mathrm{FM}}/\tau_{sf}^{\mathrm{FM},0}} = \sqrt{\tau_{\sigma}^{\mathrm{FM}}/\tau_{\sigma}^{\mathrm{FM},0}}$ and $\alpha_{\mathrm{HM}} = \sqrt{\tau_{sf}^{\mathrm{HM}}/\tau_{sf}^{\mathrm{HM},0}} = \sqrt{\tau_{\sigma}^{\mathrm{HM}}/\tau_{\sigma}^{\mathrm{HM},0}}$, both ranging from 0.1 to 10 which can be seen as a time contraction (α<1) and time expansion (α>1).

We can observe on Fig. 3.2a that the spin-accumulation $m(z)$ in the FM layer is constant for all α_{HM} but the level of the spin-population evolves linearly with α_{HM}, thus the relaxation time τ_{sf}^{HM}. This is because $T^* = 10^{-3}$ is small (confinement regime). In the heavy metal, the slope (in logscale) of the spin accumulation, or the typical evanescent length, as a function of the distance $m(z)$ is given by the spin diffusion length l_{sf}^{HM} (as it remains unchanged in Fig. 3.2a). While

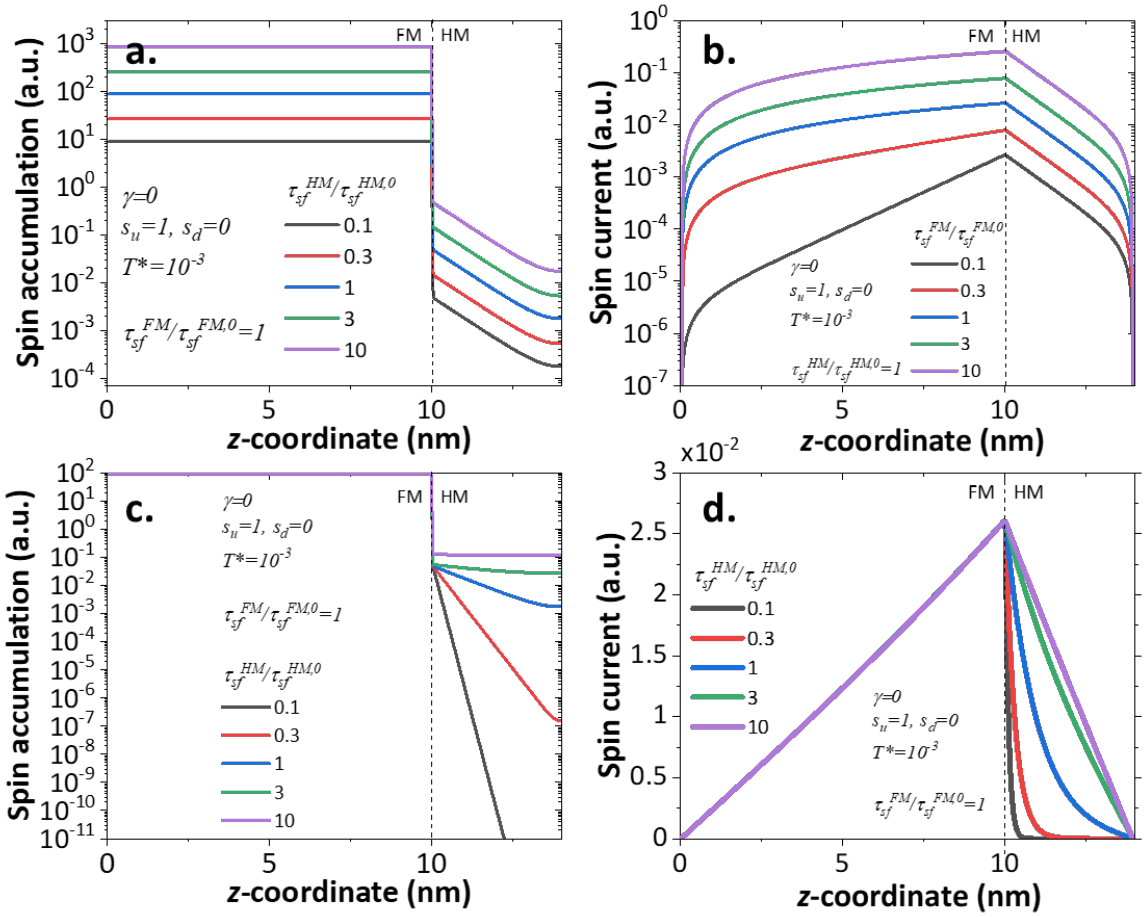

Figure 3.2: Confined case in the steady-state regime. Profile of (a) the spin accumulation and the (b) spin current while varying the spin scattering time in the FM layer by α_{FM}. Profile of the (c) spin accumulation and the (d) spin current while varying the spin scattering time in the HM layer by α_{HM}. All the calculations are performed for a spin-asymmetry of $\gamma = 0$ and interfacial transmission coefficient $T^* = 10^{-3}$ for a Co(10nm)/Pt(4nm) structure.

varying α_{HM}, we see in Fig. 3.2c that the spin-population in the FM is not affected contrary to the spin-population in the HM layer which relaxes very quickly for low values of the spin scattering time $\propto \alpha_{\text{HM}}$ (grey curve). Regarding the spin current $j_s(z)$, in all cases the results demonstrate that the boundary conditions corresponding to a pure reflection $j_s(z = z_{\text{B}}^{\pm}) = 0$ are fulfilled. In Fig. 3.2b, the spin current space profile has different slopes for the part in the FM and in the HM layers, illustrating the different spin diffusion lengths in the FM and HM layers. In the case of constant α_{FM} in Fig. 3.2d, the spin current profile $j_s(z)$ is constant in the FM layer and evolves with the spin diffusion length $l_{sf}^{\text{HM}} = \sqrt{\tilde{D}_{\text{HM}}\tau_{sf}^{\text{HM}}} \propto \alpha_{\text{HM}}$. The calculated steady-state spin transport is in agreement with the Valet-Fert model, expected for those bilayers. We will then consider the generalized time-dependent short pulse excitation to mimic the dynamical transport properties.

1.2.2 Dynamical spin-current injection: role of the spin Hall angle and the thicknesses.

We are now setting the most realistic case with an interfacial transmission for Co(10nm)/Pt(4nm) about $T^\star = 0.1$ and spin-asymmetry of the interface $\gamma = 0.5$ calculated from Dang *et al.* [231]. We launched a pumping assuming that more spin-up are launched than spin-down with a ratio 2:1, *i.e.* $s_\uparrow = 2s_\downarrow$. The pump profile is now transient, *i.e.* setting a Gaussian profile to account for the experimental femtosecond pump pulse of duration τ_p=100 fs. We recall that the reference

times are $\tau_{sf}^{\mathrm{FM}} \simeq 267$ fs, $\tau_{\sigma}^{\mathrm{FM}} \simeq 20$ fs for Co and $\tau_{sf}^{\mathrm{HM}} \simeq 20$ fs, $\tau_{\sigma}^{\mathrm{FM}} \simeq 10$ fs for Pt (see Table III.1). The obtained results are presented in Fig. 3.3a, presenting the THz spin accumulation, charge current and emitted electric field. We observe that the temporalities are well reproduced, with an THz electric field of similar shape that the ones obtained in experiments. Moreover, we compare in Fig. 3.3b the experimental and calculated bandwidth which shows a very good agreement in frequency. Note that the detection crystal response is not included in the simulations.

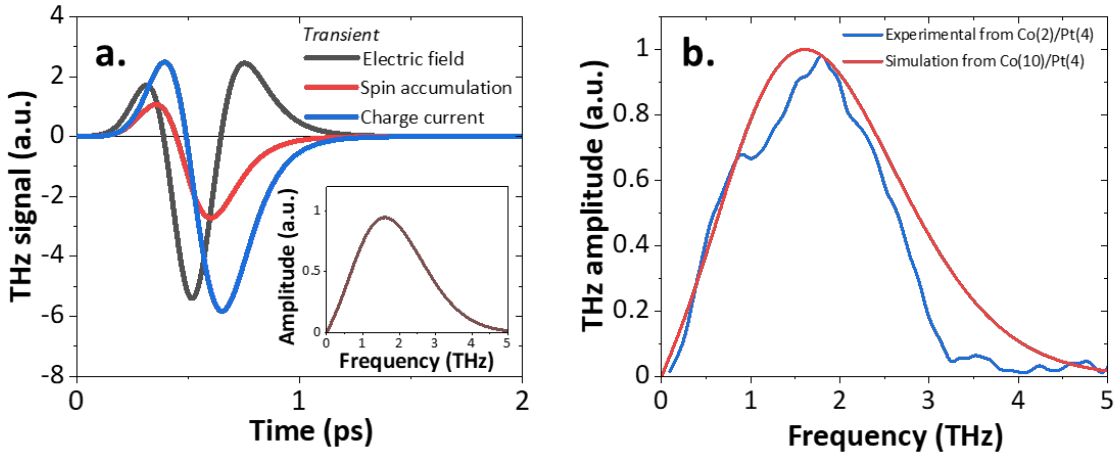

Figure 3.3: Dynamical signals obtained for the transient case. (a) Transient spin accumulation (red), charge current (blue) and THz electric field (grey) calculated for Co(10nm)/Pt(4nm). The inset presents the Fourier transform of the electric field. (b) Comparison between the experimental (blue) and calculated (red) THz bandwidth. The transmission coefficient is T^*=0.1 and the spin asymmetry is γ=0.5. Detailed parameters are given in Table III.1.

As we are able to reproduce the shape of THz transients, we further propose in Fig. 3.4a to change the spin Hall angle of Pt $\theta_{\mathrm{SHE}}^{\mathrm{Pt}}$ by a negative spin Hall angle like in W. We find that the THz polarization is indeed reversed owing to the sign of the spin Hall angle. We have also tuned the thickness of both FM and HM layers, ranging typically from 1 to 10 nm as displayed in Fig. 3.4b-c. For the case of Co(t_{Co})/Pt(4nm), the THz amplitude increases regularly with t_{Co} up to 10 nm and we can predict a saturation above this point following the value of the equivalent-spin diffusion length of Co (l_{sf}^{FM}). While we artificially reduce the spin diffusion length of Co (respectively from $1l_{sf}^{\mathrm{FM},0}$ to $0.25l_{sf}^{\mathrm{FM},0}$ and $0.1l_{sf}^{\mathrm{FM},0}$), it appears that the saturation occurs for smaller injector thickness due to spin-flip events, in agreement with expectations. In the case of Co(2nm)/Pt(t_{Pt}), we observe an strong increase of the THz amplitude up to 4 nm leading to a saturation of the emission, typical of inverse spin Hall effect origin. This is in agreement with the spin diffusion length of Pt, from which the conversion could not be increased for further Pt thicknesses as the dynamical spin accumulation in Pt is zero after this point. Indeed, the THz amplitude is proportional to the integrated spin current profile in the HM having the following form:

$$\int j_s(z)dz \propto j_s(z=0^+)\, 2l_{sf} \tanh\left(\frac{z}{2l_{sf}}\right) \tag{E3.9}$$

From those simulations, we strongly emphasis that the obtained THz signal and spectrum does not include several elements: *i*) the THz impedance Z_{THz} in metallic layers owing to their imaginary refractive index (conductivity), *ii*) the pump absorption profile $\mathcal{A}_{\mathrm{NIR}} \propto \exp(-z/l_{\mathrm{NIR}})$ where $l_{\mathrm{NIR}} = 1/\alpha_{\mathrm{NIR}}$ is the skin depth of the radiation and α_{NIR} is the absorption coefficient for a given wavelength λ_0, and *iii*) the electro-optic response of the detection crystal $H_{\mathrm{EO}}(\omega)$. The bandwidth is therefore overestimated compared to the typical measured THz signals. In this regard, the results obtained from the simulations correspond to the THz efficiency η_{THz} that we will introduce in Section III.2.2.

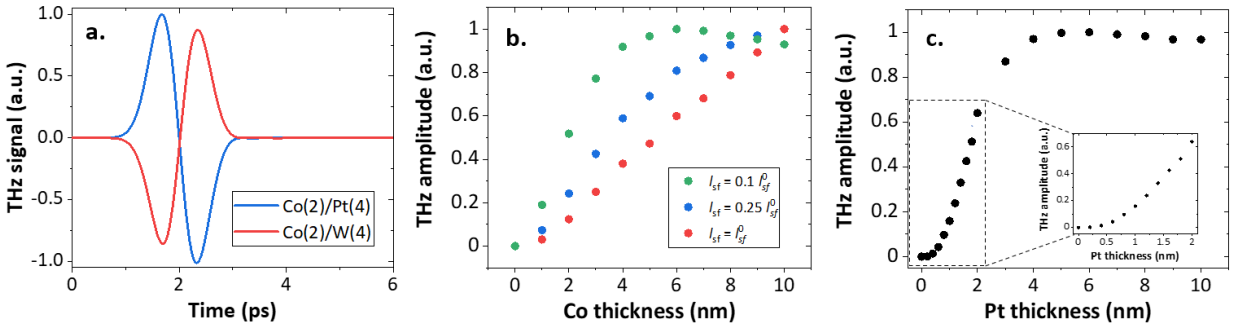

Figure 3.4: Impact of the spin Hall angle and layer thicknesses. (a) Simulated THz signals by replacing Pt with W of negative spin Hall angle, (b) THz amplitude as a function of the FM layer thickness (presently Co) for different spin diffusion lengths, and (b) THz amplitude as a function of the HM layer thickness (presently Pt). The pump duration is τ_p=100 fs, the bilayer is Co(2)/Pt(4), the interfacial transmission is T^*=0.1 and the spin-asymmetry is $\gamma = +0.5$.

1.2.3 Impact of the interfacial spin transmission and the spin-relaxation time.

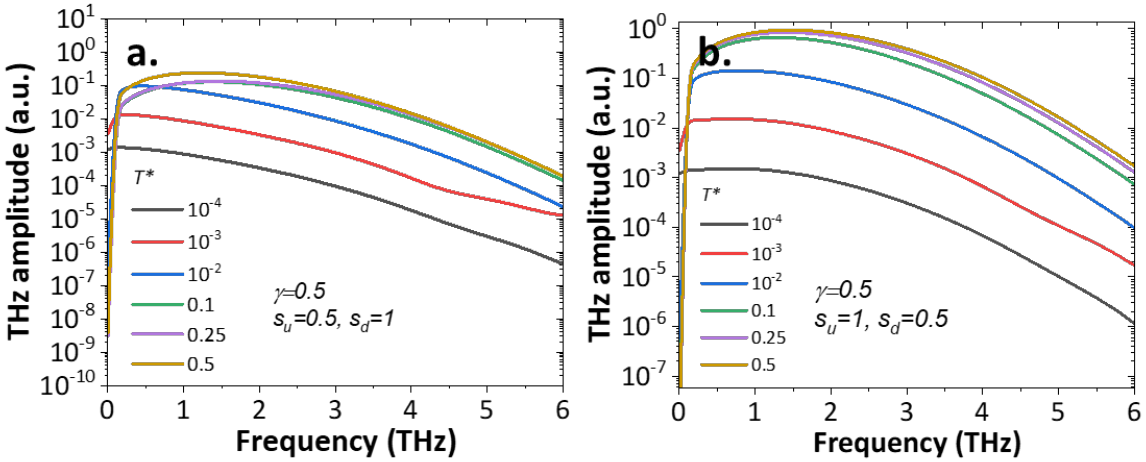

Figure 3.5: Impact of the interfacial transmission. THz amplitude as a function of the interfacial transmission coefficient T^*, ranging from $\{10^{-4}, 10^{-3}, 10^{-2}, 0.1, 0.25, 0.5\}$ and spin-asymmetry coefficient $\gamma = 0.5$, respectively for (a) $s_\uparrow$=0.5 and $s_\downarrow$=1 and (b) inverted $s_\uparrow$=1 and $s_\downarrow$=0.5. The pump duration is τ_p=100 fs and the bilayer is Co(2)/Pt(4).

We now turn towards the properties of the THz radiation from spintronic bilayers as a function of the interfacial transmission T^*. We plot in Fig. 3.5 the THz bandwidth for Co(2nm)/Pt(4nm) excited for a pump pulse of τ_p=100 fs for various transmission coefficients ranging from $\{10^{-4}, 10^{-3}, 10^{-2}, 0.1, 0.25, 0.5\}$. We can observe that in both pumping asymmetry cases, the trend is an increase of the THz amplitude with T^*. This proves that the Co/Pt interface (experimental case corresponding to $T^* \simeq 0.1$ as obtained from DFT calculations [231] with, in details, $T_\uparrow = 0.7$ and $T_\downarrow = 0.4$) is very close to the perfect interface case for THz spintronics. The amplitude saturation near maximal transmission T^* for the second pumping case $s_\uparrow = 1$ and $s_\downarrow = 0.5$ would potentially arise from the spin-asymmetry of the interface. Indeed, *i*) the majority spins have a better transmission coefficient compared to minority spins and *ii*) the carrier lifetime in the Co $\tau_\sigma \simeq 2d_{\mathrm{FM}}/v_\downarrow^{\mathrm{FM}} T_\downarrow$ has a value around $\simeq$ 100 fs matching the spin-flip time in Co.

We now turn to the dependence on the material spin relaxation properties while keeping constant the ideal transmission of Co(2nm)/Pt(4nm) ($T^* \simeq 0.1$) under a pump pulse τ_p=100 fs and a preferred minority spin pumping ($s_\downarrow > s_\uparrow$), corresponding to the experimental situation.

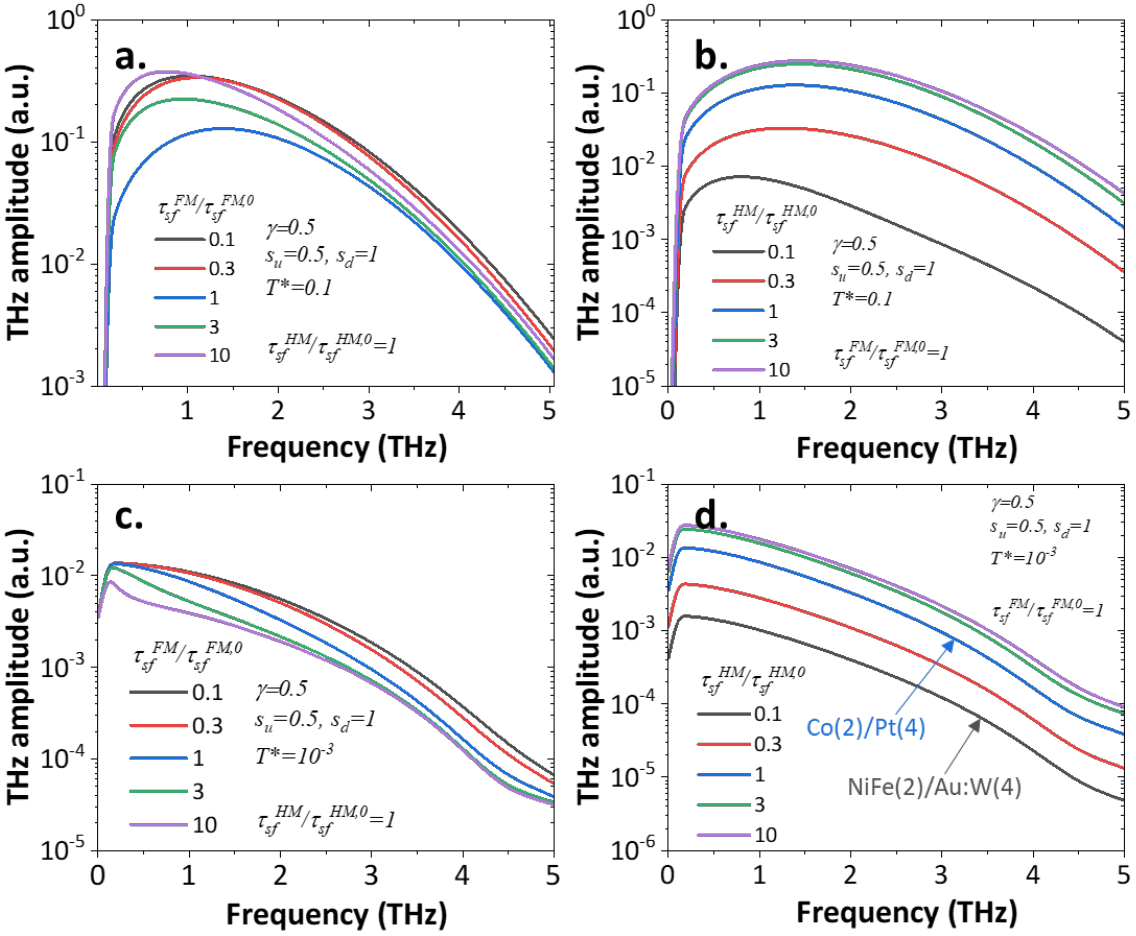

Figure 3.6: Impact of the spin scattering timescale. (a-b) Evolution of the THz amplitude as a function of (a) α_{FM} and (b) α_{HM} for the conventional case of Co/Pt interface with an interfacial transmission coefficient $T^* = 0.1$. (c-d) Evolution of the THz amplitude as a function of (c) α_{FM} and (d) α_{HM} in the confined case defined for a transmission coefficient about $T^* = 10^{-3}$. The pump duration is τ_p=100 fs and the bilayer is Co(2)/Pt(4) and the spin-asymmetry is $\gamma = +0.5$.

We report in Fig. 3.6a-c the THz amplitude (spectrum) while varying α_{FM}. In Fig. 3.6a, we see surprisingly that the THz amplitude is found to be larger for very short or very long spin timescales. On long spin lifetime (*i.e.* no spin-flip events happened during the transport in the FM layer), this trend is explained by the spin-filtering of the minority spins in the first case as identified in previous Fig. 3.5. On the short spin lifetime (*i.e.* smallest α_{FM}), the spin-flip events present a reversed spin population ($n_\uparrow > n_\downarrow$) at the interface which is converted via the efficient spin-transmission for majority spins. This trend however is the exact opposite of Fig. 3.6c in the confined geometry $T^* = 10^{-3}$ due to the reflection of the electronic population at the interface and lowered spin-flip rates in the FM layer.

We now discuss on the similar simulations in the case of varying the HM layer α_{HM} in Fig. 3.6b-d. We see that in both optimized and confined geometries for the transmission coefficient, increasing the spin-scattering time in the HM layer leads to an increase of the THz signal. This is due to a correlated increase of the spin diffusion length and subsequent dipole volume, which allows a larger conversion in the HM layer. We will be able to provide such experimental changes of the spin diffusion length (and spin scattering time) using Au-based spin Hall alloys, assimilated in Fig. 3.6d to the case of the scattering time of Pt in an Co/Pt bilayer or a smaller spin diffusion time in Au:W based alloys in a NiFe/Au:W structure owing to the high-scattering

rate in alloys [152].

1.2.4 THz response on the pump time duration.

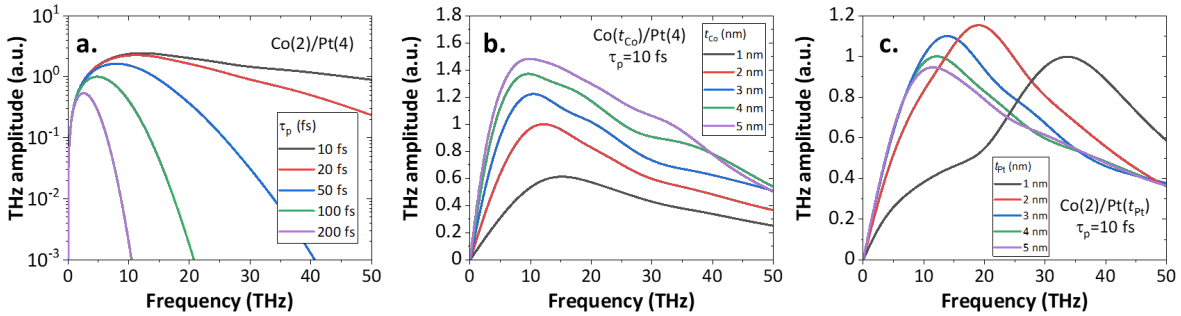

Figure 3.7: Evolution of the THz emission as a function of the pump duration. (a) Evolution of the THz signal (spectrum) *vs.* the pump duration τ_p ranging from $\{10, 20, 50, 100, 200\}$ fs . (b-c) Evolution of the THz bandwidth as a function of the (b) Co thickness in Co(t_{Co})/Pt(4) and (c) Pt thickness in Co(2)/Pt(t_{Pt}) for the shorter pump pulse τ_p=10 fs. The interfacial transmission coefficient is $T^* = 0.1$, the spin asymmetry is $\gamma = +0.5$ and the pump selectivity is $s_\uparrow$=1 and $s_\downarrow$=0 for sake of clarity.

At last, we conclude our simulations with the study of the pump time duration τ_p on the THz response. We set α_{FM}=1 and α_{HM}=1 and we consider an ideal interface ($T^* = 0.1$) for Co(2)/Pt(4) bilayer. We report in Fig. 3.7a the impact of the pump duration τ_p, varying from $\{10, 20, 50, 100, 200\}$ fs, on the THz bandwidth. We observe that the bandwidth is widened for shorter pulses. This is explained by the shorter dynamics induced by the sharper derivative of the pump profile $\partial(E^2_{\text{pump}})/\partial t$ on short pump duration times. It is to be noted that the different bandwidths for all pump durations share the same low-frequency cutoff which is linear in ω and matches the longest dynamics reachable in the system, limited by the remagnetization time τ_r (*i.e.* the induced charge current is zero if no spin-current is injected). To dive into the higher dynamics achievable with spintronic THz emitters, we set the pump pulse to τ_p=10 fs and study the impact of the FM and HM layer thickness respectively in Fig. 3.7b-c. We observe for the FM layer that the THz amplitude is larger for larger FM thickness and that the peak frequency is shifted towards lower frequencies. This could be explained by the higher probability of spin-flip in the depth of the FM layer which has a longer spin relaxation time, as previously evidenced in Fig. 3.4b. On the contrary for the HM layer, we see that the peak frequency is strongly influenced by the HM thickness as shown in Fig. 3.7c. This owns to the electronic wave that is reflected in very short Pt layer leading to *i*) the spin-flip of the electronic population at the Pt boundary and thus *ii*) the sharpening of the total spin current profile undergoing spin-charge conversion. Indeed, the crossing time $\tau_{AR} = 2d_{HM}/v_{HM}$ is about 50 fs for 2 nm of Pt, corresponding to the THz peak centered around 20 THz. This effect disappears at larger Pt thickness as the incoming and reflected electronic wave are decorrelated. The role of the Pt thickness is therefore essential for the spectroscopy of higher dynamics.

Spin current propagation and electronic interferences. Following this idea, we focus finally on the spin current relaxation timescales in Pt by studying the THz response of Co(2)/Pt(4) bilayer for a pump duration of τ_p=10 fs while varying the extension/contraction parameter $\alpha_{HM} = \{0.01, 0.1, 1, 10, 100\}$ as shown in Fig. 3.8. At very long relaxation times ($\alpha_{HM} \gg 1$), we observe that the THz peak frequency around 11 THz strongly narrows and reaches up to an order of magnitude compared to the reference case α_{HM}=1. The bandwidth after presents dips near 30 THz and 40 THz. We note that the THz peak frequency is independent of the expansion parameter α_{HM}. This behaviour is slightly encountered at very short relaxation timescales $\alpha_{HM} \ll 1$.

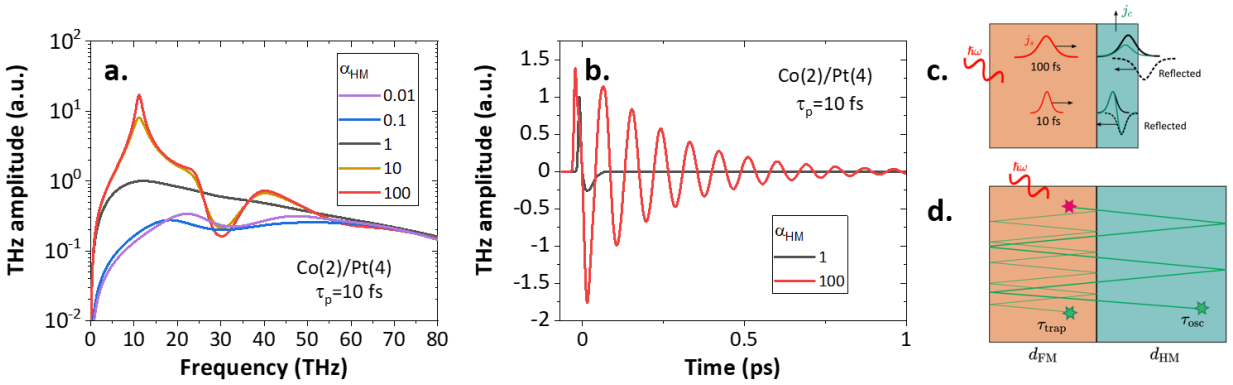

Figure 3.8: Narrowband contribution in the long relaxation time limit. (a) THz amplitude as a function of $\alpha_{HM} = \{0.01, 0.1, 1, 10, 100\}$. A narrowband contribution is found around 11 THz. (b) Time trace of the THz signal at α_{HM}=1 and α_{HM}=100 (oscillations in the time-domain). (c) Scheme of the (c) spin current wave packet sharpening and (d) electronic interferences. The pump duration is τ_p=10 fs and the bilayer is Co(2)/Pt(4). The interfacial transmission coefficient is $T^* = 0.1$, the spin asymmetry is $\gamma = +0.5$ and the pump selectivity is $s_\uparrow$=1 and $s_\downarrow$=0 for sake of clarity.

While we look at the time-response of such narrow contribution, we observe oscillations in the time-domain of period $\tau_{\rm osc} = 1/f_{\rm osc} \simeq 2T^*(d_{\rm FM} + d_{\rm HM})/v_{\rm F}$ which corresponds to the back-and-forth travel of the electronic wave in the HM layer. These variations at given frequencies are typical of electronic interferences in the wave-diffusion model owing to the longer propagation of the spin current in thin multilayers of high $\alpha_{\rm HM}$. The transient spin current travels back-and-forth in the Pt and now has a stronger probability to relax in the FM layer instead in the HM layer, owing to shorter relaxation times in the FM layer ($\alpha_{\rm FM}$=1 $\ll$ $\alpha_{\rm HM}$ $\rightarrow$100). The trapping time in the FM layer is about $\tau_{\rm trap} \simeq \tau_{\rm osc} \cdot d_{\rm FM}/(d_{\rm FM} + d_{\rm HM})$ around 30 fs, thus explaining the dip around 30 THz. Following this point, a careful engineering of the spin scattering time τ_{sf} in multilayers is required for an experimental implementation of such narrowband THz emitters. For such purposes, magnetic insulators propose an interesting platform for smaller spin-orbit coupling (thus longer relation times) but it would required a good interfacial acoustic and spin conductance to efficiently lead to the spin-current interferences. This approach is similar to the one proposed by Zhuang *et al.* [243, 197] in a slightly different manner combining metallic, dielectric and magnetic structures to envision narrowband THz emitters.

Opening on modelling the interfacial conversion. To account for interfacial conversion in spintronic bilayers, the inverse Rashba-Edelstein effect (like studied experimentally from topological insulators in Chap. IV) can be modelled via the integration of the interfacial dynamical magnetization $m_{\rm tot}^{\rm int}$, the conversion figure-of-merit $\lambda_{\rm IREE}$ and an interfacial relaxation time $\tau_{\rm int}$ as:

$$j_c^{\rm IREE}(t) \simeq \frac{e\hbar\lambda_{\rm IREE}}{\tau_{\rm int}} m_{\rm tot}^{\rm int}(t) \Rightarrow E_{\rm THz}^{\rm IREE}(t) \propto \frac{\partial m_{\rm tot}^{\rm int}(t)}{\partial t} \qquad \text{(E3.10)}$$

As an example, we give in Fig. 3.9 the time profile of the magnetization $m_{\rm tot}^{\rm int}$ at the interface of Co(2)/Pt(4) and subsequent THz amplitude (in the frequency domain) generated by the interfacial conversion as a function of the pump duration τ_p. We observe that the accumulation at the interface increases for shorter pump durations. The accumulation profile narrows for shorter duration times and in particular, the shape changes from a Gaussian shape (pump shape) to a quasi-instantaneous rise time followed by an exponential decay time. This can be understood by the pump intensity derivative $\partial(E_{\rm pump}^2)/\partial t$. This leads in the frequency domain to a broadening of the equivalent THz bandwidth for $\partial m_{\rm tot}^{\rm int}(t)/\partial t$ compared to the charge current term in the case of ISHE-type conversion which follows $\partial j_s(t)/\partial t$

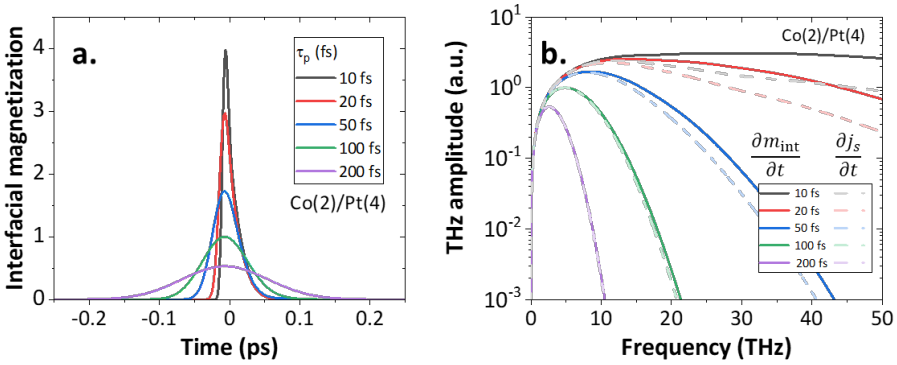

Figure 3.9: Dynamical interfacial magnetization response. (a) Time profile of the interfacial magnetization and induced charge current proportional to the derivative of the magnetization. (b) Frequency response of the charge current derived from the transient magnetization. The structure is Co(2)/Pt(4) bilayer, the interfacial transmission coefficient is $T^* = 0.1$, the spin asymmetry is $\gamma = +0.5$ and the pump selectivity is $s_\uparrow$=1 and $s_\downarrow$=0 for sake of clarity.

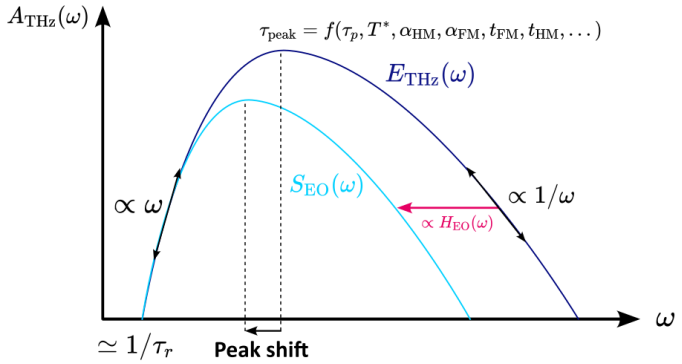

Figure 3.10: Bandwidth limitations for spintronic THz emitters. Schematic view of the generated (dark blue) and detected (light blue) THz bandwidth. The measured bandwidth is limited by the transfer function of the detector $H_{\mathrm{EO}}(\omega)$. No gap in the bandwidth is reported due to the absence of phonon absorptions.

Conclusions on the wave-diffusion model.

We have reviewed via an spin-generalized wave-diffusion model the impact of various parameters of spintronic structures on the resulting THz emission. We have evidenced that a trade-off is necessary between the FM and HM thickness (with the spin diffusion lengths), the interfacial transmission and the spin-flip parameters. A careful design of the spin-current in STEs is therefore needed to optimize both the emission performances and bandwidth. Studying these high-frequency effects in real systems would necessitate the broadband THz spectroscopy, with the maximal bandwidth reachable experimentally to fully compare the different types of STEs together. From this, we can open a discussion on a schematic understanding of the THz bandwidth from spintronic emitters as presented in Fig. 3.10. Although the low frequency cut-off is given by the remagnetizaiton time τ_r, the high-frequency cut-off is limited by both the pump duration τ_p and the highest reachable dynamics in the system, potentially the carrier lifetime τ_σ. The THz spectroscopy at high frequencies (5-10 THz) on very thin metallic layers opens therefore interesting visions for narrowband contributions, especially owing to spin-flip, spin-backflow and electronic wave engineering.

1.3 Perspectives: the generalized spin voltage model.

We now open the discussions on a recent model derivation called the generalized spin voltage developed by Rouzegar *et al.* [244]. In this scheme, the driving mechanism arises from the spin accumulation $\Delta m(t)$ as the only parameter driving the spin-injection mechanism, which represents the dynamical spin voltage $\Delta\mu_s(t) = \mu_\uparrow(t) - \mu_\downarrow(t)$ equal to the difference between the chemical potential for the two spin reservoirs at each time t, also linked to the generated spin current. One of the main conclusion of this work is that the remagnetization (spin) process occurs by thermalization with the additional reservoirs (electron, phonon, *etc.*), mainly via the electron-phonon interactions (Γ_{ep}^{-1}) happening at a timescale longer than the electron-spin scattering time (Γ_{es}^{-1}) typically >1 ps. We express the electron-phonon and electron-electron relaxation rates as:

$$\Gamma_{es}^{\mathrm{FM/HM}} = \frac{2g_{sf} + g_{tr}}{\chi_\mathrm{T}} \quad \text{and} \quad \Gamma_{es}^{\mathrm{FM}} = \frac{2g_{sf}}{\chi_\mathrm{T}} \quad \text{with} \quad \chi_\mathrm{T} = \frac{\mu_0 \mathcal{N}(\varepsilon - \varepsilon_\mathrm{F})}{\tau_{sf}} \tag{E3.11}$$

where g_{sf} and g_{tr} are the spin-flip and interface conductances, respectively, $\mathcal{N}$ is the density of states and $\chi_\mathrm{T} = \partial m/\partial\mu$ is the magnetic susceptibility. We can thus distinguish three regions of interest (illustrated in Fig. 3.11a) for the dynamics of the spin-current linked to the shape of the electric field:

- The first region, dominated by the dynamics of the electrons in the FM layer, is defined below 40 fs (>25 THz) and is strongly correlated to the pump profile $\partial E_{\mathrm{pump}}^2/\partial t$. In the most ideal picture, one would assume electron and spin temperatures to rise abruptly. Here, it is difficult to define a spin temperature and the excited s-electrons undergo inelastic scatterings (electronic lifetime of tens of fs from Zhukov *et al.* [58]) in travelling back-and-forth in the FM layer. On this image, electrons are loosing rapidly a large amount of energy, from 1.5 eV to several hundreds of meV. Interestingly, these scattering events preserve the spin orientation (in ferromagnets).

- The most interesting region is the second region between 40 fs and 200-300 fs (25 THz>ω>3-5 THz). In this region, the photo-excited spins have traveled back and forth in the FM and enter the HM layer to relax in the strong spin-orbit coupling material via $\partial\mathbf{j}_s/\partial t$ term. The equilibration is ruled out by the electron-spin relaxation time Γ_{es}^{-1}. The energy of the electrons entering the conversion material is about hundreds of meV (after a few electron-electron scattering events, typically 2-5 events) and the spin scattering time is about some hundreds of fs.

- Above 300-500 fs, the spin-charge conversion is achieved and an almost zero spin-reservoir is left to be converted. The main dynamics in this region is thus dominated by $\partial\mathbf{m}/\partial t$ as the d band starts to be repopulated again via phonon-magnon couplings. This region gives the low-frequency cutoff of the THz signal and is strongly ruled out by the electron-phonon interactions via Γ_{ep}^{-1}.

This model thus concludes first that on many systems, $\Gamma_{es}^{-1} \ll \Gamma_{ep}^{-1}$ leading to the dynamics of the spin current explained above. The second element demonstrated by this work is that as many scattering events already went in the FM layer, the role of the scattering times in the FM strongly determines the shape of the THz pulse. By increasing the transmission coefficient (fully transparent FM/HM interface), it would thus typically lead to a gain up to a order of magnitude for the THz spin current [244]. This model thus validates our electronic wave approach: for times longer than 40 fs, the electron system have a uniform temperature and an energy close to the Fermi level.

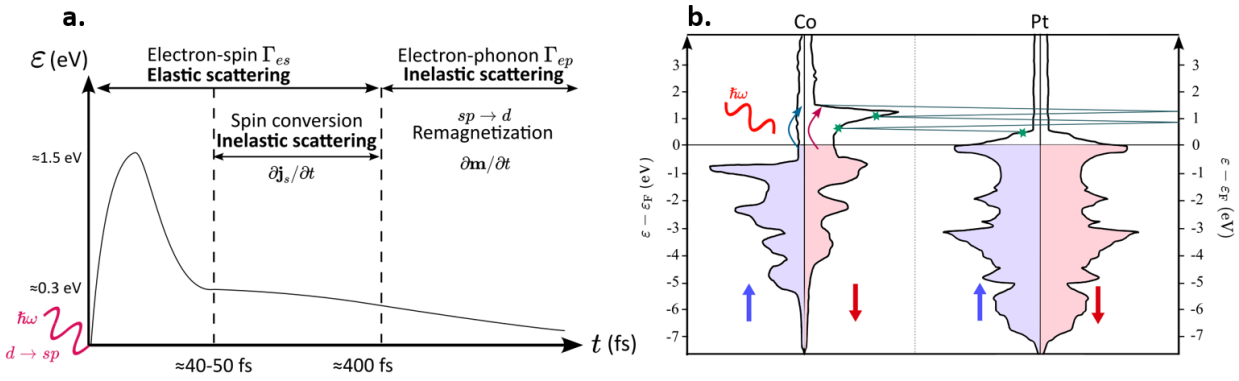

Figure 3.11: Illustration of the spin dynamics in the framework of the spin voltage model. (a) Energy profile of the hot-excited electrons as a function of time. (b) Spin-scattering processes upon ultrashort pump excitation overprinted on the density of states in a Co/Pt bilayer. The density of states are extracted from Refs. [58, 57, 245].

2 THz emission spectroscopy in the time-domain.

We now propose to experimentally implement and study such spin-orbit strategies in metallic spintronic THz emitters. The experimental technique at the heart of this thesis work is the THz emission spectroscopy in the time-domain. It allows to reconstruct in time a THz signal proportional to the THz electric field, and to access both the amplitude and the phase of the generated THz emission.

2.1 Experimental spectroscopy protocol.

Experimental setup. A complete scheme of the THz emission spectroscopy is described in Fig. 3.12. Femtosecond optical pulses are delivered by different available sources depending on the different setups in use, but the main setup uses a Ti:Sa oscillator (more details about the pump properties are available in Annex A9). The Ti:Sa oscillator delivers τ_p=100 fs pulses with a repetition rate of f_r=80 MHz centered at the wavelength λ=800 nm. The energy per impulsion is about 2-3 nJ and the pump is linearly (horizionally) polarized. The pulses generated by the Ti:Sa oscillator are separated orthogonally in two parts by a beam-splitter with a ratio 70%/30%. The first pulse is called the pump line (*i.e.* pumping the THz emitter) while the second pulse is the probe line going through the detection crystal. On the pump line near the sample, a magnetic field about 100-200 mT is applied in the thin film plane by use of permanent magnets. The samples under investigations typically possess a very low coercivity, below 10 mT, enough to saturate the in-plane magnetization [244]. The magnets are mounted on a separated rotational mount which can be slided on a rail system combined with the rotational stage where the sample is positioned. In that way, both magnetic field and sample azimuthal angles (respectively called θ and ϕ) can be independently rotated freely by 360°. In order to decorrelate non-magnetic contribution from magnetic contributions in STEs, we will focus during our investigations on the angular THz emission symmetries via the two independent rotations (θ, ϕ) as discussed in the next section (Fig. 3.16). The pump polarization can also be tuned (from linear with an angle α to circular) by means of a half-waveplate ($\lambda/2$) and quarter-waveplate ($\lambda/4$).

Before reaching the crystal, the probe line passes through a computer-controlled mechanical delay line which position shifts the probe line by $2\Delta L = c\Delta t$ where c is the light velocity and Δt is the time step between the two pump and probe pulses. Typically, for a time delay of few picoseconds, the length displacement is about few hundreds of micrometers.

The pump line, focused on the sample with a spot diameter about 200 µm, generates a THz transient which propagates on an optical path enclosed in a dry-air box to prevent the radiation absorption by ambient water present in the atmosphere. The generated THz is first collimated by a parabolic mirror of focal length 15 cm and diameter ≃7.6 cm (3"). It is then focused by a second parabolic mirror, where the THz focal point at 15 cm of distance from the focalising parabolic mirror is about 500-600 µm. At this point, the THz pulses are chopped mechanically at the frequency of $f_{\text{mod}} = 6$ kHz to perform heterodyne detection (with a flicker noise following $\propto 1/f_{\text{mod}}$). We use a lock-in amplifier locked at f_{mod} to perform the heterodyne detection. After this, the THz is collimated by another $f\#3$ parabolic mirror and a last parabolic mirror of focal length 7.5 cm and diameter ≃7.6 cm (3") focuses the THz onto the detection crystal. The f-number of a parabolic mirror is defined as the ratio between its focal distance f and its diameter D according to $f\# = f/D$. More the f-number is small and more the focal point which would be achieve will be small. A teflon (polytétrafluoroéthylène or PTFE) sheet which is THz-transparent (up to 6 THz) is placed in the THz path to block the residual NIR pump without loosing significant measurement bandwidth. This is sufficient in the 1-3 THz frequency range but for needs of high bandwidth measurements (above 5 THz to several tens of THz), a Ge wafer can be used to cut the NIR pump without loosing too much of the THz radiation by absorption.

This will not be the case in our study as we restrict our measurements to effective bandwidth $\leq$3 THz.

The two THz pulse and the NIR probe superpose spatially and temporally at the detection crystal. The NIR probe experiences a polarization change due to a change of the refractive index of the non-linear crystal induced by the THz electric field (more details are given in Annex A10 and in the next part). By tuning the delay between the THz and NIR pulses using a mechanical delay line, one can reconstruct the THz emission. All the measurements are first calibrated using a photoconductive antenna on LT-GaAs. The dark resistance is about some kΩ while the illuminated resistance is around 100 Ω. In most of our studies and if not stated otherwise, we will study the THz emission obtained in reflection geometry *i.e.* the sample is pumped and emits THz on the same edge [231]. The transmission geometry refers to a pump going through the sample from one edge and emitting the THz from the other edge.

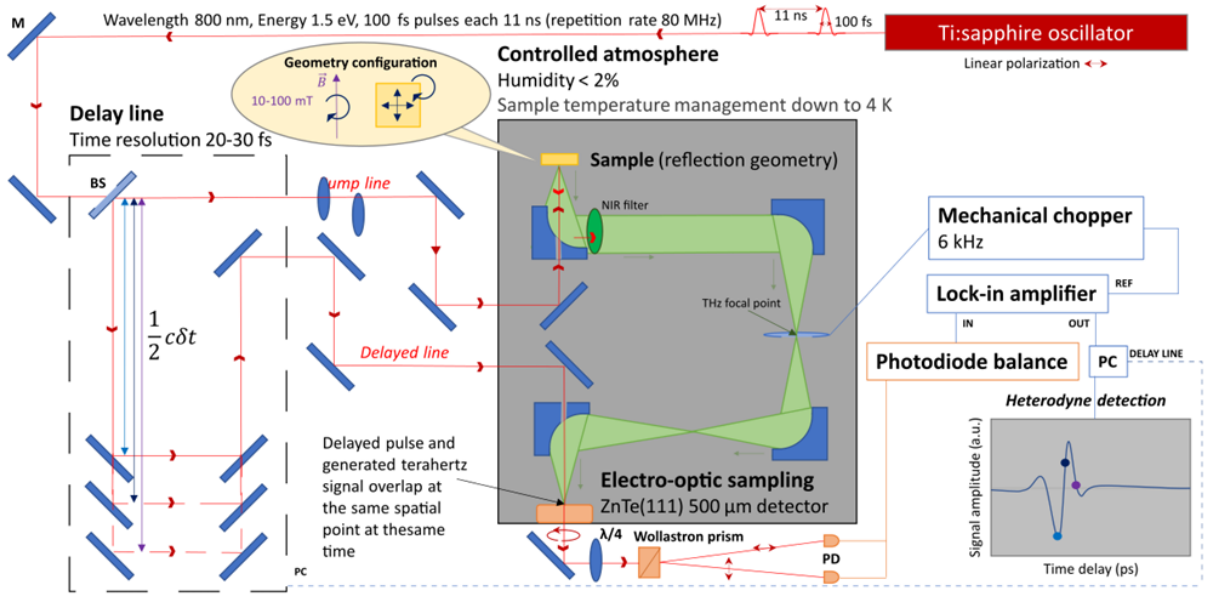

Figure 3.12: THz emission spectroscopy in the time-domain. The scheme represents the experimental setup which main elements are a femtosecond optical pump, a delay line, a THz emitter and coherent heterodyne detection via electro-optic sampling.

Cryo-cooled THz measurements. To study the THz emission as a function of temperature, cryo-cooled measurements are performed with an optical cryostat where THz windows are mounted. The sample is mounted on a cold finger (in Cu) joint with In thin sheets for good thermal contact. A small magnetic field is applied by a permanent magnet on the cold finger. The temperature can be monitored from 4 K to room temperature.

Detecting the THz signal with polarization changes by EOS and balanced photodetectors. Experimentally, the electro-optic sampling (EOS, detailed in Annex A10) rotates the probe polarization due to the THz-induced birefringence through the detection crystal (ZnTe$\langle 110\rangle$ or GaP$\langle 110\rangle$). This probe polarization rotation can be measured according to *i*) a separation of the polarization by use of a quarter-wave plate and a Wollastron prism, and *ii*) by the generation of a photo-current induced in a balanced photodetector proportional to the difference between the two horizontal (P_1) and vertical (P_2) projections of the polarization via:

$$\frac{\Delta P}{P_{\rm NIR}} = \frac{\omega_{\rm NIR} n_{\rm cr}^3 E_{\rm THz} r_{41} e_{\rm cr}}{c} \quad \text{and} \quad V_{\rm RF} = -\Delta P\, \mathcal{R}(\lambda)\, \mathcal{G} \tag{E3.12}$$

where $\Delta P = P_2 - P_1$ the power difference between the horizontal and vertical polarizations and $P_{\text{NIR}} = P_2 + P_1$ the NIR probe power going through the non-linear crystal. To measure a very small variation of the THz induced-polarization rotation, heterodyne detection is used via lock-in amplifier detection scheme able to access the rectified generated bias V_{RF} (supposing impedance matching), where $\mathcal{R}(\lambda)$ is the responsivity of the photodiode depending on the wavelength and $\mathcal{G}$ the transimpedence gain of the RF output.

Extraction of the amplitude from measurements. The measured time-resolved quantity $S_{\text{THz}}(t)$ is proportional to the THz electric field $E_{\text{THz}}(t)$ which can be derived with the THz charge current as $j_c(t)$:

$$S_{\text{EO}}(t) \propto E_{\text{THz}}(t) \propto Z(\omega)\frac{\partial j_c(t)}{\partial t} \tag{E3.13}$$

where $Z(\omega)$ is the THz impedance. The measure unit can be defined by different ways: either looking *i*) at the peak THz amplitude $E_{\text{THz}}^{\text{peak}}$, *ii*) the THz peak-peak amplitude A_{pp}, *iii*) the root mean square (RMS) A_{RMS} of the THz signal or *iv*) the integrated THz power P_{THz}. The choice of the convention does not alter the quantification of the THz efficiency as long as the convention stays consistent between different sample measurements within a same series. From here on, we have chosen to use the convention of the peak-peak amplitude A_{pp}. Besides, by the absence of electrical contacts while mapping only the free-space THz transients, THz emission spectroscopy reveals to be a very powerful non-destructive technique (below the damage threshold) to investigate ultrafast spin-current injection and spin-charge conversion phenomena in nanometer-thin multilayers.

Signal-over-noise ratio for THz time-domain spectroscopy. Although the THz emission measured in metallic STEs is of large amplitude, the measurements of the small THz signals from antiferromagnetic materials is particularly challenging due to the weak dynamical magnetization induced in those systems. To optimize the signal acquisition, we had several ways to proceed: first, we can play with the sampling step Δt which only allows to access larger frequencies. Then, we mostly varied the time constant τ_{C} (integration) on the lock-in to detect weak signals up to few µV of signals for τ_{C} ranging from hundreds of ms to few s. The last SNR enhancement method is the possibility to repeat the number of acquisitions. Following the average statistics, the SNR is expected to follow a $\sqrt{N}$ dependence, with N the number of measurement repetitions.

Measured signals: echos and water absorption. We present in Fig. 3.13 the typical THz normalized signals using THz emission spectroscopy in the case of not purged ($\simeq 30\%$ of relative humidity) and purged ($< 5\%$ of relative humidity) measurements. We notice the presence of incoherent oscillations in the time-domain that are attributed to the THz radiation absorption in water present in the ambient atmosphere. In the frequency domain, this traduces a loss of the measurement bandwidth (the cutoff of the detector is around 3 THz) at given frequencies which corresponds to the inter-molecule vibrational modes of water. The emission is in general reduced by 30% in amplitude with the presence of water absorption.

We present in Fig. 3.14a a full scan in the time-domain of the THz radiation from W/CoFeB/Pt reference emitter. We observe the presence of an additional signal around 10-12 ps which corresponds to the echos of the THz wave in the crystal (and/or in the substrate). Indeed, the time delay between the main signal and the echo coming from the crystal (or/and the substrate) can be estimated via $\Delta t_{\text{ec}} = 2N d_{\text{ec}} n_{\text{ec}}/c$ where d_{ec} and n_{ec} are the thickness and THz refractive index of the crystal (or substrate) and N is the number of back-and-forth travels. In this regard, more the detection crystal (substrate) is thin and closer the echo gets, which restricts the frequency resolution. In our case, for ZnTe$\langle 110 \rangle$(500 µm) crystal and sapphire(500µm) substrate, the thickness

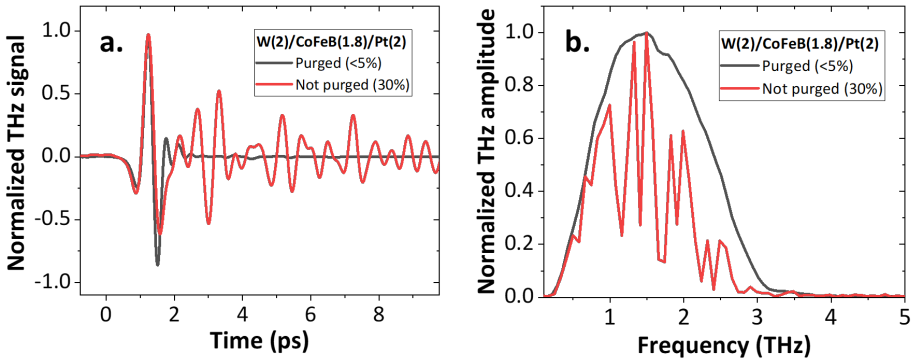

Figure 3.13: THz absorption by water in ambient atmosphere. (a) Measured THz signals (normalized) in the time-domain of W/CoFeB/Pt reference acquired under purged (<5%) and not purged (30%) conditions. (b) Obtained THz spectrum in both cases. The second case present strong absorptions of the THz radiation. The detector used is ZnTe$\langle 110 \rangle$(500 µm).

are equal and refractive index of the crystal and substrate are similar, about $n_{cr} \simeq n_s \simeq 3$, so that the two echoes arrive at the same time. For $N = 1$, the time delay is estimated around 10 ps which corresponds to the experimental measurement. In THz emission spectroscopy, the region of interest is highlighted in the orange region in Fig. 3.14a and corresponds to Fig. 3.14b. It allows to map the THz signal with a maximal resolution in frequency. Fig. 3.14c presents the integrated THz signal in the time-domain which, in the far-field, allows to reconstruct the generated THz charge current in the heterostructure. We have also displayed the absolute value of the integrated THz signal to show that one can extract the relaxation time of the THz charge current using THz emission spectroscopy. For spintronic THz emitters, this quantity is proportional to the generated THz spin current.

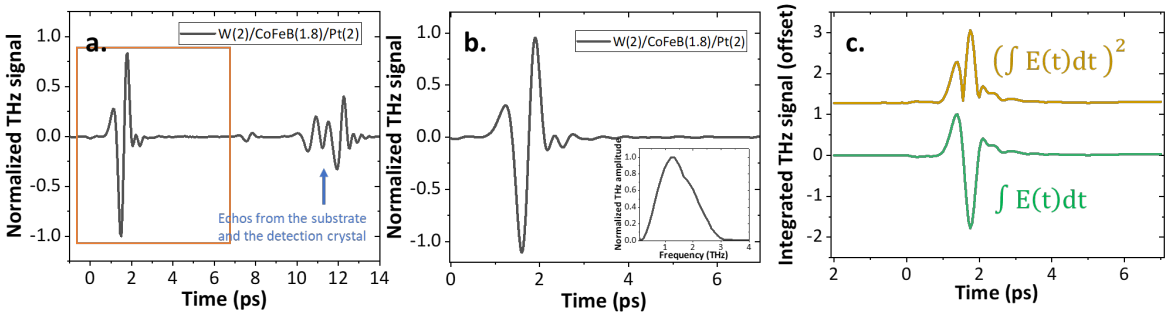

Figure 3.14: THz echo and derived THz field. (a) THz measurement for long time-trace on W/CoFeB/Pt reference. The presence of echos in the time-domain is equivalent to the wave reflections in the crystal and substrate. The orange box shows the region of interest in THz emission spectroscopy. (b) THz signal and corresponding THz spectrum (inset) in the region highlighted by an orange box. (c) Integrated THz signal (green) and absolute value of the integrated signal (yellow) which are quantities proportional to the time-resolved THz charge (and thus spin) current. The detector used is ZnTe$\langle 110 \rangle$(500 µm).

2.2 Extraction of THz efficiency by removing absorption contributions.

The measured THz electric field E_{THz} encodes the ultrafast spin current properties (that we will thereafter denote as the THz spin efficiency η_{THz}) and the spin-charge conversion efficiency, like played by the spin Hall angle θ_{SHE}. In order to extract these relevant parameters governing the spin relaxation contributing to the THz radiation, we have to consider both THz and NIR wave absorption in the heterostructure. Indeed, we have [150, 159]:

$$S_{\mathrm{EO}} = \mathcal{A}_{\mathrm{NIR}} Z(\omega)\, \theta_{\mathrm{SHE}} \eta_{\mathrm{THz}} \tag{E3.14}$$

where $\mathcal{A}_{\mathrm{NIR}}$ is the near-infrared absorption term and $Z(\omega)$ describes the effective THz impedance derived from the Tinkham formula [246] (developed in Appendix A6). For this, we make several assumptions: *i*) the total layer thickness is smaller than the wavelength, which leads to *ii*) multiple wave reflections in the heterostructure and *iii*) the substrate has been considered as infinite, in the sense that the reflections at the air/substrate interface does not make a strong contribution. In this framework, we can write the THz impedance as:

$$Z(\omega) = \frac{Z_0}{1 + n_{\mathrm{sub}}(\omega) + Z_0 \int \sigma(\omega, z) dz} \tag{E3.15}$$

with $Z_0 = 377\ \Omega$ is the free-space impedance and n_{sub} is the substrate THz refractive index. This formula computes the impedance at THz frequencies and consequently the absorption of the THz wave is directly proportional to $1/Z(\omega)$. In other words, more the conductivity is high in our multilayers, more the radiation is absorbed. One could consider a frequency-dependent conductivity based on the Drude model via $\sigma(\omega) = \sigma_{\mathrm{DC}}/(1 - i\omega\tau)$ where τ is the typical electron scattering time. However, we assume a frequency-independent conductivity $\sigma(\omega) = \sigma_{\mathrm{DC}}$ over the studied frequency range (300 GHz-3 THz) as it has been reported that the conductivity does not vary strongly with the frequency for various metals in the thin film limit [247]. The product between the free-space impedance and the sheet conductance $Z_0 G = Z_0 \sum_i t_i \sigma_i$ can be seen as an effective THz refractive index n_{eff} of the STE multilayers. To account for the near-infrared absorption, we consider a Beer-Lambert law:

$$\mathcal{A}_{\mathrm{NIR}} = \prod_i \mathcal{A}^i_{\mathrm{NIR}} = \prod_i \exp(-\alpha_i t_i) \quad \text{with} \quad \alpha_i = \frac{4\pi\kappa_i}{\lambda} \tag{E3.16}$$

where t_i is the thickness of the i-th layer, $\kappa_i = \mathrm{Im}\,(\tilde{n}_i)$ is the extinction coefficient of the i-th layer, α_i is the absorption coefficient of the i-th layer extracted for λ=800 nm. The associated tables for the values of the THz conductivities, the extinction coefficients, the absorption coefficients and the penetration depths $\delta = 1/\alpha$ gathered from various sources [248, 249] are available in Appendix A11. The NIR pump term is sometimes written by means of $\mathcal{A}_{\mathrm{NIR}} F/d_{\mathrm{tot}}$ where $\mathcal{A}_{\mathrm{NIR}}$ is the computed NIR absorption, F is the pump fluence and d_{tot} is the total layer thickness composing the emitter [160]. Interestingly, one could derive the case of additionally added layers to the same heterostructure and substrate by direct THz measurements:

$$\xi = \frac{E'}{E} \propto \frac{\mathcal{A}'_{\mathrm{NIR}}}{\mathcal{A}_{\mathrm{NIR}}} \frac{Z'}{Z} \propto \mathcal{A}^{\mathrm{add}}_{\mathrm{NIR}} \frac{1}{1 + \frac{Z}{Z_0}\Delta n_{\mathrm{eff}}} \tag{E3.17}$$

with $\Delta n_{\mathrm{eff}} = Z_0 \int \sigma_{\mathrm{add}} dz_{\mathrm{add}}$ and $\mathcal{A}^{\mathrm{add}}_{\mathrm{NIR}} = \prod_j \exp(-\alpha^{\mathrm{add}}_j t^{\mathrm{add}}_j)$. We recover that, in the case of an added insulating layer ($\sigma_{\mathrm{add}} \to 0$) or no added layer ($t_{\mathrm{add}} \to 0$), $\Delta n_{\mathrm{eff}} \to 0$ and thus the measured electric field remains identical. In the case where only one layer is added, it is possible to recover the optical absorption, the thickness or the conductivity of the additional layer by measuring the THz field ratio ξ.

Experimental link with spin-current in spintronic structures. We present in Fig. 3.15 an example of the use of THz and NIR absorption renormalization procedure on Co(2)/Pt(t_{Pt}) bilayer series. It is possible using this method to extract the THz efficiency η_{THz} which scales with the spin diffusion length of Pt. In the case of a bilayer between a FM and HM layers, the spin-current depth profile follows:

$$\tilde{j_s}(t', t_{\mathrm{HM}}) = \int_0^{t_{\mathrm{HM}}} j_s(t', z) dz = j_s(t', 0^+)\ 2l_{sf} \tanh\left(\frac{t_{\mathrm{NM}}}{2l_{sf}}\right) \tag{E3.18}$$

in the so-called hard-wall model, where the $\tanh(t_{\mathrm{NM}}/2l_{sf})$ dependence comes from the specular reflections at low thickness of the NM layer. Note that in case of a FM/HM/FM trilayer, the injected spin current $j_s(t', 0^+)$ has now the following form $(j_s(t', 0^+) + j_s(t', t_{\mathrm{HM}}))/2$ due to the second adjacent spin injector. We can therefore identify an optimum value for an efficient THz emission given by the interplay between the maximal spin current conversion and the minimal metallic layer THz absorption. This value equals the spin diffusion length of the NM, roughly 3 nm for Pt in our case. THz spectroscopy allows thus to extract informations about the ultrafast spin-related relaxation processes.

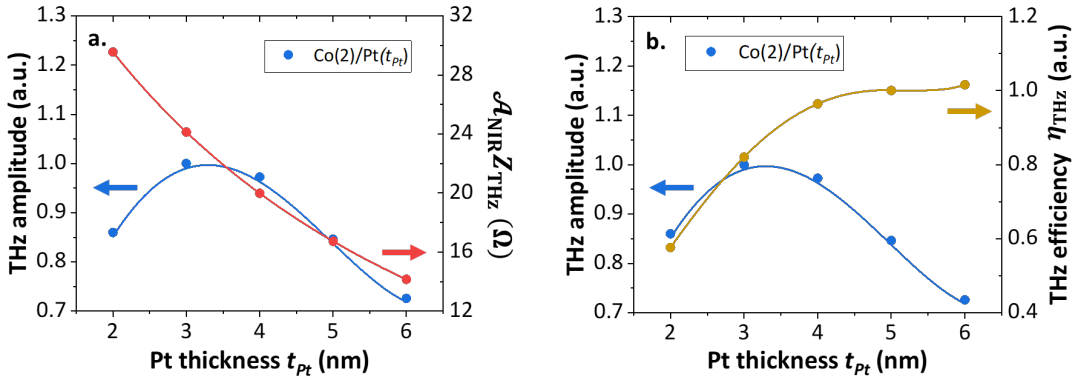

Figure 3.15: Interplay between the generated THz and the radiation absorption. (a) Representation of the experimental normalized THz amplitude (blue) and the absorption terms (red) for Co(2)/Pt(t_{Pt}) series, as a function of the Pt thickness t_{Pt}. (b) Comparison of the normalized THz efficiency (yellow) with the THz amplitude (blue) for the same series.

2.3 Extraction of the magnetic and non-magnetic components.

To extract the respective magnetic and non-magnetic contributions from measured THz signals, we perform a time-resolved sum (or difference) of two signals measured under opposite magnetizations $\pm\mathbf{M}$ (controlled by the magnetic field angle θ):

$$S_+(t) = \frac{S_{+\mathbf{M}}(t) + S_{-\mathbf{M}}(t)}{2} \quad \text{and} \quad S_-(t) = \frac{S_{+\mathbf{M}}(t) - S_{-\mathbf{M}}(t)}{2} \tag{E3.19}$$

Experimentally, a very slight tilt of the sample between the two magnetic field configurations can lead to a small shift in time of the second signal and should be corrected during the data treatment. Alternatively, this method can be implemented by considering the signal peak-peak amplitude $A_{\mathrm{pp}} = |\max(S) - \min(S)|$ and the signal phase $\Phi = \mathrm{sgn}\,(\arg(S))$. Eq. (E3.19) can therefore be rewritten as:

$$S_+ = \Phi^+ A^+_{\mathrm{pp}} = \frac{\Phi_{+\mathbf{M}} A^{\mathrm{pp}}_{+\mathbf{M}} + \Phi_{-\mathbf{M}} A^{\mathrm{pp}}_{-\mathbf{M}}}{2} \quad \text{and} \quad S_- = \Phi^- A^-_{\mathrm{pp}} = \frac{\Phi_{+\mathbf{M}} A^{\mathrm{pp}}_{+\mathbf{M}} - \Phi_{-\mathbf{M}} A^{\mathrm{pp}}_{-\mathbf{M}}}{2} \tag{E3.20}$$

This method will particularly be used in Chap. IV in order to decorrelate the spin-related phenomena from non-linear optical effects in topological insulators, or in Chap. V to identify the contribution from the Néel vector of NiO in the THz emission. In particular, we will perform this treatment as a function of the crystallographic angle ϕ, as shown in Fig. 3.16, to distinguish the interconversion symmetries from the non-linear optics symmetries.

2.4 Ultrafast spin current dynamics spectroscopy.

The measured THz signal $S_{\mathrm{EO}}(\omega)$ is a convolution between the THz electric field $E_{\mathrm{THz}}(\omega)$ and a certain transfer function $H_{\mathrm{EO}}(\omega)$ of the detector according to:

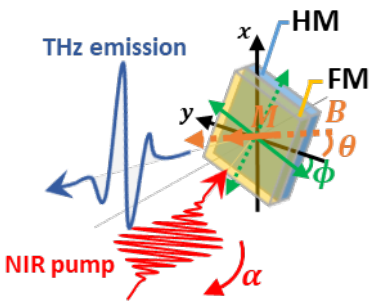

Figure 3.16: Experimental configuration of the two-independent angular rotations. The angle θ maps the in-plane rotation of the applied magnetic field with respect to e_y while the angle ϕ maps the azimuthal crystalline orientation rotation with respect to e_y (parallel to the optical table plane). The pump polarization can be tuned (linear or circular) with α the angle between the linear polarization and e_y. For sake of clarity, the pump and the generated THz pulse are tilted with respect to the sample normal which is not the case experimentally.

$$S_{\mathrm{EO}}(\omega) = H_{\mathrm{EO}}(\omega) * E_{\mathrm{THz}}(\omega) = \int H_{\mathrm{EO}}(t-t')E_{\mathrm{THz}}(t')dt' \tag{E3.21}$$

This transfer function represents the electro-optic response of the detection crystal (agreement with the electro-optic coefficient, the crystal thickness, the phase-matching, *etc.*) with respect to the THz pulses. Such transfer function can be experimentally quantified by THz transmission spectroscopy [250] of the detector as shown in Fig. 3.17. Using THz emission spectroscopy, it is possible, by subtracting the transfer function, to extract the time-resolved generated spin current and spin-charge conversion efficiency via a generalized Ohm law [83], as it will be performed on NiO/Pt system (Chap. V) in collaboration with T. Kampfrath's team (FUB), according to:

$$S_{\mathrm{THz}}(\omega) \overset{H_{\mathrm{EO}}^{-1}(\omega)}{\longrightarrow} E_{\mathrm{THz}}(\omega) \overset{\times(eZ(\omega)\theta_{\mathrm{SHE}}\lambda_{rel})^{-1}}{\longrightarrow} j_s(\omega) \overset{\mathcal{F}^{-1}}{\longrightarrow} j_s(t) \tag{E3.22}$$

Link between spin-current and THz emission spectroscopy.

From now on, we will use THz emission spectroscopy as a central technique to address the dynamical properties of the spin-injection, spin transport and spin-charge conversion in spintronic THz emitters.

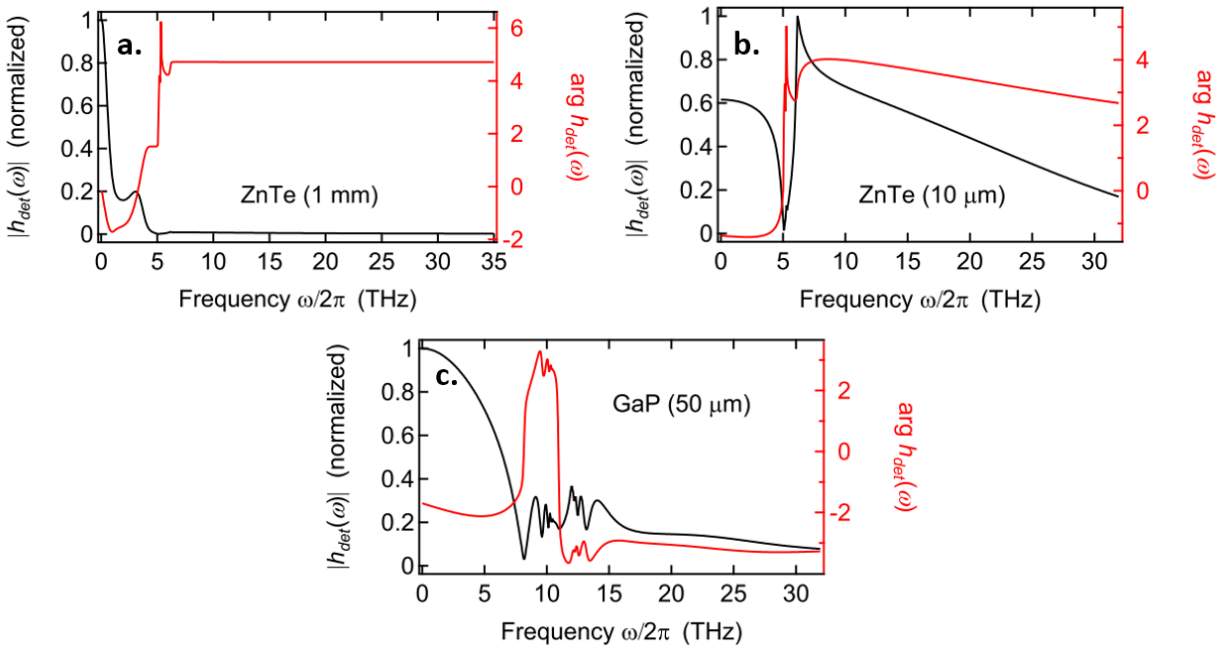

Figure 3.17: Transfer function of the electro-optic sampling. Experimental transfer functions $H_{\mathrm{EO}}(\omega)$ defined by their amplitude $|h_{\mathrm{det}}(\omega)|$ and phase $\arg(h_{\mathrm{det}}(\omega))$ as a function of the frequency, obtained for ZnTe$\langle 110\rangle$(1mm), ZnTe$\langle 110\rangle$(10μm) and GaP$\langle 110\rangle$(50μm) non-linear crystals used for detection via electro-optic sampling. Reproduced from Ref. [250].

3 3*d*/5*d* metallic THz spintronic emitters: material engineering.

Spintronics *vs.* current THz technologies. As an introductive remark, we first compare the photoconductive antenna (photo-Dember), non-linear crystal (optical rectification) and spintronic THz technologies. We report in Fig. 3.18 the THz emission from a spintronic trilayer W(2nm)/CoFeB(1.8nm)/Pt(2nm) compared to a ZnTe$\langle 110 \rangle$ (500µm) and an optimized photoconductive switch (PCS) grown on LT-GaAs (low temperature for shorter carrier lifetime) [251]. The PCS is composed of a top 500 $\times$ 500 µm^2 interdigitated antenna of width 8 µm and separation 4 µm. One Au plane acting as a THz reflector is buried around d=10 µm. A bias of $V_{\text{bias}} = 6$ V peak modulated at 25 kHz is applied on the antenna. The generated THz amplitude are normalized with respect to the spintronic emitter and we can observe that from the optimized trilayer STE, the ZnTe non-linear crystal generated THz via optical rectification is found to be smaller by an field amplitude about 25%. We then turn on the THz amplitude generated by the PCS and found an amplitude increased by a factor $\times 80$ in amplitude (corresponding to a power increased by a factor $\times 6400$) addressing that efforts are needed to propose STE as alternative THz sources. Although the performances of STE are still to be enhanced, STEs have a larger emission bandwidth (not shown here, refer to Chap. II) whereas the PCA technology cuts at lower frequencies (phonon absorption in GaAs around 8 THz).

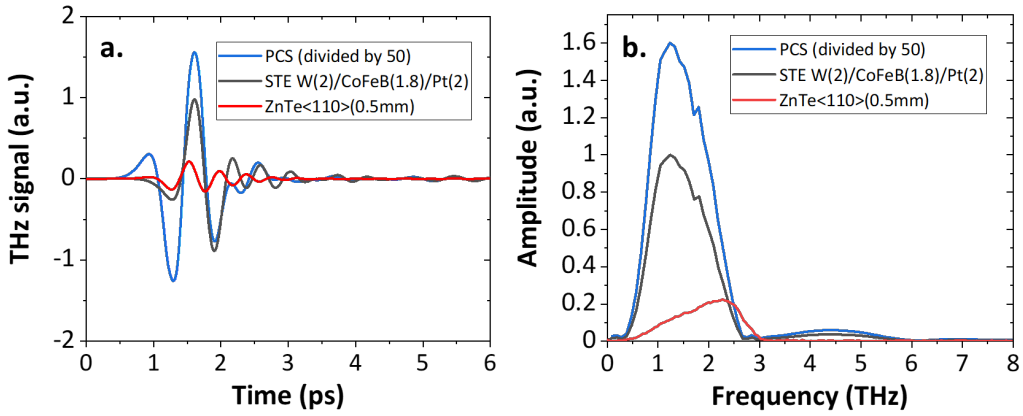

Figure 3.18: Comparing STE with actual pulsed THz technologies. (a) THz emission from a ZnTe$\langle 110 \rangle$(500µm), a photoconductive switch (PCS) and the reference spintronic trilayer W(2nm)/CoFeB(1.8nm)/Pt(2nm). (b) Measured bandwidth for the three systems. The amplitudes are normalized with respect to the spintronic emitter. Note that the THz amplitude of the PCS is divided by a factor $\times 50$.

We will now present the different investigations performed on metallic STEs. In an outline of this section, we will demonstrate that the THz emission figure-of-merit has the following form:

$$\eta_{\text{FOM}} \propto \frac{1}{2}(g_{\uparrow} + g_{\downarrow}) \underbrace{\theta_{\text{SHE}}\sigma_{xx}}_{=\sigma_{\text{SHE}}} l_{sf}|M|Z(\omega) \tag{E3.23}$$

where $g_{\uparrow} + g_{\downarrow}$ is the interfacial spin conductance term, θ_{SHE} is the spin Hall angle, σ_{xx} is the conductivity, l_{sf} is the spin diffusion length, $|M|$ is the magnetization and $Z(\omega)$ is the THz impedance. Each term will thus be separately studied in this chapter. In a perspective to address the physical challenges in ultrathin spintronic multilayers, we first propose a material engineering and conversion efficiency understanding by using *i*) spin-Hall alloys (Au:Ta, Au:W, *etc.*) of higher interconversion efficiency, or *ii*) the structure repetition strategy to increase the number of radiating THz dipoles. We then propose to study closely the spin-current propagation and tailoring in 3d/5d heterostructures by studying *i*) the spin-sink strategy, *ii*) the tuning of the electronic transmission and interfacial properties via the use of metallic inset layers (Ti, Au:W, *etc.*) between

the spin reservoir and conversion layer, and finally *iii*) the use of high spin-polarization Heusler materials. We report via those studies several tracks to enhance the THz performances derived from spintronic metallic structures.

3.1 Role of the spin-charge conversion efficiency with spin Hall alloys.

According to the spin-charge process and modelling, a larger spin Hall angle would lead to a larger THz emission power according to a θ^2_{SHE} dependence. Such high values of the spin Hall angle (compared to Pt) can be encountered in Au-based alloys, for instance between Au:Ta and Au:W alloys as reported in Table III.2 [38, 37, 39]. Those materials, previously studied [38, 39], are expected to show a large spin Hall angle due to *i*) the increase of the scattering rate by alloying and *ii*) the increase of the extrinstic contribution to the spin Hall effect. We reproduced in Fig. 3.19 the results of Ref. [39] where the authors reported the evolution of l_{sf} and θ_{SHE} for Au:W alloy as a function of W concentration (or similarly Au:W resistivity).

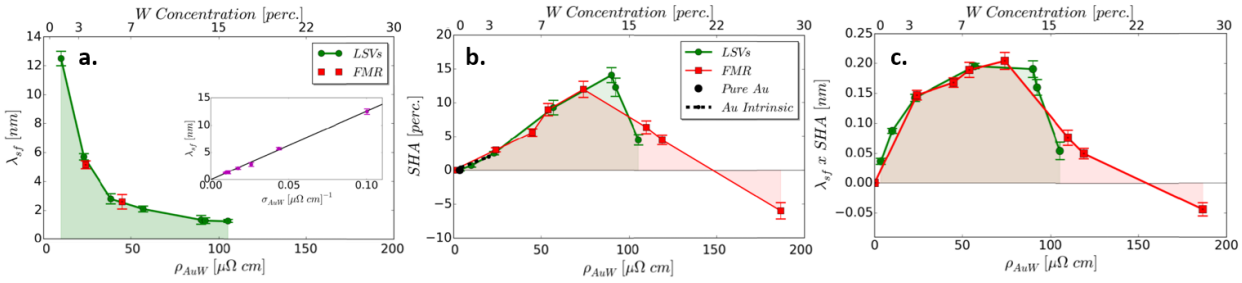

Figure 3.19: Au:W spin-Hall alloy properties. Values of (a) the spin diffusion length l_{sf}, (b) the spin Hall angle θ_{SHE} and (c) the product for Au:W spin Hall alloy as a function of the concentration of W (%) or similarly the resistivity. Reproduced from Ref. [39].

System	Pt [38, 39]	Au:W [38, 39]	Au:Ta [38, 39]
θ_{SHE}	0.06	0.15	0.25
σ_{SHE} (kΩ^{-1}.cm^{-1})	3.5	1.6	5
ρ_{xx} (μΩ.cm)	17	90	50
l_{sf} (nm)	3	3	1.5

Table III.2: Properties of Au-based spin Hall alloys compared to Pt heavy metal, without considering the interfacial spin-memory loss.

We present in Fig. 3.20a the results obtained by replacing Co/Pt by Co/X where X={Au:Ta, Au:W}. Contrary to the expected trend, we measured a THz amplitude decrease by replacing Pt with Au:W and Au:Ta, by a factor $\times 20$ in both cases. We also compared in the same measurement series Co/Pt and NiFe/Pt, which amplitude is about 90% of Co/Pt for the same thicknesses. We would relate this reduction either to a change of the interfacial spin-mixing conductance as it is known that Co/Pt is the best interface for THz spintronics [83], or related to a lowered spin-polarization (see for instance Table I.1).

To explain the discrepancy between the expected enhancement by the spin Hall angle and the measured lowered THz signals in Au-based alloys, we develop several hypothesis. First, in Au-based alloys, the spin-transport is degraded due to the dopant intermixing, which leads to a reduction of the spin diffusion length l_{sf} by a factor $\times 2$ [39]. Secondly, we discuss in terms of the resistivity of the replaced layer. For alloys, the resistivity is increased due to higher scattering (collisions) rate because of alloying, the latter evolving as $1/\tau_{\text{sc}} = v_{\text{F}}\mathcal{N}\sigma_{\text{sc}}$ where σ_{sc} is the scattering cross section. Therefore in terms of THz absorption, Au-based alloys are a more favorable playground. However, this is to put aside the change of the spin Hall conductivity $\sigma_{\text{SHE}} = \sigma_{xx}\theta_{\text{SHE}}$ in overall reduced in alloys. This shows that the spin Hall angle increase is largely compensated by

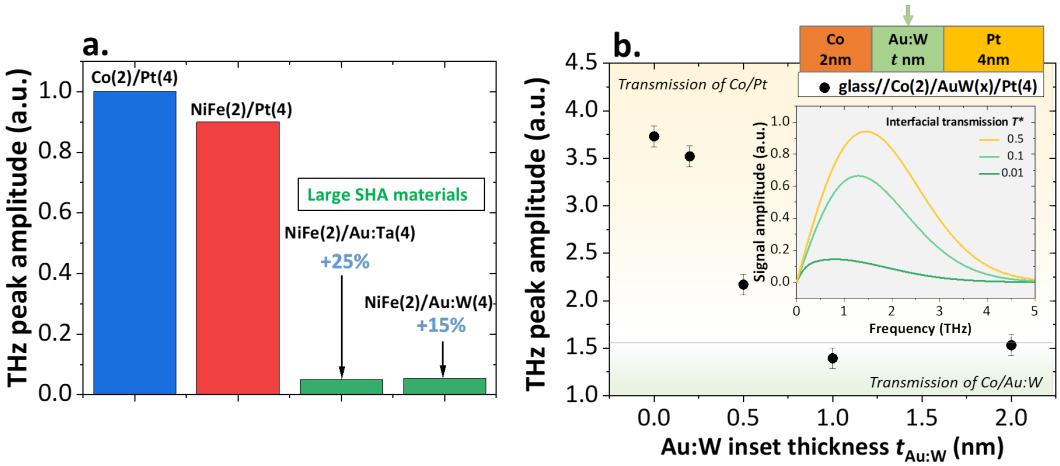

Figure 3.20: Replacing the heavy metal with large spin Hall angle Au-based alloys. (a) Histogram presenting the THz peak amplitude from Co(2)/Pt(4), NiFe(2)/Pt(4), NiFe(2)/Au:Ta(4) and NiFe(2)/Au:W(4). (b) THz peak amplitude from Co(2)/Au:W(t_{AuW})/Pt(4) as a function of the Au:W thickness t_{AuW}. The inset presents the modelled THz amplitude as a function of the interfacial transmission coefficient T^*.

the resistivity change and is the key parameter while looking at spin Hall alloys (Eq. (E3.23)). By introducing the spin Hall conductivity, the THz electric field can thus be written as [231]:

$$E_{\mathrm{THz}}(\omega) \simeq \frac{i\omega\kappa\tau_{sf}\theta_{\mathrm{SHE}}}{(1-i\omega\tau)(1-i\omega\tau_{sf})}\left(\frac{\sigma_{\mathrm{SHE}}}{\mathcal{N}(\varepsilon)e^2}j_c(\omega,z=0)\right) \quad \text{with} \quad \kappa=\frac{1}{\sqrt{\tilde{D}\tau_{sf}}} \tag{E3.24}$$

Thirdly, we also further develop the possible degradation of the interfacial transparency in Co/Au:W and Co/Au:Ta by carrying a second study where we have inserted a disordered Au:W(t_{AuW}) alloy in between Co(2nm) and Pt(4nm) as displayed in Fig. 3.20b. We observe that the THz peak amplitude decreases as a function of Au:W thickness t_{AuW}, estimated to a factor $\times 2$ up to $\times 2.5$. This is correlated to the interfacial transmission linked to the different spin conductance. To highlight this effect, we have modelled the structure where we have artificially degraded the interface by tuning the transmission coefficient T^* from 0.5 (case of Co/Pt) to 0.01. We observe a drastic reduction of the THz amplitude. Therefore at large Au:W inset thicknesses, the THz emission is hampered by the dominating interfacial properties of Au:W and prevents an efficient spin-injection for SCC in Pt.

In conclusion, we have reported three arguments to explain the strong reduction of the THz amplitude in Au-based alloys: *i*) the reduction of the spin diffusion length (factor $\times 3$), *ii*) the change of the spin Hall conductivity (factor $\times 2$) and *iii*) the reduction of the interfacial transmission (factor $\times 2$). To this, we need to add the optical pump absorption in Au-based alloys, reducing the effective pumping of the ferromagnetic reservoir. All those elements are explaining the reduction of the THz amplitude in Au-based alloys. From all these parameters, one needs to gain a better comprehension of the spin-injection properties: this will be addressed in the second part of this section via the interfacial spin-conductance.

3.2 Repetition layers strategy.

A different strategy to gain in the THz emission is to grow a heterostructure composed of N STE repetitions like Co/Pt. To avoid the electrical shunting of the THz current, it is necessary to separate the Co/Pt stacks by an insulating barrier such as AlO_x. In the regime where residual NIR pump can be absorbed in the additional $(N+1)$ Co/Pt repetition, one expects naively to multiple the obtained THz emission following the increase of the THz efficiency by $N\eta_{\mathrm{THz}}$. We

strongly emphasis on the fact that the radiated dipolar emissions of each separated repetition are in phase as the interlayer distances are much smaller than the THz wavelength.

We implemented those structures for $N = \{1, 2, 3, 4\}$ denoted as $[\text{Co(2)/Pt(2)}]_N$ on glass substrates and performed THz emission spectroscopy in reflection as displayed in Fig. 3.21. We observe an increase of the THz emission up to $N = 2$ followed by a decrease of the amplitude. The maximal enhancement at $N = 2$ is about +50% in field (about $\times 2.25$ in power). This behaviour is linked to the radiation absorption in the additional metallic layer which overcomes the enhancement of the far-field emission by the additional N-th repetition. Besides, we have also extracted the THz efficiency η_{THz} as a function of the repetition number N as displayed in the inset of Fig. 3.21. We report a linear increase of the THz efficiency as expected from the model. Those results are similar to Refs. [84, 154] for thin bilayers STEs.

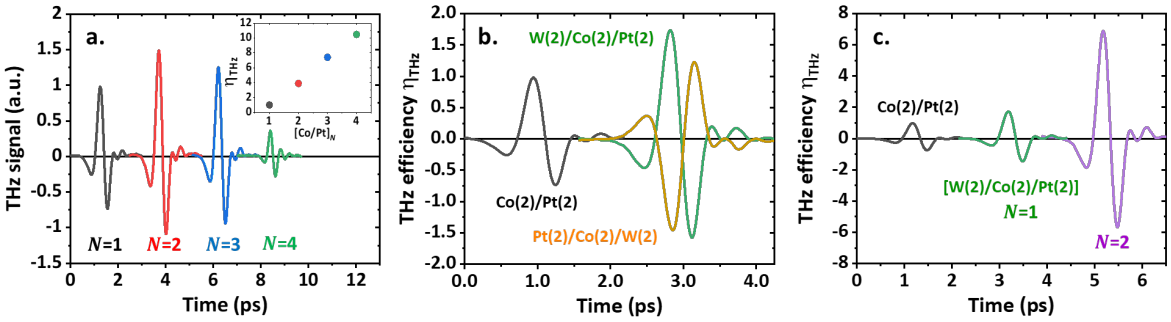

Figure 3.21: Repetition strategy of optimized STEs. (a) THz emission from $[\text{Co(2)/Pt(2)}]_N$ (separated by AlO_x(1nm) between each repetition). The inset presents the THz efficiency as a function of the N-th Co/Pt repetition. (b) THz efficiency from W(2)/Co(2)/Pt(2) and Pt(2)/Co(2)/W(2) trilayers compared to Co(2)/Pt(2) bilayer. (c) THz efficiency from Co(2)/Pt(2) bilayer, $[\text{W(2)/Co(2)/Pt(2)}]_{N=\{1,2\}}$ repeated trilayers.

To explain quantitatively this drawback, we calculate the radiation absorption *vs.* N periodic repetition(s) of identical Co/Pt multilayers from use of Section III.2.2, it comes:

$$E_{\text{THz}}^{(N)} \propto \frac{Z_0 \sum_N (\mathcal{A}_{\text{NIR}}^{\text{Co/Pt}})^N}{1 + n_{\text{sub}}(\omega) + N\, Z_0 \sum_p \sigma_p(\omega) t_p} \times (N \theta_{\text{SHE}} \eta_{\text{THz}}) \tag{E3.25}$$

where typically, each Co(2)/Pt(2) bilayer absorbs $\mathcal{A}_{\text{Co/Pt}} \simeq 26\%$ of the incoming pump. As the AlO_x spacer is insulating and infrared-transparent, it can be assumed that only the metallic N-th repetition enters in such analytical form. By deriving the geometry sum, we obtain:

$$E_{\text{THz}}^{(N)} \propto \frac{Z_0\, N_m \left(1 - \exp\left(-N/N_m\right)\right)}{1 + n_{\text{sub}}(\omega) + N\, Z_0 \sum_p \sigma_p(\omega) t_{\text{p}}} \times (N \theta_{\text{SHE}} \eta_{\text{THz}}) \tag{E3.26}$$

where we denote $N_m = l_{\text{NIR}}/d_p$ with l_{NIR} is the absorption length of the NIR pump in one repetition layer which is equal to $1/\sum_i \alpha_i$, around 6.6 nm in our case and $d_p = \sum_p t_p$ is the total metallic thickness of a repetition contributing to the dipolar emission, about 4 nm in our case. For the trilayer repetition, the spin Hall angle term becomes $\simeq \theta_{\text{SHE}}^1 + \theta_{\text{SHE}}^2$ and the NIR absorption term changes as d_p=6 nm, l_{NIR} ≃5.1 nm and $\mathcal{A}_{\text{W/Co/Pt}} \simeq 32\%$.

Implementation of the repetition strategy on optimized trilayers. We now focus on already-optimized trilayers STEs composed of W/Co/Pt following the report of Seifert *et al.* [83]. Fig. 3.21b-c presents the comparison between the THz efficiency obtained from W/Co/Pt trilayers with Co/Pt bilayer. We see that the phase of the THz radiation generated in W shares the same phase as the radiation from top Pt, enhancing the total radiation measured in free-space. With this trilayer technique, we measured a THz efficiency increased by +75% compared to the efficiency of Co/Pt bilayer. We also prepared a dual-repetition of the trilayer structure $[\text{W/Co/Pt}]_{\times 2}$ and

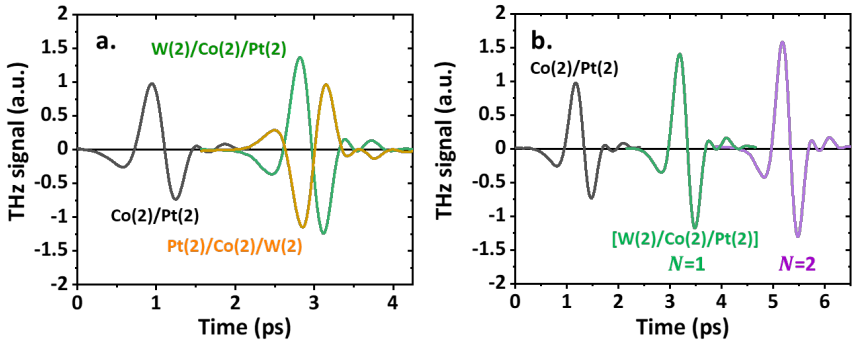

Figure 3.22: Repetition strategy of optimized trilayers STEs. (a) THz emission of trilayers W(2)/Co(2)/Pt(2) and Pt(2)/Co(2)/W(2) compared to reference bilayer Co(2)/Pt(2). (b) Implementation of the repetition strategy on trilayers $[W(2)/Co(2)/Pt(2)]_N$ with $N = \{1, 2\}$

obtained an experimental THz efficiency of the order of a factor $\times 7$ compared to single bilayer Co/Pt. However, this trend is not recovered on the measured THz signal as shown in Fig. 3.22: despite the additional W(2) layer absorbing the NIR and THz radiations, the THz emission from W(2)/Co(2)/Pt(2) is larger by a factor +40%. Even for $N = 2$ repetition of the trilayer structure, the THz amplitude from $[W/Co/Pt]_N$ is increased about a factor +60% from Co(2)/Pt(2), which is however only an enhancement about +6% compared to the single trilayer repetition case $N = 1$. The maximal THz amplitude in single trilayers (for $N = 1$) is then comparable to the maximal THz amplitude measured in repeated bilayers (for $N = 2$), about +50% from the reference bilayer Co(2)/Pt(2).

Conclusion on material optimization: spin-Hall alloys and repetition layers.

We have seen that the use of spin-Hall alloys for replacing optimized Pt layer is limited due to the higher slip-flip rate, shorter spin-diffusion length and decreased spin Hall conductivity. The repetition strategy, efficient in metallic bilayers, is however limited in trilayers due to the strong radiation absorption. Although we expect a large THz efficiency increase (up to a factor $\times 7$), we measure at maximum in the dual repetition of the trilayers a THz emission increased by +60% compared to Co(2)/Pt(2) which corresponds to a power enhancement about $\times 2.6$. As a comparison, we measured in the double repetition of the bilayer Co/Pt a maximal enhancement factor about +50% which corresponds to a power enhancement of $\times 2.25$. In all cases, the expected THz efficiency proves that margins are still possible to generate higher THz amplitude, hindered in metallic structures by the strong wave absorptions. To envision such enhancements, one could thus try to gain in radiation amplitude by using TI/FM multistacks, as topological insulators (TIs) are more resistive layers, about one order of magnitude higher compared to $5d$ transition metals. TIs will be explored in Chap. IV. In the mean time, we now provide a careful spin-current tailoring approach in thin heterostructures by use of *i*) the spin-sink strategy and *ii*) interfacial considerations to tune the electronic transmission.

3.3 Spin-sink layers.

A novel strategy that we have developed to increase the THz efficiency of metallic THz STE is the use of spin-sink layers to avoid the reflected spin-flip backflow j_s^{backflow}. Indeed, spin-current injection in a thin HM layer can suffer the reduction of the net spin current (called j_s^{HM}) due to detrimental reflection at the edge of the HM layer for thicknesses typically below the spin relaxation length l_{sf}. A spin-sink (SS) material would thus be defined as a layer acting as a pure drain of spins in which the remaining spin current j_s^{net} could be absorbed (*i.e.* relaxed). The spin-

transparency (or spin-mixing conductance) of the HM/SS interface is therefore crucial to have a noticeable enhancement effect.

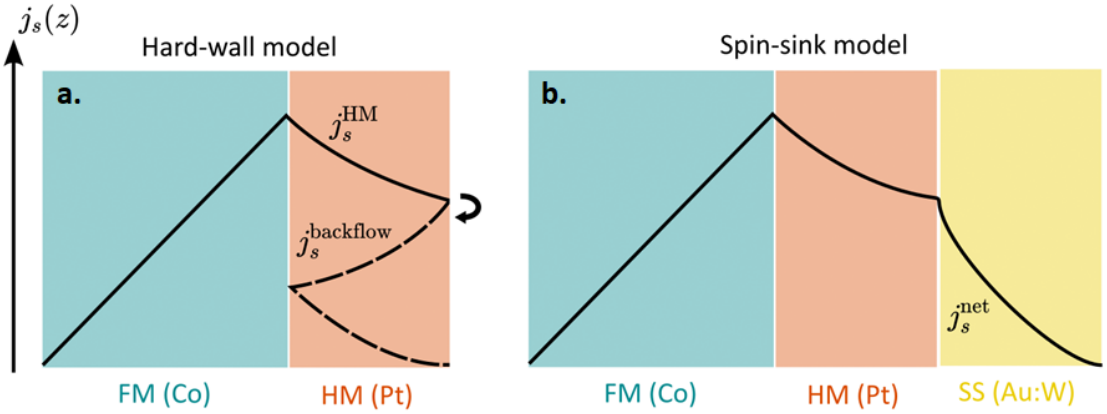

Figure 3.23: Illustration of the spin-sink strategy. (a) Conventional FM/HM structure with t_{HM} typically below the spin diffusion length l_{sf}^{HM}. The spin backflow reduces the effective converted spin-current: this is the hard-wall model. (b) Enhanced FM/HM/SS structure with the same value of t_{HM} but with an additional spin-sink layer. The injected spin-current at the FM/HM interface is identical to the first case but all the net accessible spin-current is converted. For clarity, the spin memory loss is not represented in both cases.

Modelling the spin-sink enhancement. To account the effect of the spin-sink layer, we have considered a three-layer model where the interfacial spin-resistance in the FM layer r_{FM}^s and in the HM layer r_{HM}^s are tabulated with $r^s = \rho_{xx} l_{sf}$ (as derived in Section I.4.1). The spin-sink concept is schematized in Fig. 3.23. We establish a generalized trilayer model as a function of the spin-resistance of an additional layer called the spin-sink of resistance r_{SS}^s. The demonstration from the Valet-Fert model is left to the reader in Appendix A3. We obtain:

$$\eta_{THz}(t_{HM}, r_{SS}^s) = \frac{2l_{sf}^{HM} r_{FM}^s \sinh\left(\frac{t_{HM}}{2l_{sf}^{HM}}\right)\left(r_{HM}^s \cosh\left(\frac{t_{HM}}{2l_{sf}^{HM}}\right)+r_{SS}^s \sinh\left(\frac{t_{HM}}{2l_{sf}^{HM}}\right)\right)}{r_{HM}^s\left(\left(r_{FM}^s \cosh\left(\frac{t_{HM}}{l_{sf}^{HM}}\right)+r_{HM}^s \sinh\left(\frac{t_{HM}}{l_{sf}^{HM}}\right)\right)+r_{SS}^s\left(r_{HM}^s \cosh\left(\frac{t_{HM}}{l_{sf}^{HM}}\right)+r_{FM}^s \sinh\left(\frac{t_{HM}}{l_{sf}^{HM}}\right)\right)\right)} \quad \text{(E3.27)}$$

By use of the relation $\sinh(2x) = 2\sinh(x)\cosh(x)$, we can extract two limit cases, depending on the spin-sink spin-resistance, which are noticeable: we call hard-wall (HW) model the initial model of spin-current injection from a FM into a HM of thickness t_{HM}, recovered for $r_{SS}^s \to +\infty$. The spin-sink (SS) model is derived in the limit of a spin-resistance $r_{SS}^s \to 0$ acting as a pure spin drain without interfacial scattering or spin loss, giving respectively:

$$\eta_{THz}^{ss}(t_{HM}) \underset{\text{spin-sink}}{=} \frac{l_{sf}^{HM}}{\coth\left(\frac{t_{HM}}{l_{sf}^{HM}}\right)+\frac{r_{HM}^s}{r_{FM}^s}} \quad \text{and} \quad \eta_{THz}^{hw}(t_{HM}) \underset{\text{hard-wall}}{=} \frac{l_{sf}^{HM}}{\coth\left(\frac{t_{HM}}{2l_{sf}^{HM}}\right)+\frac{r_{HM}^s}{2r_{FM}^s}\left[1+\coth^2\left(\frac{t_{HM}}{2l_{sf}^{HM}}\right)\right]} \quad \text{(E3.28)}$$

where t_{HM} and l_{sf}^{HM} are respectively the HM layer thickness and HM spin diffusion length. The spin-sink gain can thus be expressed as the area between the spin-sink model and the hard-wall model according to:

$$\mathcal{G}(t_{HM}) = \frac{\eta_{THz}^{ss}(t_{HM}) - \eta_{THz}^{hw}(t_{HM})}{\eta_{THz}^{hw}(t_{HM})} = \frac{r_{HM}^s \coth\left(\frac{t_{HM}}{2l_{sf}^{HM}}\right) + r_{FM}^s}{r_{FM}^s \cosh\left(\frac{t_{HM}}{l_{sf}^{HM}}\right) + r_{HM}^s \sinh\left(\frac{t_{HM}}{l_{sf}^{HM}}\right)} > 0 \quad \text{(E3.29)}$$

We present in Fig. 3.24a the resulting efficiencies corresponding respectively to the case of the hard-wall and the spin-sink models for two different spin diffusion lengths of Pt l_{sf}^{Pt}=2.5-3 nm. We also display in Fig. 3.24b the expected gain profile as a function of the Pt thickness t_{Pt}. We see that in the low thickness limit, $\mathcal{G}$ goes to $+\infty$ while in the large thickness regime, the gain is expected to become zero as all the conversion has been made in the thick Pt. We can say that the gain diverges close to zero because the efficiency η_{THz} evolves as t_{HM}^2 for the hard-wall model and as t_{HM} for the spin-sink model.

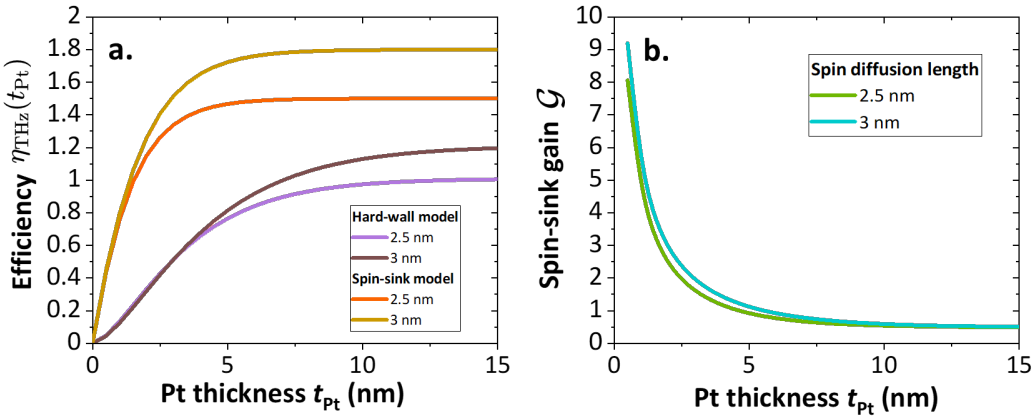

Figure 3.24: Profile of the spin-sink gain. (a) Efficiency as a function of Pt thickness t_{Pt} for the hard-wall model and the spin-sink model derived for a spin diffusion length l_{sf}=$\{2.5, 3\}$ nm. (b) Spin-sink gain $\mathcal{G}(t_{\mathrm{HM}})$ as a function of the Pt thickness t_{Pt} for l_{sf}=$\{2, 3\}$ nm (calculated down to 0.5 nm). The considered spin resistances are r_{F}^s=15 and r_{HM}^s=3 (given in units of the Sharvin resistance).

Experimental implementation using Au:W spin Hall alloy. We have implemented experimentally this strategy on Co/Pt multilayers by capping with a Au:W alloy which is well-known to be an efficient spin-sink [38, 37] with a large spin-transparency with Pt. Its spin Hall angle depends on the resistivity of the alloy (Fig. 3.19), and we focus on the range $\rho_{\mathrm{AuW}} = 87 - 130$ μΩ.cm. We select two resistivities: 117 μΩ.cm of spin Hall angle about $+15\%$ or 87 μΩ.cm of spin Hall angle about $\simeq 0\%$. The samples are deposited at room temperature by sputtering in a single deposition chamber on MgO(001) and SiHR substrates. A specifically prepared Au:W target, by means of 15% of W and 85% of Au, is used for evaporation on the samples. Calibration samples of 50 nm have been realized prior to our studies to estimated the film resistivity of Au:W about 87 μΩ.cm and 117 μΩ.cm.

We first performed measurements on the spin-sink effect in Co(2nm)/Pt(t_{Pt})/Au:W(2nm) samples as a function of the Pt thickness t_{Pt} ranging from 2 to 5 nm, as presented in Fig. 3.25. We observe that for each Pt thickness, the measured THz emission exceeds the reference emitter Co(2)/Pt(4) which is the reference (optimized) point for the bilayer. Specifically on this optimized thicknesses Co(2)/Pt(4), the spin-sink gain in THz amplitude is about +45%. At low thickness like Pt(2nm), the spin-sink gain is even more pronounced, about +80%, owing to the avoided spin backflow at the Pt surface boundary and subsequent detrimental spin reflections. By comparing with the reference Pt thickness dependence Co(2)/Pt(t_{Pt}) as presented previously in Section III.3.5, the ratio between the THz emission for Co(2)/Pt(2) and Co(2)/Pt(4) is about 13% which leads to an estimation of the spin-sink effect at 2 nm of $\times 6$ comparing with the effect of the addition of Pt(4). We thus see the importance of such Au:W spin-sink on thin Co/Pt layers to *i*) avoid the spin current backflow while *ii*) reducing the effective conductivity of the stack by using more resisitive Au:W alloy (compared to a configuration where Pt(2) would have been increased up to Pt(3-4)).

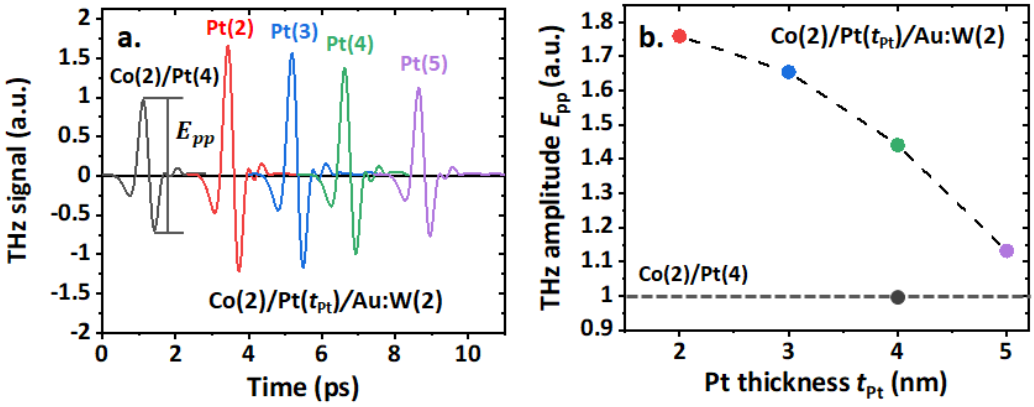

Figure 3.25: Au:W spin-sink on Co/Pt bilayers. (a) Time traces from Co(2nm)/Pt(t_{Pt})/Au:W(2nm). (b) THz peak-peak amplitude representation.

We further explore the trends of the THz efficiency in optimized spin-sink layers. By subtracting the absorption contributions from the optical conductivities (see Section III.2.2), we are able to connect the figure of merit to our spin-sink and hard-wall model as shown in Fig. 3.26. We first report a THz efficiency up to a factor of 2 for Co(2)/Pt(t_{Pt})/Au:W(2) samples compared to the Co(2)/Pt(t_{Pt}) samples. Besides, we obtain a qualitative agreement between the hard-wall and the spin-sink models with our experimental data, with an extraction of the spin diffusion length of l_{sf}=3 nm in case of the hard-wall model and l_{sf}=2.5 nm in the case of the spin-sink model. The spin-resistance derived from the trilayer model are expressed $r^s_{\mathrm{FM}} = \rho_{\mathrm{FM}}(l^{\mathrm{FM}}_{sf})^2/t_{\mathrm{FM}}$ for the FM layer and $r^s_{\mathrm{HM}} = \rho_{\mathrm{HM}} l^{\mathrm{HM}}_{sf}$ for the HM layer. By numerical application, we found about $r^s_{\mathrm{FM}} \simeq 15$ (3 fΩ.m^2) for Co and $r^s_{\mathrm{HM}} \simeq 3$ (0.6 fΩ.m^2) in case of Pt given in units of the Sharvin resistance (R_{Sh}=0.2 fΩ.m^2) as reported in Section I.4.1. Visually, the spin-sink enhancement is the area enclosed between the hard-wall curve and the spin-sink curve and is therefore maximal when the Pt thickness equals its spin diffusion length. At large thicknesses ($t_{\mathrm{HM}} \gg l^{\mathrm{HM}}_{sf}$), the gain due to the spin-sink layer is almost zero as the spin relaxation fully occurs in the HM layer. Interestingly in the low thickness regime, the spin-sink model evolves as t_{HM} while it is following t^2_{HM} for the hard-wall.

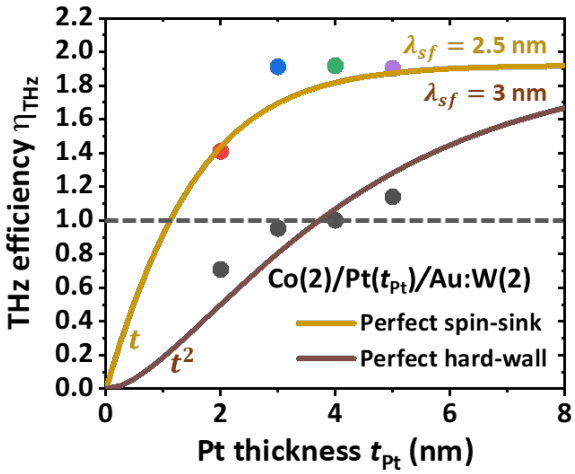

Figure 3.26: Au:W spin-sink on Co/Pt bilayers. THz efficiency presented for Co(2)/Pt(t_{Pt})/Au:W(2) (color dots) compared to Co(2)/Pt(t_{Pt}), alongside the hard-wall model (brown) and the spin-sink model (yellow).

Spin-sink trilayers. We have now employed the spin-sink strategy in already optimized dual-SCC W/CoFeB/Pt trilayers. We present respectively in Fig. 3.27a and Fig. 3.27b the results of the THz emission and THz efficiency comparing optimized W(2)/Co(2)/Pt(2), W(2)/CoFeB(2)/Pt(2) layers and $[W(2)/CoFeB(2)/Pt(2)]_{N=\{1,2\}}$ trilayer sequences. We report a reduction of the net THz emission in both optimized spin-sink samples, by -5% and -180% respectively for the spin-sink with $N = 1$ and $N = 2$. On the other hand, we observe a net increase of the THz efficiency on both $N = \{1, 2\}$ spin-sink samples, accounting for the increase of the electronic efficiency in the Pt layer. Here, the net THz emission in spin-sink implemented trilayers is reduced owing to a strong THz absorption by the metallic multistacking due to the effective increased thickness of metallic layer in the trilayers. However, we notice a similar trend for the THz efficiency using the spin-sink strategy.

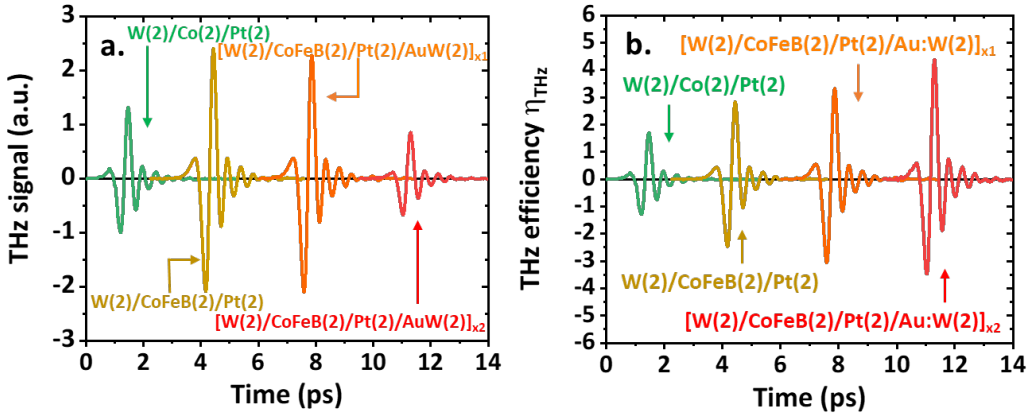

Figure 3.27: Spin-sink strategy in optimized STE trilayers. (a) THz emission and (b) THz efficiency for W(2)/CoFeB(2)/Pt(2), $[W(2)/CoFeB(2)/Pt(2)]_1$ and $[W(2)/CoFeB(2)/Pt(2)]_2$ compared to W(2)/Co(2)/Pt(2) trilayer without spin-sink.

Nature of the FM layer: Co *vs.* CoFeB. We discuss in this part the exact role of the nature of the ferromagnetic injection reservoir. As noticed in Fig. 3.27, the THz emission from the trilayers W(2)/Co(2)/Pt(2) is nearly doubled in amplitude by replacing Co(2) by CoFeB(2) (exact composition of the alloy is $Co_{60}Fe_{20}B_{20}$). Although the change of the resistivity between Co and CoFeB materials may explain a part of the results from minimization of the THz absorption (the resistivity of CoFeB is expected to be larger than for Co), we think that a larger THz emission with CoFeB may be better explained from a strong reduction of the spin-flip process in CoFeB (larger spin-resistance of the FM layer as it scales with ρ_{xx}). This will be developed further below with the use of Co_2MnGa Heusler compound of higher spin-polarization in Section III.4.2.

In conclusion, we demonstrate a significant increase of the THz efficiency by employing spin-sink layers, either on bilayers or trilayers. The enhancement ratio of the THz efficiency can reach up to a factor $\times 2$ in amplitude ($\times 4$ in power) for already optimized Pt thicknesses for the bilayers. One drawback of this method is that, by using metallic spin-sink, one may loose a part of the efficiency gain by radiation absorption in the additional metallic layers, especially for trilayers. One could thus envision to implement efficient insulating THz spin-sink layers but future challenges exploring this area will be to find insulating materials allowing a large spin-mixing conductance at the interface with a metallic SOC layer.

Importantly, this opens up perspectives to study the effect of the pump duration τ_p on the spin-sink effect. Indeed, although for long pump times the spin backflow can be avoided, this

effect might not be recovered for short pump times. Indeed, the generated electric field is proportional to the derivative of the charge current which is expected to be higher in case of spin backflow for short durations of the pump. This hypothesis, quickly addressed in Section III.1.2.4, is still to be evidenced experimentally and will be the object of further studies.

3.4 Comparative study with extracted spin-orbit torques.

In that part, we propose comparative studies of the THz emission and the spin-orbit torque measurements on the same series of spin-sink Co(2)/Pt(t_{Pt})/Au:W(2) trilayers in order to highlight a correlated increase of a spin-injection efficiency. Indeed, we would like to know if the gain evidenced in spintronic THz emitters can be transposed to spin-torque compatible spintronic devices. Extracting spin-orbit torques is performed via harmonic voltage measurements (quasi-DC) which attracted attention as an efficient technique to determine the spin Hall angle of Au-based alloys [159] or more recently to map a strong Rashba interactions in metallic multilayers [252]. In the first kind of experiments by THz emission spectroscopy, a pulsed spin-current is injected (well above the Fermi level) from Co into the active Pt layer where the ISHE converts it into a lateral charge current. In the secondary spin-torque measurement, we deal with the reciprocal experiment where a charge current flows into the Pt layer and is converted into a lateral spin current injected thereafter in the ferromagnetic layer (at the Fermi level). Such spin-current interacts with the local magnetization and is possibly able to switch the direction of the magnetization (magnetization switching experiments).

We plot in Fig. 3.28 a direct comparison of the experimental spin-sink gain $(\eta_{ss}-\eta_{hw})/\eta_{hw}$ and modelled $\mathcal{G}$ as a function of the Pt thickness t_{HM}, between two resistivities (87 and 117 μΩ.cm). We emphasis to the reader that this preliminary study does not include yet measurements on the 87 μΩ.cm for the spin-torque efficiency. Likewise from the first THz experiments, we also expect an increase of the spin-current injected at the HM/FM interface provided by the spin-sink structure in spin-torque measurements. Noticeably, we recover the same trend for the spin-sink gain related to the electronic efficiency offered by the spin-sink as derived by the trilayer model $\mathcal{G}(t_{HM})$, thus evidencing an universal law (Eq. (E3.27)).

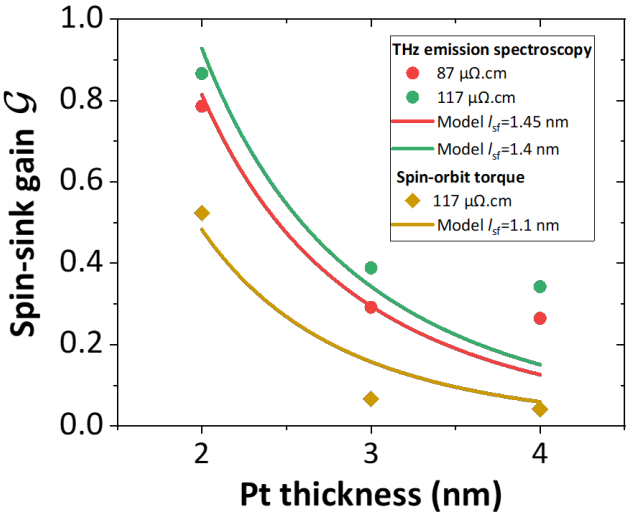

Figure 3.28: DC and THz spin-sink gain. Extracted of the spin-sink correlated gain for spin-orbit torque (DC) and THz efficiency in Co(2)/Pt(t_{Pt})/Au:W(2).

To that extend, the form of the universal law follows our previous derivation (Eq. (E3.27))

while replacing the heavy metal spin resistance at the numerator (r^s_{HM}) by a global source resistance r^s_Σ in the spin-sink enhancement. This global source resistance is equivalent to the heavy metal spin resistance r^s_{HM} in the case of THz spin current injection (η_{THz}) and to the ferromagnet spin resistance r^s_{FM} in the case of spin-torque (η_{SOT}). Here, the ferromagnetic resistance (for collinear configuration between the spins and the magnetization) can be expressed as $r^s_{\mathrm{FM}} = r_\infty \coth\left(t_{\mathrm{FM}}/l^{\mathrm{FM}}_{sf}\right)$ and the heavy metal spin resistance can be expressed as $r^s_{\mathrm{HM}} = \rho_{\mathrm{HM}} l^{\mathrm{HM}}_{sf}$. It is important to notice that for $t_{\mathrm{FM}} \gg l^{\mathrm{FM}}_{sf}$, the ferromagnetic spin resistance can be reduced to $r^s_{\mathrm{FM}} \simeq \rho_{\mathrm{FM}}(l^{\mathrm{FM}}_{sf})^2/t_{\mathrm{FM}}$ while it is equivalent to the spin-mixing resistance $1/G_{\uparrow\downarrow}$. We are able with an updated understanding to extract the value of the spin diffusion lengths in our trilayers as given in Table III.3.

Material	ρ (μΩ.cm)	l_{sf} (nm)	r^s (fΩ.m^2)	r^s/R_{Sh}	$1/G_{\uparrow\downarrow}$
Co	30	10	3	15	5
Pt	25	1.5-2	0.6	3	5

Table III.3: Values of the resisitivies, extracted spin diffusion lengths and spin-resistances for Co and Pt.

3.5 Probing of interfacial spin-current and spin-charge conversion properties.

This work, in collaboration with L. Perfetti's team, has led to a publication in Advanced Optical Materials [160].

The previous investigations motivated us to study the interfacial effects for efficient spin-current injection in metallic STEs. We refer here to the transient spin-injection in strong SOC materials, compared to the well-studied steady-state case illustrated by the FMR spin-pumping. This comparative steady-state/transient case has been addressed in the literature [231, 159] and more importantly, the two techniques of measurements, quasi-static (FMR) *vs.* transient (THz) and subsequent probed quantities are illustrated in Fig. 3.29. In particular, one specific motivation is to possibly demonstrate an interfacial passivation between FM and SOC by a neutral spin-orbit inset from selected chemical species, like played by Au or Ti [253].

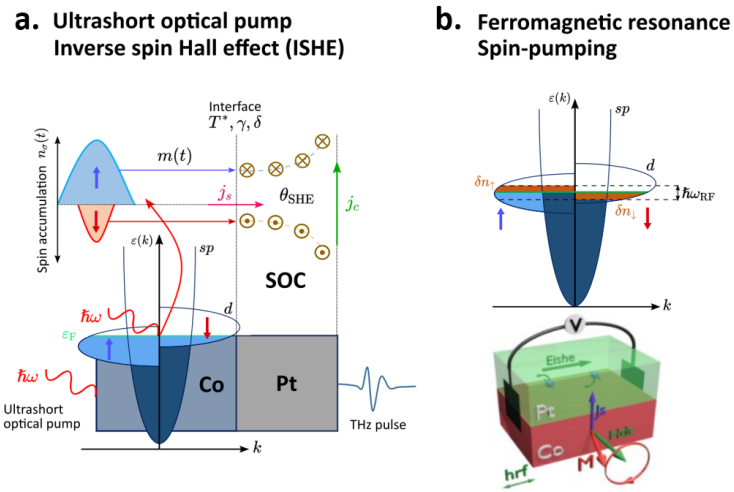

Figure 3.29: Comparison between the spin band probed via THz emission and ferromagnetic resonance. (a) Scheme of the THz emission principle on which a transient spin current (well above the Fermi level) is generated from an ultrashort optical pump. The spin current is converted into a transverse charge current in a SOC layer generating the THz free-space emission. (b) Representation of the ferromagnetic resonance probing local variations of the d band with an energy broadening $\hbar\omega_{\mathrm{RF}}$ (near the Fermi level).

First, it is to be noted that the pumped spin-current, in the case of the FMR, evolves with en-

ergies close to the Fermi level as the radio-frequency excitation $\hbar\omega_{\mathrm{RF}}$ is around few 10-100 µeV. In the case of THz emission, the excited spin-current via optical pumping $\hbar\omega_{\mathrm{NIR}}$ is a fraction of the eV. It comes that the interfacial transmission (injection) for the dynamical hot spin-polarized electrons is quasi-ballistic and therefore is linked to the sum between the two channel direct interfacial conductance $\frac{1}{2}(g_{\uparrow}+g_{\downarrow})$. However, this is to put aside the discussions of Rouzegar *et al.* [244] which propose that multiple reflections of the spin population occurs at the Co/Pt interface, allowing energy relaxation without the loss of the spin-polarization. In the case of the steady-state spin-injection, the spin-mixing conductance $g_{\uparrow\downarrow}$ is the interfacial parameter to consider.

Contribution of the spin-transmission at interfaces. In this work, we propose a systematic study comparing the ferromagnetic resonance (static regime) and THz radiation by SCC (transient regime) to account for the spin transport in FM/I/HM bilayers, where I is an interfacial inset expected to increase the spin loss at interface. To that extend, we have realized Co(2nm)/X(d)/Pt(4nm) for the THz emission spectroscopy and Co(15nm)/X(d)/Pt(5nm) for the FMR measurements where X={Ti, Au, $Au_{0.85}$:$W_{0.15}$} with thicknesses d ranging from 0 to 2 nm. Such interfacial control of a different chemistry may have the advantage of passivate/reduce the local spin-orbit interactions (Rashba field) responsible for decoherence and spin-memory loss. However, from the electronic transfer point of view, such thin layer insertion has two main effects among which *i*) the formation of a thin potential barrier reducing the spin-transmission *vs.* Co/Pt ideal interface, whereas a larger chemical mismatch may take place in the case of Co/X/Pt with X={Ti, Au or $Au_{0.85}$:$W_{0.15}$} and *ii*) a reduction of the spin-orbit interaction and spin-memory loss with Ti or Au owing to a closed 5d shell. Indeed, Co/Pt interface is known to build an excellent matching for the majority spin channel [44, 254, 231] at the Fermi level (case of spin-pumping), with $T_{\uparrow}=0.7$ and $T_{\downarrow}=0.4$. This behaviour is also present at higher energies, for instance at 1 eV from the Fermi level with $T_{\uparrow}=0.8$ and $T_{\downarrow}\simeq 0.3$ (case of generated hot-electrons for THz transients).

From the measurements, we extract the THz efficiency η_{THz} on one side and the Gilbert damping α and the spin-mixing conductance $g_{\mathrm{eff}}^{\uparrow\downarrow}$ on the other side, as presented in Fig. 3.30a-b as a function of the inset thickness d. We note a decrease of the THz efficiency with the inset thickness for the two DC and THz quantities. We note that Au and $Au_{0.85}$:$W_{0.15}$ have a comparable behaviour compared to Ti which shows in both cases a more pronounced decrease with the inset thickness d. The reduction of the THz signal indicates a decrease of the electronic transmission between FM (Co) and SOC (Pt) layers. The similar decrease observed between Au and $Au_{0.85}$:$W_{0.15}$ seems to indicate that the addition of a small W content, slightly modifying the interfacial spin-orbit interactions, does not alter/change the efficiency of the spin-charge interconversion comparing Au and Au:W in the ultrafast regime of spin-injection. In contrast, no conclusions can be raised at that stage concerning Ti except that the interleaved layers seem to alter the efficiency of spin-injection but possibly in a different way.

Fig. 3.30b displays the measurements by RF spin-pumping of the resulting Gilbert damping α together with its enhancement $\Delta\alpha$ directly correlated to the corresponding spin-mixing conductance $g_{\mathrm{eff}}^{\uparrow\downarrow}$ or spin-transmission $T_{\uparrow\downarrow}$. One observes an equivalent trend compared to the pulsed optical injection (Fig. 3.30a) with a gradual decrease of $g_{\mathrm{eff}}^{\uparrow\downarrow}$ on increasing the thickness of the interleaved layer (X={Ti, Au, $Au_{0.85}$:$W_{0.15}$}). Note that, as for the pulsed optical pumping case, the decrease for Au and Au:W resembles to each other with the same conclusions of the unchanged character of the interfacial SOI with the W content.

Even more interesting is the correlation between the spin-mixing conductance $g_{\mathrm{eff}}^{\uparrow\downarrow}$ and the THz efficiency η_{THz} displayed on Fig. 3.31c. Indeed, one observes an universal variation giving $g_{\mathrm{eff}}^{\uparrow\downarrow}$ *vs.* η_{THz} (or vice-versa η_{THz} *vs.* $g_{\mathrm{eff}}^{\uparrow\downarrow}$) described by a common and unique *universal law* irrespec-

tive of the chemical nature of the interleaved layer (Ti, Au, Au:W). As we will see, this captures the intrinsic physics of the spin-memory loss (SML) parameter δ which parametrizes the typical shape variation of $\eta_{\mathrm{THz}}(d) = \eta_{\mathrm{THz}}(g_{\mathrm{eff}}^{\uparrow\downarrow}(d))$ with d the thickness of the interlayer.

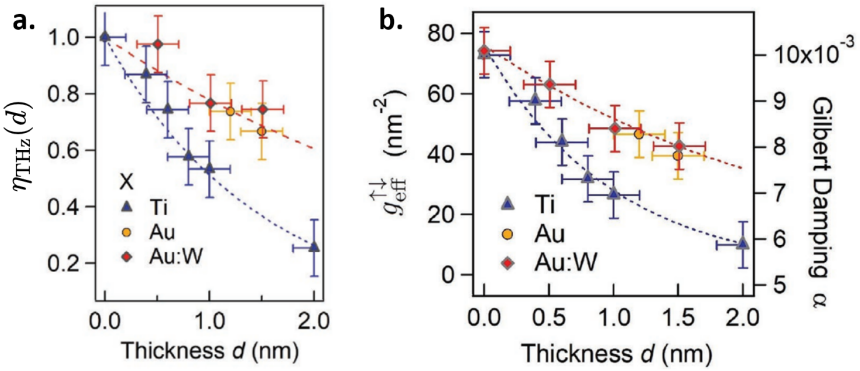

Figure 3.30: Extraction of the interfacial figures of merit in case of DC and THz transport. (a) THz efficiency and (b) spin-mixing conductance and Gilbert damping as a function of the inset thickness d. The inset is composed alternatively from Ti (blue), Au (yellow) or Au:W alloy (red).

Semi-phenomenological approach. To understand our results, we report the spin-current profile in the heterostructure with and without the Rashba interactions responsible for the spin-memory loss in Fig. 3.31a-b. When no spin-memory loss is taken into account, no spin-flip scattering event is present thus the spin-current is continuous at the interface (black curve). However, in case of the spin-memory loss, interfacial spin-orbit Rashba potentials scatter the incoming spin population (spin-flip events) which leads to a discontinuity of the spin-current at the interface [255]. We thus can see the spin-mixing conductance as directly related to the proportion of the spin-current exiting the FM layer while the THz efficiency can be regarded as proportional to the incoming spin-current into the HM. Experimentally, this is highlighted in Fig. 3.31b where we plotted the effective spin-mixing conductance, obtained by ferromagnetic resonance, as a function of the THz efficiency. We observe that a direct correlation can be evidenced between the two quantities, and the slope can be linked to the interfacial spin-memory loss. Interestingly, this behaviour is encountered for all the inset types, Ti, Au or Au:W alloy, which appears as an universal law. We thus evidence that this is a global behaviour and illustrate the role of the interfacial spin-memory loss.

We are now going to interpret the discovered *universal law* giving the variation of the effective spin-mixing conductance $g_{\uparrow\downarrow}^{\mathrm{eff}}$ *vs.* the THz efficiency η_{THz} (or reciprocally) on varying the interface quality (both quantities can be considered as unitless because given in terms of the effective transmission coefficients). Such dependence $\eta_{\mathrm{THz}}(g_{\uparrow\downarrow}^{\mathrm{eff}})$ we are searching for may be derived from the general theory of spin injection/diffusion/relaxation by considering the spin memory loss with an extended parameter δ at the Co/Pt where the interface resistance r_{B}^{*} is linked to the interfacial spin-resistance r_{I}^{s} by $r_{\mathrm{B}}^{*} = r_{\mathrm{I}}^{s}\delta$. One can then show that the electronic transmission ratio R_{SML} between the current injected in the Pt layer (the THz signal) and the current ejected from Co (spin-pumping measurements) writes [231]:

$$R_{\mathrm{SML}} = \frac{\eta_{\mathrm{THz}}}{g_{\uparrow\downarrow}^{\mathrm{eff}}} = \frac{1}{\cosh\delta + \frac{T^{*}}{\gamma_{\mathrm{SO}}}\delta\sinh\delta} \tag{E3.30}$$

with T^{*} the transmission coefficient for the majority spin and γ_{SO} is the spin-orbit parameter. From this equation, one easily derives that the slope of $g_{\mathrm{eff}}^{\uparrow\downarrow}(\eta_{\mathrm{THz}})$ is always larger than unity with a typical concave shape like the one obtained experimentally on Fig. 3.31c. The universal

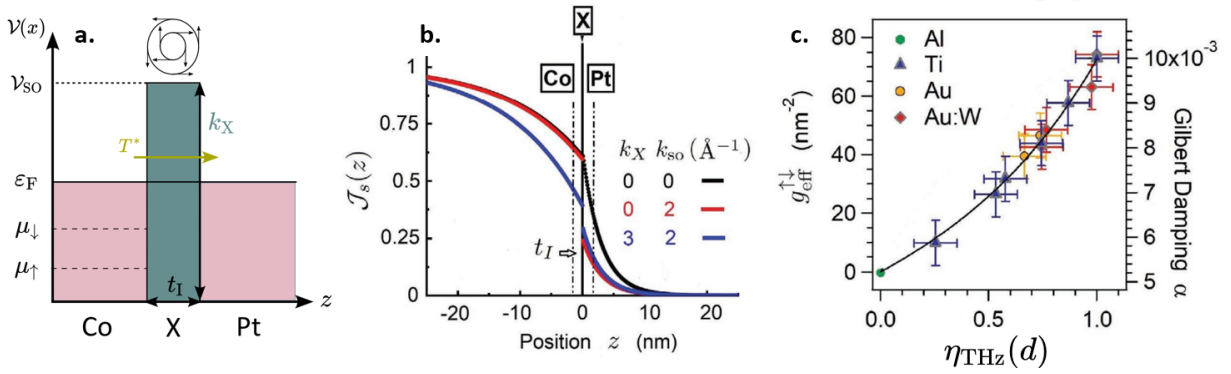

Figure 3.31: Direct evidence of the spin-memory loss from the relation between the spin-mixing conductance and the THz efficiency of Co/X/Pt multilayers. (a) Schematic representation of the interfacial Rashba potential $\mathcal{V}_{SO}$ over an interfacial region of thickness t_I. (b) Modelling of the spin-memory loss as a function of the spin-orbit scattering. k_X represents the potential step and k_{SO} the Rashba spin-orbit strength in the interfacial region of thickness t_I. (c) Experimental universal behaviour linking the out-coming and incoming spin-current via the spin-memory loss.

character of this plot together with its fitting demonstrates that the spin-memory loss parameter δ remains unchanged and that the surface Rashba spin-orbit interactions at the pristine Co/Pt is not altered by chemical insertion of Ti, Au and Au:W. Fitting the experimental data from the value of $\gamma_{SO} = 0.3$ for Pt, one extracts a spin-memory loss parameter $\delta = 0.5$ for Co/Pt interface.

Quantum modelling of the electronic transfer involving the spin-orbit interactions. To go into deeper details, we have considered a simplified spin-orbit assisted quantum transmission model to convince ourselves about the results and conclusions drawn with the semi-phenomenological approach (the reader is referred to Annex. A7 for more details). In that scheme, the interface is treated as an ideal trilayer structure Co/X/Pt with a spin current j_s propagating along the direction normal to the layers. The spin current is computed from the propagation of selected plane waves with respective conserved in-plane wavevector $k_{||}$ summed hereafter over the Fermi surface. We obtained the $j_s(z)$ profile across the interface $\delta j_s(z)$ via a refined model involving a Rashba-like term and by considering spin-dependent bulk diffusion responsible for spin-backflow.

Material	$k_F^{\uparrow}$ (Å^{-1})	$k_F^{\downarrow}$ (Å^{-1})	l_{sf} (nm)	λ (nm)
Co	$\simeq 1$	$\simeq 0.7$	10	3
Pt	$\simeq 1$	$\simeq 1$	3	1.5

Table III.4: Values of the Fermi wavevector for the two spin sectors, the spin diffusion length and the mean free path considered in the model for Co and Pt [160].

We considered the values of the Fermi wavevector (for the two spin sectors), the spin diffusion length and the mean free path for Co and Pt in Table III.4. Note that the same values for $k_F^{\uparrow}$ in Co and k_{Pt} expresses the absence of potential step between Co and Pt for the majority spin channel. This feature has to be associated to a very good band matching and optimized transmission at Co/Pt interface for majority spins [30, 231]. In order to fit the experiments, we consider an inverse spin-orbit length k_{SO} of the order of $k_{SO} = t_I m^* \alpha_R \overline{k}_F/\hbar^2 = 1.5$ Å^{-1}, where $\overline{k}_F$ is the mean value of the Fermi wavevector. By setting an interface extension of about $t_I \simeq 2$ nm, one obtains a Rashba splitting of $\alpha_R \overline{k}_F \simeq 0.4$ eV. This in good agreement with the value predicted by ab-initio calculations for the Co/Pt interface [256] and in the range of the spin-orbit strength of Pt.

We now focus on the main results on which a spin-polarized current j_s^{Co} normalized to unity and originating from Co penetrates the scattering region in a Co/X/Pt trilayer. On Fig. 3.31a, three specific cases are considered, corresponding respectively to *i*) no interfacial potentials ($\mathcal{V}_{\mathrm{X}} = 0$ or $k_{\mathrm{X}} = 0$ and $\alpha_{\mathrm{R}} = 0$ or $k_{\mathrm{SO}} = 0$), *ii*) a pure Rashba potential ($k_{\mathrm{X}} = 0$ and $k_{\mathrm{SO}} = 2$ Å^{-1}) and *iii*) both interfacial potential and Rashba interactions ($k_{\mathrm{X}} = 3$ Å^{-1} and $k_{\mathrm{SO}} = 2$ Å^{-1}). The spin current is always maximum in Co and vanishes towards zero when penetrating into Pt far away from the interface. In the absence of any quantum diffusion (black curve) and good interface matching and spin-transmission, $j_s^{(0)}$ value at the Co/Pt interface results from an equilibrium condition between bulk spin-flip rates within the two regions. The spin-current is continuous everywhere (no spin-orbit) and its value ($j_s^{(0)} \approx 0.6$) is the one expected from a pure diffusive spin-model:

$$j_s^{\mathrm{FM/HM}} = j_s^{\mathrm{FM}} \frac{r^s_{\mathrm{FM}}}{r^s_{\mathrm{FM}} + r^s_{\mathrm{HM}}} = j_s^{\mathrm{FM}} \frac{l^{\mathrm{FM}}_{sf}/\lambda^{\mathrm{FM}}}{l^{\mathrm{FM}}_{sf}/\lambda^{\mathrm{FM}} + l^{\mathrm{HM}}_{sf}/\lambda^{\mathrm{HM}}} \quad \text{where} \quad r_s \propto \frac{l^{\mathrm{FM,HM}}_{sf}}{\lambda^{\mathrm{FM,HM}}} \tag{E3.31}$$

Adding a Rashba field $k_{\mathrm{SO}} = 2$ Å^{-1} (red curve) introduces an additional diffusion potential leading to a drop of the spin-current j_s injected into Pt. $j_s(z)$ displays a strong discontinuity at the interface resulting from the spin-orbit field. The spin memory loss parameter is then given by $\delta = (j_s(z_-) - j_s(z_+))/j_s(z_-)$, where z_- and z_+ are the limiting values reached by approaching the interface from the Co and Pt side, respectively. From the chosen parameters, we extract $\delta = 0.4$, which is in agreement with the experimental value. Adding an additional spin-independent scattering potential $k_{\mathrm{X}} = 3$ Å^{-1} (blue curve) has now two main effects. j_s is favorably diffused back in the Co layer thus leading to a smaller escape spin-current out of Co and smaller spin-pumping damping. Note that, despite this additional diffusive term, j_s slightly increases in Pt owing to a reduced contribution of the Rashba field in average. The apparent spin-memory loss δ thus drops as k_{X} increases keeping fixed k_{SO}. We therefore come to the conclusions that introducing a chemical disorder at the interface by insertion of Ti, Au or $Au_{0.85}W_{0.15}$ enhances the electronic backward diffusion and decreases the spin-mixing conductance $g_{\uparrow\downarrow}$. In agreement with experiments, this process comes together with a drop of the spin memory loss δ as the interfacial Rashba parameter α_{R} is kept fixed or even decreases like in the case of Au:W. Moreover, the quasi-linear relationship between $g_{\mathrm{eff}}^{\uparrow\downarrow}$ and η_{THz} like exhibited on experiments is recovered (Fig. 3.31c) with the correct slope giving thus the range of k_{SO} for Co/Pt between 1 and 2 Å^{-1} ($\alpha_{\mathrm{R}} \simeq 0.3 - 0.4$ eV).

Conclusions on the interfacial scattering barrier and the global THz figure-of-merit.

We have reported a novel approach with the use of spin-sink layers to avoid detrimental spin reflection at the edges of thin SOC layers, typically below the spin diffusion length. The reported performances in bilayers show a doubling of the THz emission and subsequent THz efficiency in agreement with the developed spin-sink model. However, the use of spin-sink in trilayers is not as efficient owing to the absorption of the THz radiation in metallic structures. Secondly, we have realized samples in which we have inserted Ti, Au or Au:W to degrade the electronic transmission and locally probe the impact of the interface. It seems that the inset acts as a barrier for spin-polarized hot electrons injection into the conversion material due to the different spin-transmission of Co and Au, Ti and Au:W compared to the optimized interface Co/Pt. These two studies launch spin-current tailoring investigations and open perspectives on the non-metallic spin-sink layers and the careful control of the interface.

4 Take-home message and future developments.

Conclusions on spin-current tailoring in 3d/5d metallic spintronic THz emitters. In conclusion, we first developed a THz generation model accounting from the ultrafast spin-current gen-

eration, spin-injection and spin-charge conversion processes in embedded multistructures. From those studies, we have introduced an actualized figure-of-merit for the THz radiation, which accounts for the spin-orbit coupling (spin Hall angle θ_{SHE}, spin diffusion length l_{sf} and spin-polarization $\propto |M|$), the interfacial properties (spin conductance $\propto g_{\uparrow} + g_{\downarrow}$) and the THz impedence $Z(\omega)$ in the following form:

$$\eta_{\text{FOM}} \propto \frac{1}{2}(g_{\uparrow} + g_{\downarrow}) \underbrace{\theta_{\text{SHE}}\sigma_{xx}}_{=\sigma_{\text{SHE}}} l_{sf}|M|Z(\omega) \tag{E3.32}$$

From this figure of merit, we have explored several paths to enhance the THz radiation with the example of the *i*) multiple STE repetition or *ii*) the spin-sink strategy. We summarize our results in Table III.5.

Strategy	Repetition on bilayers [257]	Repetitions on trilayers [257]	Spin-sink [257]
Field amplitude	+50%	+60%	+50%
Power	× 2.25	× 2.6	× 2.25

Table III.5: Comparison of the different enhancement strategies developed in these studies, the repetition and spin-sink strategies on bilayers and on optimized trilayers with a presentation of the field amplitude and power enhancement compared to Co/Pt reference.

Take-home message on metallic spintronic THz emitters.

Metallic spintronic THz emitters offer the best perspectives of enhancement at short term, either via spin-sink strategy or high SOC layer stacking. An order of magnitude (in emission power) could be expected in future implementations, as supported by our numerical modelling (with perspectives for complex multilayers and IREE conversion). However, one of the main drawbacks of the metallic STEs is that, although they present strong interconversion efficiency, they are difficult to use in those combining methods proposed in this work due to the radiation absorption.

Therefore, we propose to look in the next part at different materials (like semi-conductors) in the example of topological insulators which present at the same time a lower conductivity while still presenting strong interfacial spin-orbit coupling to increase the global THz efficiency. We now propose perspectives for metallic spintronic THz emitters with the development of spin-orbitronics and the use of strong spin-polarization materials like in Weyl semi-metals.

4.1 Spin-orbitronics.

We discuss in this part the novel orbital-charge conversion via the so-called inverse orbital Hall effect (IOHE) for THz emission. The conversion mechanism from an orbital current into a charge current follows $j_c^{\text{IOHE}} \propto \alpha_{\text{IOHE}} j_l$ where the orbital current can be associated to $j_l = C_{ls} j_s$ where C_{ls} represents the spin-orbital conversion efficiency [258]. The orbital conversion follows the same conversion symmetry rules as for the ISHE and is thus difficult to harvest in magnetic multilayers.

To dissociate the IOHE component from light and heavy metals, Xu *et al.* [258] have studied systematically the THz contribution of the two effects from two FM reservoirs: CoFeB/X and Ni/X, where X={Cu,Pt,W,Ta} presents different spin Hall and orbital Hall angles. Interestingly, it has been both predicted [259] and reported experimentally [258] the dependence of the orbital current between different FM reservoirs: Fe, CoFeB and Ni, via a variation of the conversion coefficient C_{ls}. Moreover, whereas the polarity of the spin Hall angle of W and Ta is opposite to the one of Pt, the signs of the orbital Hall angle are the same in all three materials on which we include Cu which has a negligible spin Hall angle.

4.2 Towards larger spin-polarization for ultrafast injection using Weyl semi-metals.

This work has been published in Applied Physical Letters [257] and we acknowledge the collaboration with C. Felser's group (Max Planck Institute, Dresden) for the sample growth..

The search for high spin-polarized ferromagnetic materials is motivated by the projected enhancement of the spin-charge conversion as those effects scale directly with the initial spin-polarization of the ferromagnetic reservoir at the Fermi level. Weyl semi-metals are a particular phase of matter owing to the spin-orbit coupling in topological materials. Compared to topological insulators, the bulk band structure is nearly not gapped near the degeneracy points under the effect of spin-orbit coupling. The Weyl materials are thus semi-metals and they have been reported to carry strong anomalous spin Hall effects. They thus represent an ideal mix between ferromagnetic materials and strong spin-orbit coupling converters [184].

Electronic structure of Co_2MnGa.

Electronic structure	Number of valence electrons
Co: [Ar] $3d^7\ 4s^2$	$N_V^{Co} = 7+2 = 9$
Mn: [Ar] $3d^5\ 4s^2$	$N_V^{Mn} = 5+2 = 7$
Ga: [Ar] $3d^{10}\ 4s^2\ 4p^1$	$N_V^{Ga} = 2+1 = 3$

In this part, we will take the example of Co_2MnGa Heusler coumpound (*i.e.* the family of face-centered cubic ferromagnetic alloy materials sharing the Heusler stoichiometry A_2BC [260]). The net magnetic moment per unit cell is given by the Slater-Pauling rule $m = (N_V - 24)\mu_B$ for half-metallic ferromagnets. In Co_2MnGa, the total number of valence electrons is $N_V = 2N_V^{Co} + N_V^{Mn} + N_V^{Ga} = 28$ leading to a magnetic moment of $4\mu_B$ per unit cell.

Besides its spin-polarization at the Fermi level (see the definition of the spin-polarization in Chap. I), Co_2MnGa Heusler alloy is known to present a good spin-transparency, similar to the interface of Co/Pt [261, 262, 186]. Co_2MnGa represents thus a high potential platform for THz spintronics, as recently highlighted with the example of Co_2FeSi/Pt by Gupta *et al.* [183]. The reader is referred to the state-of-the-art (Section II.5.1) for more details.

Epitaxial growth of thin films. The epitaxial growth of Co_2MnGa is carried in collaboration with Max Planck Institute for Chemical Physics of Solids (C. Felser's group) by magnetron sputtering on MgO substrates. A co-deposition from Co, Mn and MnGa targets ensure the good stoichiometry of the deposited Co_2MnGa. The films are annealed in-situ at 600°C in ultra-high vacuum for 25 min to ensure good crystalinicity. In a first series of samples, the Co_2MnGa is fixed to 43 nm and capped with Pt(2.5nm). In a second series of samples, the Co_2MnGa thickness is varied from 8, 10, 20 and 30 nm and capped with Pt(2.5nm). More details are available in Refs. [257].

THz efficiency from Co_2MnGa/Pt Weyl thin films. We present in Fig. 3.32 the results of the THz emission from $Co_2MnGa(t_{FM})$/Pt(2nm) bilayers as a function of the Co_2MnGa thickness t_{FM} which has been varied from 8 to 30 nm. We report a sizeable THz emission for all the studied samples demonstrating the very good quality of the epitaxial growth, and in particular a strong contribution at $t_{FM} = 8$ nm leading to an amplitude enhancement reaching up to +40% compared to the one of Co(2)/Pt(4). This result is even more interesting as it involves a spin-injection reservoir four times thicker in the case of Co_2MnGa. The THz emission from Co_2MnGa/Pt decreases

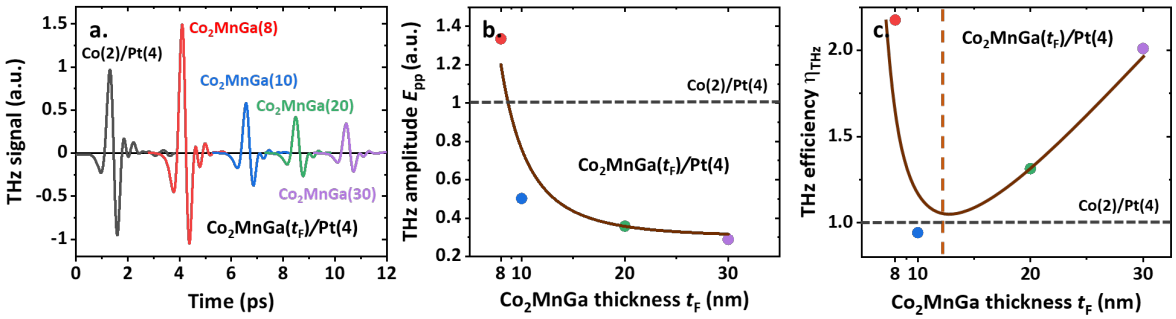

Figure 3.32: Heusler Co_2MnGa/Pt mediated THz emission. (a) Net THz emission from $Co_2MnGa(t_{FM})$/Pt(2nm) as a function of the Co_2MnGa thickness t_{FM} ranging from 8, 10, 20 and 30 nm, compared to Co(2)/Pt(4). (b) Peak-peak amplitude as a function of the Co_2MnGa thickness t_{FM}. (c) Extracted THz efficiency η_{THz} as a function of the Co_2MnGa thickness t_{FM}.

as a function of t_{FM}, assuming a non-negligible radiation absorption in the Co_2MnGa as the thickness increases. To remove the effect of the absorption in the depth of the metallic multilayers, we show in Fig. 3.32c the THz efficiency as a function of t_{FM}. We can distinguish three different regions:

- The first part, at very low thicknesses, shows a doubling of the THz efficiency compared to Co/Pt. To explain this effect, we have to consider the higher spin-polarization of Co_2MnGa compared to Co, about 130% of the one of Co. Besides, the main effect in this region is the strong increase of the FM interfacial spin-resistance r_{FM} which scales as $\rho_{xx}(l_{sf}^{FM})^2/t_{FM}$ for $t_{FM} < l_{sf}$ combined with a larger electronic transmission.
- Around $t_{FM} = 10$ nm, the THz efficiency experiences a minima which would indicate a compensation between the high spin-polarization, the decrease of the interfacial spin-resistance and the start of the conversion in the bulk of the Heusler semi-metal (self-conversion) owing to the strong anomalous Hall effect in Weyl semi-metal.
- At larger thicknesses, the self-conversion of Co_2MnGa is the most dominant part. The spin-current is in all cases fully converted, either in the depth of the Co_2MnGa or locally at the interface with Pt via the spin Hall effect in Pt. Both large spin-polarization and efficient conversion led to a THz efficiency up to two times the efficiency of Co/Pt.

Self-contribution from Co_2MnGa. We compare now in Fig. 3.33 the THz emission from a single Co_2MnGa(43nm) to a Co_2MnGa(43nm)/Pt(2.5nm) ISHE bilayer. A small radiation is measured, typically about an order of magnitude smaller than the ISHE bilayer, that we attribute to a self-SCC expected in Weyl semi-metal Co_2MnGa of however smaller amplitude than the ISHE in Pt.

In summary, we have reported the THz emission from Co_2MnGa/Pt bilayers and especially that the use of Heusler semi-metal Co_2MnGa whose properties of high spin-polarization reservoir and efficiency spin-injector are demonstrated to play favorably on the THz emission, particularly at low FM layer thicknesses. *A study of Co_2MnGa/Pt spin-charge conversion on the THz frequencies has also been proposed by our collaborators G. Bierhance and T. Kampfrath (Freie Universität Berlin) and published in Applied Physical Letters [263].*

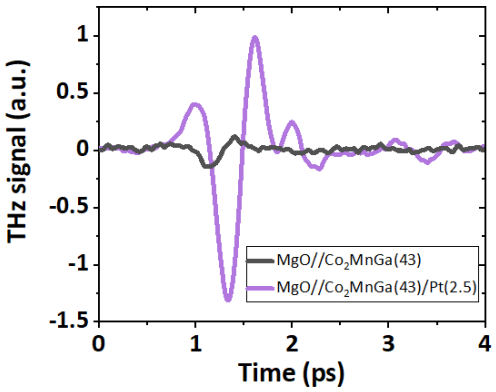

Figure 3.33: Reference measurements on Co_2MnGa. THz emission from Co_2MnGa(43nm) and Co_2MnGa(43nm)/Pt(2.5nm).

IV

Topological surface states based spin-charge conversion mapped via THz spectroscopy.

This chapter focuses on the ultrafast spin-injection at sub-picosecond timescales and the resulting THz emission via dynamical spin-charge conversion from interfacial systems, presently in Bi-based topological insulator/ferromagnet bilayers, as a probe to study the possibility of a novel type of spin-charge conversion via the inverse Rashba-Edelstein effect mediated by the topological surface states. Although very recently reported, the proof of concept of such interfacial conversion is today highly debated. In that purpose, we clearly demonstrate the high efficiency of the interconversion at the direct interface of such bilayers. These studies also address interesting dissections of the non-linear optical phenomena besides pure spin-charge effects, whose comprehensions are both needed to have the full picture of the THz generation mechanisms in topological insulators/ferromagnet bilayers.

After a short introduction discussing the main properties of topological insulators and their specific $\mathbb{Z}_2$ topology, we will first address some theoretical expectations about their ability to host the inverse Rashba-Edelstein effect. In a second step, we will motivate the experimental investigations of the THz efficiency as an elegant probe of the spin-injection and relaxation mechanisms. One of the particular advantage of topological insulator/ferromagnet structures is the gain by more than an order of magnitude in the output THz signal compared to purely optically-mediated non-magnetic contributions. Thus, we propose to study two Bi-based topological insulators engineered to pin the Fermi level in the electronic gap: $SnBi_2Te_4$/Co by doping compared to its parent material Bi_2Te_3 and $Bi_{1-x}Sb_x$/Co via stoichiometry and induced strain. Studying the isotopic angular THz conversion and thickness-dependent profiles give an important hint for interfacially-mediated conversion. The discussion is further focused on tight-binding calculations and spin-resolved ARPES measurements for $Bi_{1-x}Sb_x$ on the distinction of hybridized Rashba-type surface states *vs.* topological surface states for the interfacial conversion. We finally open perspectives on this chapter with discussions about Bi_2Se_3/WSe_2/Co trilayers combining a transition metal dichalcogenide inset between the spin-injector and the topological insulator. Here, we will show that we are able to map the transition from a relevant interface for the spin-injection to the formation of a Schottky barrier and its impact on the spin-injection.

We have collaborated with INN (S. Fragkos, E. Xenogiannopoulou, P. Tsipas, A. Dimoulas) and SOLEIL synchrotron (L. Baringthon, P. Le Fèvre) for the growth of $SnBi_2Te_4$ and Bi_2Te_3. We acknowledge the collaboration with Spintec for the TI/2D TMDC growth (M. Oliveira Ribeiro, F. Bonell, M. Jamet) and S. Husain from CNRS/Thales. We thank J.-M. George and N. Reyren from CNRS/Thales.

1 Bi-based topological insulators: a novel platform for efficient spin-charge conversion.

Interface physics, and interface spintronics, plays a central role in harvesting strong spin-orbit coupling (SOC) induced by the occurrence of interfacial symmetry-breaking electric fields or charge transfer dipoles and their subsequent applications. In particular, topological insulators (TI) offer a rich physic relative to their exotic properties [264, 265]. Their electronic band dispersion are composed of a bulk valence and conduction band separated by a certain gap, that can be small of few tens to hundreds of meV (the conventional picture of a semi-conductor) but also present in its gap, Dirac-like electron dispersive topologically-protected surface states whose spin-locking properties make the spin perpendicular to the momentum. For that, it is necessary to consider the two components of the spin-orbit coupling: bulk and interfacial Rashba surface potential [266]. In the absence of magnetism, the topological protection arises from the time-reversal symmetry $\mathcal{T}$. This leads to an interesting system combining insulating properties in the material bulk and quantized conductive states at the surface with enhanced spin-orbit properties. They are of particular interest in spintronics and opto-electronics owing to their surface states manipulation with predicted strong interfacial spin-charge conversion and high band polarizability. Such topological materials have been firstly reported in 2D HgTe-CdTe crystal quantum wells (QW) by Bernevig *et al.* [267], and then in 3D TIs by using Bi-based material platform for its high spin-orbit coupling [268].

Time-reversal operator.

We define as $\mathcal{T} : t \mapsto -t$ the time-reversal operation which reverses the time direction. We call time-reversal symmetry or $\mathcal{T}$-symmetry the physical variables which are even under the action of $\mathcal{T}$ while other physical variables are odd under the action of $\mathcal{T}$. For instance, the position $\mathbf{r}$ is even under the action of $\mathcal{T}$ while the velocity $\mathbf{v}$ is changed to $-\mathbf{v}$ (odd under the action of $\mathcal{T}$). Following those arguments, we deduce the action of $\mathcal{T}$ on the electric field $\mathbf{E}$ and the magnetic field $\mathbf{B}$: the electric field involves the charge and the position of the charged particles (Coulomb law) and is therefore even under the action of $\mathcal{T}$. On the contrary, the magnetic field (similarly the magnetization of ferromagnets) considers, in addition, the velocity of the charged particles (Biot and Savart law) and therefore is odd under the action of the time-reversal operator $\mathcal{T}$.

1.1 Topological order.

Two main ingredients are needed to obtain a strong topological insulator: a small electronic gap of the order of hundreds of meV, and a $\mathbb{Z}_2$ topological invariant, illustrating the time-reversal symmetry present in the system [269].

Conventions for the 2D and 3D topological invariant.

By definition, a $\mathbb{Z}_2$ topological invariant means that, for a two-dimensional or three-dimensional system belonging to the *AII* symmetry class, the topological invariant Q can only take two possible values, either $Q = 1$ (topological insulator) or $Q = 0$ (trivial insulator phase). The convention differs between mathematicians and physicists and the notation $Q = \pm 1$ is sometimes encountered. The symmetry class *AII* only means that the operation of time-reversal symmetry $\mathcal{T}^2 = -1$ is allowed (owing to the spin 4π-rotation invariance) but not the operations of particle-hole symmetry $\mathcal{P} = 0$ nor chiral symmetry $\mathcal{C} = 0$. The symmetry class *AII* corresponds to the special unitary group SU($2n$) notation. In our study, we will focus on 3D topological insulators (and not on 2D systems): here, the topological invariant $\mathbb{Z}_2$ represents a generalization of the Chern number for the case of the electron spin (and not the charge).

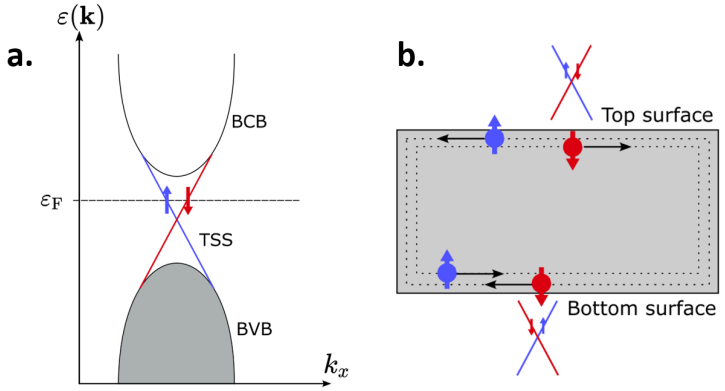

Figure 4.1: Schematic band structure of topological insulators. (a) Relation dispersion in a topological insulator. The TSS are spin-polarized to lift the Kramers degeneracy, except at the Dirac point. (b) Schematic representation of the surface conduction where the chirality of the TSS imposes that the spin-up and spin-down propagates in opposite directions, thus preventing back-scattering.

The electronic band structure of a topological insulator thus combines a semiconductor-like structure with a (small) electronic gap (typically around few tens to hundreds of meV, see Table IV.1) and more importantly a band inversion where the energy of the top of the valence band is higher than the energy of the bottom of the conduction band. It results to the presence of topologically-protected surface states presenting a graphene-like linear dispersion relation with $\mathbf{k}$ near the Brillouin zone center (Γ):

$$\varepsilon(\mathbf{k}) = \pm \hbar v_F |\mathbf{k}| \tag{E4.1}$$

System	$Bi_{1-x}Sb_x$ [270]	$SnBi_2Te_4$ [271]	Bi_2Te_3 [269]	Bi_2Se_3 [272]
ε_g (meV)	20-40	200	170	300-350

Table IV.1: Electronic gap of studied topological insulators, $Bi_{1-x}Sb_x$, $SnBi_2Te_4$, Bi_2Te_3 and Bi_2Se_3, at the Γ point.

Surface electronic and spin-polarized band structure of topological insulators. The spin-orbit interactions involved in the system Hamiltonian lift the spin-degeneracy of the bands depending on the electron spin σ. This leads to the presence of different energy bands for the two spin channels $\sigma_\pm$. However, it exists peculiar points where the bottom and top bands merge which leads to a two-fold degenerated energy, always occurring in pairs. These points, called

Dirac points, present a Kramers degeneracy and are in this sense called Kramers (surface) topological invariants Λ (or sometimes time-reversal invariant momentum points, or TRIMs). The TRIM points Λ_i are thus specific high-symmetry points of the Brillouin zone where the electronic states are degenerated. In other terms, the Kramers theorem states that for half-integer spin (one-half for electrons), each eigenstate is at least doubly degenerated at a TRIM point. For $\mathbf{k} \neq \Lambda_i$, the degeneracy is lifted by the spin-orbit coupling. By symmetry in the hexagonal Brillouin zone for Bi-based compounds, the Kramers invariant are found in high-symmetry points such as the center of the Brillouin zone (Γ point) or on the edges of the Brillouin zone on $\bar{\text{M}}$ points. The spin-polarized band structure $\varepsilon(\mathbf{k}, \sigma)$ is presented projected onto the spin-polarization along σ_x and σ_y which are the components of interest for the spin-charge conversion (as we have $\sigma_z \times \mathbf{k}_z = \mathbf{0}$ along the interface normal). The dispersion relation of the TSS follows the particular symmetries:

$$\varepsilon(k) = \varepsilon(-k) \quad \text{and} \quad \sigma(-k) = -\sigma(k) \tag{E4.2}$$

More interestingly, this means that the electron transport is spin-polarized and the transport is curly closed on all the material surfaces. One spin-electron flows towards $-k$ while the opposite spin-electron flows to $+k$ as shown in Fig. 4.1b, which will be the origin of surface states mediated spin-charge conversion. At equilibrium, the net charge is cancelled out but not the spin current. For 3D topological insulator, the topological nature of their surface states is given by the number of crossings of the surface states with the Fermi level ΔN between two consecutive topological invariants Λ_i and Λ_j:

$$\Delta N(\Lambda_i, \Lambda_j) \equiv \begin{cases} \mod 2n+1 & \rightarrow \text{Strong topological insulator } (\mathbb{Z}_2 = 1) \\ \mod 2n & \rightarrow \text{Trivial insulator } (\mathbb{Z}_2 = 0) \end{cases} \tag{E4.3}$$

This is the origin of the $\mathbb{Z}_2$ invariant. At the Fermi level, the electronic transport onto the TSS is only ensured at the surface of the system via one electronic state and thus with a conductance being the quantified conductance $G_0 = e^2/\hbar$. This has for instance been observed in Bi_2Se_3 by using THz conductivity measurements to extract the quantified conductance as a function of the number of quintuple layers (QL) [273]. The topological protection of the TSS means that adding a supplementary system to the TI will not alter the electronic properties of the TSS as long as the material is trivial and does not alter the $\mathcal{T}$-symmetry. Thus in theory, systems breaking the $\mathcal{T}$-symmetry (like magnetic materials used in this work) may alter the TSS.

1.2 Interfacial spin-charge interconversion via inverse Rashba-Edelstein effect.

The inverse Rashba-Edelstein effect presented in Chap. I on 2D free electron gas, can be recovered with topological insulators. In the case of topological surface states, only one spin-textured band is encountered at the Fermi level as shown in Fig. 4.2. In this picture, the Rashba coefficient α_{R} can be identified by the spin-orbit velocity (band velocity) of the topological surface states $\partial\varepsilon/\partial\mathbf{k} = \hbar v_{\text{F}}$ (linear dispersion). It comes, with in a similar form of Eq. (E1.28):

$$j_c = \frac{e\hbar}{m}\Delta k \Delta m = e\Delta m v_{\text{SO}} \tag{E4.4}$$

where Δk and Δm refers to the Fermi surface shift on a single spin-textured Fermi contour (contrary to the Rashba-Edelstein effect in 2DEGs). We will see that the ideal picture of an isotropic spin-texture of the topological surface states is not always assured, especially in Bi-based TI compounds owing to the six-fold surface warping of the Fermi contour. However, the derived interfacial spin-charge conversion profile is expected to be independent from an additional Fermi surface warping term, as supported by our theoretical prediction in the frame of the linear response theory (Annex A2).

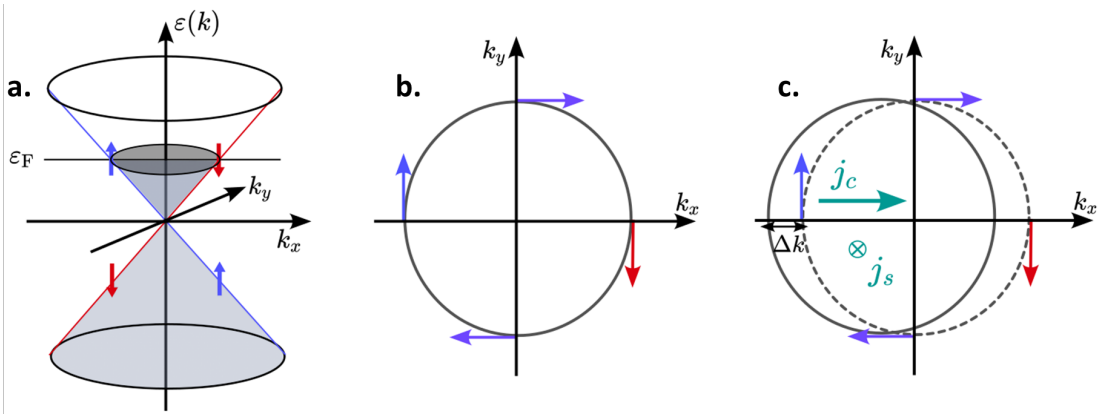

Figure 4.2: Inverse Rashba-Edelstein effect onto topological surface states of a topological insulator. (a) Dirac-like band dispersion of the spin-polarized topological surface states. (b) Fermi surface presenting a chiral spin-texture. (c) Upon the application of a spin-current j_s (along z), the Fermi surface shifts in the k-space by Δk due to the spin-polarized bands, leading to the generation of a transverse charge current j_c.

1.3 Topological protection, surface states hybridization, surface exchange and charge transfer: the effect of a magnetic contact.

To make topological insulators efficient spintronic devices, a prerequisite is to experimentally realize a magnetic contact in a TI/FM-like structure. A challenging question, which still remains an open-ended and very debated question nowadays, is the stability of the TSS after the deposition of such magnetic contact. Indeed, the theory predicts that the topological order may be altered due to the breaking of time-reversal symmetry $\mathcal{T}$. The hybridization of the time-reversal invariant by the magnetic exchange depends on the orientation of the magnetic perturbation. Considering a simple Rashba model, in the case of in-plane magnetic field (along $\mathbf{e}_x$ for the demonstration), the Hamiltonian changes to:

$$\mathcal{H} = \mathcal{H}_0 + \lambda_{SO}(k_y\sigma_x - k_x\sigma_y) + B_x\sigma_x = \mathcal{H}_0 + \lambda_{SO}((k_y + B_x)\sigma_x - k_x\sigma_y) \quad \text{(E4.5)}$$

where we have introduced $\lambda_{SO} = \hbar v_{SO}$ with the spin-orbit velocity v_{SO}. In a textbook case, the in-plane magnetic field can thus be associated to shift of $k'_y = k_y - B_x$ of the spin-polarized surface states which shifts the topological contour. Similarly, in the case of out-of-plane magnetic field (along $\mathbf{e}_z$), the Hamiltonian is not anymore compatible with the $\mathcal{T}$-symmetry and the topological protection vanishes:

$$\mathcal{H} = \mathcal{H}_0 + \lambda_{SO}(k_y\sigma_x - k_x\sigma_y) + B_z\sigma_z \quad \text{(E4.6)}$$

that would lead to the hybridization of the surface states in a Rashba-like texture, as illustrated in the inset of Fig. 4.3c. To try to answer this important point, we now give experimental details. Although ARPES is a useful surface-sensitive method to observe in-situ the TSS for uncapped topological insulators, it becomes a blind method to observe the conservation of the TSS, as soon as a capping is deposited, the photo-excited electrons are extracted from the top surface of the capping layer, even for a 0.5 nm-thick ferromagnet.

Recent references have claimed to observe remaining TSS after magnetic capping in TI/FM systems, for instance in Bi_2Se_3/Fe [274, 275], Bi_2Se_3/Au [276], Bi_2Te_3/Te [277] and BiSbTe/Cr [278]. In more details, Wray *et al.* [279] have claimed to observe a transition of the surface states of Bi_2Se_3 during ferromagnetic Fe deposition (up to 1.2 Å). They reported through a systematic ARPES study that the band structure shifts to lower energies, and so the Fermi level cuts more highly the bulk conduction bands. Moreover, due to the hybridization of the topological surface states, an electronic gap opens due to the massive Dirac bands (shown schematically in

Fig. 4.3c). However, the authors reported on the creation of new spin-degenerated surface states near the bulk conduction bands. The central discussion that arises from this is that the topological character might not be necessary to obtain Rashba-Edelstein type of spin-charge conversion as long as the spin degeneracy of the surface states is lifted.

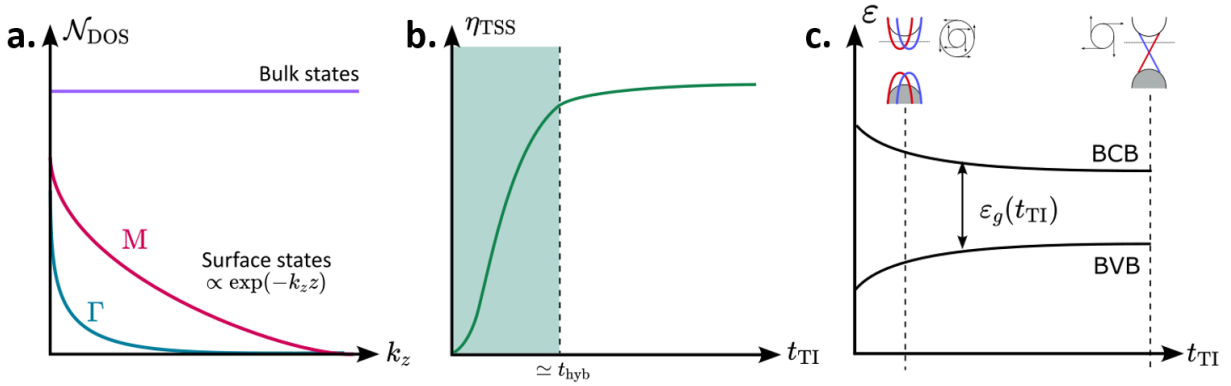

Figure 4.3: Evolution of the TSS profile. (a) Schematic of the out-of-plane dispersion of the TSS density of states near the Γ point (blue) and the M point (red), and the bulk bands (violet). (b) Hybridization profile of the SCC efficiency η_{TSS} in the ultrathin thickness limit. (c) Evolution of the electronic gap as a function of the topological insulator thickness t_{TI} with respect to out-of-plane confinement effects.

Interfacial charge transfer. Moreover, the conservation of the TSS properties is not the only key ingredient to consider. We also need to carefully take into account the charge transfer mediated by the chemical interfacial composition which would shift the Fermi level. The contact between a semiconducting bulk TI and a ferromagnetic material from the transition metals family would result in the formation of a Schottky barrier. The interfacial biasing would result to a shift of the bands with respect to the Fermi level, thus possibly leading to *i*) a crossing of the bulk bands or *ii*) a Fermi level lying in the bandgap, due to interfacially-located charges and depending on the initial band structure of the TI [280, 281]. A potential track for investigating this Fermi energy shift would be to probe the Schottky barrier by means of THz surge currents response using oblique optically-mediated pumping (see the discussions in Section II.2.2).

In 3D topological insulators, the efficient conversion may be hampered by the presence of bulk conduction bands at the Fermi level, which may not be totally true if the bulk bands take part in the SCC via ISHE for instance. This intrinsic problem is often encountered with Bi_2Se_3 where the Fermi level generally lies in the bulk conduction bands as this material is often natively n-doped due to the presence of Se vacancy defects [281]. The Fermi level control is thus a challenging issue in 3D TIs. To tackle this electronic band management, two approaches can be used to efficiently avoid bulk conduction band contributions at the Fermi level crossing. The first approach, that we will implement in the $SnBi_2Te_4$ topological insulator, is to pin the Fermi level by doping the topological insulator with Sn. The second approach will be to increase the electronic gap via confinement effects in very thin layers of $Bi_{1-x}Sb_x$ as detailed in Ref. [282]. In the scope of this thesis, we intuitively present THz emission spectroscopy as an interesting tool to probe the surface states and their interconversion in fully-stacked TI/FM structures.

Topological insulator in the very thin limit: topological surface states coupling and hybridization. Lastly, we address the case of topological surface states coupling in the very thin limit, typically smaller than several tens of nm. In the case of 3D topological insulators, hybridization between the top and bottom TSS is an issue which needs to be included in the balance. The surface states are mostly localized at the interface of the materials but in reality, they weakly penetrate the material's bulk and a non-zero TSS density of states is encountered on the bulk region

near the interface. The surface states are therefore called evanescent states *i.e.* the density of states follows an exponential decay as a function of depth $\propto \exp(-k_z t_{\mathrm{hyb}})$ (Fig. 4.3a) with an evanescent length of the TSS estimated about 3 QL ($\simeq$ 3 nm) for Bi_2Se_3 [281]. Therefore, for a topological insulator thickness equal or below this evanescent length t_{hyb}, the two surface states start to couple together: this is the hybridization of the TSS. For pure Bi, the reader is referred to the theoretical study of Ishida *et al.* [283] represented in Fig. 4.4.

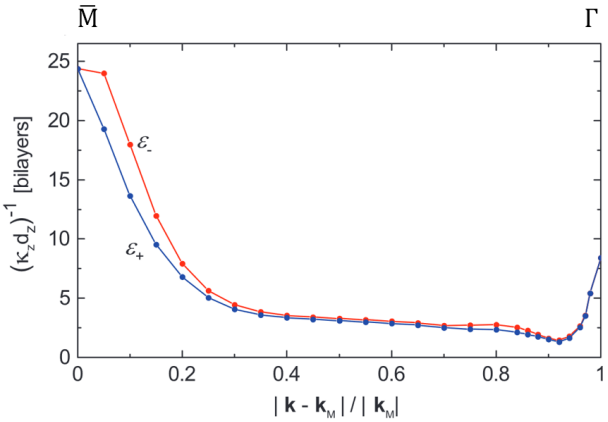

Figure 4.4: Evanescence of the topological surface states. Decay length of the two TSS (blue and red) of Bi(111) along the $\Gamma\bar{\mathrm{M}}$ direction. Adapted from Ref. [283].

This crossover between a 3D TI and an 2D non-TI due to the loss of the TSS by their hybridization at very low thicknesses has been widely reported in the literature for Bi_2Se_3 [272, 281]. As shown in Fig. 4.3b, the coupling of the two top and bottom TSS leads to the disappearance of the TSS because the two initial TSS at the two edges are spin-texture opposed. Following the Kramers theorem, the density of states has to be non-degenerated for the two spin orientations which would not be the case if the two TSS merge together. This therefore creates an opening of the electronic gap and the disappearance of the TSS in the ultrathin limit of topological systems, with a gap reaching up to $\Delta \simeq 0.25$ eV for the thinnest limit of 2 QL [281]. Another important cause of this effect is the reduction of the surface Rashba potential due to the weakening of the surface potential variation in ultrathin thicknesses. Although the Fermi velocity remains constant, the Rashba coefficient drops in the ultrathin region. For instance in Bi_2Se_3, the Rashba coefficient α_{R} changes from 2.8 eV.Å at 6 QL to 0 eV.Å below 3 QL as reported by Zhang *et al.* [281]. This can be understood as a potential disappearance of the SCC process in the ultrathin film limit as depicted in Fig. 4.3b.

This behaviour is also conjugated to another effect that goes with the reduction of the thickness for ultrathin topological insulator: the increase of the electronic gap by confinement effects [282]. A reduction of the thickness induces first a quantization of the band distribution along the k_z dispersion profile (continuum of states to discrete levels) evolving as $(n/t_{\mathrm{TI}})^2$, with n the quantized bulk band index and t_{TI} the thin film thickness, which implies an increase of the electronic gap in the very thin film limit.

1.4 Optical non-linearities in topological insulators: towards spin-related phenomena.

Topological insulators material growth and investigations of their properties had a rapid upturn around their experimental discovery in the early 2000s, with ARPES as a central technique to study the TSS electronic properties. It is only very recently that research on TIs regained a strong interest, with the theoretical prediction of a large interfacial spin-charge conversion in TIs [284].

From ARPES to optically-induced THz currents. Although ARPES is a technique of choice for studying TSS electronic states, the integration of TIs into complex and embedded magnetic structures (spin-injection, spin-conversion layer, metallic capping, *etc.*) makes it more complex to access both their electronic and optical properties. Following this idea, a novel research axis opened up from the 2010s with the study of photo-induced effects in topological insulators, mostly via their THz shift-current response and inverse photogalvanic effects as highlighted recently in Refs. [107, 109, 285, 286]. Even if this domain offers rich physics, our interest here lies in the magnetic-component of the THz signal addressing the spin-injection and spin-charge conversion dynamical properties. Launched with the work of Liu *et al.* [287] in 2018, the study focuses on spin-related phenomena in TIs that are typically about one order of magnitude larger than second-order non-linear effects in TIs. The approach that we follow is thus to treat pure non-magnetic optical effects in TIs as spurious effects as they do not participate to the spin-injection nor spin-charge conversion [106].

The reader is referred to the previous Section II.2.2 for a systematic presentation of such optical effects in non-linear media. In TIs, the electronic gap is often of the order of few hundreds of meV thus preventing a strong contribution from the optical rectification as our pump is always above 1.5 eV. We may then extract three possible contributions from non-linear optical effects with *i*) injection currents (via circular photogalvanic effect), unlikely in our case as we restrict solely our studies to linear pump polarization, *ii*) shift currents (via linear photogalvanic effect) and *iii*) surge currents via surface-depletion field and photo-Dember effect. Arising from the symmetry of hexagonally-shaped and inversion-symmetry breaking at the surface of topological insulators, we generally expect a $\cos(3\phi)$ dependence of the THz shift currents in topological insulators. In our reflection geometry experiments, we would expect a negligible contribution from normal charge currents as in the case of surge currents (surface-depletion field, photo-Dember effect), except if the sample is slightly tilted (misaligned) from the pumping incidence.

From THz non-linearities to spin-orbit related phenonema. We will now focus on the THz spin-injection and spin-relaxation as recently evidenced in Bi_2Te_3/Co [164] or in Bi_2Se_3/Co [168]. For that goal, we will help from the Kubo linear response theory in Annex A2 for the calculations of the spin-charge conversion response tensors σ^y_{xz} and κ_{xy}, respectively in case of inverse spin Hall and inverse Rashba-Edelstein effects. We have theoretically reported an isotropic conversion profile as a function of the crystalline orientation ϕ, and particularly, this argument still holds in case of hexagonally-structured of different spin-textured warping of the topological surface states in topological insulators. We now present our investigations on $SnBi_2Te_4$, Bi_2Te_3, $Bi_{1-x}Sb_x$ and Bi_2Se_3 in ferromagnetic contact with Co to address the interfacial SCC process.

2 Bi_2Te_3 and stoichiometric $SnBi_2Te_4$ family.

2.1 An engineered topological insulator with Fermi level pinning.

We present in this part our collaborative study with INN and SOLEIL synchrotron published in Advanced Optical Materials [271] about the ultrafast spin-charge conversion in Bi_2Te_3 and $SnBi_2Te_4$ topological insulators.

The scientific considerations behind the choice of $(SnBi_2Te_4)_n(Bi_2Te_3)_m$ epitaxial materials is to find a way to set free from the contributions of the bulk conduction bands of its parent material Bi_2Te_3, *i.e.* by tuning the Fermi level to cut only the topological surface states. In particular in Bi_2Se_3 and Bi_2Te_3, the Fermi level cuts additional bulk bands that could interfere with the conversion on the surface states. Although the THz emission in FM/TI multistacks has been reported with the topological insulator being Bi_2Te_3 [164] or Bi_2Se_3 [200], we propose to study the THz emission on a TI/FM system where the TI has been carefully engineered to have an absence of bulk conduction bands crossing at the Fermi level: $SnBi_2Te_4$. Such engineering is performed in $SnBi_2Te_4$ via a careful doping with Sn inducing charge transfer as performed previously on Bi_2Se_3 [288]. Experimentally, the epitaxial growth and the Fermi level control has been successfully reported by our collaborators at INN (Institute of Nanoscience and Nanotechnology in Greece) following the report of Fragkos *et al.* [289] in 2021. For a careful alloying with stoichiometric $SnBi_2Te_4$, the parasitic contribution of the bulk conduction bands is demonstrated to be minimal. The derivation has been performed for various stoichiometric ratio and the interested reader is referred to Ref. [289] for more details. After a structural and topological characterization of $SnBi_2Te_4$, we will study the spin-injection and spin-charge conversion in $SnBi_2Te_4$/Co bilayers. First, we quickly address the topological insulators based on Bi and Te compounds which present an hexagonal Fermi surface warping term.

Topological insulator with hexagonal warping terms. Following the discovery of topological surface states in TIs composed of Bi-based compounds [290], Fu [291] has theoretically predicted in 2009 the deformation of the Fermi contour of the surface states in Bi_2Te_3 due to the spin-orbit coupling, thus adding an extra hexagonal warping term. The energy dispersion finally reads:

$$\varepsilon_{\pm}(\mathbf{k}) = \varepsilon_0(k) \pm \sqrt{v_k^2 k^2 + \lambda_{SO}^2 k^6 \cos^2(3\phi)} \tag{E4.7}$$

where $\varepsilon_{\pm}$ is the energy of the lower (upper) band, $\mathbf{k} = (k\cos\phi, k\sin\phi)$ is the wave vector where ϕ is defined as the azimuthal angle with respect to the ΓK direction, λ_{SO} is the spin-orbit coupling strength and $v_k = v(1+\alpha k^2)$ is the Dirac velocity taking into account such correction for relativistic Dirac electrons. Note that the $\varepsilon_0(k)$ term represents the energy of free-like electrons. The addition of a warping from the ideal circular Fermi surface may generate a variation of the spin-texture along the Fermi contour with the appearance of a spin-polarization along the normal direction (z). This is particularly the case in $SnBi_2Te_4$ with a six-fold symmetry Fermi contour.

2.2 Topological surfaces states of $SnBi_2Te_4$.

$SnBi_2Te_4$ is a material presenting a rhombohedral unit cell (*P3m1*) and is composed of Van der Waals layers, each layer being composed of seven rows of atoms (respectively Te-Bi-Te-Sn-Te-Bi-Te) as shown in Fig. 4.5a. This stacking is denoted thereafter as a septuple layer (SL) which thickness is about 1.2 nm. The structural characterization is available in more details in Ref. [289]. The projected 2D Brillouin zone shows a hexagonal shape with $\bar{\Gamma}$, $\bar{K}$ and $\bar{M}$ the points of symmetry as shown in Fig. 4.5b.

We present in Fig. 4.6a the resulting band structure calculated at INN by density functional theory (DFT) for $SnBi_2Te_4$(5SL). At the Fermi level, we observe that the crossing with the band

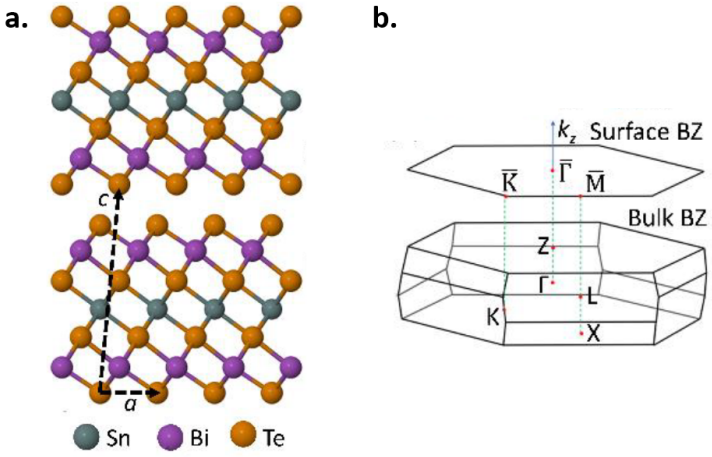

Figure 4.5: Structural characterization of $SnBi_2Te_4$. (a) Crystallographic arrangement of $SnBi_2Te_4$ presenting the septuple layer (SL). (b) 3D Brillouin zone and its 2D projection along the surface normal.

structure occurs only at the level of a single topological surface states in the region close to the $\bar{\Gamma}$ point. The experimental growth is conducted on Si substrates with an InAs(35nm) buffer to tune the lattice mismatch. Fig. 4.6b-c presents the experimental observation of the TSS performed by ARPES. We report a linear dispersion of the band structure near the $\bar{\Gamma}$ point, characteristic of topological surface states, with a gap between the closest bulk valence band around 0.2 eV near the $\bar{M}$ point. Moreover, the Fermi surface presents, as expected, an hexagonal warping of the TSS.

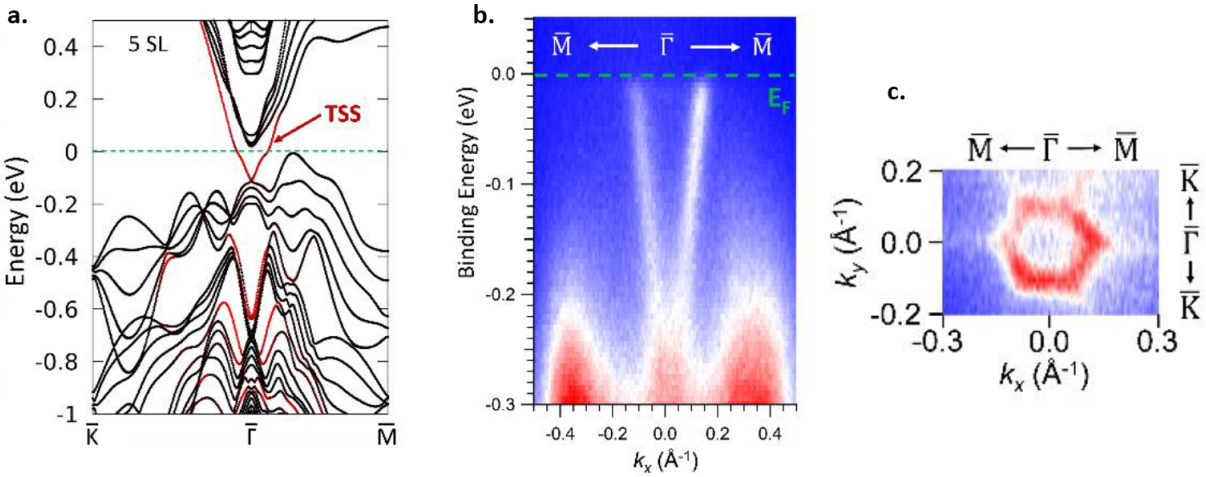

Figure 4.6: Band structure of $SnBi_2Te_4$. (a) Calculated band structure for $SnBi_2Te_4$(5SL) presenting the topological surface states crossing (red) at the Fermi level (dotted green line). (b) Band dispersion along the $\bar{\Gamma}\bar{M}$ direction in $SnBi_2Te_4$(5SL). (c) Experimental Fermi surface presenting an hexagonal shape in $SnBi_2Te_4$(5SL).

This demonstrates *i*) the very good epitaxial growth of the stoichiometric $SnBi_2Te_4$ compound and *ii*) the effective control of the band structure with respect to the Fermi level, able to cross the TSS. We focus now on samples composed of $SnBi_2Te_4$ with thicknesses varying like 5SL, 8SL and 13SL (*resp.* 5.9, 9.4 and 16.2 nm), on top of which we grew a FM contact with Co, of thickness ranging from 2 to 4 nm and capped with a 2.5-3 nm-thick naturally oxidized AlO_x layer. A dual conversion $SnBi_2Te_4$(5SL)/Co(2nm)/Pt(2.5nm) sample will be proposed: here, the ultrafast spin-current would escape from both interfaces, leading to a conversion in Pt with ISHE and at $SnBi_2Te_4$/Co interface. A Bi_2Te_3(5QL)/Co(1.5nm) sample (QL stands for quintuple layers) is

grown as a reference to compare the spin-injection and spin-charge conversion efficiency in this parent topological compound. Complementary ARPES data displayed in Fig. 4.7 presents the experimental band structure of Bi_2Te_3 ($R\bar{3}m$). We see that contrary to the case of $SnBi_2Te_4$, we measure additionally to the TSS, a contribution from bulk conduction bands (BCB) at the center of the Brillouin zone, demonstrating the presence at the Fermi level of those disturbing bands in the spin-conversion process.

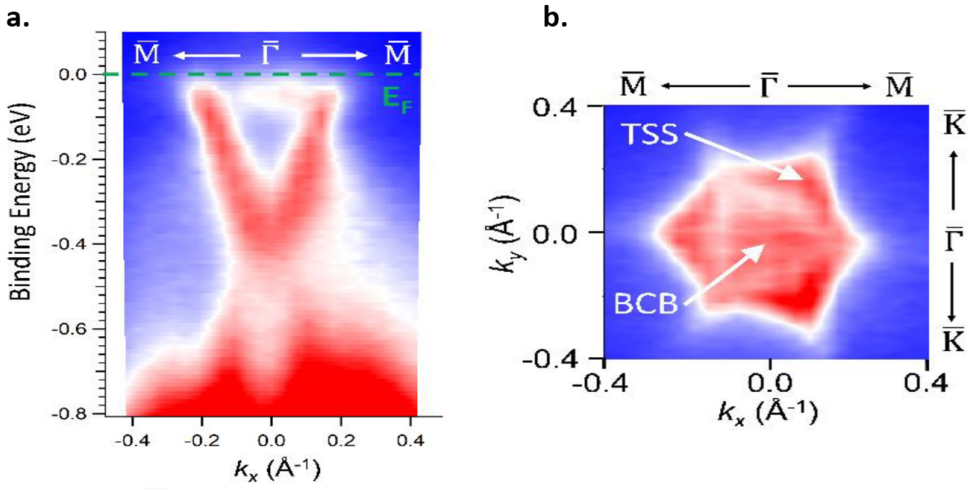

Figure 4.7: Band structure of Bi_2Te_3. (a) Band dispersion along the $\bar{\Gamma}\bar{M}$ direction. (b) Experimental Fermi surface where both the TSS and the bulk conduction band (BCB) are mapped.

2.3 THz emission features from $SnBi_2Te_4$/Co bilayers.

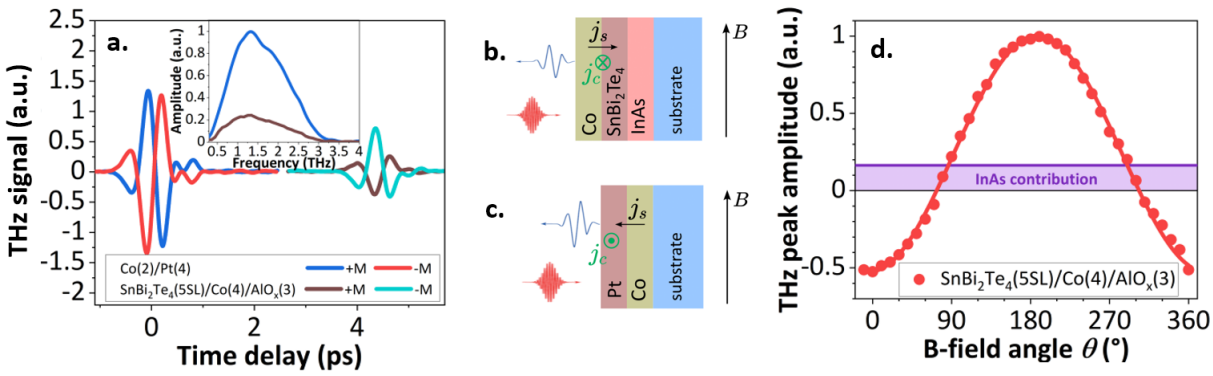

Figure 4.8: THz emission features from $SnBi_2Te_4$ bilayers. (a) THz emission from $SnBi_2Te_4$/Co (brown and light blue) compared to Co/Pt (blue and red), respectively at positive and negative applied magnetic fields. Representation of the THz generation in (b) $SnBi_2Te_4$/Co and (c) Co/Pt addressing a different spin current escape for a same sign of the interconversion process. (d) THz peak amplitude from $SnBi_2Te_4$/Co as a function of the magnetic field angle θ.

We address now via the THz emission spectroscopy method (in the time-domain, see Section III.2.1) the ultrafast spin-current injection properties and related spin-charge conversion mechanism in those optimized TI/FM bilayers. To that extend, we reported in Fig. 4.8a the THz emission from $SnBi_2Te_4$/Co(4)/AlO_x(3) heterostructure compared with standard metallic spintronic THz emitter Co(2)/Pt(4). We report two key elements: the first is the presence of a sizeable THz signal, comparable to Co/Pt, about 30% in signal amplitude. The second is the inversion of the THz polarization (electric field) of $SnBi_2Te_4$/Co compared to Co/Pt under the same orientation of the external magnetic field. This demonstrates that the sign of the

interconversion efficiency α_{SCC} is equal to the sign of the positive spin Hall angle sign of Pt owing to the different spin current escape in both heterostructures (see panels in Fig. 4.8b-c). Moreover, by switching the magnetic field orientation, we measured a partial reversal of the THz signal indicating that the signal is composed of two contributions that we further explore in the next parts: a magnetic contribution of strong interest as we are searching for evidence of strong spin-injection and spin-charge conversion mechanism, and a non-magnetic contribution owing to pure optical effects.

To address the THz polarization generated from these heterostructures, we have performed angular measurements as shown in Fig. 4.8d by rotating the in-plane magnetic field by an angle θ thus rotating the in-plane magnetization of Co $\mathbf{M}(\theta)$, following the definition proposed in Section III.2.3. In a second part, we will define as ϕ the crystallographic azimuthal orientation, where both angles θ and ϕ can be rotated independently. We recover an uniaxial dependence $\propto \cos(\theta)$ as reported previously on spintronic based THz emission which is in agreement with the THz polarization rules (isotropic emission combined with the detector response, see Section II.3.2). Interestingly, this angular response is superposed with a constant offset (of amplitude about 20% of the maximum signal) which traduces a non-magnetic response to the total signal.

2.4 Spin THz efficiency.

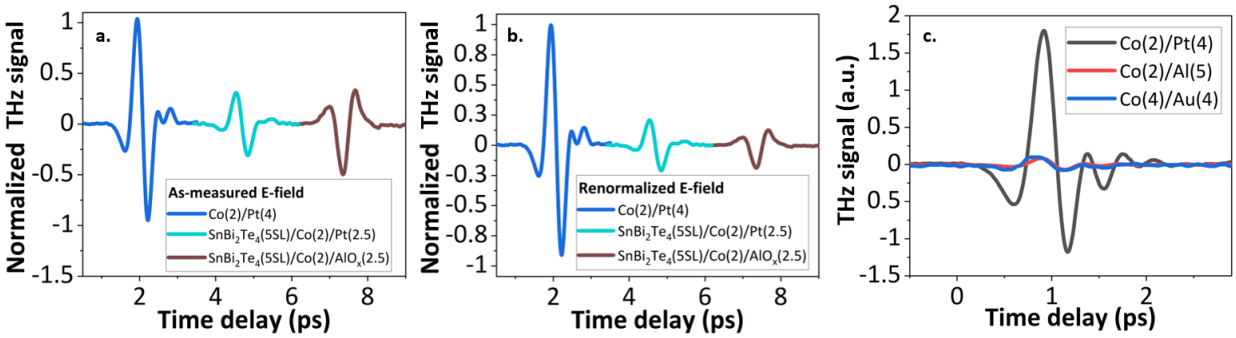

Figure 4.9: Addressing the spin-charge conversion efficiency in $SnBi_2Te_4$ topological insulator. (a) Measured THz emission and (b) extracted THz efficiency presented for Co(2)/Pt(4), $SnBi_2Te_4$(5SL)/Co(2)/Pt(2.5) and $SnBi_2Te_4$(5SL)/Co(2)/AlO_x(2.5). (c) THz contribution from additional layers in spintronic structures, presently Co(2nm)/Pt(4nm) (grey), Co(2nm)/Al(5nm) (red) and Co(4nm)/Au(4nm) (blue) addressing the negligible role of the self-emission in Co.

To perform the absorption renormalization treatment following the procedure proposed in Section III.2.2, we have considered a resistivity of $SnBi_2Te_4$ around 400 µΩ.cm extracted from Hall measurements, and assumed to be independent on the $SnBi_2Te_4$ thickness in the range from 5 to 13 SL. The resistivity $\rho = 1/en_1\mu_1$ has been extracted using a measured carrier density around $n_1 = 2 \times 10^{13}$ cm^{-2} and carrier mobility of $\mu_1 = 588$ cm^2.V^{-1}.s^{-1} and we refer the reader to Ref. [289] for more details.

We present in Fig. 4.9a-b the measured and renormalized THz magnetic signals from Co(2)/Pt(4) reference *vs.* $SnBi_2Te_4$(5SL)/Co(2)/AlO_x(2.5) sample and dual-SCC $SnBi_2Te_4$(5SL)/Co(2)/Pt(2.5) sample. We first observe that the single-SCC in $SnBi_2Te_4$/Co reaches up to 30% compared to the one of Pt. While combining two dual SCC conversions of identical sign (Pt and $SnBi_2Te_4$/Co), we observe that the renormalized THz signal is of the same phase as Pt, indicating the dominant role of Pt in the overall SCC. However, the total THz efficiency is reduced compared to the pure THz signal of Pt which shows the sizeable contribution of the interconversion efficiency in $SnBi_2Te_4$ that we estimate about 30% of the one of Pt.

To exclude the role of NIR-transparent AlO_x layer and the impact of the Co self-radiation to the THz emission, we displayed in Fig. 4.9c the THz efficiency obtained from contribution from Co(2nm)/Pt(4nm), Co(4nm)/Au(4nm) and Co(2nm)/Al(5nm) which can be dissociated into a metallic Al(2nm) and naturally oxidized AlO_x(3nm) layer. We observe that the emission from the reference Co/Al bilayer is more than one order of magnitude smaller than Co/Pt. The same interpretation can be drawn for Co/Au bilayer. This is linked to the absence of strong spin Hall dissipation channel to convert a spin current into a charge current in both Al and Au, and also the absence of major self-emission process in ferromagnetic Co [292, 293]. Here, the THz emission mainly arises from two effects: *i*) the magnetic dipole radiation proportional to $\partial\mathbf{m}/\partial t$ and to *ii*) a small contribution from the AHE in Co (self conversion in the FM layer).

2.5 Separation of the non-magnetic contributions to the THz emission.

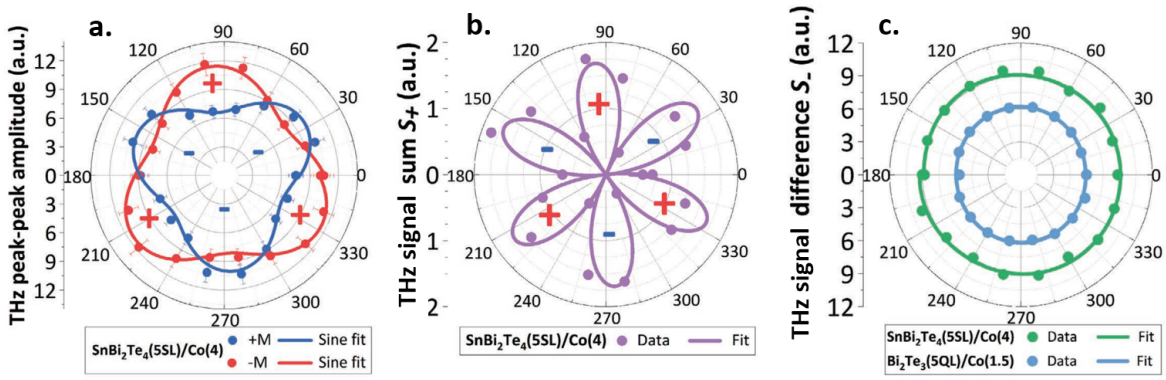

Figure 4.10: Crystalline angular dependence on the THz emission from $SnBi_2Te_4$/Co. (a) Measured THz emission of $SnBi_2Te_4$(5SL)/Co(4nm) as a function of magnetic field polarity $\pm B$, respectively for positive $+\mathbf{M}$ and negative $-\mathbf{M}$ thereafter followed by the extraction of (b) the treated non-magnetic and (c) the magnetic component on the THz signal. The $\pm$ label on each lobe represents the THz signal phase. The magnetic component of $SnBi_2Te_4$(5SL)/Co(4nm) (green) is compared to the extracted magnetic component of Bi_2Te_3(5QL)/Co(1.5nm).

As the overall signal contains mixed non-magnetic and magnetic signals, it is necessary to separate both terms following the method proposed in Section III.2.3 and to discuss about the role of the Fermi level pinning and interface interconversion in those TI/FM systems. For this, we have plotted in Fig. 4.10a the THz signal from $SnBi_2Te_4$(5SL)/Co(4nm)/AlO_x(3nm) as a function of the crystallographic orientation ϕ from 0° to 360° for the two magnetic field polarities $\pm B$. We observe two angular profiles shifted by 60° and composed of an isotropic background on which is imprinted a three-fold axis symmetry. From these data, it is possible to extract respectively in Fig. 4.10b and Fig. 4.10c the respective optical and magnetic contribution *vs.* the crystallographic orientation ϕ. Typically, the non-magnetic maximal amplitude is about 15-20% of the total THz emission while the magnetic-contribution we are searching for, represents 75% of the total THz emission.

Non-magnetic contribution. We first focus on the non-magnetic optical contribution for which we detail the time-trace in Fig. 4.10a. We observe a three-fold symmetry $\cos(3\phi)$ with a phase reversal on each lobe and a sizeable offset about 30%. The same data is plotted in Fig. 4.10b in an angular plot. Fig. 4.10c displays the same signal after having subtracted the constant offset, making apparent a $\cos(3\phi)$ polar dependence ($\pm$ signs denote the signal phase). These symmetries are confirmed by additional measurements on a reference InAs buffer (only) of thickness 35 nm as presented in Fig. 4.12. We observe *i*) a THz signal independent of the applied magnetic field orientation and *ii*) a three-fold ($\cos(3\phi)$) emission symmetry as a function of the

azimuthal angle ϕ.

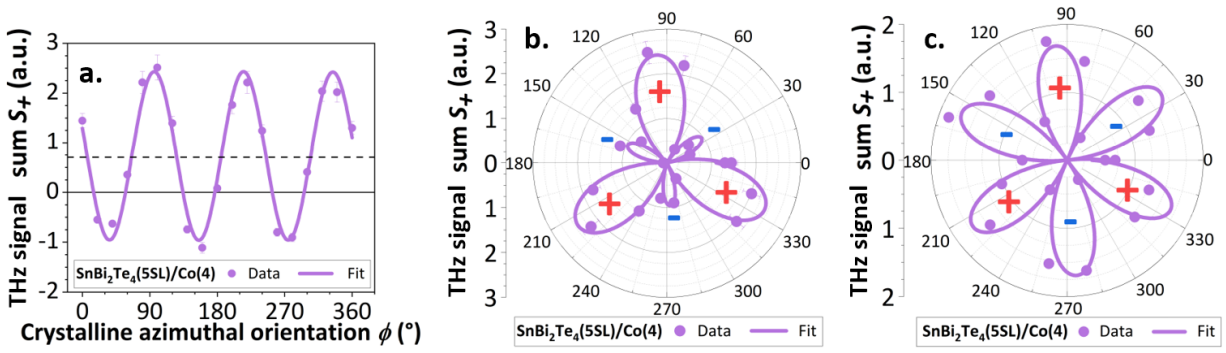

Figure 4.11: Symmetries of the non-magnetic contribution from InAs/SnBi$_2$Te$_4$/Co bilayer. (a) Extracted contribution without any additional treatment. The dashed black line represents a non-zero offset that shifts the $\cos(3\phi)$ dependence. (b) Identical data plotted in an angular plot. The $\pm$ label represents the phase of the signal. (c) Contribution where the constant offset has been subtracted. We identify clearly the $|\cos(3\phi)|$ contribution.

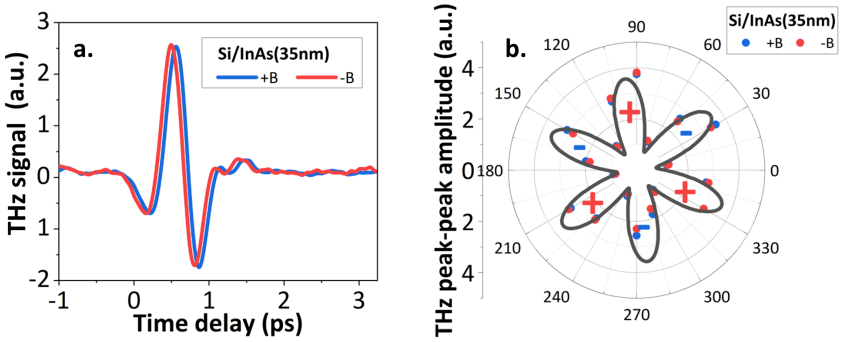

Figure 4.12: THz emission from InAs buffer. (a) THz emission insensitivity under magnetic field ($\pm B$) respectively in blue and red, at fixed azimuthal sample orientation ($\phi \simeq 100°$). (b) Azimuthal THz emission profile from InAs(35nm) demonstrating a $\cos(3\phi)$ symmetry. Interestingly, the THz phase reverses on each lobe separated by $30°$.

In summary, the non-magnetic contribution can be described by two terms of different symmetries: a three-fold symmetry evidences an effect mediated via second-order surface optical rectification $\chi^{(2)}$ as reported for InAs material by Reid *et al.* [111]. Moreover, the constant offset may be associated to a slight out-of-plane tilt of the sample which would characterize the normal dipole generated via surge currents and potentially with the photo-Dember effect.

2.6 SnBi$_2$Te$_4$ thickness dependence and azimuthal angular profile.

In this final part, we focus on the major spin-injection THz emission possibly arising from the topological surface states contribution. We remind that we have beforehand extracted the magnetic contribution on the THz signals and also performed a renormalization treatment to extract the THz efficiency η_{THz} (removing the THz absorption in the multilayers, see Section III.2.2). We can now focus on the variations of the bare THz efficiency as a function of the SnBi$_2$Te$_4$ thickness and crystallographic orientation ϕ.

To predict the thickness dependence of interfacially-mediated conversion, we present in Fig. 4.13a the expected thickness dependence of the THz efficiency η_{THz} comparing the ISHE (bulk) *vs.* the IREE (interfacial) interconversion profile. Conventionally and as reported above throughout Chap. III, the evolution of the THz measured signal in case of ISHE evolves up to

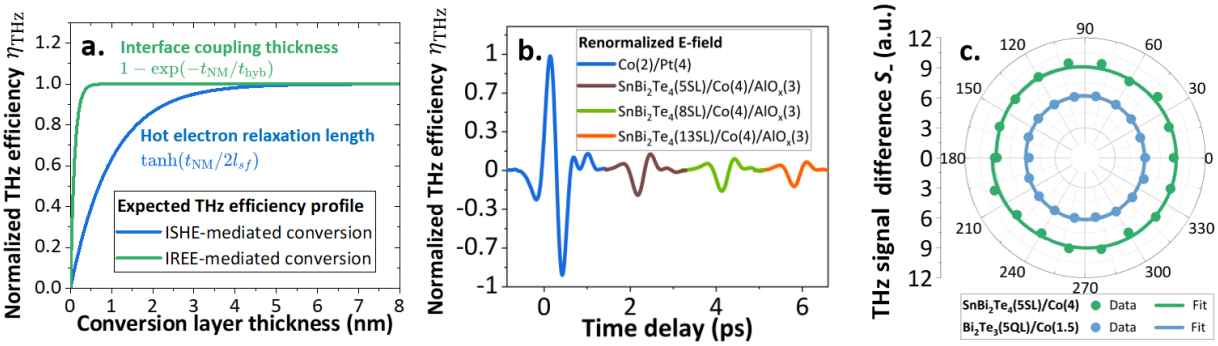

Figure 4.13: Interfacially-mediated interconversion. (a) Expected THz efficiency thickness profile for ISHE (bulk) interconversion (blue) *vs.* IREE (interface) interconversion. (b) Experimental thickness dependence of the THz efficiency on $SnBi_2Te_4(t_{TI})$/Co(4) for t_{TI} ranging from 5, 8 and 13 SLs, compared to Co(2)/Pt(4). (c) Angular conversion profile of the magnetic component in $SnBi_2Te_4$/Co (green) and Bi_2Te_3/Co (light blue).

a typical lengthscale approaching the spin diffusion length l_{sf} before decreasing progressively due to the THz absorption induced by $1/\mathcal{A}_{NIR}Z(\omega)$ in the material bulk. The THz efficiency η_{THz} is thus evolving as $\tanh(t_{NM}/2l_{sf})$ for ISHE. In the case of the IREE, the THz efficiency as a function of the thickness has the following form $1-\exp(-t_{NM}/t_{hyb})$ where t_{NM} is the thickness of the conversion layer and the saturation length t_{hyb} can be represented as the minimal coupling thickness between the top and bottom interfaces as the extension/penetration of the length of the TSS in the bulk, *i.e.* as soon as the two surfaces states are decoupled from one another (discussions in Section IV.1.3). This reasoning starts to be shared by the scientific community as a way to probe, via THz emission spectroscopy, the eventuality of interfacial conversion mediated by surface states in topological insulators/ferromagnet heterosturctures [164, 167, 163].

Experimentally, we have performed a thickness dependence of the THz efficiency η_{THz} in $SnBi_2Te_4$/Co samples as a function of the $SnBi_2Te_4$ thickness, ranging from 5SL to 13SL, as shown in Fig. 4.13. We observe an almost constant level of signal in favor of an interfacially mediated emission. Indeed, even at large thicknesses of $SnBi_2Te_4$ presently 13SL $\simeq$ 16.2 nm, the signal remains sizeable. Besides, the occurrence of a significant THz signal at the lowest thickness accessible (5SL) demonstrates the very good crystalline quality of the epitaxial thin films. Indeed, when one imagines the thickness dependence at low thicknesses, the signal would have started to drop below the minimal coupling thickness (called t_{hyb}) which describes the coupling or hybridization between the two surface states (top and bottom interfaces). Such low coupling thickness has been already reported by our collaborators at INN [294] on Bi_2Se_3 on AlN substrate down to 3 QL $\simeq$ 2.88 nm (quintuple layers) and is strongly depend on the deposited material quality influenced by the substrate and specific growth conditions. The second hint measurement performed on $SnBi_2Te_4$ and Bi_2Te_3 is the extraction of the azimuthal variation $\eta_{THz}(\phi)$, connected to the interconversion profile, presented in Fig. 4.13. We directly observe an isotropic contribution on both systems and a smaller amplitude for Bi_2Te_3 compared to its optimized compound $SnBi_2Te_4$ by a factor $\simeq$ 30%. This is to connect with the discussion detailed in Annex A2 where we demonstrated that the spin-charge conversion profile is expected to be isotropic in both case of ISHE and IREE, with respect to the azimuthal crystalline orientation ϕ, even for hexagonally shaped topological surface states.

Due to the ferromagnetic contact with $SnBi_2Te_4$, a possible distortion of the topological surface states may occur without however destroying the whole spin-momentum locking properties, and may lead to a transformation of the TSS into spin-polarized Rashba states. However, several references available in the literature reported the conversion of such hybridized states with a

thin $3d$ ferromagnetic contact, and we referred the reader to the discussion we had previously on this particular issue (found in Section IV.1.3). The second element induced by the ferromagnetic contact is the charge transfer at the interface which would result in a shift of the Fermi level with respect to the interfacial band dispersion of $SnBi_2Te_4$. This is a particular point where we are insensitive in ARPES as this surface-sensitive technique would only give access to the electrons extracted from the top ferromagnetic contact, thus avoiding the collection of the electrons from the TI surface. THz emission spectroscopy can be an alternative technique to address this point. Indeed, we can observe a larger conversion efficiency in $SnBi_2Te_4$/Co compared to Bi_2Te_3/Co, possibly linked to a drastic reduction of the conversion in Bi_2Te_3 assumed by the presence of bulk conduction bands at the Fermi level. This would demonstrate an efficient Fermi level pinning in $SnBi_2Te_4$.

Conclusions and perspectives for $SnBi_2Te_4$/Co THz emission spectroscopy.

We have reported in this study the efficient THz spin-charge conversion in $SnBi_2Te_4$ down to 5SL ($\simeq$ 5.9 nm) with a FM contact with Co, and a net THz amplitude about 20% of Co/Pt reference emitter. After extraction of the THz efficiency, we report a spin-charge conversion efficiency $\alpha_{SCC} = +20\%$ of the spin Hall angle of Pt, sharing the same sign. This material has been carefully designed to avoid the crossing of the bulk conduction bands at the Fermi level, bands which can be parasitic in the spin-charge conversion process. By comparing $SnBi_2Te_4$ to Bi_2Te_3 parent material, we report a larger THz amplitude owing to the careful pinning of the Fermi level in the bandgap. We have moreover performed a systematic study of the emission symmetries in $SnBi_2Te_4$/Co bilayers demonstrating an isotropic conversion profile and a $SnBi_2Te_4$ thickness independent THz signal. Those two elements are in favor of an interfacially-mediated spin-charge conversion in $SnBi_2Te_4$, but the exact nature of the process, whether it would be inverse Rashba-Edelstein effect or an interfacial-enhancement of the inverse spin Hall effect, remains challenging to claim. THz emission spectroscopy reveals to be here a powerful and interesting experiment to investigate and probe the dynamical spin-charge and spin-current properties in TI/FM thin film heterostructures.

We thus propose in the next part the study of $Bi_{1-x}Sb_x$ topological insulator alloy which allow more control of the profile of the TSS, whether it would be via the Sb doping concentration or exerted strains induced by stiochiometry. Besides, its electronic structure can be calculated and would be an interesting tool to estimate the interfacial conversion profile as well as the possibility of an inverse Rashba-Edelstein conversion.

3 $Bi_{1-x}Sb_x$ alloy.

This work has been realized in collaboration with SOLEIL synchrotron (L. Baringthon, P. Le Fèvre, F. Bertran) and C2N (G. Patriarche, A. Lemaître). The growth of $Bi_{1-x}Sb_x$, detailed in a previous work [270], and the (S)ARPES characterization has been performed in the frame of a previous joint thesis [295]. We acknowledge the collaboration with co-workers from UMPhy (D. She, N. Reyren, J.-M. George). A manuscript concerning the THz spectroscopy characterization is currently under peer-review [296].

Historically, $Bi_{1-x}Sb_x$ has been the first three-dimensional topological insulator to be experimentally investigated, following the growth in 2008 by Hsieh *et al.* [56] which revealed the existence of topological surface states. The extracted band velocities in the vicinity of the Fermi level of $Bi_{1-x}Sb_x$ are about $v_x \simeq 8 \times 10^4$ m.s^{-1} and $v_y \simeq 10^6$ m.s^{-1} respectively along k_x and k_y directions [56], which are comparable with the one of graphene $|\mathbf{v}| = 10^6$ m.s^{-1}, thus identifying $Bi_{1-x}Sb_x$ as a promising material. $Bi_{1-x}Sb_x$ has recently been highlighted as a very strong spin-charge conversion system to be envisioned in spintronic devices [54, 297]. The main stake studying this material holds in its capacity to tune the bulk bandgap while applying a compressive strain on the c axis of the hexagonal structure. This allows to pin the topological surface states precisely in between the bulk bands to avoid parasitic transport at the Fermi level. Our study mostly focuses on the significant ultrafast spin-charge conversion in epitaxially grown $Bi_{1-x}Sb_x$/Co bilayers, larger in amplitude than any TI/FM system and above the reference emitter Co/Pt, evidencing $Bi_{1-x}Sb_x$ as an interesting platform for spintronic applications. We address here, by THz emission spectroscopy, the major role of the interface in the spin-charge conversion process.

Giant spin Hall effect in $Bi_{1-x}Sb_x$.

Khang *et al.* [54] reported a giant spin Hall effect in $Bi_{1-x}Sb_x$ from magneto-transport measurements, claiming a value about $\theta_{SHE} \simeq 52$. But intuitively from the definition of the spin Hall angle which is the ratio between the output charge current and the incoming spin current, how could we understand this, meaning it converts more spins than the injected number of spins into the system? To explain this, we have to consider the additional contributions of the interface (IREE) to the SCC, owing to the strong helical spin-momentum locking.

3.1 Crystallographic structure of $Bi_{1-x}Sb_x$.

As Bi and Sb share the same crystallographic structure (*A7* structure), $Bi_{1-x}Sb_x$ alloys will adopt such structure with slight deviations from the ideal case as the doping with Sb will drive locally a change of the lattice parameter and also of the bandgap value through stoichiometry changes. The reference lattice parameters of Bi and Sb are given in Ref. [298]. The elementary unit cell of the $Bi_{1-x}Sb_x$ alloy is represented by a tilted rhombohedral cell (symmetry group n°166 - $R\bar{3}m$) dissociated into bilayers (BL) with a BL thickness about $\simeq 1$ Å) as depicted in Fig. 4.14a. The BLs are decomposed as a succession of the A-B-C atomic sequence (following BC→CA→AB permutation) and are separated by a gap (denoted also as an inter-BL distance) about 3 Å which can be assimilated to a Van der Waals gap as presented in Fig. 4.14b. Therefore, we will refer to the total inter-BL and intra-BL distances as 1 BL $\simeq$ 4 Å. The sketch of the structure of $Bi_{1-x}Sb_x$ along the (111) direction (top view) is presented in Fig. 4.14c. We identify the atoms from the A row (*resp.* C row) as below (above) the atoms from the B row. Interestingly, the plane formed by the (111) direction and the $\Gamma\bar{M}$ direction is a symmetry plane. This point will be particularly important when addressing the THz non-magnetic components.

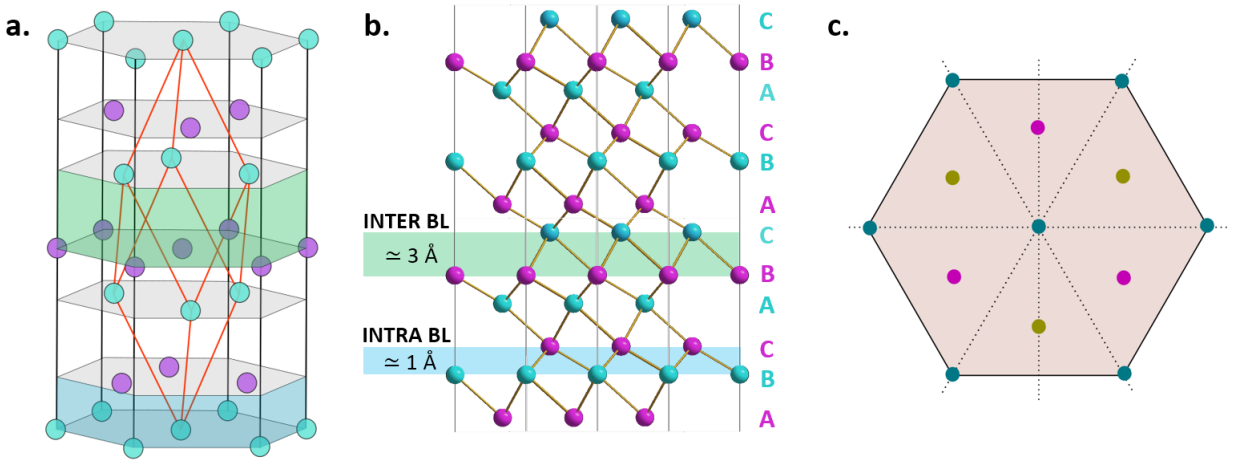

Figure 4.14: Unit cell of $Bi_{1-x}Sb_x$. (a) Rhombohedral unit cell of $Bi_{1-x}Sb_x$ presenting the bilayers and the van der Waals-like gap. (b) Side view presenting the A-B-C repetition and the inter and intra BL distances. (c) Surface view along (111) presenting the even and odd planes of $Bi_{1-x}Sb_x$.

3.2 Topological band structure and ARPES characterization.

The dispersion of the topological surface states in $Bi_{1-x}Sb_x$ depends on the Sb concentration (x), as schematically illustrated in Fig. 4.15 [299, 300]. First, we start from pure Bi ($x = 0$) presenting a semimetallic character as no indirect gap exists between the top of the valence band T and the bottom of the conduction band L_s. Those two bands are connected via two different surface states S_1 and S_2 which both join at the top of the valence band L_a at the $\bar{M}$ point. At the $\bar{M}$ TRIM point, the two surface states can meet, forming a doubled spin-degenerate point, or each of the two surface states can meet the valence or conduction bands separately. Between 7% and 13% of Sb content, a band inversion exists at the $\bar{M}$ point where the L_a valence band becomes the conduction band owing to the L_s band inversion. This opens a gap between the conduction band at the $\bar{M}$ point and the T valence band illustrating the semimetal-to-semiconductor transition. The two surfaces states S_1 and S_2 respectively connect to the conduction band L_a and the valence band L_s. An odd number of crossing $\Delta N = \Delta N(\Lambda_i = \Gamma, \Lambda_j = \bar{M}) = 3 + 2 = 5$ between the two surface states S_1, S_2 and the Fermi level denote a topological insulator behaviour. Between 30% and 60% of Sb, even though there is an odd number of crossings between S_1, S_2 and the Fermi level, the electronic gap is closed due to the upward shift of the H valence band. We recover a semimetallic behaviour as for pure Sb ($x = 1$) between the valence band H and the conduction band L_a. Two ingredients are thus needed to obtain the topological surface states: a band inversion at the $\bar{M}$ point and the (positive) indirect gap opening, both leading to an odd number of crossings between the surface states and the Fermi level [299, 300].

Semimetallic behaviour.

A semimetal present a crossing of the Fermi level with a valence band and a conduction band but at different wavevectors. The fraction of holes between the Fermi level and the top of the valence band can participate to the transport with the electrons included between the bottom of the conduction band and the Fermi level. From neutrality arguments, the number of holes is equal to the number of electrons [301].

Studies led by Baringthon *et al.* [270] reported the very good thin film quality of $Bi_{1-x}Sb_x$ grown at SOLEIL synchrotron (Saclay, France). The growth of $Bi_{1-x}Sb_x$ is demonstrated to remain epitaxial for various substrates of different lattice mismatches (InSb, BaF_2 and Si). Connected to the deposition chamber, ARPES technique allowed to access the band dispersion of $Bi_{1-x}Sb_x$ in

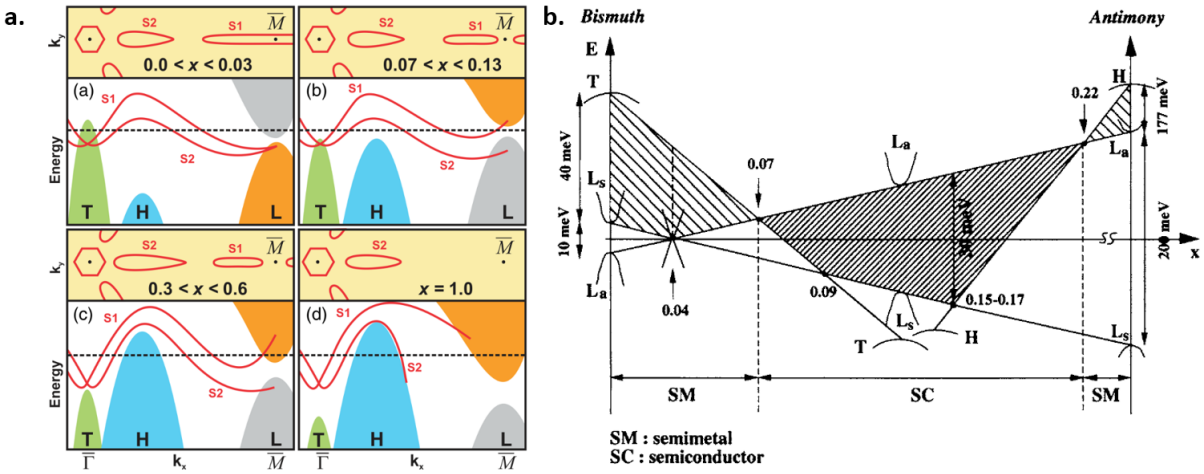

Figure 4.15: Evolution of band structure of $Bi_{1-x}Sb_x$ topological insulator as a function of the Sb concentration x. The top panels represent the projection of the TSS onto the Fermi surface while the bottom panels present the relation dispersion in the $\Gamma\bar{M}$ direction. The TSS are labelled S_1 and S_2 (in red). (b) Quantitative evolution of the valence and conduction bands at the $\bar{M}$ point as a function of Sb dopant concentration x. Adapted respectively from Refs. [299, 300].

the reciprocal space, as shown in Fig. 4.16 for $Bi_{1-x}Sb_x$ with $x = 0.21$ and thicknesses ranging from 2.5 to 15 nm (6 BLs to 36 BLs). The reader is referred to Ref. [270] for a systematic Sb concentration study of the TSS in the 7% to 30% range. Back to $x = 0.21$, we identify near the Γ point the hexagonal electron pocket P_1 at the core of the Brillouin zone. Along $\overline{\Gamma M}$, this is followed by the hole petal P_2 (above the Fermi level) and the last electron pocket P_3 near the $\bar{M}$ point. One conclusion of the study is the ability to set free from the parasitic contribution of bulk bands by increasing the gap via stoichiometry and strain engineering in very thin films [298, 300]. First, the Sb addition leads to the inversion of the L_a and L_s bands at the $\bar{M}$ point allowing the opening of a gap, and secondly, it follows the description of the confinement effect in thin films proposed by Ito *et al.* [282]. Baringthon *et al.* demonstrated the topological insulator character of grown $Bi_{1-x}Sb_x$, down to 2.5 nm, recovered via an odd number of crossing with the Fermi level, $\Delta N = \{3, 5, 5\}$ respectively for 2.5, 5 and 15 nm. This TI platform is thus particularly interesting to study in THz spintronics for enhancing the spin-charge interconversion process efficiency.

3.3 Spin-polarized density of states: spin-resolved ARPES and tight-binding calculations of $Bi_{1-x}Sb_x$.

Before focusing into THz spin-charge profile measurements, it is necessary to consider the spin-polarization of the TSS by performing both experimental and related band calculations. Indeed, any type of inverse Rashba-Edelstein conversion would need a strong TSS spin-splitting to efficiently generate a transverse charge current. To that extend, we will respectively consider several variations of the $Bi_{1-x}Sb_x$ thickness/concentration parameters: *i*) a thickness of $Bi_{1-x}Sb_x$ of 5 nm with Sb concentrations ranging from 7%, 15% and 21%, *ii*) a thickness dependence from 2.5 nm, 5 nm and 15 nm for a Sb concentration of 15% and *iii*) an energy dependence at $\varepsilon - \varepsilon_F$ about 0 eV, -0.3 eV and -0.7 eV (from the Fermi level) for $Bi_{0.79}Sb_{0.21}$(5nm). We then extract the value of the inverse Rashba-Edelstein tensor κ_{xy} in energy for $Bi_{1-x}Sb_x$ as a function of the concentration and thickness.

Tight-binding calculations of the TSS. To date, theoretical predictions of the topological surface states bands of $Bi_{1-x}Sb_x$ requested some efforts from the scientific community to consider the lattice, electronic bandgap and electronic Dirac bands as a function of Sb concentration. It

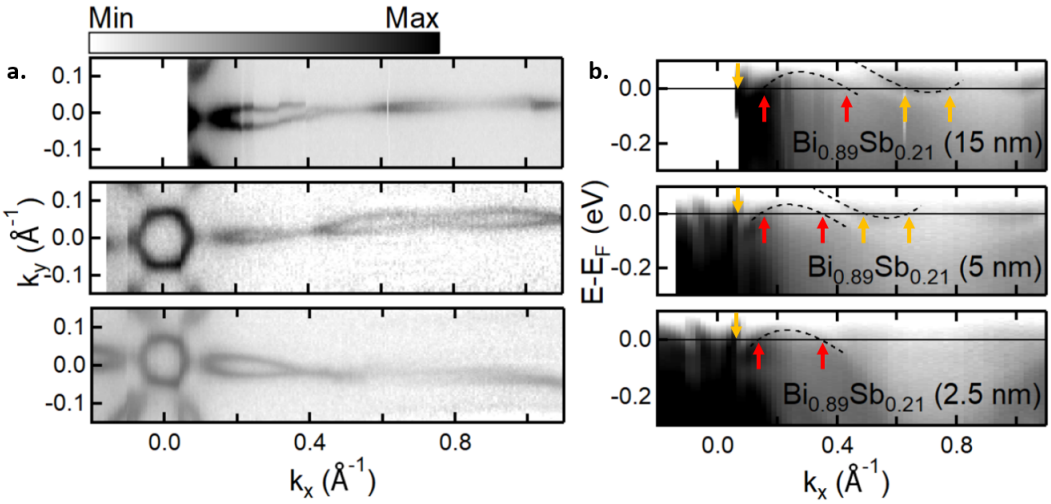

Figure 4.16: ARPES characterization of $Bi_{1-x}Sb_x$ along the $\Gamma\bar{M}$ direction. (a) Fermi surfaces from $Bi_{0.79}Sb_{0.21}$ with thickness 15 nm, 5 nm and 2.5 nm (from top to bottom). (b) Band dispersion of $Bi_{1-x}Sb_x$ with thickness 15 nm, 5 nm and 2.5 nm (from top to bottom). The red arrows correspond to the S_2 crossing points and the orange arrows correspond to the S_1 crossing points. Reproduced from Ref. [270].

started with the work of Liu and Allen [298] in 1995 who provided a bulk description of Bi and Sn separately. It was followed in 2008 by the first parametrization of the alloy by Teo *et al.* [301] in the bulk. The inclusion of the surface potential has been proposed first in 2016 by Saito *et al.* [302] who incorporated surface Rashba potential from the pure Bi case, with however an incomplete description of the conduction band. It was followed in the same year by a proposition of Ohtsubo and Kimura [303] who proposed three different sets of parametrization able to better describe the gap and the energy dispersion in the conduction band, however without including Rashba terms.

Our tight-binding (TB) approach follows the reasoning of Saito *et al.* [302] on pure Bi(111) bulk by extending it to the case of various alloy parameters where the surface-potential Rashba terms are tabulated more finely by help of experimental ARPES characterization. The tight-binding model has been implemented by H. Jaffrès, and we participated together in the interpretations of the model results. The total system Hamiltonian in the spin-polarized sp^3 basis can be decomposed as:

$$\mathcal{H}_{\text{tot}} = \mathcal{H}_0 + \mathcal{H}_{\text{SO}} + \mathcal{H}_{\text{SR}} \tag{E4.8}$$

where $\mathcal{H}_{\text{SO}} = (\hbar/4m^2c^2)((\nabla\mathcal{V} \times \hat{\mathbf{p}}) \cdot \hat{\sigma})$ is the core $6p$ spin-orbit interaction Hamiltonian and $\mathcal{H}_{\text{SR}}$ is the additional Rashba surface-potential terms described afterwards. Compared to Saito *et al.* [302] tight-binding calculations on pure Bi(111), it is necessary to adopt a different parametrization of the hopping terms for the alloy $Bi_{1-x}Sb_x$, by performing a mean-field treatment via the virtual crystal approximation [301]:

$$V_{\text{C}}^{\text{BiSb}} = x\, V_{\text{C}}^{\text{Sb}} + (1 - x^2)\, V_{\text{C}}^{\text{Bi}} \tag{E4.9}$$

where x is the Sb content, V_{C}^{Sb} and V_{C}^{Bi} are the respective hopping parameters of Sb and Bi taken from Ref. [298]. This specific parametrization allows to recover the topological window as in the phase diagram *vs.* Sb content, like described in Ref. [300]. To include the interfacial Rashba effect of the top bilayer representing the surface (*i.e.* between this last BL and the vacuum), we have considered additional hopping terms like proposed with the help of two γ_{sp} and γ_{pp} parameters for sp^3 system Hamiltonian (hexagonal symmetry) [302, 304]. The initial proposal of introducing an additional (or effective) γ_{pp} parameter was done by Petersen and Hedegård [266] to describe the surface Rashba-split band of Au. This is represented in $Bi_{1-x}Sb_x$ by including extra hopping terms in the form:

$$\mathcal{H}_{i,j}^{\mathrm{SR}} = \begin{cases} \pm\gamma_{pp}\cos(\theta_{ij}), & (i,j) = (p_x,p_z) \text{ or } (p_z,p_x) \\ \pm\gamma_{pp}\sin(\theta_{ij}), & (i,j) = (p_y,p_z) \text{ or } (p_z,p_y) \\ \pm\gamma_{sp}, & (i,j) = (s,p_z) \text{ or } (p_z,s) \end{cases} \tag{E4.10}$$

where θ_{ij} represents the angle of the bond between the two neighbours that we consider in-plane, and γ_{sp} (γ_{pp}) accounts for the hopping terms between the s and p orbitals (respectively, p_x and p_y) as given in Table IV.2.

Sb concentration (x)	$x = 0$ [302]	$x = 0.07$ [270]	$x = 0.15$ [296]
γ_{sp} (eV)	0.45	0.3	0.3
γ_{pp} (eV)	-0.27	-0.4	-0.5

Table IV.2: Surface Rashba hopping terms γ_{sp} and γ_{pp} in the tight-binding calculations, respectively for pure Bi ($x = 0$) and $Bi_{1-x}Sb_x$ compound ($x = 0.07$ and $x = 0.15$).

Tight-binding spin-resolved texture of the TSS in $Bi_{0.93}Sb_{0.07}$(5nm). On Fig. 4.17a are represented the 3D first Brillouin zone of the rhombohedral structure of $Bi_{1-x}Sb_x$ compound as well as the projected 2D first Brillouin zone of the hexagonal stacking of a multilayer structure. We present in Fig. 4.17b the electronic dispersion of the TSS and bulk bands calculated for $Bi_{0.93}Sb_{0.07}$(5nm) (or 12 BLs) resulting from slab tight-binding calculations. By definition, we define k_x direction as the $\Gamma\bar{M}$ direction and k_y direction along $\Gamma\bar{K}$. We observe in Fig. 4.17b the resulting spin-resolved band dispersion of $Bi_{1-x}Sb_x$(5nm) calculated for a wavevector along the k_x ($\Gamma\bar{M}$) direction. The spin-polarization σ_y exactly projects along the normal k_y direction. The two surfaces states S_1 and S_2 have an opposite spin-polarization σ_y. We also note that the presence of spin-polarized states in the conduction band around $\varepsilon - \varepsilon_F = +0.85$ eV that are called resonant surface states [305, 306]. Fig. 4.17c reports the density of states with the presence of the electron pocket P_1 at the center of the Brillouin zone and the P_2 (hole) and P_3 (electron) pockets. The blue hexagon represents the edge of the Brillouin zone.

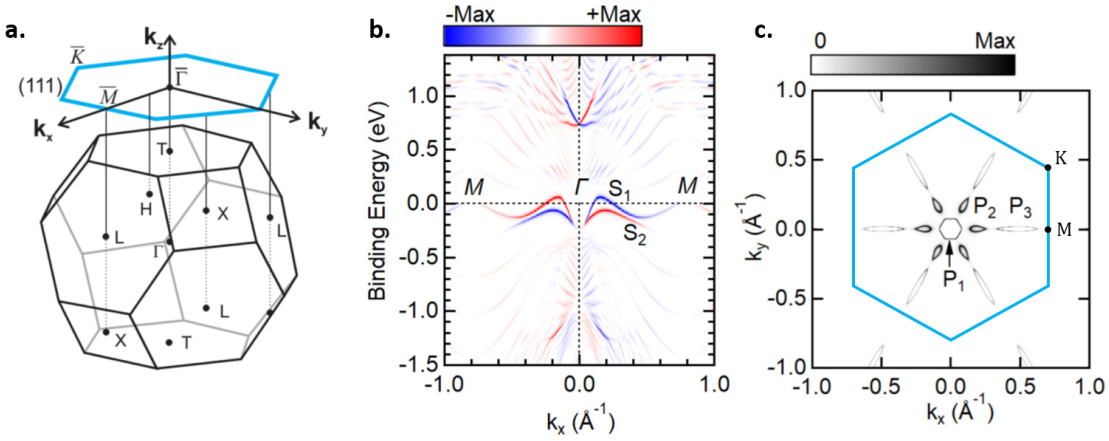

Figure 4.17: Calculated band structure of $Bi_{1-x}Sb_x$(5nm). (a) 3D first Brillouin zone and its 2D projection perpendicular to k_z along (111). (b) Calculated σ_y spin-polarized relation dispersion of $Bi_{1-x}Sb_x$ of thickness 5 nm (12 BL) for $x = 0.07$ along k_x in the $\Gamma\bar{M}$ direction. (c) Fermi surface presenting the central electron pocket P_1, the hole pocket P_2 and the electron pocket P_3 near $\bar{M}$. The blue hexagon presents the 2D Brillouin zone. Left and middle/right panels are respectively adapted from Refs. [299, 270].

Experimental spin-resolved texture of the TSS. We first present the spin-resolved ARPES (SR-ARPES) measurements and data performed at SOLEIL synchrotron at room temperature as shown in Fig. 4.18a. At the Fermi level, one observes that the six electron petals and the inner

hexagonal pocket are spin-polarized. In the case of the six electron petals, for positive k_x the σ_y polarization is positive while it is negative for negative k_x. In the inner pocket, we report the opposite spin-texture, presently a negative σ_y spin-texture for positive k_x and positive σ_y negative k_x. In parallel, we have realized tight-binding calculations of the TSS spin-polarization, which will be detailed in the next paragraph. Fig. 4.18b proposes the calculated spin-polarization of the TSS at the Fermi level (for temperature $T = 0$). We report a qualitative agreement between the measured and calculated spin-polarization with an identical projection of σ_y. We can also access the chirality of the spin-texture on the different hole and electron petals as defined by $C = \frac{1}{|\mathbf{k}|}(\mathbf{e}_z \times \mathbf{k}) \cdot \sigma$ imprinted on the experimental density of states as shown in Fig. 4.18c by black arrows. We confirm experimentally that the winding of the spin-texture is opposite between the central electron pocket P_1 and the hole petals P_2. In summary, the experimental spin-resolved density of states demonstrates the very good epitaxial growth of $Bi_{1-x}Sb_x$ with a projected spin-polarization σ_y compliant with the theoretical expectations, related to a well defined spin-momentum locking as addressed in the dedicated literature.

Resonant surface states.

Above the Fermi level ($\varepsilon - \varepsilon_F \simeq +0.85$ eV), the presence of spin-polarized states, called resonant surface states, has been theoretically predicted and experimentally studied [305, 306]. To probe those states normally inaccessible as they are empty at equilibrium, the method recently employed is to pump electrons into those states at the right energy and to perform time-resolved ARPES measurements (pump-probe) so that one is able to access to the dynamical relaxation of excited electrons from those resonant states.

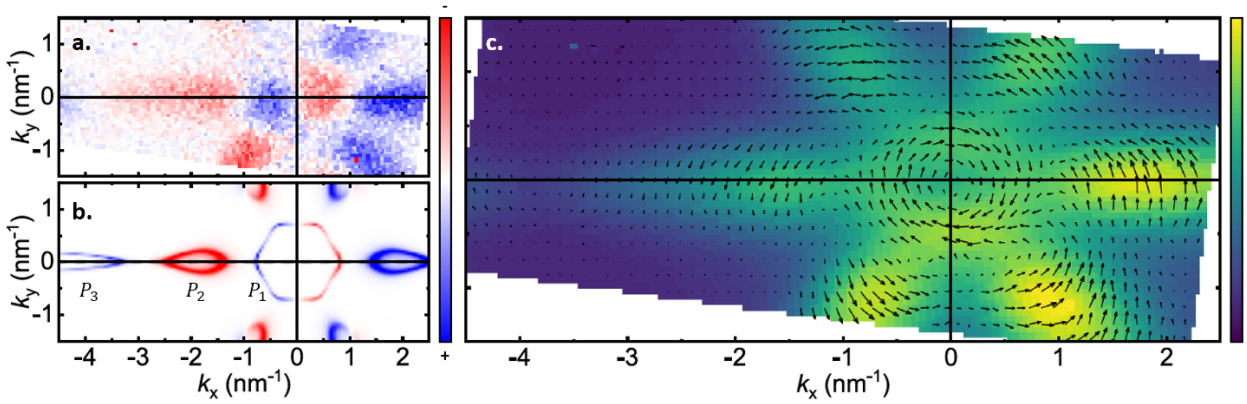

Figure 4.18: Spin-resolved density of states of $Bi_{0.85}Sb_{0.15}$(5nm) grown on Si(111). (a) Experimental spin-resolved ARPES presenting in red (blue) the negative (positive) spin-polarization σ_y. The experimental measurements, performed at room temperature, are in agreement with the (b) calculated spin-polarization σ_y via tight-binding treatment with a symmetry-axis along k_x and an anti-symmetric axis along k_y. (c) Experimental density of states (yellow) on which the spin-chirality is superposed (black arrows).

Density of states *vs.* the $Bi_{1-x}Sb_x$ thickness (Sb concentration of 15%). To address the evolution of the TSS as a function of the $Bi_{1-x}Sb_x$ thickness and the subsequent spin-charge conversion processes, we present in Fig. 4.19 the σ_y projected density of states from $Bi_{0.75}Sb_{0.15}$ with thicknesses ranging from 2.5 nm, 5 nm and 15 nm. As the Kramers theorem lifts the spin-degeneracy leading to the presence of two surface states S_1 and S_2 near the Γ and $\bar{M}$ TRIMs (only), the spin-texture at the surface respects $\sigma = \mathbf{k} \times \mathbf{e}_z$. In the $k_x = \Gamma\bar{M}$ direction, the spin-texture is exactly polarized along $\pm\sigma_y$. As we reduce the thickness of the $Bi_{1-x}Sb_x$ slab, we observe that the surface states are still present with no major changes near the Γ point. We also note that the number of bands in the bulk conduction and valence is reduced with the thickness

due to the confinement effects as the separation in energy increases.

To understand the presence of the TSS for a 5 nm thin $Bi_{1-x}Sb_x$ layer, we have to think about the decay length of the TSS. According to Ishida *et al.* [283] (reproduced in Fig. 4.4), the evanescent length remains small in Bi: near the Γ point, it is known to be very short, about <2 BL (about <1 nm) while it does not vary much between Γ and up to 0.65 $Å^{-1}$ of $\Gamma\bar{M}$ direction towards the $\bar{M}$ point (decay length about <5 BL (<2.5 nm)). At the exact $\bar{M}$ point, the evanescence can be very large, more than 24 BL (around 12 nm) and seems to diverge [283, 307]. This behaviour is mapped by the tight-binding calculations where we see that the TSS density profile near the $\bar{M}$ point varies much compared to the TSS near the Γ point. This evidences that the interfacial inverse Rashba-Edelstein effect would more likely occur on the Γ point due to a slight change of the topological surface states in this zone.

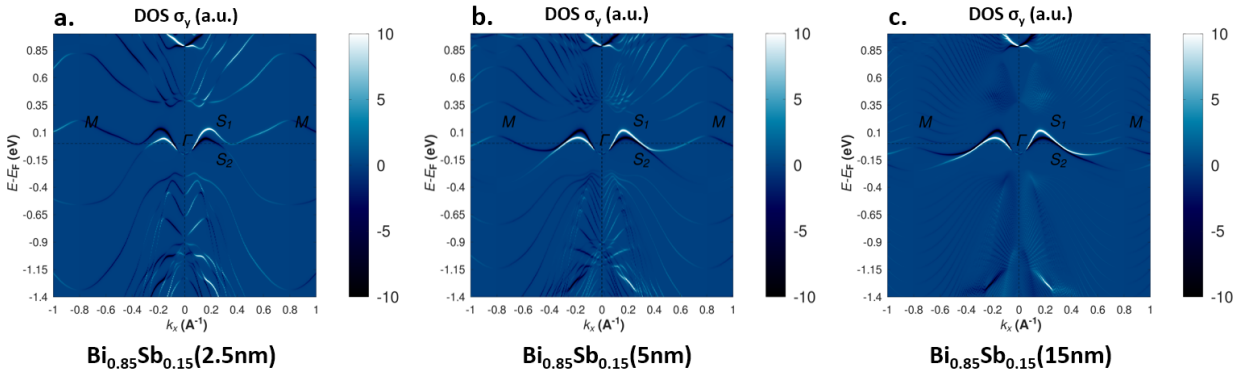

Figure 4.19: Evolution of the TSS of $Bi_{1-x}Sb_x$ as a function of the thickness. Spin-projected σ_y density of states (DOS) of $Bi_{0.85}Sb_{0.15}$ for (a) 2.5 nm, (b) 5 nm and (c) 15 nm, calculated by tight-binding.

Spin-resolved Fermi surface and chirality as a function of the energy. We focus now on the spin-polarized Fermi surface via tight-binding slab calculations on $Bi_{0.79}Sb_{0.21}$(5nm). Addressing this point is of crucial importance as the hot electron transport is distributed in energy due to optical pumping and subsequent relaxation processes. We present in Figs. 4.20, 4.21 and 4.22 the σ_x and σ_y spin-polarizations and the chirality C defined as $C = \frac{1}{|\mathbf{k}|}(\mathbf{e}_z \times \mathbf{k}) \cdot \sigma$, respectively *i*) at the Fermi level ($\varepsilon - \varepsilon_F = 0$ eV), *ii*) at $\varepsilon - \varepsilon_F = -0.3$ eV and *iii*) at $\varepsilon - \varepsilon_F = -0.7$ eV.

At the Fermi level, the P_1, P_2 and P_3 petals are recovered. Opposite k_y changes the sign for σ_x while k_x preserves the sign for σ_x. Reciprocally, k_y preserves the sign for σ_y and k_x changes the sign for σ_y. The chirality shows that the inner P_1 pocket is negatively polarized as well as the P_3 electron petal while the P_2 hole pocket is positively polarized.

We then consider the spin-polarization in the bulk valence bands, where depopulation of the carriers can happen by optically-induced pumping. First, at an energy cut at $\varepsilon - \varepsilon_F$=-0.3 eV, we observe a strong spin-polarization of the bands, possibly participating to the (interfacial) spin-charge conversion. However, we note that in the $\Gamma\bar{M}$ direction, the bands are poorly spin-polarized close to the Γ point. The resulting effect would thus be negligible. At last, we focus on an energy cut at lower energy $\varepsilon - \varepsilon_F$=-0.7 eV. We see that the band structure is more complex owing to the multiple bulk bands crossing at this energy level, but is still spin-polarized. We note the presence of spin-textured states of large spin-polarization. In all cases of the contribution of the valence bands to the spin-charge conversion process, we observe *i*) a pretty large spin-polarization of *ii*) spin-textured states. Besides, summing all the contributions of positive and negative chirality C (from the core to the edge of the Brillouin zone) would lead to an overall very weak contribution to the (interfacial) spin-charge conversion. This hypothesis

is also reinforced by the fact that depopulating the band down to $\varepsilon - \varepsilon_F$=-0.7 eV would be very small. We will see further below (Fig. 4.25) that the bulk valence bands contribute slightly to the interfacial conversion via the expression of the inverse Rashba-Edelstein tensor κ_{xy}, where it will appear clear that the spin-charge conversion is exacerbated only on the two surface states S_1 and S_2.

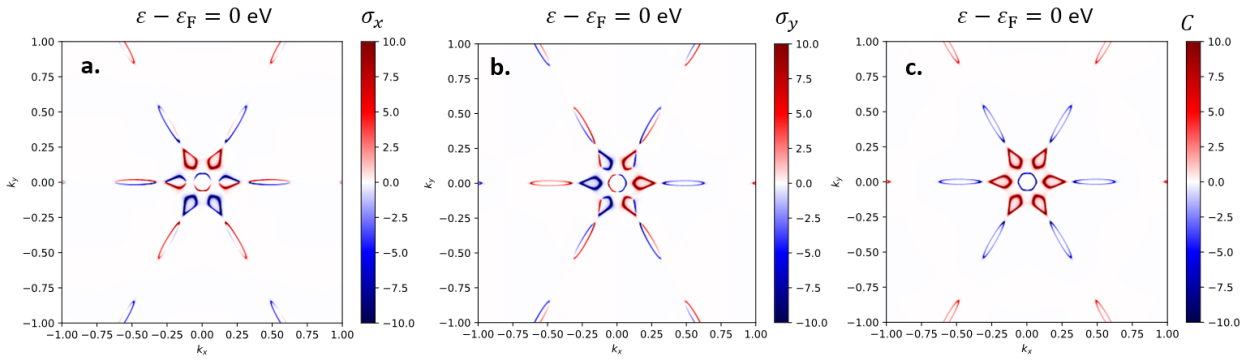

Figure 4.20: Spin-polarized Fermi surface at the Fermi level. (a) σ_x, (b) σ_y spin-polarization and (c) spin chirality C at $\varepsilon - \varepsilon_F = 0$ eV, for $Bi_{0.79}Sb_{0.21}$(5nm).

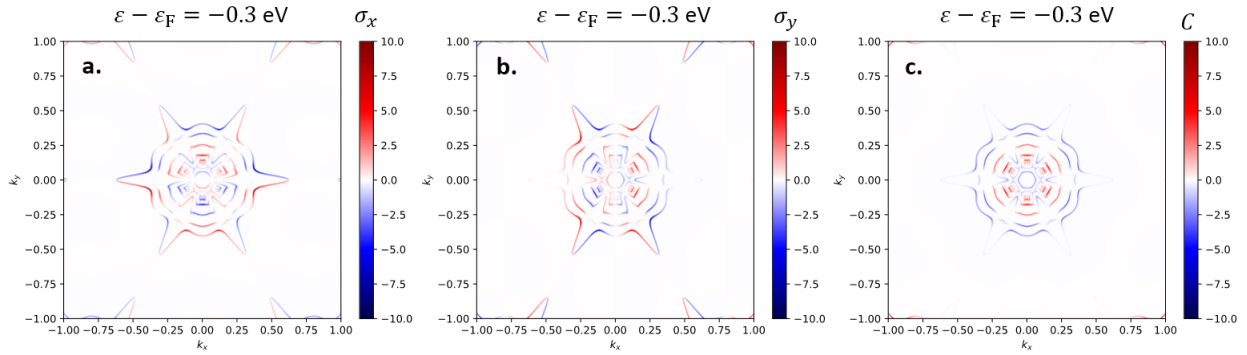

Figure 4.21: Spin-polarized energy cut in the bulk valence bands. (a) σ_x, (b) σ_y spin-polarization and (c) spin chirality C at $\varepsilon - \varepsilon_F = -0.3$ eV, for $Bi_{0.79}Sb_{0.21}$(5nm).

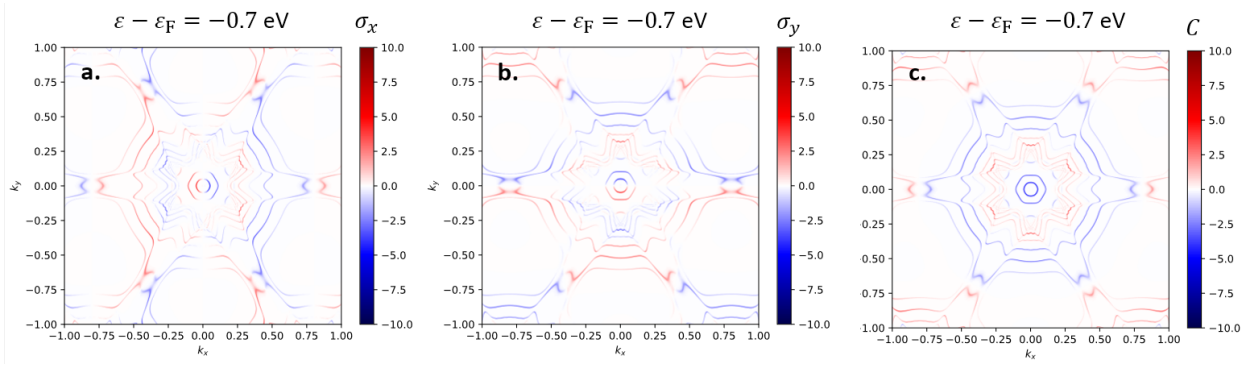

Figure 4.22: Spin-polarized energy cut in the bulk valence bands. (a) σ_x, (b) σ_y spin-polarization and (c) spin chirality C at $\varepsilon - \varepsilon_F = -0.7$ eV, for $Bi_{0.79}Sb_{0.21}$(5nm).

Inverse Rashba-Edelstein tensor. To address the interfacial spin-charge conversion mediated by IREE, we calculate the inverse Rashba-Edelstein tensor κ_{xy} as derived from the linear response

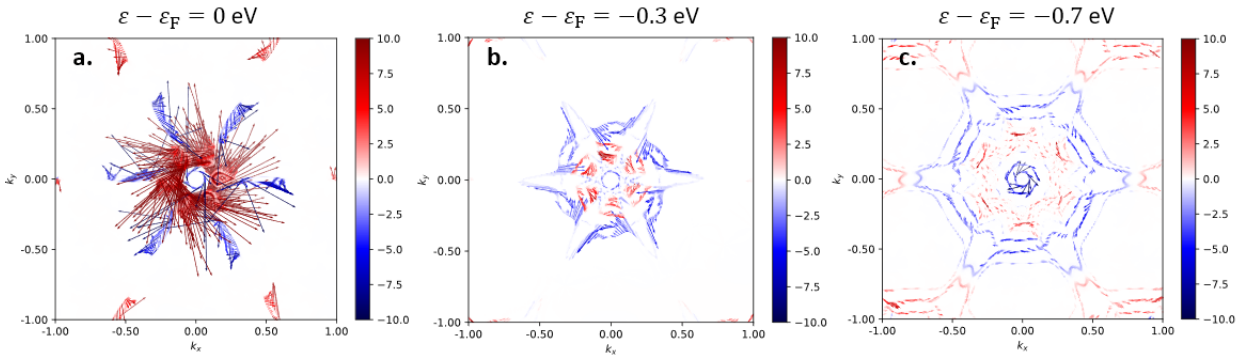

Figure 4.23: Directional chirality and spin-texture Chirality (color) and warping of the spin-texture (arrows) for the following energy cuts: (a) $\varepsilon - \varepsilon_F = 0$ eV, (b) $\varepsilon - \varepsilon_F = -0.3$ eV and (c) $\varepsilon - \varepsilon_F = -0.7$ eV, for $Bi_{0.79}Sb_{0.21}$(5nm).

theory (Annex A2), *vs.* the energy with respect to the Fermi level $\varepsilon - \varepsilon_F$. First, we report in Fig. 4.24a the calculated density of states per atom as a function of the energy for $Bi_{0.79}Sb_{0.21}$(5nm) integrated over the whole thickness. We clearly identify the bulk valence band (BVB) and the bulk conduction band (BCB) separated by a gap of about 0.3 eV, with the Fermi level pinned in the gap. We focus in Fig. 4.24b in the gap region where we notice the presence of a non-zero density of states at the Fermi level and at 0.08 eV above the Fermi level, which respectively corresponds to the TSS density of states for S_1 and S_2. We represent in Fig. 4.24c the separated contribution for each BL (of the full 12 BL-thick (5 nm) structure) where we observe that the maximal amplitude of the S_1 and S_2 TSS density are the largest for the first and twelfth (last) BL, respectively identifying the bottom and top interface.

The calculated density of states of $Bi_{1-x}Sb_x$ has to be compared to the calculations of the spin-charge conversion process by the linear response theory (Annex A2). We present in Fig. 4.25c the results of the inverse Rashba-Edelstein tensor κ_{xy} expressed in units of the spin Hall conductivity. We have recalled in panels of Fig. 4.25a-b the DOS and especially focus on the bandgap region. The calculations of the inverse Rashba-Edelstein tensor has been carried by considering *i*) a typical mean-free path $\lambda \simeq 10$ nm (which is also the in-plane spin relaxation length) along the surface corresponding to a mean elastic lifetime of about $\tau_{sf} \simeq 30$ fs. We also considered *ii*) the sum of the contributions of each $Bi_{1-x}Sb_x$ layers, from the top surface to the middle of the slab, where the top TSS are assumed to be largely evanescent (typically 3 BLs corresponding to about 0.6 nm). We thus neglect the contribution from the bottom interface of the $Bi_{1-x}Sb_x$ slab with however no direct contact with the 2 nm-thick Co spin-injector. A direct equivalence between the IREE tensor κ_{xy} and the IREE length λ_{IEE} is proposed in Annex A8.

From the linear Kubo response (Annex A2), we observe in Fig. 4.25c that the amplitude of the inverse Rashba-Edelstein tensor scales with the spin Hall conductivity of Pt σ_{SHE}^{Pt}, with values around 2500 $\Omega^{-1}.cm^{-1}$ and 1000 $\Omega^{-1}.cm^{-1}$, respectively by neglecting and considering the spin-memory loss (in Co/Pt) [44]. The κ_{xy} response is shown to be *i*) positive and quite strong in the valence band for the electronic energy below the Fermi level by about 1 eV and *ii*) negative in the conduction band above the bandgap for electron energy in the range of a fraction of the eV. We focus on the energy region near the bandgap in Fig. 4.25d to identify the role of the TSS density of states in the conversion. We see that κ_{xy} is non-zero and we focus on $Bi_{0.79}Sb_{0.21}$ for three different thicknesses of 2.5 nm, 5 nm and 15 nm. The IREE conversion profile is composed of a tripolar shape with a Fermi level crossing the first positive lobe in the present calculations. We observe a similar shape of the tensor *vs.* the energy for all thicknesses with a certain amplitude increase in the low-thickness limit. We observe in particular that for the TSS S_1 and S_2 presenting a weak contribution to the local density of states, the inverse Rashba-Edelstein tensor response is

the largest at the energies matching the TSS presence. It thus traduces a large spin-momentum locking on the TSS. When we renormalize the value of the tensor with the $Bi_{1-x}Sb_x$ thickness as shown in Fig. 4.25f, we observe that the renormalized conversion profile is almost independent of the thickness. One may thus conclude on a pure interfacial contribution to the IREE via the TSS, which scales almost with the spin Hall conductivity of Pt of typical spin-diffusion length of 2.5 to 3 nm.

Reciprocally to check that the interconversion occurs on the TSS at the surface of $Bi_{1-x}Sb_x$, we report in Fig. 4.25e the tensor contribution as a function of the BL index of the whole $Bi_{1-x}Sb_x$ structure. In particular, we observe that the contribution from the top and bottom BL are *i*) identical in absolute amplitude but *ii*) opposed to each other in sign due to the opposite spin-texture of the two top and bottom TSS. We have chosen $Bi_{1-x}Sb_x$ topological insulator in which we predict near the Fermi level a strong contribution from the inverse Rashba-Edelstein tensor (from energies varying from -0.2 to 0.4 eV). Although we know quite well the surface Rashba potentials for the top $Bi_{1-x}Sb_x$ surface by SARPES measurements, it is however difficult to probe the bottom interface in contact with the substrate, thus the surface potentials in this region remain unknown. We have deliberately chosen in previous calculations sign-opposed Rashba surface potentials between the two top and bottom surfaces.

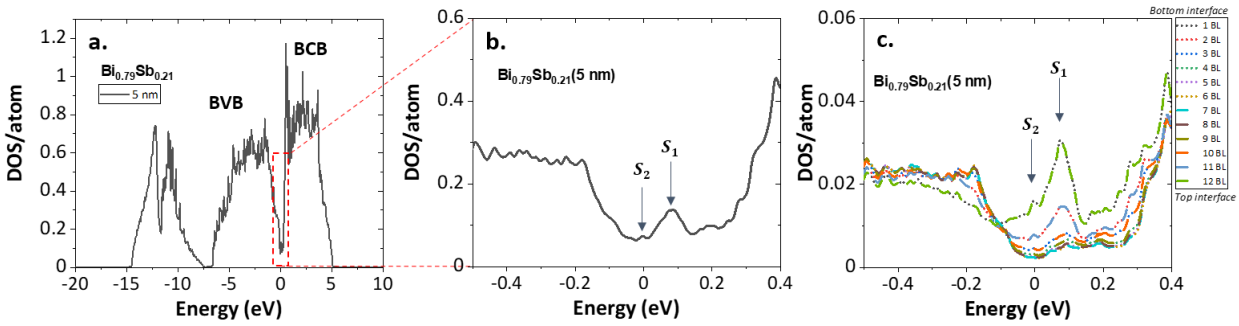

Figure 4.24: Calculated density of states of $Bi_{0.79}Sb_{0.21}$(5nm) as a function of the energy. (a) Density of states integrated on the full $Bi_{1-x}Sb_x$ thickness, including the bulk valence band (BVB) and bulk conduction band (BCB). (b) Density of states centered around the electronic gap where the contribution from the two TSS S_1 and S_2 is noticeable. (c) Evolution of the BL contribution to the density of states from the first to the twelfth BL.

Alternatively, we have plotted in Fig. 4.26 the inverse Rashba-Edelstein tensor of $Bi_{1-x}Sb_x$(5nm) as a function of the Sb concentration, ranging from 21%, 30% and 40%. Two elements can be noticed: first, we see that the tensor amplitude increases with the concentration. Secondly, we see that the tensor profile shifts towards higher energies with the Sb concentration. This result is surprising as we expect the loss of the topological character of the surface states for 40% of Sb. Therefore, this tensor seems to indicate that the topological character of the surface states (*i.e.* $Bi_{1-x}Sb_x$ trivial phase) might not be essentially needed to generate a strong interfacial conversion, that can be mediated by spin-textured hybridized Rashba-like surface states.

As a summary to both theoretical and experimental spin-polarization of $Bi_{1-x}Sb_x$ compound, we report a strong spin-polarization compatible with a inverse Rashba-Edelstein spin-charge conversion mechanism. However, it is important to note that the ferromagnetic contact with Co induces a lot of questions (Fermi level shift, conservation of the topological surface states, *etc.*) and those interrogations are difficult to be addressed in ARPES (surface-sensitive extraction) and also in tight-binding calculations due to the interface region. We thus propose THz emission spectroscopy as a very valuable probing technique to study the dynamical spin-charge conversion at spintronic interfaces, and in particular, with promising $Bi_{1-x}Sb_x$ system.

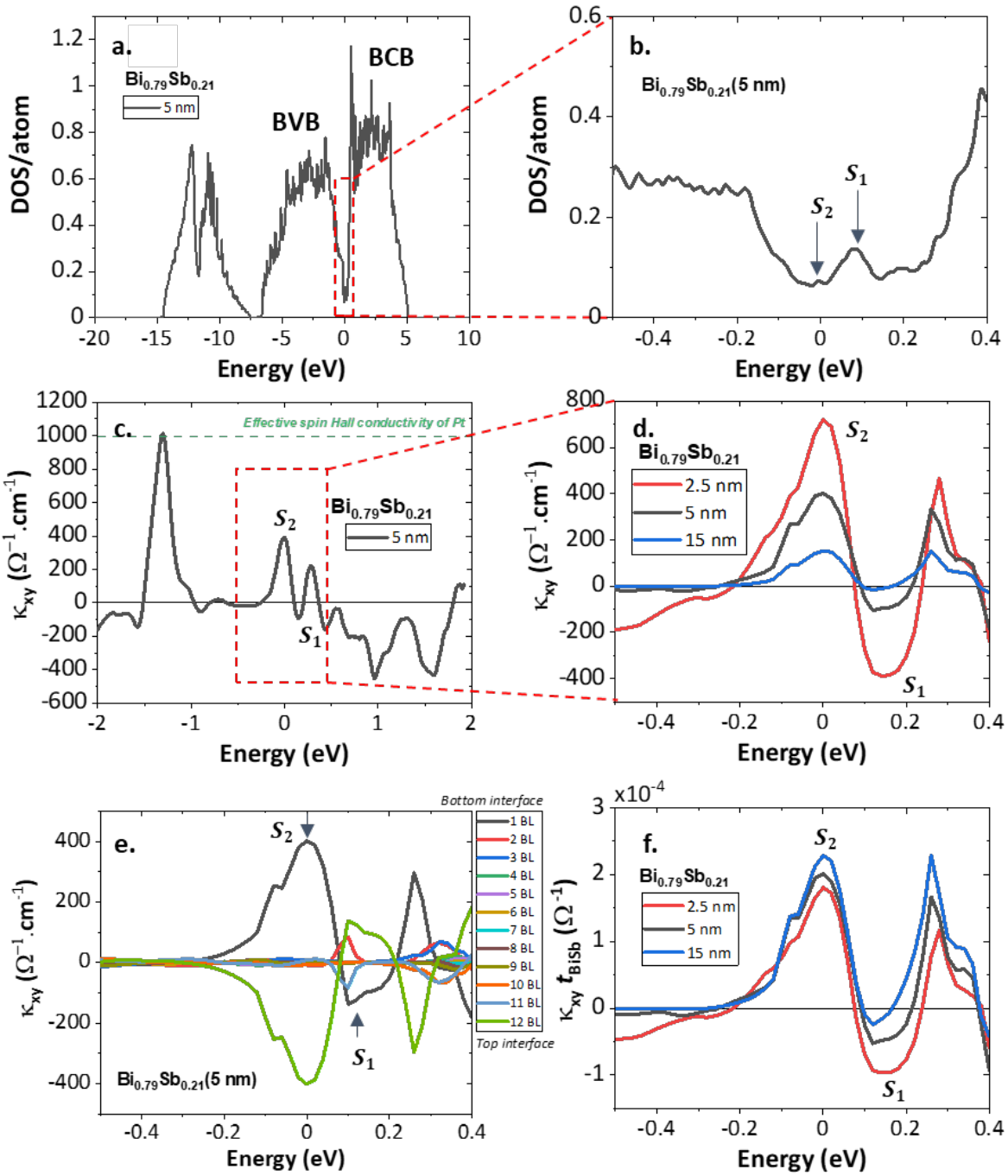

Figure 4.25: Calculated inverse Rashba-Edelstein tensor κ_{xy} of $Bi_{0.79}Sb_{0.21}$ as a function of the energy. (a) Density of states integrated on the full $Bi_{1-x}Sb_x$ thickness, including the bulk valence band (BVB) and bulk conduction band (BCB). (b) Density of states centered around the electronic gap where the contribution from the two TSS S_1 and S_2 is noticeable. (c) Conversion profile *vs.* the energy, integrated on $Bi_{1-x}Sb_x$(5nm) full thickness and given in the units of the spin Hall conductivity for comparison with the effective spin Hall conductivity of Pt (green dotted line). (d) Focus on the gap region where the Fermi level is pinned. The conversion is presented as a function of the $Bi_{1-x}Sb_x$ thickness, respectively 2.5 nm, 5 nm and 15 nm. (e) Separated contribution of the BL in the conversion tensor, from the first to the twelfth BL. (f) Inverse Rashba-Edelstein tensor renormalized with the $Bi_{1-x}Sb_x$ thickness demonstrating an interfacial-type of the conversion. In details, we considered a mean free path $\lambda \simeq 10$ nm and a mean elastic lifetime $\tau_\sigma \simeq 30$ fs.

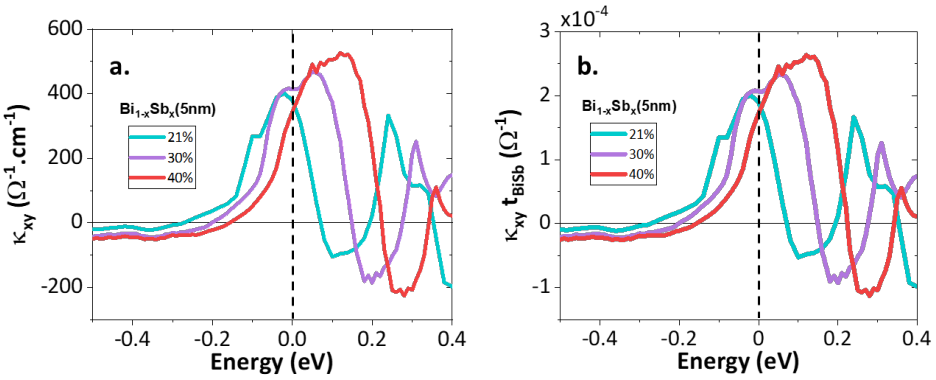

Figure 4.26: Evolution of the inverse Rashba-Edelstein tensor κ_{xy} as a function of the Sb concentration. (a) Energy profile of κ_{xy} for different Sb concentrations ranging from 21%, 30% and 40%. (b) Renormalized energy profile of κ_{xy} considering the $Bi_{1-x}Sb_x$(5nm) thickness for the same Sb concentration range.

3.4 THz interfacial spin-charge conversion in $Bi_{1-x}Sb_x$/Co: experiments.

To address the spin-injection and transient spin-charge conversion in embedded heterostructures, we performed THz emission spectroscopy on high-quality grown $Bi_{1-x}Sb_x$/Co samples. The study is separated in several measurements on different sample batches. Initial $Bi_{1-x}Sb_x$ is deposited on BaF_2, Si and SiHR but our study focuses on SiHR samples except stated otherwise. After the deposition of the ferromagnetic Co (ranging from 2 to 4 nm depending on the series, on top of $Bi_{1-x}Sb_x$), the sample is capped to prevent oxidation, either with a 3 nm-thick naturally oxidized AlO_x, or with a 4-6 nm-thick metallic Au (depending on the sample series). We will focus later on: *i*) a $Bi_{1-x}Sb_x$ concentration dependence (two series with $x = \{0.1, 0.21, 0.3, 0.4\}$ and *ii*) $x = \{0.07, 0.15, 0.30\}$), *iii*) a substrate dependence and *iv*) a capping dependence to show that those parameters do not influence the THz spin-charge conversion processes, of major interest in this study. We will then be able to focus on *v*) a $Bi_{1-x}Sb_x$ thickness dependence and *vi*) angular measurements as a function of the applied magnetic field $B(\theta)$ and the crystalline orientation of the sample ϕ to address the spin-charge conversion origin in those TI/FM bilayers.

First, we present in Fig. 4.27 the THz emission features from $Bi_{1-x}Sb_x$/Co bilayers derived from the THz emission spectroscopy setup presented in Section III.2.1. We report a THz signal which is larger in amplitude compared to Co/Pt, of about +50% (x2.25 in power) for thin 5 nm $Bi_{1-x}Sb_x$. By switching the applied magnetic field direction, we clearly observe a reversal of the THz phase which is a criterion fulfilled to assign spin-charge conversion mechanism as the major THz emission mechanism. Similarly to the investigation of $SnBi_2Te_4$, we observe that for the same polarity of the magnetic field, the THz phase is opposed in $Bi_{1-x}Sb_x$/Co compared to Co/Pt owing to the different direction of the spin current escape. This demonstrates that the interconversion sign of $Bi_{1-x}Sb_x$ is positive as the one of the spin Hall angle of Pt. Notably, we report almost no non-magnetic (second-order optical) contributions in this $Bi_{1-x}Sb_x$ bilayer. The full magnetic field orientation $B(\theta)$ dependence is performed on the same sample and proposed in Fig. 4.27c. Along a full θ rotation, we observe a typical $\cos(\theta)$ emission pattern with a phase reversal for opposite magnetic field direction, an experimental proof in favor of spin-charge process in $Bi_{1-x}Sb_x$/Co bilayers. No sizeable asymmetry in the emission lobes are reported, contrary to the one observed in $SnBi_2Te_4$, which again is in favor of a very small non-magnetic contributions in the present bilayers [167].

Impact from the material growth: the choice of the substrate and non-magnetic capping. We have first investigated the role of different substrates chosen among from BaF_2, Si and SiHR

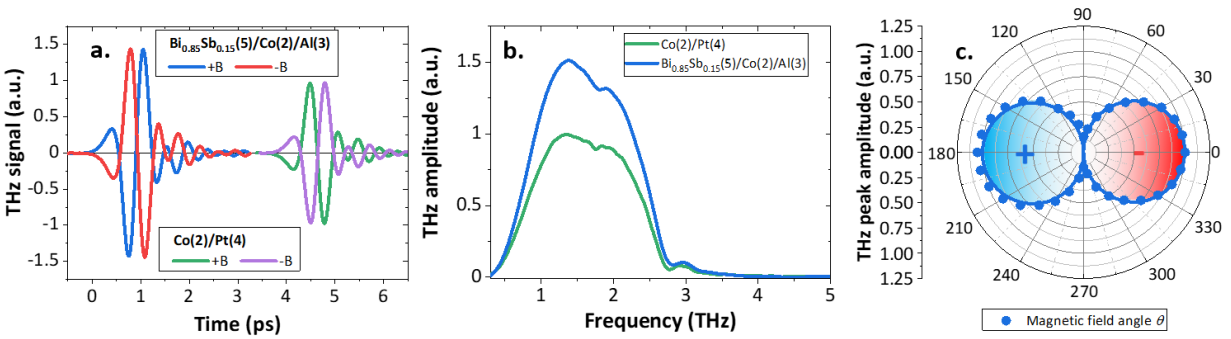

Figure 4.27: THz emission features of $Bi_{1-x}Sb_x$/Co. (a) THz radiation measured from $Bi_{1-x}Sb_x$(5nm)/Co(2nm)/AlO_x(3nm) on Si substrate compared to Co(2nm)/Pt(4nm) for two magnetic field configurations $\pm B$. (b) Measured THz bandwidth for $Bi_{1-x}Sb_x$ compared to Co(2nm)/Pt(4nm). (c) THz peak amplitude from $Bi_{1-x}Sb_x$(5 nm)/Co(2nm)/AlO_x(3nm) as a function of the magnetic field direction $\mathbf{B}(\theta)$. The $\pm$ signs stand for the THz phase reversal.

(also taken their growth advantages into account) like presented in Fig. 4.28. Interestingly, we notice a significant difference in the THz amplitudes on the three substrates for identical thin film deposition. This could arise mostly from: *i*) the THz refractive index which would have for effect to change the THz absorption in those multilayers or *ii*) a change of the topological insulator properties due to the variation of the strain induced by the substrate lattice mismatch with $Bi_{1-x}Sb_x$. Even if the THz amplitude is larger with BaF_2 substrate, it is a very brittle substrate which renders difficult the sample manipulation for the growth and characterization. Moreover, BaF_2 is responsible for charging effects upon ARPES experiments, and thus we decided not to select BaF_2 substrate for future characterizations. For optimal growth conditions and in order to limit the impact of potential THz non-linearities originating from the substrate, our study will mainly focus on $Bi_{1-x}Sb_x$ grown on SiHR substrates, very adapted to THz emission spectroscopy.

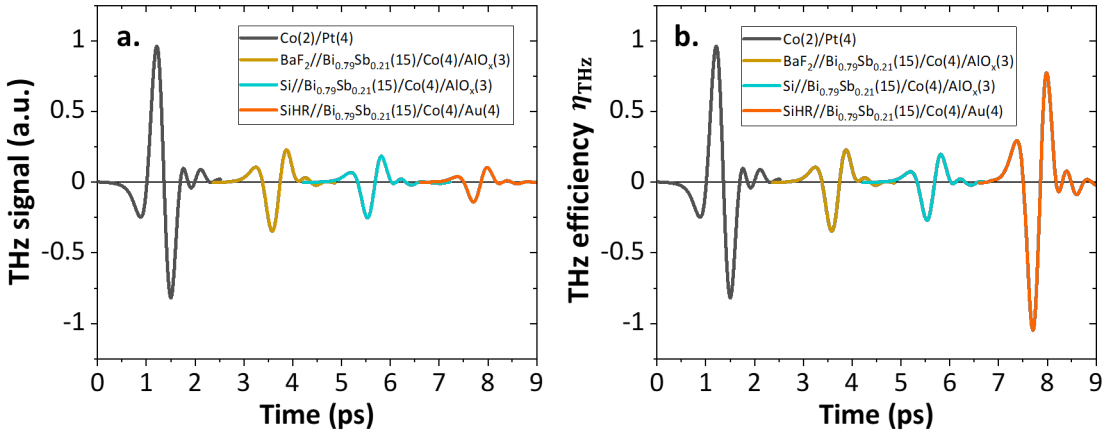

Figure 4.28: Impact of the substrate to the THz emission from $Bi_{1-x}Sb_x$/Co bilayers. (a) Measured THz emission and (b) extracted THz efficiency for $Bi_{0.79}Sb_{0.21}$(15nm)/Co(4nm)/Al(3nm) (or Au(4nm) in case of SiHR substrate, explaining the strong efficiency difference) on BaF_2, Si and SiHR, compared to Co(2nm)/Pt(4nm).

A second material issue is the nature of the capping layer. Due to the available capping sources depending on the different $Bi_{1-x}Sb_x$ growth runs, we report in Fig. 4.29 the reference measurements from the FM/NM (non-magnetic) capping, presently either Co/Al and Co/Au. In both cases, we measure a small THz signal with a characteristic reversal of the polarization

upon magnetic field direction reversal, indicating that the main origin of the THz signal is due to spin-injection and spin-charge conversion processes. The measured amplitude for Co/Al is about 10% in THz amplitude compared to Co/Pt ISHE (respectively about 5% in THz amplitude for Co/Au). The latter emission from Co/Au is smaller compared to Co/Al because of the increased THz absorption due to the increase of the Au conductivity. We attribute this small THz signal to the self-conversion or AHE in Co, owing to the large typical spin relaxation length for hot electrons (about several tens of nm) well larger than the film thickness. In the future studies, we neglect this contribution compared to the large spin-charge conversion originating from $Bi_{1-x}Sb_x$, typically more than one order of magnitude larger. To account for the effect of the non-magnetic metallic capping Au in THz absorption, we will subtract the absorption contribution from the time-trace of the THz emission (see procedure in Section III.2.2).

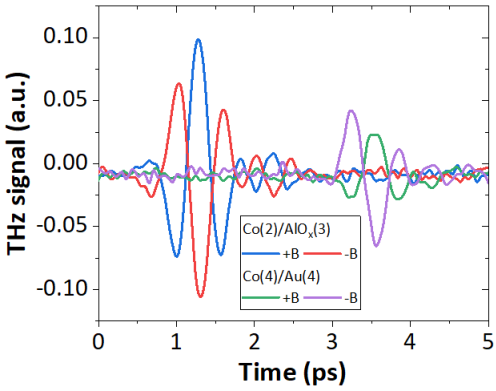

Figure 4.29: Impact of the non-magnetic capping. THz emission from Co/Al and Co/Au presented for the two magnetic field polarities $\pm\mathbf{B}$. The amplitudes are normalized with respect to Co/Pt.

Sb concentration dependence on the THz emission from $Bi_{1-x}Sb_x$ bilayers. We then proceed in the ultrafast response of $Bi_{1-x}Sb_x$/Co (upon 100 fs optical pulses) by tuning the $Bi_{1-x}Sb_x$ concentration for two different series: *i*) $x = \{0.1, 0.21, 0.3, 0.4\}$ with a thickness of 15 nm and *ii*) $x = \{0.07, 0.15, 0.30\}$ with a thickness of 5 nm. The results are respectively plotted in Figs. 4.30 and 4.31. Although several parameters are changed, such as the $Bi_{1-x}Sb_x$ thickness, the Co thickness or the metallic/insulating capping (changed from Au in the first series from naturally oxidized AlO_x in the second series), we observe in both series a sizeable signal as large as Co/Pt reference systems. The extracted THz efficiency demonstrates a robust spin-charge conversion efficiency in all materials. The THz efficiencies obtained in the Sb content region from 7% to 30% are very significant and start to decrease for concentration above. This is to put aside with the ARPES measurements as a function of the $Bi_{1-x}Sb_x$ concentration, addressing the presence of the TSS in this concentration range [270]. The smaller amplitude measured above 30%, presently at 40%, may be the demonstration of the reduction of the interconversion when the surface states change morphology.

Role of the $Bi_{1-x}Sb_x$/Co interface in the spin-related phenomena. Now that we have evidenced the role of the spin-charge conversion in the THz emission process and the negligible influence of the capping layer, we focus on the crucial role of the interface. To that goal, we have grown a sample where a metallic inset of Al(5nm) is inserted between Co and the $Bi_{1-x}Sb_x$ layer in order to decouple the TSS from the ferromagnetic contact induced exchange interactions. The THz measurements are presented in Fig. 4.32a. We observe that the THz signal from $Bi_{1-x}Sb_x$(15nm)/Al(5nm)/Co(4nm)/AlO_x(3nm) is strongly reduced compared to $Bi_{1-x}Sb_x$(15nm)/Co(4nm)/AlO_x(3nm), at the same level as the weak non-magnetic

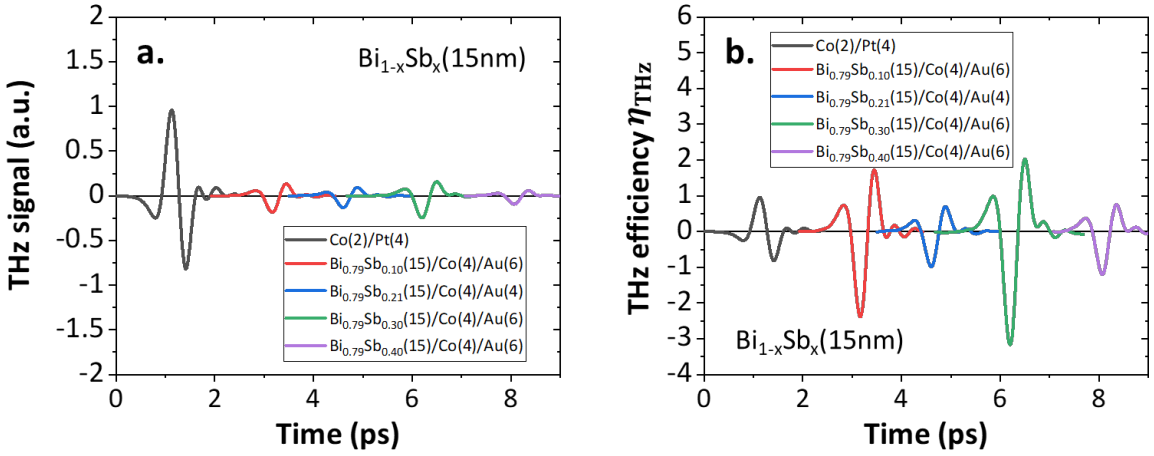

Figure 4.30: Dependence of the $Bi_{1-x}Sb_x$ concentration on the THz signal. (a) Measured THz emission and (b) extracted THz efficiency from $Bi_{1-x}Sb_x$(15nm)/Co(4nm)/Au(4-6nm) on SiHR, where the Sb concentration x ranges with $x = \{0.1, 0.21, 0.3, 0.4\}$.

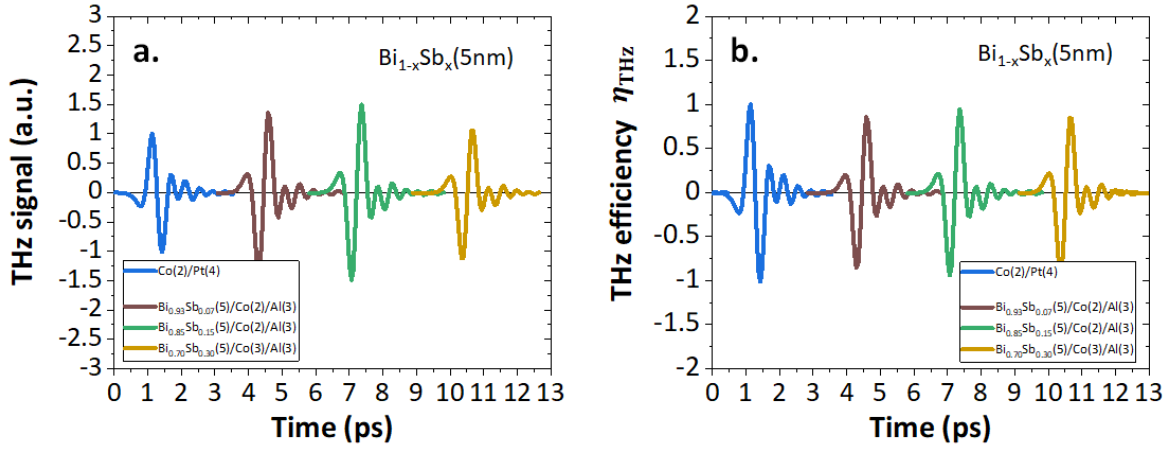

Figure 4.31: Dependence of the $Bi_{1-x}Sb_x$ concentration on the THz signal. (a) Measured THz emission and (b) extracted THz efficiency from $Bi_{1-x}Sb_x$(5nm)/Co(2-3nm)/AlO_x(3nm) on Si, where the Sb concentration x ranges with $x = \{0.07, 0.15, 0.3\}$.

contributions arising from $Bi_{1-x}Sb_x$(15nm)/AlO_x(3nm) that we will discuss in the next paragraph. The measured ratio is typically about 7-10% and the change of the THz impedance introduced by the Al(5nm) inset cannot account alone for this high reduction of the THz signal. To understand this effect, we proceed to transmission electron microscopy (TEM) and electron energy loss spectroscopy (EELS) characterization to study the spatial distribution of the atoms composing the multistack as displayed in Fig. 4.32b-c. We can observe that for the $Bi_{1-x}Sb_x$(15nm)/Co(4nm)/AlO_x(3nm) sample, the interface is very smooth and that there is no interdiffusion of atoms in the layers. We clearly observe that this is not the case in the $Bi_{1-x}Sb_x$(15nm)/Al(5nm)/Co(3nm)/AlO_x(3nm) sample where the inset of Al(5nm) strongly interdiffuses in the layer. This creates a very rough interface with interdiffusive chemical species that prevents the efficient spin injection from Co towards $Bi_{1-x}Sb_x$ and most likely destroys the topological surface states of $Bi_{1-x}Sb_x$.

Non-magnetic contributions in $Bi_{1-x}Sb_x$. As shown in Fig. 4.32a, we have grown a single layer of $Bi_{1-x}Sb_x$(15nm) without Co capped by AlO_x(3nm) to quantify the non-magnetic contri-

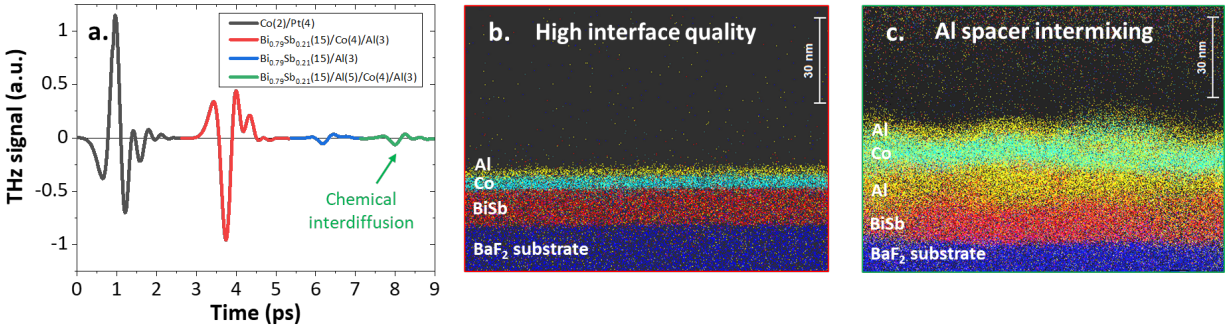

Figure 4.32: Addressing the role of the interface for THz efficiency. (a) THz emission from $Bi_{0.79}Sb_{0.21}$(15nm)/Co(4nm)/AlO_x(3nm), $Bi_{0.79}Sb_{0.21}$(15nm)/AlO_x(3nm) and $Bi_{0.79}Sb_{0.21}$(15nm)/Al(5nm)/Co(4nm)/AlO_x(3nm) on Si substrates, compared to Co(2)/Pt(4). (b-c) Transmission electron microscopy (TEM) images captured for (b) the sample $Bi_{0.79}Sb_{0.21}$(15nm)/Co(4nm)/AlO_x(3nm) and (c) the sample $Bi_{0.79}Sb_{0.21}$(15nm)/Al(5nm)/Co(4nm)/AlO_x(3nm).

butions in our bilayers composed of $Bi_{1-x}Sb_x$. We observe a reduced THz emission, about 5% of the signal derived from $Bi_{1-x}Sb_x$(15nm)/Co(4)/AlO_x(3nm). This result goes in the direction of weak non-magnetic (non-linear optical) effects in our epitaxially grown $Bi_{1-x}Sb_x$/Co samples. In particular, we can exclude the circular photogalvanic effect here as the pump polarization is kept linear.

This result is in contrast with the study of Park *et al.* [167] where the authors reported the presence of a non-magnetic contribution in $Bi_{1-x}Sb_x$/Co larger than in our films but still about one order of magnitude smaller than the magnetic contribution. The authors linked it to the occurrence of shift currents arising from $Bi_{1-x}Sb_x$ twin domains in their samples due to van der Waals-type interactions [167] and to a misorientation of the out-of-plane direction of $Bi_{1-x}Sb_x$. This discrepancy between the two studies reinforces the need of very high crystalline quality samples, especially for the interfacial spin-charge related considerations. In our study, ARPES and SARPES show a well defined crystalline structure with a six-fold petals structure (rotation by 60°) suggesting the presence of a single domain in our case, contrary to Park *et al.* [167]. Indeed, in the case of twin domain rotated by 30°, the petals would have presented a twelve-fold symmetry every 30° which is not the case in our study. Besides, the spot of the pump light for ARPES at the Cassiopée beamline is around 50 to 100 µm (similar to our pump excitation in THz measurements), addressing similar domain size probed in both experiments. This demonstrates the importance of the epitaxial growth performed at the Cassiopée beamline at SOLEIL synchrotron. We can thus exclude the shift current mechanism as the origin of any THz contribution in our bilayers and we relate this negligible non-magnetic signal to surge currents (potentially photo-Dember and surface-depletion field effects) present only due to a small misalignment of the sample with the normal direction. In the rest of the study, we thus neglect the very small non-magnetic contributions in the THz emission from our epitaxially-grown $Bi_{1-x}Sb_x$/Co samples.

Temperature dependence of the $Bi_{1-x}Sb_x$/Co THz emission. We investigate in Fig. 4.33 a temperature dependence of the THz emission from $Bi_{1-x}Sb_x$(15nm)/Co(4)/Au(4) from 4 K to room temperature. We observe a continuous decrease of the THz emission at lower temperature, with a maximum amplitude decrease about -14% at 4 K from 300 K. We assign this dependence to *i*) the change of conductivity of the metallic capping (Pt and Au) [308] and *ii*) to the decrease of the electrical resistance of Si/$Bi_{1-x}Sb_x$ [295], thus inducing a larger THz absorption. However, as the electrical resistivity of $Bi_{1-x}Sb_x$ is about one order of magnitude higher than metallic cappings (Co or Au), it cannot contribute too much to the THz absorption $\propto 1/Z(\omega)$ and the main contribution thus seems to occur from metallic cappings (Co and Au).

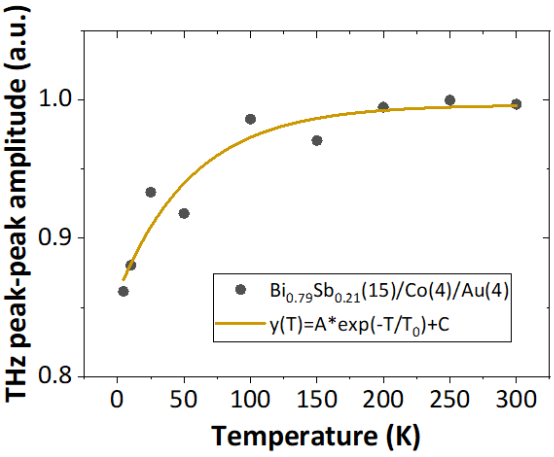

Figure 4.33: Temperature dependence of the THz emission from $Bi_{0.79}Sb_{0.21}$(15nm)/Co(4nm)/Au(4nm) from 4K to 300K.

3.5 Identifying the spin-charge conversion nature via THz angular mapping, thickness dependence and spin-current relaxation dynamics.

THz efficiency *vs.* the $Bi_{1-x}Sb_x$ thickness and spin-charge conversion angular mapping. As we have now identified spin-charge conversion mechanism as the major part of the THz emission and that the interface and topological surface states seem to play a major role, we now turn to the crystallographic angular (ϕ) dependence of the THz spin-charge interconversion of $Bi_{1-x}Sb_x$. For that, we have plotted the resulting THz efficiency profile *vs.* the crystalline orientation ϕ as shown in Fig. 4.34a (details in Annex A2). We observe an almost isotropic THz emission which demonstrates an isotropic spin-charge conversion. These measurements well support a spin-charge related emission mechanism. Besides, we also performed a $Bi_{0.79}Sb_{0.21}(t_{\mathrm{TI}})$ thickness dependence of the THz measurements where t_{TI} varies from 2.5 nm, 5 nm and 15 nm as presented in Fig. 4.34b. We recover a thickness-independent THz efficiency η_{THz}, of similar amplitude as Co(2)/Pt(4). This indicates the very efficient spin-charge conversion magnitude of $Bi_{1-x}Sb_x$, of the same order of magnitude than the spin Hall angle of Pt. The thickness-independent signal can be assigned to the linear response of the spin-charge conversion (inverse Rashba-Edelstein tensor derived in Annex A2) of $Bi_{1-x}Sb_x$ surface states thus linking the presence of interfacial-type conversion. Moreover, another demonstration in favor of a TSS-based THz emission is the constant level of signal for the thinnest $Bi_{1-x}Sb_x$ sample (2.5 nm), well smaller than the standard spin diffusion length (between 3 to 8 nm) which would have the following profile $\tanh(t_{\mathrm{NM}}/2l_{sf})$ *vs.* the converter thickness. This indicates a SCC occurring on surface states characterized by a very weak evanescence presently smaller than 1.2 nm (3 BL) close to the Γ point (up to 0.65 k_x with k_x along $\Gamma\bar{\mathrm{M}}$) like calculated by Ishida *et al.* [283] for Bi and by tight-binding calculations for $Bi_{1-x}Sb_x$. Indeed, for interfacially-mediated interconversion via the TSS, one would expect the following dependence $1-\exp\left(-t_{\mathrm{TI}}/t_{\mathrm{hyb}}\right)$ where t_{hyb} is the TSS evanescence thickness. A second thickness dependence on $Bi_{0.85}Sb_{0.15}(t_{\mathrm{TI}})$ has been performed as illustrated in Fig. 4.35. We observe that the obtained efficiency at 5 nm (respectively 50 nm) is about $\times 1.3$ compared to Co/Pt (respectively $\times 0.6$). The decrease of the THz efficiency in $Bi_{1-x}Sb_x$ at high thickness (50 nm) would be more likely related to a change of the spin-charge conversion, as the spin-injection properties depend mostly on the interface which would not change drastically from 5 to 50 nm thick $Bi_{1-x}Sb_x$ layers. Therefore, the spin-charge conversion is addressed to be less efficient in $Bi_{1-x}Sb_x$(5nm), possibly owing to a hampering from multiple bulk bands. On the contrary, the 5 nm-thick $Bi_{1-x}Sb_x$ efficiency is importantly reported to overcome the one of Co/Pt metallic spintronic THz reference by 50%, evidencing the use of topological insulators for high THz emission devices.

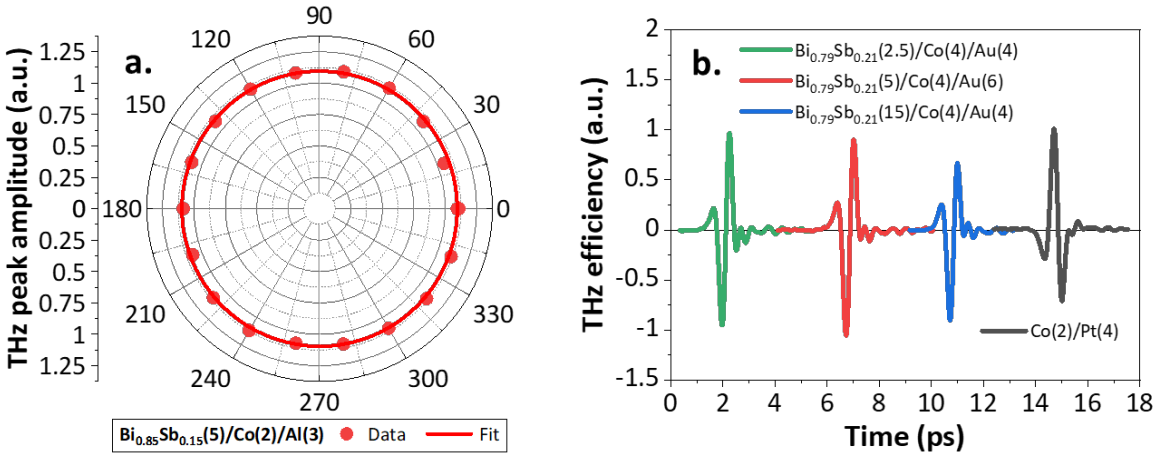

Figure 4.34: Addressing the interfacial spin-charge conversion in $Bi_{1-x}Sb_x$/Co. (a) THz angular conversion profile as a function of the crystalline orientation ϕ of a $Bi_{1-x}Sb_x$(5nm)/Co(2nm)/AlO_x(3nm) sample. (b) Thickness dependence of the THz efficiency η_{THz} for $Bi_{0.21}Sb_{0.79}(t_{TI})$/Co(3nm)/Au(4-6nm) samples with t_{TI} ranging from 2.5 nm, 5 nm and 15 nm, on SiHR substrates, compared to Co(2nm)/Pt(4nm).

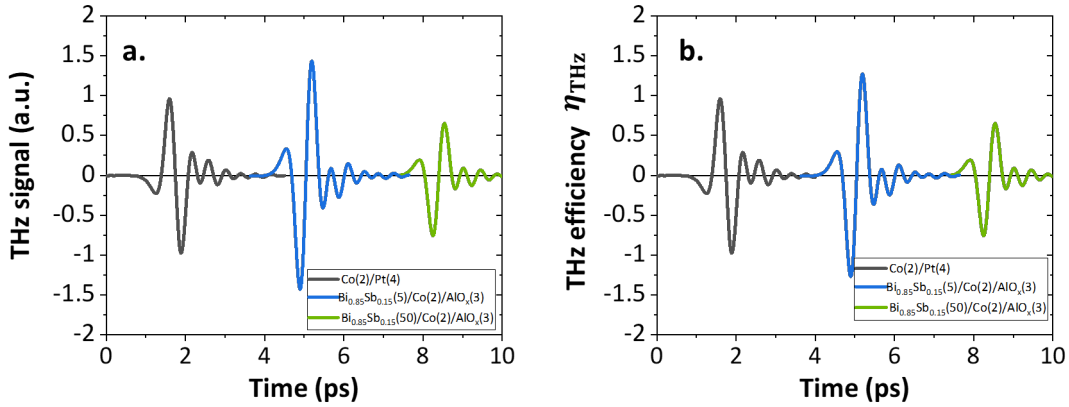

Figure 4.35: Thickness-dependence THz measurements of $Bi_{1-x}Sb_x$/Co. (a) THz emission and (b) THz efficiencies for $Bi_{0.85}Sb_{0.15}$ thickness of 5 and 50 nm on Si substrate, compared to Co/Pt.

Ultrafast spin-current extraction in $Bi_{1-x}Sb_x$/Co bilayers. *This part has been performed in collaboration with G. Bierhance, T. Kampfrath (FUB) during a visiting period at Berlin for the extraction of the ultrafast spin current dynamics in $Bi_{1-x}Sb_x$/Co [309].*

We now turn to the extraction of the THz spin-current from the measured THz radiation obtained while pumping with very short pulses (derived by a Ti:Sa oscillator of pulse duration of 10 fs, central wavelength of 800 nm, pulse energy of 1 nJ and a repetition rate of 80 MHz) by our collaborators at Freie University Berlin (T. Kampfrath's team). Pumping with such ultrashort pulses would lead to generate and detect high frequency THz dynamics (>5-10 THz) corresponding to a time-resolution about very few tens of fs on the extracted spin-current. Following the method in Section III.2.4 considering the transfer function of the electro-optic detection, we extracted the (normalized) spin-current dynamics $j_s(t)$ as a function of time from $Bi_{1-x}Sb_x$/Co bilayers compared to W/CoFeB/Pt and Co/Pt STE reference. We study the last $Bi_{1-x}Sb_x$(5nm) for 7%, 15% and 30% and the thicker $Bi_{1-x}Sb_x$(50nm) for 15% of Sb content. Typically, the observed quick current rise time are about <100 fs for all the samples, sharing the same slope which indicates the same ultrafast demagnetization origin. The spin current decay time is however manifold and can be fitted using:

$$j_s(t) = \Theta(t) \exp\left(-\frac{t}{\tau_{\text{int}}}\right) \tag{E4.11}$$

where $\Theta(t)$ is the Heaviside function and τ_{int} is the fitting relaxation time. From our experimental data (not shown here), we are able to extract longest relaxation time on the thicker sample whose dynamics is similar to the W/CoFeB/Pt reference. On the contrary, all the $Bi_{1-x}Sb_x$(5nm) samples are found to have dynamics similar to the Co/Pt reference sample. The observed relaxation times at the interface τ_{int} are about 50 fs in $Bi_{1-x}Sb_x$/Co samples, below the spin scattering time (about several hundreds of fs). Faure *et al.* [310] reported the inelastic electron scattering time (with loss of energy) in Bi as a function of the fluence, ranging from several hundreds of fs for low fluences to several tens of fs in the high fluence regime. In the regime of fluence used in THz spectroscopy using Ti:Sa oscillators, the accessible fluence is of the order of few hundreds of µJ.cm^{-2}, which put our study in the low fluence range. Besides, studies reported in TR-ARPES that the hot electrons generated in the FM layer quickly relax to 0.3 eV after 30 fs [58].

Therefore, one may assume the following picture: the generated hot electrons in Co quickly relax their energy from 1.5 eV to 0.3 eV within a timescale typically smaller than 30 fs [58], before even reaching the interface with $Bi_{1-x}Sb_x$. The hot spin-polarized electrons are therefore injected at 0.3 eV from the Fermi level (injection through the Schottky barrier) and before reaching the surface states at the interface to be efficiently converted. The reader is referred to Section III.1.3 for a detailed discussion of the generalized spin voltage model similar to this picture on metallic structures, and proposed by Rouzegar *et al.* [244] as well as typical electronic relaxation timescales [58].

3.6 Comparison with the literature and summary.

The strong competition in the community for the investigation of the ultrafast interfacial spin-charge conversion in topological insulators led to the publication of two major meantime studies [166, 167] on $Bi_{1-x}Sb_x$/Co. We discuss the conclusions raised in those two papers which are, for some elements, in contradiction with our study.

First, Sharma *et al.* [166] reported a spin Hall-like conversion scenario in amorphous FeGaB/$Bi_{0.85}Sb_{0.15}$. Via spin-pumping and THz emission spectroscopy measurements, they reported a spin Hall angle of $\theta_{\text{SHE}}^{\text{BiSb}} = 0.01$. Interestingly, even in presence of amorphous layers, they measured a spin-mixing conductance about $g_{\uparrow\downarrow}^{\text{BiSb}} \simeq 5 \times 10^{19}$ m^{-2} and they estimate the resistivity of their $Bi_{0.85}Sb_{0.15}$ about 10^3 µΩ.cm. In particular, the THz extracted effective current reported in Fig. 8 of Ref. [166] showed a typical increase and saturation up to the spin diffusion length estimated about $l_{sf}^{\text{BiSb}} \simeq 7.9$ nm, that would indicate a ISHE-like scenario. To explain such discrepancy with our current conclusion, we point out that the amorphous deposition in their case would possibly prevent *i*) the formation of the TSS, *ii*) a strong conversion via the interfacial effects and *iii*) strong spin-injection, owing to a loss of crystallinicity of the $Bi_{1-x}Sb_x$, whereas we have shown in our experiments that a smooth epitaxial interface is needed for a good spin-injection and potentially interfacial spin-conversion. Moreover, our thickness dependence of the THz efficiency is in contradiction with their results. We report high values of the THz efficiency even below their extracted spin diffusion length and especially at 2.5 nm. We thus could not exclude a part of the contribution originating from the spin Hall effect in the bulk of the material, with however additional major interfacial conversion in the low thickness regime owing to spin-textured surface states.

Secondly, Park *et al.* [167] very recently reported the coexistence of the surface states-enhanced conversion of higher amplitude than pure bulk mechanisms in epitaxial $Bi_{1-x}Sb_x$/Co films.

They reported a $Bi_{1-x}Sb_x$ thickness and concentration dependence and report respectively *i*) that the SCC needs to build up over very low minimal thickness about 7 nm, which is an element addressing the hybridization of the TSS below this point as presented before in Section IV.1.3. Secondly, *ii*) the THz emission increases across the topological phase transition *vs.* the Sb concentration.

This shows the strong interest of the community for this peculiar system, and in particular indicates that our results set the international state-of-the-art concerning the investigation of topological insulators/ferromagnet hybrid structures via THz spectroscopy. Moreover, it shows that the exact origin of the interconversion is highly debated in the community as our three studies are on some elements in contraction with one another. However, we all report the strong interest for high spin-charge conversion in $Bi_{1-x}Sb_x$ topological insulator.

Conclusions and perspectives for $Bi_{1-x}Sb_x$/Co interfacial spin-charge conversion.

We have reported the strong THz emission from $Bi_{1-x}Sb_x$/Co bilayers, of amplitude about the same order of magnitude (or larger) than Co/Pt reference emitter. Moreover, a thickness-dependent study and an isotropic conversion profile *vs.* the crystallographic angle reveal an interfacially-mediated conversion. The dependence of the signal as a function of the alloy concentration does not show any elements that could indicate the presence of topological surface state mediated conversion for concentrations beyond 40% of Sb. The concentrations studied are respectively 10, 21, 30 and 40% of Sb and we show that there is a specifically enhanced THz emission around 30% of Sb. This is in very good agreement with the tight-binding modelling. To address the origin of the interconversion, either via inverse spin Hall effect, interfacial conversion and/or inverse Rashba-Edelstein effect in $Bi_{1-x}Sb_x$/Co, we have performed spin-resolved ARPES which reveals a strong spin-momentum locking of the topological surface states at the Fermi level. A tight-binding model is in full agreement with the obtained results and allows us to predict a sizeable interfacial conversion. However in our study, we could not exclude spin Hall type conversion whereas the trends point towards the possibility of an interfacial conversion without the need of topological surface states. On this point, simple spin-textured Rashba-like surface states seem to be sufficient to generate such THz charge current via interfacial spin-charge conversion.

The next steps of studying the interconversion efficiency will be performed on $Bi_{1-x}Sb_x$ grown on MnGa synthetic ferromagnetic layer of perpendicular magnetic anisotropy and will be carried out by D. She in the framework of her thesis work.

4 Future prospects for interfacial interconversion.

Conclusions on topological insulator-based spintronic THz emitters. As a conclusion to this chapter, we have demonstrated the strong conversion from TI/FM bilayers leading to substantial THz radiation in free-space, higher than the metallic reference Co/Pt in the case of $Bi_{1-x}Sb_x$/Co. We compare the net THz amplitude from the studied systems with the metallic references in Fig. 4.36 and propose in Table IV.3 a comparison of the THz efficiency mapping the spin-injection and spin-charge conversion amplitude between those systems. The role of the interface is crucial in those systems, for both *i*) the high spin-mixing conductance (as reported in Fe/Bi/Bi_2Se_3 [311]) and *ii*) the strong interfacial interconversion. We have seen that the purely interfacially-mediated conversion in TI/FM bilayers is highly discussed in the scientific community. Presently in the systems, we have been able to study, $SnBi_2Te_4$/Co and $Bi_{1-x}Sb_x$/Co (and further Bi_2Se_3/WSe_2/Co in a complementary study), it is challenging to separate between the role of the topological surface states, the Rashba-like surface states and the bulk states to address the inverse Rashba-Edelstein effect in the interconversion process. It appears from our study that THz emission spectroscopy is an useful method to probe those problematic in complex multilayers and that, most likely, the topological character of the surface states might not be an essential ingredient for the conversion, as they could potentially be altered due to the ferromagnetic contact.

System	$Bi_{1-x}Sb_x$/Co [296]	$SnBi_2Te_4$/Co [271]	Bi_2Te_3/Co [271]	Bi_2Se_3/Co	Co/Pt [231]	W/CoFeB/Pt [257]
S_{THz}	1.5	0.2	$\simeq$ 0.1	$\simeq$ 0.2	1	3-4
α_{SCC}^{THz}	1.3	0.3	0.1	$\simeq$ 0.2	1	2

Table IV.3: Comparison of the THz emission (field amplitude) and THz efficiencies between topologically-based emitters and metallic spintronic THz emitters (normalized with respect to Co/Pt).

These works also evidence the negligible non-magnetic contributions in TIs, arising from the surge currents and shift currents. Our main focus were in this work to probe the spin-injection but interesting physics could be established by looking carefully to those contributions. As those effects are also influenced by the pump polarization, it would be a good point to study in the future in details via pump-polarization dependent measurements.

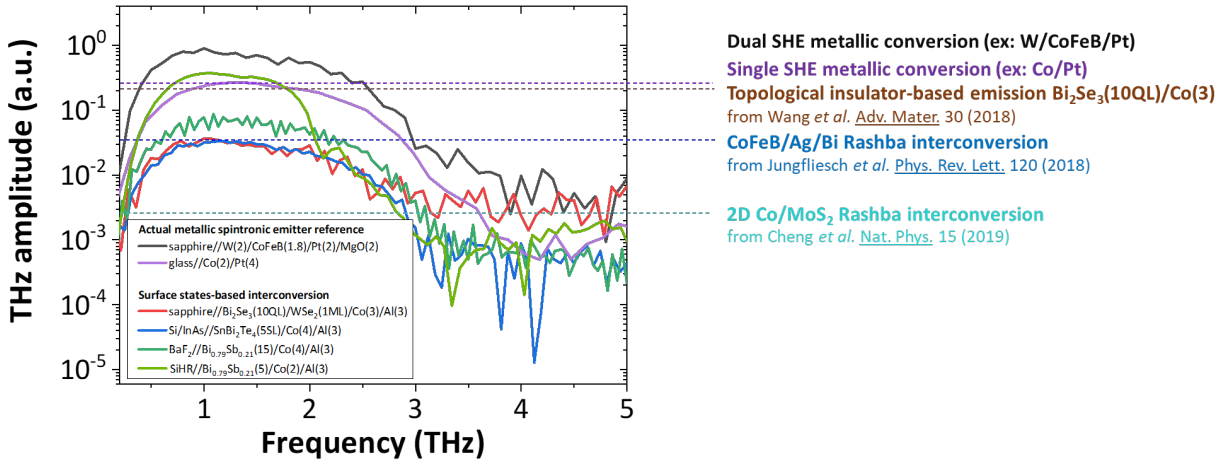

Figure 4.36: Comparison of the different topological insulators-based and 2D-based spintronic THz emitters studied in the frame of this thesis work. Emitted radiation presented in the spectral domain, from interfacially-mediated $Bi_{1-x}Sb_x$/Co, Bi_2Se_3/Co, Bi_2Te_3/Co and $SnBi_2Te_4$/Co compared to metallic spintronic THz emitters W/CoFeB/Pt and Co/Pt and sources developed in the literature.

4.1 Bi_2Se_3 and 2D transition metal dichalcogenide WSe_2 inset.

In this perspective study performed in collaboration with SPINTEC (M. Jamet, F. Bonell at CEA Grenoble, France for the structure growth), we propose the following structure TI/TDMC/FM with $Bi_2Se_3/WSe_2/Co$ where we envisioned in the first place the use of a semi-conducting transition metal dichalcogenide (TMDC) inset (presently WSe_2) to prevent the potential alteration of the TSS of Bi_2Se_3 by avoiding the direct contact between the FM reservoir and the TI. The second objective is to try to map an enhancement of the global SCC via a double interfacial SCC mechanism respectively *i*) in the 2D layer and *ii*) at the interface with the TI. Indeed, 2D materials have been recently studied for their high spin-orbit coupling at the interface, inducing a spin-splitting of free-electron like dispersion and thus enabling the feasibility of inverse Rashba-Edelstein effect spin-charge conversion [170]. An article on this work is currently under preparation [312].

4.1.1 Growth and material characterization.

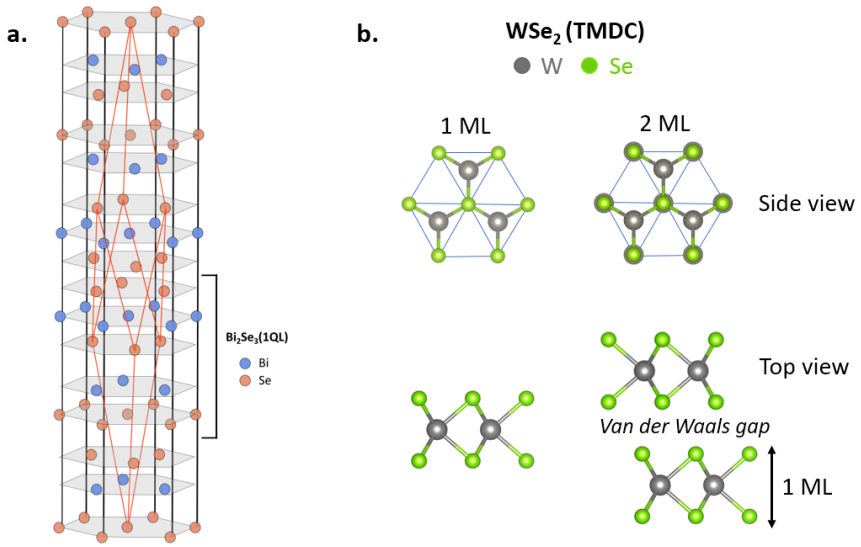

Figure 4.37: Separated crystallographic structure of Bi_2Se_3 and WSe_2. (a) Structure of Bi_2Se_3 topological insulator and of (b) WSe_2 transition metal dichalcogenide.

We present in Fig. 4.37 the crystalline structure of Bi_2Se_3 and WSe_2. As already mentioned previously, Bi_2Se_3 is a topological insulator known for presenting both topologically surfaces states mixed with the presence of bulk conduction bands at the Fermi level [281]. Bi_2Se_3 ($R\bar{3}m$) grows by forming quintuple layers (QL) formed by the rows Se-Bi-Se-Bi-Se with a thickness around 1 nm per QL [313, 314]. On the other hand, WSe_2 is a semiconducting TMDC known for its high non-linear susceptibility $\chi^{(2)}$ [174, 315]. As for many materials from the TMDC family, WSe_2 is expected to display a change in its electronic structure due to the direct to indirect bandgap transition as a function of the thickness [316] as represented in Fig. 4.38. For 1 ML, WSe_2 is reported to have a direct bandgap and should present an indirect bandgap for thickness above or equal to 2 ML. The electronic band structure of WSe_2 bulk crystal presents an indirect bandgap about 1.3 eV. Those changes in the electronic structure are thus expected to drive consequent variations in the optical response. WSe_2 monolayers (ML) are actually composed of three atomic layers, composed successively of rows of Se-W-Se, but we will employed in the rest of the study the notation widely used in the literature (ML). The monolayers stacking occurs via Van der Waals interactions between two neighbouring Se atom rows [316].

Growth of the $Bi_2Se_3/WSe_2/Co$ structure. The epitaxial growth is performed by molecular beam epitaxy (MBE), starting with the Bi_2Se_3 on sapphire substrate. It is continued with the

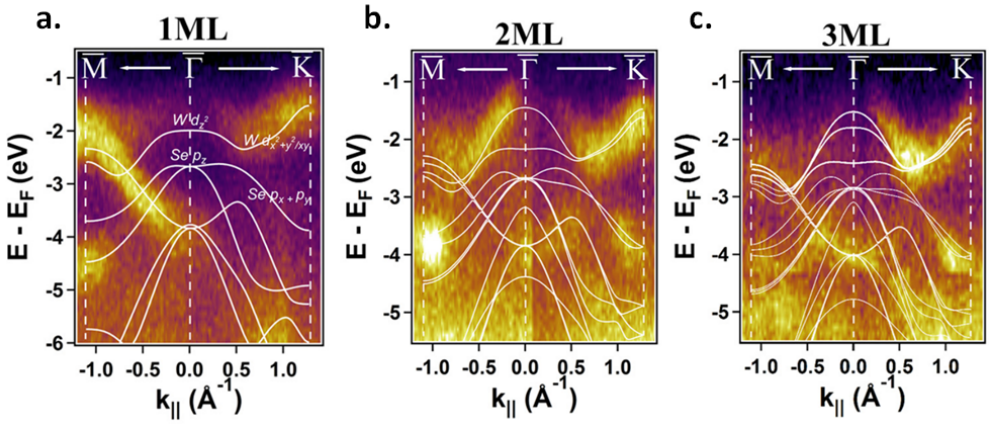

Figure 4.38: Evolution of the band structure of WSe_2 with the thickness. Measured band dispersion by ARPES on WSe_2 with thickness ranging from (a) 1 ML, (b) 2 ML and (c) 3 ML. Adapted from Ref. [316].

growth of WSe_2 then capped with the ferromagnetic injector Co(3nm). We have realized various multistacked samples where the WSe_2 is inserted between the topological insulator Bi_2Se_3 and the metallic ferromagnetic reservoir Co. The inset thickness t_{TMDC} ranges from 0 to 3 ML. The structure is capped with naturally oxidized AlO_x(3nm) to prevent the oxidation of Co. We will thus see the potential impact of the semiconducting spacer WSe_2 to *i*) prevent a possible loss of the topological surface states of Bi_2Se_3 due to the FM contact, and *ii*) to increase the interfacial spin-charge conversion due to the strong interfacial spin-orbit coupling, as a function of WSe_2 thickness.

However, one important point when building such TMDC/metallic contact is the potential hybridization of the 2D states at the interface leading to the transformation of the pure semiconducting state of the TMDC to a metallic behaviour. If we consider the simple case where the TMDC remains semiconducting, this opens a new interrogation about the efficient injection of spins in the TMDC through a Schottky barrier with a large gap semiconductor. This issue has been addressed by Sanchez *et al.* [317] where they report, *inter alia*, the injection of spin-polarized holes from a NiFe reservoir electrode to the valence band of WSe_2 in a spin-LED device. It has also been reported the possible transformation into a metallic behaviour with a ferromagnetic contact in the structure Ni(111)/WSe_2, theoretically studied by DFT calculations by reshaping the interface via a supercell [318].

Our present study is decomposed as follows: we will first focus on the THz response of Bi_2Se_3/Co bilayers before emphasizing on the respective non-magnetic contributions and magnetic contributions into trilayers of Bi_2Se_3/WSe_2/Co with the WSe_2 thickness ranging from 1 to 3 ML. Prior to our study, the number of layers of WSe_2 has been controlled using Raman spectroscopy (not shown here).

4.1.2 THz emission features from Bi_2Se_3/Co multilayer.

We now study the response of such TI/TMDC/FM trilayers by THz emission spectroscopy (details in Section III.2.1). Prior to our studies by inserting TMDC WSe_2 layer ranging from 1 to 3 ML, we report in Fig. 4.39a the THz emission from Bi_2Se_3(10QL)/Co(3nm)/AlO_x(3nm) multistack free of WSe_2. The measured THz amplitude is sizeable compared to Co(2)/Pt(4), about 30%. Similarly to our previous studies on $SnBi_2Te_4$ and $Bi_{1-x}Sb_x$, we observe a different THz signal phase for identical magnetic field orientation between Co(2nm)/Pt(4nm) and Bi_2Se_3(10QL)/Co(3nm)/AlO_x(3nm): this is mediated by the different spin-current escape in the layers, thus showing that the interconversion of Bi_2Se_3/Co is of the same sign as the ISHE in

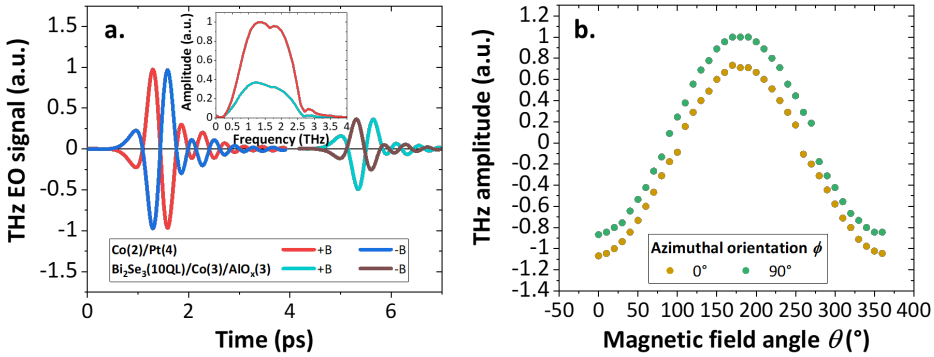

Figure 4.39: THz emission features from initial Bi_2Se_3/Co multilayer. (a) Measured THz emission of Bi_2Se_3(10QL)/Co(3nm)/AlO_x(3nm) compared to Co(2nm)/Pt(4nm) reference for the two field configurations $\pm B$. The inset presents the Fourier transform of the signals under positive magnetic field. (b) THz emission as a function of full magnetic field rotation (θ ranges from 0° to 180°). The measurements are performed for two crystalline orientations (a) $\phi = 0°$ and (b) ϕ=180°.

Pt. We observe that the THz amplitude is smaller than the one obtained for $Bi_{1-x}Sb_x$ by about a factor $\times 3.75$ and sensitively similar to the amplitude obtained in $SnBi_2Te_4$/Co. Besides, we observe similarly to our study on $SnBi_2Te_4$ the presence of an asymmetric THz emission as a function of the magnetic field. This convolution is also confirmed by the THz amplitude *vs.* the magnetic field angle θ reported in Fig. 4.39b, which presents the normalized THz response *vs.* the applied magnetic field angle θ. The main $\cos(\theta)$ dependence reflects the magnetic component but we also observe that for the two different orientations ϕ=0° or 90°, the angular profile is offset. This leads to a higher absolute value of the THz amplitude for a fixed crystalline orientation ϕ=0° (*ex.* for θ=180°, and inversely with a smaller absolute value for θ=0°) compared to a different orientation ϕ=90°. This offset thus corresponds to the non-magnetic component and one needs to quantify it more carefully as a function of the crystalline orientation ϕ.

To dive into the effective role of the spin-charge conversion in those multilayers, we performed the extraction of the respective magnetic and non-magnetic components from the THz transients by following the method proposed in Section III.2.3. We report in Fig. 4.40a the THz response as a function of the crystalline orientation ϕ for initial sample Bi_2Se_3(10QL)/Co(3nm)/AlO_x(3nm). The overall contribution can be straightforwardly mapped by using a $\cos(3\phi)$ dependence mapping the non-magnetic response, shifted by a constant offset illustrating the magnetic response. The non-magnetic response plotted in Fig. 4.40c presents a $\cos(3\phi)$ dependence and can be explained by several hypothesis: *i*) $\chi^{(2)}$ related effects (optical rectification could be excluded as Bi_2Se_3 do not present high non-linear susceptibility, and we are pumping above the bandgap) or *ii*) shift currents (owing to the potential presence of twin domains), whereas the slight offset can be associated to *iii*) surge currents arising from the photo-Dember and surface-depletion field effects. On the other hand, the magnetic contribution in Fig. 4.40b displays an almost isotropic response in favor of a spin-charge conversion mechanism.

4.1.3 Thickness dependence of the emission symmetries in Bi_2Se_3/WSe_2/Co.

We then proceed with the study of Bi_2Se_3(10QL)/WSe_2(t_{TMDC})/Co(3nm) multilayers as a function of the WSe_2 thickness t_{TMDC}. We follow the same extraction method and we report in Fig. 4.41 the obtained THz amplitude as a function of the crystallographic angle ϕ, for WSe_2 thickness t_{TMDC} of 1 ML, 2 ML and 3 ML. We observe that the obtained symmetries are different and more complex as they seem to carry different non-magnetic contributions arising from both the TI and the TMDC layers. We then extract in details the different magnetic and non-magnetic parts of the three samples while varying the WSe_2 thicknesses.

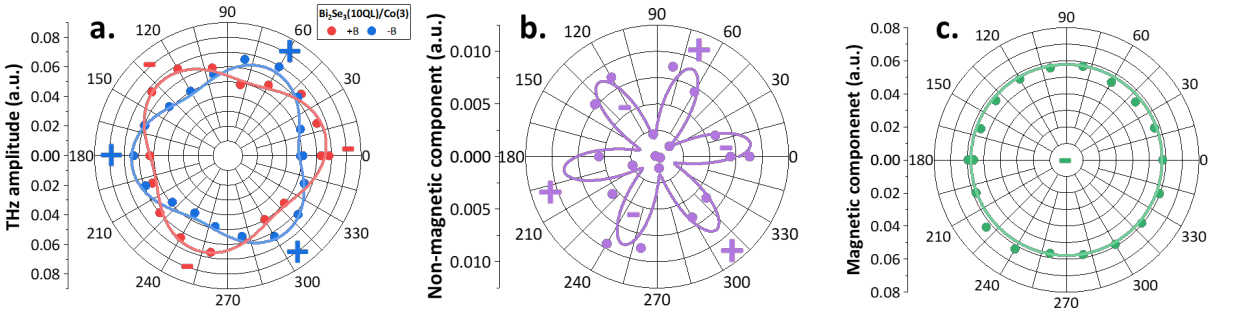

Figure 4.40: Emission symmetries of Bi_2Se_3/Co. (a) Measured THz amplitude for the two magnetic field polarities $\pm B$, (b) THz non-magnetic component and (c) magnetic component from Bi_2Se_3(10QL)/Co(3nm)/AlO_x(3nm) as a function of the crystallographic orientation ϕ. The amplitude is presented as a fraction of Co(2nm)/Pt(4nm) reference.

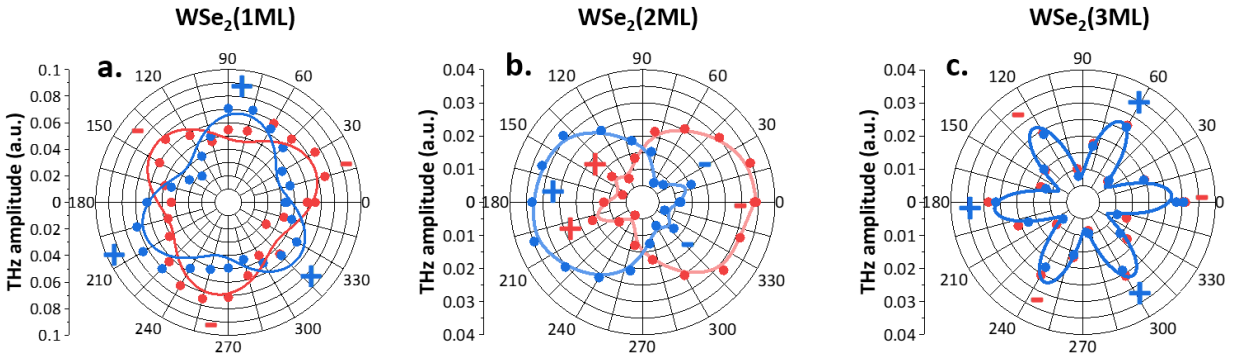

Figure 4.41: Evolution of the THz response symmetries as a function of WSe_2 thickness. Measured THz amplitude from Bi_2Se_3(10QL)/WSe_2(t_{TMDC})/Co(2nm)/AlO_x(3nm) as a function of the crystallographic orientation ϕ for $\pm B$ magnetic fields (red and blue). The WSe_2 thickness t_{TMDC} ranges from (a) 1 ML, (b) 2 ML, (c) 3 ML. The amplitude is presented as a fraction of Co(2nm)/Pt(4nm) reference.

Non-magnetic contributions from both Bi_2Se_3 and WSe_2 layers. We first observe the different symmetries of the non-magnetic contributions for the four samples with WSe_2 thickness t_{TMDC} ranging from 0 to 4 ML as displayed in Fig. 4.42 (and Fig. 4.45, not in polar plot). First, for t_{TMDC}=0 ML, we previously found a three-fold symmetry that would indicate a THz non-magnetic contribution (optical response) owing possibly to *i*) optical rectification, *ii*) shift currents or *iii*) surge currents. The first hypothesis seems unlikely as Bi_2Se_3 is not reported to present a strong non-linear susceptibility $\chi^{(2)}$ and that our pump is well above the bandgap. Then, the hypothesis of shift currents could be conceivable with respect to the potential presence of twin domains. Then, surge currents via the photo-Dember effect and surface-depletion field could also be present in the form of a constant offset in Bi_2Se_3, in a similar way as we have identified it on $SnBi_2Te_4$ previously [271]. Besides, we see that the symmetries are different for 1 ML, 2 ML and 3 ML with equivalent $\cos(3\phi)$ response for the 1 ML and 3 ML samples. This is in striking contrast with the symmetry of the non-magnetic part obtained on the 2 ML sample which appears as a $\cos(\phi)$ dependence. Moreover, we see that the amplitude of the non-magnetic contribution increases as a function of the WSe_2 thickness.

This is to be correlated with the reports in the literature indicating optical rectification in WSe_2 monolayers via a strong non-linear susceptibility $\chi^{(2)} \simeq 5$ nm.V^{-1} [315]. Such optical rectification process depends on the parity of the monolayer thickness of WSe_2 related to symmetry considerations, and this would explain the different emission symmetries observed for 1 ML, 3 ML (on one side) and 2 ML (on the other side). Indeed, for an even number of WSe_2 layers, the second-order optical susceptibility $\chi^{(2)}$ is vanishing as the space group is D^3_{3d} (which presents inversion

symmetry) while for an odd number of WSe_2, the space group is D^3_{3h} (which breaks inversion symmetry) and allows optical rectification. This has been reported in WSe_2 [315, 319] as well as in MoS_2 [173]. It remains the physical interpretation about the two-fold symmetry encountered for 2 ML. As optical rectification is not allowed in the 2 ML configuration by crystallographic symmetry arguments, we would likely attribute the $\cos(\phi)$ dependence to surge currents such as the photo-Dember and surface-depletion field effects, but it would require a slight sample misorientation with the azimuth normal.

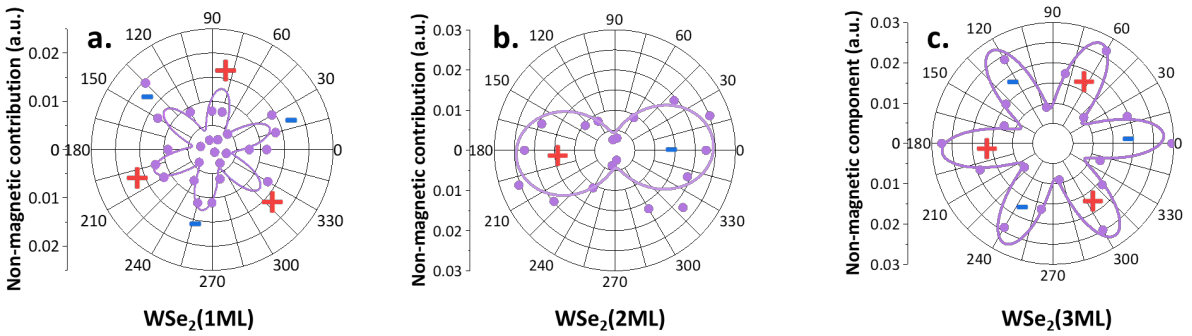

Figure 4.42: Evolution of the non-magnetic THz response symmetries as a function of WSe_2 thickness. THz non-magnetic contribution from Bi_2Se_3(10QL)/WSe_2(t_{TMDC})/Co(2nm)/AlO_x(3nm) as a function of the crystallographic orientation ϕ. The WSe_2 thickness t_{TMDC} ranges from (a) 1 ML, (b) 2 ML, (c) 3 ML. The amplitude is presented as a fraction of Co(2nm)/Pt(4nm) reference.

Comparison with the reference samples. In order to confirm that the $\cos(3\phi)$ symmetries determined experimentally are in agreement with the number of layers for WSe_2, we performed reference measurements on a Bi_2Se_3(10QL)/WSe_2(3ML)/AlO_x(3nm) sample without Co as shown in Fig. 4.43. We measure an almost-zero amplitude for the magnetic contribution and a non-magnetic contribution evolving as $\cos(3\phi)$ of sizeable amplitude. This dependence would agree with optical rectification arising from the WSe_2 layer as well as the smaller contribution from Bi_2Se_3 shift and surge currents.

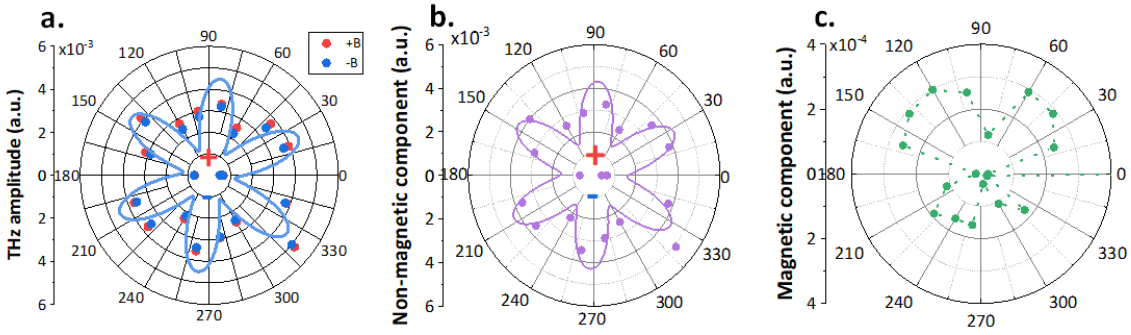

Figure 4.43: Reference THz emission symmetries measurements on Bi_2Se_3/WSe_2/AlO_x. (a) Measured THz emission from Bi_2Se_3(10QL)/WSe_2(3ML)/AlO_x(3nm) as a function of azimuthal angle ϕ, for +B and -B with extracted (b) non-magnetic component and (c) magnetic component. The amplitude is presented as a fraction of Co(2nm)/Pt(4nm) reference.

Magnetic component of the THz emission as a function of the WSe_2 thickness. As we have now assigned the non-magnetic part symmetries in Bi_2Se_3/WSe_2/Co multilayers, we can focus on the magnetic component related to spin-injection and spin-charge conversion. This is presented in Fig. 4.44 as a function of the WSe_2 thickness. We observe that in all cases, the magnetic

component is almost isotropic with respect to the crystallographic orientation ϕ and that the amplitude is significantly decreasing as the WSe_2 thickness increases. We note however slight variations of the magnetic component as a function of the crystalline orientation ϕ that we address in the next section.

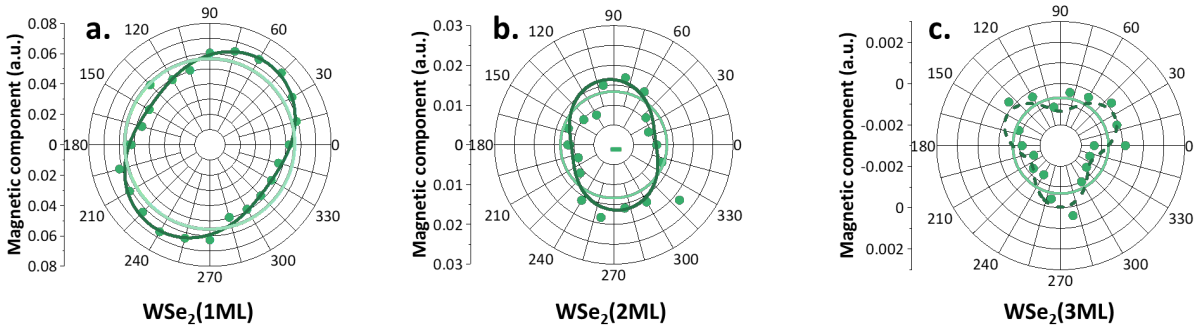

Figure 4.44: Evolution of the magnetic THz response symmetries as a function of WSe_2 thickness. THz magnetic contribution from Bi_2Se_3(10QL)/WSe_2(t_{TMDC})/Co(2nm)/AlO_x(3nm) as a function of the crystallographic orientation ϕ. The WSe_2 thickness t_{TMDC} ranges from (a) 1 ML, (b) 2 ML and (c) 3 ML. The amplitude is presented as a fraction of Co(2nm)/Pt(4nm) reference.

Discussions about the WSe_2 thickness dependence. To have a clear picture of the obtained symmetries, we plot in Fig. 4.45 (not in polar plot for sake of clarity) the obtained THz amplitude of both magnetic and non-magnetic component as a function of the WSe_2 thickness. Surprisingly, we also notice a possible $\cos(2\phi)$ dependence of the magnetic component in the WSe_2(1ML) and WSe_2(2ML) sample. This intriguing result can be possibly explained by magnetic shift current whose amplitude is very weak, and has not been studied extensively in the literature. One explanation can also include the orbital interconversion, but this will thus be the starting point of further studies.

To summarize our measurements, we show in Fig. 4.46 the net absolute amplitude of the THz magnetic and non-magnetic parts as a function of the WSe_2 thickness (t_{TMDC}). In details, we report that the THz magnetic component from Bi_2Se_3/WSe_2/Co samples is decreasing as a function of the WSe_2 thickness. We have several hypothesis to explain this effect: *i*) as the magnetic component is correlated to the spin-injection efficiency, it is possible that we map the formation of the semiconductor/metal barrier (Schottky barrier) with large bandgap WSe_2 in contact with Co. However on this point, it is important to account *ii*) the potential effects of the hybridization (metallisation) of the TMDC layer in direct contact with metallic Co in the low-thickness limit. Besides, it is also important to address the second part of the magnetic contribution related to the spin-charge conversion. In this case, a smaller amplitude of the THz magnetic component could suggest *iii*) a potential alteration of the interfacial conversion mediated via the surface states of Bi_2Se_3. However, no element could affirm this hypothesis at this point of the study. It is also possible that *iv*) an interconversion at WSe_2/Co takes place but with an opposite sign thus cancelling both conversion at Bi_2Se_3 interface and WSe_2/Co interface. On this particular point about the hybridization of WSe_2 in contact with ferromagnetic Co, *v*) it is poorly reported the effect of the magnetic proximity effects induced by WSe_2/Co contact and one could assume that the first ML of WSe_2 could be magnetized due to the exchange interactions induced by Co.

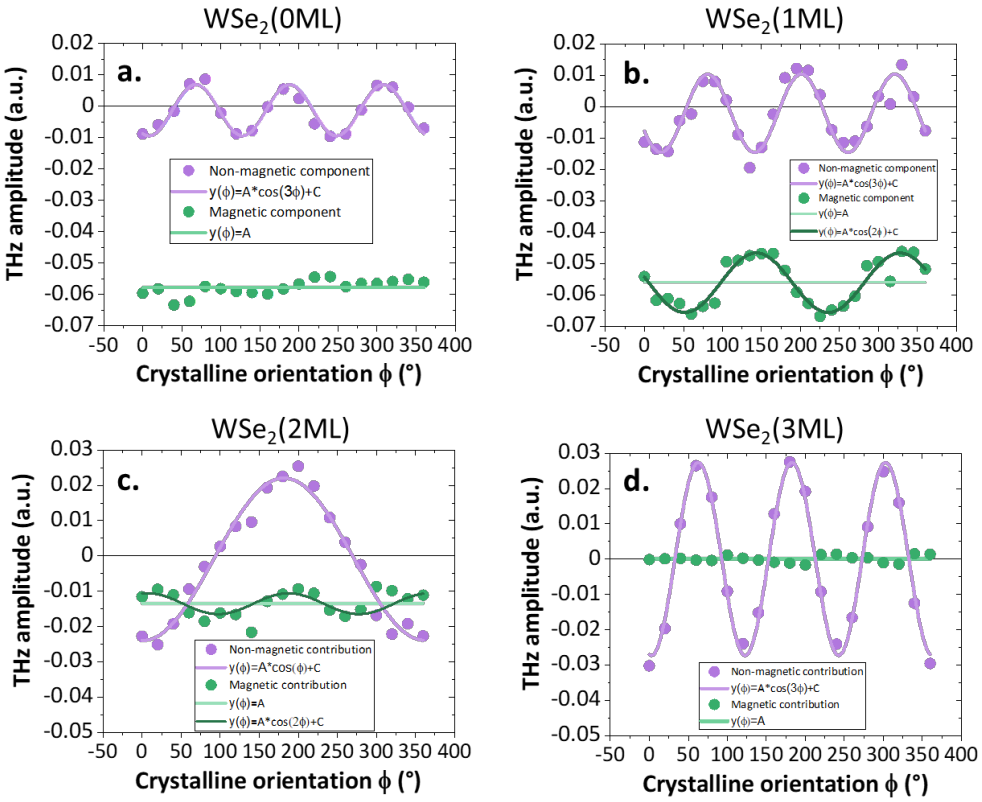

Figure 4.45: Evolution of the non-magnetic and magnetic component symmetries in Bi_2Se_3/WSe_2/Co as a function of the WSe_2 thickness. THz non-magnetic (purple) and magnetic (green) contributions from Bi_2Se_3(10QL)/WSe_2(t_{TMDC})/Co(2nm)/AlO_x(3nm) as a function of the crystallographic orientation ϕ. The WSe_2 thickness t_{TMDC} ranges from (a) 0 ML, (b) 1 ML, (c) 2 ML and (d) 3 ML. The amplitude is presented as a fraction of Co(2nm)/Pt(4nm) reference.

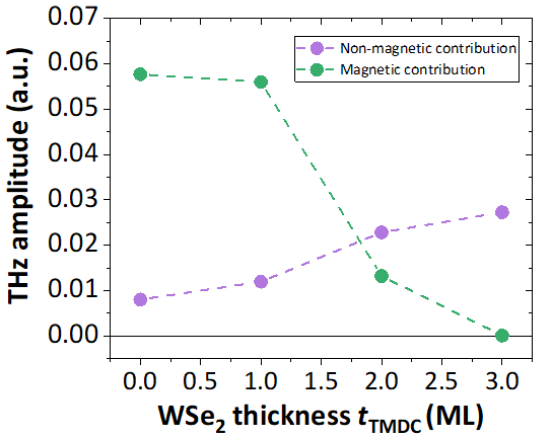

Figure 4.46: Evolution of the THz contributions *vs.* the WSe_2 thickness. THz non-magnetic component (violet) and magnetic component (green) as a function of the WSe_2 thickness. The dotted lines are a guide for the eyes. The amplitude is presented as a fraction of Co(2nm)/Pt(4nm) reference.

Conclusions and perspectives on Bi_2Se_3/WSe_2/Co THz emission spectroscopy.

We have reported in this preliminary study the role of the spin-injection and spin-charge conversion in complex Bi_2Se_3/WSe_2/Co multilayers. It appears that the non-magnetic contributions in those samples dominate as the WSe_2 increases while the magnetic part is decreasing. This should be associated to the formation of a Schottky barrier preventing an efficient spin-injection at the Bi_2Se_3 interface. No element seems to address a potential gain in the spin-charge conversion owing to the strong interfacial spin-orbit coupling in 2D TMDC WSe_2. This initial study calls further investigations via pump-polarization dependence to carefully address the dynamical properties in those embedded multilayers. These results will be soon correlated to future experimental investigations led by ferromagnetic resonance and inverse spin Hall effect by spin-pumping.

4.2 Control of the Fermi level and fully-implemented interfacial systems.

Inset barrier from semiconducting WSe_2 to metallic VSe_2. To set free from the hampering of the Schottky barrier caused by WSe_2 semi-conductor contact, it would be interesting to look at metallic-type 2D materials. For that, we have envisioned to used VSe_2 metallic phase which has recently been reported in contact with Bi_2Se_3 topological insulator by Park *et al.* [320]. The authors reported that from an interfacial charge transfer engineering, *i*) persistent topological surface states are mapped in the Bi_2Se_3/VSe_2 heterojunction. Besides, *ii*) the charge transfer allows an electronic level shift (about few tens of meV) for the bulk states of the topological insulator, allowing a non-destructive Fermi level pinning. The third and most important element is that *iii*) using metallic-type VSe_2 would avoid forming a Schottky barrier at the interface and would have a good spin-mixing conductance with the ferromagnetic metal, thus being an efficient system for spin-injection and spin-filtering to study in the future.

Electrical control of the Fermi level. One possibility to study the TSS contribution to the interconversion is the ability to tune the Fermi level by electrical gating to pin precisely the Fermi level in the gap, crossing only the TSS. This would be experimentally feasible by applying a gate voltage on the back of the sample substrate (such as highly doped Si). However, this can lead to new interrogations about *i*) the good epitaxial growth on such substrate or *ii*) the addition of non-magnetic contributions from semi-conducting substrates that would need to be taken into account in the THz efficiency extraction process.

Towards fully-implemented interfacial systems. Besides, research motives to probe the strong interfacial conversion in purely 2D-integrated systems, for instance in recently evidenced THz emission from Fe_3GeTe_2/Bi_2Te_3 [169] where the amplitude is higher by a factor of $\times 2$ compared to the pure non-magnetic contributions in topological insulators, or by use of a 2D ferromagnet in contact with high spin-orbit coupling 2D material.

V

Antiferromagnetic order based THz emission.

This chapter develops the study of the spin-related THz emission by replacing the ferromagnetic metallic layer by different insulating antiferromagnetic materials in the spintronic THz emitter structure. Antiferromagnets, discovered by Louis Néel during his thesis in 1932 (and afterwards awarding him the Nobel prize in 1970), have gained strong interest recently in the spintronic community for their intrinsic properties: robustness to parasitic magnetic field, absence of stray fields and high frequency dynamics. They host strong application perspectives for building compact and high-speed rate THz spintronic devices whether it would be for THz detection schemes, robust magnetic memories or tunable THz sources in free-space.

After presenting some of the current challenges of antiferromagnetic spintronics, we will develop how one can excite coherent THz magnons in insulating antiferromagnet NiO thin films capped with Pt via two mechanisms: either *i*) the well-known quasi-instantaneous off-resonant optical spin-torque in (111) oriented NiO or *ii*) via ultrafast spin-phonon interactions in (001) oriented NiO. By measuring various NiO/Pt bilayers with different growth orientations and thicknesses, we demonstrate the crucial role of the antiferromagnet symmetries in these mechanisms. Specifically, we unravel in this study a novel generation mechanism to generate magnons in (001) orientated NiO thin films compared to (111) orientation. We discuss the different contributions linked to phononic transport and in particular the ultrafast spin-phonon interactions, *i.e.* the role of ultrafast magneto-strictive effects unreported until now, or the incoherent phonon heat with potential spin-Seebeck contributions. Thereafter, we give some insights about the perspectives of the use of canted insulating antiferromagnets such as α-Fe_2O_3 (hematite) or $TmFeO_3$ (proposed in Annex A14) in which we report a THz signal owing to the presence of both antiferromagnetic and weak magnetic order induced by the canting.

We acknowledge the collaboration with O. Gueckstock, T. Seifert, T. Kampfrath (Freie Universität Berlin) for the THz spin-current extraction, M. Mattern, M. Bargheer (University of Potsdam) for the ultrafast X-ray characterization, O. Gomonay for the Néel vector dynamics theory and H. Meer, C. Schmitt, J. Sinova, M. Kläui (Johannes Gutenberg Universität Mainz) as well as R. Ramos, T. Kikkawa, E. Saitoh (Tohoku University), S. T. B. Goennenwein (University of Konstanz) and S. Geprägs (Walther-Meißner-Institut) for the NiO/Pt bilayers growth.

1 Motivations for antiferromagnetic spin-based THz devices.

Antiferromagnetic (AFM) spintronics has recently emerged as a challenging research area for energy-efficient manipulation of the spin-information at very high frequencies [321, 322, 323]. Contrary to ferromagnetic materials, the exchange coupling $J < 0$ strongly couples the neighbouring spins antiferromagnetically (*i.e.* the neighbouring moments are in the antiparallel direction) which corresponds to an exchange field H_{E} from hundreds to thousands of Tesla in various antiferromagnetic materials [324]. This leads to the robustness of antiferromagnetic materials to external magnetic fields, the absence of a net macroscopic magnetization and thus the absence of stray fields. Besides, this high exchange interaction directly scales the eigenfrequencies of the magnon modes in the THz range, contrary to ferromagnets where the resonant frequency $\omega_{\mathrm{FM}} = \gamma H_{\mathrm{A}}$ is given only by the anisotropy field H_{A} (γ is the gyromagnetic ratio). This intuitively gives more than two orders of magnitude between the mode frequency of ferromagnets and mode frequencies of antiferromagnets (as proportional to $\sqrt{H_{\mathrm{E}}}$).

Antiferromagnets thus offer an interesting platform for developing compact and stable magnetic memories [325] as the absence of stray fields allows to reduce the storage area size without encountering magnetic perturbations while increasing the speed rate in order to access to the stored information [326]. Alternatively, antiferromagnets are also targeted to be used in various spin-torque schemes [327] or in logical elements for neuromorphic computing [328]. Another perspective is to develop THz sources and achieve ultrafast magnonic current sources. With a view to functionalize and build efficient spintronic devices based on antiferromagnetic materials, three key factors are necessary. The first element to be fulfilled lies in the AFM dynamics which allow for instance the electrical writing at THz frequencies [326]. Beyond the case of antiferromagnets with broken inversion-symmetry (such as Mn_2Au, CuMnAs), controlling the antiferromagnetic order requires to induce a symmetry-breaking which can be achieved at interfaces. The good interfacial transmission of the spin information is crucial, and have recently been demonstrated via large spin-mixing conductances in case of metal/metal contact IrMn/Pt with $g_r = 6.9 \times 10^{18}$ m^{-2} [329, 191], comparable with interfaces between metallic ferromagnets and heavy metals, or in case of insulating/heavy metal contact NiO/Pt, which reaches up to 2×10^{14} Ω^{-1}.m^{-2} [330]. Besides, insulating antiferromagnets are considered as an efficient spintronic platform due the good transport of the spin-information, as reported in various works like in α-Fe_2O_3 [331] or in $YFeO_3$ [332]. More particularly in this chapter, we will focus on insulating antiferromagnets, which present a low magnetic damping α_{AF} that thus narrows the resonance linewidth which scales with $\Delta\omega_{\mathrm{AF}} \propto \alpha_{\mathrm{AF}} H_{\mathrm{E}}$. Such materials are thus a platform of choice to develop narrowband THz devices or magnonic circuits carrying spin-wave over long distances [333].

From THz spin-orbit torque oscillators to narrowband detectors and opto-magnonics. A strong interest for antiferromagnetic platform relies on envisioned THz antiferromagnetic-based devices. THz spin Hall nano-oscillators (SHNO) is the high-frequency extension of the spin-torque nano-oscillator (STNO) limited to the GHz regime. In the case of insulating AFMs, it has been proposed SHNOs devices where the electrical charge current injection in an adjacent heavy metal could generate steady-state oscillation of the Néel vector by interfacial spin-orbit torque [148].

One can also envision this type of AFM heterostructures to develop AFM opto-spintronics devices with narrowband tunability of the THz radiation for emission and detection purposes [334]. Furthermore, the application of DC bias on AFM/HM THz detectors could efficiently tune the AFM resonant frequencies by modifying the (relatively) small anisotropy field as envisioned by Safin *et al.* [329, 335]. Detector sensitivity of the order of 10^2 to 10^3 V.W^{-1} have been pre-

dicted [329] which would make AFM based THz detectors promising and responsive radiation devices. Besides, narrowband THz emitters using a metal/dielectric/magnetic structures have been theoretically described [243, 197] with a promising use of ultrafast strong magnetostrictions, present in insulating antiferromagnets.

The experimental work on the dynamics of AFM/HM heterostructres is strongly motivated by the possibility to achieve narrowband and tunable abilities. Broadband THz radiation from bilayers including an AFM compound has been observed in Co/Mn_2Au [190] metallic system and the authors demonstrated the use of AFMs as an ultrafast converter. More recently, a first experimental demonstration of ultrafast spin-injection from a magnonic current, leading to subsequent THz emission in a AFM/HM structure, has been recently published by Qiu *et al.* [194]. This was associated to the injection of ultrafast magnons generated from NiO into heavy metal Pt for spin-to-charge conversion. However, this study does not provide a clear evidence of the presence of AFM magnon modes and focused only on the well-known inverse Cotton-Mouton effect (ICME) as the excitation mechanism. We will provide later promising perspectives on a similar system.

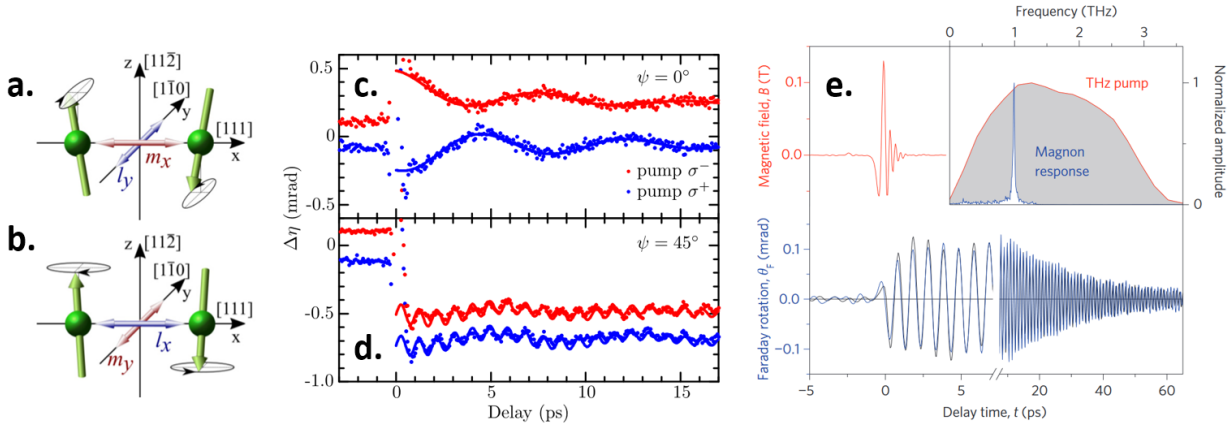

Figure 5.1: Probing THz modes in antiferromagnets. (a-b) Illustration of the 0.17 THz (top) and 1.1 THz mode (bottom) of NiO. (c-d) Off-resonant pumping of the Néel vector precession mapped by time-resolved Kerr spectroscopy in NiO. Both low and high frequency mode are mapped. (e) Resonant pumping of the out-of-plane mode of NiO. Strong THz fields of the order of MV.cm^{-1} are needed to generate a response measurable by Faraday rotation. Figures adapted respectively from [336, 188].

Probing the magnon modes of antiferromagnets. Accessing the THz magnon modes of antiferromagnets still remains a challenge nowadays. Indeed, the key question is the following: how can we efficiently map and exploit the ultrafast dynamics of the Néel vector of a fully compensated antiferromagnet where the static magnetization $\mathbf{m} = (\mathbf{M}_1 + \mathbf{M}_2)/2$ vanishes? Indeed, even for out-of-equilibrium excitations of the Néel vector, we are only sensitive to the magnetization variations $\Delta\mathbf{m}$, very weak in those systems.

One method employed by researchers was the pump-probe spectroscopy, via an off-resonant pumping of the magnon modes while a probe beam passes through the excited material and sees its polarization changed due to the interaction with, either the uncompensated moments put off their equilibrium state by the Faraday rotation, or the compensated moment via the Cotton-Mouton effect [337]. By varying the probe delay, it is possible to reconstruct the AFM mode dynamics as performed by Tzschaschel *et al.* [336] and reproduced in Fig. 5.1b. With recent progress on intense THz pulses generation, Kampfrath *et al.* [188] have coherently excited and detected THz spin waves in NiO single crystals with an on-resonant pumping using THz pulses of 0.4 MV.cm^{-1} (corresponding to a pulsed magnetic field about 0.1 T). The 1.1 THz out-of-plane

mode of NiO has been resolved in time using Faraday rotation as displayed in Fig. 5.1e. Similarly, Nishitani *et al.* [338] have reported the observation of a THz emission from NiO single crystal.

Kerr and Faraday rotation.

The Kerr rotation is the tilt of the reflected probe polarization by an angle θ_K due to the interaction with the magnetic moments $\mathbf{m}$ of a sample. Similarly, the Faraday rotation is the tilt of a transmitted probe polarization by an angle θ_F while interacting with the magnetization $\mathbf{m}$ during its transmission through the sample, following:

$$\theta_F(d,t) = \mathcal{V} d \, (\mathbf{k} \cdot \mathbf{M}(t)) \tag{E5.1}$$

where $\mathcal{V}$ is called the Verdet constant given in rad.T^{-1}.m^{-1}.

Although the possibility to observe coherent 1 THz out-of-plane mode of NiO in bulk crystals showed the dynamics of the induced magnetization variation $\Delta\mathbf{m}$, it could not be extended to very thin films of NiO due to the weak dipolar field induced by the AFM modes [338, 188]. Therefore, it is a challenging task to provide an active manipulation of this high-frequency mode to efficiently functionalize THz antiferromagnetic materials. During this thesis, a novel approach emerged via the development of THz emission spectroscopy on thin films of antiferromagnetic layers capped with heavy metals. Accessing the dynamical spin current carried by the magnon modes is here made possible via the thin capping of a heavy metal (like Pt) to efficiently convert the generated spin current into a transverse charge current (leading to THz transients in free space). Here, the role of the interface is central to induce detectable processes addressing the antiferromagnetic order, such as spin-torque and spin-charge conversion.

As mentioned previously, a very recent paper by Qiu *et al.* [194] accessed to broad THz transients generated by femtosecond short infrared pulses on a NiO(111)/Pt bilayer. They directly evidenced the link between the Néel order of NiO and the THz emission in free-space, opening new perspectives to manipulate the antiferromagnetic order on ultrafast timescales. However, one could question about *i*) the absence of mapping of the high frequency mode in NiO in those bilayers, rising interrogations about the link between the THz emission and the AFM magnon modes, and *ii*) the repeatability of the observation of ultrafast spin-current generation in NiO. Our study, performed at the same time as Qiu *et al.* and presented in this chapter, answers this particular point as we report coherent 1.1 THz narrowband emission in free space on NiO(001)/Pt thin films together with new excitation mechanisms led by spin-phonon interaction.

2 Spin arrangement and dynamics in antiferromagnets.

Within the broad family of antiferromagnetic materials, we distinguish two main classes of antiferromagnets, presently the easy-plane antiferromagnets like NiO and the easy-axis antiferromagnets like $TmFeO_3$ [339]. In both cases, to describe the dynamics of the antiferromagnetic order in those systems, one speaks from the Néel vector $\mathbf{n}$ (the notation $\mathbf{l}$ is sometimes encountered) defined as the difference between the two sublattice magnetizations:

$$\mathbf{n} = (\mathbf{M}_1 - \mathbf{M}_2)/2 \tag{E5.2}$$

Indeed, in absence of an (strong) external magnetic field (or Dzyaloshinskii-Moriya interaction field H_D), AFM materials have a compensated spin texture $\mathbf{m} = 0$. When applying a field along the main anisotropy axis of the system, the transition to a canted state happens at the spin-flop field H_{SF}. The energy associated to H_{SF} also corresponds to the energy gap of the lowest AFM mode ω_{AF} with:

$$H_{SF} = \sqrt{2H_A H_E} \Rightarrow \omega_{AF} = \gamma\sqrt{2H_A H_E} \tag{E5.3}$$

where ω_{AF} is the angular frequency of the lowest AFM mode (which depends on the anisotropy field $H_A \rightarrow H_{Ax}, H_{Az}$ in some materials) and γ is the gyromagnetic ratio. In the case of canted antiferromagnets, a sizeable DMI field H_D cants the two sublattice magnetizations which leads to a net magnetization, however without modifying the antiferromagnetic mode frequencies [340]. Typical values of anisotropy parameters are given in Table V.1 for selected antiferromagnets. We display in Fig. 5.2 the expected dispersion of the magnon modes in easy-plane and easy-axis antiferromagnets. Interestingly, the two magnon modes are circularly polarized and degenerated at zero field in the case of easy-axis antiferromagnets while the modes are linearly polarized but their degeneracy is splitted at zero field in easy-plane antiferromagnets. In the latter case, it allows to generate a magnon flow at zero magnetic field.

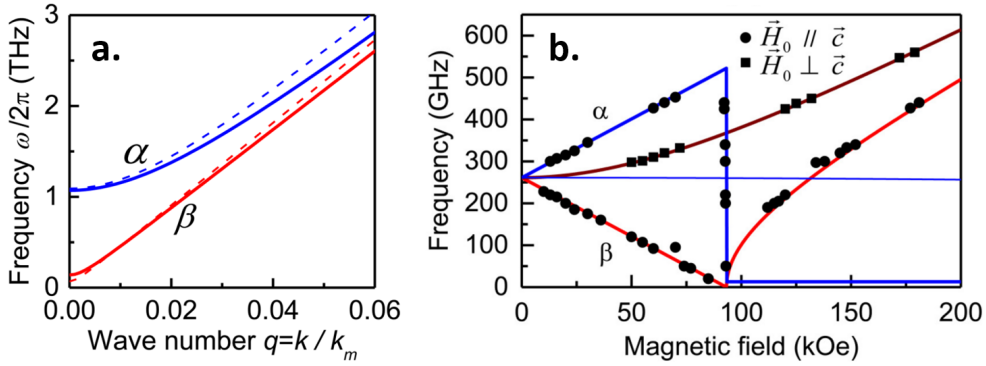

Figure 5.2: Dispersion of the magnon modes for easy-plane and easy-axis antiferromagnets. (a) Dispersion of the two magnon branches of NiO as a function of the wave number q (close to the center of the Brillouin zone) at room temperature. (b) Dispersion of the two magnon modes of MnF_2 easy-axis antiferromagnet as a function of the applied magnetic field. Note that α refers to the high-frequency mode ω_{Az} while β refers to the low-frequency mode ω_{Ax}. Adapted from Rezende *et al.* [339].

Material	Type	H_E (kOe)	H_D (kOe)	H_{Ax} (kOe)	ω_{Ax} (THz)	H_{Az} (kOe)	ω_{Az} (THz)
NiO [339]	Easy-plane	9 684	-	0.11	0.140	6.35	1.07
α-Fe_2O_3 [341]	Easy-plane	10 000	23	1	0.022	-	-
$TmFeO_3$ [341]	Easy-axis	5 500	40	0.6 $\times 10^{-3}$	0.3	-	-

Table V.1: Values of the exchange field H_E, anisotropy field H_{Ax}, H_{Az} and zero-field mode frequencies ω_{Ax}, ω_{Az} for different antiferromagnetic materials NiO, α-Fe_2O_3 and $TmFeO_3$. The two last antiferromagnets are also canted antiferromagnets.

2.1 Modelling the dynamics of the antiferromagnetic order.

Under an external excitation $\mathbf{\Gamma}$, the antiferromagnetic order can undergo precessional motion, either uniform ($\mathbf{k} = 0$) or not ($\mathbf{k} \neq 0$), following the energy absorption by the sublattice magnetizations. We describe below the dynamics of an easy-plane antiferromagnet such as NiO by considering the following model referred to as the *sigma model* [342, 343]:

$$\mathbf{n}_0 \times (\ddot{\delta\mathbf{n}} + \underbrace{2\gamma_{AF}\dot{\delta\mathbf{n}}}_{\text{damping}} - \underbrace{c^2\Delta\delta\mathbf{n}}_{\text{magnon propagation}} + \underbrace{\omega_{AF}^2(T)\delta\mathbf{n}}_{\text{anisotropy term}}) = \gamma^2 H_E \underbrace{(\mathbf{n}_0 \times \mathbf{\Gamma})}_{\text{excitation}} \tag{E5.4}$$

where $\mathbf{n}_0$ represents the initial state of the Néel vector, $\mathbf{n} = \mathbf{n}_0 + \delta\mathbf{n}$ is the dynamical Néel vector presenting variations $\delta\mathbf{n}(\omega)$ from its initial state, $\gamma_{AF} = \gamma\alpha_{AF}H_E$ is related to the damping term α_{AF}, c is the magnon velocity, ω_{AF} is the mode frequency depending on the temperature T

and H_E is the exchange field. $\mathbf{\Gamma}$ represents the external torque applied to the Néel vector. Therefore, solving the above equation of the Néel vector dynamics allows to compute the dynamical magnetization according to $\Delta\mathbf{m} = (\mathbf{n}_0 \times \delta\dot{\mathbf{n}})/(\gamma H_E)$.

2.2 NiO: a model easy-plane insulating antiferromagnet.

As a textbook example that will be important in the understanding of NiO/Pt THz emission study, we show in Fig. 5.3 the magnetic structure of NiO easy-plane insulating antiferromagnet. NiO has a Néel temperature of T_N=523 K [344]. Below the Néel temperature, the magnetic moments of Ni lie in the (111) planes which are oppositely arranged between neighbouring (111) planes [345]. We refer as $\mathbf{M}_1$ and $\mathbf{M}_2$ the successively opposed magnetic moments ordering at equilibrium. Due to the contraction of NiO along the $\langle 111 \rangle$ directions, the (111) planes are four-fold degenerated, which corresponds to four possible T-domains (twin domains). In each T-domain, the spins can point in three equivalent $\langle 112 \rangle$ directions (towards each triangle vertex) which are denoted as S-domains (spin domains). This leads to 12 possible magnetic domain orientations. However in our case, the growth favours only one T-domain to be selected due to the presence of strains [346]. In NiO, one needs to distinguish the two anisotropy fields, *i.e.* the small easy-axis H_{Ax} in the (111) plane and hard-axis H_{Az} anisotropy fields as given in Table V.1. This leads to the presence two degenerated magnon modes [339], one at low frequency ω_{Ax} and one at high frequency ω_{Az}. In easy-plane antiferromagnets like NiO, the precession modes of the sublattice magnetizations $\mathbf{M}_1$ and $\mathbf{M}_2$ are strongly elliptically polarized, as displayed in Fig. 5.3b-c, and the combination of the dynamical sublattice magnetizations leads to a linearly polarized Néel vector $\mathbf{n}(t)$. For NiO, the low-frequency mode is around ω_{Ax}=180 GHz while the high-frequency mode is at ω_{Az}=1.1 THz. Keeping the example of NiO, the out-of-plane mode ω_{Az} can be seen as oscillations $\delta\mathbf{n}$ pointing out of the easy-plane along $[111]$ in case of (111) oriented NiO or along $[5\ 5\ 19]$ for NiO(001). Symmetry considerations thus allow the detection of the high-frequency mode in NiO(111) oriented samples, contrary to the low-frequency mode as displayed in Fig. 5.4.

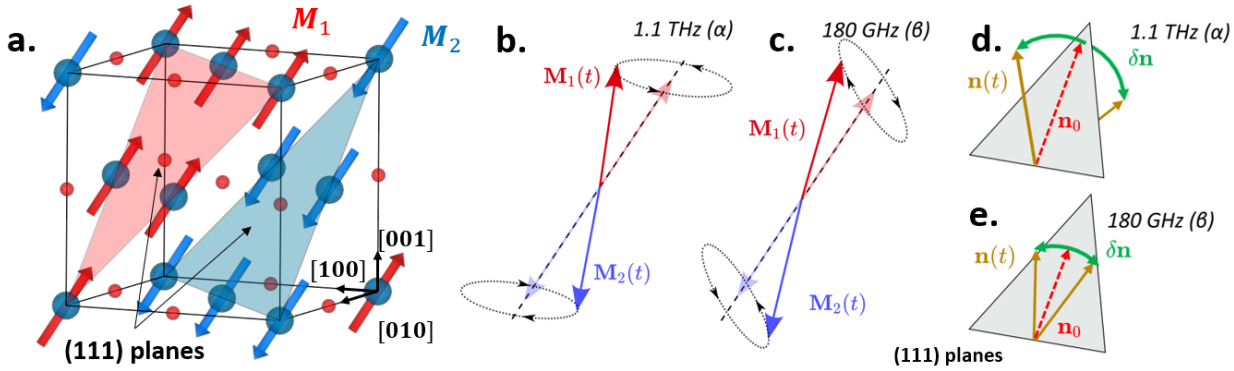

Figure 5.3: Magnetic arrangement of easy-plane antiferromagnet NiO. (a) Crystallographic structure of NiO with the magnetic structure represented. (b-c) Elliptical precession of the sublattice magnetizations for the two magnon modes and (d-e) corresponding Néel vector dynamics for the two magnon modes.

3 Combined emission of coherent and broadband THz magnons in NiO/Pt bilayers.

This work presented below is related to the preprint currently available on arXiv [347]. Most of the studied samples has been grown by H. Meer, C. Schmitt, M. Kläui (Johannes Gutenberg Universität Mainz) and R. Ramos, T. Kikkawa, E. Saitoh (Tohoku University). The NiO(111)(110nm)/Pt(2nm) sample has been

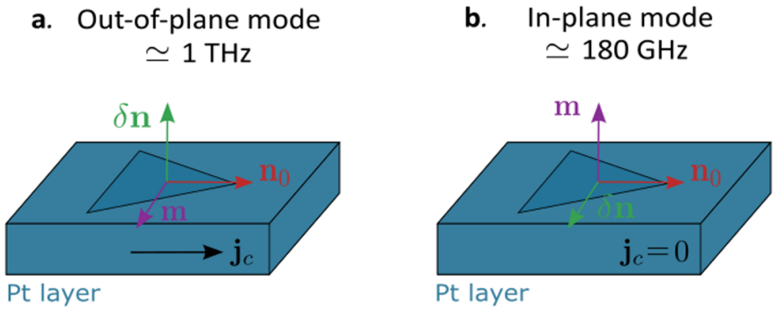

Figure 5.4: Selection rules for probing the magnon modes in (111) oriented NiO. (a) Out-of-plane (high-frequency) and (b) in-plane (low-frequency) modes of NiO. Due to the Pt contact with NiO, only the high-frequency mode inducing a dynamical magnetization oriented perpendicular to the interface normal can be mapped in our current THz emission spectroscopy geometry.

grown by S. T. B. Goennenwein (University of Konstanz) and S. Geprägs (Walther- Meißner-Institut). We acknowledge O. Gueckstock, T. Seifert and T. Kampfrath for the THz spin current dynamics extraction, M. Mattern and M. Bargheer for the ultrafast X-ray diffraction characterization and O. Gomonay for the modelling of the THz magnetization dynamics.

Following the powerful use of THz emission spectroscopy to probe in spintronic multistacks, we present in this part our study on NiO antiferromagnet capped with Pt to probe the dynamics of the Néel vector.

3.1 Observation of THz magnons by inverse spin Hall effect in NiO thin films.

Growth of the studied bilayers. The NiO layers were grown by reactive magnetron sputtering on MgO(001) or MgO(111) substrates depending on the targeted orientation of NiO. NiO layers are deposited in a mixed atmosphere containing Ar (gas flow of 15 sccm) and O_2 (gas flow of 0.7 sccm in most cases, but could be monitored to 1.5 sccm). Note that 1 sccm is equivalent to 1 $cm^3.min^{-1}$ at standard temperature and pressure. The thicknesses of NiO ranges from 10 to 100 nm and are afterwards capped by Pt(2nm) in-situ after cooling down the sample to room temperature. More details are available in Refs. [346, 348].

THz emission of NiO/Pt bilayers. We report in Fig. 5.5 the THz emission from NiO(001) (10nm)/Pt(2nm) bilayer. The generated signal is composed of two parts: *i*) a short pulse followed by *ii*) periodic oscillations in the time domain with a period of about 1 ps. These features respectively correspond in the frequency domain (inset of Fig. 5.5) to *i*) a broadband response up to 3 THz (cut-off frequency of the used ZnTe ⟨110⟩ 500 µm) and to *ii*) a narrowband contribution centered at 1.1 THz. This second feature can be linked to the high-frequency mode of NiO probed in emission configuration here (*i.e.* not in transmission spectroscopy as discussed before [188, 349, 338, 336]). The long-lived oscillations up to 10 ps seem to indicate a low magnetic damping in those bilayers and thus demonstrate the high thin film growth quality of NiO/Pt bilayers. We also notice the presence of what seems to be the second harmonic $2\omega_{AF}$ at 2 THz of the high-frequency magnon mode. The second harmonic seems to be shifted compared to its expected position around 2.2 THz, which is likely due to the cutoff frequency of the detector (around 3 THz due to the condition of phase-matching, see Section III.2.1 and Annex A10). Indeed, only the lowest frequency components near the $2\omega_{AF}$ central peak would be resolved, which artificially cuts the peak maxima although present at higher frequencies. It is however to be noted that the THz amplitude of the signal is weak compared to standard metallic spintronic THz emitters, by about three order of magnitude. This is due to the fact that *i*) the emission sensitivity is linked to $\Delta\mathbf{m}$ which is very weak in fully compensated excited antiferromagnets and

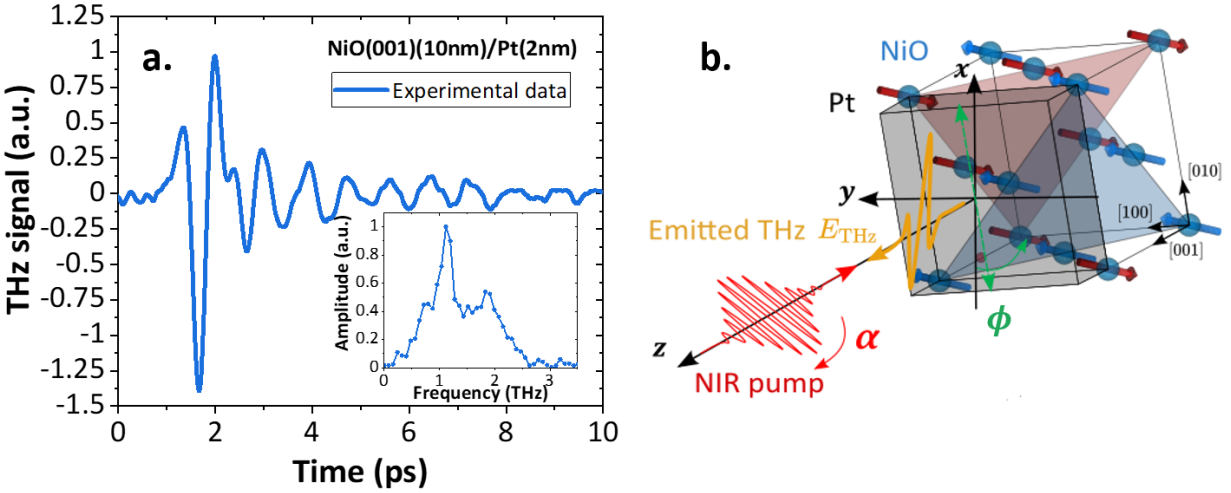

Figure 5.5: THz emission features from NiO(001)/Pt bilayer. (a) Signal from NiO(001)(10nm)/Pt(2nm) presenting short pulse (broadband) and the presence of oscillations of period around 1 ps. The inset presents the spectrum of the measured signal which shows the broadband and narrowband contribution centered around 1.1 THz. (b) Sketch of the experimental configuration. The pump polarization is noted as α and the crystallographic orientation is noted as θ.

ii) that the spin-mixing conductance between an insulating antiferromagnet and a heavy metal is generally lower by an order of magnitude compared to the metallic antiferromagnet/heavy metal interface [330].

Excitation related to the antiferromagnetic order. To link the THz emission to the Néel order, we performed angular measurements in which we rotated the sample in-plane to access the emission anisotropy *vs.* the crystalline orientation of the sample ϕ (we recall that a scheme of THz angular measurements is proposed in Section III.2.3). We report in Fig. 5.6a an uniaxial emission oriented at $\phi = \phi_0 \simeq 35°$ from the (011) sample edge. This is consistent with the observations of Meer *et al.* [350] and Schmitt *et al.* [346] in which the authors report a domain along this particular axis [5 5 19]. Interestingly, Fig. 5.6b shows that the phase of both the broad contribution and of the measured oscillations reverses while rotating the azimuthal crystalline orientation from $\phi = \phi_0$ to $\phi = \phi_0 + 180°$. This indicates that an AFM order origin is linked to the THz signal and to the 1.1 THz oscillations. Moreover, our observation is coherent with the quasi-mono domain structure (domains larger than 100×100 µm^2) as reported in those thin films [350] and measured in Kerr imagery as shown in Fig 5.6c (following the method described by [351]). This would address a mono-domain excitation via our pump, knowing our pump diameter is about 200 µm^2 in this study. On the contrary, if we would have been in presence of multi-domain state, we would have measured three-fold symmetry contributions to the angular dependence of the THz emission as reported by Qiu *et al.* [194], as a function of the crystallographic orientation ϕ due to the relative orientation of the domains by $\pm 120°$.

On the other hand, we studied various samples of different growth conditions, for instance by changing the O_2 rate (from 0.7 sccm (low gas flow) to 1.5 sccm (high gas flow)). We report in Fig. 5.8 the THz emission from two samples grown by different methods, of same thicknesses, respectively low (sample A) and high (sample B) O_2 gas flow and with high crystalline quality in both samples as measured in XRD. We notice the absence of the oscillations in sample B referred as "strong" magnetic damping. Besides, the amplitude in this sample is reduced compared to the amplitude produced by sample A. It demonstrates the sensitivity of the THz emission depending on the growth conditions. The origin of this discrepancy is yet unclear and several hypothesis

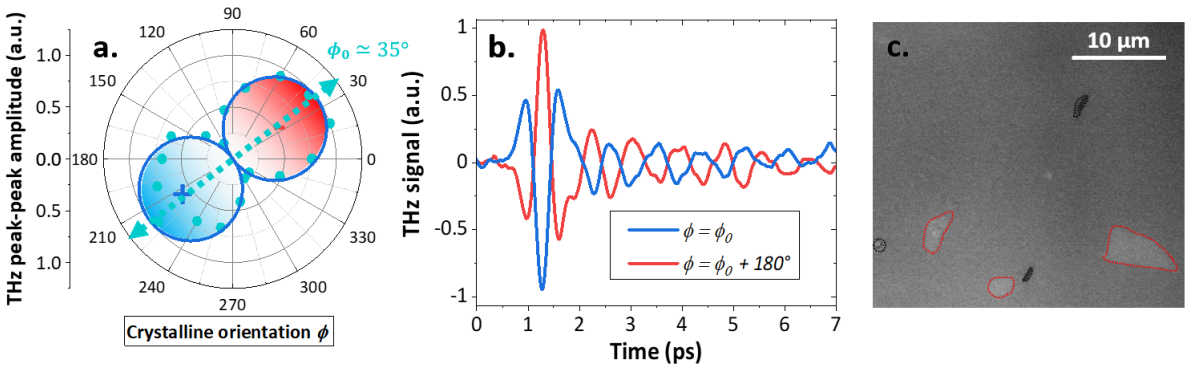

Figure 5.6: Crystallographic dependence of the THz emission in NiO(001)(10nm)/Pt(2nm). (a) THz peak-peak amplitude as a function of ϕ ranging from 0° to 360°. (b) Time traces of the THz phase reversal taken at $\phi = \phi_0$ and $\phi = \phi_0 + 180°$. (c) Kerr imagery of the large AFM quasi-mono domain states. The small white domains, of different orientation compared to the large mono grey domain, are highlighted in red. Defects appear in black.

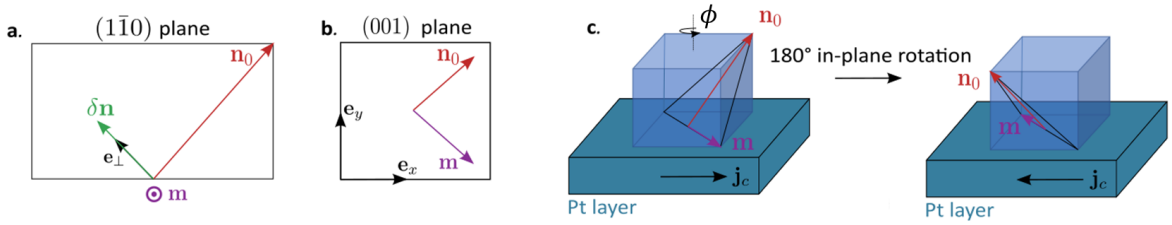

Figure 5.7: Projection of the initial Néel vector $\mathbf{n}_0$, its dynamical variations $\delta\mathbf{n}$ and the induced magnetization $\mathbf{m}$ in the (a) $(1\bar{1}0)$ and (b) (001) plane. (c) To understand the crystallographic dependence results, we represent the rotation of the Néel vector (thus induced magnetization) by ϕ=180°.

can be formulated: either *i*) a change of the magnetic texture in NiO(001) samples with a change of the magnetic damping γ_{AF} (under studies in M. Kläui's group, Johannes Gutenberg University, Mainz) or *ii*) a variation of the magneto-strictive coefficient λ_{11}, a parameter which holds a central role in the THz oscillations generation as we will discussed further below.

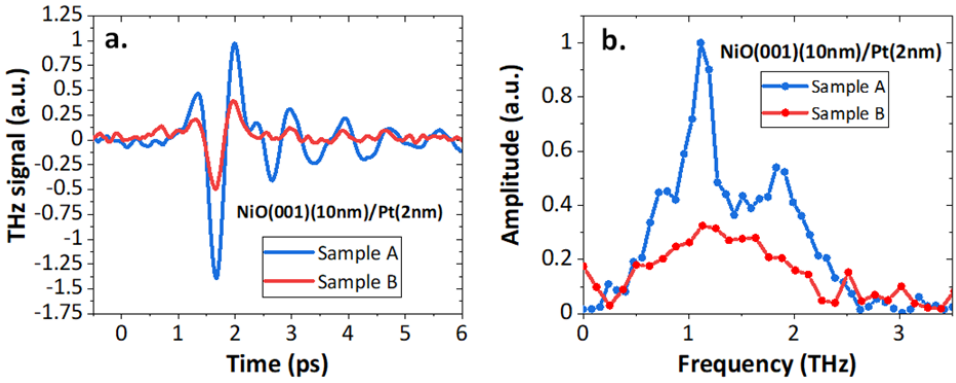

Figure 5.8: Impact of the magnetic quality on the THz emission. (a) THz signal in time-domain for sample A and sample B, grown respectively at low (0.7 sccm) and high (1.5 sccm) O_2 gas flow. (b) Spectra of the measured THz signal where the 1 THz oscillation mode could not be mapped in sample B.

Inverse spin Hall effect as the conversion and emission process. To address the emission process underlying in NiO/Pt thin films, we first replaced the Pt layer by a W layer presenting an opposite spin Hall angle sign as presented in Fig. 5.9a for a (111) sample. We observe a reversal of the THz polarization which is a hint for inverse spin Hall effect based emission following the THz

polarization rules presented in Section II.3.2. Besides, for a (001) thin film, we measured the THz emission by flipping the sample, *i.e.* the substrate now faces the pump in reflection geometry, as shown in Fig. 5.9b. We also measured a polarization reversal of the emitted THz radiation in favor of electrical dipolar radiation following the opposite spin current flow $j_s \rightarrow -j_s$, thus allowing to discard a magnetic dipolar radiation in those bilayers. This trend is also confirmed by ISHE in W for NiO(001) in Fig. 5.9c with a phase reversal of the 1.1 THz oscillations.

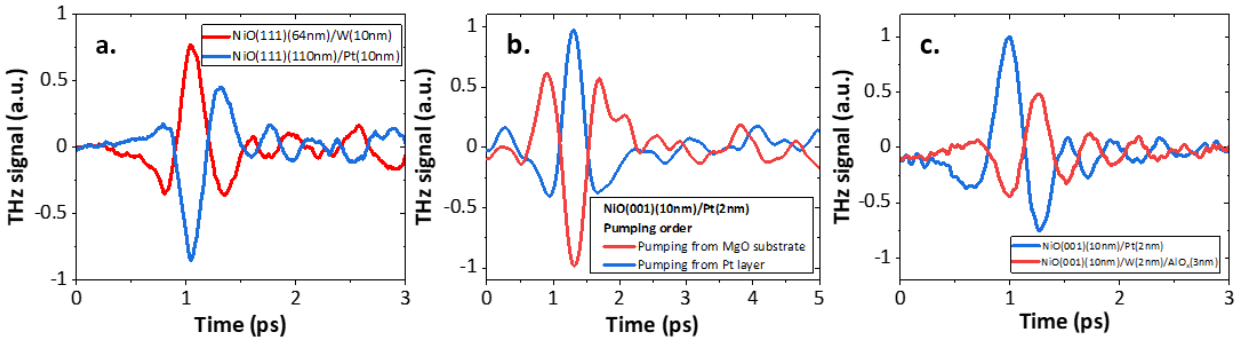

Figure 5.9: Evidencing ISHE as the THz emission origin in NiO/Pt. (a) Reported THz emission on NiO(111) by replacing the Pt(10nm) (blue) by W(10nm) (red). (b) THz signal by alternating the pump side, respectively from the MgO substrate side (red) and the Pt side (blue). (c) Reported THz emission on NiO(001) by replacing Pt(2nm) (blue) by W(2nm) (red). The THz polarization reversal points to ISHE-based emission.

The study of the emission mechanism is pursued by a fluence dependence of the THz emission as presented in Fig. 5.10a. We observe a linear dependence of the THz signal with the pump power addressing spin-charge conversion process as recovered in spintronic THz emitters [133]. We do not observe any saturation of the THz emission indicating that the NIR pump fluence range is below the damage threshold throughout the entire study: we are therefore in the linear regime. We also measured the THz emission from NiO/Pt bilayers as a function of an applied magnetic field. A magnetic field of 100-200 mT is applied in-plane with an angle θ from the optical table normal and is varied in the positions $\theta = \{0°, 90°, 180°\}$. The THz signal with an applied magnetic field is after compared to a reference signal measured without the application of a magnetic field. We observe that in all configurations, the THz signal is identical and that THz oscillations are recovered. This magnetic field insensitivity of the THz emission indicates that the emission is linked to the antiferromagnetic order (note that the values of the applied magnetic field are below the spin-flop transition, thus the antiferromagnetic order is unperturbed) and not to uncompensated moments that could easily switch direction under an applied magnetic field.

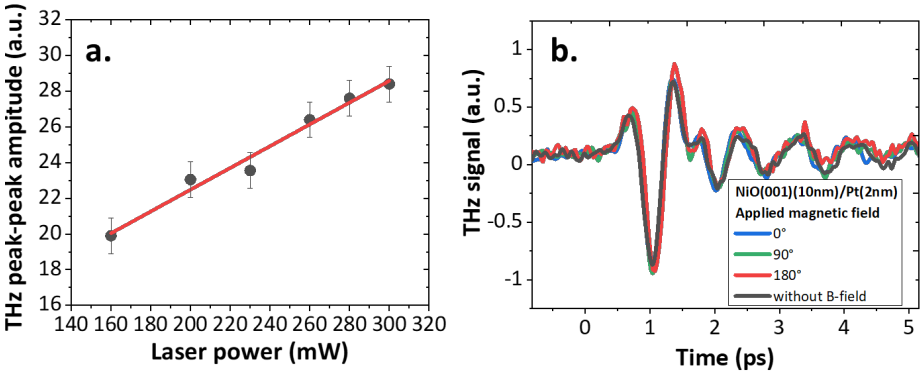

Figure 5.10: Fluence and magnetic field dependence. THz emission from NiO(001)(10nm)/Pt(2nm) as a function of (a) the pump fluence and (b) the applied magnetic field for $\theta = \{0°, 90°, 180°\}$ (or without a magnetic field).

Excluding proximity effects at the NiO/Pt interface. To exclude proximity effects in our current understanding of the phenomena, we realized a sample with a Cu(2nm) inserted between NiO and Pt to prevent induced magnetization on the first layers of Pt. The results are displayed in Fig. 5.11 and shows a enhancement of the THz signal in this sample, about an order of magnitude. It shows that the THz emission does not arise from the proximity-induced magnetism in Pt due to the presence of the Cu interlayer in the first case. To then understand the origin of the enhancement, we compared the signal with a THz emission from NiO(10nm)/Pt(4nm). The results are displayed in Fig. 5.11b and we still observe an enhancement factor about $\times 7$ between Cu(2nm)/Pt(2nm) and Pt(4nm) for the same thickness of metallic layers. Several hypothesis can enter into account: *i*) the thermal electronic conductivity of Cu ($\kappa_e^{\mathrm{Cu}} \simeq 396$ W.m^{-1}.K^{-1} for Cu *vs.* $\kappa_e^{\mathrm{Pt}} \simeq 66$ W.m^{-1}.K^{-1} for Pt) [72, 352], *ii*) the magnetic texture of NiO in contact with Cu, *iii*) the NiO/Cu interface that would have a better spin-mixing conductance and/or acoustic impedance matching compared to the one of NiO/Pt and finally *iv*) an enhanced propagation of both spin and strain waves, as Cu is known to be a good transport material for both quantities [72]. One must notice indeed in parallel that the spin diffusion length l_{sf} of Pt is around 2-3 nm. This last element could also include potentially a more efficient pump absorption by the additional Cu layer to transfer more energy to the lattice via electron-phonon interactions [72].

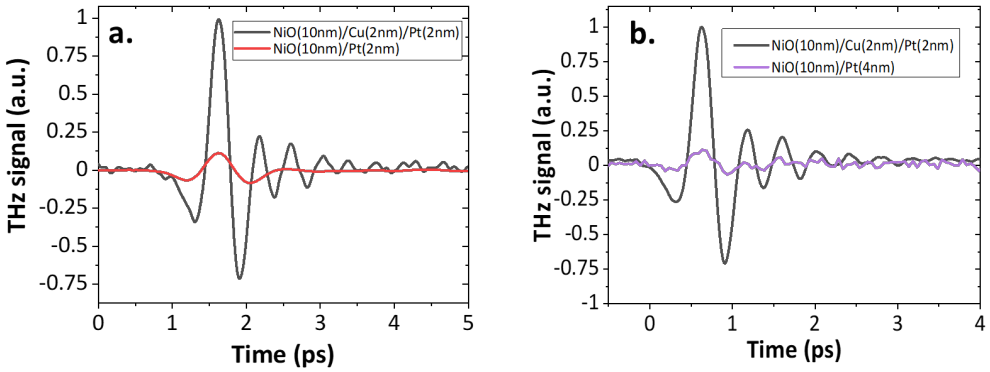

Figure 5.11: Excluding proximity effects in Pt. (a) Comparison of the THz emission from NiO(10nm)/Cu(2nm)/Pt(2nm) and NiO(10nm)/Pt(2nm). (b) To account for the additional Cu(2nm) metallic inset that could change the measured THz response, we also measure NiO(10nm)/Pt(4nm). The NiO orientation is (001).

Summary about the contribution from the Néel order and spin-charge conversion.

In summary, we have demonstrated that the THz emission is indeed of Néel order origin. The THz emission process is made via the inverse spin Hall effect in Pt giving us the opportunity to study the AFM order dynamics in NiO, as the small spin-current injected in Pt arise from the dynamics of the Néel vector $\delta\mathbf{n}(t)$. We can now focus on the origin of the spin current excitation in NiO/Pt bilayers via THz emission spectroscopy.

3.2 Magneto-optical torque: inverse Faraday and Cotton-Mouton effects.

To understand the origin of the magnon flow generation mechanisms in NiO/Pt bilayers, we have systematically studied the THz emission of NiO(t_{NiO})/Pt(2nm) by varying both the NiO thickness, ranging from 5 to 110 nm, and the NiO growth orientation, either on (001) or (111) orientations. Historically, research has first focused on the direct interaction between light illumination and NiO(111) magnetic moments to induce a change of a probe polarization which was thereafter detected [336, 353, 349, 338]. Qiu *et al.* [194] notably published a study on THz emission from NiO(111)/Pt bilayers in which the authors say that the spin current excitation is of

direct magneto-optical torque origin. In this part, we will evidence that different processes can be considered in the case of NiO/Pt bilayers with two (001) and (111) orientations to generate THz spin currents.

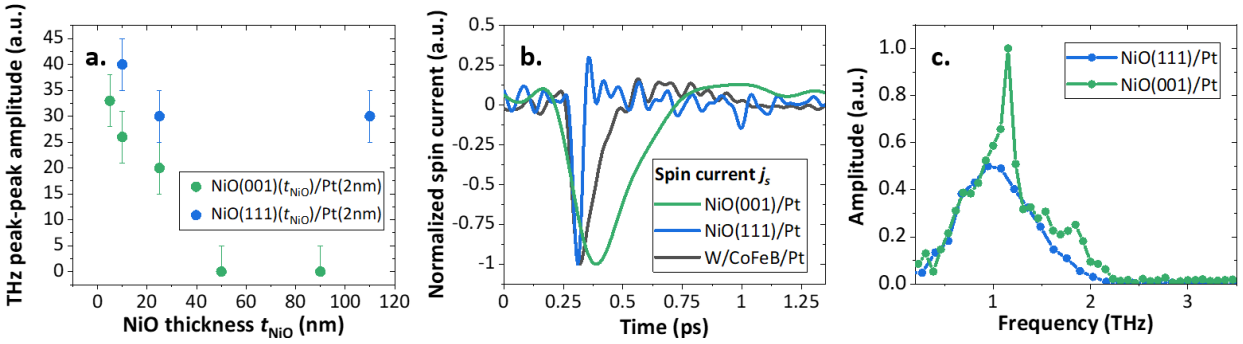

Figure 5.12: Impact on the NiO orientation and thickness on the THz emission in NiO/Pt bilayers. (a) THz peak-peak amplitude of NiO(t_{NiO})/Pt as a function of the NiO thickness t_{NiO}, ranging from 5 to 110 nm, and orientation ((001) or (111)). (b) Extracted THz spin current as a function of time for W/CoFeB/Pt (grey), NiO(111)/Pt (blue) and NiO(001)/Pt (green). (c) THz amplitude comparison between NiO(001)/Pt and NiO(111)/Pt.

Thickness dependence of the THz emission from NiO/Pt bilayers. We first extract the NiO(t_{NiO})/Pt thickness dependence of the THz emission as a function of the NiO orientation. Fig. 5.12a presents the NiO/Pt THz response for different thickness and growth orientations. We have measured the THz emission from NiO(t_{NiO})/Pt as a function of NiO thickness t_{NiO} (ranging from 5 to 110 nm) for both orientations. We extract from the thickness dependence that the emission amplitude decreases with the NiO thickness t_{NiO} in both cases. This evidences the crucial role of the interface to the emission via magnon contribution, but also possibly a change of the magnetic structure depending on the NiO thickness [350, 330]. One can note that, only magnons generated and propagating close to the interface with Pt would be efficiently converted whereas those travelling from longer lengthscale ($t_{NiO} > l_{sf}^{NiO}$) would scatter and result in a less efficient conversion. It can also be suggested the relaxation of the static strain in the high NiO thickness limit [350, 330]. Importantly, the mapping of the THz oscillations is only reported in (001) oriented samples of low thicknesses, typically 5 and 10 nm. As a comparison, we display in Fig. 5.12c the THz spectrum comparison between NiO(001)/Pt and NiO(111)/Pt where the absence of oscillations is reported in the latter. Another strong element is the measured THz amplitude at large NiO thicknesses. In the case of (001) oriented samples, the THz signals drops to zero very quickly whereas for (111) orientation, we map a negligible thickness dependence of the THz emission, still sizeable at large NiO thickness, presently NiO(111)(110nm)/Pt(10nm). This is also to put aside with the reported presence (*resp.* absence) of 1.1 THz oscillations in (001) (*resp.* (111)) oriented NiO that we discuss in the next section. At this point, the THz sizeable emission at large thickness on NiO(111)(110nm)/Pt(10nm) could potentially be explained by optically-dependent excitation process which would in principle be independent on the NiO thickness, contrary to (001) grown samples.

Ultrafast spin-current extraction on NiO/Pt bilayers. Complementary to those measurements, we performed THz spin current extraction from the two (001) and (111) orientations, compared to W/CoFeB/Pt metallic spintronic reference as displayed in Fig. 5.12b. The spin-current extraction method is detailed in Section III.2.4 and in Refs. [250, 354] and represents the integration of the THz electric field. Typically, the spin current transients present two noticeable timescales: an ultrafast spin current rise time τ_{rise} and afterwards a spin current decay with time τ_{decay}. Thz THz spin current extraction is therefore a useful technique to extract the dynamical spin current properties and identify the underlying excitation processes. We report in Table V.2

the extracted spin current decay and rise times for NiO(001)/Pt, NiO(111)/Pt and reference sample W/CoFeB/Pt. Note that the minimal detection time is <50 fs (limited by the pump pulse duration) and shorter dynamics could thus not be resolved.

System	NiO(001)/Pt	NiO(111)/Pt	W/CoFeB/Pt
τ_{rise} (fs)	200-250	<50	70
τ_{decay} (fs)	300	<50	250

Table V.2: Extracted spin current dynamics from NiO(001)/Pt, NiO(111)/Pt and W/CoFeB/Pt.

It is surprising that we observe different trends for the two NiO/Pt samples of different orientations. First, in standard metallic STEs such as W/CoFeB/Pt, the rise time is typically govern by the excitation process and the ultrafast demagnetization time. Moreover, the decay time is typically ruled out by the relaxation processes, for instance the spin-electron relaxation timescale [244]. In NiO(111)/Pt, both rise and decay time are very short, of the order of the resolution limit, which would indicate an instantaneous system response. Only few effects have such quasi-instantaneous time response and we would relate this here to off-resonant Raman-type torque (that we would call optical-spin torque) as previously reported in NiO [353, 336]. It is important to note that the pump energy (1.5 eV) is below the bandgap of NiO, excluding multi-photon processes. In NiO(001)/Pt, however, the rise and decay times are build up on longer timescales which would address thermally-mediated effects, for instance via the pump photon absorption in Pt and related thermal heating [354].

Pump polarization dependence on NiO/Pt thin films depending on their orientations. We first systematically study the impact of the pump polarization on the THz emission in both orientations (111) and (001) as respectively presented in Fig. 5.13 and 5.14. Our pump polarization study consists in collecting the THz emission as a function first *i*) of the linear polarization angle α and after *ii*) of the ratio between the linear pump and the circular pump polarization of helicity $\sigma_{\pm}$ respectively for left and right-handed polarizations (details in Section III.2.1).

- NiO(111) pump polarization dependence.

On the (111) oriented NiO/Pt bilayers, we measure a THz signal dependent on the pump polarization. For the linear polarization, the THz peak amplitude follows a $\cos(2\alpha)$ dependence and the THz signal drops by half while pumping the NiO(111)/Pt bilayers by a circularly polarized pump. Moreover, no trace of the 1.1 THz oscillation mode could be detected on the (111) oriented NiO. This result is in agreement with the report of Qiu *et al.* [194] about optically-mediated effects.

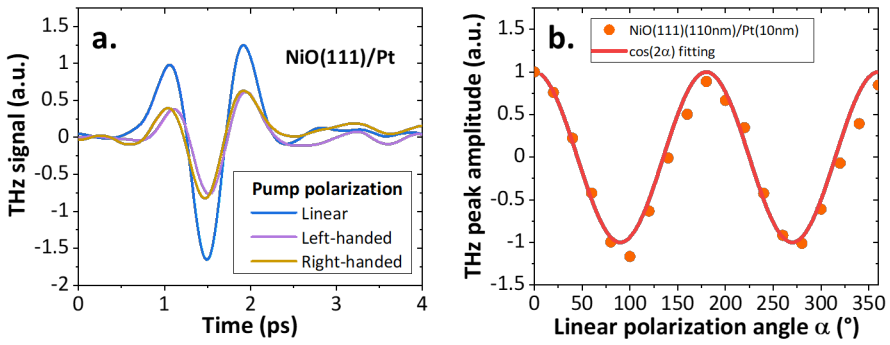

Figure 5.13: Polarization dependent THz signal in (111) oriented films. (a) THz signals for linear (blue) and circular pump polarization (purple and yellow) alongside the (b) THz peak-peak amplitude as a function of the linear pump polarization (angle α) in NiO(111)(110nm)/Pt(10nm).

- NiO(001) pump polarization dependence.

On the (001) oriented NiO/Pt bilayers, a drastically different behaviour is mapped as a function of the pump polarization. We observe that, for both linear pump polarization rotation (angle α) and circular pump polarization, an pump polarization independent THz signal is measured. This is an unexpected behaviour, and has not been reported in the literature in NiO/Pt bilayers. This would address a thermal origin of the excitation process in (001) oriented NiO compared to the optical-dependent excitation process in NiO(111) samples.

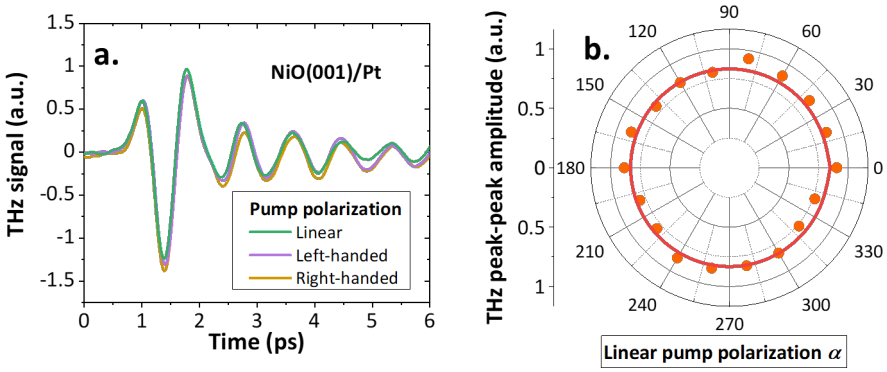

Figure 5.14: Polarization independent THz signal in (001) oriented films. (a) THz signals for linear (green) and circular pump polarization (purple and yellow) alongside (b) the THz peak-peak amplitude as a function of the linear pump polarization (angle α) in NiO(001)(25nm)/Pt(2nm).

Discussions of the light-matter interactions in NiO/Pt bilayers. To summarize, from the results of all the measurements we have presented previously, we identified two different mechanisms to the spin current excitation. The first mechanism, happening on (111) oriented samples, presents a pump-polarization dependence and ultrashort dynamics, which is therefore compatible with an off-resonant optical-spin torque via the inverse Cotton-Mouton effect (Fig. 5.15) as captured in the literature [353, 336]. The second mechanism, present only on (001) oriented samples, seems to originate from a thermal build-up due to the larger spin current dynamics. Regarding the origin of the excitation mechanism in (111) oriented NiO, we can first discard the inverse Faraday effect (IFE) involving circularly polarized light for several reasons. First, *i*) the linear pump polarization contribution to the THz emission is larger than for circular pump polarization, and *ii*) we do not report any change of THz phase in the case of left or right-handed circular pump polarization. We can then associate the pump polarization dependence on (111) orientation to the so-called inverse Cotton-Mouton effect (ICME).

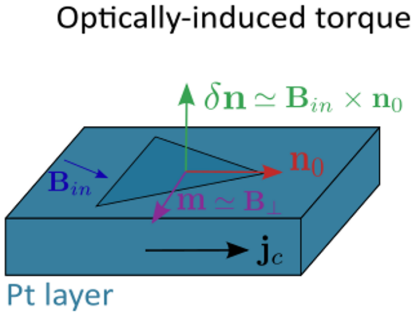

Figure 5.15: Symmetry of the optically-induced torque. Non-zero optically-induced torque in NiO(111).

To account for the relative contribution of the light-matter interaction in NiO/Pt bilayers, we physically describe the interaction of an external force $\mathbf{\Gamma}$ induced by the interaction with the AFM Néel vector $\mathbf{n}$ via its interaction Hamiltonian:

$$\mathbf{\Gamma} = \frac{\partial \mathcal{H}_{\text{int}}}{\partial \mathbf{n}} \tag{E5.5}$$

In the case of inverse Cotton-Mouton effect (ICME), the light-matter Hamiltonian is phenomenologically described by:

$$\mathcal{H}_{\text{int}} = g_{ijkl} n_i n_j E_k E_l^* \quad \overset{(E5.5)}{\Rightarrow} \quad \mathbf{\Gamma}_i^{\text{ICME}} = g_{ijkl} n_{0j} E_k E_l \tag{E5.6}$$

where g_{ijkl} are the phenomenological coefficients of the fourth rank tensor that describes the light-matter interaction, $E_k E_l^*$ is the pump intensity polarized along $E_k E_l^*$ and $n_i n_j$ are the component of the Néel vector. Using the Voigt notation and choosing the frame $\mathbf{e}_x \parallel [100]$, $\mathbf{e}_y \parallel [010]$ and $\mathbf{e}_z \parallel [001]$, the non-trivial components of the g-tensor are $g_{11} = g_{22} = g_{33}$, $g_{44} = g_{55} = g_{66}$ and $g_{12} = g_{23} = g_{31}$. The phenomenological light-matter interaction tensor associated with ICME can thus be written as:

$$g = \begin{bmatrix} g_{11} & g_{12} & g_{12} & 0 & 0 & 0 \\ g_{12} & g_{11} & g_{12} & 0 & 0 & 0 \\ g_{12} & g_{12} & g_{11} & 0 & 0 & 0 \\ 0 & 0 & 0 & g_{44} & 0 & 0 \\ 0 & 0 & 0 & 0 & g_{44} & 0 \\ 0 & 0 & 0 & 0 & 0 & g_{44} \end{bmatrix} \tag{E5.7}$$

Voigt notation.

The Voigt notation permits to reduce the number of indices for a symmetrical tensor like the phenomenological light-matter interactions g_{ijkl} or the phenomenological magnetostrictions λ_{ijkl} as discussed later. For instance, the initial tensor g_{ijkl} is rewritten g_{IJ} with I, J indices ranging now from 1 to 6.

In case of (111) NiO orientation, we have $n_{0j} \propto \mathbf{e}_x + \mathbf{e}_y + \mathbf{e}_z$ and $\mathbf{e}_\perp$ being the interface normal. For (001) NiO orientation, we have $n_{0j} \propto \mathbf{e}_z$ and $\mathbf{e}_\perp \propto \mathbf{e}_x$. The torques are thus expressed as:

$$\begin{cases} \Gamma \cdot \mathbf{e}_\perp = \dfrac{E_{\text{in}}^2}{3\sqrt{2}} \left(g_{44} + (3g_{44} - 2g_{11} + 4g_{12}) \cos(2\alpha)\right) & \text{for (111)} \\ \Gamma \cdot \mathbf{e}_\perp = \dfrac{E_{\text{in}}^2}{3\sqrt{2}} \left(2(g_{11} - 2g_{12}) + 4g_{44} \sin(2\alpha)\right) & \text{for (001)} \end{cases} \tag{E5.8}$$

From the two expressions of the ICME, several elements can be raised. First, it comes that the ICME is linear with the pump power $P_{\text{in}} = E_{\text{in}}^2$, in line with our experiments. Secondly, it can be seen that the two ICME contributions are mathematically non-zero in both orientations. However, our experiment points out to a negligible ICME in (001) oriented films, which observations are also in line with reports in the literature [336, 194]. Therefore, we would assume the coefficient g_{44} to be smaller compared $(g_{11} - 2g_{12})$ which gives the isotropic contribution in (001) oriented films in NiO and pump-dependent signal in (111).

Discussions about the optically-induced contribution.

We have here addressed the ICME excitation mechanism in NiO/Pt which depends on the orientation of the NiO layer, either (001) or (111). After identifying experimentally drastically different behaviours for the pump polarization dependence on the THz emission, accompanied by the different trends for both thickness and spin-current dynamics for two NiO orientations, we explain the THz spin current excitation in (111) films via a phenomenological description of the ICME as recovered in the literature [353, 336]. Although we predict a non-zero ICME for both orientations, we expect a smaller amplitude of the ICME for (001) orientation as the pump polarization dependent part of the ICME is govern only by g_{44}. This is not the case for (111) orientation where a combination of all the phenomenological tensor rules the polarization-dependent part of the ICME. We can thus assume this coefficient to be small compared to $(g_{11} - 2g_{12})$, which would explain the absence of polarization-dependent signal in (001) oriented films. Besides, the hypothesis of the ICME could not explain the presence of oscillations in NiO(001)/Pt. The conclusion is thus that we could not discard the ICME in (001) films but estimate that the polarization-independent part of the ICME is small compared to a thermally-mediated effect.

3.3 THz dynamics driven by ultrafast thermal excitations.

3.3.1 Ultrafast lattice response upon optical pumping.

While the spin current excitation mechanism in (111) films via off-resonant optical-spin torque has been clearly identified by our measurements, we now discuss the excitation mechanism in (001) oriented films. To deepen our comprehension on this supposed thermally-mediated mechanism, we studied the lattice dynamical response in collaboration with the group of M. Bargheer (Potsdam University). Indeed, in insulators, the heat transport is governed by the phonon propagation due to the absence of conduction electrons, contrary to the diffusive electronic heat in metals.

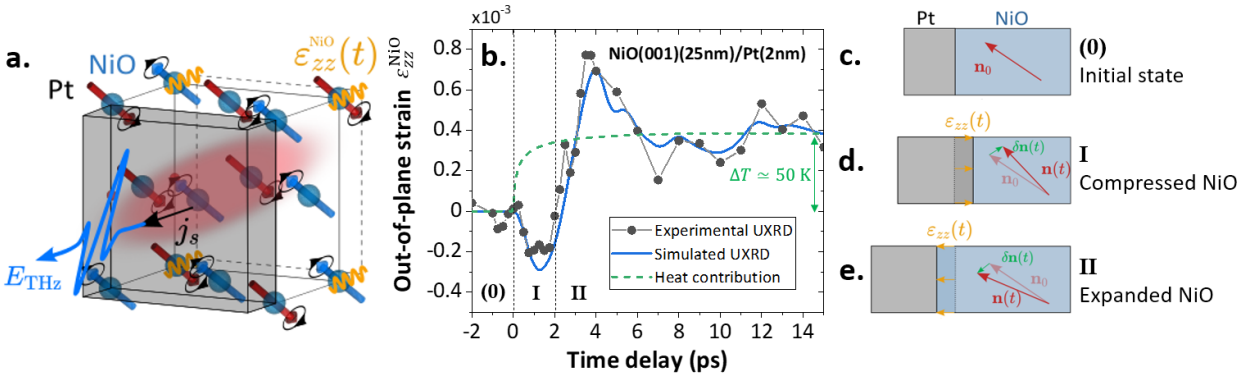

Figure 5.16: Lattice dynamics in NiO(001)/Pt after a femtosecond NIR pump excitation. (a) Scheme of the lattice dynamics in NiO(001)(25nm)/Pt(2nm) bilayer, where the out-of-plane strain plays a major role. (b) Measured mean NiO out-of-plane strain $\varepsilon_{zz}^{NiO}(t)$ as a function of time. A one-dimension temperature model allows to simulate the magneto-striction and heat contributions *vs.* time. The sketches on the right panel present respectively the NiO and Pt layers in (c) the initial conditions, (d) in case of contraction of NiO and (e) under expansion of NiO.

We studied the time-resolved response of the phonons experimentally by probing the lattice using ultrafast X-ray diffraction (UXRD) after a NIR pump of the NiO(001)(25nm)/Pt(2nm) bilayer. The experimental method is described more precisely in Annex. A13 and Refs. [352, 355, 356]. To that extend, we have followed the intensity of the NiO(004) recip-

rocal space peak to track the variation of the out-of-plane strain $\varepsilon_{zz}(t) = \Delta q_z/q_z$ as a function of time as presented in Fig. 5.16. The measured small amplitude for NiO(25nm) prevents for measuring thinner NiO samples where the oscillations have been recorded but we can extrapolate the phonon transport to NiO(5nm) and NiO(10nm) thicknesses.

We observe from the UXRD measurements three interesting features (grey curve): *i*) we first measure a negative out-of-plane strain which denotes a reduction of the out-of-plane lattice constant *i.e.* a contraction of the lattice up to 2 ps. Then, *ii*) the out-of-plane strain is positive (and increasing) which indicates an expansion of the lattice up to 4 ps. After 4 ps, *iii*) the lattice constant is still extended but at a slower rate as far as the system go towards equilibrium. However, this response at longer timescales is superimposed by an offset value (around 0.4×10^{-3}) which would decay on much longer timescales (>0.1 ps) [357] and which would correspond to a temperature increase in NiO about 50 K mediated by incoherent phonon propagation.

To analyze this experiment, we simulated the total strain response by using the 1D *udkm1Dsim* Python toolbox [358] (details are available in Annex A13). We were able to identify two different responses to the phonon transport. One first evidences a coherent strain wave generated from the Pt layer initial expansion. The time profile is extracted from the strain map (Annex A13) averaged over the NiO layer thickness: this is the blue curve of Fig. 5.16. Besides, the second contribution owns to the thermal build-up in NiO over longer timescales mediated by incoherent phonon propagation (inelastic scattering in the Pt which then transfers the energy to the system). The time profile of this contribution modelled in the temperature map is displayed in dotted green line in Fig. 5.16.

Briefly, we experimentally measured a strain wave generated from hot Pt lattice expansion and launched into NiO layer after the NIR pump. Strain and heat transport simulations in the bilayers precise this ultrafast strain profile (Annex A13). It is composed of a strain wave mediated by coherent phonon propagation and is superimposed with a incoherent phonon propagation inducing a temperature elevation. We have now proven that an ultrafast strain wave propagates through NiO, scene of sizeable magneto-striction [350]. We can now start to estimate those magneto-strictions before deducing the dynamics of the Néel vector using the evaluated strain and temperature maps.

3.3.2 Thermo-magneto-elastic coherent response of NiO/Pt bilayers.

The use of magneto-striction at the ultrafast timescales to tune the magnetic properties of materials has been reported recently in antiferromagnetic NiO single crystals [359, 360] or in magnetic insulator Bi:YIG [361] as a function of the pump energy. In this part, we assess the major role of the metallic Pt capping into launching a strain wave of high amplitude. Before modelling the system response using the profile of the strain wave and the heat contribution, we present in this part the symmetry of such thermo-magneto-elastic effect (TME) in NiO, that can be phenomenologically described as:

$$\mathcal{H}_{\text{int}} = \lambda_{ijkl} n_i n_j \varepsilon_{kl} \quad \overset{(E5.5)}{\Rightarrow} \quad \mathbf{\Gamma}_i^{\text{TME}} = \lambda_{11} n_{0z} \varepsilon_{zz}(z,t) \mathbf{e}_{\perp z} \tag{E5.9}$$

where λ_{ijkl} is the magneto-elastic coefficient following the same structure as g_{ijkl} and ε_{zz} is the out-of-plane strain launched by the pump heating in Pt. The total out-of-plane strain can be assimilated to a coherent part (strain wave) and an incoherent part (thermal changes) via $\varepsilon_{zz} = \varepsilon_{zz}^{\text{sw}} + \varepsilon_{zz}^{\text{th}}$ with $\varepsilon_{zz}^{\text{th}} = \zeta \Delta T(z,t)$ and ζ represents a material-dependent expansion/dilatation coefficient. The magneto-elastic tensor shrinks to λ_{11} in the case of strain wave launched in the direction normal to the interface. By symmetry considerations displayed in Fig. 5.17, we have:

$$n_{0z} \cdot \mathbf{e}_z = 0 \quad \text{for (111)} \quad \text{and} \quad n_{0z} \cdot \mathbf{e}_z = 0.46 \quad \text{for (001)} \tag{E5.10}$$

The TME torque therefore vanishes in case of (111) oriented NiO, in line with experimental results. In case of (001) orientation, the TME torque is non-zero and the induced tilt of the Néel vector (in the linear regime) can be estimated via:

$$\beta = \arccos\left(\mathbf{n}(t)\cdot\mathbf{e}_z\right) = \frac{\varepsilon_{zz}^{\mathrm{NiO}}\lambda_{11}\gamma}{2\gamma_{\mathrm{AF}}} \tag{E5.11}$$

with $\gamma_{\mathrm{AF}} = \gamma\alpha_{\mathrm{AF}}H_{\mathrm{E}}$. The first strain wave contribution is the leading contribution to the magneto-acoustic strain allowing dynamical magneto-striction in NiO. Typically in NiO thin films, Schmitt *et al.* [346] have reported in the static range an experimental value of the out-of-plane magneto-striction coefficient about $\lambda_{11} = 3\times10^{7}$ J.m^{-3}. The measured maximum strain wavefront is about $\varepsilon_{zz}^{\max} = 0.6\times10^{-3}$ for a fluence of 10 mJ.cm^{-2} (as extracted from Fig. 5.16). In a first approximation, the strain scales linearly with the fluence which thus gives a wavefront strain of $\varepsilon_{zz}^{\max} = 6\times10^{-5}$ for the fluence used in THz spectroscopy (10 µJ.cm^{-2}). We estimate the tilt of the Néel vector about $\beta = 0.3°$ for an out-of-plane strain launched from Pt in NiO. This corresponds to a dynamical magnetization given by $\Delta\mathbf{m} = (\mathbf{n}_0\times\delta\dot{\mathbf{n}})/(\gamma H_{\mathrm{E}})$, estimated around 1 A.m^{-1}.

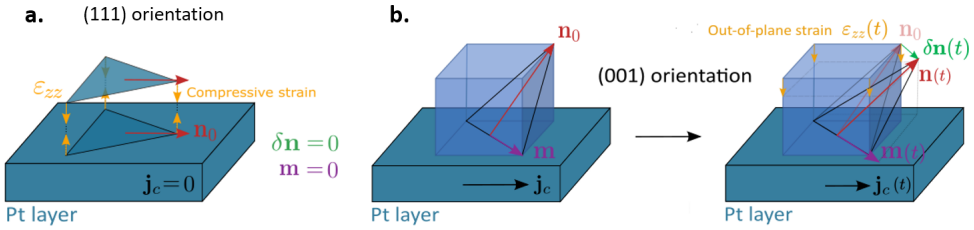

Figure 5.17: Symmetry of the strain-induced thermo-magneto-elastic effect in case of (111) and (001) oriented NiO. (a) Vanishing strain-induced torque as the projection of n_{0z} is zero in case of NiO(111). (b) In the case of (001) orientation, under excitation, the Néel vector $\mathbf{n}(t) = \mathbf{n}_0 + \delta\mathbf{n}(t)$ is reduced due to magneto-strictions from the bipolar strain-wave $\varepsilon_{zz}(t)$ and thus launches a dynamical magnetization $\mathbf{m}(t)$ to be converted via ISHE in Pt.

Modelling the system response using ultrafast magneto-strictions. Up to now, we have demonstrated the presence of ultrafast strains inducing strong magneto-strictions in NiO. It typically launches a precession of the Néel vector with a tilt estimated about $\beta = 0.3°$.

To understand how this excitation profile can generate combined narrow 1 THz and broadband response, we modelled the magnetization dynamics by considering the dual system response via both strain wave propagation and temperature contributions as input for Eq. (5.5). Two elements have been considered in this model. First, we include the important magneto-striction effect for NiO, *i.e.* the tilt of magnetic order under strain application. It is to be noted that we do not consider a potential variation of the exchange field $H_{\mathrm{E}}(T)$ and peak frequency $\omega_{\mathrm{AF}}^2(T)$ as a function of temperature, as we work at $T \ll T_{\mathrm{N}}$. The material parameters of NiO have carefully been chosen with a Gilbert damping of $\alpha_{\mathrm{AF}} = 0.006$ corresponding to $\gamma_{\mathrm{AF}}/2\pi$ = 0.16 THz, the high-frequency mode is $\omega_{\mathrm{AF}}/2\pi$ = 1.08 THz and with a magnon velocity of $c = 10$ nm.ps^{-1}.

We present respectively in Fig. 5.18a and Fig. 5.18b the magneto-acoustic strain and temperature contribution on the antiferromagnetic-based THz emission. We call those contributions E_{MAS} and E_{T}, respectively. We observe that both contributions present a large amplitude near the high-frequency mode of NiO around 1.1 THz and we even distinguish the second-harmonic of this mode in the heat contribution near 2.2 THz. We performed a ponderated sum between those two contributions in the form $E_{\mathrm{TOT}} = aE_{\mathrm{MAS}} + bE_{\mathrm{T}}$ to directly model the measured THz signal as

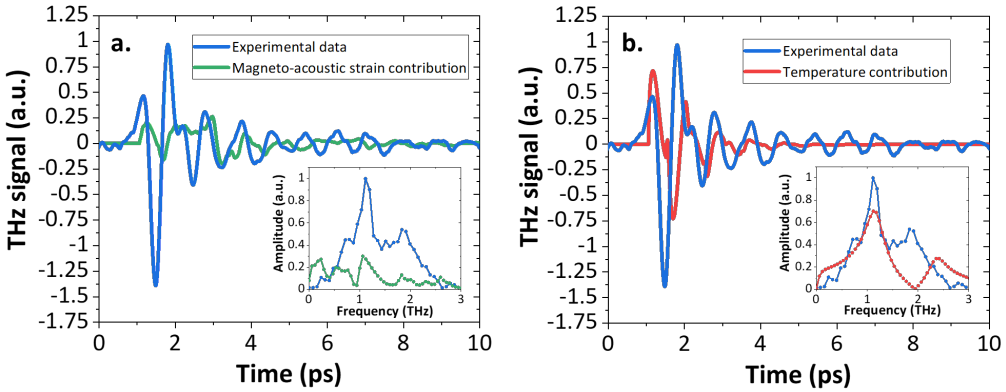

Figure 5.18: Magneto-acoustic stain and temperature contributions to the THz emission in NiO/Pt. (a) Calculated THz magneto-acoustic strain contribution E_{MAS} (green) compared to the experimental THz signal (blue), presented in the time-domain. The inset presents the normalized calculated THz magneto-acoustic contribution E_{MAS} in the frequency domain. (b) Calculated THz contribution E_{T} (red) compared to the experimental THz signal (blue), presented in the time-domain. The inset presents the normalized calculated THz contribution E_{T} in the frequency domain. Modelling for NiO(001)(10nm)/Pt(2nm).

displayed in Fig. 5.19. It appears a qualitative agreement between the experimental data and the modelling, reproducing both the broadband and narrowband contribution with the oscillations in time. The fitting points to the following values of $a = -0.3$ and $b = 0.7$ for the magneto-acoustic and temperature contributions, respectively. It seems that the contributions associated with the temperature to the Néel vector dominates the broadband response, but also plays a role in the response at 1.1 THz.

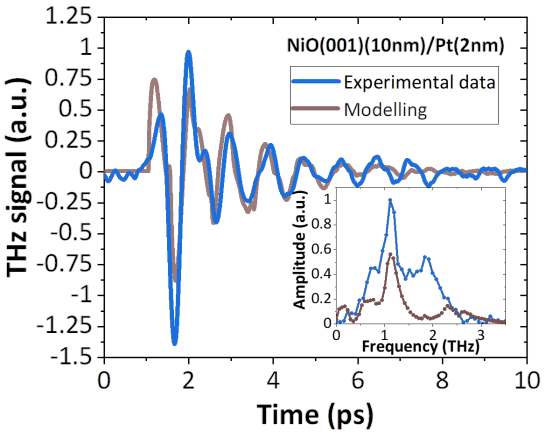

Figure 5.19: Magnetization dynamics modelling compared to the experimental signal. THz signal (in blue) compared to the magnetization dynamics modelling (brown) which reproduces qualitatively the THz response in (a) the time-domain and (b) normalized in the frequency domain.

Positioning our study with the current research on ultrafast magneto-strictions. We also report a similar study by our collaborators at Johannes Gutenberg University (Mainz) and Kaiserslautern Technische Universität [357] where the authors measured a subpicosecond reduction of the Néel vector in NiO/Pt bilayer upon NIR pump, a behaviour which is not recovered on bare NiO samples. A similar understanding in the role of Pt electronic heating and the efficient interfacial transfer of energy (directly in the spin reservoir or via phonon interactions) is also pointed out as central in an efficient spin excitation. It also illustrates the efficiency of ultrafast thermally-

driven control of the AFM order including magneto-striction and potentially spin-Seebeck related effects that we will discuss in the next section.

Summary about the strain-induced contribution.

In summary, we have highlighted the role and importance of the ultrafast lattice response to the Néel dynamics. We modelled this ultrafast spin-phonon response and obtained a qualitative agreement between the experimental data and the simulations of the out-of-equilibrium magnetization dynamics in NiO. We thus evidenced the respective role of the coherent strain wave, which induces a direct thermo-magneto-elastic effect, and of the incoherent phonon propagation on the magnetization dynamics in NiO. These results further open discussions on the heat contributions, and perspectives for ultrafast control of the AFM order.

3.3.3 Uncoherent phonon propagation and thermal effects.

We now focus on the uncoherent phonon propagation contributions taking the form of temperature changes and potential spin-Seebeck effects. As mentioned previously, we can discard the the temperature dependence of the exchange field, anisotropy field and resonant frequencies for $T \ll T_{\mathrm{N}}$. The discussions now focus on the spin-Seebeck contributions to the THz emission.

Linear spin-Seebeck effect. We first address the potential conventional (linear) spin-Seebeck effect [362, 363] in NiO/Pt bilayers. The presence of a temperature imbalance $\Delta T = T_{\mathrm{Pt}} - T_{\mathrm{NiO}}$ between hot Pt and cold NiO creates an out-of-plane temperature gradient ∇T which would result in a spin current generation proportional to:

$$j_s^{\mathrm{SSE}} \propto S_{\mathrm{SSE}} \nabla T \tag{E5.12}$$

where S_{SSE} is called the spin-Seebeck coefficient conventionally given in pA.cm.K^{-1}. It is important in the context of NiO/Pt to differentiate between this linear spin-Seebeck effect [364], illustrated in Fig. 5.20, and the non-linear spin-Seebeck effect, associated to ultrafast interfacial spin torques induced by the thermal gradient ∇T [354].

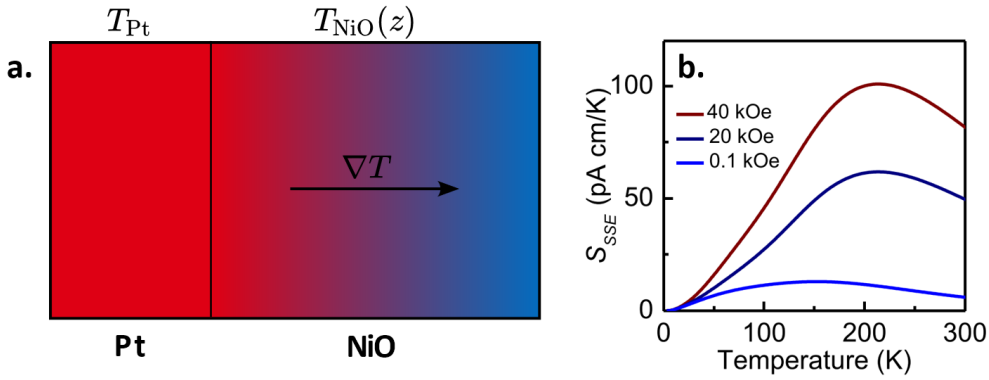

Figure 5.20: Linear spin-Seebeck effect in NiO/Pt. (a) Temperature gradient at the interface between hot Pt and cold NiO generating an interfacially-normal spin current in the NiO layer. (b) Calculated spin Seebeck coefficient in NiO/Pt as a function of temperature. Right panel is adapted from Ref. [364].

First, the linear spin-Seebeck effect needs the presence of an interfacial temperature gradient which is the case in NiO/Pt system. At zero magnetic field, the two magnon branches of NiO (low and high frequency modes) degeneracy is already lifted (explaining the small signal at magnetic fields as low as 0.1 kOe as shown in Fig. 5.20b), the difference in population density

between the two modes can lead to a non-zero magnon spin current as calculated for reasonable excitations in Fig. 5.20b as a function of temperature [365, 364].

In the case of an easy-axis antiferromagnet (like $KCoF_3$), the two magnon modes are degenerated at zero magnetic field, thus preventing a contribution from the SSE. To induce a contribution, a magnetic field needs to be applied. This lifts the degeneracy, and the magnon branches energy gap $\Delta\varepsilon(H)$ evolves linearly with H as shown schematically in Fig. 5.2b. Recently, Kholid *et al.* [366] observed in $KCoF_3$/Pt a temperature-dependent THz emission, with maximal SSE around the Néel temperature. Far below the Néel temperature, the SSE signal increases linearly with the fluence up to a saturation value. The process of the linear spin-Seebeck effect can be viewed in terms of Fig. 5.21. Indeed, the pump-induced effective electronic temperature T_e scales linearly with the increase of the pump fluence (corresponding to the spreading of the electronic population in energy as $\mu_e \propto \Delta T_e$ with μ_e the chemical potential) so that magnons with higher energies ($\varepsilon > \varepsilon_0$) can be accessed when increasing the pump fluence and then contributes to the magnonic current. At high pump fluences (or close to the Néel temperature), the bands are fully populated and the signal saturates, potentially transitioning to the case of the non-linear spin-Seebeck contribution discussed below.

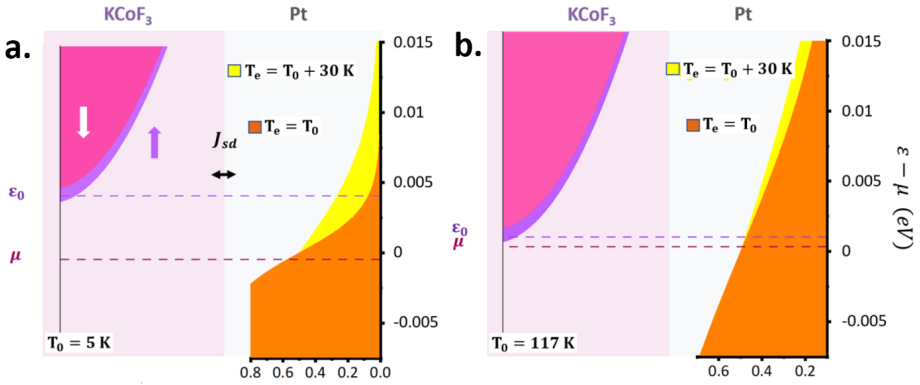

Figure 5.21: Addressing the sub-picosecond spin-Seebeck effects in antiferromagnets. (a-b) Scheme of the band diagram of $KCoF_3$/Pt bilayer, respectively below and close to the Néel transition T_N. The photo-excited electronic population (in yellow is the electronic population spreading in energy) induces an interfacial transfer of the energy via the exchange J_{sd} exciting the spin-splitted magnon population of $KCoF_3$ (pink and violet), only in the temperature region where $\varepsilon_0 > \mu_e$ (where μ_e is the chemical potential), either induced by the antiferromagnet temperature T or by the equivalent fluence-increased electron energy spreading. This model can be seen as the linear spin-Seebeck effect. Adapted from Ref. [366].

Non-linear spin-Seebeck effect. Secondly, we discuss the eventuality of a non-linear spin-Seebeck effect in NiO/Pt as illustrated in Fig. 5.22 which accounts for the ultrafast interfacial spin torque induced by the thermal gradient ∇T. For this purpose, we follow the transient spin-Seebeck derivations proposed by Seifert *et al.* [354] in YIG/Pt, and recently adapted by Kholid *et al.* [366] in $KNiF_3$. The torque induced by the spin fluctuations $\mathbf{s}_{\mathrm{Pt}}$ in the Pt layer can be written as:

$$\boldsymbol{\Gamma}_{\mathrm{SSE}} = H_{\mathrm{curr}} \left(\mathbf{s}_{\mathrm{Pt}} \times \mathbf{n}\right) \tag{E5.13}$$

where H_{curr} is a phenomenological constant depending mostly on the NiO/Pt interface. In average, the spin fluctuations are zero, *i.e.* $\langle \mathbf{s}_{\mathrm{Pt}}(t) \rangle = 0$, however they can generate non-zero fluctuations of the Néel vector $\delta\mathbf{n}(t)$. The spin-torque can therefore be written as $\delta\mathbf{n}(t) \propto \mathbf{s}_{\mathrm{Pt}}(t) \times \mathbf{n}_0$ and up to a second order term in $\delta\mathbf{n}(t)$, we have in the time-domain ($t' > t$):

$$\begin{aligned}
\boldsymbol{\Gamma}_{\mathrm{SSE}}(t') &= H_{\mathrm{curr}}(\mathbf{s}_{\mathrm{Pt}}(t') \times \mathbf{n}(t')) && \text{(E5.14)}\\
&= H_{\mathrm{curr}}(\mathbf{s}_{\mathrm{Pt}}(t') \times \mathbf{n}_0 + \mathbf{s}_{\mathrm{Pt}}(t') \times \delta\mathbf{n}(t')) && \text{(E5.15)}\\
&= H_{\mathrm{curr}}(\mathbf{s}_{\mathrm{Pt}}(t') \times \mathbf{n}_0 + \mathbf{s}_{\mathrm{Pt}}(t') \times \mathbf{s}_{\mathrm{Pt}}(t) \times \mathbf{n}_0) && \text{(E5.16)}\\
&= H_{\mathrm{curr}}\langle \mathbf{s}_{\mathrm{Pt}}(t') \times \mathbf{n}_0(\mathbf{s}_{\mathrm{Pt}}(t) \cdot \mathbf{n}_0)\rangle && \text{(E5.17)}
\end{aligned}$$

In the frequency domain, it comes:

$$\begin{aligned}
\boldsymbol{\Gamma}_{\mathrm{SSE}}(\omega) &= H_{\mathrm{curr}}(\mathbf{s}_{\mathrm{Pt}}(\omega) \times \mathbf{n}(\omega)) && \text{(E5.18)}\\
&= H_{\mathrm{curr}}(\mathbf{s}_{\mathrm{Pt}}(\omega) \times \mathbf{n}_0 + \mathbf{s}_{\mathrm{Pt}}(\omega) \times \delta\mathbf{n}(\omega)) && \text{(E5.19)}\\
&= \frac{\gamma^2 H_{\mathrm{curr}}^2 H_{\mathrm{E}}}{\omega^2 + 2i\gamma_{\mathrm{AF}}\omega - \omega_{\mathrm{AF}}^2}\langle \mathbf{s}_{\mathrm{Pt}}(\omega) \times \mathbf{n}_0(\mathbf{s}_{\mathrm{Pt}}(\omega) \cdot \mathbf{n}_0)\rangle && \text{(E5.20)}
\end{aligned}$$

as we accounted for the following fluctuations of the Néel vector in the frequency domain:

$$\delta\mathbf{n}(\omega) = \frac{\gamma^2 H_{\mathrm{E}} H_{\mathrm{curr}}}{\omega^2 + 2i\gamma_{\mathrm{AF}}\omega - \omega_{\mathrm{AF}}^2}\mathbf{s}_{\mathrm{Pt}} \qquad \text{(E5.21)}$$

In this framework, although the temporal mean value of $\langle \mathbf{s}_{\mathrm{Pt}}(t)\rangle$ is zero, the spin torque induced by the fluctuations of $\mathbf{s}_{\mathrm{Pt}}(t)$ is non-zero. The time-dependence of the spin-spin correlations according to Seifert *et al.* [354] can be expressed as $\langle \mathbf{s}_{\mathrm{Pt}}(t) \cdot \mathbf{s}_{\mathrm{Pt}}(t')\rangle \propto \nabla T(t)\delta(t - t')$ where $\nabla T(t)$ is the time-dependent temperature gradient at the NiO/Pt interface. We recover thus identical symmetry for the non-linear SSE and thermo-magneto-elastic effect with however, different time-dependence of the generated THz signals.

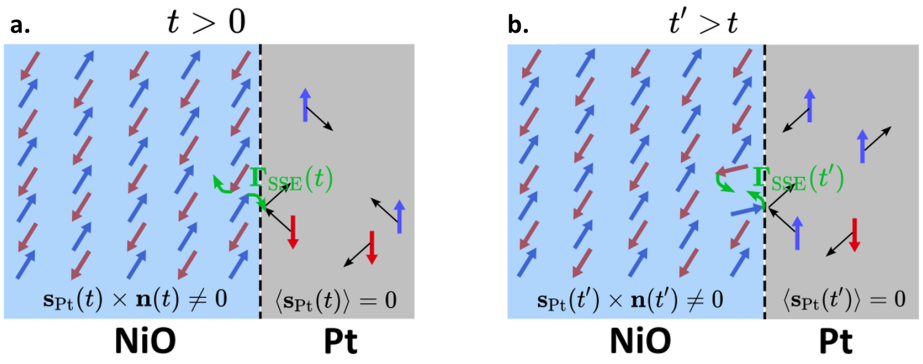

Figure 5.22: Spin-fluctuations and non-linear spin-Seebeck effect. (a) Effect of the spin-fluctuations $\mathbf{s}_{\mathrm{Pt}}$ in Pt inducing a torque Γ_{SSE} on the sublattice magnetizations of NiO at time $t > 0$. (b) At a time $t' > t$, another spin-fluctuations from Pt see a different magnetic texture inducing a different effect of the torque Γ_{SSE}.

This effect has also been reported by Kholid *et al.* [366] in easy-axis $KNiF_3$/Pt where the magnon gap (97 GHz, 0.4 meV) is much smaller than the electronic temperature. Similarly to the case of $KCoF_3$ at high laser fluences [366], the authors report a decreasing SSE signal with the temperature as $\propto (1 - T/T_{\mathrm{N}})^3$ and no impact of the pump fluence. In this view, the signal would originate from a mechanism similar to the results obtained on YIG/Pt [354], possibly via the spin-fluctuations mechanisms $\mathbf{s}_{\mathrm{Pt}}(t)$ and can be regarded as the non-linear SSE in our study. Indeed, as the magnon bands are already fully filled, the linear SSE cannot take place. Instead, the pump-induced heating ΔT_e creates spin fluctuations $\mathbf{s}_{\mathrm{Pt}}(t)$ in Pt at the interface between the AFM and Pt. The generated spin-fluctuations only have an impact on the magnon population of the AFM

via short-range electron-magnon correlations. The torque induced by the Pt spin-fluctuations is non-zero in the AFM near the interface and leads to subsequent spin-pumping into Pt, thereafter converted by ISHE in Pt.

Comparison with experiments and discussions. To address these potential two spin-Seebeck contributions experimentally, we performed a series of experiments. First, we performed a temperature dependence of the THz emission from NiO/Pt with a temperature ranging from 4 K to 300 K as displayed in Fig. 5.23. We measured a THz signal for all temperatures but no clear trend can be extracted from the temperature dependence, which it is not in line with a linear spin-Seebeck effect as described theoretically in Ref. [365], shown in Fig. 5.20.

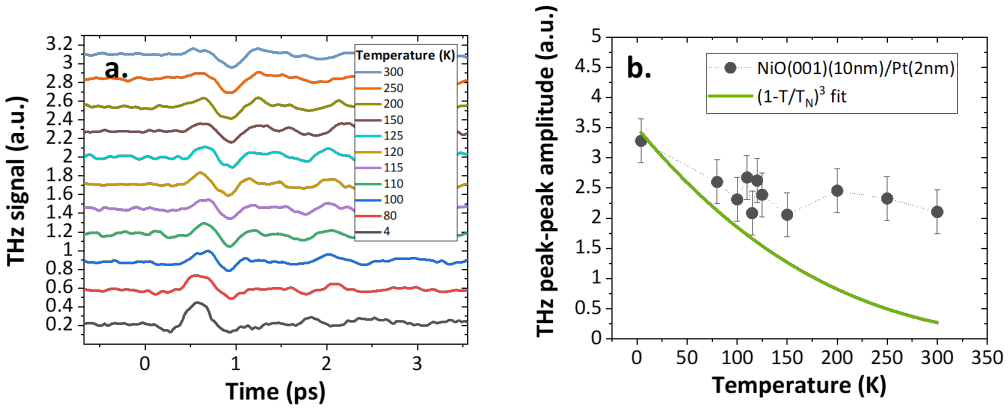

Figure 5.23: Temperature dependence on the THz emission from NiO(001)(10nm)/Pt(2nm). (a) Offset THz time traces of NiO(001)(10nm)/Pt(2nm) and (b) peak-peak amplitude of the THz emission ranging from 4 K to room temperature.

Secondly, regarding the potential non-linear spin-Seebeck contribution, we notice that *i*) the expected trend scaling with $(1 - T/T_{\mathrm{N}})^3$, as highlighted from the recent studies [366, 354], is not recovered on our temperature dependence, as shown in Fig. 5.23b. Besides, *ii*) our experimental fluence dependence demonstrates a linear regime, shown in Fig. 5.10a. We can thus also exclude a dominating non-linear spin-Seebeck contribution.

General conclusion on THz emission in NiO/Pt bilayers.

To conclude, we report a combined broad and narrowband 1.1 THz contribution from NiO/Pt bilayers excited by a NIR pump. After demonstrating that the emission arises from the ISHE conversion of a dynamical change of the Néel vector, a systematical study including pump polarization dependence, thickness dependence and sample growth orientation dependence indicates two different spin current mechanisms in (111) and (001) oriented samples. THz spin-current extraction also addresses two different dynamics of the mechanisms. The first mechanism, an off-resonant optical-spin torque happens via the inverse Cotton-Mouton effect as evidenced in the literature before, and we measured its ultrafast response. The second effect, pump-polarization independent, is here reported for the first time. Upon pumping, a strain wave is launched from hot expanding Pt and exerted ultrafast magneto-strictions in NiO which reduces the Néel vector and excites the out-of-plane mode of NiO. This injects a net spin current detected via THz emission spectroscopy. A qualitative agreement is obtained between experiments and magnetization dynamics modelling, addressing both strain and heat contributions to the THz current. The first strain-mediated effect is highlighted in this study for the first time, while the heat contributions show a behaviour that go beyond the scope standard spin-Seebeck effects (none of the reported effects in the literature seem to support our findings).

Future works on this topic would include the fine control of the induced strain by engineering the metallic strain launcher material. This would open on-resonant pumping of the Néel vector of NiO, with a potential enhancement of the narrowband amplitude and a possible tuning of the resonant frequency. One could also try to lower the pump fluence for two reasons: *i*) first to limit the temperature increase in NiO to focus on the magneto-strictive contributions and *ii*) to reduce the Pt heating and study the out-coupling of the THz radiation from the Néel vector between the free-space and the Pt transducer of finite temperature.

4 Perspectives for antiferromagnetic-based pulsed THz emitters.

4.1 Narrowband emission tunability by electrical control.

Our study has been the first to demonstrate the coherent narrowband THz emission centered around the high-frequency mode of NiO, therefore paving the way to narrowband emission tunability. Indeed, over the past years, researchers have studied the impact of the temperature, magnetic field, electrical currents, *etc.* to manipulate the Néel vector response. For instance, it could be possible to efficiently sweep the antiferromagnetic resonance frequency by applying DC current which allows to change the anisotropy of the antiferomagnetic materials as suggested in AFM based THz detectors [329]. It would result in a direct control of the narrowband THz emission. This approach is proposed in the detection regime (*i.e.* detection over the THz range on the AFMR which is down-converted (rectified) into a DC bias) and we propose the use of such bias application to tune the emission frequency of the AFMR. DC currents could also compensate the magnetic damping and thus the resonance linewidth, possibly leading to auto-oscillations [148]. Another perspective to control narrowband THz emission is the use of ultrafast strain as theoretically predicted in Refs. [243, 197] in an embedded metallic strain transducer/dielectric/magnet to finely tune the applied strain on the (antiferro)magnet and to separate the pump-induced temperature increase in the metallic transducer on one side and the pure coherent strain wave inducing magneto-striction in the antiferromagnetic layer.

4.2 THz emission from canted easy-plane antiferromagnet α-Fe_2O_3/Pt through the Morin transition.

A certain class of antiferromagnets presents a canted moment due to the DMI interactions. This cants the two sublattice magnetizations and leads to the presence of a net weak magnetic moment. The interest for such systems thus rely on the ability to manipulate the small canted ferromagnetic order $\mathbf{m}$ as well as the antiferromagnetic order $\mathbf{n}$, which are correlated to one another. To that extend, we will focus on the α-Fe_2O_3 antiferromagnet, but the reader is also referred to a preliminary study on $TmFeO_3$/Pt in Annex. A14.

α-Fe_2O_3: a canted easy-plane antiferromagnet. Hematite (α-Fe_2O_3) is an easy-axis antiferromagnet at low temperature, presenting a canting that leads to the presence of both antiferromagnetic and ferromagnetic order. The transition temperature between the easy-axis antiferromagnet and the canted easy-plane antiferromagnet at high temperatures is called the Morin transition about T_M=260 K [62]. It hosts strong potential to manipulate the antiferromagnetic order via the tailoring of the small canted ferromagnetic moment, as via THz pulse induced Néel vector switching [367]. The study of such antiferromagnetic systems presenting both an antiferromagnetic and ferromagnetic ordering has been given a lot of credit in the community, for instance with the recent study of Qiu *et al.* [195] in Fe_2O_3 and we propose further below some complementary experiments on such systems.

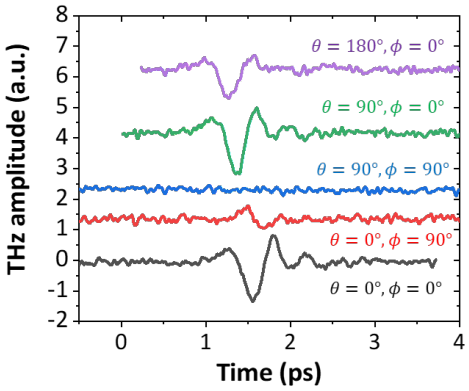

Figure 5.24: THz emission from α-Fe_2O_3/Pt bilayer. THz emission from α-Fe_2O_3(500µm)/Pt(10nm) bilayer as a function of the magnetic field orientation (θ) and crystalline orientation (ϕ) from the initial magnetic moment direction.

Report of THz emission from α-Fe_2O_3/Pt bilayers. The reader is referred to Ref. [331] for more details about the sample growth. We present in Fig. 5.24 the THz emission from α-Fe_2O_3(500µm)/Pt(10nm) bilayer with α-Fe_2O_3 cutted along the R-plane ($[1\bar{1}02]$). We report a sizeable THz emission from α-Fe_2O_3(500µm)/Pt(10nm) thin films. We have measured the THz emission from several configurations for both magnetic field (θ) and crystalline orientation (ϕ) where in both cases the initial orientation corresponds to the direction perpendicular to the initial magnetization. We observe that no signal is measured when the crystallographic orientation at ϕ=90° contrary to the sizeable signals recorded at ϕ=0°. When the magnetic field is flipped from θ=0° to θ=180°, the recorded signal is of smaller amplitude although the signal phase is not reversed. Those elements would indicate the strong contribution of the antiferromagnetic order to the THz emission compared to the canted magnetic moment. It would address the insensitivity of the weak moment under a weak magnetic field (100-200 mT) due to the strong easy-plane anisotropy in the system. These results are in agreement with the recent study of Qiu *et al.* [195] although the temperature dependence of the THz emission from α-Fe_2O_3/Pt through the Morin

transition has not been explored by the authors.

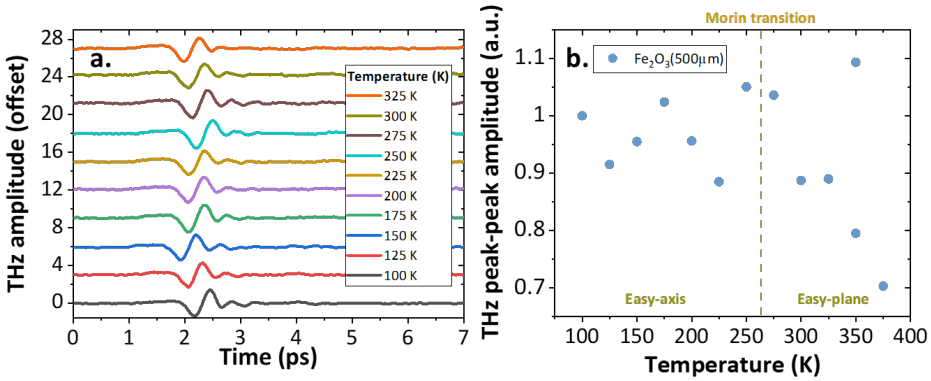

Figure 5.25: Temperature dependence of the THz emission from α-Fe_2O_3/Pt bilayer. (a) THz emission time trace from α-Fe_2O_3(500µm)/Pt(10nm) and (b) THz peak-peak amplitude as a function of temperature from 100 to 325 K. The two regions separated by the Morin transition are represented.

We thus performed a temperature dependence of the THz emission from 100 K to 350 K as shown in Fig. 5.25. A THz signal is measured in each case. From this, we have extracted the THz peak-peak amplitude as a function of the temperature. We observe an almost constant level of signal up to 275 K and then a decrease of the signal. To explain this, we have shown the expected Morin transition of α-Fe_2O_3 near T_M=260 K. The decrease at high temperature would be associated to the weakness of the induced magnetic moment with temperature, as the Néel temperature is reported around $T_N \simeq$900 K. Future studies would look at the optical *vs.* spin-phonon interactions in this transition region to understand their respective interactions with the compensated and weak moments. In brief summary, THz emission spectroscopy reveals to be an interesting tool to probe both antiferromagnetic and ferromagnetic ordering in α-Fe_2O_3, which could be controlled by low magnetic field. This will also be pursed in the scope of further studies to evidence contributions of coherent magnon modes as highlighted in NiO/Pt.

VI

Engineering spintronic THz emitters: from device integration to continuous THz waveform.

This final chapter focuses on the integration and engineering perspectives for spintronic THz emitters. Indeed, compared to the well-established semiconductor sources which have a certain technological maturity, these recent spintronic THz emitters are at their infancy and have considerable potential, with a range of approaches, to enhance their performances. This will permit THz spintronic sources to become further relevant to applications, as needed for instance in industrial and medical practice.

In this chapter, we present different tracks to efficiently functionalize spintronic THz emitters. We will adapt the photonic strategies previously developed in the literature (near-infrared cavity for efficient pump interaction with the structure) to the THz frequencies to increase the emission efficiency via, for instance, the study of THz cavities and THz anti-reflective coatings (adaptation of optical impedance) to efficiently emit in free-space. We will also focus on the role of the substrate, including thermal diffusion or harvesting lost power in the substrate by THz metallic reflector (proposed in Annex A16). A second part of this chapter will be dedicated to the theoretical prediction of continuous-wave (CW) THz emission achievement on spintronic THz emitters derived via photo-mixing, by use of previously developed wave-diffusion modelling. We then conclude with insights of interesting future developments for spintronic THz emitters.

In the following chapter, we collaborate with I. Sagnes (C2N) for the realization of buried THz cavities. We thank N. Nilforoushan (LPENS) for performing the fluence dependence on the STE on sapphire with the Yb-doped fiber based amplifier. We also propose in the end of this chapter to study numerically the CW THz from STE structures in close collaboration with M. Vanwolleghem's team (IEMN).

1 Challenges for high power spintronic THz emitters.

Currently, spintronic THz technology would benefit in performance increases such that they can be transposed to everyday applications. For example, using femtosecond oscillators, they have relatively low emitted electric fields (tens of V.cm^{-1}). With amplified systems, spintronic THz emitters (STE) can reach noticeable emission power (several hundreds of µW) with maximum field amplitude about hundreds of V.cm^{-1} [133] in the case of single-cycle THz pulse, whereas their low optical-to-THz conversion efficiency is typically about $P_{\text{out}}/P_{\text{in}} \simeq 10^{-5}$ [141], which limits the integration of their unique properties (such as polarization tunability or large bandwidth) into efficient devices. Even if their performances are comparable to non-linear crystals and that the emission bandwidth is broader due to the absence of phonon absorptions in metallic STEs, the amplitude is still far below the range obtained by using photoconductive switches (PCS), with electric fields that can reach several hundreds of V.cm^{-1} using femtosecond oscillators [368]. In particular, photoconductive switches offer the most interesting emission platform for low THz range with femtosecond oscillators while non-linear crystals are widely used with amplified systems. Owing to their faster relaxation dynamics, spintronic THz emitters thus propose an interesting approach to be used flexibly with amplified (low repetition rate) and oscillator (high repetition rate) sources. To increase the emission efficiency, research (and this work) has focused on highly efficient STE by designing new materials, more efficient spin-charge conversion, *etc.* However, all enhancement strategies shall be integrated together to deliver a high power THz source. Although the material research is well addressed in the literature and in the scope of the previous chapters, less efforts have been placed on photonic engineering on both near-infrared (NIR) and THz frequencies, even if some works have shown that NIR optical cavities allow a better pump absorption and lead to stronger THz transient generation [142, 198].

Therefore in order to functionalize spintronic THz emitters, we have explored several paths and in particular we provide interesting transpositions of NIR strategies to the THz domain. We will first start to give theoretical description of the THz wave propagation in the thin film limit. We then have explored several paths to enhance the THz emission power from spintronic THz emitters by means of heterostructure design in reflection geometry: anti-reflective coatings, buried metallic planes to reflect the THz wave, buried THz cavities and thermal management. In the end, we will afterwards focus on estimating the CW THz power derived by spintronic photomixing, in collaboration with IEMN (Lille) which have experimentally generated CW THz in free-space from STEs.

2 Confinement and amplification of the THz wave.

Although efforts have been put in STEs coupled with antennas to shape charge current oscillations and to increase the THz emitted field using electronic approaches [201, 200], few techniques have been imported from the (infrared) optics community to enhance the THz radiation. We thus propose in the following part to transpose cavity-based [251] and anti-reflection coatings to the THz frequency domain.

2.1 Wave impedance matching.

Before starting the experimental implementation, we recall that the far-field THz electric field $E_{\text{THz}}(\omega)$ radiating from the charge current $j_c(\omega)$ can be expressed in frequency as:

$$E_{\text{THz}}(\omega) \propto i\omega \cdot Z(\omega) j_c(\omega) \tag{E6.1}$$

and we see that for low characteristic impedance $Z(\omega)$ (derived from the Tinkham formula in Annex A6), the THz electric field goes to zero. The THz characteristic impedance, involved many

times in the previous studies for characterizing the THz absorption in the multilayer, represents in a sense a coupling efficiency of the STE with the free-space of impedance $Z_0 = 377\ \Omega$ as:

$$Z(\omega) = \frac{Z_0}{1 + n_s(\omega) + Z_0 \int \sigma(\omega, z) dz} \tag{E6.2}$$

We present in Fig. 6.1 the four working configurations of a standard STE (typically W/CoFeB/Pt) of equivalent THz refractive index $\delta n = Z_0 \int \sigma(\omega, z) dz$, deposited on a substrate of refractive index n_s. We can establish the reflection coefficient at asymmetric interfaces in the general case as:

$$R = \left(\frac{n_1 - n_2}{n_1 + n_2} \right)^2 \tag{E6.3}$$

where n_1 and n_2 are respectively the THz refractive index from both sides of the interface. We recall that a full list of THz and NIR refractive indices is available in Annex A11. Contrary to optical gap semi-conductor based photo-conductive antennas, STEs can be used in various reflection and transmission configurations for both optical pump and generated THz emission. We describe the effective coupling of the THz generated from the STE with free-space [101] in the four configurations:

(1) in the first configuration, the pump is from the STE side and the THz is detected from the substrate side. This is the most ideal case, as for dielectric and semi-conducting substrates of high permittivity $\epsilon_s = n_s^2$, most of the generated THz radiation power is emitted towards the substrate side due to the progressive optical impedance matching. This can also be understood as a small reflection coefficient R_{ES} at the STE/substrate interface and thereafter at the substrate/air interface (R_{SA}) with:

$$R_{\text{ES}} = \left(\frac{\delta n - n_s}{\delta n + n_s} \right)^2 \quad \text{and} \quad R_{\text{SA}} = \left(\frac{n_s - n_0}{n_s + n_0} \right)^2 \quad \text{with} \quad n_0 = 1 < n_s \ll \delta n \tag{E6.4}$$

(2) in the second configuration, easier to implement, the pump hits the sample from the STE side and the THz is also detected from the STE side: this is the reflection geometry that is widely used in our studies. We find that in this case, the reflection coefficient R_{EA} of the air/STE interface is very high. The THz radiation is thus making important back-and-fourth travels in the heterostructure and the characteristic impedance $Z(\omega) = Z_0/(1 + n_s + \delta n)$ is small, we have:

$$R_{\text{EA}} = \left(\frac{\delta n - n_0}{\delta n + n_0} \right)^2 \quad \text{with} \quad n_0 = 1 < n_s \ll \delta n \tag{E6.5}$$

(3-4) the third and fourth configurations are respectively equivalent to the first and second configurations, supposing that the substrate is transparent to the NIR radiation. In particular, we stress on the low THz radiation coupling with free-space in the fourth case, identical to the second case.

It is therefore needed an enhancement strategy for STE in the reflection geometry (from the STE side) to increase the radiation efficiency. We will see in the following studies different paths to achieve this goal, via top dielectric anti-reflective coatings (ARC) or with buried THz cavities.

2.2 Quarter-wavelength resonant THz cavities.

Scientific context for resonant THz. A useful strategy to increase the THz radiation power from STE is the use of THz cavities. Due to the long radiation wavelength in the THz range (from hundreds of microns to several microns), it is sometimes challenging to implement such cavities in embedded nanostructures. We first present the example of the THz Tamm cavity reported by

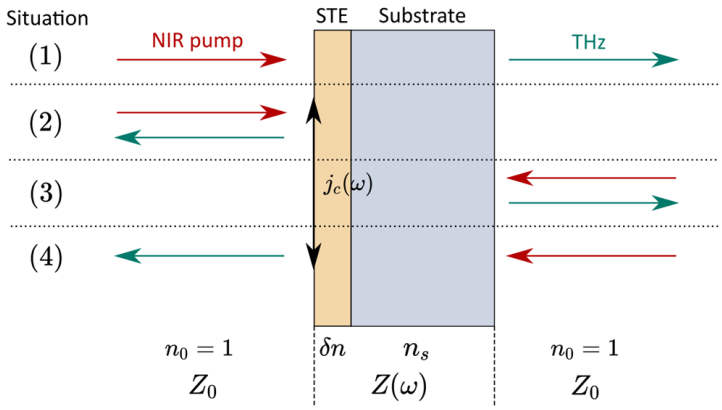

Figure 6.1: STE derived THz radiation out-coupling with free-space. Four cases are depicted here. (1) Pumping from the top STE and detecting the THz radiation from the substrate side. (2) Pumping from the top STE and detecting from the STE side. (3) Pumping from the bottom substrate side and detecting from the substrate side. (4) Pumping from the substrate side and pumping from the STE side.

Messelot *et al.* [369] which combines a very-high quality reflector composed of a metallic plane (Au) and a distributed Bragg reflector (DBR). In brief, the DBR is a repetition of vacuum and Si layers of carefully engineered thicknesses so that constructive interferences are built up as the THz is reflected from the Au plane. The reached quality factor Q is about 230 at 1 THz. Unfortunately, this type of structure would not be compatible with the spintronic THz emitter configuration due to the poor field escape from the metallic plane, as we will see in our metallic planes based THz cavity. Alternatively, Zhang *et al.* [370] proposed a THz photonic crystal cavity based on the repetition of vacuum and Si layers. It causes, depending on the frequency, constructive or destructive interferences as a function of the position in the vacuum layer. This technique might not be as ideal in our case as the resonant modes are difficult to tailor.

Definition of the Q-factor.

For resonating cavities of electromagnetic waves, we define the Q-factor as the ratio between the resonance frequency ν_0 and the spectral broadening at the resonance $\Delta\nu$. More the coupling is strong, more the Q-factor is high and more the photon duration time τ in the cavity is high:

$$Q = \frac{\nu_0}{\Delta\nu} = 2\pi\tau\nu_0 \tag{E6.6}$$

Another approach, making the bridge with an efficient implementation with THz emitters (photoconductive antennas) has been previously proposed by Hawecker *et al.* [251]. The structure is composed of an interdigitated photoconductive antenna below which a Au plane is buried thus delimiting a cavity with a GaAs interlayer about tens of microns between the top interdigitated pattern and the buried Au plane. The thickness of the GaAs interlayer is matching the so-called $\lambda/4$ cavity conditions. The authors reported an strong enhancement gain of $\times 7.5$ in emission power. This structure seems therefore more suitable as it involves already the THz emitter active-area in the cavity.

$\lambda/4$ cavities. Although some techniques might not be well suited for our aim with STE, the previously presented literature showed that the reflection of a THz wave on a designed $\lambda_0/(4n_c)$ cavity (also called quarter wavelength resonant cavity) provokes constructive interferences and thus an enhancement of the emitted THz wave. We denote as λ the wavelength in the material and λ_0 the free-space wavelength. We note that in the spintronic structure (of total multilayer thickness d), the very thin film approximation is fulfilled with $d \ll \lambda$, and thus we assume the

phase shift due to propagation of the THz wave in the material to be negligible. In the $\lambda/4$ cavity, the opposed phase shift of $\pm\pi$ due to the reflection of the incoming wave on metallic planes leads to a field enhancement. The quarter wavelength resonant cavity conditions can be written as:

$$d_c = \frac{\lambda}{4} = \frac{\lambda_0}{4n_c} \Rightarrow \nu = \frac{c}{4d_c n_c} \tag{E6.7}$$

where n_c is the THz refractive index in the cavity, d_c is the effective thickness of the cavity and c is the light velocity. This resonance leads to a very narrowband enhancement at the frequency ν, tunable as a function of the refractive index n_c.

Modelling. To understand the role of the $\lambda/4$ cavity in STE-based structures, we performed finite element method (FEM)-based numerical simulations using COMSOL Multiphysics [371]. Although the previously derived characteristic impedance $Z(\omega)$ using the Tinkham formula is valid in the thin film limit, it can diverge as we consider an additional layer of the order of the wavelength $\lambda = \lambda_0/n_c$ and thus we propose to simulate by FEM-based model to obtain a more realistic picture of the THz wave propagation in thick layers. We have set an oscillating charge current $j_c(\omega)$ at the very surface of the STE. Note that the NIR pump and subsequent absorption are not computed in the simulations. Modelling details are available in Annex A15.

We first present in Fig. 6.2 the modelling of a reference STE on conventional GaAs substrate. We observe oscillations of the electric field in the substrate corresponding to the Fabry-Pérot modes due to the reflection of the field at the back of the substrate. A high part of the radiation is collected towards the detector (on top) but a non-negligible part is also emitted from the substrate side and thus lost experimentally. We remark that the higher emission on top of the emitter owns to the fact that the input charge current is locally set at the very interface with air, thus already radiating in air (contrary to the reality). From the calculated THz electric field as a function of the frequency ν and the position, it is possible to obtain a figure of merit of the directive THz emission by integrating the THz field amplitude over a hemispherical region representing the detector in the far-field region: $E_{\mathrm{THz}}^{\mathrm{int}} = \int_{\mathcal{D}} E_{\mathrm{THz}} dl$ (thus given in V). The obtained profile of the integrated electric field as a function of frequency (shown in Fig. 6.2c) decreases with frequency and will be used as a reference for future calculations to compare the enhancement between different structures. Moreover, the region at low frequency (around 0.3 GHz) is not accounting for the remagnetization time (typically $\tau_r \simeq 1 - 10$ ps) of the STE which gives the low frequency cutoff of the THz emission in experiments.

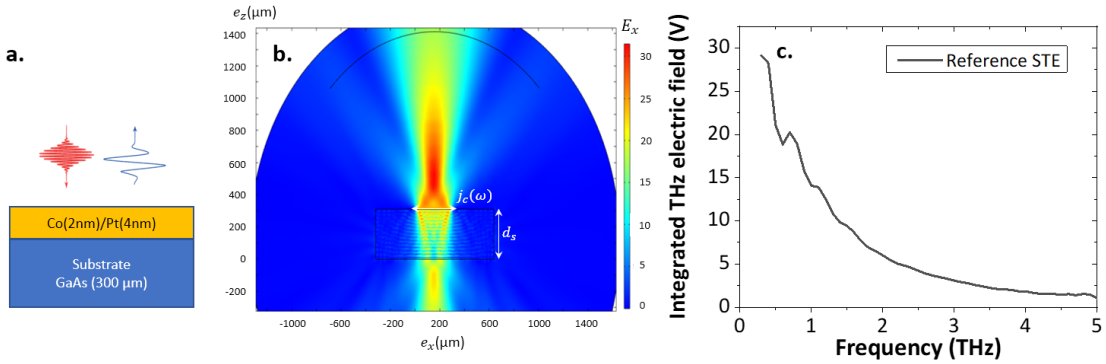

Figure 6.2: Simulated frequency response of the THz emission from STE reference. (a) Schematic representation of the structure. (b) Representation of the modelled structure respectively with dynamical charge current $j_c(\omega)$ where the x-component of the THz electric field (at 2 THz) is represented. (c) Integrated (over the hemispherical area) electric field as a function of the frequency. Note that the THz emission is overestimated on the STE side (top) as the input charge current is set numerically at the top interface (thus, already radiating in air).

We represent in Fig. 6.3a-b the structures that will be studied numerically and experimentally: a home-grown Co(2nm)/Pt(4nm) is respectively deposited on a GaAs(11µm) cavity terminated by *i*) a AlGaAs(200nm) cavity-ending or *ii*) a Ti/Au(200nm) based-cavity. The substrate is SI-GaAs(300µm) (SI stands for semi-insulating). We present in Fig. 6.3c-d, respectively for the AlGaAs-based and Au-based cavities, the x-component of the THz electric field for 2 THz. We interestingly observe that in the case of AlGaAs, Fabry-Pérot oscillations in the substrate are recovered. This behaviour is not encountered on Au-based cavity which can be explained as a high THz absorber (or reflector) with the Au planes. In those simulations, we get the integrated THz field magnitude on the hemispherical region. We plot in Fig. 6.3e the integrated THz field as a function of the frequency for the reference STE, the AlGaAs-based and Au-based cavities. We see that the profiles are very similar and in particular superposed between the reference and AlGaAs. To extract a figure of merit of the cavity-based structures, we plot in Fig. 6.3f the field enhancement ratio $\eta_c = E_{\text{cavity}}/E_{\text{ref}}$. We see that the enhancement ratio is quite weak, around 5% in mean value between 1 and 3 THz. This effect from the simulations might be explained by *i*) the change of the THz STE refractive index due to the addition of a highly conductive Au plane. We recall that the THz refractive index is defined by a real and imaginary part $n_{\text{THz}} + i\kappa_{\text{THz}}$, the latter describing the attenuation of the wave. This term participates in the simulations to the absorption of the wave. Alternatively, this effect could also come from *ii*) numerical consideration due to the modelling of the thin Au plane (meshing) compared to the wavelength.

Experimental implementation. Following the path of THz cavities proposed by Hawecker *et al.* [251], we study the role of a buried THz cavity to enhance the THz emission of STE in the reflection geometry (maximizing the generated electric field from the top surface). To that extend, we have built in collaboration with C2N (I. Sagnes) samples on SI-GaAs(300µm) substrates on which we have inserted a GaAs layer of 11 µm to match the quarter wavelength condition $d_e \simeq \lambda/(4n_e)$. The fabrication process is done via metal wafer bonding technique and the interested reader can find details in Ref. [251]. The cavity is delimited between the STE (Co(2)/Pt(4)) and a buried plane of thickness 200 nm, either semiconducting AlGaAs or metallic Ti/Au as schematically displayed in Figs. 6.3a and 6.3b. We present in Fig. 6.4a the experimental characterization measured in the time-domain. We denote an electric field amplitude enhancement of +32% ($\times 1.74$ in power) in both structures compared to the reference sample SI-GaAs//STE. The metallic Au plane does not read a stronger confinement of the THz wave (and thus a stronger enhancement ratio) compared to the cavity delimited by AlGaAs. We now turn to the results in the frequency domain shown in Fig. 6.4b where we observe that the field enhancement ratio (>1) compared to the reference sample is more pronounced between 2 and 3 THz for the metallic Au based cavity compared to the one build on AlGaAs, around +50%. This is particularly evident in Fig. 6.4 which presents the ratio of the field enhancement between the cavity with Au and with AlGaAs. The amplitude is enhanced by +50% around 2.5 THz in Au based sample compared to AlGaAs, which could indicate the presence of the cavity effect in Au based sample.

Interpretations for the THz absorption. Surprisingly, the cavity effect is not encountered in both FEM simulations and experimental implementation, whereas we expected a stronger field enhancement for the latter due to the stronger field confinement in the GaAs cavity. To explain this drawback, we can easily approximate the electric field difference from the two structures by considering the THz impedance variation, derived from the Tinkham formula (Annex A6), under the change(s) in the heterostructure following:

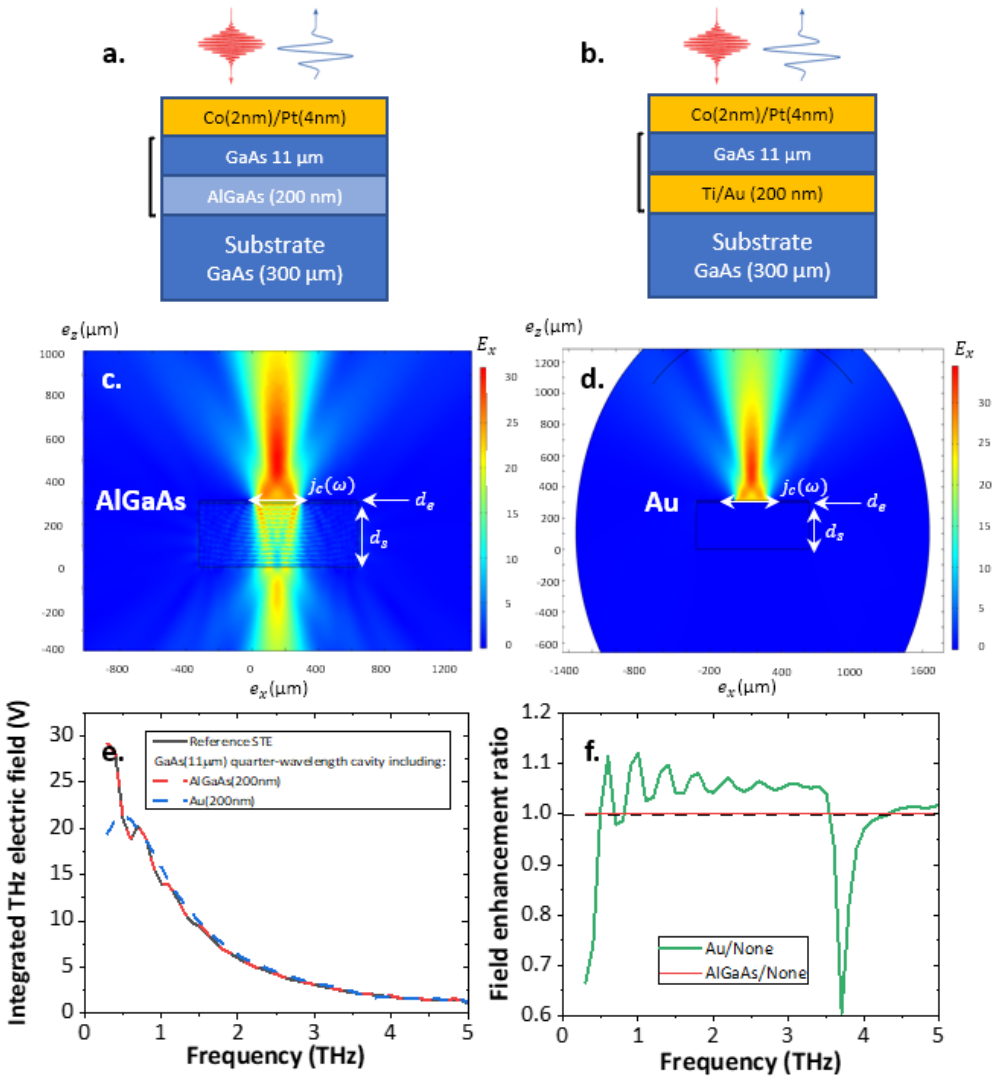

Figure 6.3: Simulated buried $\lambda/4$ cavities in STE design. (a-b) Schematical representation of the structure in the case of (a) AlGaAs(200nm) and (b) Au(200nm) terminated cavities. (c-d) Representation of the modelled structure respectively with (c) AlGaAs(200nm) and (d) Au(200nm) where the x-component of the THz electric field (at 2 THz) is represented. (e) Integrated (over the hemispherical area) electric field as a function of the frequency for the three structures *i.e.* the reference and the two cavities. (f) Field enhancement ratio for AlGaAs-based cavity compared to Au-based cavity, as a function of the frequency.

$$\frac{E'}{E} \propto \frac{Z'}{Z} = \frac{1}{1 + \frac{Z_{\text{ini}}}{Z_0}\Delta n} \tag{E6.8}$$

$$\text{with } \Delta n = Z_0 \int \Delta\sigma(z')dz' \quad \text{(case of fixed substrate but varying multistack)} \tag{E6.9}$$

where Z_{ini} represents the initial THz impedance of the sample with the buried AlGaAs plane. The addition/removal/replacement of an additional layer includes an effective refractive index Δn in the multistack owing to an effective change of the conductivity $\Delta\sigma$ and thickness Δz. The use of this model seems *a priori* to be justified as we consider absorbing multilayer of thicknesses smaller than the THz wavelength (in both free-space or in the metallic material). We represent in Fig. 6.5 the relative variation $\Delta Z/Z_{\text{ini}}$ for the two structures. Between AlGaAs and Au based samples, we estimate this ratio about a factor $\times 150$ which could explain the reduced THz amplitude measured experimentally. Moreover, contrary to the implemented design on optimized photoconductive switches [251], no interdigitation are present on the STE surface which strongly

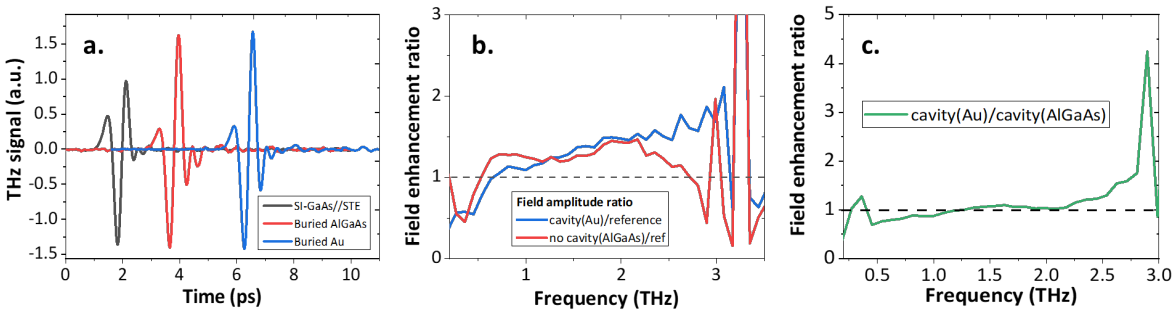

Figure 6.4: Experimental buried cavity-based STEs. (a) Measured THz emission from AlGaAs (red) and Au (blue) based buried THz cavities. The reference sample is SI-GaAs//STE (black). (b) Enhancement ratio (electric field) presented in the frequency domain. An enhancement around +30% is reported experimentally. (c) Experimentally measured ratio between the two enhancements from Au based cavity and AlGaAs based cavity demonstrating specifically an enhancement at higher frequencies (from 2 to 3 THz) of +50% on Au based buried cavity compared AlGaAs based cavity.

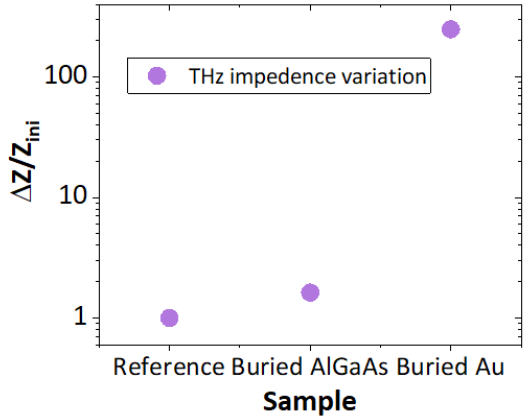

Figure 6.5: Variation of the structure impedance. Calculated THz impedance variation for the two structures GaAs(300µm)//AlGaAs(200nm)/GaAs(11µm)/Co(2nm)/Pt(4nm) and GaAs(300µm)//Au(200nm)/GaAs(11µm)/Co(2nm)/Pt(4nm) compared to the reference GaAs(300µm)//Co(2nm)/Pt(4nm).

restricts the amplified electric field in the GaAs cavity and thus leads to its absorption in the two metallic layers, progressively via multiple reflections. This interesting result opens perspectives about future cavity designs, for instance the use of a non-metallic cavity (strong refractive index and non-metallic layers) and patterning of the STE surface to allow the enhanced electric field to radiate in free-space.

3 Quasi-index matching structures.

Scientific context. Quasi-index matching structures, also called anti-reflective coatings (ARC), find various uses to avoid the unwanted reflections of electromagnetic waves. For instance, they are used in THz meta-materials [372] to suppress the additional reflections of a near-infrared probe while still allowing an efficient and unperturbed pumping of nano-structures of interest using an intense THz pump. Recent research now also include the search of THz ARCs to suppress the Fabry-Pérot reflections at interfaces. The back and forth travel $2d_s$ of the THz wave in the substrate of refractive index n_s provokes a measurable echo at $2Nd_sn_s/c$ (where N is the number of travels in the substrate) which would limit the spectral resolution of measured THz signals using time-domain spectroscopy. Zhou *et al.* [373] proposed a broadband THz anti-reflection coating using graphene. Alternatively, Nenno *et al.* [100] predicted the use of ARC on STEs to increase the conversion efficiency up to a factor $\times 2$ in a dual ARC structure in transmission geometry.

ARCs typically consist of an additional dielectric layer of refractive index n_e that suppresses the wave reflected from the substrate interface. The ARC layer thickness d_e is chosen to match the $\lambda/4$ criterion as it gives constructive interferences of the wave reflected from the substrate interface (as schematically represented in Fig. 6.6). In details, the refractive index of the ARC is chosen according to the Rayleigh's film condition:

$$n_e = \sqrt{n_0 n_s} \tag{E6.10}$$

to avoid the wave reflection due to the presence of a strong refractive index difference between the substrate of index n_s and air of index $n_0 = 1$. One of the limitation of quarter-wavelength ARC is that they are by definition narrowband (centered at $\nu = c/4d_en_e$).

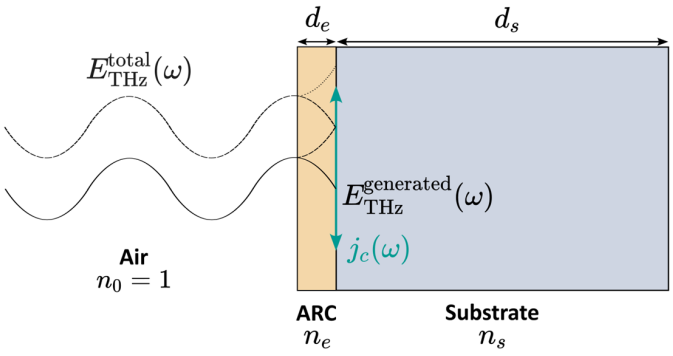

Figure 6.6: Principle of the anti-reflective coating. The emitted wave $E_{\mathrm{THz}}^{\mathrm{generated}}(\omega)$ generated by the transient charge current $j_c(\omega)$ propagates *i*) in free-space and *ii*) in the ARC where the wave is reflected at the interface with the substrate. The reflected part passing through the ARC coherently interfere with the emitted wave and the total electric field detected $E_{\mathrm{THz}}^{\mathrm{total}}(\omega)$ is thus of higher amplitude. The refraction at the interfaces has been neglected, as well as the effective propagative wavelength contraction for clarity.

3.1 Parylene polymer as a top anti-reflective coating.

To implement such ARC-based STE, we have decided to use parylene-C polymer coating, well used in the electronic community for encapsulation, which has a THz refractive index around $n_e^{\mathrm{THz}} = 1.6$ to build a top NIR-transparent ARC (of quarter-wavelength $\lambda/4$ design), avoiding the reflection of the THz radiation between the STE and the substrate. The parylene layer matches the Rayleigh's film conditions for substrate refractive indices ranging around $n_s^{\mathrm{THz}} \simeq 3.5$ like GaAs (3.6) or sapphire (3.3). The simulated parylene thickness is taken around $d = 25$ µm as it is matching $d = \lambda/(4n_e)$ where λ is the free space wavelength around 150 µm, corresponding to

a central frequency around $\nu = 2$ THz. We thus have an echo from the second, third, ..., N-th reflection which arrives at time $\Delta t = 2Nd_e n_e/c$. In our case for parylene, we estimate the time delay around $\Delta t = N \times 250$ fs so that the first contributions arrive practically in phase with the THz pulse: the measured electric field is expected to be enhanced (constructive interferences).

Modelling. To extract a field enhancement ratio $\eta_{\text{ARC}} = E_{\text{ARC}}/E_{\text{ref}}$ by using this ARC-based STE, we performed numerical simulations via finite elements methods (FEM) using COMSOL Multiphysics [371] described in Annex. A15. We modelled the ARC-based STE structure by considering a substrate of thickness $d_s = 300$ µm and of refractive index n_s capped with an ARC of thickness $d_e = 25$ µm and refractive index n_e. We have set a charge current density $j_c(\omega)$ on the STE as depicted in Fig. 6.7a. Note that the NIR pump and subsequent absorption are not computed in the simulations. A reference composed of the exact same structure without the ARC is calculated. We present in Fig. 6.7b the equivalent THz field amplitude integrated over a hemispherical area reproducing the detection. Note that a non-negligible electric field is recovered at low frequency (around 0.3 THz) as the remagnetization time is not computed in this simulation whereas it sets the low frequency cutoff in STE structures. Nonetheless, we see that the amplitude obtained with the ARC-based structure is larger between 1 and 3 THz and to understand it, we have plotted in Fig. 6.7c the field enhancement ratio η_{ARC}. We see that the obtained field enhancement reaches at maximum +65% (power enhancement $\times 2.7$) at 2 THz which is the frequency calculated from the $\lambda/4$ condition, thus confirming our theoretical expectations. Notably, the part above 4 THz is explained by numerical noise as the meshing has to follow the diminution of the wavelength at high frequencies. We have limited the meshing shrinking to avoid too long calculation times as we focused mainly experimentally in the range up to 3 THz.

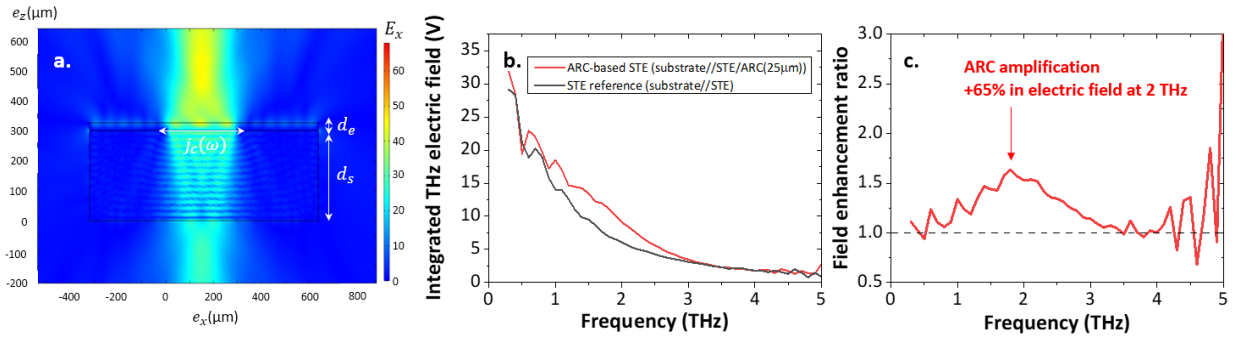

Figure 6.7: Simulated ARC-based STE enhancement. (a) Graphical representation of the x-component of the THz electric field at 2 THz projected on the ARC structure. (b) Integrated (over the hemispherical area) electric field as a function of the frequency for the two structures. (c) Field enhancement ratio obtained from ARC-based STE as a function of the frequency

Experimental realization. The experimental implementation of the ARC-based STE structure has been realized on various STE structures (Co/Pt bilayer, W/CoFeB/Pt optimized trilayer, *etc.*) grown on several substrates (GaAs, sapphire, MgO, *etc.*) followed by the deposition thereafter on top of a parylene polymer layer of thickness about 21 µm (controlled by the parylene supplier). First, the deposition of such high thickness dielectric layer already represents a challenging experimental implementation that we have unlocked here on STEs. We focus on the following results on the optimized STE trilayer W/CoFeB/Pt deposited on sapphire which is actually the reference STE in the community. We report in Fig. 6.8 the experimental results on this structure. We see that the global THz signal is increased by looking at the peak-peak amplitude, by a factor $\times 1.5$. The measured enhancement (the ratio between the ARC-based structure *vs.* the reference STE) reads an amplification in field about +52% ($\times 2.3$ in power enhancement) at 2.3 THz. We find a close agreement between the simulation and the experimental film implementation. We note that the

centered frequency of enhancement is shifted compared to the simulation results. This is due to the thickness difference of the experimentally deposited anti-reflective coating layer. Indeed, it can be shown that the frequency shift $\delta\nu = c\delta d_e/(4d_e^2 n_e)$ is estimated around 0.3 THz for a thickness difference δd_e=4 µm, in agreement with our results. One could also notice the constant offset in the experimental enhancement ratio (of value ≃1.25) that could potentially arise from an enhancement of the NIR pump interaction with parylene (of refractive index $n_e^{\mathrm{NIR}} \simeq 1.6 - 1.7$ [374]) and will make the point of further studies.

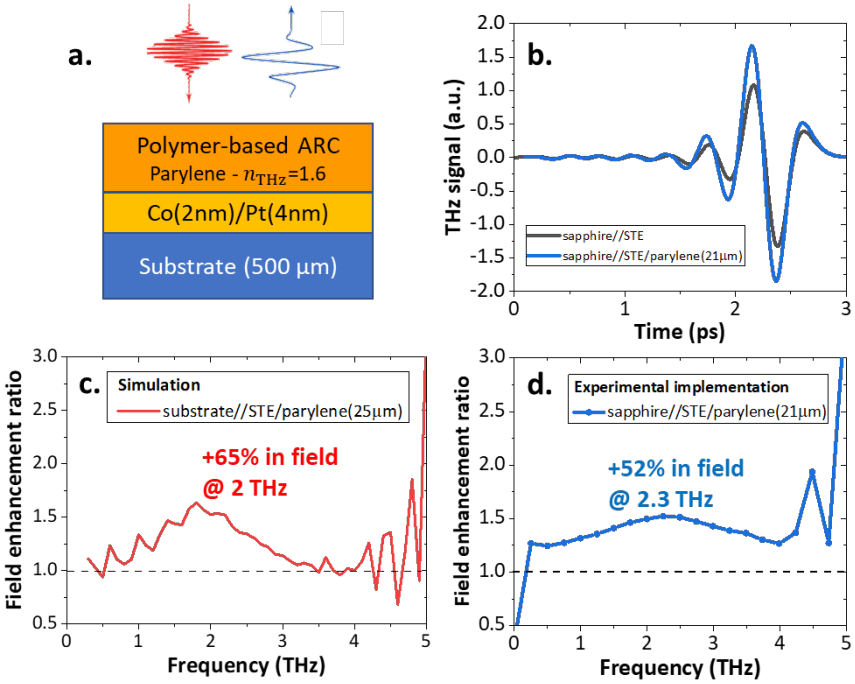

Figure 6.8: Anti-reflective coating (ARC) capped STEs. (a) Representation of the implemented ARC structure in reflection geometry. (b) Measured THz emission from standalone STE and ARC-based STE. (c-d) Presentation of the field enhancement ratio comparing (c) simulations and (d) experimental measurements. The simulated structure is substrate//STE/parylene(25µm) and the experimental structure is sapphire//STE/parylene(21µm).

In summary, this result demonstrates the first successful implementation of such ARC structures on STEs. This will come as a complementary tool to enhance the THz emission power in already-optimized samples (implemented near-infrared cavity from Herapath *et al.* [142], *etc.*). Especially, this enhancement in reflection geometry can also be envisioned in the transmission geometry by stacking an additional ARC layer on the back of the substrate to have an even smoother transition, that will be the point of future studies.

4 Continuous THz wave emission by means of spintronic-based structures.

4.1 Current state-of-the-art of CW THz.

THz continuous waveform (CW) sources are of importance for spectroscopy applications and telecommunications, and offer very fine frequency tuning [124]. THz CW has been widely explored in the THz community, either from the optical side with cryo-cooled QCL [375, 124] or from the electronics using up-conversion or photoconductive antennas as photomixer sources where the optical laser emission is down-converted to the THz range [101]. Typically, the power obtained from photomixers sources reaches up to a few mWs for millimeters waves (tens of GHz) and rapidly decreases while entering the THz region, down to few µW of CW power or less. This is represented in Fig. 6.10. Indeed, the THz gap above 2 THz is today hardly accessible, with only narrowband and low-temperature operation THz QCLs [124]. The advantage of STE is their operation on the full THz spectrum, demonstrated in the pulsed regime and that can be transferred to the CW regime [376]. THz spintronic-based photomixers are therefore planned to be widely tunable in the whole spectrum of the THz domain. In this part, we will demonstrate theoretically the CW operation of STE-photomixers and estimate their frequency and amplitude response.

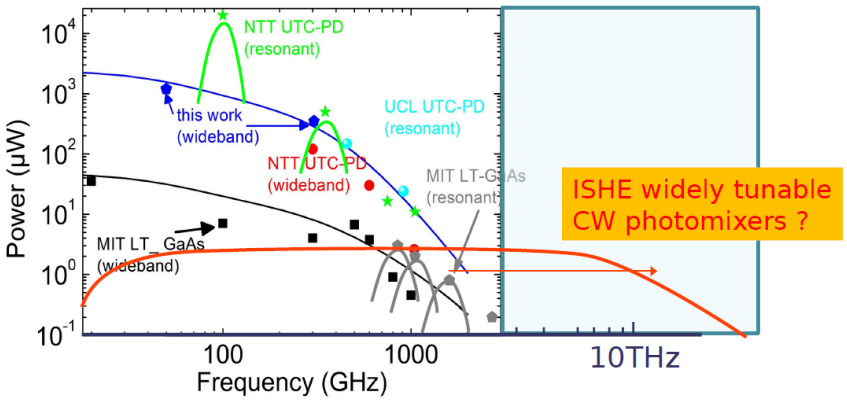

Figure 6.9: Outlook on CW THz performances obtained by photomixing. THz CW photomixing from the current available electronic sources including photo-conducting antennas (on LT-GaAs substrates) and uni-traveling-carrier photodiode (UTC-PD), compared to envisioned CW derived from STE-photomixer (red). Courtesy of M. Vanwolleghem (IEMN Lille).

4.2 Optical photomixing pump profile and pulsed-to-CW efficiency ratio.

We first start by detailing the optical photomixing principle as schematically represented in Fig. 6.10. In details, we pump using two detuned pumps E_1 and E_2 of respective frequencies ω_1 and ω_2 that can be decomposed with respect to a common ground frequency $\omega_1 = \omega_0 + \omega_{\mathrm{THz}}/2$ and $\omega_2 = \omega_0 - \omega_{\mathrm{THz}}/2$, following the argumentation of Preu *et al.* [101]. The total incident pump electric field (and power) can therefore be written as:

$$\begin{aligned} E_{\mathrm{pump}} &= E_1 + E_2 = E_0 \exp(i\omega_0 t)\left(\exp(i\omega_{\mathrm{THz}} t) + \exp(-i\omega_{\mathrm{THz}} t)\right) = 2E_0 \exp(i\omega_0 t)\cos(\omega_{\mathrm{THz}} t/2) \\ P_{\mathrm{pump}} &= 4E_0^2 \cos^2(\omega_{\mathrm{THz}} t/2) = 2E_0^2(1+\cos(\omega_{\mathrm{THz}} t)) \end{aligned} \tag{E6.11}$$

The generated THz CW electric field is linked to the derivative of the time-dependent pump electric field as $E_{\mathrm{CW}}^{\mathrm{THz}} \propto \nu_{\mathrm{THz}} \sin(2\pi\nu_{\mathrm{THz}} t)$ with $2\pi\nu_{\mathrm{THz}} = \omega_{\mathrm{THz}}$.

Estimation of the pulsed-to-CW efficiency ratio. We then estimate the ratio of the THz emission from STE in the expected CW regime compared to the pulsed case. In the pulsed STE case,

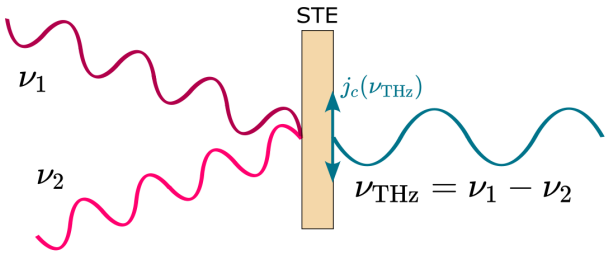

Figure 6.10: Photomixing based CW STE. Representation of the CW THz generation principle by photomixing where two detuned optical CW sources of beatnote frequency ν_1 and ν_2 lead to the generation of a CW THz emission with $\nu_{\mathrm{THz}} = \nu_1 - \nu_2$.

a THz pulse of duration τ_{THz} is emitted upon the NIR pumping modelled as a Gaussian pulse $P_{\mathrm{pump}} = (1/f_r)\exp(-\omega^2\tau_{\mathrm{NIR}}^2/4)$ where τ_{NIR} is the pump pulse duration. As recovered experimentally, we consider that the THz electric field is proportional to the pump power $E_{\mathrm{THz}} = \alpha P_{\mathrm{pump}}$. The CW-equivalent optical power derived from the pulse regime can be written as:

$$P_{\mathrm{pulse}}^{\mathrm{THz}} = f_r P_{\mathrm{pulse}}^{(1)} = f_r \int_{\mathbb{R}} E_{\mathrm{THz}}^2(t)dt = f_r \frac{\alpha^2}{2\pi}\int_{\mathbb{R}} \omega^2 P_{\mathrm{pump}}^2(\omega)d\omega = \frac{2\alpha^2}{\sqrt{\pi}\tau_{\mathrm{NIR}}^3 f_r} \tag{E6.12}$$

We now write the CW emission power by considering a CW pump term as $P_{\mathrm{pump}}(t) = \sin^2(2\pi\nu_{\mathrm{THz}}t)$. We thus have:

$$P_{\mathrm{CW}}^{\mathrm{THz}} = \int_{\mathbb{R}} E_{\mathrm{THz}}^2(t)dt = \frac{\alpha^2}{2\pi}\int \omega^2\delta(\omega - \omega_{\mathrm{THz}})d\omega = \alpha^2\omega_{\mathrm{THz}}^2 \tag{E6.13}$$

The CW-to-pulsed ratio between the pulsed emission regime of the STE and the envisioned CW regime can thus be written as:

$$\eta_{\mathrm{CW}} = \frac{P_{\mathrm{CW}}^{\mathrm{THz}}}{P_{\mathrm{pulse}}^{\mathrm{THz}}} = \frac{\sqrt{\pi}}{2}\tau_{\mathrm{NIR}}^3 f_r \omega_{\mathrm{THz}}^2 \tag{E6.14}$$

Typically for values of ν_{THz}=1 THz, f_r=80 MHz (oscillator) and τ_{NIR}=100 fs, we estimate the pulsed-to-CW ratio about η_{CW}=10^{-8}. This is a challenging signal to be measured as it is expected around the pW (compared to µW in pulsed regime) but interestingly, we see that the ratio evolves as ω_{THz}^2 and the ratio will thus be around 10^{-6} around 10 THz. We thus propose to simulate the THz CW response from STE using our 1D-FDTD method.

4.3 THz CW modelling by the wave-diffusion model.

To understand the effect of the spintronic THz photomixing, we performed 1D-FDTD simulations using the wave-modelling implemented in Chap. III with a CW-based pumping at a frequency $\nu_{\mathrm{THz}} = 1/T_{\mathrm{period}} = \omega_{\mathrm{THz}}/2\pi$. For that, we consider a pump power profile of the following form:

$$\mathcal{P}_0^{\mathrm{CW}}(\sigma, \mathbf{r}, t) = s_\sigma A \sin^2(2\pi\nu_{\mathrm{THz}}t) \tag{E6.15}$$

where A is the normalization coefficient and s_σ is the spin-asymmetric pump ratio that we fix to 1:0 (majority spins) for convenience. To compare the integrated THz power $P_{\mathrm{THz}} = \int E_{\mathrm{THz}}^2(\omega)d\omega$ between the pulsed and CW emission, we normalize the two pulsed and CW pumps on the totally computed time ΔT =0.1 ns which is the maximal time we can compute for a time step of dt =1 fs, thus corresponding to an artificial repetition rate of $f_r = 1/\Delta T$ =10 GHz.

Simulation results. We have performed FDTD simulations (wave-diffusion model developed in Chap. III) to try to illustrate this theoretically expected behaviour, respectively at fixed pulse duration (τ_{NIR} =100 fs) as a function of the beatnote frequency ν_{THz}, and alternatively at fixed beatnote frequency (ν_{THz}=1 THz) as a function of the pulse duration τ_{NIR} as presented in Fig. 6.11. We first notice that for the interesting study case comparing the power from CW photomixing with ν_{THz}=1 THz and from the pulsed case with τ_{NIR}=100 fs and artificial f_r=10 GHz, we obtain numerically a pulsed-to-CW ratio about $\eta_{\mathrm{CW}} = 7 \times 10^{-6}$, in agreement with the theoretical derivation predicting a value $\simeq 10^{-5}$ for the computed parameters. We also see that the pulsed-to-CW ratio evolves very closely to a dependence following ω_{THz}^2 and τ_{NIR}^3, excepted for the short dynamics region. The trend at longer dynamics (shown in yellow) is in very well agreement with the theoretical understanding of the CW-operation of STE that we have developed before.

However, one notes that for very high frequency and short pulse duration, the simulations results are diverging in the short dynamics region from the previously established understanding. Several elements could account this behaviour like the necessity of finding an interplay between the computation limitation (time of calculation, memory use, *etc.*) and the smallest time step available for accuracy (typically $dt \simeq$1 fs). This discussion is similar for highest CW beatnote frequency (as the pump oscillations are of small period, typically around 10 fs). Even if we have used a very narrow time step (about 1 fs short), caution is needed about the interpretation of the modelling in those regions as they do not follow the expected trend.

Towards a new understanding of spintronic THz photomixing. Nonetheless, the theoretical prediction is also to reformulate as one considers very short dynamics, around 20 fs down to 10 fs which is similar to the typical spin scattering time in the system. Following the derivation proposed by Preu *et al.* [101] for PCAs, it would be interesting to define the high-frequency roll-off of our STE system corresponding to $\nu_{\mathrm{rel}} = 1/2\pi\tau_{\mathrm{rel}}$ where τ_{rel} is the main relaxation time of our system, presently the spin-flip scattering time. In the high-frequency range, the pulsed-to-CW ratio would evolves as ν_{THz}^{-2}. This is currently under investigation, and the pulsed-to-CW ratio would have the following form:

$$\eta = \frac{P_{\mathrm{CW}}}{P_{\mathrm{pulse}}} \simeq \frac{(\omega_{\mathrm{THz}}\tau_{\mathrm{rel}})^2}{4(\omega_{\mathrm{THz}}\tau_{\mathrm{rel}})^2 + (1-(\omega_{\mathrm{THz}}\tau_{\mathrm{rel}})^2)^2} f_r \tau_{\mathrm{NIR}} \tag{E6.16}$$

Towards an experimental implementation of spintronic THz photomixing. Following this theoretical understanding of the radiation performances of STE-photomixers, recent experiments have been conducted by our collaborators at IEMN (P. Koleják, G. Lezier, M. Vanwolleghem), demonstrating the experimental operation of STE-photomixing [377]. Measured amplitudes are about few hundreds of fW at 1 THz. Although this obtained power is weak, especially compared to photoconductive switches based photomixing (typically, few µW can be achieved), this result is central and promises STE-photomixing operation for frequencies above 2 THz, which is a region hard to cover nowadays. Moreover, we have also demonstrated numerically that, compared to current electronic THz photomixer sources, the pulsed-to-CW efficiency is expected to increase as ω_{THz}^2, so that the projected factor already reaches $\times 4$ for the THz CW power at 2 THz. Upon future optimization and high-frequency photomixing, one could envision in the future the CW power to reach few µW with spintronic THz photomixing [377].

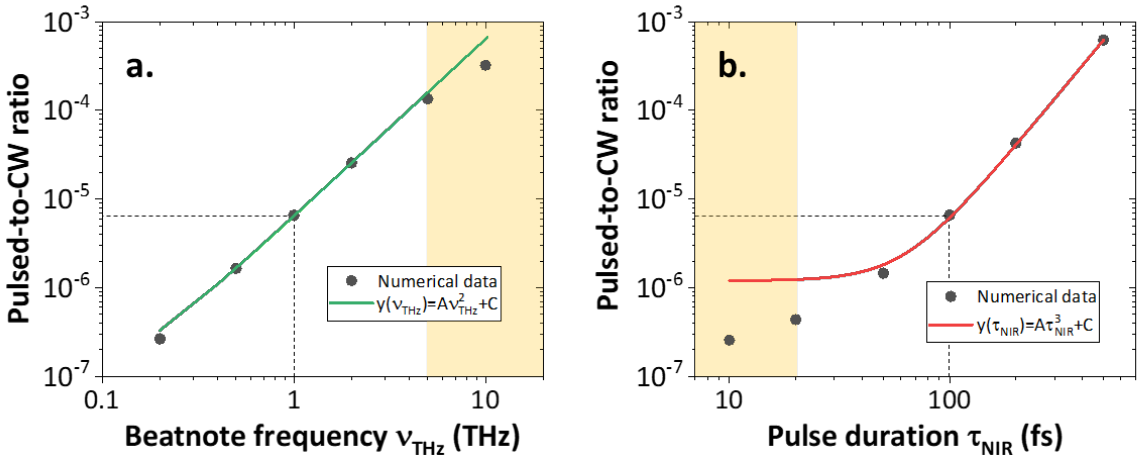

Figure 6.11: Modelling CW THz efficiency compared to the pulsed working regime. (a) Impact of the CW pump frequency ν_{THz} on the pulsed-to-CW ratio (for fixed pump pulse duration τ_{NIR}=100 fs). (b) Impact of the pulse duration τ_{NIR} on the pulsed-to-CW ratio (for fixed CW frequency ν_{THz}=1 THz). The orange region shows the limits of our current understanding.

5 Conclusions and projected implementations.

Perspectives for engineering and functionalizing spintronic THz emitters.

In conclusion, we have explored several ways to functionalize STEs. First, we increased the radiation power by considering buried THz cavities followed with ARC structures which efficiencies are reported in Table VI.1 compared to the recent literature. We have also demonstrated the theoretical working of CW-based STE photomixers, highlighting the challenges ahead owing to the expected low THz emission power if no careful engineering of the emission is performed before.

From this work, we can now present a global strategy for the ideal STE structure, that would combined the following strategies, for instance in transmission: the STE would be pumped in transmission geometry from *i*) a well-defined NIR cavity as proposed by Herapath *et al.* [142]. The facing layer would be enclosed with a well-engineered ARC as we proposed with parylene coating. Alternatively, in the reflection geometry, we can propose a buried metallic reflector, potentially combined with a distributed Bragg reflector (DBR), to fully reflect the generated THz wave, and a top ARC to avoid losing the reflected component.

5.1 Role of the substrate: thermal management and THz refractive index.

Finally, we have started to look at the impact of the substrate thermal conductivity to efficiently provide STE with thermal management as recently studied by Vogel *et al.* [141]. Indeed, an enhanced heat diffusion would likely benefit for STEs, comparing for instance the thermal conductivity of sapphire and MgO to the ones of CVD diamond or AlN given in Table VI.2. The effect of a high thermal conductivity substrate is expected at higher fluences, avoiding the saturation of the emission as the NIR generated heat would be evacuated more easily. This might also be linked to a better out-coupling of the generated radiation from hot STE with free-space.

Experimental realization. We present in Fig. 6.12a the implemented structure. The STE is deposited at the same time on both sapphire and CVD diamond substrates. We further look at the

Year	Structure	Field enhancement	Power enhancement
	Near-infrared pump collection		
2019	NIR Bragg mirror [142]	+100%	$\times 4$
2022	NIR photonic crystal [198]	-	-
	THz transposed photonic strategies		
2022	Parylene-based THz ARC (This work)	+60%	$\times 2.56$
2022	Buried Au THz cavity (This work)	+32%	$\times 1.74$
	Antenna-coupling and plasmonics		
2018	Photoconductive antenna enhanced STE [200]	x10 (below 1 THz)	x100 (below 1 THz)
2019	Coupled-antenna at 1550 nm [201]	$\times 2.4$	$\times 5.76$
2021	Bow-tie antenna [205]	+48% to +98%	$\times 2.3$ to $\times 3.9$
2022	Gold-nanorods plasmonics STE [209]	$\times 2.4$	$\times 5.76$
2022	Rectangular antenna [206]	$\times 4.2$	$\times 17.6$

Table VI.1: Targeted THz enhancement for the different implemented engineering approaches for spintronic THz emitters.

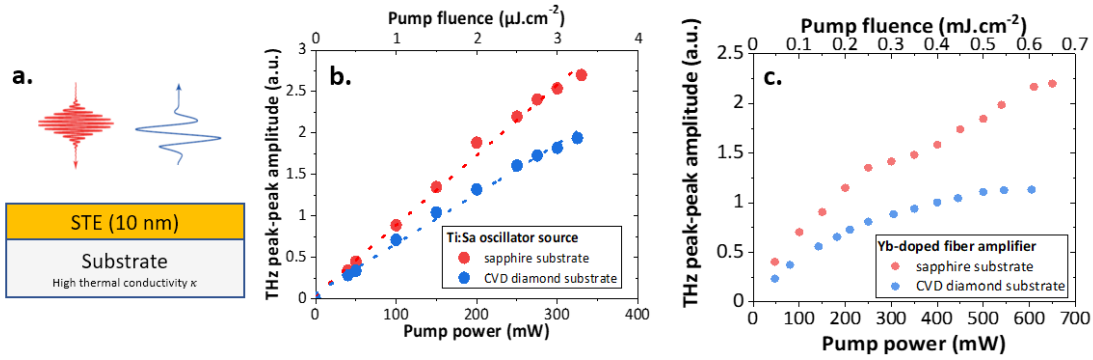

Figure 6.12: Influence of the substrate heat diffusivity. (a) Schematics of the realized structure. (b-c) THz peak-peak amplitude from W/CoFe/Pt STE grown on sapphire or CVD diamond, as a function of the fluence, (b) in the low fluence regime derived from an oscillator or (c) in the high fluence regime derived from an amplifier.

response of the STE at low pump fluences using a Ti:Sa oscillator (repetition rate 80 MHz, pulse width 120 fs, central wavelength 800 nm, pulse energy 3 nJ, more details in Dang *et al.* [231]) and at higher pump fluences using a Yb-doped fiber amplifier (repetition rate 200 kHz, pulse width 23 fs, pulse energy 200 µJ, more details in Nilforoushan *et al.* [378]), respectively in Figs. 6.12b and 6.12c. Surprisingly, we do not see a strong difference in the THz amplitude from STE on sapphire and CVD diamond. By calculating the impact of the different THz refractive indices between sapphire $n_{\mathrm{THz}} + i\kappa_{\mathrm{THz}} = 3.3 + 0.045i$ and CVD diamond $n_{\mathrm{THz}} + i\kappa_{\mathrm{THz}} = 2.5 + 0.1i$, we expect a THz amplitude reduction of -4% for the CVD diamond based STE. However, at the high pump fluence regime, the saturation on CVD diamond compared to sapphire is unexpected.

Material	CVD diamond [379]	Sapphire [380]	AlN [381]	MgO [382]
Thermal conductivity κ (W.m^{-1}.K^{-1})	>1800	45	320	30

Table VI.2: Thermal conductivity at 300 K for selected substrates: CVD diamond, sapphire, AlN and MgO.

This would indicate that the role of the thermal conductivity might not be predominant in the high fluence regime of STE (especially using amplified sources) and we can also address here a possible saturation of the demagnetization process with such high fluences. In the future developments, we aim to prospect active thermal management system to build more efficient STEs. Notably, a careful interplay between the conductivity and the THz refractive would need to be made, as the THz electric field is evolving as $\propto 1/n_s$.

5.2 Spintronic coupled THz antennas and resonators.

The coupling between electrical and optical impedance has not been explored in the frame of these studies. We can cite as an interesting example the diabolo-shaped antenna proposed by Talara *et al.* [205]. From their metallic composition, STEs are therefore an interesting playground for designing THz antennas and resonators. An interesting point to study in the future is also the evolution of the optical impedance with free-space as a function of the pump power via a heat-dissipater and the electrical coupling with an antenna, all in a combined structure. Typically, a power enhancement about a factor $\simeq 25$ could be achieved with all the enhancement paths presented before (including ARCs ($\times 2.6$), NIR Bragg mirror ($\times 4$) and antenna-coupled STE (at minima $\times 2.3$)), and this would allow strong capabilities to tune the THz performances derived from STEs in their saturation regime.

5.3 Experimental integrations of THz spintronics-based functionalities.

STE technological maturity is rapidly increasing, with recent proof-of-concepts that illustrate for instance the use of highly-scalable plastic bendable substrates for practical uses. Jin *et al.* [199] recently suggested the use of polyethylene terephthalate (PET) as firstly reported in 2016 by Wu *et al.* [85]. The THz emission resulting of such integrated structures does not vary with the bending angle for instance (up to a bending angle of 24° [199]) and allow spectroscopy measurements. Alternatives routes to integrate spintronic THz emitters with existing technologies has been also proposed with liquid crystals [383] to control the polarization. Tong *et al.* [384] have also reported the use of Co/Pt and Co/W alternates to pattern coded spintronics, where the polarization can be spatially controlled by use of an optical mask. We can also predict the use of spintronic heterostructures for broadband THz detection.

Conclusions and perspectives

THz spintronics and spintronic THz emitters represent a fast-growing and very promising research topic, aiming to probe ultrafast dynamics of correlated systems, and potentially realizing efficient and novel ultrafast THz sources. Such optically excited spin emitters already possess advantages owing to their low fabrication cost, broadband response, controllable polarization, and their ease of implementation in existing systems, as well as their robustness over time, making them ideal candidates for THz devices. Throughout this thesis, we have aimed to present new concepts, insights and enhancement strategies for spintronic THz emitters. We have investigated a range of areas in this newly emerged domain of THz spintronics, from the spin-injection to spin-to-charge conversion efficiency and spin-relaxation processes in multilayers. In details, we have focused on material optimization (spin Hall alloys, multilayer repetition strategies, Weyl semimetals) and on the role of spin-interfaces (spin-sink and interfacial scattering comprehension) in metallic systems. We further showed the use of strong spin-orbit coupling quantum materials (topological insulators) in THz emission. This is followed by narrowband THz emitters with insulating antiferromagnets compared to the broadband emission in other systems. Finally, we showed the first steps to enhance THz emitters by means of photonic engineering.

- **Metallic THz emitters relying 3*d*/5*d* systems.**

We have demonstrated that diverse approaches exist to enhance the efficiency of metallic spintronic THz emitters based on ferromagnetic/heavy metal heterostructures. We proposed first a material-based approach to increase the interconversion efficiency, with spin Hall alloys (*e.g.* Au:W, Au:Ta) which showed the necessary trade-off between the spin Hall angle, the spin Hall conductivity and the spin-diffusion length in high-scattering rate alloys. We then studied the strategy of repeated multilayers, in which we reported a power performance increased by $\times 2.25$. An important interplay between the spin-charge conversion efficiency and THz absorption in the depth of metallic layers has been evidenced. We have also shown that the replacement of $3d$ ferromagnetic material by a Weyl semi-metal from the Heusler family (*e.g.* Co_2MnGa) permits a strong THz efficiency (increase of a factor $\times 2$) in those heterostructures owing to a lowered THz absorptive conductivity and higher spin-polarization. Another approach consisted in the careful tailoring of the spin-current and spin-interfaces by use of spin-sinks (*e.g.* Au:W). Owing to the good spin-transparency with ferromagnets and a reduced conductivity compared to their heavy metals counterpart, an effective spin-relaxation in spin-sinks avoids detrimental reflections in thin spin-orbit coupling material designed for efficient spintronic THz emitters, with the report of a THz amplitude gain by a factor $\times 2$. We also demonstrated the central role of the interface transmission and interfacial scattering events, reducing the THz efficiency derived from metallic layers. Beyond pure performance metrics, we show that THz spectroscopy of the generated current transients from such nanometer-thin spintronic structures permits an in-depth comprehension of the ultrafast spin-related injection, relaxation and conversion processes down to the sub-picosecond timescale. This has also been supported by the development of the wave-diffusion model to understand and predict the ultrafast spin-current propagation and tailoring in multilayers.

- **Topological insulator-based systems for efficient THz spintronics.**

In contrast to fully metallic systems, we have demonstrated novel spintronic THz structures on topological insulators from the Bi-based family, taking advantage of their strong interfacial spin-orbit coupling properties. In these systems (*e.g.* $SnBi_2Te_4$/Co and $Bi_{1-x}Sb_x$/Co), we show a careful Fermi level pinning in the bandgap by material doping, stoichiometry as well as strain engineering. The topological surface states (confirmed by angular photoemission spectroscopy) contributions to the THz spin-charge conversion and subsequent THz emission have been discussed in the frame of the inverse Rashba-Edelstein effect and the potential hybridization of the surface states under the effect of *i*) the ferromagnetic contact, *ii*) charge transfer effects and *iii*) in the very thin topological insulator thickness limit. This work has highlighted that THz emission spectroscopy is a powerful tool to probe spin-injection and spin-current relaxation mechanisms, for instance with the mapping of a Schotkky barrier formation in Bi_2Se_3/WSe_2/Co. In particular, we have shown in the prototypical $Bi_{1-x}Sb_x$/Co bilayer a net THz power gain at least a factor $\times 2.25$ compared to the reference bilayer Co/Pt metallic emitter. An extensive crystallographic azimuthal profile of the THz emission, as well as thickness-dependence of the topological insulator allows to separate the non-linear optical contribution in topological insulator/ferromagnetic multistacked structures, typically an order of magnitude smaller than the spin-related injection and relaxation processes (magnetic contribution). From the extensive experimental and theoretical developments, we conclude on a majority interfacial spin-charge conversion mechanism in topological insulators systems in contact with a ferromagnet, with the possibility of the inverse Rashba-Edelstein effect mediated by hybridized Rashba-like spin-textured surface states. The topological protection does not seem, from our studies, required to induce an efficient interfacial spin-current interconversion. This opens up interesting developments for highly integrated topological THz spintronic devices, taking advantage of their strong interfacial spin-orbit coupling properties while still in direct contact with spin-injectors in complex multistructures.

- **Antiferromagnetic systems for coherent narrowband THz emission.**

An important perspective in the THz spintronic field is related to the possibility of spectrally narrowband THz emitters via antiferromagnetic-based structures (*e.g.* NiO, α-Fe_2O_3 and $TmFeO_3$,) owing to the THz dynamics of the antiferromagnetic Néel vector. Here, we demonstrate for the first time, in easy-plane NiO/Pt bilayers, the presence of coherent narrowband contribution centered at 1.1 THz *i.e.* the out-of-plane mode of the Néel vector of NiO. After demonstrating that the THz generation process is a result of the spin current generation by the reduction of the Néel vector of NiO and subsequent spin-charge conversion in Pt via ISHE, we highlight two radically different mechanisms between (111) and (001) oriented NiO thin films. While instantaneous off-resonant Raman-like spin-optical torque is at the origin of the (111)-based THz emission, the exact origin of the (001) mechanism is highly debated in the scientific community. Here, we provide evidence that ultrafast spin-phonon interactions are at the heart of (001)-oriented NiO THz emission. In particular, one has to disentangle coherent strain wave contribution shrinking the Néel vector via ultrafast magneto-strictions from incoherent phonon propagation. Interestingly in the latter case, one needs to separate two components: the linear spin-Seebeck effect from the non-linear spin Seebeck effect, which represents the interfacial spin-torque induced by thermal gradient excited spin-fluctuations in the adjacent heavy metal. However, we could not account nor discard these two heat contributions in NiO/Pt bilayers, as discussed very recently in the literature. A strong perspective awaiting spintronic THz emitters is the future application of efficient strain-transducers and launched magneto-strictions to control the narrowband THz emission, via static electrical control or launched via strain waves induced by ultrafast pump heating. These materials also launch the possibility of THz detection via the interaction of the Néel vector with the driving THz electric field.

- **Towards the engineering and functionalization of spintronic THz emitters.**

Lastly, we show perspectives on the application of photonic engineering strategies transposed on THz frequencies to enhance the emission. The use of anti-refractive coatings allows to enhance the radiation coupling with free-space, permitting a power enhancement of about $\times 2.4$. Cavity-based spintronic THz emitters are also a promising way to enhance the radiation efficiency on higher frequencies. We also theoretically predicted spintronic photomixer to derive THz continuous waveform (narrowband) emission in free-space. The combination of photonic engineering of the near-infrared pump and generated THz radiation promises a potential route towards THz enhancement.

As a closing remark, our findings represent significant advances in the comprehension of the THz generation and sub-picosecond dynamics in nanometer-thin optically excited spintronic heterostructures. As this study mostly identified the generated dynamics in the 1-5 THz range, one would find pertinent in the future to explore the spectroscopy of ultrabroadband dynamics in the 5-10 THz range, offering promising insights to both understand the fundamental relaxation of spin currents and enhance the spintronic THz emitters to achieve a full covering of the THz range. Beyond the operation of broadband spintronic THz emitters, this work proposes a novel vision for narrowband THz operation with the tuning of the electronic wave interferences in thin metallic layers, the theoretical report of the spintronic photomixing concept and with the development of antiferromagnetic-based emitters. On this last point, we focused the THz emission from fully-compensated insulting antiferromagnets, but one could take advantage of canted antiferromagnets to evaluate both responses of the weak ferromagnetic moment and antiferromagnetic order under ultrafast magneto-strictions. Moreover, as we reported that such magneto-strictive effects depend on the symmetry of the material, one could try to study the evolution of the THz response for a system varying with the temperature (for instance α-Fe_2O_3 across the Morin transition). Further, tunable THz detectors could also be envisioned with spintronic concepts, by counting on Zeeman-type torque in thin magnetic layers to account for large detection bandwidth due to the absence of phonons. This thesis paves the way towards highly efficient THz sources. Combining all the presented enhancement strategies (material, interfaces, optical and THz wave engineering, *etc.*) and counting on novel degrees of freedom relying on the interfacial conversion with high spin-orbit materials, one could potentially target a gain in THz power by at least an order of magnitude ($\times 25$ as derived from our perspectives relying on antenna-coupled and photonic engineered spintronic THz sources). For all these reasons, our proposal for narrowband and topological-based THz emitters promise highly-integrated efficient spintronic THz platforms and represent the future generation of THz spintronic sources.

Bibliography

[1] N. W. Ashcroft and N. D. Mermin, Physique des solides. Les Ulis Cedex A, France: EDP Sciences, 2002. OCLC: 1004989344. 6, 21

[2] P. Mohn and E. P. Wohlfarth, "The Curie temperature of the ferromagnetic transition metals and their compounds," Journal of Physics F: Metal Physics, vol. 17, pp. 2421–2430, Dec. 1987. 7

[3] R. J. Soulen, J. M. Byers, M. S. Osofsky, B. Nadgorny, T. Ambrose, S. F. Cheng, P. R. Broussard, C. T. Tanaka, J. Nowak, J. S. Moodera, A. Barry, and J. M. D. Coey, "Measuring the Spin Polarization of a Metal with a Superconducting Point Contact," Science, vol. 282, pp. 85–88, Oct. 1998. 7

[4] S. X. Huang, T. Y. Chen, and C. L. Chien, "Spin polarization of amorphous CoFeB determined by point-contact Andreev reflection," Applied Physics Letters, vol. 92, p. 242509, June 2008. 7

[5] L. Liu, C.-F. Pai, Y. Li, H. W. Tseng, D. C. Ralph, and R. A. Buhrman, "Spin-Torque Switching with the Giant Spin Hall Effect of Tantalum," Science, vol. 336, pp. 555–558, May 2012. 7, 16

[6] H. Sato, P. Chureemart, F. Matsukura, R. W. Chantrell, H. Ohno, and R. F. L. Evans, "Temperature-dependent properties of CoFeB/MgO thin films: Experiments versus simulations," Physical Review B, vol. 98, p. 214428, Dec. 2018. 7

[7] R. Winkler, Spin-orbit coupling effects in two-dimensional electron and hole systems. No. v. 191 in Springer tracts in modern physics, Berlin ; New York: Springer, 2003. 7

[8] F. Hellman, A. Hoffmann, Y. Tserkovnyak, G. S. Beach, E. E. Fullerton, C. Leighton, A. H. MacDonald, D. C. Ralph, D. A. Arena, H. A. Dürr, P. Fischer, J. Grollier, J. P. Heremans, T. Jungwirth, A. V. Kimel, B. Koopmans, I. N. Krivorotov, S. J. May, A. K. Petford-Long, J. M. Rondinelli, N. Samarth, I. K. Schuller, A. N. Slavin, M. D. Stiles, O. Tchernyshyov, A. Thiaville, and B. L. Zink, "Interface-induced phenomena in magnetism," Reviews of Modern Physics, vol. 89, p. 025006, June 2017. 8, 9

[9] A. Brataas, G. Bauer, and P. Kelly, Non-collinear magnetoelectronics, vol. 427. Elsevier, physics reports ed., Apr. 2006. 8, 10, 22, 24

[10] T. Valet and A. Fert, "Theory of the perpendicular magnetoresistance in magnetic multilayers," Physical Review B, vol. 48, pp. 7099–7113, Sept. 1993. 8, 227

[11] C. Petitjean, D. Luc, and X. Waintal, "Unified Drift-Diffusion Theory for Transverse Spin Currents in Spin Valves, Domain Walls, and Other Textured Magnets," Physical Review Letters, vol. 109, p. 117204, Sept. 2012. 8, 20

[12] K. V. Shanavas, Z. S. Popović, and S. Satpathy, "Theoretical model for Rashba spin-orbit interaction in *d* electrons," Physical Review B, vol. 90, p. 165108, Oct. 2014. 9

[13] F. Herman, S. Skillman, and J. Arents, "Atomic Structure Calculations," Journal of The Electrochemical Society, vol. 111, no. 3, p. 87C, 1964. 9

[14] R. D. Cowan, The theory of atomic structure and spectra. No. 3 in Los Alamos series in basic and applied sciences, Berkeley: University of California Press, 1981. 9

[15] S. A. Wolf, D. D. Awschalom, R. A. Buhrman, J. M. Daughton, S. von Molnár, M. L. Roukes, A. Y. Chtchelkanova, and D. M. Treger, "Spintronics: A Spin-Based Electronics Vision for the Future," Science, vol. 294, pp. 1488–1495, Nov. 2001. 8

[16] A. Andrae and T. Edler, "On Global Electricity Usage of Communication Technology: Trends to 2030," Challenges, vol. 6, pp. 117–157, Apr. 2015. 9

[17] B. Dieny, I. L. Prejbeanu, K. Garello, P. Gambardella, P. Freitas, R. Lehndorff, W. Raberg, U. Ebels, S. O. Demokritov, J. Akerman, A. Deac, P. Pirro, C. Adelmann, A. Anane, A. V. Chumak, A. Hirohata, S. Mangin, S. O. Valenzuela, M. C. Onbaşlı, M. d'Aquino, G. Prenat, G. Finocchio, L. Lopez-Diaz, R. Chantrell, O. Chubykalo-Fesenko, and P. Bortolotti, "Opportunities and challenges for spintronics in the microelectronics industry," Nature Electronics, vol. 3, pp. 446–459, Aug. 2020. 9

[18] C. Chappert, A. Fert, and F. N. Van Dau, "The emergence of spin electronics in data storage," Nature Materials, vol. 6, pp. 813–823, Nov. 2007. 9

[19] P. Barla, V. K. Joshi, and S. Bhat, "Spintronic devices: a promising alternative to CMOS devices," Journal of Computational Electronics, vol. 20, pp. 805–837, Apr. 2021. 9

[20] S. Manipatruni, D. E. Nikonov, C.-C. Lin, T. A. Gosavi, H. Liu, B. Prasad, Y.-L. Huang, E. Bonturim, R. Ramesh, and I. A. Young, "Scalable energy-efficient magnetoelectric spin–orbit logic," Nature, vol. 565, pp. 35–42, Jan. 2019. 9

[21] M. N. Baibich, J. M. Broto, A. Fert, F. N. Van Dau, F. Petroff, P. Etienne, G. Creuzet, A. Friederich, and J. Chazelas, "Giant Magnetoresistance of (001)Fe/(001)Cr Magnetic Superlattices," Physical Review Letters, vol. 61, pp. 2472–2475, Nov. 1988. 9, 10

[22] P. Grünberg, R. Schreiber, Y. Pang, M. B. Brodsky, and H. Sowers, "Layered Magnetic Structures: Evidence for Antiferromagnetic Coupling of Fe Layers across Cr Interlayers," Physical Review Letters, vol. 57, pp. 2442–2445, Nov. 1986. 9

[23] W. Thomson, "XIX. On the electro-dynamic qualities of metals: Effects of magnetization on the electric conductivity of nickel and of iron," Proc. R. Soc. Lond., vol. 8, pp. 546–550, 1857. 11

[24] T. McGuire and R. Potter, "Anisotropic magnetoresistance in ferromagnetic 3*d* alloys," IEEE Transactions on Magnetics, vol. 11, pp. 1018–1038, July 1975. 11

[25] E. C. Stoner and E. P. Wohlfarth, "A mechanism of magnetic hysteresis in heterogeneous alloys," Philosophical Transactions of the Royal Society of London, vol. Series A, Mathematical and Physical Sciences, no. 240, pp. 599–642, 1948. 11

[26] A. Karsenty, "A Comprehensive Review of Integrated Hall Effects in Macro-, Micro-, Nanoscales, and Quantum Devices," Sensors, vol. 20, p. 4163, July 2020. 12

[27] N. Nagaosa, J. Sinova, S. Onoda, A. H. MacDonald, and N. P. Ong, "Anomalous Hall effect," Reviews of Modern Physics, vol. 82, pp. 1539–1592, May 2010. 13

[28] M. Dyakonov and V. Perel, "Current-induced spin orientation of electrons in semiconductors," Physics Letters A, vol. 35, pp. 459–460, July 1971. 13

[29] J. E. Hirsch, "Spin Hall Effect," Physical Review Letters, vol. 83, pp. 1834–1837, Aug. 1999. 13

[30] T. H. Dang, Q. Barbedienne, D. Q. To, E. Rongione, N. Reyren, F. Godel, S. Collin, J. M. George, and H. Jaffrès, "Anomalous Hall effect in 3d/5d multilayers mediated by interface scattering and nonlocal spin conductivity," Physical Review B, vol. 102, p. 144405, Oct. 2020. 13, 15, 23, 97, 234

[31] J. Smit, "The spontaneous hall effect in ferromagnetics I," Physica, vol. 21, pp. 877–887, Jan. 1955. 13

[32] J. Smit, "The spontaneous hall effect in ferromagnetics II," Physica, vol. 24, pp. 39–51, Jan. 1958. 13

[33] C. L. Chien and C. R. Westgate, eds., The Hall Effect and Its Applications. Boston, MA: Springer US, 1980. 13

[34] G.-Y. Guo, S. Maekawa, and N. Nagaosa, "Enhanced Spin Hall Effect by Resonant Skew Scattering in the Orbital-Dependent Kondo Effect," Physical Review Letters, vol. 102, p. 036401, Jan. 2009. 13

[35] L. Berger, "Side-Jump Mechanism for the Hall Effect of Ferromagnets," Physical Review B, vol. 2, pp. 4559–4566, Dec. 1970. 13, 14

[36] S. Lowitzer, M. Gradhand, D. Ködderitzsch, D. V. Fedorov, I. Mertig, and H. Ebert, "Extrinsic and Intrinsic Contributions to the Spin Hall Effect of Alloys," Physical Review Letters, vol. 106, p. 056601, Feb. 2011. 14

[37] P. Laczkowski, H. Jaffrès, W. Savero-Torres, J.-C. Rojas-Sánchez, Y. Fu, N. Reyren, C. Deranlot, L. Notin, C. Beigné, J.-P. Attané, L. Vila, J.-M. George, and A. Marty, "Evaluation of spin diffusion length of AuW alloys using spin absorption experiments in the limit of large spin-orbit interactions," Physical Review B, vol. 92, p. 214405, Dec. 2015. 15, 16, 85, 90

[38] P. Laczkowski, J.-C. Rojas-Sánchez, W. Savero-Torres, H. Jaffrès, N. Reyren, C. Deranlot, L. Notin, C. Beigné, A. Marty, J.-P. Attané, L. Vila, J.-M. George, and A. Fert, "Experimental evidences of a large extrinsic spin Hall effect in AuW alloy," Applied Physics Letters, vol. 104, p. 142403, Apr. 2014. 15, 16, 85, 90

[39] P. Laczkowski, Y. Fu, H. Yang, C. Bouard, P. Warin, V. Maurel, M. Chshiev, and A. Marty, "Large enhancement of the spin Hall effect in Au by side-jump scattering on Ta impurities," Physical Review B, p. 5, 2017. 15, 16, 24, 85

[40] Y. K. Kato, R. C. Myers, A. C. Gossard, and D. D. Awschalom, "Observation of the Spin Hall Effect in Semiconductors," Science, vol. 306, pp. 1910–1913, Dec. 2004. 15

[41] J. Wunderlich, B. Kaestner, J. Sinova, and T. Jungwirth, "Experimental Observation of the Spin-Hall Effect in a Two-Dimensional Spin-Orbit Coupled Semiconductor System," Physical Review Letters, vol. 94, p. 047204, Feb. 2005. 15

[42] S. O. Valenzuela and M. Tinkham, "Direct electronic measurement of the spin Hall effect," Nature, vol. 442, pp. 176–179, July 2006. 15

[43] J. Sinova, S. O. Valenzuela, J. Wunderlich, C. Back, and T. Jungwirth, "Spin Hall effects," Reviews of Modern Physics, vol. 87, pp. 1213–1260, Oct. 2015. 15

[44] J.-C. Rojas-Sánchez, N. Reyren, P. Laczkowski, W. Savero, J.-P. Attané, C. Deranlot, M. Jamet, J.-M. George, L. Vila, and H. Jaffrès, "Spin Pumping and Inverse Spin Hall Effect in Platinum: The Essential Role of Spin-Memory Loss at Metallic Interfaces," Physical Review Letters, vol. 112, p. 106602, Mar. 2014. 16, 23, 24, 65, 95, 127

[45] C.-F. Pai, L. Liu, Y. Li, H. W. Tseng, D. C. Ralph, and R. A. Buhrman, "Spin transfer torque devices utilizing the giant spin Hall effect of tungsten," Applied Physics Letters, vol. 101, p. 122404, Sept. 2012. 16

[46] Q. Hao and G. Xiao, "Giant Spin Hall Effect and Switching Induced by Spin-Transfer Torque in a $W/Co_{40}Fe_{40}B_{20}/MgO$ Structure with Perpendicular Magnetic Anisotropy," Physical Review Applied, vol. 3, p. 034009, Mar. 2015. 16

[47] R. Yu, B. F. Miao, L. Sun, Q. Liu, J. Du, P. Omelchenko, B. Heinrich, M. Wu, and H. F. Ding, "Determination of spin Hall angle and spin diffusion length in β-phase-dominated tantalum," Physical Review Materials, vol. 2, p. 074406, July 2018. 16

[48] T. Wang, W. Wang, Y. Xie, M. A. Warsi, J. Wu, Y. Chen, V. O. Lorenz, X. Fan, and J. Q. Xiao, "Large spin Hall angle in vanadium film," Scientific Reports, vol. 7, p. 1306, Dec. 2017. 16

[49] L. Onsager, "Reciprocal Relations in Irreversible Processes. I.," Physical Review, vol. 37, pp. 405–426, Feb. 1931. 16

[50] Y. A. Bychkov and I. Rashba, "Properties of a 2D electron gas with lifted spectral degeneracy," Soviet Journal of Experimental and Theoretical Physics Letters, vol. 39, p. 78, Jan. 1984. ADS Bibcode: 1984JETPL..39...78B. 16

[51] V. Edelstein, "Spin polarization of conduction electrons induced by electric current in two-dimensional asymmetric electron systems," Solid State Communications, vol. 73, pp. 233–235, Jan. 1990. 16

[52] J. C. R. Sánchez, L. Vila, G. Desfonds, S. Gambarelli, J. P. Attané, J. M. De Teresa, C. Magén, and A. Fert, "Spin-to-charge conversion using Rashba coupling at the interface between non-magnetic materials," Nature Communications, vol. 4, p. 2944, Dec. 2013. 17, 18

[53] J.-C. Rojas-Sánchez, S. Oyarzún, Y. Fu, A. Marty, C. Vergnaud, S. Gambarelli, L. Vila, M. Jamet, Y. Ohtsubo, A. Taleb-Ibrahimi, P. Le Fèvre, F. Bertran, N. Reyren, J.-M. George, and A. Fert, "Spin to Charge Conversion at Room Temperature by Spin Pumping into a New Type of Topological Insulator: α-Sn Films," Physical Review Letters, vol. 116, p. 096602, Mar. 2016. 18

[54] N. H. D. Khang, Y. Ueda, and P. N. Hai, "A conductive topological insulator with large spin Hall effect for ultralow power spin–orbit torque switching," Nature Materials, vol. 17, pp. 808–813, Sept. 2018. 18, 49, 119

[55] A. R. Mellnik, J. S. Lee, A. Richardella, J. L. Grab, P. J. Mintun, M. H. Fischer, A. Vaezi, A. Manchon, E.-A. Kim, N. Samarth, and D. C. Ralph, "Spin-transfer torque generated by a topological insulator," Nature, vol. 511, pp. 449–451, July 2014. 18

[56] D. Hsieh, D. Qian, L. Wray, Y. Xia, Y. S. Hor, R. J. Cava, and M. Z. Hasan, "A topological Dirac insulator in a quantum spin Hall phase," Nature, vol. 452, pp. 970–974, Apr. 2008. 18, 119

[57] V. P. Zhukov, E. V. Chulkov, and P. M. Echenique, "Lifetimes and inelastic mean free path of low-energy excited electrons in Fe, Ni, Pt, and Au: *Ab initio* GW + T calculations," Physical Review B, vol. 73, p. 125105, Mar. 2006. 19, 64, 75

[58] V. P. Zhukov and E. V. Chulkov, "The femtosecond dynamics of electrons in metals," Physics-Uspekhi, vol. 52, pp. 105–136, Feb. 2009. 19, 64, 74, 75, 137

[59] J. Tang and K. L. Wang, "Electrical spin injection and transport in semiconductor nanowires: challenges, progress and perspectives," Nanoscale, vol. 7, no. 10, pp. 4325–4337, 2015. 20

[60] R. J. Elliott, "Theory of the Effect of Spin-Orbit Coupling on Magnetic Resonance in Some Semiconductors," Physical Review, vol. 96, pp. 266–279, Oct. 1954. 20

[61] Y. Yafet, "g-Factors and Spin-Lattice Relaxation of Conduction Electrons," in Solid State Physics, vol. 14, pp. 1–98, Elsevier, 1963. 20

[62] R. Lebrun, A. Ross, O. Gomonay, V. Baltz, U. Ebels, A.-L. Barra, A. Qaiumzadeh, A. Brataas, J. Sinova, and M. Kläui, "Long-distance spin-transport across the Morin phase transition up to room temperature in ultra-low damping single crystals of the antiferromagnet α-Fe_2O_3," Nature Communications, vol. 11, p. 6332, Dec. 2020. 21, 173

[63] R. Landauer, "Spatial Variation of Currents and Fields Due to Localized Scatterers in Metallic Conduction," IBM Journal of Research and Development, vol. 1, pp. 223–231, July 1957. 22

[64] T. Gilbert, "A Phenomenological Theory of Damping in Ferromagnetic Materials," IEEE Transactions on Magnetics, vol. 40, pp. 3443–3449, Nov. 2004. 24

[65] Y. Tserkovnyak, A. Brataas, and G. E. W. Bauer, "Spin pumping and magnetization dynamics in metallic multilayers," Physical Review B, vol. 66, p. 224403, Dec. 2002. arXiv: cond-mat/0208091. 24, 25

[66] T. Taniguchi and H. Imamura, "Critical current of spin-transfer-torque-driven magnetization dynamics in magnetic multilayers," Physical Review B, vol. 78, p. 224421, Dec. 2008. 24, 25

[67] E. Beaurepaire, J.-C. Merle, A. Daunois, and J.-Y. Bigot, "Ultrafast Spin Dynamics in Ferromagnetic Nickel," Physical Review Letters, vol. 76, pp. 4250–4253, May 1996. 26, 27, 46

[68] A. V. Kimel, A. Kirilyuk, P. A. Usachev, R. V. Pisarev, A. M. Balbashov, and T. Rasing, "Ultrafast non-thermal control of magnetization by instantaneous photomagnetic pulses," Nature, vol. 435, pp. 655–657, June 2005. 26

[69] B. Koopmans, M. van Kampen, J. T. Kohlhepp, and W. J. M. de Jonge, "Ultrafast Magneto-Optics in Nickel: Magnetism or Optics?," Physical Review Letters, vol. 85, pp. 844–847, July 2000. 26

[70] B. Koopmans, G. Malinowski, F. Dalla Longa, D. Steiauf, M. Fähnle, T. Roth, M. Cinchetti, and M. Aeschlimann, "Explaining the paradoxical diversity of ultrafast laser-induced demagnetization," Nature Materials, vol. 9, pp. 259–265, Mar. 2010. 26, 27

[71] U. Ritzmann, P. M. Oppeneer, and P. Maldonado, "Theory of out-of-equilibrium electron and phonon dynamics in metals after femtosecond laser excitation," Physical Review B, vol. 102, p. 214305, Dec. 2020. 26

[72] M. Deb, E. Popova, S. Zeuschner, M. Hehn, N. Keller, S. Mangin, G. Malinowski, and M. Bargheer, "Generation of spin waves via spin-phonon interaction in a buried dielectric thin film," Physical Review B, p. 9, 2021. 27, 159

[73] M. Battiato, Superdiffusive Spin Transport and Ultrafast Magnetization Dynamics: Femtosecond spin transport as the route to ultrafast spintronics. PhD thesis, Uppsala University, Sept. 2013. 27

[74] M. Battiato, K. Carva, and P. M. Oppeneer, "Theory of laser-induced ultrafast superdiffusive spin transport in layered heterostructures," Physical Review B, vol. 86, p. 024404, July 2012. 27, 62, 64, 65, 66

[75] B. Koopmans, J. J. M. Ruigrok, F. D. Longa, and W. J. M. de Jonge, "Unifying Ultrafast Magnetization Dynamics," Physical Review Letters, vol. 95, p. 267207, Dec. 2005. 27

[76] A. Barman and A. Haldar, "Time-Domain Study of Magnetization Dynamics in Magnetic Thin Films and Micro- and Nanostructures," in Solid State Physics, vol. 65, pp. 1–108, Elsevier, 2014. 27, 28

[77] C. D. Stanciu, F. Hansteen, A. V. Kimel, A. Kirilyuk, A. Tsukamoto, A. Itoh, and T. Rasing, "All-Optical Magnetic Recording with Circularly Polarized Light," Physical Review Letters, vol. 99, p. 047601, July 2007. 27

[78] T. Kampfrath, M. Battiato, P. Maldonado, G. Eilers, J. Nötzold, S. Mährlein, V. Zbarsky, F. Freimuth, Y. Mokrousov, S. Blügel, M. Wolf, I. Radu, P. M. Oppeneer, and M. Münzenberg, "Terahertz spin current pulses controlled by magnetic heterostructures," Nature Nanotechnology, vol. 8, pp. 256–260, Apr. 2013. 27, 28, 217

[79] Z. Jin, A. Tkach, F. Casper, V. Spetter, H. Grimm, A. Thomas, T. Kampfrath, M. Bonn, M. Kläui, and D. Turchinovich, "Accessing the fundamentals of magnetotransport in metals with terahertz probes," Nature Physics, vol. 11, pp. 761–766, Sept. 2015. 27

[80] M. Battiato, K. Carva, and P. M. Oppeneer, "Superdiffusive Spin Transport as a Mechanism of Ultrafast Demagnetization," Physical Review Letters, vol. 105, p. 027203, July 2010. 28, 62, 64, 65, 66, 217

[81] A. Melnikov, I. Razdolski, T. O. Wehling, E. T. Papaioannou, V. Roddatis, P. Fumagalli, O. Aktsipetrov, A. I. Lichtenstein, and U. Bovensiepen, "Ultrafast Transport of Laser-Excited Spin-Polarized Carriers in Au / Fe / MgO (001)," Physical Review Letters, vol. 107, p. 076601, Aug. 2011. 28, 217

[82] T. J. Huisman, R. V. Mikhaylovskiy, J. D. Costa, F. Freimuth, E. Paz, J. Ventura, P. P. Freitas, S. Blügel, Y. Mokrousov, T. Rasing, and A. V. Kimel, "Femtosecond control of electric currents in metallic ferromagnetic heterostructures," Nature Nanotechnology, vol. 11, pp. 455–458, May 2016. 28, 43, 46, 217

[83] T. Seifert, S. Jaiswal, U. Martens, J. Hannegan, L. Braun, P. Maldonado, F. Freimuth, A. Kronenberg, J. Henrizi, I. Radu, E. Beaurepaire, Y. Mokrousov, P. M. Oppeneer, M. Jourdan, G. Jakob, D. Turchinovich, L. M. Hayden, M. Wolf, M. Münzenberg, M. Kläui, and T. Kampfrath, "Efficient metallic spintronic emitters of ultrabroadband terahertz radiation," Nature Photonics, vol. 10, pp. 483–488, July 2016. 28, 43, 45, 46, 47, 82, 85, 87, 217, 218

[84] D. Yang, J. Liang, C. Zhou, L. Sun, R. Zheng, S. Luo, Y. Wu, and J. Qi, "Powerful and Tunable THz Emitters Based on the Fe/Pt Magnetic Heterostructure," Advanced Optical Materials, vol. 4, pp. 1944–1949, Dec. 2016. 28, 47, 48, 54, 87

[85] Y. Wu, M. Elyasi, X. Qiu, M. Chen, Y. Liu, L. Ke, and H. Yang, "High-Performance THz Emitters Based on Ferromagnetic/Nonmagnetic Heterostructures," Advanced Materials, vol. 29, p. 1603031, Jan. 2017. 28, 46, 47, 191

[86] M. Tonouchi, "Cutting-edge terahertz technology," Nature Photonics, vol. 1, pp. 97–105, Feb. 2007. 30, 40

[87] B. Ferguson and X.-C. Zhang, "Materials for terahertz science and technology," Nature Materials, vol. 1, pp. 26–33, Sept. 2002. 30

[88] S. S. Dhillon, M. S. Vitiello, E. H. Linfield, A. G. Davies, M. C. Hoffmann, J. Booske, C. Paoloni, M. Gensch, P. Weightman, G. P. Williams, E. Castro-Camus, D. R. S. Cumming, F. Simoens, I. Escorcia-Carranza, J. Grant, S. Lucyszyn, M. Kuwata-Gonokami, K. Konishi, M. Koch, C. A. Schmuttenmaer, T. L. Cocker, R. Huber, A. G. Markelz, Z. D. Taylor, V. P. Wallace, J. A. Zeitler, J. Sibik, T. M. Korter, B. Ellison, S. Rea, P. Goldsmith, K. B. Cooper, R. Appleby, D. Pardo, P. G. Huggard, V. Krozer, H. Shams, M. Fice, C. Renaud, A. Seeds, A. St, J. E. Cunningham, and M. B. Johnston, "The 2017 terahertz science and technology roadmap," Appl. Phys., p. 50, 2017. 30, 31, 38, 42, 59

[89] J. P. Guillet, B. Recur, L. Frederique, B. Bousquet, L. Canioni, I. Manek-Hönninger, P. Desbarats, and P. Mounaix, "Review of Terahertz Tomography Techniques," Journal of Infrared, Millimeter, and Terahertz Waves, vol. 35, pp. 382–411, Apr. 2014. 30

[90] S. J. Oh, J. Choi, I. Maeng, J. Y. Park, K. Lee, Y.-M. Huh, J.-S. Suh, S. Haam, and J.-H. Son, "Molecular imaging with terahertz waves," Optics Express, vol. 19, p. 4009, Feb. 2011. 30

[91] S. Yamaguchi, Y. Fukushi, O. Kubota, T. Itsuji, T. Ouchi, and S. Yamamoto, "Brain tumor imaging of rat fresh tissue using terahertz spectroscopy," Scientific Reports, vol. 6, p. 30124, Sept. 2016. 30, 31

[92] A. J. Fitzgerald, V. P. Wallace, M. Jimenez-Linan, L. Bobrow, R. J. Pye, A. D. Purushotham, and D. D. Arnone, "Terahertz Pulsed Imaging of Human Breast Tumors," Radiology, vol. 239, pp. 533–540, May 2006. 31

[93] V. P. Wallace, A. J. Fitzgerald, E. Pickwell, R. J. Pye, P. F. Taday, N. Flanagan, and T. Ha, "Terahertz Pulsed Spectroscopy of Human Basal Cell Carcinoma," Applied Spectroscopy, vol. 60, pp. 1127–1133, Oct. 2006. 31

[94] F. Wahaia, G. Valusis, L. M. Bernardo, A. Almeida, J. A. Moreira, P. C. Lopes, J. Macutkevic, I. Kasalynas, D. Seliuta, R. Adomavicius, R. Henrique, and M. Lopes, "Detection of colon cancer by terahertz techniques," Journal of Molecular Structure, vol. 1006, pp. 77–82, Dec. 2011. 31

[95] C. Ketchazo, Imagerie dans le domaine terahertz: considérations radiométriques pour l'imagerie en mode passif. PhD thesis, Université de Grenoble, Grenoble, 2006. 31

[96] H. Dely, T. Bonazzi, O. Spitz, E. Rodriguez, D. Gacemi, Y. Todorov, K. Pantzas, G. Beaudoin, I. Sagnes, L. Li, A. G. Davies, E. H. Linfield, F. Grillot, A. Vasanelli, and C. Sirtori, "10 Gbit.s $^{-1}$ Free Space Data Transmission at 9 µm Wavelength With Unipolar Quantum Optoelectronics," Laser & Photonics Reviews, vol. 16, p. 2100414, Feb. 2022. 31

[97] H. Ketelsen, R. Mästle, L. Liebermeister, R. Kohlhaas, and B. Globisch, "THz Time-Domain Ellipsometer for Material Characterization and Paint Quality Control with More Than 5 THz Bandwidth," Applied Sciences, vol. 12, p. 3744, Apr. 2022. 31, 56

[98] J. Treutell, Multiplixel heterodyne receiver at submillimeter wavelength for atmospheric sounding. PhD thesis, Observatoire de Paris, Paris, 2011. 31

[99] C. Cohen-Tannoudji, J. Dupont-Roc, and G. Grynberg, Photons et atomes : introduction à l'électrodynamique quantique. Savoirs actuels, EDP Sciences, cnrs editions ed., 1987. 32, 228, 229

[100] D. M. Nenno, R. Binder, and H. C. Schneider, "Simulation of Hot-Carrier Dynamics and Terahertz Emission in Laser-Excited Metallic Bilayers," Physical Review Applied, vol. 11, p. 054083, May 2019. 33, 63, 64, 65, 183

[101] S. Preu, G. H. Döhler, S. Malzer, L. J. Wang, and A. C. Gossard, "Tunable, continuous-wave Terahertz photomixer sources and applications," Journal of Applied Physics, vol. 109, p. 061301, Mar. 2011. 33, 39, 45, 177, 186, 188

[102] T. J. Huisman and T. Rasing, "THz Emission Spectroscopy for THz Spintronics," Journal of the Physical Society of Japan, vol. 86, p. 011009, Jan. 2017. 34

[103] Y. Huang, Z. Yao, C. He, L. Zhu, L. Zhang, J. Bai, and X. Xu, "Terahertz surface and interface emission spectroscopy for advanced materials," Journal of Physics: Condensed Matter, vol. 31, p. 153001, Apr. 2019. 34, 35

[104] S. Casalbuoni, H. Schlarb, B. Schmidt, P. Schmüser, B. Steffen, and A. Winter, "Numerical studies on the electro-optic detection of femtosecond electron bunches," Physical Review Special Topics - Accelerators and Beams, vol. 11, p. 072802, July 2008. 34, 238

[105] J. E. Sipe and A. I. Shkrebtii, "Second-order optical response in semiconductors," Physical Review B, vol. 61, pp. 5337–5352, Feb. 2000. 35

[106] L. Gao, Z. Addison, E. J. Mele, and A. M. Rappe, "Intrinsic Fermi-surface contribution to the bulk photovoltaic effect," Physical Review Research, vol. 3, p. L042032, Nov. 2021. 35, 110, 229

[107] L. Braun, G. Mussler, A. Hruban, M. Konczykowski, T. Schumann, M. Wolf, M. Münzenberg, L. Perfetti, and T. Kampfrath, "Ultrafast photocurrents at the surface of the three-dimensional topological insulator Bi_2Se_3," Nature Communications, vol. 7, p. 13259, Dec. 2016. 35, 110

[108] Y. Kinoshita, N. Kida, T. Miyamoto, M. Kanou, T. Sasagawa, and H. Okamoto, "Terahertz radiation by subpicosecond spin-polarized photocurrent originating from Dirac electrons in a Rashba-type polar semiconductor," Physical Review B, vol. 97, p. 161104, Apr. 2018. 35

[109] J. W. McIver, D. Hsieh, H. Steinberg, P. Jarillo-Herrero, and N. Gedik, "Control over topological insulator photocurrents with light polarization," Nature Nanotechnology, vol. 7, pp. 96–100, Feb. 2012. 35, 46, 110

[110] D. A. Bas, R. A. Muniz, S. Babakiray, D. Lederman, J. E. Sipe, and A. D. Bristow, "Identification of photocurrents in topological insulators," Optics Express, vol. 24, p. 23583, Oct. 2016. 35, 36

[111] M. Reid, I. V. Cravetchi, and R. Fedosejevs, "Terahertz radiation and second-harmonic generation from InAs: Bulk versus surface electric-field-induced contributions," Physical Review B, vol. 72, p. 035201, July 2005. 36, 116

[112] V. Apostolopoulos and M. E. Barnes, "THz emitters based on the photo-Dember effect," Journal of Physics D: Applied Physics, vol. 47, p. 374002, Sept. 2014. 36

[113] J. Maysonnave, S. Huppert, F. Wang, S. Maero, C. Berger, W. de Heer, T. B. Norris, L. A. De Vaulchier, S. Dhillon, J. Tignon, R. Ferreira, and J. Mangeney, "Terahertz Generation by Dynamical Photon Drag Effect in Graphene Excited by Femtosecond Optical Pulses," Nano Letters, vol. 14, pp. 5797–5802, Oct. 2014. 37, 41

[114] Q. Chen, M. Tani, Z. Jiang, and X.-C. Zhang, "Electro-optic transceivers for terahertz-wave applications," Journal of the Optical Society of America B, vol. 18, p. 823, June 2001. 37

[115] H. Rubens and O. von Baeyer, "LXXX. On extremely long waves, emitted by the quartz mercury lamp," The London, Edinburgh, and Dublin Philosophical Magazine and Journal of Science, vol. 21, pp. 689–695, May 1911. 38

[116] F. F. Sizov, "Brief history of THz and IR technologies," Semiconductor Physics, Quantum Electronics & Optoelectronics, vol. 22, pp. 67–79, Mar. 2019. 38

[117] J. Faist, F. Capasso, D. L. Sivco, C. Sirtori, A. L. Hutchinson, and A. Y. Cho, "Quantum Cascade Laser," Science, vol. 264, pp. 553–556, Apr. 1994. 38

[118] A. Khalatpour, A. K. Paulsen, C. Deimert, Z. R. Wasilewski, and Q. Hu, "High-power portable terahertz laser systems," Nature Photonics, vol. 15, pp. 16–20, Jan. 2021. 38

[119] R. Köhler, A. Tredicucci, F. Beltram, H. E. Beere, E. H. Linfield, A. G. Davies, D. A. Ritchie, R. C. Iotti, and F. Rossi, "Terahertz semiconductor-heterostructure laser," Nature, vol. 417, pp. 156–159, May 2002. 38, 39

[120] Q. Lu, F. Wang, D. Wu, S. Slivken, and M. Razeghi, "Room temperature terahertz semiconductor frequency comb," Nature Communications, vol. 10, p. 2403, Dec. 2019. 39

[121] Y. C. Shen, P. C. Upadhya, E. H. Linfield, H. E. Beere, and A. G. Davies, "Ultrabroadband terahertz radiation from low-temperature-grown GaAs photoconductive emitters," Applied Physics Letters, vol. 83, pp. 3117–3119, Oct. 2003. 39

[122] S. Lepeshov, A. Gorodetsky, A. Krasnok, E. Rafailov, and P. Belov, "Enhancement of terahertz photoconductive antenna operation by optical nanoantennas: Enhancement of terahertz photoconductive antenna operation by optical nanoantennas," Laser & Photonics Reviews, vol. 11, p. 1600199, Jan. 2017. 40

[123] T. Ishibashi and H. Ito, "Uni-traveling-carrier photodiodes," Journal of Applied Physics, vol. 127, p. 031101, Jan. 2020. 39, 40

[124] M. Razeghi, "Recent progress of widely tunable, CW THz sources based QCLs at room temperature," International Journal of Terahertz Science and Technology, vol. 10, no. 4, pp. 87–151, 2017. 39, 186

[125] J. M. Blackledge, A. Boretti, L. Rosa, and S. Castelletto, "Fractal Graphene Patch Antennas and the THz Communications Revolution," IOP Conference Series: Materials Science and Engineering, vol. 1060, p. 012001, Feb. 2021. 40

[126] F. Sizov and A. Rogalski, "THz detectors," Progress in Quantum Electronics, vol. 34, pp. 278–347, Sept. 2010. 40

[127] T. Crowe, W. Bishop, D. Porterfield, J. Hesler, and R. Weikle, "Opening the terahertz window with integrated diode circuits," IEEE Journal of Solid-State Circuits, vol. 40, pp. 2104–2110, Oct. 2005. 40

[128] A. Fisher, Y. Park, M. Lenz, A. Ody, R. Agustsson, T. Hodgetts, A. Murokh, and P. Musumeci, "Single-pass high-efficiency terahertz free-electron laser," Nature Photonics, vol. 16, pp. 441–447, June 2022. 40

[129] H. Roskos, M. Thomson, M. Kreß, and T. Löffler, "Broadband THz emission from gas plasmas induced by femtosecond optical pulses: From fundamentals to applications," Laser & Photonics Review, vol. 1, pp. 349–368, Dec. 2007. 40, 41

[130] H. Hamster, A. Sullivan, S. Gordon, W. White, and R. W. Falcone, "Subpicosecond, electromagnetic pulses from intense laser-plasma interaction," Physical Review Letters, vol. 71, pp. 2725–2728, Oct. 1993. 40

[131] S. Liu, C. Lu, Z. Fan, S. Wang, P. Li, X. Chen, J. Pan, Y. Xu, Y. Liu, and X. Wu, "Modulated terahertz generation in femtosecond laser plasma filaments by high-field spintronic terahertz pulses," Applied Physics Letters, vol. 120, p. 172404, Apr. 2022. 41, 45

[132] F. Sizov, "Terahertz radiation detectors: the state-of-the-art," Semiconductor Science and Technology, vol. 33, p. 123001, Dec. 2018. 41

[133] T. Seifert, S. Jaiswal, M. Sajadi, G. Jakob, S. Winnerl, M. Wolf, M. Kläui, and T. Kampfrath, "Ultrabroadband single-cycle terahertz pulses with peak fields of 300 kV.cm^{-1} from a metallic spintronic emitter," Applied Physics Letters, vol. 110, p. 252402, June 2017. 43, 45, 158, 176

[134] L. Cheng, Z. Li, D. Zhao, and E. E. M. Chia, "Studying spin–charge conversion using terahertz pulses," APL Materials, vol. 9, p. 070902, July 2021. 43

[135] Z. Feng, H. Qiu, D. Wang, C. Zhang, S. Sun, B. Jin, and W. Tan, "Spintronic terahertz emitter," Applied Physics, p. 16, 2021. 43

[136] T. S. Seifert, L. Cheng, Z. Wei, T. Kampfrath, and J. Qi, "Spintronic sources of ultrashort terahertz electromagnetic pulses," Applied Physics Letters, vol. 120, p. 180401, May 2022. 43

[137] C. Bull, S. M. Hewett, R. Ji, C.-H. Lin, T. Thomson, D. M. Graham, and P. W. Nutter, "Spintronic terahertz emitters: Status and prospects from a materials perspective," APL Materials, vol. 9, p. 090701, Sept. 2021. 43

[138] E. T. Papaioannou and R. Beigang, "THz spintronic emitters: a review on achievements and future challenges," Nanophotonics, vol. 0, Dec. 2020. 43

[139] J. Walowski and M. Münzenberg, "Perspective: Ultrafast magnetism and THz spintronics," Journal of Applied Physics, vol. 120, p. 140901, Oct. 2016. 43

[140] Y. Liu, H. Cheng, Y. Xu, P. Vallobra, S. Eimer, X. Zhang, X. Wu, T. Nie, and W. Zhao, "Separation of emission mechanisms in spintronic terahertz emitters," Physical Review B, vol. 104, p. 064419, Aug. 2021. 44

[141] T. Vogel, A. Omar, S. Mansourzadeh, F. Wulf, N. M. Sabanés, M. Müller, T. S. Seifert, A. Weigel, G. Jakob, M. Kläui, I. Pupeza, T. Kampfrath, and C. J. Saraceno, "Average power scaling of THz spintronic emitters efficiently cooled in reflection geometry," Optics Express, vol. 30, p. 20451, June 2022. 45, 48, 176, 189

[142] R. I. Herapath, S. M. Hornett, T. S. Seifert, G. Jakob, M. Kläui, J. Bertolotti, T. Kampfrath, and E. Hendry, "Impact of pump wavelength on terahertz emission of a cavity-enhanced spintronic trilayer," Applied Physics Letters, p. 6, 2019. 45, 53, 55, 176, 185, 189, 190

[143] E. T. Papaioannou, G. Torosyan, S. Keller, L. Scheuer, M. Battiato, V. K. Mag-Usara, J. L'huillier, M. Tani, and R. Beigang, "Efficient Terahertz Generation Using Fe/Pt Spintronic Emitters Pumped at Different Wavelengths," IEEE Transactions on Magnetics, vol. 54, pp. 1–5, Nov. 2018. 45

[144] V. K. Mag-usara, M. C. Escaño, C. E. Petoukhoff, G. Torosyan, L. Scheuer, J. Madéo, J. Afalla, M. L. Talara, J. E. Muldera, H. Kitahara, D. R. Bacon, M. Nakajima, K. Dani, E. T. Papaioannou, R. Beigang, and M. Tani, "Optimum excitation wavelength and photon energy threshold for spintronic terahertz emission from Fe/Pt bilayer," iScience, vol. 25, p. 104615, July 2022. 45, 47

[145] I. Ilyakov, N. Agarwal, J.-C. Deinert, J. Liu, A. Yaroslavtsev, L. Foglia, G. Kurdi, R. Mincigrucci, E. Principi, G. Jakob, M. Kläui, T. S. Seifert, T. Kampfrath, S. Kovalev, R. E. Carley, A. O. Scherz, and M. Gensch, "Terahertz-wave decoding of femtosecond extreme-ultraviolet light pulses," Optica, vol. 9, p. 545, May 2022. 45, 46

[146] G. Torosyan, S. Keller, L. Scheuer, R. Beigang, and E. T. Papaioannou, "Optimized Spintronic Terahertz Emitters Based on Epitaxial Grown Fe/Pt Layer Structures," Scientific Reports, vol. 8, p. 1311, Dec. 2018. 46

[147] J. Gorchon, S. Mangin, M. Hehn, and G. Malinowski, "Is terahertz emission a good probe of the spin current attenuation length?," Applied Physics Letters, vol. 121, p. 012402, July 2022. 47, 48

[148] R. Cheng, D. Xiao, and A. Brataas, "Terahertz Antiferromagnetic Spin Hall Nano-Oscillator," Physical Review Letters, vol. 116, p. 207603, May 2016. 47, 150, 172

[149] M. A. Wahada, E. Şaşıoğlu, W. Hoppe, X. Zhou, H. Deniz, R. Rouzegar, T. Kampfrath, I. Mertig, S. S. P. Parkin, and G. Woltersdorf, "Atomic Scale Control of Spin Current Transmission at Interfaces," Nano Letters, vol. 22, pp. 3539–3544, May 2022. 47

[150] O. Gueckstock, L. Nádvorník, M. Gradhand, T. S. Seifert, G. Bierhance, R. Rouzegar, M. Wolf, M. Vafaee, J. Cramer, M. A. Syskaki, G. Woltersdorf, I. Mertig, G. Jakob, M. Kläui, and T. Kampfrath, "Terahertz Spin-to-Charge Conversion by Interfacial Skew Scattering in Metallic Bilayers," Advanced Materials, p. 2006281, Jan. 2021. 47, 79

[151] D. M. Nenno, L. Scheuer, D. Sokoluk, S. Keller, G. Torosyan, A. Brodyanski, J. Lösch, M. Battiato, M. Rahm, R. H. Binder, H. C. Schneider, R. Beigang, and E. T. Papaioannou, "Modification of spintronic terahertz emitter performance through defect engineering," Scientific Reports, vol. 9, p. 13348, Dec. 2019. 47, 62, 63

[152] G. Li, R. Medapalli, R. V. Mikhaylovskiy, F. E. Spada, T. Rasing, E. E. Fullerton, and A. Kimel, "THz emission from Co/Pt bilayers with varied roughness, crystal structure, and interface intermixing," Physical Review Materials, vol. 3, p. 084415, Aug. 2019. 47, 71

[153] J. Liu, K. Lee, Y. Yang, Z. Li, R. Sharma, L. Xi, T. Salim, C. Boothroyd, Y. M. Lam, H. Yang, M. Battiato, and E. E. Chia, "Spintronic Terahertz Emitters in Silicon-Based Heterostructures," Physical Review Applied, vol. 18, p. 034056, Sept. 2022. 47

[154] Z. Feng, R. Yu, Y. Zhou, H. Lu, W. Tan, H. Deng, Q. Liu, Z. Zhai, L. Zhu, J. Cai, B. Miao, and H. Ding, "Highly Efficient Spintronic Terahertz Emitter Enabled by Metal-Dielectric Photonic Crystal," Advanced Optical Materials, vol. 6, p. 1800965, Dec. 2018. 48, 87

[155] K. Neeraj, A. Sharma, M. Almeida, P. Matthes, F. Samad, G. Salvan, O. Hellwig, and S. Bonetti, "Terahertz charge and spin transport in metallic ferromagnets: The role of crystalline and magnetic order," Applied Physics Letters, vol. 120, p. 102406, Mar. 2022. 48

[156] W. Zhang, P. Maldonado, Z. Jin, T. S. Seifert, J. Arabski, G. Schmerber, E. Beaurepaire, M. Bonn, T. Kampfrath, P. M. Oppeneer, and D. Turchinovich, "Ultrafast terahertz magnetometry," Nature Communications, vol. 11, p. 4247, Dec. 2020. 48

[157] P. Agarwal, Y. Yang, J. Lourembam, R. Medwal, M. Battiato, and R. Singh, "Terahertz spintronic magnetometer (TSM)," Applied Physics Letters, vol. 120, p. 161104, Apr. 2022. 48

[158] D. S. Bulgarevich, Y. Akamine, M. Talara, V. Mag-usara, H. Kitahara, H. Kato, M. Shiihara, M. Tani, and M. Watanabe, "Terahertz Magneto-Optic Sensor/Imager," Scientific Reports, vol. 10, p. 1158, Dec. 2020. 48

[159] M. Meinert, B. Gliniors, O. Gueckstock, T. S. Seifert, L. Liensberger, M. Weiler, S. Wimmer, H. Ebert, and T. Kampfrath, "High-Throughput Techniques for Measuring the Spin Hall Effect," Physical Review Applied, vol. 14, p. 064011, Dec. 2020. 49, 79, 93, 94

[160] J. Hawecker, T. Dang, E. Rongione, J. Boust, S. Collin, J. George, H. Drouhin, Y. Laplace, R. Grasset, J. Dong, J. Mangeney, J. Tignon, H. Jaffrès, L. Perfetti, and S. Dhillon, "Spin Injection Efficiency at Metallic Interfaces Probed by THz Emission Spectroscopy," Advanced Optical Materials, p. 2100412, June 2021. 49, 80, 94, 97, 218

[161] M. B. Jungfleisch, Q. Zhang, W. Zhang, J. E. Pearson, R. D. Schaller, H. Wen, and A. Hoffmann, "Control of Terahertz Emission by Ultrafast Spin-Charge Current Conversion at Rashba Interfaces," Physical Review Letters, vol. 120, p. 207207, May 2018. 49, 50

[162] C. Zhou, Y. Liu, Z. Wang, S. Ma, M. Jia, R. Wu, L. Zhou, W. Zhang, M. Liu, Y. Wu, and J. Qi, "Broadband Terahertz Generation via the Interface Inverse Rashba-Edelstein Effect," Physical Review Letters, vol. 121, p. 086801, Aug. 2018. 49

[163] X. Wang, L. Cheng, D. Zhu, Y. Wu, M. Chen, Y. Wang, D. Zhao, C. B. Boothroyd, Y. M. Lam, J.-X. Zhu, M. Battiato, J. C. W. Song, H. Yang, and E. E. M. Chia, "Ultrafast Spin-to-Charge Conversion at the Surface of Topological Insulator Thin Films," Advanced Materials, vol. 30, p. 1802356, Dec. 2018. 49, 50, 117, 219

[164] M. Tong, Y. Hu, Z. Wang, T. Zhou, X. Xie, X. Cheng, and T. Jiang, "Enhanced Terahertz Radiation by Efficient Spin-to-Charge Conversion in Rashba-Mediated Dirac Surface States," Nano Letters, p. acs.nanolett.0c03079, Dec. 2020. 49, 110, 111, 117, 219

[165] X. Chen, H. Wang, C. Wang, C. Ouyang, G. Wei, T. Nie, W. Zhao, J. Miao, Y. Li, L. Wang, and X. Wu, "Efficient Generation and Arbitrary Manipulation of Chiral Terahertz Waves Emitted from Bi_2Te_3-Fe Heterostructures," Advanced Photonics Research, vol. 2, p. 2000099, Apr. 2021. 49, 58, 219

[166] V. Sharma, W. Wu, P. Bajracharya, D. Q. To, A. Johnson, A. Janotti, G. W. Bryant, L. Gundlach, M. B. Jungfleisch, and R. C. Budhani, "Light and microwave driven spin pumping across FeGaB-BiSb interface," Physical Review Materials, vol. 5, p. 124410, Dec. 2021. 49, 137

[167] H. Park, S. Rho, J. Kim, H. Kim, D. Kim, C. Kang, and M. Cho, "Topological Surface-Dominated Spintronic THz Emission in Topologically Nontrivial $Bi_{1-x}Sb_x$ Films," Advanced Science, p. 2200948, May 2022. 49, 117, 130, 134, 137, 219

[168] H. Park, K. Jeong, I. Maeng, K. I. Sim, S. Pathak, J. Kim, S.-B. Hong, T. S. Jung, C. Kang, J. H. Kim, J. Hong, and M.-H. Cho, "Enhanced Spin-to-Charge Conversion Efficiency in Ultrathin Bi_2Se_3 Observed by Spintronic Terahertz Spectroscopy," ACS Applied Materials & Interfaces, p. acsami.1c03168, May 2021. 49, 110, 219

[169] X. Chen, H. Wang, H. Liu, C. Wang, G. Wei, C. Fang, H. Wang, C. Geng, S. Liu, P. Li, H. Yu, W. Zhao, J. Miao, Y. Li, L. Wang, T. Nie, J. Zhao, and X. Wu, "Generation and Control of Terahertz Spin Currents in Topology-Induced 2D Ferromagnetic Fe_3GeTe_2 | Bi_2Te_3 Heterostructures," Advanced Materials, vol. 34, p. 2106172, Mar. 2022. 50, 147

[170] H. Yang, S. O. Valenzuela, M. Chshiev, S. Couet, B. Dieny, B. Dlubak, A. Fert, K. Garello, M. Jamet, D.-E. Jeong, K. Lee, T. Lee, M.-B. Martin, G. S. Kar, P. Sénéor, H.-J. Shin, and S. Roche, "Two-dimensional materials prospects for non-volatile spintronic memories," Nature, vol. 606, pp. 663–673, June 2022. 50, 51, 140

[171] A. K. Geim and I. V. Grigorieva, "Van der Waals heterostructures," Nature, vol. 499, pp. 419–425, July 2013. 50

[172] J. F. Sierra, J. Fabian, R. K. Kawakami, S. Roche, and S. O. Valenzuela, "Van der Waals heterostructures for spintronics and opto-spintronics," Nature Nanotechnology, vol. 16, pp. 856–868, Aug. 2021. 50

[173] X. Wen, Z. Gong, and D. Li, "Nonlinear optics of two-dimensional transition metal dichalcogenides," InfoMat, vol. 1, pp. 317–337, Sept. 2019. 50, 144

[174] K. Si, Y. Huang, Q. Zhao, L. Zhu, L. Zhang, Z. Yao, and X. Xu, "Terahertz surface emission from layered semiconductor WSe_2," Applied Surface Science, vol. 448, pp. 416–423, Aug. 2018. 50, 140

[175] A. Jakhar, D. S. Arya, S. Ghosh, and S. Das, "Zero-Biased and Broadband (0.1-1.5 THz) Terahertz Detector Using Dirac Semimetal-Platinum Telluride ($PtTe_2$)," IEEE Sensors Letters, vol. 6, pp. 1–4, July 2022. 50

[176] C. Cheng, J.-T. Sun, X.-R. Chen, H.-X. Fu, and S. Meng, "Nonlinear Rashba spin splitting in transition metal dichalcogenide monolayers," Nanoscale, vol. 8, no. 41, pp. 17854–17860, 2016. 50

[177] Y. C. Cheng, Z. Y. Zhu, M. Tahir, and U. Schwingenschlögl, "Spin-orbit–induced spin splittings in polar transition metal dichalcogenide monolayers," EPL (Europhysics Letters), vol. 102, p. 57001, June 2013. 51

[178] V. Zatko, M. Galbiati, S. M.-M. Dubois, M. Och, P. Palczynski, C. Mattevi, P. Brus, O. Bezencenet, M.-B. Martin, B. Servet, J.-C. Charlier, F. Godel, A. Vecchiola, K. Bouzehouane, S. Collin, F. Petroff, B. Dlubak, and P. Seneor, "Band-Structure Spin-Filtering in Vertical Spin Valves Based on Chemical Vapor Deposited WS_2," ACS Nano, p. acsnano.9b08178, Nov. 2019. 51

[179] L. Cheng, X. Wang, W. Yang, J. Chai, M. Yang, M. Chen, Y. Wu, X. Chen, D. Chi, K. E. J. Goh, J.-X. Zhu, H. Sun, S. Wang, J. C. W. Song, M. Battiato, H. Yang, and E. E. M. Chia, "Far out-of-equilibrium spin populations trigger giant spin injection into atomically thin MoS_2," Nature Physics, vol. 15, pp. 347–351, Apr. 2019. 51

[180] D. Khusyainov, A. Guskov, S. Ovcharenko, N. Tiercelin, V. Preobrazhensky, A. Buryakov, A. Sigov, and E. Mishina, "Increasing the Efficiency of a Spintronic THz Emitter Based on WSe_2/FeCo," Materials, vol. 14, p. 6479, Oct. 2021. 51

[181] L. Nádvorník, O. Gueckstock, L. Braun, C. Niu, J. Gräfe, G. Schütz, H. Takagi, T. S. Seifert, P. Kubaščík, A. K. Pandeya, A. Anane, H. Yang, A. Bedoya-Pinto, S. S. P. Parkin, M. Wolf, H. Nakamura, and T. Kampfrath, "Terahertz spin-to-charge current conversion in stacks of ferromagnets and the transition-metal dichalcogenide $NbSe_2$," arXiv preprint, no. arXiv:2208.00846, p. 19, 2022. 51

[182] K. Cong, E. Vetter, L. Yan, Y. Li, Q. Zhang, Y. Xiong, H. Qu, R. D. Schaller, A. Hoffmann, A. F. Kemper, Y. Yao, J. Wang, W. You, H. Wen, W. Zhang, and D. Sun, "Coherent control of asymmetric spintronic terahertz emission from two-dimensional hybrid metal halides," Nature Communications, vol. 12, p. 5744, Dec. 2021. 51

[183] R. Gupta, S. Husain, A. Kumar, R. Brucas, A. Rydberg, and P. Svedlindh, "Co_2FeAl Full Heusler Compound Based Spintronic Terahertz Emitter," Advanced Optical Materials, vol. 9, p. 2001987, May 2021. 51, 52, 100

[184] B. Yan and C. Felser, "Topological Materials: Weyl Semimetals," Annual Review of Condensed Matter Physics, vol. 8, pp. 337–354, Mar. 2017. 51, 100

[185] S. Heidtfeld, R. Adam, T. Kubota, K. Takanashi, D. Cao, C. Schmitz-Antoniak, D. E. Bürgler, F. Wang, C. Greb, G. Chen, I. Komissarov, H. Hardtdegen, M. Mikulics, R. Sobolewski, S. Suga, and C. M. Schneider, "Generation of terahertz transients from $Co_2Fe_{0.4}Mn_{0.6}Si$ -Heusler-alloy/normal-metal nanobilayers excited by femtosecond optical pulses," Physical Review Research, vol. 3, p. 043025, Oct. 2021. 51

[186] C. Guillemard, S. Petit-Watelot, J.-C. Rojas-Sánchez, J. Hohlfeld, J. Ghanbaja, A. Bataille, P. Le Fèvre, F. Bertran, and S. Andrieu, "Polycrystalline Co_2Mn-based Heusler thin films with high spin polarization and low magnetic damping," Applied Physics Letters, vol. 115, p. 172401, Oct. 2019. 52, 100

[187] A. Mann, J. Walowski, M. Münzenberg, S. Maat, M. J. Carey, J. R. Childress, C. Mewes, D. Ebke, V. Drewello, G. Reiss, and A. Thomas, "Insights into Ultrafast Demagnetization in Pseudogap Half-Metals," Physical Review X, vol. 2, p. 041008, Nov. 2012. 52

[188] T. Kampfrath, A. Sell, G. Klatt, A. Pashkin, S. Mährlein, T. Dekorsy, M. Wolf, M. Fiebig, A. Leitenstorfer, and R. Huber, "Coherent terahertz control of antiferromagnetic spin waves," Nature Photonics, vol. 5, pp. 31–34, Jan. 2011. 52, 151, 152, 155

[189] T. Kampfrath, K. Tanaka, and K. A. Nelson, "Resonant and nonresonant control over matter and light by intense terahertz transients," Nature Photonics, vol. 7, pp. 680–690, Sept. 2013. 52

[190] Y. Ni, Z. Jin, B. Song, X. Zhou, H. Chen, C. Song, Y. Peng, C. Zhang, F. Pan, G. Ma, Y. Zhu, and S. Zhuang, "Temperature-Dependent Terahertz Emission from Co/Mn_2Au Spintronic Bilayers," physica status solidi (RRL) – Rapid Research Letters, vol. 15, p. 2100290, Oct. 2021. 52, 151

[191] O. Gueckstock, R. L. Seeger, T. S. Seifert, S. Auffret, S. Gambarelli, J. N. Kirchhof, K. I. Bolotin, V. Baltz, T. Kampfrath, and L. Nádvorník, "Impact of gigahertz and terahertz transport regimes on spin propagation and conversion in the antiferromagnet IrMn," Applied Physics Letters, vol. 120, p. 062408, Feb. 2022. 52, 53, 150

[192] C. Li, B. Fang, L. Zhang, Q. Chen, X. Xie, N. Xu, Z. Zeng, Z. Wang, L. Fang, and T. Jiang, "Terahertz Generation via Picosecond Spin-to-Charge Conversion in $IrMn_3$/Ni-Fe Heterojunction," Physical Review Applied, vol. 16, p. 024058, Aug. 2021. 52

[193] X. Wu, H. Wang, H. Liu, Y. Wang, X. Chen, P. Chen, P. Li, X. Han, J. Miao, H. Yu, C. Wan, J. Zhao, and S. Chen, "Antiferromagnetic-Ferromagnetic Heterostructure-based Field-Free Terahertz Emitters," Advanced Materials, p. 2204373, Aug. 2022. 52

[194] H. Qiu, L. Zhou, C. Zhang, J. Wu, Y. Tian, S. Cheng, S. Mi, H. Zhao, Q. Zhang, D. Wu, B. Jin, J. Chen, and P. Wu, "Ultrafast spin current generated from an antiferromagnet," Nature Physics, vol. 17, pp. 388–394, Mar. 2021. 52, 53, 151, 152, 156, 159, 161, 163

[195] H. Qiu, T. S. Seifert, L. Huang, Y. Zhou, C. Zhang, J. Wu, K. Fan, Q. Zhang, D. Wu, C. Song, B. Jin, J. Chen, and P. Wu, "Manipulating THz Spin Current Dynamics by the Dzyaloshinskii-Moriya Interaction in Antiferromagnetic Hematite," arXiv preprint, no. arXiv:2209.10175, p. 21, 2022. 53, 173

[196] C. Sun, H. Yang, A. Brataas, and M. B. A. Jalil, "Terahertz Spin-Current Pulses from an Off-Resonant Antiferromagnet," Physical Review Applied, vol. 17, p. 034028, Mar. 2022. 53

[197] S. Zhuang and J.-M. Hu, "Excitation and detection of coherent sub-terahertz magnons in ferromagnetic and antiferromagnetic heterostructures," npj Computational Materials, vol. 8, p. 167, Aug. 2022. 53, 72, 151, 172

[198] P. Koleják et al., "Highly Efficient Terahertz Spintronic Emitter Integrated with Optimized Photonic Crystal," in preparation, 2022. 54, 176, 190

[199] Z. Jin, Y. Peng, Y. Ni, G. Wu, B. Ji, X. Wu, Z. Zhang, G. Ma, C. Zhang, L. Chen, A. V. Balakin, A. P. Shkurinov, Y. Zhu, and S. Zhuang, "Cascaded Amplification and Manipulation of Terahertz Emission by Flexible Spintronic Heterostructures," Laser & Photonics Reviews, p. 2100688, June 2022. 54, 191

[200] M. Chen, Y. Wu, Y. Liu, K. Lee, X. Qiu, P. He, J. Yu, and H. Yang, "Current-Enhanced Broadband THz Emission from Spintronic Devices," Advanced Optical Materials, p. 1801608, Dec. 2018. 54, 111, 176, 190

[201] U. Nandi, M. S. Abdelaziz, S. Jaiswal, G. Jakob, O. Gueckstock, S. M. Rouzegar, T. S. Seifert, M. Kläui, T. Kampfrath, and S. Preu, "Antenna-coupled spintronic terahertz emitters driven by a 1550 nm femtosecond laser oscillator," Applied Physics Letters, vol. 115, p. 022405, July 2019. 54, 55, 176, 190

[202] Z. Jin, S. Zhang, W. Zhu, Q. Li, W. Zhang, Z. Zhang, S. Lou, Y. Dai, X. Lin, G. Ma, and J. Yao, "Terahertz Radiation Modulated by Confinement of Picosecond Current Based on Patterned Ferromagnetic Heterostructures," physica status solidi (RRL) – Rapid Research Letters, vol. 13, p. 1900057, Sept. 2019. 54, 55

[203] W. Wu, S. Lendinez, M. Taghipour Kaffash, R. D. Schaller, H. Wen, and M. B. Jungfleisch, "Modification of terahertz emission spectrum using microfabricated spintronic emitters," Journal of Applied Physics, vol. 128, p. 103902, Sept. 2020. 54, 56

[204] M. T. Hibberd, D. S. Lake, N. A. B. Johansson, T. Thomson, S. P. Jamison, and D. M. Graham, "Magnetic-field tailoring of the terahertz polarization emitted from a spintronic source," Applied Physics Letters, vol. 114, p. 031101, Jan. 2019. 55, 56

[205] M. Talara, D. S. Bulgarevich, C. Tachioka, V. K. Mag-usara, J. Muldera, T. Furuya, H. Kitahara, M. C. Escaño, Q. Guo, M. Nakajima, G. Torosyan, R. Beigang, M. Watanabe, and M. Tani, "Efficient terahertz wave generation of diabolo-shaped Fe/Pt spintronic antennas driven by a 780 nm pump beam," Applied Physics Express, vol. 14, p. 042008, Apr. 2021. 55, 190, 191

[206] M. Talara, D. Bulgarevich, K. Kobayashi, H. Kitahara, t. furuya, M. C. Escaño, M. Watanabe, and M. Tani, "Impact of various spintronic antenna structures driven by a 795-nm pump beam to terahertz (THz) wave generation," Applied Physics Express, Oct. 2022. 55, 190

[207] B. Y. Shahriar, B. N. Carnio, E. Hopmann, and A. Y. Elezzabi, "Enhanced directive terahertz radiation emission from a horn antenna-coupled W/Fe/Pt spintronic film stack," Applied Physics Letters, vol. 119, p. 092402, Aug. 2021. 55

[208] C. Rathje, R. v. Seggern, N. Meyer, C. Denker, M. Munzenberg, and S. Schafer, "Emission Properties of Structured Spintronic Terahertz Emitters," 2019 44th International Conference on Infrared, Millimeter, and Terahertz Waves (IRMMW-THz), pp. 1–2, Sept. 2019. 56

[209] S. Liu, F. Guo, P. Li, G. Wei, C. Wang, X. Chen, B. Wang, W. Zhao, J. Miao, L. Wang, Y. Xu, and X. Wu, "Nanoplasmonic-Enhanced Spintronic Terahertz Emission," Advanced Materials Interfaces, vol. 9, p. 2101296, Jan. 2022. 56, 190

[210] B. Song, Y. Song, S. Zhang, K. Jin, W. Zhu, Q. Li, Z. Zhang, X. Lin, Y. Dai, X. Yan, G. Ma, Z. Jin, and J. Yao, "Controlling terahertz radiation with subwavelength blocky patterned CoFeB/Pt heterostructures," Applied Physics Express, vol. 12, p. 122003, Dec. 2019. 56

[211] W. Hoppe, J. Weber, S. Tirpanci, O. Gueckstock, T. Kampfrath, and G. Woltersdorf, "On-Chip Generation of Ultrafast Current Pulses by Nanolayered Spintronic Terahertz Emitters," ACS Applied Nano Materials, vol. 4, pp. 7454–7460, July 2021. 56

[212] H. Niwa, N. Yoshikawa, M. Kawaguchi, M. Hayashi, and R. Shimano, "Switchable generation of azimuthally- and radially-polarized terahertz beams from a spintronic terahertz emitter," Optics Express, vol. 29, p. 13331, Apr. 2021. 56

[213] O. Gueckstock, L. Nádvorník, T. S. Seifert, M. Borchert, G. Jakob, G. Schmidt, G. Woltersdorf, M. Kläui, M. Wolf, and T. Kampfrath, "Modulating the polarization of broadband terahertz pulses from a spintronic emitter at rates up to 10 kHz," Optica, vol. 8, p. 1013, July 2021. 57

[214] G. Lezier, P. Koleják, J.-F. Lampin, K. Postava, M. Vanwolleghem, and N. Tiercelin, "Fully reversible magnetoelectric voltage controlled THz polarization rotation in magnetostrictive spintronic emitters on PMN-PT," Applied Physics Letters, vol. 120, p. 152404, Apr. 2022. 57

[215] A. Chaurasiya, Z. Li, R. Medwal, S. Gupta, J. R. Mohan, Y. Fukuma, H. Asada, E. E. M. Chia, and R. S. Rawat, "Active Magnetoelectric Control of Terahertz Spin Current," arXiv preprint, no. 2111.13823, 2021. Publisher: arXiv Version Number: 1. 57

[216] P. Agarwal, L. Huang, S. Ter Lim, and R. Singh, "Electric-field control of nonlinear THz spintronic emitters," Nature Communications, vol. 13, p. 4072, Dec. 2022. 57

[217] P. Koleják, G. Lezier, K. Postava, J.-F. Lampin, N. Tiercelin, and M. Vanwolleghem, "360° Polarization Control of Terahertz Spintronic Emitters Using Uniaxial FeCo/$TbCo_2$/FeCo Trilayers," ACS Photonics, vol. 9, pp. 1274–1285, Apr. 2022. 57

[218] S. M. Hewett, C. Bull, A. M. Shorrock, C.-H. Lin, R. Ji, M. T. Hibberd, T. Thomson, P. W. Nutter, and D. M. Graham, "Spintronic terahertz emitters exploiting uniaxial magnetic anisotropy for field-free emission and polarization control," Applied Physics Letters, vol. 120, p. 122401, Mar. 2022. 57

[219] W. Wu, S. Lendinez, M. T. Kaffash, R. D. Schaller, H. Wen, and M. B. Jungfleisch, "Controlling polarization of spintronic THz emitter by remanent magnetization texture," Applied Physics Letters, vol. 121, p. 052401, Aug. 2022. 57

[220] D. Schulz, B. Schwager, and J. Berakdar, "Nanostructured Spintronic Emitters for Polarization-Textured and Chiral Broadband THz Fields," ACS Photonics, vol. 9, pp. 1248–1255, Apr. 2022. 57, 58

[221] Y. Ogasawara, Y. Sasaki, S. Iihama, A. Kamimaki, K. Z. Suzuki, and S. Mizukami, "Laser-induced terahertz emission from layered synthetic magnets," Applied Physics Express, vol. 13, p. 063001, June 2020. 57

[222] Q. Zhang, Y. Yang, Z. Luo, Y. Xu, R. Nie, X. Zhang, and Y. Wu, "Terahertz Emission From an Exchange-Coupled Synthetic Antiferromagnet," Physical Review Applied, vol. 13, p. 054016, May 2020. 57

[223] M. Fix, R. Schneider, J. Bensmann, S. Michaelis de Vasconcellos, R. Bratschitsch, and M. Albrecht, "Thermomagnetic control of spintronic THz emission enabled by ferrimagnets," Applied Physics Letters, vol. 116, p. 012402, Jan. 2020. 57

[224] M. Fix, R. Schneider, S. Michaelis de Vasconcellos, R. Bratschitsch, and M. Albrecht, "Spin valves as magnetically switchable spintronic THz emitters," Applied Physics Letters, vol. 117, p. 132407, Sept. 2020. 57

[225] C. Liu, S. Wang, S. Zhang, Q. Cai, P. Wang, C. Tian, L. Zhou, Y. Wu, and Z. Tao, "Active spintronic-metasurface terahertz emitters with tunable chirality," Advanced Photonics, vol. 3, Oct. 2021. 58

[226] P. Li, S. Liu, X. Chen, C. Geng, and X. Wu, "Spintronic terahertz emission with manipulated polarization (STEMP)," Frontiers of Optoelectronics, vol. 15, p. 12, Dec. 2022. 58

[227] F.-F. Stiewe, T. Winkel, Y. Sasaki, T. Tubandt, T. Kleinke, C. Denker, U. Martens, N. Meyer, T. S. Parvini, S. Mizukami, J. Walowski, and M. Münzenberg, "Spintronic emitters for super-resolution in THz-spectral imaging," Applied Physics Letters, vol. 120, p. 032406, Jan. 2022. 58

[228] S.-C. Chen, Z. Feng, J. Li, W. Tan, L.-H. Du, J. Cai, Y. Ma, K. He, H. Ding, Z.-H. Zhai, Z.-R. Li, C.-W. Qiu, X.-C. Zhang, and L.-G. Zhu, "Ghost spintronic THz-emitter-array microscope," Light: Science & Applications, vol. 9, p. 99, Dec. 2020. 58

[229] P. Li, S. Liu, Z. Liu, M. Li, H. Xu, Y. Xu, H. Zeng, and X. Wu, "Laser terahertz emission microscopy of nanostructured spintronic emitters," Applied Physics Letters, vol. 120, p. 201102, May 2022. 58

[230] Z. Bai, Y. Liu, R. Kong, T. Nie, Y. Sun, H. Li, T. Sun, C. Pandey, Y. Wang, H. Zhang, Q. Song, G. Liu, M. Kraft, W. Zhao, X. Wu, and L. Wen, "Near-field Terahertz Sensing of HeLa Cells and *Pseudomonas* Based on Monolithic Integrated Metamaterials with a Spintronic Terahertz Emitter," ACS Applied Materials & Interfaces, vol. 12, pp. 35895–35902, Aug. 2020. 58

[231] T. H. Dang, J. Hawecker, E. Rongione, G. Baez Flores, D. Q. To, J. C. Rojas-Sanchez, H. Nong, J. Mangeney, J. Tignon, F. Godel, S. Collin, P. Seneor, M. Bibes, A. Fert, M. Anane, J.-M. George, L. Vila, M. Cosset-Cheneau, D. Dolfi, R. Lebrun, P. Bortolotti, K. Belashchenko, S. Dhillon, and H. Jaffrès, "Ultrafast spin-currents and charge conversion at 3*d*-5*d* interfaces probed by time-domain terahertz spectroscopy," Applied Physics Reviews, vol. 7, p. 041409, Dec. 2020. 62, 67, 69, 77, 86, 94, 95, 96, 97, 139, 190, 218, 234

[232] M. Beens, R. A. Duine, and B. Koopmans, "An s-d model for local and non-local spin dynamics in laser-excited magnetic heterostructures," arXiv:2005.03905 [cond-mat], May 2020. arXiv: 2005.03905. 62

[233] M. Beens, R. A. Duine, and B. Koopmans, "Modeling ultrafast demagnetization and spin transport: The interplay of spin-polarized electrons and thermal magnons," Physical Review B, vol. 105, p. 144420, Apr. 2022. 62

[234] Y. Yang, S. Dal Forno, and M. Battiato, "Transfer-matrix description of heterostructured spintronics terahertz emitters," Physical Review B, vol. 104, p. 155437, Oct. 2021. 62

[235] D. M. Nenno, B. Rethfeld, and H. C. Schneider, "Particle-in-cell simulation of ultrafast hot-carrier transport in Fe/Au heterostructures," Physical Review B, vol. 98, p. 224416, Dec. 2018. 62

[236] S. Kaltenborn, Y.-H. Zhu, and H. C. Schneider, "Wave-diffusion theory of spin transport in metals after ultrashort-pulse excitation," Physical Review B, vol. 85, p. 235101, June 2012. 63, 64, 218

[237] J. Wieczorek, A. Eschenlohr, B. Weidtmann, M. Rösner, N. Bergeard, A. Tarasevitch, T. O. Wehling, and U. Bovensiepen, "Separation of ultrafast spin currents and spin-flip scattering in Co/Cu(001) driven by femtosecond laser excitation employing the complex magneto-optical Kerr effect," Physical Review B, vol. 92, p. 174410, Nov. 2015. 65

[238] D. Gall, "Electron mean free path in elemental metals," Journal of Applied Physics, vol. 119, p. 085101, Feb. 2016. 65

[239] J. Bass and W. P. Pratt, "Spin-diffusion lengths in metals and alloys, and spin-flipping at metal/metal interfaces: an experimentalist's critical review," Journal of Physics: Condensed Matter, vol. 19, p. 183201, May 2007. 65

[240] R. Freeman, A. Zholud, Z. Dun, H. Zhou, and S. Urazhdin, "Evidence for Dyakonov-Perel-like Spin Relaxation in Pt," Physical Review Letters, vol. 120, p. 067204, Feb. 2018. 65

[241] A. Fert and S.-F. Lee, "Theory of the bipolar spin switch," Physical Review B, vol. 53, pp. 6554–6565, Mar. 1996. 65, 66

[242] K. Carva, M. Battiato, D. Legut, and P. M. Oppeneer, "*Ab initio* theory of electron-phonon mediated ultrafast spin relaxation of laser-excited hot electrons in transition-metal ferromagnets," Physical Review B, vol. 87, p. 184425, May 2013. 66

[243] S. Zhuang, P. B. Meisenheimer, J. Heron, and J.-M. Hu, "A Narrowband Spintronic Terahertz Emitter Based on Magnetoelastic Heterostructures," ACS Applied Materials & Interfaces, p. acsami.1c13461, Oct. 2021. 72, 151, 172

[244] S. M. Rouzegar, L. Brandt, L. Nádvorník, D. A. Reiss, A. L. Chekhov, O. Gueckstock, C. In, M. Wolf, T. S. Seifert, P. W. Brouwer, G. Woltersdorf, and T. Kampfrath, "Laser-induced terahertz spin transport in magnetic nanostructures arises from the same force as ultrafast demagnetization," arXiv preprint, vol. 2103, p. 11710, 2021. 74, 76, 95, 137, 161

[245] D. A. Papaconstantopoulos, Handbook of the Band Structure of Elemental Solids. Boston, MA: Springer US, 2015. 75

[246] R. E. Glover and M. Tinkham, "Conductivity of Superconducting Films for Photon Energies between 0.3 and 4 0 k T c," Physical Review, vol. 108, pp. 243–256, Oct. 1957. 80, 232

[247] N. Laman and D. Grischkowsky, "Terahertz conductivity of thin metal films," Applied Physics Letters, vol. 93, p. 051105, Aug. 2008. 80

[248] E. D. Palik, Handbook of Optical Constants of Solids. Academic Press Handbook, 1985. 80, 240

[249] W. S. M. Werner, K. Glantschnig, and C. Ambrosch-Draxl, "Optical Constants and Inelastic Electron-Scattering Data for 17 Elemental Metals," Journal of Physical and Chemical Reference Data, vol. 38, pp. 1013–1092, Dec. 2009. 80, 240

[250] T. Seifert, Spintronics with Terahertz Radiation: Probing and driving spins at highest frequencies. PhD thesis, Freie Universität Berlin, Dec. 2017. 82, 83, 160

[251] J. Hawecker, V. Pistore, A. Minasyan, K. Maussang, J. Palomo, I. Sagnes, J.-M. Manceau, R. Colombelli, J. Tignon, J. Mangeney, and S. S. Dhillon, "Cavity-based photoconductive sources for real-time terahertz imaging," Photonics Research, vol. 8, p. 858, June 2020. 84, 176, 178, 180, 181

[252] S. Krishnia, Y. Sassi, F. Ajejas, N. Reyren, S. Collin, A. Fert, J.-M. George, V. Cros, and H. Jaffres, "Large interfacial Rashba interaction and giant spin-orbit torques in atomically thin metallic heterostructures," June 2022. arXiv:2205.08486 [cond-mat]. 93

[253] J. Ryu, S. Lee, K. Lee, and B. Park, "Current-Induced Spin–Orbit Torques for Spintronic Applications," Advanced Materials, vol. 32, p. 1907148, Sept. 2020. 94

[254] A. J. Berger, E. R. J. Edwards, H. T. Nembach, O. Karis, M. Weiler, and T. J. Silva, "Determination of the spin Hall effect and the spin diffusion length of Pt from self-consistent fitting of damping enhancement and inverse spin-orbit torque measurements," Physical Review B, vol. 98, p. 024402, July 2018. 95

[255] L. Zhu, D. C. Ralph, and R. A. Buhrman, "Effective Spin-Mixing Conductance of Heavy-Metal–Ferromagnet Interfaces," Physical Review Letters, vol. 123, p. 057203, Aug. 2019. 96

[256] A. Manchon, H. C. Koo, J. Nitta, S. M. Frolov, and R. A. Duine, "New perspectives for Rashba spin–orbit coupling," Nature Materials, vol. 14, pp. 871–882, Sept. 2015. 97, 234

[257] J. Hawecker, E. Rongione, A. Markou, S. Krishnia, F. Godel, S. Collin, R. Lebrun, J. Tignon, J. Mangeney, T. Boulier, J.-M. George, C. Felser, H. Jaffrès, and S. Dhillon, "Spintronic THz emitters based on transition metals and semi-metals/Pt multilayers," Applied Physics Letters, vol. 120, p. 122406, Mar. 2022. 99, 100, 139, 218

[258] Y. Xu, F. Zhang, Y. Liu, R. Xu, Y. Jiang, H. Cheng, A. Fert, and W. Zhao, "Inverse Orbital Hall Effect Discovered from Light-Induced Terahertz Emission," arXiv preprint, no. arXiv:2208.01866, 2022. Publisher: arXiv Version Number: 1. 99

[259] D. Go, F. Freimuth, J.-P. Hanke, F. Xue, O. Gomonay, K.-J. Lee, S. Blügel, P. M. Haney, H.-W. Lee, and Y. Mokrousov, "Theory of current-induced angular momentum transfer dynamics in spin-orbit coupled systems," Physical Review Research, vol. 2, p. 033401, Sept. 2020. 99

[260] T. Graf, S. S. P. Parkin, and C. Felser, "Heusler Compounds—A Material Class With Exceptional Properties," IEEE Transactions on Magnetics, vol. 47, pp. 367–373, Feb. 2011. 100

[261] B. S. D. C. S. Varaprasad, A. Rajanikanth, Y. K. Takahashi, and K. Hono, "Enhanced Spin Polarization of Co $_2$ MnGe Heusler Alloy by Substitution of Ga for Ge," Applied Physics Express, vol. 3, p. 023002, Feb. 2010. 100

[262] C. Guillemard, S. Petit-Watelot, L. Pasquier, D. Pierre, J. Ghanbaja, J.-C. Rojas-Sánchez, A. Bataille, J. Rault, P. Le Fèvre, F. Bertran, and S. Andrieu, "Ultralow Magnetic Damping in Co_2Mn -Based Heusler Compounds: Promising Materials for Spintronics," Physical Review Applied, vol. 11, p. 064009, June 2019. 100

[263] G. Bierhance, A. Markou, O. Gueckstock, R. Rouzegar, Y. Behovits, A. L. Chekhov, M. Wolf, T. S. Seifert, C. Felser, and T. Kampfrath, "Spin-voltage-driven efficient terahertz spin currents from the magnetic Weyl semimetals Co $_2$ MnGa and Co $_2$ MnAl," Applied Physics Letters, vol. 120, p. 082401, Feb. 2022. 101

[264] J. E. Moore, "The birth of topological insulators," Nature, vol. 464, pp. 194–198, Mar. 2010. 104

[265] M. Z. Hasan and C. L. Kane, "*Colloquium* : Topological insulators," Reviews of Modern Physics, vol. 82, pp. 3045–3067, Nov. 2010. 104

[266] L. Petersen and P. Hedegård, "A simple tight-binding model of spin–orbit splitting of *sp*-derived surface states," Surface Science, vol. 459, pp. 49–56, July 2000. 104, 122

[267] B. A. Bernevig, T. L. Hughes, and S.-C. Zhang, "Quantum Spin Hall Effect and Topological Phase Transition in HgTe Quantum Wells," Science, vol. 314, pp. 1757–1761, Dec. 2006. 104

[268] L. Fu, C. L. Kane, and E. J. Mele, "Topological Insulators in Three Dimensions," Physical Review Letters, vol. 98, p. 106803, Mar. 2007. 104

[269] Y. Ando, "Topological Insulator Materials," Journal of the Physical Society of Japan, vol. 82, p. 102001, Oct. 2013. 104, 105

[270] L. Baringthon, T. H. Dang, H. Jaffrès, N. Reyren, J.-M. George, M. Morassi, G. Patriarche, A. Lemaitre, F. Bertran, and P. Le Fèvre, "Topological surface states in ultrathin $Bi_{1-x}Sb_x$layers," Physical Review Materials, vol. 6, p. 074204, July 2022. 105, 119, 120, 121, 122, 123, 132

[271] E. Rongione, S. Fragkos, L. Baringthon, J. Hawecker, E. Xenogiannopoulou, P. Tsipas, C. Song, M. Mičica, J. Mangeney, J. Tignon, T. Boulier, N. Reyren, R. Lebrun, J. George, P. Le Fèvre, S. Dhillon, A. Dimoulas, and H. Jaffrès, "Ultrafast Spin-Charge Conversion at $SnBi_2Te_4$/Co Topological Insulator Interfaces Probed by Terahertz Emission Spectroscopy," Advanced Optical Materials, p. 2102061, Feb. 2022. 105, 111, 139, 143, 219, 225

[272] L. Wu, M. Brahlek, R. Valdés Aguilar, A. V. Stier, C. M. Morris, Y. Lubashevsky, L. S. Bilbro, N. Bansal, S. Oh, and N. P. Armitage, "A sudden collapse in the transport lifetime across the topological phase transition in $(Bi_{1-x}In_x)_2Se_3$," Nature Physics, vol. 9, pp. 410–414, July 2013. 105, 109

[273] B. C. Park, T.-H. Kim, K. I. Sim, B. Kang, J. W. Kim, B. Cho, K.-H. Jeong, M.-H. Cho, and J. H. Kim, "Terahertz single conductance quantum and topological phase transitions in topological insulator Bi_2Se_3 ultrathin films," Nature Communications, vol. 6, p. 6552, May 2015. 106

[274] M. R. Scholz, J. Sánchez-Barriga, D. Marchenko, A. Varykhalov, A. Volykhov, L. V. Yashina, and O. Rader, "Tolerance of Topological Surface States towards Magnetic Moments: Fe on Bi_2Se_3," Physical Review Letters, vol. 108, p. 256810, June 2012. 107

[275] J. Honolka, A. A. Khajetoorians, V. Sessi, T. O. Wehling, S. Stepanow, J.-L. Mi, B. B. Iversen, T. Schlenk, J. Wiebe, N. B. Brookes, A. I. Lichtenstein, P. Hofmann, K. Kern, and R. Wiesendanger, "In-Plane Magnetic Anisotropy of Fe Atoms on Bi_2Se_3(111)," Physical Review Letters, vol. 108, p. 256811, June 2012. 107

[276] M. Fanetti, I. Mikulska, K. Ferfolja, P. Moras, P. Sheverdyaeva, M. Panighel, A. Lodi-Rizzini, I. Píš, S. Nappini, M. Valant, and S. Gardonio, "Growth, morphology and stability of Au in contact with the Bi_2Se_3(0001) surface," Applied Surface Science, vol. 471, pp. 753–758, Mar. 2019. 107

[277] K. Hoefer, C. Becker, S. Wirth, and L. Hao Tjeng, "Protective capping of topological surface states of intrinsically insulating Bi_2Te_3," AIP Advances, vol. 5, p. 097139, Sept. 2015. 107

[278] L. Yu, L. Hu, J. L. Barreda, T. Guan, X. He, K. Wu, Y. Li, and P. Xiong, "Robust Gapless Surface State against Surface Magnetic Impurities on $(Bi_{0.5}Sb_{0.5})_2Te_3$ Evidenced by *In Situ* Magnetotransport Measurements," Physical Review Letters, vol. 124, p. 126601, Mar. 2020. 107

[279] L. A. Wray, S.-Y. Xu, Y. Xia, Y. S. Hor, D. Qian, A. V. Fedorov, H. Lin, A. Bansil, R. J. Cava, and M. Z. Hasan, "Observation of topological order in a superconducting doped topological insulator," Nature Physics, vol. 6, pp. 855–859, Nov. 2010. 107

[280] L. A. Wray, S.-Y. Xu, Y. Xia, D. Hsieh, A. V. Fedorov, Y. S. Hor, R. J. Cava, A. Bansil, H. Lin, and M. Z. Hasan, "A topological insulator surface under strong Coulomb, magnetic and disorder perturbations," Nature Physics, vol. 7, pp. 32–37, Jan. 2011. 108

[281] Y. Zhang, K. He, C.-Z. Chang, C.-L. Song, L.-L. Wang, X. Chen, J.-F. Jia, Z. Fang, X. Dai, W.-Y. Shan, S.-Q. Shen, Q. Niu, X.-L. Qi, S.-C. Zhang, X.-C. Ma, and Q.-K. Xue, "Crossover of the three-dimensional topological insulator Bi_2Se_3 to the two-dimensional limit," Nature Physics, vol. 6, pp. 584–588, Aug. 2010. 108, 109, 140

[282] S. Ito, M. Arita, J. Haruyama, B. Feng, W.-C. Chen, H. Namatame, M. Taniguchi, C.-M. Cheng, G. Bian, S.-J. Tang, T.-C. Chiang, O. Sugino, F. Komori, and I. Matsuda, "Surface-state Coulomb repulsion accelerates a metal-insulator transition in topological semimetal nanofilms," Science Advances, vol. 6, p. eaaz5015, Mar. 2020. 108, 109, 121

[283] H. Ishida, "Decay length of surface-state wave functions on Bi(111)," Journal of Physics: Condensed Matter, vol. 29, p. 015002, Jan. 2017. 109, 125, 135

[284] W. Han, Y. Otani, and S. Maekawa, "Quantum materials for spin and charge conversion," npj Quantum Materials, vol. 3, p. 27, Dec. 2018. 109

[285] T. Schumann, T. Kleinke, L. Braun, N. Meyer, G. Mussler, J. Kampmeier, D. Grützmacher, E. Schmoranzerova, K. Olejník, H. Reichlová, C. Heiliger, C. Denker, J. Walowski, T. Kampfrath, and M. Münzenberg, "Circular photogalvanic effects in topological insulator/ferromagnet hybrid structures," arXiv preprint, no. 2202.01522, 2022. Publisher: arXiv Version Number: 1. 110

[286] S. Y. Hamh, S.-H. Park, S.-K. Jerng, J. H. Jeon, S.-H. Chun, and J. S. Lee, "Helicity-dependent photocurrent in a Bi_2Se_3 thin film probed by terahertz emission spectroscopy," Physical Review B, vol. 94, p. 161405, Oct. 2016. 110

[287] Y. Liu, J. Besbas, Y. Wang, P. He, M. Chen, D. Zhu, Y. Wu, J. M. Lee, L. Wang, J. Moon, N. Koirala, S. Oh, and H. Yang, "Direct visualization of current-induced spin accumulation in topological insulators," Nature Communications, vol. 9, p. 2492, Dec. 2018. 110

[288] D. Hsieh, Y. Xia, D. Qian, L. Wray, J. H. Dil, F. Meier, J. Osterwalder, L. Patthey, J. G. Checkelsky, N. P. Ong, A. V. Fedorov, H. Lin, A. Bansil, D. Grauer, Y. S. Hor, R. J. Cava, and M. Z. Hasan, "A tunable topological insulator in the spin helical Dirac transport regime," Nature, vol. 460, pp. 1101–1105, Aug. 2009. 111

[289] S. Fragkos, L. Baringthon, P. Tsipas, E. Xenogiannopoulou, P. Le Fèvre, P. Kumar, H. Okuno, N. Reyren, A. Lemaitre, G. Patriarche, J.-M. George, and A. Dimoulas, "Topological surface states in epitaxial $(SnBi_2Te_4)_n(Bi_2Te_3)_m$ natural van der Waals superlattices," Physical Review Materials, vol. 5, p. 014203, Jan. 2021. 111, 114, 219

[290] Y. Xia, D. Qian, D. Hsieh, L. Wray, A. Pal, H. Lin, A. Bansil, D. Grauer, Y. S. Hor, R. J. Cava, and M. Z. Hasan, "Observation of a large-gap topological-insulator class with a single Dirac cone on the surface," Nature Physics, vol. 5, pp. 398–402, June 2009. 111

[291] L. Fu, "Hexagonal Warping Effects in the Surface States of the Topological Insulator Bi_2Te_3," Physical Review Letters, vol. 103, p. 266801, Dec. 2009. 111, 226

[292] Q. Zhang, Z. Luo, H. Li, Y. Yang, and X. Zhang, "Terahertz emission from anomalous Hall effect in a single-layer ferromagnet," Physical Review Applied, vol. 12, no. 054027, p. 22, 2019. 115

[293] H. Zhang, Z. Feng, J. Zhang, H. Bai, H. Yang, J. Cai, W. Zhao, W. Tan, F. Hu, B. Shen, and J. Sun, "Laser pulse induced efficient terahertz emission from Co/Al heterostructures," Physical Review B, vol. 102, p. 024435, July 2020. 115

[294] P. Tsipas, E. Xenogiannopoulou, S. Kassavetis, D. Tsoutsou, E. Golias, C. Bazioti, G. P. Dimitrakopulos, P. Komninou, H. Liang, M. Caymax, and A. Dimoulas, "Observation of Surface Dirac Cone in High-Quality Ultrathin Epitaxial Bi_2Se_3 Topological Insulator on AlN(0001) Dielectric," ACS Nano, vol. 8, pp. 6614–6619, July 2014. 117

[295] L. Baringthon, Élaboration et caractérisation de phases topologiques de l'alliage $Bi_{1-x}Sb_x$ pour la conversion spin charge. PhD thesis, Université Paris-Saclay, 2022. 119, 134, 219

[296] E. Rongione, L. Baringthon, D. She, G. Patriarche, R. Lebrun, A. Lemaître, M. Morassi, N. Reyren, M. Mičica, J. Mangeney, J. Tignon, F. Bertran, S. Dhillon, P. Le Fèvre, H. Jaffrès, and J.-M. George, "Spin-momentum locking and ultrafast spin-charge conversion in ultrathin epitaxial $Bi_{1-x}Sb_x$ topological insulator.," submitted, 2023. 119, 123, 139, 219, 225

[297] Z. Chi, Y.-C. Lau, X. Xu, T. Ohkubo, K. Hono, and M. Hayashi, "The spin Hall effect of Bi-Sb alloys driven by thermally excited Dirac-like electrons," Science Advances, vol. 6, p. eaay2324, Mar. 2020. 119

[298] Y. Liu and R. E. Allen, "Electronic structure of the semimetals Bi and Sb," Physical Review B, vol. 52, pp. 1566–1577, July 1995. 119, 121, 122

[299] H. M. Benia, C. Straßer, K. Kern, and C. R. Ast, "Surface band structure of $Bi_{1-x}Sb_x(111)$," Physical Review B, vol. 91, p. 161406, Apr. 2015. 120, 121, 123

[300] B. Lenoir, H. Scherrer, and T. Caillat, "Chapter 4 An overview of recent developments for BiSb Alloys," in Semiconductors and Semimetals, vol. 69, pp. 101–137, Elsevier, 2001. 120, 121, 122

[301] J. C. Y. Teo, L. Fu, and C. L. Kane, "Surface states and topological invariants in three-dimensional topological insulators: Application to $Bi_{1-x}Sb_x$," Physical Review B, vol. 78, p. 045426, July 2008. 120, 122

[302] K. Saito, H. Sawahata, T. Komine, and T. Aono, "Tight-binding theory of surface spin states on bismuth thin films," Physical Review B, vol. 93, p. 041301, Jan. 2016. 122, 123

[303] Y. Ohtsubo and S.-i. Kimura, "Topological phase transition of single-crystal Bi based on empirical tight-binding calculations," New Journal of Physics, vol. 18, p. 123015, Dec. 2016. 122

[304] C. R. Ast and I. Gierz, "s p -band tight-binding model for the Bychkov-Rashba effect in a two-dimensional electron system including nearest-neighbor contributions from an electric field," Physical Review B, vol. 86, p. 085105, Aug. 2012. 122

[305] H. Hedayat, D. Bugini, H. Yi, C. Chen, X. Zhou, G. Cerullo, C. Dallera, and E. Carpene, "Ultrafast evolution of bulk, surface and surface resonance states in photoexcited Bi_2Te_3," Scientific Reports, vol. 11, p. 4924, Dec. 2021. 123, 124

[306] C. Jozwiak, J. A. Sobota, K. Gotlieb, A. F. Kemper, C. R. Rotundu, R. J. Birgeneau, Z. Hussain, D.-H. Lee, Z.-X. Shen, and A. Lanzara, "Spin-polarized surface resonances accompanying topological surface state formation," Nature Communications, vol. 7, p. 13143, Dec. 2016. 123, 124

[307] I. Aguilera, H.-J. Kim, C. Friedrich, G. Bihlmayer, and S. Blügel, "Z_2 topology of bismuth," Physical Review Materials, vol. 5, p. L091201, Sept. 2021. arXiv: 2108.12674. 125

[308] M. Matthiesen, D. Afanasiev, J. R. Hortensius, T. C. van Thiel, R. Medapalli, E. E. Fullerton, and A. D. Caviglia, "Temperature dependent inverse spin Hall effect in Co/Pt spintronic emitters," Applied Physics Letters, vol. 116, p. 212405, May 2020. 134

[309] G. Bierhance et al., "Terahertz dynamic signatures of spin accumulation and spin-to-charge conversion at topological insulator–ferromagnet interfaces," in preparation, 2022. 136

[310] J. Faure, J. Mauchain, E. Papalazarou, M. Marsi, D. Boschetto, I. Timrov, N. Vast, Y. Ohtsubo, B. Arnaud, and L. Perfetti, "Direct observation of electron thermalization and electron-phonon coupling in photoexcited bismuth," Physical Review B, vol. 88, p. 075120, Aug. 2013. 137

[311] C. Sun, H. Yang, and M. B. A. Jalil, "Enhanced subterahertz spin-current transients via modulation of cross-sublattice damping in uniaxial antiferromagnets," Physical Review B, vol. 105, p. 104407, Mar. 2022. 139

[312] E. Rongione, M. Ribeiro Oliveria, A. Wright, S. Husain, M. Mičica, T. Denneulin, R. Lebrun, J.-M. George, H. Jaffrès, M. Jamet, and S. Dhillon, "Topological insulator, transition metals dichalcogenides and ferromagnets junctions in the generation of ultrafast THz photocurrents," in preparation, 2023. 140, 219

[313] M. Han, J. Ma, H. Xu, and Y. Liu, "Two-step vapor transport deposition of large-size bridge-like Bi_2Se_3 nanostructures," CrystEngComm, vol. 17, no. 44, pp. 8449–8456, 2015. 140

[314] J. G. Analytis, J.-H. Chu, Y. Chen, F. Corredor, R. D. McDonald, Z. X. Shen, and I. R. Fisher, "Bulk Fermi surface coexistence with Dirac surface state in Bi_2Se_3: A comparison of photoemission and Shubnikov-de Haas measurements," Physical Review B, vol. 81, p. 205407, May 2010. 140

[315] J. Ribeiro-Soares, C. Janisch, Z. Liu, A. L. Elías, M. S. Dresselhaus, M. Terrones, L. G. Cançado, and A. Jorio, "Second Harmonic Generation in WSe_2," 2D Materials, vol. 2, p. 045015, Dec. 2015. 140, 143, 144

[316] P.-C. Yeh, W. Jin, N. Zaki, D. Zhang, J. T. Liou, J. T. Sadowski, A. Al-Mahboob, J. I. Dadap, I. P. Herman, P. Sutter, and R. M. Osgood, "Layer-dependent electronic structure of an atomically heavy two-dimensional dichalcogenide," Physical Review B, vol. 91, p. 041407, Jan. 2015. 140, 141

[317] O. L. Sanchez, D. Ovchinnikov, S. Misra, A. Allain, and A. Kis, "Valley Polarization by Spin Injection in a Light-Emitting van der Waals Heterojunction," Nano Letters, vol. 16, pp. 5792–5797, Sept. 2016. 141

[318] T. Garandel, Structure électronique des interfaces Co(0001)/MoS_2 et Ni(111)/WSe_2 pour l'injection de spin dans un semi-conducteur bidimensionnel. PhD thesis, INSA Toulouse, 2017. 141

[319] H. G. Rosa, Y. W. Ho, I. Verzhbitskiy, M. J. F. L. Rodrigues, T. Taniguchi, K. Watanabe, G. Eda, V. M. Pereira, and J. C. V. Gomes, "Characterization of the second- and third-harmonic optical susceptibilities of atomically thin tungsten diselenide," Scientific Reports, vol. 8, p. 10035, Dec. 2018. 144

[320] T. G. Park, J. H. Jeon, S.-H. Chun, S. Lee, and F. Rotermund, "Ultrafast interfacial carrier dynamics and persistent topological surface states of Bi_2Se_3 in heterojunctions with VSe_2," Communications Physics, vol. 5, p. 182, Dec. 2022. 147

[321] T. Jungwirth, X. Marti, P. Wadley, and J. Wunderlich, "Antiferromagnetic spintronics," Nature Nanotechnology, vol. 11, p. 11, 2016. 150

[322] V. Baltz, A. Manchon, M. Tsoi, T. Moriyama, T. Ono, and Y. Tserkovnyak, "Antiferromagnetic spintronics," Reviews of Modern Physics, vol. 90, p. 015005, Feb. 2018. 150

[323] O. Gomonay, T. Jungwirth, and J. Sinova, "Concepts of antiferromagnetic spintronics," physica status solidi (RRL) - Rapid Research Letters, vol. 11, p. 1700022, Apr. 2017. 150

[324] M. L. Néel, "Propriétés magnétiques des ferrites ; ferrimagnétisme et antiferromagnétisme," Annales de Physique, vol. 12, no. 3, pp. 137–198, 1948. 150

[325] P. Wadley, B. Howells, J. Zelezny, C. Andrews, V. Hills, R. P. Campion, V. Novak, F. Freimuth, Y. Mokrousov, A. W. Rushforth, K. W. Edmonds, B. L. Gallagher, and T. Jungwirth, "Electrical switching of an antiferromagnet," Science, vol. 351, pp. 587–590, Feb. 2016. arXiv:1503.03765 [cond-mat]. 150

[326] K. Olejník, T. Seifert, Z. Kašpar, V. Novák, P. Wadley, R. P. Campion, M. Baumgartner, P. Gambardella, P. Němec, J. Wunderlich, J. Sinova, P. Kužel, M. Müller, T. Kampfrath, and T. Jungwirth, "Terahertz electrical writing speed in an antiferromagnetic memory," Science Advances, vol. 4, p. eaar3566, Mar. 2018. 150

[327] J. Železný, P. Wadley, K. Olejník, A. Hoffmann, and H. Ohno, "Spin transport and spin torque in antiferromagnetic devices," Nature Physics, vol. 14, pp. 220–228, Mar. 2018. 150

[328] A. Mitrofanova, A. Safin, O. Kravchenko, S. Nikitov, and A. Kirilyuk, "Optically initialized and current-controlled logical element based on antiferromagnetic-heavy metal heterostructures for neuromorphic computing," Applied Physics Letters, vol. 120, p. 072402, Feb. 2022. 150

[329] A. Safin, V. Puliafito, M. Carpentieri, G. Finocchio, S. Nikitov, P. Stremoukhov, A. Kirilyuk, and A. Slavin, "Electrically tunable detector of THz-frequency signals based on an antiferromagnet," Applied Physics Letters, p. 7, 2020. 150, 151, 172

[330] L. Baldrati, A. Ross, T. Niizeki, C. Schneider, R. Ramos, J. Cramer, O. Gomonay, M. Filianina, T. Savchenko, D. Heinze, A. Kleibert, E. Saitoh, J. Sinova, and M. Kläui, "Full angular dependence of the spin Hall and ordinary magnetoresistance in epitaxial antiferromagnetic NiO(001)/Pt thin films," Physical Review B, vol. 98, p. 024422, July 2018. 150, 156, 160

[331] A. Ross, R. Lebrun, O. Gomonay, D. A. Grave, A. Kay, L. Baldrati, S. Becker, A. Qaiumzadeh, C. Ulloa, G. Jakob, F. Kronast, J. Sinova, R. Duine, A. Brataas, A. Rothschild, and M. Kläui, "Propagation Length of Antiferromagnetic Magnons Governed by Domain Configurations," Nano Letters, vol. 20, pp. 306–313, Jan. 2020. 150, 173

[332] S. Das, A. Ross, X. X. Ma, S. Becker, C. Schmitt, F. van Duijn, E. F. Galindez-Ruales, F. Fuhrmann, M.-A. Syskaki, U. Ebels, V. Baltz, A.-L. Barra, H. Y. Chen, G. Jakob, S. X. Cao, J. Sinova, O. Gomonay, R. Lebrun, and M. Kläui, "Anisotropic long-range spin transport in canted antiferromagnetic orthoferrite $YFeO_3$," Nature Communications, vol. 13, p. 6140, Oct. 2022. 150

[333] A. V. Chumak, P. Kabos, M. Wu, C. Abert, C. Adelmann, A. O. Adeyeye, J. Akerman, F. G. Aliev, A. Anane, A. Awad, C. H. Back, A. Barman, G. E. W. Bauer, M. Becherer, E. N. Beginin, V. A. S. V. Bittencourt, Y. M. Blanter, P. Bortolotti, I. Boventer, D. A. Bozhko, S. A. Bunyaev, J. J. Carmiggelt, R. R. Cheenikundil, F. Ciubotaru, S. Cotofana, G. Csaba, O. V. Dobrovolskiy, C. Dubs, M. Elyasi, K. G. Fripp, H. Fulara, I. A. Golovchanskiy, C. Gonzalez-Ballestero, P. Graczyk, D. Grundler, P. Gruszecki, G. Gubbiotti, K. Guslienko, A. Haldar, S. Hamdioui, R. Hertel, B. Hillebrands, T. Hioki, A. Houshang, C.-M. Hu, H. Huebl, M. Huth, E. Iacocca, M. B. Jungfleisch, G. N. Kakazei, A. Khitun, R. Khymyn, T. Kikkawa, M. Klaui, O. Klein, J. W. Klos, S. Knauer, S. Koraltan, M. Kostylev, M. Krawczyk, I. N. Krivorotov, V. V. Kruglyak, D. Lachance-Quirion, S. Ladak, R. Lebrun, Y. Li, M. Lindner, R. Macedo, S. Mayr, G. A. Melkov, S. Mieszczak, Y. Nakamura, H. T. Nembach, A. A. Nikitin, S. A. Nikitov, V. Novosad, J. A. Otalora, Y. Otani, A. Papp, B. Pigeau, P. Pirro, W. Porod, F. Porrati, H. Qin, B. Rana, T. Reimann, F. Riente, O. Romero-Isart, A. Ross, A. V. Sadovnikov, A. R. Safin, E. Saitoh, G. Schmidt, H. Schultheiss, K. Schultheiss, A. A. Serga, S. Sharma, J. M. Shaw, D. Suess, O. Surzhenko, K. Szulc, T. Taniguchi, M. Urbanek, K. Usami, A. B. Ustinov, T. van der Sar, S. van Dijken, V. I. Vasyuchka, R. Verba, S. V. Kusminskiy, Q. Wang, M. Weides, M. Weiler, S. Wintz, S. P. Wolski, and X. Zhang, "Advances in Magnetics Roadmap on Spin-Wave Computing," IEEE Transactions on Magnetics, vol. 58, pp. 1–72, June 2022. 150

[334] P. Němec, M. Fiebig, T. Kampfrath, and A. V. Kimel, "Antiferromagnetic opto-spintronics," Nature Physics, vol. 14, pp. 229–241, Mar. 2018. 150

[335] A. Safin, S. Nikitov, A. Kirilyuk, V. Tyberkevych, and A. Slavin, "Theory of Antiferromagnet-Based Detector of Terahertz Frequency Signals," Magnetochemistry, vol. 8, p. 26, Feb. 2022. 150

[336] C. Tzschaschel, K. Otani, R. Iida, T. Shimura, H. Ueda, S. Günther, M. Fiebig, and T. Satoh, "Ultrafast optical excitation of coherent magnons in antiferromagnetic NiO," Physical Review B, vol. 95, p. 174407, May 2017. 151, 155, 159, 161, 162, 163, 164

[337] K. Grishunin, E. A. Mashkovich, A. V. Kimel, A. M. Balbashov, and A. K. Zvezdin, "Excitation and detection of terahertz coherent spin waves in antiferromagnetic α-Fe_2O_3," Physical Review B, vol. 104, p. 024419, July 2021. 151

[338] J. Nishitani, K. Kozuki, T. Nagashima, and M. Hangyo, "Terahertz radiation from coherent antiferromagnetic magnons excited by femtosecond laser pulses," Applied Physics Letters, vol. 96, p. 221906, May 2010. 152, 155, 159

[339] S. M. Rezende, A. Azevedo, and R. L. Rodríguez-Suárez, "Introduction to antiferromagnetic magnons," Journal of Applied Physics, vol. 126, p. 151101, Oct. 2019. 152, 153, 154

[340] A. Gurevich and G. Melkov, Magnetization Oscillations and Waves. CRC Press, crc press ed., 1996. 153

[341] I. Boventer, H. Simensen, A. Anane, M. Kläui, A. Brataas, and R. Lebrun, "Room-Temperature Antiferromagnetic Resonance and Inverse Spin-Hall Voltage in Canted Antiferromagnets," Physical Review Letters, vol. 126, p. 187201, May 2021. 153

[342] H. V. Gomonay and V. M. Loktev, "Spin transfer and current-induced switching in antiferromagnets," Physical Review B, vol. 81, p. 144427, Apr. 2010. 153

[343] E. V. Gomonay and V. M. Loktev, "Spintronics of antiferromagnetic systems (Review Article)," Low Temperature Physics, vol. 40, pp. 17–35, Jan. 2014. 153

[344] W. L. Roth, "Neutron and Optical Studies of Domains in NiO," Journal of Applied Physics, vol. 31, pp. 2000–2011, Nov. 1960. 154

[345] I. Sänger, V. V. Pavlov, M. Bayer, and M. Fiebig, "Distribution of antiferromagnetic spin and twin domains in NiO," Physical Review B, vol. 74, p. 144401, Oct. 2006. 154

[346] C. Schmitt, L. Baldrati, L. Sanchez-Tejerina, F. Schreiber, A. Ross, M. Filianina, S. Ding, F. Fuhrmann, R. Ramos, F. Maccherozzi, D. Backes, M.-A. Mawass, F. Kronast, S. Valencia, E. Saitoh, G. Finocchio, and M. Kläui, "Identification of Néel Vector Orientation in Antiferromagnetic Domains Switched by Currents in NiO/Pt Thin Films," Physical Review Applied, vol. 15, p. 034047, Mar. 2021. 154, 155, 156, 166

[347] E. Rongione, O. Gueckstock, M. Mattern, O. Gomonay, H. Meer, C. Schmitt, R. Ramos, J. Sinova, H. Jaffrès, M. Mičica, J. Mangeney, S. T. B. Goennenwein, S. Geprägs, M. Kläui, M. Bargheer, T. S. Seifert, S. Dhillon, and R. Lebrun, "Emission of coherent THz magnons in an antiferromagnetic insulator triggered by ultrafast spin-phonon interactions," arXiv preprint, vol. arXiv:2205.11965, p. 11, 2022. 154, 220

[348] J. Fischer, O. Gomonay, R. Schlitz, K. Ganzhorn, N. Vlietstra, M. Althammer, H. Huebl, M. Opel, R. Gross, S. T. B. Goennenwein, and S. Geprägs, "Spin Hall magnetoresistance in antiferromagnet/heavy-metal heterostructures," Physical Review B, vol. 97, p. 014417, Jan. 2018. 155

[349] J. Nishitani, T. Nagashima, and M. Hangyo, "Coherent control of terahertz radiation from antiferromagnetic magnons in NiO excited by optical laser pulses," Physical Review B, vol. 85, p. 174439, May 2012. 155, 159

[350] H. Meer, F. Schreiber, C. Schmitt, R. Ramos, E. Saitoh, O. Gomonay, J. Sinova, L. Baldrati, and M. Kläui, "Direct Imaging of Current-Induced Antiferromagnetic Switching Revealing a Pure Thermomagnetoelastic Switching Mechanism in NiO," Nano Letters, vol. 21, pp. 114–119, Jan. 2021. 156, 160, 165, 220, 221

[351] F. Schreiber, L. Baldrati, C. Schmitt, R. Ramos, E. Saitoh, R. Lebrun, and M. Kläui, "Concurrent magneto-optical imaging and magneto-transport readout of electrical switching of insulating antiferromagnetic thin films," Applied Physics Letters, vol. 117, p. 082401, Aug. 2020. 156

[352] J. Pudell, M. Mattern, M. Hehn, G. Malinowski, M. Herzog, and M. Bargheer, "Heat Transport without Heating?—An Ultrafast X-Ray Perspective into a Metal Heterostructure," Advanced Functional Materials, vol. 30, p. 2004555, Nov. 2020. 159, 164

[353] T. Higuchi, N. Kanda, H. Tamaru, and M. Kuwata-Gonokami, "Selection Rules for Light-Induced Magnetization of a Crystal with Threefold Symmetry: The Case of Antiferromagnetic NiO," Physical Review Letters, p. 4, 2011. 159, 161, 162, 164

[354] T. S. Seifert, S. Jaiswal, J. Barker, S. T. Weber, I. Razdolski, J. Cramer, O. Gueckstock, S. F. Maehrlein, L. Nadvornik, S. Watanabe, C. Ciccarelli, A. Melnikov, G. Jakob, M. Münzenberg, S. T. B. Goennenwein, G. Woltersdorf, B. Rethfeld, P. W. Brouwer, M. Wolf, M. Kläui, and T. Kampfrath, "Femtosecond formation dynamics of the spin Seebeck effect revealed by terahertz spectroscopy," Nature Communications, vol. 9, p. 2899, Dec. 2018. 160, 161, 168, 169, 170, 171

[355] S. P. Zeuschner, M. Mattern, J.-E. Pudell, A. von Reppert, M. Rössle, W. Leitenberger, J. Schwarzkopf, J. E. Boschker, M. Herzog, and M. Bargheer, "Reciprocal space slicing: A time-efficient approach to femtosecond X-ray diffraction," Structural Dynamics, vol. 8, p. 014302, Jan. 2021. 164, 243

[356] D. Schick, A. Bojahr, M. Herzog, C. v. K. Schmising, R. Shayduk, W. Leitenberger, P. Gaal, and M. Bargheer, "Normalization schemes for ultrafast X-ray diffraction using a table-top laser-driven plasma source," Review of Scientific Instruments, vol. 83, p. 025104, Feb. 2012. 164, 243

[357] S. Wust, C. Seibel, H. Meer, P. Herrgen, C. Schmitt, L. Baldrati, R. Ramos, T. Kikkawa, E. Saitoh, O. Gomonay, J. Sinova, Y. Mokrousov, H. C. Schneider, M. Kläui, B. Rethfeld, B. Stadtmüller, and M. Aeschlimann, "Indirect optical manipulation of the antiferromagnetic order of insulating NiO by ultrafast interfacial energy transfer," arXiv preprint, 2022. arXiv:2205.02686. 165, 167

[358] D. Schick, A. Bojahr, M. Herzog, R. Shayduk, and M. Bargheer, "udkm1Dsim—A simulation toolkit for 1D ultrafast dynamics in condensed matter," Computer Physics Communications, p. 10, 2014. 165, 244

[359] D. Bossini, M. Pancaldi, L. Soumah, M. Basini, F. Mertens, M. Cinchetti, T. Satoh, O. Gomonay, and S. Bonetti, "Ultrafast Amplification and Nonlinear Magnetoelastic Coupling of Coherent Magnon Modes in an Antiferromagnet," Physical Review Letters, vol. 127, p. 077202, Aug. 2021. 165

[360] Y. Windsor, D. Zahn, R. Kamrla, J. Feldl, H. Seiler, C.-T. Chiang, M. Ramsteiner, W. Widdra, R. Ernstorfer, and L. Rettig, "Exchange-Striction Driven Ultrafast Nonthermal Lattice Dynamics in NiO," Physical Review Letters, vol. 126, p. 147202, Apr. 2021. 165

[361] L. Soumah, D. Bossini, A. Anane, and S. Bonetti, "Optical Frequency Up-Conversion of the Ferromagnetic Resonance in an Ultrathin Garnet Mediated by Magnetoelastic Coupling," Physical Review Letters, vol. 127, p. 077203, Aug. 2021. 165

[362] J. Xiao, G. E. W. Bauer, K.-c. Uchida, E. Saitoh, and S. Maekawa, "Theory of magnon-driven spin Seebeck effect," Physical Review B, vol. 81, p. 214418, June 2010. 168

[363] M. Schreier, A. Kamra, M. Weiler, J. Xiao, G. E. W. Bauer, R. Gross, and S. T. B. Goennenwein, "Magnon, phonon, and electron temperature profiles and the spin Seebeck effect in magnetic insulator/normal metal hybrid structures," Physical Review B, vol. 88, p. 094410, Sept. 2013. 168

[364] S. M. Rezende, R. L. Rodríguez-Suárez, and A. Azevedo, "Diffusive magnonic spin transport in antiferromagnetic insulators," Physical Review B, vol. 93, p. 054412, Feb. 2016. 168, 169

[365] S. M. Rezende, A. Azevedo, and R. L. Rodríguez-Suárez, "Magnon diffusion theory for the spin Seebeck effect in ferromagnetic and antiferromagnetic insulators," Journal of Physics D: Applied Physics, vol. 51, p. 174004, May 2018. 169, 171

[366] F. N. Kholid, D. Hamara, A. F. B. Hamdan, G. N. Antonio, R. Bowen, D. Petit, R. Cowburn, R. V. Pisarev, D. Bossini, and C. Ciccarelli, "The importance of the interface for picosecond spin pumping in antiferromagnet-heavy metal heterostructures," arXiv preprint, vol. arXiv:2208.08332, p. 21, 2022. 169, 170, 171

[367] L. Huang, Y. Zhou, H. Qiu, T. Guo, F. Pan, B. Jin, and C. Song, "Terahertz pulse-induced Néel vector switching in α-Fe_2O_3/Pt heterostructures," Applied Physics Letters, vol. 119, p. 212401, Nov. 2021. 173

[368] N. M. Burford and M. O. El-Shenawee, "Review of terahertz photoconductive antenna technology," Optical Engineering, vol. 56, p. 010901, Jan. 2017. 176

[369] S. Messelot, C. Symonds, J. Bellessa, J. Tignon, S. Dhillon, J.-B. Brubach, P. Roy, and J. Mangeney, "Tamm Cavity in the Terahertz Spectral Range," ACS Photonics, vol. 7, pp. 2906–2914, Oct. 2020. 178

[370] Q. Zhang, M. Lou, X. Li, J. L. Reno, W. Pan, J. D. Watson, M. J. Manfra, and J. Kono, "Collective non-perturbative coupling of 2D electrons with high-quality-factor terahertz cavity photons," Nature Physics, vol. 12, pp. 1005–1011, Nov. 2016. 178

[371] "COMSOL Multiphysics." 179, 184, 247

[372] M. Pancaldi, R. Freeman, M. Hudl, M. C. Hoffmann, S. Urazhdin, and S. Bonetti, "Anti-reflection coating design for metallic terahertz meta-materials," Optics Express, vol. 26, no. 3, pp. 2917–2927, 2018. 183

[373] Y. Zhou, X. Xu, F. Hu, X. Zheng, W. Li, P. Zhao, J. Bai, and Z. Ren, "Graphene as broadband terahertz antireflection coating," Applied Physics Letters, vol. 104, p. 051106, Feb. 2014. 183

[374] R. R. A. Callahan, K. G. Pruden, G. B. Raupp, and S. P. Beaudoin, "Downstream oxygen etching characteristics of polymers from the parylene family," Journal of Vacuum Science & Technology B: Microelectronics and Nanometer Structures, vol. 21, no. 4, p. 1496, 2003. 185

[375] Q. Lu, D. Wu, S. Sengupta, S. Slivken, and M. Razeghi, "Room temperature continuous wave, monolithic tunable THz sources based on highly efficient mid-infrared quantum cascade lasers," Scientific Reports, vol. 6, p. 23595, July 2016. 186

[376] P.-K. Lu, A. d. J. Fernandez Olvera, D. Turan, T. S. Seifert, N. T. Yardimci, T. Kampfrath, S. Preu, and M. Jarrahi, "Ultrafast carrier dynamics in terahertz photoconductors and photomixers: beyond short-carrier-lifetime semiconductors," Nanophotonics, vol. 0, Mar. 2022. 186

[377] P. Koleják et al., "Spintronic inverse spin hall photomixing: demonstration of THz CW and frequency comb generation," in preparation, 2022. 188

[378] N. Nilforoushan, T. Apretna, C. Song, T. Boulier, J. Tignon, S. Dhillon, M. Hanna, and J. Mangeney, "Ultra-broadband THz pulses with electric field amplitude exceeding 100 kV/cm at a 200 kHz repetition rate," Optics Express, vol. 30, p. 15556, Apr. 2022. 190, 237

[379] D. Twitchen, C. Pickles, S. Coe, R. Sussmann, and C. Hall, "Thermal conductivity measurements on CVD diamond," Diamond and Related Materials, vol. 10, pp. 731–735, Mar. 2001. 190

[380] S. Burghartz and B. Schulz, "Thermophysical properties of sapphire, AlN and $MgAl_2O_4$ down to 70 K," Journal of Nuclear Materials, vol. 212-215, pp. 1065–1068, Sept. 1994. 190

[381] Z. Cheng, Y. R. Koh, A. Mamun, J. Shi, T. Bai, K. Huynh, L. Yates, Z. Liu, R. Li, E. Lee, M. E. Liao, Y. Wang, H. M. Yu, M. Kushimoto, T. Luo, M. S. Goorsky, P. E. Hopkins, H. Amano, A. Khan, and S. Graham, "Experimental observation of high intrinsic thermal conductivity of AlN," Physical Review Materials, vol. 4, p. 044602, Apr. 2020. 190

[382] A. Slifka, B. Filla, and J. Phelps, "Thermal conductivity of magnesium oxide from absolute, steady-state measurements," Journal of Research of the National Institute of Standards and Technology, vol. 103, p. 357, July 1998. 190, 245

[383] Y. Sun, Y. Xu, H. Li, Y. Liu, F. Zhang, H. Cheng, S. Tao, H. Wang, W. Hu, Y. Lu, C. Zhao, T. Nie, W. Zhao, Q. Guo, and L. Wen, "Flexible Control of Broadband Polarization in a Spintronic Terahertz Emitter Integrated with Liquid Crystal and Metasurface," ACS Applied Materials & Interfaces, p. acsami.2c04782, June 2022. 191

[384] M. Tong, Y. Hu, W. He, S. Hu, X. Cheng, and T. Jiang, "Light-Driven Spintronic Heterostructures for Coded Terahertz Emission," ACS Nano, p. acsnano.2c02160, May 2022. 191

[385] V. Litvinov, Magnetism in Topological Insulators. Cham: Springer International Publishing : Imprint: Springer, 1st ed. 2020 ed., 2020. 225

[386] M. P. Marder, Condensed Matter Physics. Hoboken, NJ, USA: John Wiley & Sons, Inc., Oct. 2010. 225

[387] K. Shen, G. Vignale, and R. Raimondi, "Microscopic Theory of the Inverse Edelstein Effect," Physical Review Letters, vol. 112, p. 096601, Mar. 2014. 225

[388] A. Johansson, J. Henk, and I. Mertig, "Theoretical aspects of the Edelstein effect for anisotropic two-dimensional electron gas and topological insulators," Physical Review B, vol. 93, p. 195440, May 2016. 225, 226

[389] S. Vajna, E. Simon, A. Szilva, K. Palotas, B. Ujfalussy, and L. Szunyogh, "Higher-order contributions to the Rashba-Bychkov effect with application to the Bi/Ag(111) surface alloy," Physical Review B, vol. 85, p. 075404, Feb. 2012. 226

[390] K.-W. Kim, K.-J. Lee, J. Sinova, H.-W. Lee, and M. D. Stiles, "Spin-orbit torques from interfacial spin-orbit coupling for various interfaces," Physical Review B, vol. 96, p. 104438, Sept. 2017. 233

[391] V. Amin, J. Zemen, and M. Stiles, "Interface-Generated Spin Currents," Physical Review Letters, vol. 121, p. 136805, Sept. 2018. 233

[392] V. P. Amin, P. M. Haney, and M. D. Stiles, "Interfacial spin-orbit torques," Journal of Applied Physics, vol. 128, p. 151101, Oct. 2020. arXiv: 2008.01182. 233

[393] A. Yariv, Quantum electronics. New York: Wiley, 3rd ed., 1989. 238, 239, 240

[394] B. Pradarutti, G. Matthäus, S. Riehemann, G. Notni, S. Nolte, and A. Tünnermann, "Highly efficient terahertz electro-optic sampling by material optimization at 1060nm," Optics Communications, vol. 281, pp. 5031–5035, Oct. 2008. 238

[395] G. Gallot and D. Grischkowsky, "Electro-optic detection of terahertz radiation," Journal of the Optical Society of America B, vol. 16, p. 1204, Aug. 1999. 238

[396] P. C. M. Planken, H.-K. Nienhuys, H. J. Bakker, and T. Wenckebach, "Measurement and calculation of the orientation dependence of terahertz pulse detection in ZnTe," Journal of the Optical Society of America B, vol. 18, p. 313, Mar. 2001. 238, 239, 240

[397] A. Schneider and P. Günter, "Measurement of the terahertz-induced phase shift in electro-optic sampling for an arbitrary biasing phase," Applied Optics, vol. 45, p. 6598, Sept. 2006. 238

[398] A. Nahata, A. S. Weling, and T. F. Heinz, "A wideband coherent terahertz spectroscopy system using optical rectification and electro-optic sampling," Applied Physics Letters, vol. 69, pp. 2321–2323, Oct. 1996. 239

[399] G. Zhao, R. N. Schouten, N. van der Valk, W. T. Wenckebach, and P. C. M. Planken, "Design and performance of a THz emission and detection setup based on a semi-insulating GaAs emitter," Review of Scientific Instruments, vol. 73, pp. 1715–1719, Apr. 2002. 239, 240

[400] B. Wu, L. Cao, Q. Fu, P. Tan, and Y. Xiong, "Comparison of the Detection Performance of Three Nonlinear Crystals for the Electro-optic Sampling of a FEL-THz Source," Proceedings of the 5th Int. Particle Accelerator Conf., vol. IPAC2014, pp. 3 pages, 0.489 MB, 2014. Artwork Size: 3 pages, 0.489 MB ISBN: 9783954501328 Medium: PDF Publisher: JACoW, Geneva, Switzerland. 239, 240

[401] P. Salén, M. Basini, S. Bonetti, J. Hebling, M. Krasilnikov, A. Y. Nikitin, G. Shamuilov, Z. Tibai, V. Zhaunerchyk, and V. Goryashko, "Matter manipulation with extreme terahertz light: Progress in the enabling THz technology," Physics Reports, vol. 836-837, pp. 1–74, Dec. 2019. 239, 240

[402] J. Dai, J. Zhang, W. Zhang, and D. Grischkowsky, "Terahertz time-domain spectroscopy characterization of the far-infrared absorption and index of refraction of high-resistivity, float-zone silicon," Journal of the Optical Society of America B, vol. 21, p. 1379, July 2004. 240, 241

[403] F. Sanjuan and J. O. Tocho, "Optical properties of silicon, sapphire, silica and glass in the Terahertz range," in Latin America Optics and Photonics Conference, (Sao Sebastiao), p. LT4C.1, OSA, 2012. 240, 241

[404] R. Kitamura, L. Pilon, and M. Jonasz, "Optical constants of silica glass from extreme ultraviolet to far infrared at near room temperature," Applied Optics, vol. 46, p. 8118, Nov. 2007. 240, 241

[405] T. Henning and H. Mutschke, "Low-temperature infrared properties of cosmic dust analogues," Astronomy and Astrophysics, p. 12, 1997. 240, 241

[406] A. M. Hofmeister, E. Keppel, and A. K. Speck, "Absorption and reflection infrared spectra of MgO and other diatomic compounds," Monthly Notices of the Royal Astronomical Society, vol. 345, pp. 16–38, Oct. 2003. 240, 241

[407] M. Naftaly and R. E. Miles, "Terahertz time-domain spectroscopy of silicate glasses and the relationship to material properties," Journal of Applied Physics, vol. 102, p. 043517, Aug. 2007. 240, 241

[408] V. Kubarev, "Optical properties of CVD-diamond in terahertz range and its applications on the NovoFEL," in 2007 Joint 32nd International Conference on Infrared and Millimeter Waves and the 15th International Conference on Terahertz Electronics, (Cardiff), pp. 863–865, IEEE, Sept. 2007. 240, 241

[409] A. Majkić, U. Puc, A. Franke, R. Kirste, R. Collazo, Z. Sitar, and M. Zgonik, "Optical properties of aluminum nitride single crystals in the THz region," Optical Materials Express, vol. 5, p. 2106, Oct. 2015. 240, 241

[410] A. Markou, D. Kriegner, J. Gayles, L. Zhang, Y.-C. Chen, B. Ernst, Y.-H. Lai, W. Schnelle, Y.-H. Chu, Y. Sun, and C. Felser, "Thickness dependence of the anomalous Hall effect in thin films of the topological semimetal Co_2MnGa," Physical Review B, vol. 100, p. 054422, Aug. 2019. 240, 241

[411] R. A. Faregh, A. Boochani, S. R. Masharian, and F. H. Jafarpour, "The surface effect on the thermodynamic stability, half-metallic and optical properties of $Co_2MnGa(001)$ films: a DFT study," International Nano Letters, vol. 9, pp. 339–348, Dec. 2019. 240, 241

[412] K. J. Palm, J. B. Murray, T. C. Narayan, and J. N. Munday, "Dynamic Optical Properties of Metal Hydrides," ACS Photonics, vol. 5, pp. 4677–4686, Nov. 2018. 240

[413] A. D. Rakić, "Algorithm for the determination of intrinsic optical constants of metal films: application to aluminum," Applied Optics, vol. 34, p. 4755, Aug. 1995. 240

[414] X. Wang, R. Y. Engel, I. Vaskivskyi, D. Turenne, V. Shokeen, A. Yaroslavtsev, O. Grånäs, R. Knut, J. O. Schunck, S. Dziarzhytski, G. Brenner, R.-P. Wang, M. Kuhlmann, F. Kuschewski, W. Bronsch, C. Schüßler-Langeheine, A. Styervoyedov, S. S. P. Parkin, F. Parmigiani, O. Eriksson, M. Beye, and H. A. Dürr, "Ultrafast manipulation of the NiO antiferromagnetic order *via* sub-gap optical excitation," Faraday Discussions, p. 10.1039.D2FD00005A, 2022. 240

[415] M. Rinzan, A. Perera, S. Matsik, H. Liu, M. Buchanan, G. von Winckel, A. Stintz, and S. Krishna, "Terahertz absorption in AlGaAs films and detection using heterojunctions," Infrared Physics & Technology, vol. 47, pp. 188–194, Oct. 2005. 240, 241

[416] M. Querry, "Optical Constants of Minerals and Other Materials from the Millimeter to the Ultraviolet," in Contractor Report CRDEC-CR-88009, 1987. 240, 241

[417] L. Berger, "Emission of spin waves by a magnetic multilayer traversed by a current," Physical Review B, vol. 54, pp. 9353–9358, Oct. 1996. 242

[418] J. Slonczewski, "Current-driven excitation of magnetic multilayers," Journal of Magnetism and Magnetic Materials, vol. 159, pp. L1–L7, June 1996. 242

[419] D. Ralph and M. Stiles, "Spin transfer torques," Journal of Magnetism and Magnetic Materials, vol. 320, pp. 1190–1216, Apr. 2008. 242

[420] A. Manchon, J. Železný, I. Miron, T. Jungwirth, J. Sinova, A. Thiaville, K. Garello, and P. Gambardella, "Current-induced spin-orbit torques in ferromagnetic and antiferromagnetic systems," Reviews of Modern Physics, vol. 91, p. 035004, Sept. 2019. 242

[421] M. Hayashi, J. Kim, M. Yamanouchi, and H. Ohno, "Quantitative characterization of the spin-orbit torque using harmonic Hall voltage measurements," Physical Review B, vol. 89, p. 144425, Apr. 2014. 242

[422] R. Shayduk, V. Vonk, B. Arndt, D. Franz, J. Strempfer, S. Francoual, T. F. Keller, T. Spitzbart, and A. Stierle, "Nanosecond laser pulse heating of a platinum surface studied by pump-probe X-ray diffraction," Applied Physics Letters, vol. 109, p. 043107, July 2016. 245

[423] H. Watanabe, "Thermal constants for Ni, NiO, MgO, MnO and CoO at low temperatures," Thermochimica Acta, vol. 218, pp. 365–372, May 1993. 245

[424] T. Barron, W. Berg, and J. Morrison, "On the heat capacity of crystalline magnesium oxide," Proceedings of the Royal Society of London. Series A. Mathematical and Physical Sciences, vol. 250, pp. 70–83, Feb. 1959. 245

[425] M. J. Duggin, "The thermal conductivities of aluminium and platinum," Journal of Physics D: Applied Physics, vol. 3, pp. L21–L23, May 1970. 245

[426] R. MacFarlane, J. Rayne, and C. Jones, "Temperature dependence of elastic moduli of iridium," Physics Letters, vol. 20, pp. 234–235, Feb. 1966. 245

[427] S. Collard and R. McLellan, "High-temperature elastic constants of platinum single crystals," Acta Metallurgica et Materialia, vol. 40, pp. 699–702, Apr. 1992. 245

[428] N. Uchida and S. Saito, "Elastic Constants and Acoustic Absorption Coefficients in MnO, CoO, and NiO Single Crystals at Room Temperature," The Journal of the Acoustical Society of America, vol. 51, pp. 1602–1605, May 1972. 245

[429] M. A. Durand, "The Temperature Variation of the Elastic Moduli of NaCl, KCl and MgO," Physical Review, vol. 50, pp. 449–455, Sept. 1936. 245

[430] R. S. Krishnan, R. Srinivasan, S. Devanarayanan, and B. R. Pamplin, Thermal Expansion of Crystals: International Series in The Science of The Solid State. Burlington: Elsevier Science, 1979. OCLC: 1040263736. 245

[431] S. K. Agrawal, J. Narain, and J. Shanker, "Investigation of the Equation of State and the Grüneisen Parameters for Transition Metal Oxides," physica status solidi (b), vol. 123, pp. 497–501, June 1984. 245

[432] L. C. Bartel and B. Morosin, "Exchange Striction in NiO," Physical Review B, vol. 3, pp. 1039–1043, Feb. 1971. Publisher: American Physical Society. 245

[433] G. K. White and O. L. Anderson, "Grüneisen Parameter of Magnesium Oxide," Journal of Applied Physics, vol. 37, pp. 430–432, Jan. 1966. 245

[434] D. Zahn, H. Seiler, Y. W. Windsor, and R. Ernstorfer, "Ultrafast lattice dynamics and electron–phonon coupling in platinum extracted with a global fitting approach for time-resolved polycrystalline diffraction data," Structural Dynamics, vol. 8, p. 064301, Nov. 2021. 245

[435] A. V. Kimel, A. Kirilyuk, A. Tsvetkov, R. V. Pisarev, and T. Rasing, "Laser-induced ultrafast spin reorientation in the antiferromagnet $TmFeO_3$," Nature, vol. 429, pp. 850–853, June 2004. 246

[436] A. V. Kimel, C. D. Stanciu, P. A. Usachev, R. V. Pisarev, V. N. Gridnev, A. Kirilyuk, and T. Rasing, "Optical excitation of antiferromagnetic resonance in $TmFeO_3$," Physical Review B, vol. 74, p. 060403, Aug. 2006. 246, 247

[437] J. Zhang, M. Białek, A. Magrez, H. Yu, and J.-P. Ansermet, "Antiferromagnetic resonance in $TmFeO_3$ at high temperatures," Journal of Magnetism and Magnetic Materials, vol. 523, p. 167562, Apr. 2021. 246

Résumé de la thèse

- **Contexte scientifique de la spintronique THz.**

La spintronique terahertz (THz) est un domaine de recherche récent et prometteur [80, 81, 78, 82, 83], à la fois pour la recherche fondamentale (dynamique de relaxation ultra-rapide de spins) mais également vers des applications ciblées (télécommunications, médical, spectroscopie large-bande, *etc.*). Elle combine la spintronique, également appelée électronique de spin, qui a vocation à remplacer l'électronique traditionelle en utilisant la manipulation de spins électroniques comme porteuse de l'information numérique, et la gamme fréquentielle du THz qui correspond à des temps extrêmement courts, de l'ordre de la picoseconde (ps, 10^{-12} s), et à des énergies autour du millielectronvolt (meV), ce qui en fait une radiation intéressante pour sonder le gap de matériaux supraconducteurs, la dynamique des magnons (ondes de spin), la réponse des phonons dans les matériaux, *etc.*

La spintronique THz consiste donc en la génération et la manipulation d'ondes éléctromagnétiques THz (10^{12} Hz) en espace libre par un processus de pompage optique femtoseconde (fs, 10^{-15} s) d'une hétérostructure spintronique nanométrique (Fig. F.1a) composée d'un matériau ferromagnétique de la famille $3d$ (*e.g.* Co) et d'un métal lourd à fort couplage spin-orbite de la famille $5d$ (*e.g.* Pt). Cette pompe ultra-rapide, dérivée d'un laser impulsionel (centrée sur une longueur d'onde $\lambda \simeq 800$ nm (10^{-9} m) dans le proche infrarouge), donne naissance à un courant de spin femtoseconde suite à une désaimantation du matériau ferromagnétique. Ce courant de spin est diffusif car l'énergie apportée par la pompe (1.5 eV) promeut les électrons de la bande d porteuse du magnétisme, vers les bandes hybridées sp des électrons de conduction (diffusifs). Aussi, ce courant de spin pénètre dans le matériau à fort couplage spin-orbite où un mécanisme particulier, appelé conversion spin-charge, convertit le courant de spin en un courant de charge transverse. Cette déflection des électrons en fonction de leurs spins est appelée l'effet Hall de spin inverse (ISHE). Ce courant de charge transitoire donne lieu à une radiation THz en espace libre suivant les équations de Maxwell (émission dipolaire). Une détection électro-optique est ensuite utilisée pour caractériser les pulses THz, leurs amplitudes et leurs bandes spectrales d'émission. Les avantages de ces sources spintroniques THz sont leur large bande d'émission (Fig. F.1b-c) ainsi que le contrôle de la polarization (oscillations du champ éléctrique de la lumière) par application d'un champ magnétique extérieur. Cette thèse se positionne donc au coeur de cette thématique de recherche, qui regroupe à la fois l'investigation des mécanismes d'interconversion nouveaux en spintronique, et les performances d'émetteurs/détecteurs innovants dans la gamme du THz. Deux chapitres introductifs présentent respectivement les enjeux de recherche en spintronique (Chap. I) et en THz en espace libre (Chap. II) et donnent les notions abordées pendant la thèse (couplage spin-orbite, électronique de spin, génération et manipulation de pulses THz, état de l'art des émetteurs/détecteurs THz).

- **Des émetteurs spintroniques THz métalliques de la famille $3d$/$5d$.**
Collaboration: L. Perfetti (LSI)

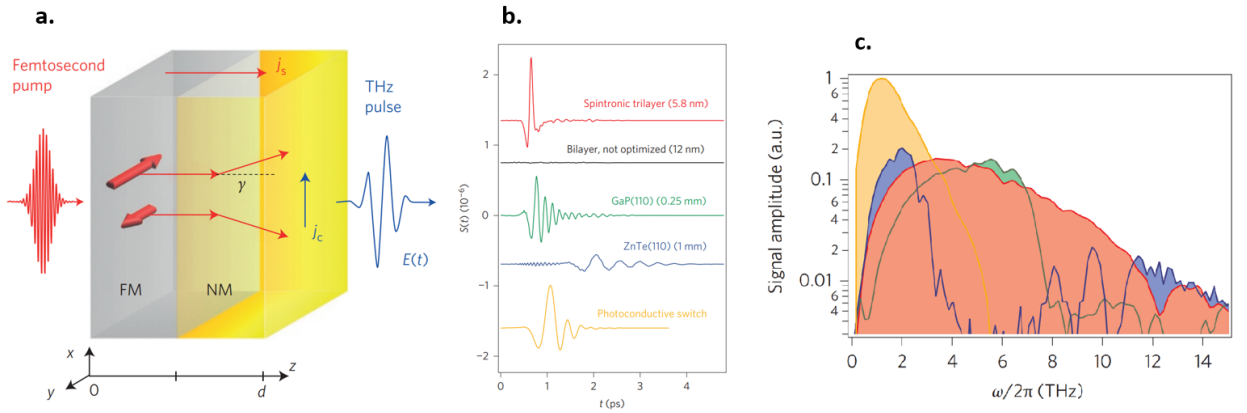

Figure F.1: Emetteurs THz spintronique. (a) Principe de fonctionnement. (b) Comparison des signaux temporels THz entre un émetteur spintronique W/CoFeB/Pt de 5.8 nm d'épaisseur, un émetteur spintronique non-optimisé de 12 nm d'épaisseur, des cristaux non-linéaires de GaP$\langle 110 \rangle$(250µm) et de ZnTe$\langle 110 \rangle$(1mm) ainsi qu'une antenne photoconductrice. (c) Comparaison du spectre THz émis par les émetteurs précédents. Adapté de Ref. [83] et présenté dans le Chap. II.

Dans un premier chapitre (Chap. III) à la fois expérimental et numérique, nous détaillons les pistes d'amélioration possibles des émetteurs métalliques spintroniques. Ces émetteurs présentent actuellement les meilleures performances d'émission, ainsi que les perspectives d'amélioration les plus rapides à court terme. Un ordre de grandeur dans le champ éléctrique THz émis (puissance émise augmentée d'un facteur $\times 100$) est envisagé dans les prochaines années avec ce type d'émetteur. Au cours de ce travail de recherche, nous avons mis en lumière le rôle de la diffusion de spin pour une génération THz efficace, à travers le développement d'un modèle numérique de *wave-diffusion* [236, 231] (diffusion ondulatoire). Ce modèle nous permet d'établir une figure de mérite de l'émission basée sur la longueur de diffusion de spin l_{sf}, l'amplitude de la conversion par l'angle de spin Hall θ_{SHE}, la résistivité ρ_{xx} pour limiter les pertes radiatives, ainsi que d'autres facteurs incluant l'efficacité d'injection de spin et les interfaces (Fig. F.2a). Expérimentalement, la diffusion de spin peut être contrôlée par une couche additionelle de *spin-sink* (drain de spin) [257]. Nous montrons qu'en utilisant une couche de Au:W(2), nous pouvons augmenter l'émission THz de +60% (en champ éléctrique). Une autre stratégie présentée consiste en multipliant les plans d'émission (Fig. F.2b-c) pour atteindre un optimum d'émission à $N = 2$ répétitions de Co(2)/Pt(2) pour une augmentation de +50% en amplitude. De plus, le rôle des interfaces est mis en avant, avec une expérience consistant à mesurer l'émission THz d'une structure Co/X/Pt où X est un insert d'Au, Ti ou Au:W de quelques nm qui a pour but d'ajouter des potentiels Rashba d'interface. Nous remarquons que l'amplitude décroit en fonction, selon une loi universelle caractérisée par un modèle, ce qui traduit que l'ajout d'un insert réduit les capacités d'une injection de spin efficace depuis le matériau ferromagnétique (Co) vers le matériau à conversion spin-charge (Pt) [160]. Nous étudions également un semi-metal de Weyl (Co_2MnGa) qui présente une plus forte polarisation de spin au niveau de Fermi, ce qui est censé accroître l'émission THz résultante. Nous démontrons un gain d'un facteur $\times 2$ dans l'efficacité THz résultante [257].

- **Conversion spin-charge d'interface via les états de surface d'isolants topologiques sondée par spectroscopie THz d'émission.**
  Collaboration: P. Lefèvre (Soleil synchrotron), A. Lemaître (C2N), J.-M. George (UMPhy)

Dans un second chapitre (Chap. IV), nous proposons un nouveau type d'émetteurs spintroniques THz basés sur des hétérostructures entre un métal ferromagnétique (*e.g.* Co) et un isolant topologique de la famille du Bi (*e.g.* Bi_2Se_3, Bi_2Te_3, $Bi_{1-x}Sb_x$, *etc.*). Ces matériaux, en plus de

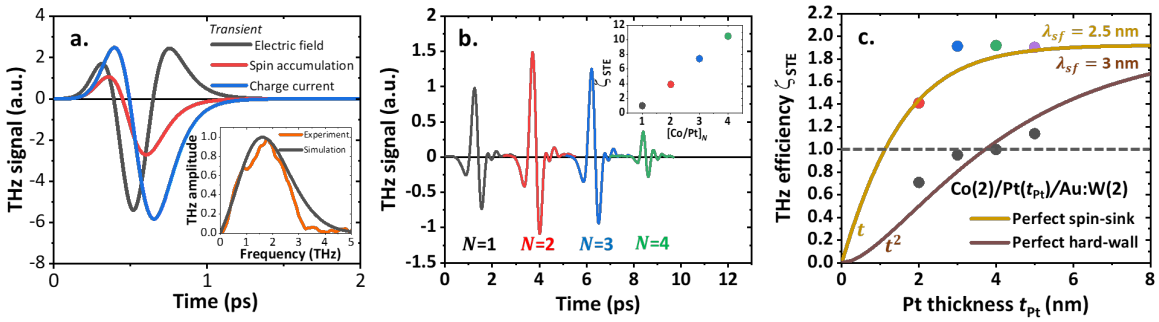

Figure F.2: Avancées sur les émetteurs THz spintronique métalliques. (a) Signaux THz simulées par notre modèle *wave-diffusion* en accord avec l'expérience. (b) Stratégie de répétition dans les couches $[\text{Co(2)/Pt(4)}]_N$ de une à quatre répétitions séparées par AlO_x(1). (c) Stratégie du *spin-sink* (drain de spin) dans Co(2)/Pt(t_{Pt})/Au:W(2) démontrant une efficacité électronique d'un facteur $\times 2$. Figures extraites du Chap. III.

posséder une résistivité électrique d'un ordre de grandeur plus grande que celle des métaux (environ autour de 100-1000 µΩ.cm), portent à leur surface des états conducteurs polarisés en spin, ce qui en fait une plateforme idéale pour étudier des interconversions d'interface portées par l'effet Rashba-Edelstein inverse (IREE) [164, 165, 163, 168, 167]. Nous nous sommes concentrés dans un premier temps sur $SnBi_2Te_4$, où une stœchiométrie précise du dopant Sn permet de fixer le niveau de Fermi entre la bande de valence et la bande de conduction dans le but d'éviter des contributions parasites dans la conversion spin-charge [289]. Nous observons une émission (et donc une interconversion) isotrope en fonction de l'orientation crystalline dans le plan (angle azimuthal ϕ). De plus, une extraction de l'efficacité THz η_{THz} nous permet de mesurer une interconversion constante en fonction de l'épaisseur jusqu'à 5 SL (5.9 nm), signe d'une conversion d'interface [271]. Pour aller plus loin dans notre étude, nous étudions l'alliage $Bi_{1-x}Sb_x$ où *i*) la croissance stable de couches ultrafines a été demontrée [295] et *ii*) la texture de spin au niveau de Fermi a été mesurée expérimentalement par nos collaborateurs au synchrotron SOLEIL [296]. Cette texture hélicale (Fig. F.3a-c), mesurée par spectroscopie de photo-émission résolue en angle et en spin, est un ingrédient essentiel pour obtenir une conversion d'interface de type Rashba-Edelstein. Nous avons ensuite réalisé la caractérisation de l'émission THz par adjonction d'une couche de Co (Fig. F.3d), et nous mesurons une émission nette augmentée d'un facteur $\times 1.5$ en champ électrique ($\times 2.25$ en puissance). Des mesures en fonction de l'orientation crystalline ϕ et de l'épaisseur pointent vers une conversion d'interface ((Fig. F.3e)). Ces mesures sont ensuite corrélées à un modèle de liaisons fortes qui nous permet d'extraire la longueur inverse de Rashba-Edelstein, autour de 0.3 nm sur les états de surface au niveau de Fermi, ce qui démontre la possibilité d'une conversion d'interface dans nos bicouches combinant isolant topologique et métal ferromagnétique (Fig. F.3f). Enfin, nous discutons en fin de chapitre l'effet de l'insertion, entre un isolant topologique (Bi_2Se_3) et un matériau ferromagnétique (Co), d'une couche atomiquement fine de dichalcogénures de métaux de transition (WSe_2) sur l'émission THz résultante. Ces matériaux bidimensionels sont typiquement des semi-conducteurs à gap (optique) modulable, de gap direct pour un monolayer, à gap indirect au-delà d'un monolayer d'épaisseur. En fonction de l'épaisseur de l'insert de WSe_2, nous observons que l'amplitude des composantes magnétiques et non-magnétiques évoluent ainsi que leurs symmétries d'émission (en fonction de l'orientation crystalline ϕ). En particulier, nous associons une diminution de la composante magnétique à la réduction de l'injection de spin en lien avec la formation d'une barrière Schottky entre le Co métallique et le WSe_2 semiconducteur [312]. Dans le même temps, l'augmentation de la composante non-magnétique est associée à des contributions THz additonnelles dans le WSe_2 et dont les symmétries d'émission sont imposées par la parité du nombre de couches.

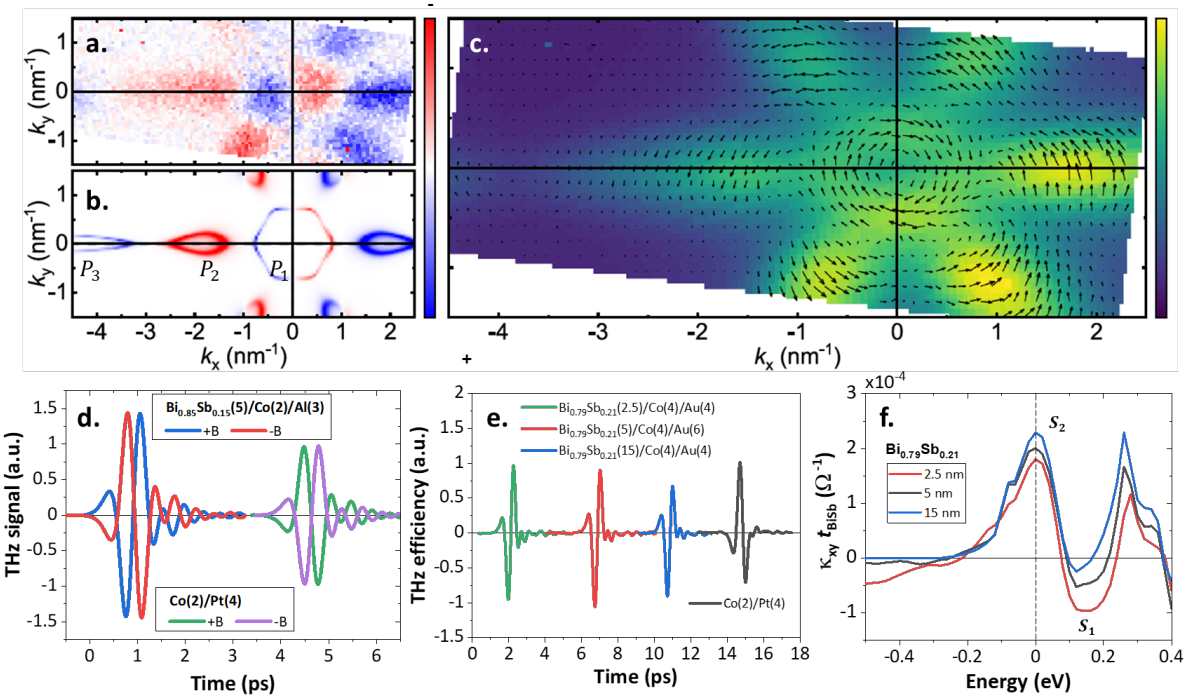

Figure F.3: Nouveau type d'émetteur spintronique à base d'isolants topologiques. (a) Mesures SARPES de la projection σ_y du spin pour $Bi_{0.85}Sb_{0.15}$(5) comparé aux (b) calculs en liasons fortes. (c) Verrouillage *spin-momentum* de la surface de Fermi pour $Bi_{0.85}Sb_{0.15}$(5) measuré par (S)ARPES. (d) Emission THz à partir de $Bi_{0.85}Sb_{0.15}$(5)/Co(2) comparé à Co(2)/Pt(4). Le gain en puissance est d'un facteur $\times 2.25$. (e) Efficacité électronique THz η_{THz} en fonction de l'épaisseur de $Bi_{1-x}Sb_x$. Le profil indépendent de l'épaisseur est corroborré par (f) les calculs en liaisons fortes démontrant un profil de conversion IREE indépendent de l'épaisseur.

- **Emission THz à bande étroite génerée par l'ordre antiferromagnétique.**
  Collaboration: O. Gomonay, M. Klaüi (JGU), T. Kampfrath (FUB), E. Saitoh (Tohoku)

Dans un troisième chapitre (Chap. V), nous remplaçons la composante ferromagnétique de l'émetteur par un matériau antiferromagnétique où les deux sous-réseaux magnétiques sont agencés de manière antiparallèle. Cette propriété est fixée par le champ d'échange intense entre les deux sous-réseaux et fixe les modes propres de résonnance de ces matériaux dans la gamme THz et sont donc des structures particulièrement intéressantes à étudier dans cette thèse. Nous nous concentrons principalement sur NiO/Pt de deux orientations différentes: (001) et (111) [350]. Nous observons pour la première orientation (001) une émission présentant des oscillations dans le domaine temporel (Fig. F.4a), dont la période correspond, après transformée de Fourier, à une contribution à bande étroité centrée autour de 1.1 THz, qui correspond au mode hors-plan du vecteur de Néel dans NiO [347]. Ces oscillations ne sont pas observées dans le cas NiO(111)/Pt. Des études préliminaires nous permettent de déterminer que l'émission est bien d'origine liée au vecteur de Néel (par anisotropie de l'émission en fonction de l'orientation crystallographique ϕ et par imagerie Kerr). De plus, nous montrons que le mécanisme d'émission est lié à la conversion ISHE dans le métal $5d$ en remplaçant le Pt par du W, à angle de spin Hall négative. Ces études préliminaires nous permettent de nous concentrer ensuite sur les mécanismes de génération du courant de spin. Après des études en fonction de la polarisation de la pompe, de l'épaisseur du NiO et de la dynamique du courant de spin, nous pouvons affirmer que deux mécanismes distincts ont lieu dans NiO et qu'ils dépendent de l'orientation de la couche de NiO (Fig. F.4b). Pour NiO(111), le mécanisme de génération se passe par un effet d'interaction pompe-matière, quasi-instantané et de type Raman non-résonant qui peut être vu comme l'effet Cotton-Mouton inverse. La nouveauté dans notre étude est la mise en lumière du second

mécanisme de génération de courant de spin sur des orientations NiO(001), où un mécanisme thermique est dominant. Par une étude approfondie de la réponse dynamique des phonons (qui régissent le transport thermique dans les isolants) par diffraction par rayons X ultra-rapides (équipe de M. Bargheer, Université de Potsdam), nous observons que le pompage optique du Pt crée localement du chauffage et induit la génération d'une onde de compression/dilatation qui se propage dans la bicouche (Fig. F.4c). Cette onde de compression/dilatation, lancée au sein du NiO, crée une précession des moments magnétiques. En effet, le NiO est un matériau connu pour être un matériau magnéto-strictif [350]. Cela induit donc une précession du vecteur de Néel qui se répercute sur l'injection du courant de spin (et donc de l'émission THz). Des simulations (O. Gomonay, Université de Mayence) confirment cette interprétation physique en modélisant la dynamique du vecteur de Néel sous égale excitation. Cette thématique de recherche ouvre des perspectives intéressantes sur l'émission à bande étroite par des matériaux à résonance THz et par effets magnéto-acoustiques.

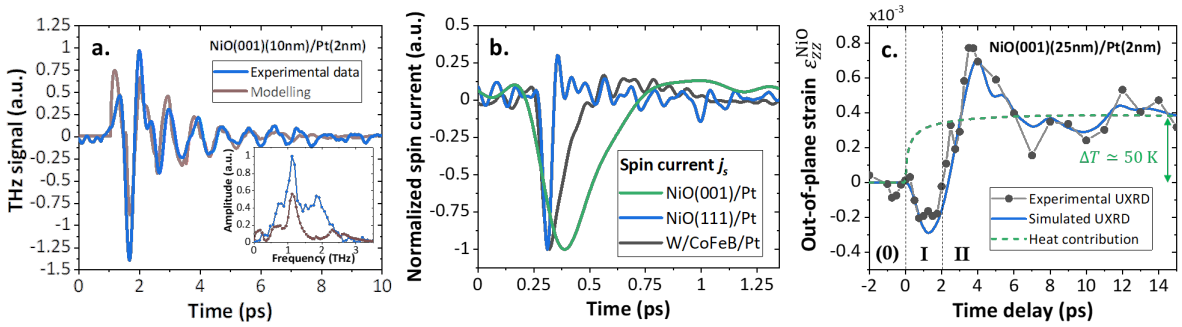

Figure F.4: Emission THz à base de structures antiferromagnétiques: NiO/Pt. (a) Signal THz (bleu) présentant des contributions large bande et à bande étroite à partir d'une bicouche NiO(001)/Pt. La contribution à bande étroite est centrée sur le mode haute-fréquence du vecteur de Néel à 1.1 THz. Les simulations corroborent nos mesures expérimentales. (b) Dynamique du courant de spin à partir de W/CoFeB/Pt, NiO(111)/Pt et NiO(001)/Pt présentant des dynamiques radicalement différentes et en faveur, respectivement, d'effets optiques et thermiques pour les deux orientations de NiO. (c) Profil de la déformation du réseau (paramètre hors plan) en fonction du temps à partir de mesures de diffraction à rayons X ultra-rapides. Deux contributions d'onde de choc de compression (bleu) et d'élévation thermique (vert) peuvent être dissociées et contribuent, par magnéto-striction, à l'excitation du vecteur de Néel.

- **Ingénérie et fonctionnalisation des émetteurs spintroniques THz.**
  Collaboration: I. Sagnes (C2N), M. Vanwolleghem (IEMN)

Enfin, dans un quatrième chapitre (Chap. VI), nous présentons des pistes d'amélioration des émetteurs spintroniques THz basées sur des stratégies transposées de l'optique et de la photonique. Nous utilisons des cavités THz et des couches anti-reflets pour augmenter la puissance THz émise par un facteur $\times 1.4$ et $\times 1.6$ (respectivement en Figs. F.5a-b). Nous démontrons également théoriquement la possibilité de générer du THz continu par photo-mélange sur une hétérostructure spintronique (Fig. F.5c). Nous ouvrons aussi des perspectives sur l'utilisation de strétégies adaptés de l'éléctronique haute fréquence (antennes et couplage radiatif) pour fonctionaliser les émetteurs THz spintroniques.

- **Conclusion générale et perspectives.**

En conclusion, cette thèse couvre un domaine large de la physique de la spintronique THz. Nous avons montré qu'en plus de pouvoir améliorer la puissance d'émission -a minima- d'un

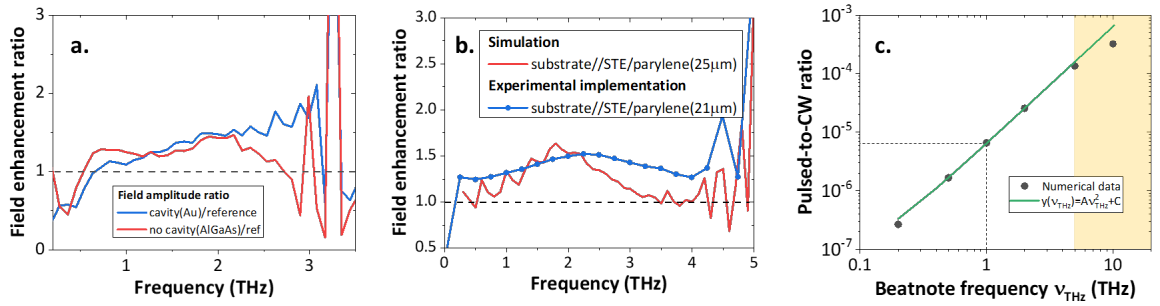

Figure F.5: Perspectives d'ingénierie THz des émetteurs spintroniques. (a) Gain (en champ électrique) mesuré sur des cavités THz à base de GaAs entérré. (b) Gain (en champ électrique) mesuré sur des couches anti-reflets THz à base de parylène. (c) Résultats numériques démontrant le principe d'émission CW THz par photomélange. Le ratio émission pulsée/émission CW est prédit être plus grand à plus haute fréquence.

facteur $\times 25$ (en amplitude) à moyen terme avec les dispositifs métalliques (drain de spin, répétitions, couplage radiatif par des antennes THz, *etc.*), une recherche sur des matériaux quantiques nouveaux comme les isolants topologiques est souhaitable. En effet, nous avons montré que ces matériaux présentent une texture de spin hélicale, appelée verrouillage *spin-momentum*, qui permet de convertir, à l'échelle de la picoseconde, une accumulation de spin en un courant de charge transverse via l'effet d'interface Rashba-Edelstein inverse par des états hybridés de type Rashba. La spectrocopie THz d'émission se révèle ici une sonde idéale pour étudier ce type de conversion à l'échelle de quelques centaines de femtosecondes. Un gain en amplitude d'un facteur $\times 1.5$ est déjà démontré sur des couches non-optimisées et leur intégration avec d'autres couches promet une augmentation des performances de dispositifs spitronique THz topologique. De plus, les émetteurs THz spintroniques peuvent être fonctionnalisés en utilisant des couches antiferromagnétiques présentant des modes THz propres et permettant une génération à bande étroite. Nous reportons pour la première fois dans notre étude une contribution cohérente au vecteur de Néel par des effets magnéto-strictifs ultra-rapides induits par une onde de compression/dilatation amenée par le transducteur Pt. Enfin, nous étudions les cavités et couches anti-reflets THz pour ingénierer les émetteurs spintroniques THz et proposons théoriquement une plage de fonctionnement du mode pulsé au mode CW (par photo-mélange). Un futur effort devra être amené dans la communauté sur le développement de détecteurs THz à base d'héterostructures spintroniques ou encore sur l'usage de dispositifs spintroniques THz comme sonde locale de phénomènes ultra-rapides (dynamique de courants de spin, couplage THz-matière, physique non-linéaire, *etc.*).

Appendix

This Appendix section is composed of several parts:

- First, Annex A1 presents the physical constants used in the scope of this work as well as usual conversions of physical quantities and the acronyms used in this work.
- Then, we propose needed derivations in our studies in a dedicated theoretical part:
  - Annex A2 develops the calculations of the spin-charge conversion in the linear response theory.
  - Annex A3 presents the Valet-Fert model for deriviating the spin-current propagation profile in the steady-state regime.
  - Annex A4 develops the different THz radiation mechanisms in free-space.
  - Annex A5 details the continuity equations at interfaces for the wave-diffusion model (from Chap. III).
  - Annex A6 presents the derivation of the Tinkham formula.
  - Annex A7 develops the spin-orbit assisted quantum modelling to account for the step potential-like interface (from Co/X/Pt study in Chap. III).
  - Annex A8 presents the equivalence of the Rashba tensor in terms of inverse Rashba-Edelstein length (from the study developed in Chap. IV).
- Finally, we discuss on the experimental developments performed during our studies:
  - Annex A9 presents the properties of our optical pump pulses.
  - Annex A10 presents the electro-optic sampling and phase-matching in non-linear crystals as used in our detection scheme.
  - Annex A11 references the tabulated near-infrared and THz absorption coefficients.
  - Annex A12 presents the spin-torque experiments (from Chap. III).
  - Annex A13 presents the ultrafast X-ray diffraction experimental method (from Chap. V).
  - Annex A14 presents our preliminary study on the THz emission from canted rare-earth antiferromagnet $TmFeO_3$/Pt (from Chap. V).
  - Annex A15 presents the finite-element method and the simulated structure parametrization to calculate the THz response of an engineered spintronic emitter (from Chap. VI).
  - Annex A16 develops our preliminary study on the impact of a buried metallic plane to reflect the emitted THz wave in reflection geometry (from Chap. VI).

A1 Physical constants, usual conversions and list of acronyms.

Physical constant	**Value**
Velocity of light in vacuum c	3×10^8 m.s^{-1}
Planck constant h	6.63×10^{-34} J.s
Reduced Planck constant $\hbar$	$h/(2\pi) = 1.05 \times 10^{-34}$ J.s
Free space impedance Z_0	377 Ω
Electron charge e	1.6×10^{-19} C
Electron mass m_e	9.1×10^{-31} kg
Vacuum permeability μ_0	$4\pi \times 10^{-7}$ kg.m.A^{-2}.s^{-2}
Vacuum permittivity ϵ_0	8.85×10^{-12} F.m^{-1}
Bohr magneton μ_B	$e\hbar/(2m_e) = 9.27 \times 10^{-24}$ A.m^2
Boltzmann constant k_B	1.38×10^{-23} J.K^{-1}

Physical quantity	**Unit conversion**
Energy	1 eV = 1.6×10^{-19} J
Rydberg energy	1 Ry = 13.6 eV
Length	1" = 2.54 cm
Temperature	$\theta_K = \theta_C + 273.15$
Magnetic field	1 Oe = $10^3/4\pi$ A.m^{-1}
Magnetic induction	1 T = 10^4 Oe = 10^4 G
Magnetization	1 erg.Oe^{-1}.cm^{-3} = 10^3 A.m^{-1}

Acronym	**Signification**
FM	Ferromagnet
HM	Heavy metal
SS	Spin-sink
AHE	Anomalous Hall effect
SML	Spin memory loss
SCC	Spin-charge conversion
FMR	Ferromagnetic resonance
FFT	(Fast) Fourier transform
EO(S)	Electro-optic (sampling)
QCL	Quantum cascade laser
STE	Spintronic THz emitter
HW	Hard wall (model)
ML, BL, QL, SL	monolayer, bilayer, quintuple layer, septuple layer
TB	Tight binding (calculations)
(I)SHE	(Inverse) spin Hall effect
(I)REE	(Inverse) Rashba-Edelstein effect
TI	Topological insulator
TSS	Topological surface states
(TR)(S)ARPES	(Time-resolved) (Spin-resolved) Angular Photoemission Spectroscopy
DFT	Density functional theory
TMDC	Transition metal dichalcogenide
AFM	Antiferromagnets
AFMR	Antiferromagnetic resonance
TDS	Time-domain spectroscopy
NIR	Near-infrared
DC/AC	Direct current / Alternating current
(I)FE	(Inverse) Faraday effect
(I)CME	(Inverse) Cotton-Mouton effect
(U)XRD	(Ultrafast) X-ray diffraction
SSE	Spin-Seebeck effect
STT	Spin-transfer torque
MRAM	Magnetic random access memory
RF	Radio-frequency
PCA/PCS	Photo-conductive antenna / Photo-conductive switch
BCB/BVB	Bulk conduction (valence) bands

A2 Calculations of the spin-charge conversion in the linear response theory.

A2.1 Derivation of the interconversion tensors from the Kubo formula.

In this section, we derive theoretically the inverse spin-charge conversion profile via the inverse spin Hall tensor σ_{xy}^{SHE} (assimilated to the spin Hall conductivity) and the inverse Rashba-Edelstein tensor $\hat{\lambda}_{\text{IREE}}$. We start with the well-known Kubo formula [385, 386] and the theory of the linear response which states that under a time-dependent external perturbation, the system under consideration will follow a linear response (neglecting higher order terms). This will allow us to derive the angular response of the interconversion (angular profile) mediated by topological surface states (warping) as experimentally characterized in Chap. IV.

Inverse spin Hall effect tensor. From the Kubo formula, we relate the spin Hall conductivity $\hat{\sigma}_{xy}^{\text{SHE}} \equiv \hat{\sigma}_{xz}^{y}$ to the Berry curvature Ω_n^{xz} via a transverse Hall conductivity and by introducing the longitudinal ($\mathbf{e}_x$) and transverse ($\mathbf{e}_z$) velocities from the velocity operator $\hat{\mathbf{v}} = \partial\mathcal{H}/\partial\mathbf{p}$. We define the spin current operator as $\hat{J}_{zy} = \hat{\mathbf{v}}_z\hat{\sigma}_y$. It comes from the Kubo formula:

$$\sigma_{xz}^{y} = \frac{2e^2\hbar}{(2\pi)^2}\sum_{m,n\ ;\ m\neq n}\int_{\text{BZ}}\left(f_n(\mathbf{k}) - f_m(\mathbf{k})\right)\frac{\text{Im}\left[\langle\psi_{n\mathbf{k}}|\,\hat{v}_x\,|\psi_{m\mathbf{k}}\rangle\,\langle\psi_{m\mathbf{k}}|\,\hat{\sigma}_y\hat{v}_z\,|\psi_{n\mathbf{k}}\rangle\right]}{(\varepsilon_{n\mathbf{k}} - \varepsilon_{m\mathbf{k}})^2 + \Gamma^2}d^2\mathbf{k} \tag{EA2.1}$$

$$= -\frac{e^2}{\hbar(2\pi)^2}\sum_{n}\int_{\text{BZ}} f_n(\mathbf{k})\Omega_n^{xz}(\mathbf{k})d^2\mathbf{k} \tag{EA2.2}$$

where e the electron charge, $\hbar$ the reduced Planck constant, $\Gamma = \hbar/\tau_{\text{relax}}$ the typical elastic energy broadening, $|n\rangle$ and $|m\rangle$ the band indices for the wavevector $\mathbf{k}$. $\psi_{i\mathbf{k}}$ is the electronic state associated with energy $\varepsilon_{i\mathbf{k}}$ and $f_i(\mathbf{k})$ is the Fermi filling factor. We have used the definition of the Berry curvature as:

$$\Omega_n^{xz}(\mathbf{k}) = 2i\hbar^2\sum_{m\neq n}\frac{\left[\langle\psi_{n\mathbf{k}}|\,\hat{v}_x\,|\psi_{m\mathbf{k}}\rangle\,\langle\psi_{m\mathbf{k}}|\,\hat{\sigma}_y\hat{v}_z\,|\psi_{n\mathbf{k}}\rangle\right]}{(\varepsilon_{n\mathbf{k}} - \varepsilon_{m\mathbf{k}})^2} \tag{EA2.3}$$

Inverse Rashba-Edelstein effect tensor. In the case of interfacial inverse Rashba-Edelstein effect, it is necessary not to consider only the density of states projected on the Fermi level $\mathcal{N}(\varepsilon_{\text{F}})$ but also to address the spin-texture warping $\hat{\sigma}_y$ at the Fermi level. We focus in this paragraph about the expected conversion response via IREE contribution mediated by the TSS in studied non-centrosymmetric topological insulators ($SnBi_2Te_4$, $Bi_{1-x}Sb_x$, *etc.*). This discussion is also mentioned in our published articles [271, 296]. The inverse Rashba-Edelstein tensor λ_{IREE} can be written according to the formalism introduced by Shen *et al.* [387]:

$$\lambda_{\text{IREE}} = \frac{\hbar^3}{2\pi m^*}\sum_{m,n\ ;\ m\neq n}\int_{\text{BZ}}\left(f_n(\mathbf{k}) - f_m(\mathbf{k})\right)\frac{\text{Im}\left[\langle\psi_{n\mathbf{k}}|\,\hat{v}_x\,|\psi_{m\mathbf{k}}\rangle\,\langle\psi_{m\mathbf{k}}|\,\hat{\sigma}_y\,|\psi_{n\mathbf{k}}\rangle\right]}{(\varepsilon_{n\mathbf{k}} - \varepsilon_{m\mathbf{k}})^2 + \Gamma^2}d^2\mathbf{k} \tag{EA2.4}$$

where m^* is the electron effective mass. For our purpose, we will consider for now on the intraband terms with $|n\rangle = |m\rangle$ dealing with pure diffusive effects on the topological surface states.

A2.2 Interfacial conversion angular profile *vs.* crystalline orientation.

In this derivation, we also account for the effect of the six-fold TSS warping in the case of C_{3v} symmetry as included by Johansson *et al.* [388] to estimate the angular response of the studied

topological insulators. Projecting the in-plane wavevector $\mathbf{k} := (k\cos(\phi-\phi_{\rm R}), k\sin(\phi-\phi_{\rm R}))$ onto a particular crystallographic direction (*e.g.* $\phi_{\rm R}=0 \Leftrightarrow \overline{\Gamma{\rm M}}$ in the reciprocal space), one finally obtains:

$$\begin{aligned}\lambda_{\rm IREE}(\theta,\phi_{\rm R}) &= \frac{\hbar^3}{2\pi m^*}\int_{\rm BZ} d\phi\ \hat{v}_x(\phi,\phi_{\rm R})\hat{\sigma}_y(\phi,\theta,\phi_{\rm R})\sum_n \frac{f_n(k)d^2k}{\Gamma^2}\\ &= \frac{\hbar^3}{2\pi m^*\Gamma}\int_0^{2\pi} d\phi\ \hat{v}_x(\phi,\phi_{\rm R})\hat{\sigma}_y(\phi,\theta,\phi_{\rm R})\left(\frac{d^2k}{d\varepsilon}\right)\\ &= \frac{\hbar^3}{2\pi m^*\Gamma}\int_0^{2\pi} d\phi\ \hat{v}_x(\phi,\phi_{\rm R})\hat{\sigma}_y(\phi,\theta,\phi_{\rm R})\mathcal{N}(\phi,\phi_{\rm R})\end{aligned} \tag{EA2.5}$$

where we have introduced the density of states $\mathcal{N}(\varepsilon) = (d^2k/d\varepsilon)$, θ the orientation of out-of-equilibrium injected spins (in-plane magnetization or magnetic field), $\phi_{\rm R}$ the in-plane sample orientation and ϕ the generic azimuthal angle. Therefore, the conversion symmetries are given by the integrated product between the longitudinal group velocity, the spin orientation, and the density of states. For C_{3v} symmetry systems, the energy dispersion relation including Rashba term [291, 389, 388] reads:

$$\varepsilon_{\pm}(\mathbf{k}) = \frac{\hbar^2k^2}{2m} \pm \sqrt{\alpha_{\rm R}^2k^2 + \lambda^2k^6\cos^2(3\phi)} \tag{EA2.6}$$

with $\alpha_{\rm R}$ the Rashba coefficient (velocity) and λ a coefficient describing the strength of the six-fold anisotropy term. Thus we assume the spin accumulation, group velocity and density of states to have the following symmetries [388]:

$$\begin{aligned} v_x(\phi,\phi_{\rm R}) &\equiv \cos(\phi) + 3\lambda\cos(3(\phi-\phi_{\rm R}))\left[\cos(\phi_{\rm R})\cos(\phi-\phi_{\rm R}) + \sin(\phi_{\rm R})\sin(\phi-\phi_{\rm R})\right]\\ \sigma_y(\phi,\theta,\phi_{\rm R}) &\equiv \frac{1}{2}\left(1+\sin(\phi+\phi_{\rm M})\right)\times\left(1+3\beta\cos^2(3(\phi-\phi_{\rm R}))\right)\\ \mathcal{N}(\phi,\phi_{\rm R}) &\equiv 1+\gamma\cos^2(3(\phi-\phi_{\rm R}))\end{aligned}$$

where λ,β,γ are three coefficients describing the anisotropy (hexagonal warping) of each involved physical quantity. One obtains the general isotropic response $\lambda_{\rm IREE}$ arising from the properties of the linear response theory:

$$\lambda_{\rm IREE}(\theta,\phi_{\rm R}) = \kappa_{xy}(\theta) = \frac{\pi}{32}(3\beta(8+18\lambda+3\gamma(2+5\lambda)) + 2(8+12\lambda+\gamma(4+9\lambda)))\sin(\theta) \tag{EA2.7}$$

independent of the crystallographic orientation $\phi_{\rm R}$. This will confirm our results of isotropic THz emission evidenced in Chap. IV. This fulfills the dipolar symmetry for the THz emission *vs.* the in-plane magnetic field direction.

Response of an hexagonal system from symmetry arguments. We derive in this section the response for an anisotropic system admitting a hexagonal symmetry, like the Fermi contour of studied topological surface states. We can express the response $\mathcal{J}$ of the system as:

$$\mathcal{J}_i = \sigma_{ij}\xi_j \tag{EA2.8}$$

where σ_{ij} is the response tensor and ξ_j is the excitation tensor. We place ourselves in the $(i,j)=(x,y)$ plane as displayed in Fig. A2.1. We represent, for hexagonal symmetry, the fact that the system is invariant under a rotation of $2\pi/3$ as:

$$\mathcal{J}_i = \tilde{\mathcal{J}}_i \Rightarrow \tilde{\sigma}_{ij}\xi_j = \mathcal{R}\sigma_{ij}\mathcal{R}^{-1}\xi_j = \sigma_{ij}\xi_j \tag{EA2.9}$$

where we have introduced the rotation matrix $\mathcal{R}$:

$$\mathcal{R} = \mathcal{R}\left(\frac{2\pi}{3}\right) = \begin{bmatrix} 1/2 & -\sqrt{3}/2 \\ \sqrt{3}/2 & 1/2 \end{bmatrix} \tag{EA2.10}$$

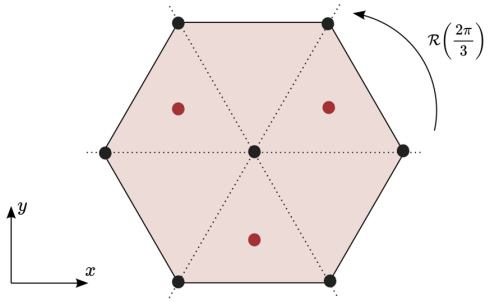

Figure A2.1: Angular response of hexagonal symmetry systems. The system is invariant under a $2\pi/3$ rotation.

By identification (we neglect the index notation for clariry), we have for an hexagonal system:

$$\tilde{\sigma} = \begin{bmatrix} \tilde{\sigma}_{xx} & \tilde{\sigma}_{xy} \\ \tilde{\sigma}_{yx} & \tilde{\sigma}_{yy} \end{bmatrix} = \begin{bmatrix} 1/2 & -\sqrt{3}/2 \\ \sqrt{3}/2 & 1/2 \end{bmatrix} \begin{bmatrix} \sigma_{xx} & \sigma_{xy} \\ \sigma_{yx} & \sigma_{yy} \end{bmatrix} \begin{bmatrix} 1/2 & \sqrt{3}/2 \\ -\sqrt{3}/2 & 1/2 \end{bmatrix} = \sigma \tag{EA2.11}$$

with $\sigma_{xy} \neq \sigma_{yx}$. By identification, it comes:

$$\tilde{\sigma}_{xx} = \frac{1}{4}\sigma_{xx} + \frac{3}{4}\sigma_{yy} - \frac{\sqrt{3}}{4}(\sigma_{xy} + \sigma_{yx}) = \sigma_{xx} \tag{EA2.12}$$

$$\tilde{\sigma}_{xy} = \frac{1}{4}\sigma_{xy} - \frac{3}{4}\sigma_{yx} + \frac{\sqrt{3}}{4}(\sigma_{xx} - \sigma_{yy}) = \sigma_{xy} \tag{EA2.13}$$

$$\tilde{\sigma}_{yx} = \frac{1}{4}\sigma_{yx} - \frac{3}{4}\sigma_{xy} + \frac{\sqrt{3}}{4}(\sigma_{xx} + \sigma_{yy}) = \sigma_{yx} \tag{EA2.14}$$

$$\tilde{\sigma}_{yy} = \frac{1}{4}\sigma_{yy} + \frac{3}{4}\sigma_{xx} + \frac{\sqrt{3}}{4}(\sigma_{xy} + \sigma_{yx}) = \sigma_{yy} \tag{EA2.15}$$

Therefore, it comes the symmetry of the σ tensor according to $\sigma_{xx} = \sigma_{yy}$ and $\sigma_{yx} = -\sigma_{xy}$, which is typical of an isotropic system:

$$\sigma = \begin{bmatrix} \sigma_{xx} & \sigma_{xy} \\ -\sigma_{xy} & \sigma_{xx} \end{bmatrix} \tag{EA2.16}$$

A3 Derivation of the spin current profile in spin-sink layers from the Valet-Fert model.

We derive here a expression of the spin-current profile following the Valet-Fert model [10]. We first make the assumption of the steady-state regime so that the differential equations ruling the spin accumulation μ_s and spin current j_s are:

$$\nabla^2 \mu_s = \frac{\mu_s}{l_{sf}^2} \quad \text{and} \quad j_s = -e\frac{l_{sf}}{r^s}\nabla\mu_s \tag{EA3.1}$$

We distinguish our system by a ferromagnetic layer of thickness t_{FM}, a heavy metal of thickness t_{HM} and a spin-sink of thickness t_{SS}. For sake of simplicity, we consider that the two inner interfaces do not present spin memory loss, i.e. $\delta_{\mathrm{FM/HM}} = t^{\mathrm{I}}_{\mathrm{FM/HM}}/l_{sf}^{\mathrm{FM/HM}} = 0$ and $\delta_{\mathrm{FM/HM}} = t^{\mathrm{I}}_{\mathrm{HM/SS}}/l_{sf}^{\mathrm{HM/SS}} = 0$. The solution to Eq. (EA3.1) can be written for each layer i as:

$$\mu_s^{(i)}(z) = A_i \exp\left(\frac{z}{l_{sf}^i}\right) + B_i \exp\left(-\frac{z}{l_{sf}^i}\right) \tag{EA3.2}$$

$$j_s^{(i)}(z) = \frac{1}{r_i^s}\left(A_i \exp\left(\frac{z}{l_{sf}^i}\right) - B_i \exp\left(-\frac{z}{l_{sf}^i}\right)\right) \tag{EA3.3}$$

The continuity equations for the spin accumulation and spin current (in absence of spin memory loss) reads:

$$\mu_s^{(i)}(z = z_{ij}^{\text{int}}) = \mu_s^{(j)}(z = z_{ij}^{\text{int}}) \quad \text{and} \quad j_s^{(i)}(z = z_{ij}^{\text{int}}) = j_s^{(j)}(z = z_{ij}^{\text{int}}) \tag{EA3.4}$$

for each adjacent layer (i, j). Besides, on the edge from the ferromagnetic side, we have a condition of spin current injection, and on the other side the spin current vanishes at the edge of the spin-sink material:

$$j_s^{(F)}(z = 0) = j_0 \quad \text{and} \quad j_s^{(\text{SS})}(z = z_{\text{SS}}) = 0 \tag{EA3.5}$$

A4 THz emission mechanisms in free-space.

A4.1 Case of the classical dipolar oscillator.

We develop in this part the properties of the dipolar radiation in the near-field and far-field regime, separated regions which can be identified as respectively under and above a distance from the emitter equivalent to $3\lambda_0$ where λ_0 is the free-space wavelength. From Ref. [99], we consider the case of an oscillating dipole $\mathbf{r}_a(t) = \mathbf{a}_0 \cos(\omega_0 t)$ leading to a radiation whose electric field admit the following form:

$$\mathbf{E}(\mathbf{r}, t) = \frac{q}{4\pi\epsilon_0}(k_0^2 \mathbf{a}_0 + \nabla(\mathbf{a}_0 \cdot \nabla))\frac{\cos(k_0 r - \omega_0 t)}{r} \tag{EA4.1}$$

From this, the expanded term can allow to identify three regions:

$$\mathbf{E}(\mathbf{r}, t) = \frac{q}{4\pi\epsilon_0}\left(3\frac{\mathbf{r}(\mathbf{a}_0 \cdot \mathbf{r})}{r^2} - \mathbf{a}_0\right)\left(\frac{\cos(k_0 r - \omega_0 t)}{r^3}\right) \tag{EA4.2}$$

$$+ \frac{q}{4\pi\epsilon_0}\left(3\frac{\mathbf{r}(\mathbf{a}_0 \cdot \mathbf{r})}{r^2} - \mathbf{a}_0\right)\left(k_0\frac{\sin(k_0 r - \omega_0 t)}{r^2}\right) \tag{EA4.3}$$

$$+ \frac{q}{4\pi\epsilon_0}\left(\mathbf{a}_0\frac{\mathbf{r}(\mathbf{a}_0 \cdot \mathbf{r})}{r^2}\right)\left(k_0^2\frac{\cos(k_0 r - \omega_0 t)}{r}\right) \tag{EA4.4}$$

The first term vanishes as $1/r^3$ and is thus very localized at the dipole surface. The second term evolves as $1/r^2$ and typically maps the near-field emission (spherical wave) with $a_0\omega \propto j_c$. The last term evolves as $1/r$ which is the far-field component with $a_0\omega^2 \propto \partial j_c \partial t$. In the case of one oscillator, we have:

$$E = \frac{e}{4\pi\epsilon_0 r} a_0 k^2 = \frac{e}{4\pi\epsilon_0 r}\frac{a_0\omega^2}{c^2} \tag{EA4.5}$$

The output power can be expressed as:

$$\frac{\partial P_{\text{out}}}{\partial t} = \frac{\partial}{\partial t}\int_\Omega \epsilon E^2 dV = \frac{e^2}{4\pi\epsilon c^3}(a_0\omega^2)^2 = \frac{e^2}{4\pi\epsilon c^3}\left(\frac{\partial j_c}{\partial t}\right)^2 \tag{EA4.6}$$

A4.2 Quantum equivalence: the Fermi golden rule for emission.

We discuss in this part the Fermi golden rule for spontaneous emission of a single photon (of energy $\varepsilon_{ph} = \hbar\omega$ with ω in the THz range). From the formalism of Ref. [99], we have the following Fermi golden rule owing to the dipolar term of the Hamiltonian where we have defined Γ_{em} the emission rate (τ_{em} is the response time) as:

$$\Gamma_{em} = \frac{1}{\tau_{em}} = \frac{2\pi}{\hbar}\sum_{k,n}(\langle kn|\, ev_k A\,|nk\rangle)^2 \mathcal{N}(\varepsilon_{\text{ph}}) \tag{EA4.7}$$

where e is the electron mass, v_k is the electron velocity, A is the vector potential and $\mathcal{N}$ is the photon density of states. The electric dipole generated is a sum over the $|k,n\rangle$ intraband electronic states, as the electric dipole is a term proportional to the intraband processes only [106]. By writing the electric field $e\mathbf{E} = -\nabla\mathbf{V} - e\partial\mathbf{A}/\partial t$, we have:

$$\frac{1}{\tau_{em}} = \frac{2\pi}{\hbar}\left(e\left(\sum_{k,n} V_k\right)A\right)^2 \mathcal{N}(\varepsilon_{ph}) = \frac{2\pi e^2}{\hbar}\left(\frac{E}{\omega}\right)^2\left(\sum_{k,n} V_k\right)\mathcal{N}(\varepsilon_{ph}) \tag{EA4.8}$$

where E can be seen as the electric field corresponding to a single-photon emission. By introducing the generated charge current $j_c = e\sum_k v_k$ (and by integrating over the volume dV), we have:

$$\frac{1}{\tau_{em}} = \frac{2\pi}{\hbar\varepsilon\omega^2}(\epsilon E^2) j_c^2 \mathcal{N}(\varepsilon_{\text{ph}}) \Longrightarrow \frac{1}{\tau_{\text{em}}} = \frac{2\pi}{\hbar\epsilon\omega^2}\int_{dV}(\epsilon E^2) j_c^2 \frac{n^3\omega^2}{2\pi^2\hbar c^3} \tag{EA4.9}$$

It comes the expression of the output THz power, and we have in case of an emission origin from a spin-charge conversion process (where the charge current via $j_c \propto \theta_{\text{SCC}}(j_s \times v)$):

$$P_{\text{out}} = \frac{\hbar\omega}{\tau_{\text{em}}} = \frac{\theta_{\text{SCC}}^2 n l_{sf}}{\pi\epsilon_0 c^3}\frac{\partial P_{\text{in}}}{\partial t}^2 \tag{EA4.10}$$

A4.3 Comparing electric and magnetic dipolar radiations.

We derive in this section the expression of the electric field induced by an electric (or magnetic) dipolar radiation.

Charge current derivation. A pulsed charge current j_c is generated at the front surface of the spintronic THz emitter. Therefore, owing to the Ohm law, Maxwell-Faraday and Maxwell-Ampère equations, we have:

$$\frac{\sigma}{\epsilon_0 c}\frac{\partial\mathbf{E}}{\partial t} + \frac{1}{c^2}\frac{\partial^2\mathbf{E}}{\partial t^2} = \nabla^2\mathbf{E} \tag{EA4.11}$$

The last equation is called the wave equation. Assuming in a plane wave $\mathbf{E} = \mathbf{E}_0\exp(-i\omega t)\exp(i\mathbf{k}\cdot\mathbf{r})$ as a solution, we have in the frequency domain:

$$\left(\frac{-i\omega\sigma}{\epsilon_0 c} - \frac{\omega^2}{c^2}\right)\mathbf{E} = -\mathbf{k}^2\mathbf{E} \Rightarrow k^2 = \frac{\omega^2}{c^2}n^2 = \frac{\omega^2}{c^2}\left(1 + \frac{i\sigma c}{\omega\epsilon_0}\right) \tag{EA4.12}$$

in absence of time-dependence of any external magnetic field which allows us to compute the THz refractive index.

Expression of the magnetic dipolar radiation. Starting with Maxwell-Ampère and Maxwell-Faraday equations, we can derive the magnetic wave equation:

$$\nabla \times \nabla \times \mathbf{B} = -\mu_0 \epsilon_0 \frac{\partial^2 \mathbf{B}}{\partial t^2} \tag{EA4.13}$$

with $\mathbf{B} = \mu_0(\mathbf{H} + \mathbf{M}(t))$ where $\mathbf{M}(t)$ is the dynamical magnetization, equivalent to the source term that for simplicity will be considered as a point source $\delta(z)$ corresponding to a finite thickness d_{FM}. We consider as solution a plane wave that can be written in the near-field as:

$$\left(k^2 - \frac{\omega^2}{c^2} n^2\right) \mathbf{B} = -\mu_0^2 \epsilon_0 \omega^2 \mathbf{M}(\omega) d_{\mathrm{FM}} \delta(z) \tag{EA4.14}$$

where n is the THz refractive index and ω the THz oscillation frequency. Finally, it comes:

$$\mathbf{E}_{\mathrm{M}}(\omega) = -\frac{i\omega n Z(\omega) d_{\mathrm{FM}} \mathbf{M}(\omega)}{c} \tag{EA4.15}$$

Magnitude comparison between electric dipolar radiation and magnetic dipolar radiation. To compare in the near field the two dipolar radiations, we assume an electric dipole radiation E_{js} owing to the spin-charge conversion of a spin current j_s, and an magnetic dipole radiation E_m, to have respectively the following expressions:

$$E_{js} \propto e Z_0 \theta_{\mathrm{SHE}} l_{sf} j_s \quad \text{with} \quad j_s = (m^* d_{\mathrm{FM}} M / \tau_{sf} \hbar) \tag{EA4.16}$$

$$E_m \propto \frac{n Z_0 d_{\mathrm{FM}}}{c} \frac{M}{\tau_r} \tag{EA4.17}$$

where e is the electron charge, $\hbar$ the reduced Planck constant, $m^* \simeq \hbar k_{\mathrm{F}} / v_{\mathrm{F}}$ the effective electron mass linked to the Fermi velocity v_{F} (nm.ps^{-1}) and the Fermi wavevector ($k_{\mathrm{F}} \simeq 10^9$ m^{-1}), Z_0=377 Ω is the free-space impedance, $c = 1/\sqrt{\epsilon_0 \mu_0}$ the light velocity, θ_{SHE} is the spin Hall angle, M is the magnetization, $\tau_r \simeq$ 1-10 ps is the remagnetization time, $\tau_{sf} \simeq$ 10-100 fs is the spin scattering time, $n = \sqrt{\sigma / \varepsilon_0 \omega_r}$ the THz refractive index with ω_r the corresponding THz pulsation (about 10^{12} rad.s^{-1}). The ratio between the two quantities can be estimated to a factor $\simeq 50$ and is expressed as:

$$\frac{E_{js}}{E_m} \equiv \frac{e l_{sf} \theta_{\mathrm{SHE}} m^* c}{n \hbar} \frac{\tau_r}{\tau_{sf}} \equiv \frac{e}{\hbar} \frac{\tau_r}{\tau_{sf}} \theta_{\mathrm{SHE}} l_{sf} m^* \sqrt{\frac{\omega_r}{\mu_0 \sigma}} \tag{EA4.18}$$

A5 Continuity equations for the wave-diffusion model.

Conditions at the inner interfaces: the importance of interfacial transmission in multilayers. Eqs. (E3.3) are valid in the bulk of the i-th layer, but the two regions are separated by an interface which needs a particular treatment. The continuity equations stands at the interface regarding the spin and charge transport, in particular we have the continuity of the charge current j_c:

$$j_c(z = 0^+, t) = j_c(z = 0^-, t) \tag{EA5.1}$$

$$\Leftrightarrow j_\uparrow(z = 0^+, t) + j_\downarrow(z = 0^+, t) = j_\uparrow(z = 0^-, t) + j_\downarrow(z = 0^-, t) \tag{EA5.2}$$

However, the spin current j_s might not be conserved at the interface due to some potential interfacial spin-flip events. The manifestation of the spin-current discontinuity at the interface can be written as:

$$\Delta j_s^{\text{int}} = j_s(z=0^+,t) - j_s(z=0^-,t) \tag{EA5.3}$$
$$= \left[j_\uparrow(z=0^+,t) - j_\downarrow(z=0^+,t)\right] - \left[(j_\uparrow(z=0^-,t) - j_\downarrow(z=0^-,t)\right] \tag{EA5.4}$$
$$= 2v_{\uparrow\downarrow}^{\text{int}} m_{\text{tot}}^{\text{int}}(t) \tag{EA5.5}$$

where $v_{\uparrow\downarrow}^{\text{int}}$ is the interfacial scattering velocity and we have introduced the interfacial magnetization $m_{\text{tot}}^{\text{int}}$ as:

$$m_{\text{tot}}^{\text{int}}(t) = m(z=0^+,t) + m(z=0^-,t) \tag{EA5.6}$$
$$= \big(n_\uparrow(z=0^+,t) - n_\downarrow(z=0^+,t)\big) + \big(n_\uparrow(z=0^-,t) - n_\downarrow(z=0^-,t)\big) \tag{EA5.7}$$

In details, the spin-current expression at the interface can be derived in the following form:

$$\begin{aligned} j_\sigma(z=0^-,t) &= 2\left(v_{\sigma\sigma}^{\text{int}}\left[n_\sigma(z=0^-,t) - n_\sigma(z=0^+,t)\right] + v_{\sigma\sigma'}^{\text{int}}\left[n_\sigma(z=0^-,t) - n_{-\sigma}(z=0^+,t)\right]\right) \\ j_\sigma(z=0^+,t) &= 2\left(v_{\sigma\sigma}^{\text{int}}\left[n_\sigma(z=0^+,t) - n_\sigma(z=0^-,t)\right] + v_{\sigma\sigma'}^{\text{int}}\left[n_{-\sigma}(z=0^-,t) - n_\sigma(z=0^+,t)\right]\right) \end{aligned} \tag{EA5.8}$$

with the interfacial (transfer) velocities are determined $v_{\sigma\sigma'}^{\text{int}}$, depending on their spins, from the transmission coefficient:

$$v_{\sigma\sigma'} = v_{\text{F}} T_{\sigma\sigma'} \Longleftrightarrow \begin{bmatrix} v_{\uparrow\uparrow} & v_{\uparrow\downarrow} \\ v_{\downarrow\uparrow} & v_{\downarrow\downarrow} \end{bmatrix} = v_{\text{F}} \begin{bmatrix} T_{\uparrow\uparrow} & T_{\uparrow\downarrow} \\ T_{\downarrow\uparrow} & T_{\downarrow\downarrow} \end{bmatrix} \tag{EA5.9}$$

At the interface, the spin-flip probability $p_{sf} = 1 - \exp(-\delta)$ can be linked to the ratio between the parallel and antiparallel transmission $(\sqrt{2}T_{\uparrow\downarrow})/\sqrt{T_{\uparrow\uparrow} + T_{\downarrow\downarrow}}$. Importantly, it comes in the steady-state regime the approximation:

$$j_\sigma \simeq v_{\text{F}} T n_\sigma \Longrightarrow j_s \simeq v_{\text{F}} T m \tag{EA5.10}$$

Edge conditions and border spin-flip scattering events. We now focus on the boundary regions of the materials, always two in a multistack of layers (thereafter referred at positions $z_{\text{B}}^{\pm}$). To account for potential spin-flip at the boundaries, we integrate the following scattered population n_σ^{out} depending on the incoming population n_σ^{in}:

$$n_\sigma^{\text{out}} = \frac{p_{sf}}{2} n_{-\sigma}^{\text{in}} + \left(1 - \frac{p_{sf}}{2}\right) n_\sigma^{\text{in}} \tag{EA5.11}$$

where p_{sf} is the probability of spin-flip events at the interface. At the edges $z = z_{\text{B}}^{\pm}$ (left $(-)$ and right $(+)$ external boundaries), we consider specular electron reflections ($R = 1$) so that the net border electrical current j_c is zero which can be also written:

$$j_c(z = z_{\text{B}}^{\pm}) = j_\uparrow(z = z_{\text{B}}^{\pm}, t) + j_\downarrow(z = z_{\text{B}}^{\pm}, t) \tag{EA5.12}$$
$$= 0 \tag{EA5.13}$$

$$j_s(z = z_{\text{B}}^{\pm}) = j_\uparrow(z = z_{\text{B}}^{\pm}, t) - j_\downarrow(z = z_{\text{B}}^{\pm}, t) \tag{EA5.14}$$
$$= \left(\frac{p_{sf}}{2 - p_{sf}}\right) m(z = z_{\text{B}}^{\pm}) \left(\frac{v_{\text{F}}^{\uparrow} + v_{\text{F}}^{\downarrow}}{2}\right) \tag{EA5.15}$$

We verify well that in case of no border spin-flip events, the initial and final spin populations cancelled each other and there is no net spin current. In case of border spin-flip, the residual spin current is directly proportional to the net border magnetization $m(z = z_{\text{B}}^{\pm})$.

A6 Derivation of the Tinkham formula.

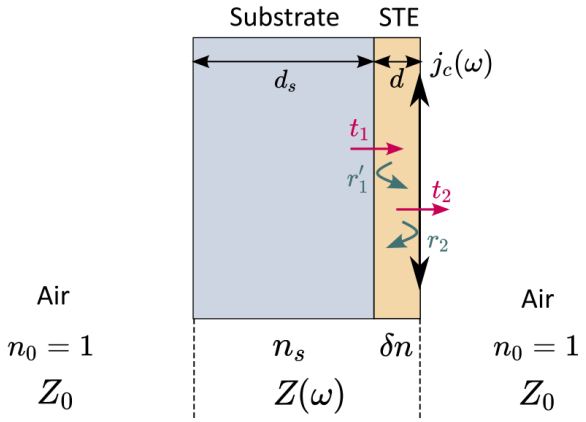

Figure A6.1: Derivation of the Tinkham formula. Schematics of the spintronic THz emitter of refractive index δn and thickness d on a substrate of index n_s and thickness d_s.

We derive in this Appendix the Tinkham formula [246] accounting for the THz absorption in a thin metallic multilayer. We start by considering the following geometry displayed in Fig. A6.1. The heterostructure is composed of a substrate of thickness d_s and refractive index n_s on which is deposited the emitter of thickness d and refractive index δn. We consider the surrounding media to be air of refractive index $n_0 = 1$. A THz source $j_c(\omega)$ oscillates at the metal surface (dipolar radiation of dispersion $k^2 = n^2\omega^2/c^2$). We call t_i (r_i) the transmission (reflection) at the i-th interface defined as:

$$r_1' = \frac{n - n_s}{n + n_s}, \quad r_2 = \frac{n - n_0}{n + n_0}, \quad t_1 = \frac{2n}{n + n_s}, \quad t_2 = \frac{2n}{n + n_0}, \tag{EA6.1}$$

The effective transmission coefficient which includes the multiple reflections can be written as:

$$t^* = t_2 t_1 + t_2(r_2 r_1' \exp(2ikd)) + t_2(r_2 r_1' \exp(4ikd)) + ... \tag{EA6.2}$$

$$= t_2 \sum_{N=2j} (r_1' r_2 \exp(ikd))^N = \frac{t_2}{1 - r_1' r_2 \exp(2ikd)} \tag{EA6.3}$$

For a metal, the refractive index $n = \sqrt{\epsilon}$ can be expressed via $\epsilon = \epsilon_r + i\sigma/\omega\epsilon_0$ where σ is the metal conductivity following the Drude model:

$$\sigma = \frac{\sigma_{\text{DC}}}{1 - i\tau\omega} \tag{EA6.4}$$

which leads to a strong metallic refractive index $n \gg n_0, n_s$. For thin metallic multilayers, typically well below the wavelength , we consider $\exp(2i\omega dn/c) \ll 1$ we have:

$$t^* = \frac{\frac{2n}{n+n_0}}{1 - \left(\frac{n-n_s}{n+n_s}\right)\left(\frac{n-n_0}{n+n_0}\right)\left(\frac{2i\omega dn}{c} + 1\right)} \tag{EA6.5}$$

$$= \frac{2n(n+n_s)}{(n+n_s)(n+n_0) - (n-n_s)(n-n_0)\left(\frac{2i\omega dn}{c} + 1\right)} \tag{EA6.6}$$

$$\simeq \frac{n+n_s}{n_0 + n_s - \frac{i\omega dn^2}{c}} = \frac{n+n_s}{n_0 + n_s + Z_0\sigma d} \tag{EA6.7}$$

Finally, it comes:

$$Z(\omega) = \frac{Z_0}{n_0 + n_s + Z_0 \int \sigma(\omega, z) dz} \tag{EA6.8}$$

A7 Modelling of the electronic transfer involving spin-orbit interactions.

Definition of the Hamiltonian. This Appendix develops the spin-orbit assisted quantum model to account for the interfacial scattering following the study of interfacial spin-injection and spin-charge conversion in Co/X/Pt trilayers proposed in Section III.3.5.

***i*) SOI assisted electronic quantum transmission at Co/X/Pt interfaces.**
The partitioned Hamiltonian in Co and Pt reads:

$$\hat{\mathcal{H}} = \frac{\hat{\mathbf{p}}^2}{2m^*} - \Delta_{\text{ex}} \hat{\mathbf{m}} \cdot \hat{\sigma} + \hat{\mathcal{V}} \tag{EA7.1}$$

where $\hat{\mathbf{p}} = -i\hbar\nabla_z$ is the impulsion operator, m^* is the effective mass, $\hat{\mathbf{m}}$ is the magnetization and $\Delta_{\text{ex}} \simeq 2$ eV is the exchange coupling for Co. $\hat{\mathcal{V}}_{\text{Co}} = 0$ represents the energy position of the bottom of the spin-averaged $3d$ Co bands. Along the same idea, for Pt, we set $\Delta_{\text{ex}} = 0$ together with $\hat{\mathcal{V}}_{\text{Pt}} \simeq -1$ eV equal to the bottom of the $5d$ Pt band and representative of the offset of the work function between the two metals. The important feature is to add an interfacial potential parameterized by $\hat{\mathcal{V}}_{\text{S}}$ and written in a Dirac-like form and expressed by [390, 391, 392]:

$$t_{\text{I}} \hat{\mathcal{V}}_{\text{S}} \delta(z) = t_{\text{I}} \left[\mathcal{V}_{\text{X}} + \mathcal{V}_{\text{ex}} \hat{\mathbf{m}} \cdot \hat{\sigma} + \frac{\alpha_{\text{R}}}{\hbar} (\hat{\mathbf{p}} \times \mathbf{e}_n) \cdot \hat{\sigma} \right] \delta(z) \tag{EA7.2}$$

where z is the coordinate in the depth of the layer, t_{I} is the effective interface thickness. $\hat{\mathcal{V}}_{\text{S}}$ may be described by three different parameters: $\mathcal{V}_{\text{X}} = \hbar^2 k_{\text{X}}/t_{\text{I}} m^*$ is the average potential barrier, the second term ($\mathcal{V}_{\text{ex}}$) represents a possible interface exchange that we will not consider henceforth ($\mathcal{V}_{\text{ex}} = 0$). The last term is the Rashba interaction scaled by $\alpha_{\text{R}} = \frac{\hbar^2}{am^*} \left(\frac{k_{\text{SO}}}{k_{\text{F}}} \right)$. We solved the quantum transport problem by matching the different wavefunctions $\psi_{k_{\parallel}}(z)$ involving $\mathcal{V}_{\text{S}}$. This is performed by imposing a quantum step of magnitude $\hat{k}_{\text{S}} = am^* \hat{\mathcal{V}}_{\text{S}} \phi(0)/\hbar^2$ in the current wave keeping continuous both the wavefunction and the current flux making then the relationship between the generalized surface potential energy $\mathcal{V}_{\text{S}}$ with a corresponding surface wavevector $\hat{k}_{\text{S}}$.

***ii*) Spin and spin-current diffusion in the bulk layers.**
Our calculations also consider the diffusive spin backflow by introducing spin-diffusion terms in the two bulk regions. We have calculated self-consistently the two spin distribution functions $f_\sigma(z,k) = f_\sigma^{(0)}(z,k) + \left(g_\sigma^{(1)}(z) \cos(\theta_k) + \Delta n_\sigma(z) \right) \delta(\varepsilon - \varepsilon_{\text{F}})$ away from the equilibrium described by $f_\sigma^{(0)}(z,k)$, and where $g_\sigma^{(1)}(z)$ and $\Delta n_\sigma(z)$ stand respectively for the Fermi sphere displacement (the spin-dependent current writes $j_\sigma = e\mathcal{N}(\varepsilon_{\text{F}}) g_\sigma^{(1)}$ where $\mathcal{N}(\varepsilon_{\text{F}})$ is the density of states at the Fermi level) and the spin-accumulation $\Delta m = \Delta n_\uparrow - \Delta n_\downarrow$. Both diffusive spin currents and spin-relaxation in the bulk regions writes:

$$\delta j_s(z) = \frac{\sigma^*}{e} \frac{\partial \Delta m(z)}{\partial z} \quad \text{and} \quad \frac{\partial \left[\delta j_s(z) \right]}{\partial z} = \frac{\sigma^*}{e l_{sf}^2} \Delta m(z) \tag{EA7.3}$$

The solution is obtained by matching the coherent spin-current to its diffusive expression in both regions at the vicinity of the interface.

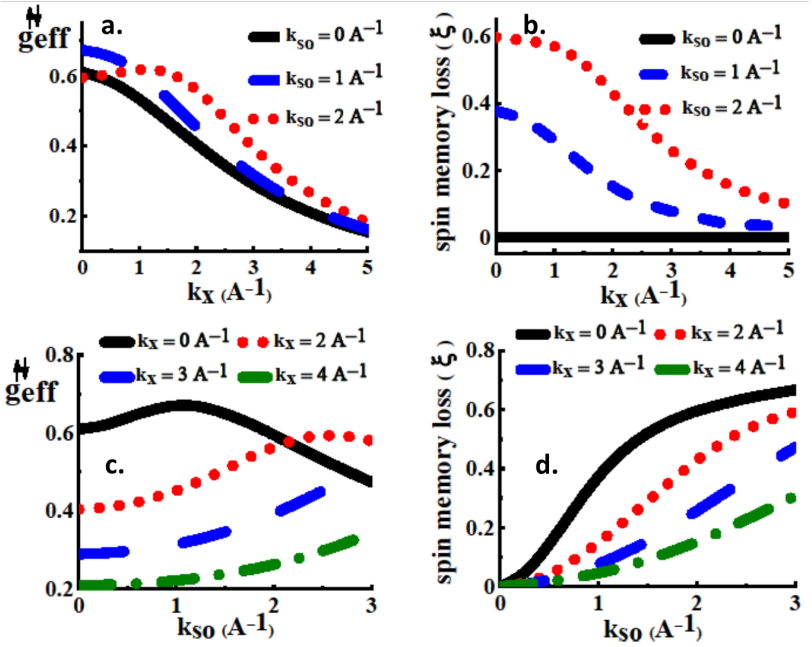

Figure A7.1: Variations of the interfacial spin parameters as a function of the interfacial potentials. (a) Spin mixing conductance $g_{\text{eff}}^{\uparrow\downarrow}$ in units of transmission coefficient T^* and (b) spin-memory loss ξ calculated *vs.* the interface potential k_X for different spin-orbit parameters ($k_{SO} = 0, 1, 2$ Å^{-1}). (c) Spin-mixing conductance $g_{\text{eff}}^{\uparrow\downarrow}$ in units of transmission coefficient T^* and (d) spin-memory loss ξ calculated *vs.* spin-orbit parameters k_{SO} for different interface potential (k_X=0, 2, 3 and 4 Å^{-1}). Non-zero k_{SO} is responsible for spin-memory loss.

***iii*) Physical parameters.**

We considered for Co Fermi wavevectors of $k_F^{\uparrow} \simeq 1$ Å^{-1}, $k_F^{\downarrow} \simeq 0.7$ Å^{-1} for the two spin sectors, together with a spin-diffusion length $l_{sf}^{Co} = 10$ nm (mean free path λ^{Co}=3 nm). A value $k_{Pt} \simeq 1$ Å^{-1} and $l_{sf}^{Pt} = 3$ nm (mean-free path for Pt λ^{Pt}=1.5 nm) has been chosen for Pt. Note that the same values for $k_F^{\uparrow}$ and k_{Pt} expresses the absence of potential step between Co and Pt for the majority spin channel. This feature has to be associated to a very good band matching and optimized transmission at Co/Pt interface for spin $\uparrow$ electrons [231, 30]. In order to fit the experiments, we consider an inverse spin-orbit length k_{SO} of the order of $k_{SO} = t_I m^* \alpha_R \bar{k}_F / \hbar^2 = 1.5$ Å^{-1}. By setting an interface extension of about $t_I \simeq 2$ nm. One obtains a Rashba splitting of $\alpha_R \bar{k}_F \simeq 0.4$ eV. This in good agreement with the value predicted by ab-initio calculations for the Co/Pt interface [256] and in the range of the spin-orbit strength of Pt.

Modelling: results and analyses. The conclusions raised in the devoted section are even more clear when focusing on the variation of $g_{\text{eff}}^{\uparrow\downarrow}$ (in units of the transmission coefficient T with $g_{\text{eff}}^{\uparrow\downarrow} = \frac{e^2}{h}\Sigma_{k_\parallel} T(k_\parallel)$) and spin memory loss ξ *vs.* the different potential parameters, k_X and k_{SO}. Fig. A7.1a-b displays the variation of $g_{\text{eff}}^{\uparrow\downarrow}$ and ξ *vs.* k_X from 0 to 5 Å^{-1} for different values of the spin-orbit parameter $k_{SO} = 0, 1, 2$ Å^{-1}. Note that 9 electrons per Co atom, a 2D density of 13 atoms.nm^{-2} and an average spin-transmission coefficient of $T \simeq 0.6$ yields to 70 channels.nm^{-2} for $g_{\text{eff}}^{\uparrow\downarrow}$, close to the measured value (Fig. 3.30b). As expected, $g_{\text{eff}}^{\uparrow\downarrow}$ drops on increasing k_X in almost any situation as $k_X \gtrsim k_{SO}$ due to a stronger back scattering. However, calculations evidence an increase of $g_{\text{eff}}^{\uparrow\downarrow}$ in the range $k_X \lesssim k_{SO}$ for $k_{SO} = 2$ Å^{-1} showing a certain correlation between both potentials. In parallel, we evidence a clear drop of the spin-memory loss ξ with k_X hiding more and more the role of the spin-orbit interaction k_{SO} although kept fixed. The spin memory loss drops from $\xi = 0.43$ to $\xi = 0.15$ when k_X increases from 2 Å^{-1} to 4 Å^{-1} for $k_{SO} = 2$ Å^{-1}. In the same vein, Fig. A7.1c-d displays respectively $g_{\text{eff}}^{\uparrow\downarrow}$ and spin-memory loss parameter ξ *vs.* k_{SO} for different

values of k_X. Quite surprisingly, $g_{\text{eff}}^{\uparrow\downarrow}$ increases with the Rashba spin-orbit potential k_{SO} within a certain range, $k_{SO} \lesssim k_X$, (see also Fig. A7.1a). This demonstrates an enhancement of the spin-current escape from Co as spin-orbit interactions increase. On the other hand, Fig. A7.1d clearly reveals the strong increase of the spin memory loss with k_{SO} for any k_X. Since we assume that the interface Co/X/Pt does not have a band matching as good as Co/Pt, the introduction of an interlayer has the effect of reducing the transmission of spin current via a chemical blocking of transport spin-channels. In our model this effect corresponds to an increase of the interface barrier $\mathcal{V}_X$. Moreover, it comes conjointly with a reduction of the Rashba parameter k_{SO} that accounts for a moderate spin-orbit passivation. Figure A7.1b reveals that a larger potential step $\mathcal{V}_X = 0.3$ eV (obtained with k_{SO}=1.5 Å^{-1}) reduces the current $j_s(z_+)$ as well as the spin memory loss jump ξ. The parameter ξ corresponds to the $j_s(z_+)$ of the Hamiltonian with $\mathcal{V}_X > 0$ (namely Co/X/Pt with an interlayer X of finite thickness d divided by $j_s(z_+)$ obtained for $\mathcal{V}_X = 0$ (namely the bare Co/Pt interface).

A8 Equivalence to the inverse Rashba-Edelstein length in $Bi_{1-x}Sb_x$/Co interfacial conversion.

IREE is scaled by the characteristic IREE length Λ_{IEE} whereas the ISHE is scaled by the spin-Hall conductivity (SHC) $\sigma_{\text{SHC}} = \sigma_{xz}^{y}$. In order to compare the efficiency of the two different processes, one must compare Λ_{IEE} to the product $\theta_{\text{SHE}}\lambda_{sf}$ where $\theta_{\text{SHE}} = \sigma_{\text{SHC}} \times \rho_{xx}$ refers to the effective spin-Hall angle and l_{sf} is the spin-diffusion length. One can thus transform Λ_{IEE} to an equivalent SHC according to $\Lambda_{\text{IEE}} = \sigma_{\text{IEE}}\rho_{xx} \times \lambda_{sf} = \sigma_{\text{IEE}} r_s$ with $r_s = \tau_s/e^2\mathcal{N}_{\text{DOS}}^{\text{3D}}\lambda_{sf}$ the spin resistance. We arrive at the following formula to compare with σ_{SHE} (if non-zero):

$$\sigma_{\text{IEE}} = \frac{1}{2\sqrt{3}\pi^2}\left(\frac{e^2}{\hbar}\right)k_{\text{F}}^2\Lambda_{\text{IEE}} \tag{EA8.1}$$

We display in Fig. A8.1 the equivalence between the inverse Rashba-Edelstein tensor κ_{xy} and the inverse Rashba-Edelstein length $\Lambda_{xy}^{\text{IREE}}$ for the tight-binding calculations displayed in Chap. IV.

A9 Properties of the ultrafast pulsed sources.

Pump spectrum. Following the mode locking of the laser, allowing the generation of light pulses, the pump spectrum results in a broadening around a central frequency ($\nu_0 = c/\lambda_0 = 373.3$ THz) according to a certain dispersion $\delta\nu$. In practical, more the pulse is short in time, more the pump spectrum is broaden. Our laser system, centered at $\lambda_0 = 803$ nm, owns the spectrum shown in Fig. A9.1. With the help of a Gaussian fitting of the following form:

$$y(\lambda, w) = \frac{A}{w\sqrt{\frac{\pi}{2}}}\exp\left(-2\frac{(\lambda-\lambda_0)^2}{w^2}\right) \tag{EA9.1}$$

the spectral broadening is given by the full width at half-maximum (FWHM) $\Delta\lambda = \sqrt{2\ln 2}w$=8.2 nm which corresponds in frequency to a broadening of $\Delta\nu$=3.75 THz.

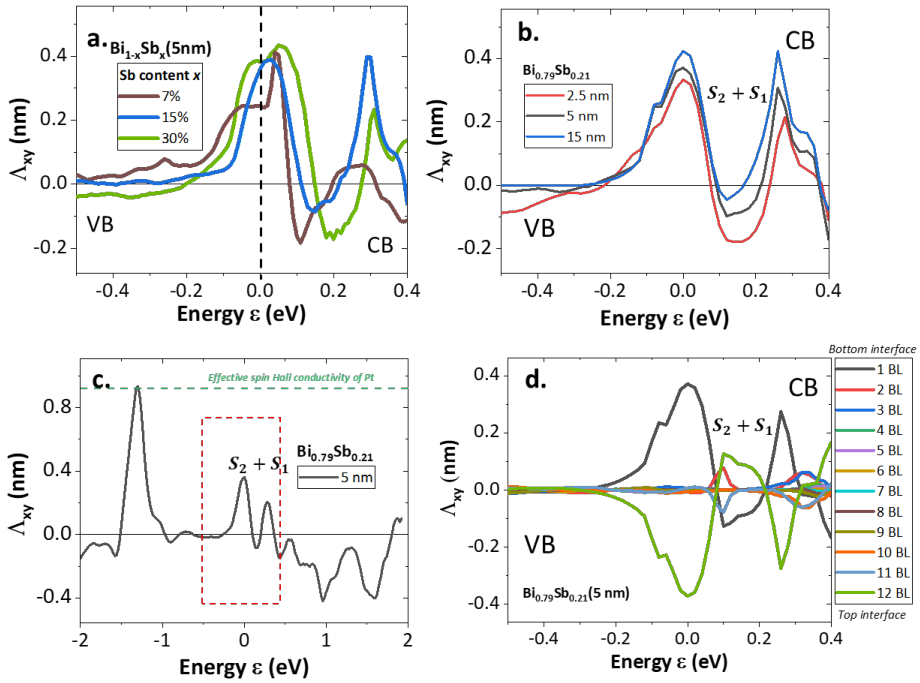

Figure A8.1: Equivalent calculations of the inverse Rashba-Edelstein length $\Lambda_{xy}^{\text{IREE}}$. (a) Renormalized energy profile for (a) different Sb concentrations ranging from 7%, 10% and 30% and (b) different $Bi_{1-x}Sb_x$ thicknesses (2.5, 5 and 15 nm). (c) Conversion profile *vs.* the energy from -2 to 2 eV, integrated on $Bi_{1-x}Sb_x$(5nm) full thickness and serves as a comparison with the inverse spin Hall effect in Pt (green dotted line). (d) Separated contribution of the BL in the conversion efficiency, from the first to the twelfth BL. In details, we considered a mean free path $\lambda \simeq 10$ nm and a mean elastic lifetime $\tau_\sigma \simeq 30$ fs.

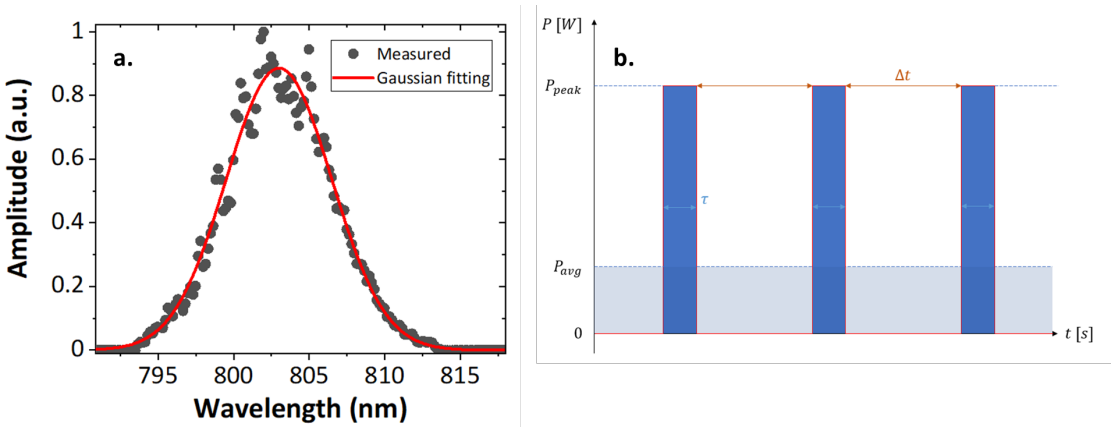

Figure A9.1: Properties of the ultrafast pump. (a) Spectral components of our laser pump system (Ti:Sa oscillator) acquired with a spectrometer (black) and fitted using a Gaussian fit (red). The spectrum is centered around $\lambda_0 = 803$ nm. (b) Laser pump profile.

Towards shorter pulses: attosecond physics.

The theoretical limit for generating the shortest pulses depends on two elements: first, to generate the shortest pulses means in Fourier domain that the bandwidth enlarges. However it exists a lower limit to the maximal bandwidth accessible: the pulse is called Fourier-transform-limited *i.e.* following the imposed oscillator bandwidth. Secondly, the pulse duration is limited by the optical cycle which is defined as the propagation of one period of wavelength. For instance at $\lambda_0 = 800$ nm, the optical cycle is $\lambda_0/c \simeq 2.67$ fs. Therefore, to generate attosecond pulses, the wavelength is to be reduced in the ultra-violet light range (the pump energy is thus increased).

Pump power, energy and effective duty-cycle. Pulsed pump emission regimes differ from continuous wave: indeed, pulsed regime can reach high peak amplitude. Conventionally, pulsed laser systems are defined according to the following physical quantities :

- Temporalities: the pulse width τ_p, the repetition rate $f_{rep} = 1/\Delta t$ with Δt the interval between two consecutive pulses, with the duty cycle $\tau_p/\Delta t$
- Peak quantities: the energy per pulse ε_p where the energy carried by the photons is expressed as $\varepsilon = h\nu = hc/\lambda$ where h is the Planck constant, c is the velocity of light in vacuum and λ is the radiation wavelength. The peak power is defined as $P_{\text{peak}} = \varepsilon_p/\tau_p$
- Averaged quantities: the laser fluence $F = \varepsilon_p/S$ (given in J.m^{-2}), the average power P_{avg} and $S = \pi r^2$ the spot surface (of radius r)

From the definitions, it comes:

$$P_{peak} = P_{avg} f_{rep} \tau_p \quad \text{with} \quad P_{avg} = F S \tau_p f_{rep}^2 \tag{EA9.2}$$

Laser system	Wavelength	Pulse duration	Repetition rate	Pulse period	Energy per pulse
Ti:Sa oscillator	800 nm	100 fs	80 MHz	12.5 ns	3.75 nJ
Ti:Sa oscillator	800 nm	15 fs	1 GHz	1 ns	0.3 nJ
Yb-doped amplifier	1030 nm	23 fs	200 kHz	5 µs	215 µJ

Table A9.1: Experimental details of the ultrafast sources used in our studies.

THz collection, radiation power and conversion efficiency. Following the method described in [378], the conversion efficiency is defined as the ratio between the input pumping power P_{pump} and the output THz power $P_{\text{THz}} \propto |E_{\text{THz}}|^2$, as:

$$\eta = \frac{P_{\text{pump}}}{P_{\text{THz}}} \quad \text{with} \quad E_{\text{THz}} = \sqrt{\frac{2I_{\text{peak}}}{c\varepsilon_0}} \quad \text{with} \quad I_{\text{peak}} = \frac{2P_{\text{peak}}}{\pi r^2} \tag{EA9.3}$$

A10 Electro-optic sampling and phase-matching in non-linear crystals.

We detail in this part the detection technique of the THz transients by electro-optic sampling (EOS) in non-linear crystals. The THz emission spectroscopy setup is detailed in Section III.2.1.

In anisotropic crystals, the propagation of light is different along the crystallographic axis: this is called the birefringence. In uniaxial crystals, the linear birefringence is described by two different refractive indices for two directions perpendicular to the propagating axis, conventionally by

an ordinary refractive index n_o and an extraordinary refractive index n_e. Between the two proper optical axis, it results a wavefront phase difference which results in a beam polarization variation between the input surface and the output surface of a birefringent crystal.

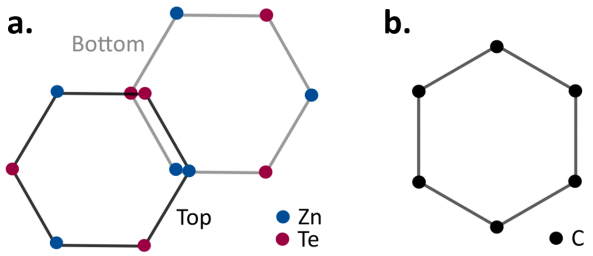

Figure A10.1: Non-centrosymmetric crystals. Crystal structure of (a) non-centrosymmetric ZnTe$\langle 110 \rangle$ surface and (b) centrosymmetric graphene.

In particular, in presence of an electric field in a non-linear (second-order) non-centrosymmetric crystals, the propagation of the light polarization ellipsoid is given by introducing the electro-optic tensor $\mathbf{r}_{ij}$ following the derivation of Yariv [393]:

$$\underbrace{\left(\frac{1}{n^2}\right)_1 x^2 + \left(\frac{1}{n^2}\right)_2 y^2 + \left(\frac{1}{n^2}\right)_3 z^2}_{\text{birefringence}} + \underbrace{2\left(\frac{1}{n^2}\right)_4 yz + 2\left(\frac{1}{n^2}\right)_5 xz + 2\left(\frac{1}{n^2}\right)_6 xy}_{\text{electro-optic effect}} = 1 \qquad \text{(EA10.1)}$$

where $i = \{1, ..., 6\}$ represent the six tensor components $\{x^2, y^2, z^2, yz, xz, xy\}$. In absence of an electric field, the first three indices $i = \{1, 2, 3\}$ represent the conventional birefringence term $1/n_i^2$ and the three mixed terms given by $i = \{4, 5, 6\}$ are vanishing. The variation of the refractive index can be more readily formulated as:

$$\Delta\left(\frac{1}{n^2}\right)_i = \sum_{j=1}^{3} \mathbf{r}_{ij} E_j \qquad \text{(EA10.2)}$$

where $\mathbf{r}$ is a 6x3 matrix coding the electro-optic effect. Depending on the crystal point group, the electro-optic coefficients can possibly vanish by symmetry arguments. The electro-optic tensor has been computed by Yariv [393] for various symmetries and we will consider here the particular example of the $\bar{4}3m$ point group for ZnTe and GaP which crystallize in the zinc-blende arrangement [104]. In this configuration, only the coefficients $r_{41} = r_{52} = r_{63}$ are non-zero and are equals. It is also possible to empirically parameterize the refractive index change Δn following the Sellmeier equations, for instance in case of ZnTe and GaP, in order to numerically compute the electro-optic response *vs.* the frequency. The reader may refer to Refs. [104, 394, 395] for more details. In the case of $\bar{4}3m$, it comes from Planken [396] and Schneider [397] that the phase shift Γ is expressed as:

$$\Gamma = \frac{2\pi e_{\text{cr}}}{\lambda_{\text{NIR}}} \Delta n = \frac{\omega_{\text{NIR}} n_{\text{cr}}^3 E_{\text{THz}} r_{41} e_{\text{cr}}}{2c} (\cos\alpha \sin 2\phi + 2 \sin\alpha \cos 2\phi) \qquad \text{(EA10.3)}$$

with $\lambda_{\text{NIR}} = 2\pi c/\omega_{\text{NIR}}$ the free-space NIR wavelength, e_{cr} and n_{cr} respectively the crystal thickness and refractive index on NIR frequencies, α is the angle of the THz polarization with respect to the [001] crystallographic axis and ϕ is the angle of the probe-beam polarization with respect to the same crystal [001] axis.

Phase-matching and detection bandwidth. However, the description of the light electric field only by a temporal distribution does not catch the full picture of the reality. For that, we need to consider the spatial distribution of the propagating electric field in a non-linear media. The

electromagnetic wave is fully described by considering a dependence $E(\mathbf{r},t) = E(t)\exp(-i\mathbf{k}\cdot\mathbf{r})$ with $|\mathbf{k}| = n(\omega)\omega/c$. This leads to the so-called phase-matching [398] between the probe and the THz pulse, given in the case of electro-optic sampling by:

$$l_c = \frac{\pi}{\Delta k} = \frac{\pi c}{\omega_{\mathrm{THz}}|n_{\mathrm{NIR}} - n_{\mathrm{THz}}|} \tag{EA10.4}$$

where l_c is the coherence length, typically the thickness of the non-linear crystal required for detecting the frequency component ω_{THz} of the THz pulse. This condition is only valid in a certain frequency range imposed by the NIR and THz properties of the optical media and it defines a phase-matching bandwidth, limiting the high cutoff frequency of the THz detection of non-linear crystals. Typically, the thicker the crystal, the shorter the bandwidth but the larger the electro-optic signal owing to the propagation in the crystal thickness. One has also to consider in the bandwidth response the crystal phonon modes, appearing around 5 THz for ZnTe and 10 THz for GaP and restricting the detection bandwidth. We give in Table A10.1 some crystals parameters for the two crystals that we will use in our studies: ZnTe$\langle 110\rangle$ and GaP$\langle 110\rangle$.

Crystal	Electro-optic coefficient	n_{cr}	Phonon frequency f_0	Point group
ZnTe [393, 396, 399, 400, 401]	r_{41}=3.9 pm.V^{-1}	2.8-3.22-3.9	$\simeq$5.3 THz	$\bar{4}3m$
GaP [393, 400, 401]	r_{41}=0.97 pm.V^{-1}	3.31	$\simeq$10 THz	$\bar{4}3m$

Table A10.1: Detection crystal parameters. Non-linear electro-optic constant r_{41}, real part of the refractive index n_{cr} (for λ_{NIR}=800 nm), phonon mode frequency f_0 and point group for ZnTe and GaP non-linear crystals.

A11 Optical and electrical properties of materials.

We detail in this Annex the values of the NIR and THz absorption. We recall that the THz electric field is proportional to:

$$E_{\mathrm{THz}} \propto S_{\mathrm{THz}} \propto \mathcal{A}_{\mathrm{NIR}} Z(\omega) \eta_{\mathrm{THz}} \alpha_{\mathrm{SCC}} \tag{EA11.1}$$

Near-infrared absorption. The NIR absorption is computed by means of the so-called Beer-Lambert law:

$$\mathcal{A}_{\mathrm{NIR}} = \prod_i \mathcal{A}^i_{\mathrm{NIR}} = \prod \exp(-\alpha_i t_i) \quad \text{with} \quad \alpha_i = \frac{4\pi\kappa_i}{\lambda} \quad \text{and} \quad l^i_{\mathrm{NIR}} = \frac{1}{\alpha_i} \tag{EA11.2}$$

where κ is the extinction coefficient, α the absorption coefficient and l_{NIR} the absorption length at a given wavelength λ (=800 nm in our case). We provide in Table A11.1 the values of the absorption coefficients as given from different sources in the literature [248].

Material	n_{NIR}	κ_{NIR}	α (cm^{-1})	l_{NIR} (nm)	Reference
Air	1	0	-	-	-
ZnTe	2.8-3.22	-	-	-	[393, 396, 399, 400, 401]
GaP	3.31	-	-	-	[393, 400, 401]
Si	3.4-3.6	-	-	-	[402, 403]
SiO_2	1.9-2	-	-	-	[404, 405, 403]
MgO	3-4	-	-	-	[406]
Glass	1.9-2.1	-	-	-	[407]
Sapphire	3.3	-	-	-	[403]
CVD diamond	2.4	-	-	-	[408]
AlN	3.0-3.1	-	-	-	[409]
Co	-	-	7.5×10^5	13	[248]
Cu	-	-	7.82×10^6	12.8	[249]
CoFeB	-	-	7.5×10^5	13	[248]
Pt	-	-	7.7×10^5	13	[248]
Co_2MnGa	-	-	4.7×10^5	21	[410, 411]
AuW*	-	-	8.8×10^5	11.7	(*)
Ti	-	-	3.97×10^5	25	[412]
Au	-	-	9.7×10^5	10	[249]
W	-	-	4.3×10^5	23	[248]
AlO_x	-	-	1.15×10^6	8	[413]
Al	-	-	1.3×10^6	7.7	[413]
NiO	-	-	1860	> 5 µm	[414]
AlGaAs	4	-	1860	> 5 µm	[415]
GaAs**	3.68	0.085	-	-	[415]
Parylene	1.6-1.7	-	-	-	-
BaF_2	1.6-1.7	-	-	-	[416]

Table A11.1: Near-infrared absorption. Values considered for the NIR refractive index $n_{\mathrm{NIR}} + i\kappa_{\mathrm{NIR}}$, the absorption coefficient α (considered for λ=800 nm) and the penetration depth l_{NIR} depending on the material. *The AuW near-infrared absorption is estimated from the optical absorptions of Au and W following $\alpha_{\mathrm{AuW}} = x\alpha_{\mathrm{W}} + (1-x)\alpha_{\mathrm{Au}}$ where x is the content of W in the alloy.

THz absorption. The THz absorption is accounted via the THz structure impedance $Z(\omega)$ in the thin film limit (multiple reflections). The derivation of the Tinkham formula is proposed in Annex A6. The THz impedance can be written by means of:

$$Z(\omega) = \frac{Z_0}{1 + n_s(\omega) + Z_0 \int \sigma(\omega, z) dz} \tag{EA11.3}$$

where ω is the THz frequency, $Z_0 = \sqrt{\mu_0/\epsilon_0}$=377 Ω is the free-space impedance, n_s is the THz refractive index of the substrate and $\sigma(\omega, z)$ is the conductivity of the thin film(s). We propose in Table A11.2 the values considered for the THz absorption.

Material	n_{THz}	κ_{THz}	ρ (μΩ.cm)	Reference
Air	1	0	-	-
Si	3.4-3.6	-	-	[402, 403]
SiO_2	1.9-2	-	-	[404, 405, 403]
MgO	3-4	-	-	[406]
Glass	1.9-2.1	-	-	[407]
Sapphire	3.3	-	-	[403]
CVD diamond	2.4	-	-	[408]
AlN	3.0-3.1	-	-	[409]
Co	-	-	29	Magneto-transport
Cu	-	-	8.5	Magneto-transport
CoFeB	-	-	130	Magneto-transport
Pt	-	-	30	Magneto-transport
Co_2MnGa	-	-	120	[410, 411]
AuW	-	-	87-117	Magneto-transport
Ti	-	-	200	Magneto-transport
Au	-	-	2.5-25	Magneto-transport
W	-	-	25	Magneto-transport
Al	-	-	40	Magneto-transport
AlO_x	-	-	-	-
AlGaAs	4	-	-	[415]
GaAs**	3.6	0.05	-	[415]
Parylene	1.6	-	-	-
BaF_2	2.7	-	-	[416]

Table A11.2: THz absorption. Values considered for the DC resistivity ρ depending on the material. Resistivity values are obtained from magneto-transport measurements in the thin film approximation. **GaAs presents a phonon absorption mode around 8 THz.

A12 Spin-orbit torque and spin-transfer torque.

Ultimate spintronics technological goal is to achieve magnetization switching by electrical control, thus allowing to access/write/erase the stored magnetic information more easily. It can be envisioned via the second revolution of spintronics as played by the discovery of spin-transfer torque. The reciprocal effect of spin-pumping has been predicted in 1996 by Berger [417] and Slonczewski [418]. Spin-transfer torque (STT) and spin-orbit torque (SOT) consist of a transfer of spin angular momentum from the conduction electrons (electrical current) to the local magnetization. Whereas the STT refers to the spin-polarization of the conduction electrons by a fixed ferromagnet (hard magnetization or in fixed layers), the SOT refers to the injection of a non-local spin-current from a high SOC material (via SHE) or interface (REE). These torques can potentially achieve electrically-induced magnetization switching without the need of applying a macroscopic magnetic field [419, 420]. This effect is schematically represented in Fig. A12.1.

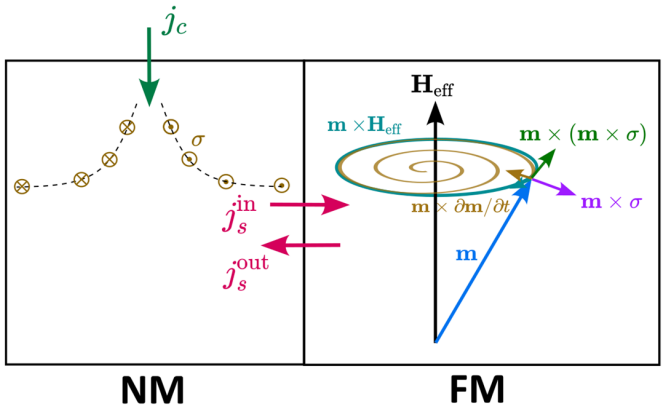

Figure A12.1: Spin-orbit torque. An injected charge current j_c is converted in a strong SOC material into a spin-polarized current j_s^{in} injected into a neighbouring ferromagnet. The spin current transfers part of its angular momentum to the magnetization $\mathbf{m}$ via the action of the damping-like torque $\mathbf{m} \times (\mathbf{m} \times \sigma)$ and field-like torque $\mathbf{m} \times \sigma$, inducing magnetization precession and concurrent spin pumping j_s^{out}.

Experimentally, a charge current j_c is injected into a heavy metal which allows the generation of a transverse spin current j_s via ISHE and injected into the FM layer. As the FM presents spontaneously a non-zero magnetization below its Curie temperature and consequently a large exchange potential energy ($J_{sd} \simeq 0.2$ eV), the injection of a spin current from the heavy metal leads to a transfer of angular momentum, from the intrinsic angular momentum of the spin-polarized current j_s to the net magnetization $\mathbf{m}$. The magnetization starts to precess: this mechanism is called spin-transfer torque which can potentially induces magnetization switching or subsequent magnetoresistance effects [421].

In details, the action of the angular momentum transfer leads to an additional term in the Laudau-Lifschitz-Gilbert equation which adds the so-called Slonczewski contributions. Additional spin-orbit torque can be generally separated into two terms orthogonal to the magnetization, written as :

$$\mathbf{T}_{\text{SO}} = \mathbf{T}_{\parallel} + \mathbf{T}_{\perp} = \underbrace{\tau_{\text{DL}}\mathbf{m} \times (\mathbf{m} \times \sigma)}_{\text{damping-like torque}} + \underbrace{\tau_{\text{FL}}(\mathbf{m} \times \sigma)}_{\text{field-like torque}} \tag{EA12.1}$$

where $\mathbf{T}_{\perp}$ is the damping-like component (also called Slonczewski torque) of the spin-orbit torque mainly linked to the ISHE contribution whereas $\mathbf{T}_{\parallel}$ is the field-like component mostly describing the IREE contribution to the spin-orbit torque. In FM/HM bilayers, the field-like component H_{FL} is assumed to be negligible compared to the damping-like contribution H_{DL} as it is directly linked to the imaginary part of the spin-mixing conductance $\text{Im}(g_{\text{eff}}^{\uparrow\downarrow})$ (reciprocally, the

damping-like contribution is related to the real part of the spin-mixing conductance $\mathrm{Re}(g_{\mathrm{eff}}^{\uparrow\downarrow})$). Besides, the contribution of the Oersted field (due to the current flowing into the metallic slab) is in general opposite to the field-like torque. It can be shown that Oersted contribution is collinear to the field-like torque due to symmetry contributions.

Oersted field.

The Oersted field arises from the Maxwell-Ampère equation, in which a charge current j_{HM} flowing in a metal (of thickness t_{eff}) generates a curved closed magnetic field B_{Oe} (the reciprocal effect of the magnetic induction arises from Maxwell-Faraday equation). In the first view, we can approximate the Oersted field as:

$$B_{\mathrm{Oe}} = \mu_0 H_{\mathrm{Oe}} = \mu_0 j_{\mathrm{HM}} \frac{t_{\mathrm{eff}}}{2} \tag{EA12.2}$$

The precession of the magnetization generates a second spin current term entering into the heavy metal through spin pumping effect, with the applied current density $j_{\mathrm{AC}} = I_{\mathrm{AC}}/S$ where I_{AC} is the input AC current and S is the injection cross section. A common convention is to consider the spin-orbit torque efficiency (given in $\mathrm{A}^{-1}.\mathrm{m}^2$):

$$\xi_{\mathrm{DL}}^{j} = \left(\frac{2e}{\hbar}\right) \frac{\mu_0 H_{\mathrm{DL}} M_s t_{\mathrm{eff}}}{j_{\mathrm{AC}}}, \quad \xi_{\mathrm{FL}}^{j} = \left(\frac{2e}{\hbar}\right) \frac{\mu_0 H_{\mathrm{FL}} M_s t_{\mathrm{eff}}}{j_{\mathrm{AC}}} \tag{EA12.3}$$

where we have distinguished the respective efficiency of the damping-like and field-like torques, with M_s the saturation magnetization, t_{eff} the effective conduction thickness of the metal. One can also write down the efficiency which takes the form of an effective spin Hall conductivity $\sigma_{\mathrm{SHE}}^{*}$ and spin Hall angle $\theta_{\mathrm{SHE}}^{*}$ (including the interfacial transmission), as a function of the interface spin transparency T^* linked to the spin-mixing conductance $g_{\mathrm{eff}}^{\uparrow\downarrow}$, with ρ_{xx} the longitudinal resistivity of the heavy metal, n the carrier density and μ the carrier mobility:

$$\xi_{\mathrm{DL}}^{j} = T^* \underbrace{\sigma_{\mathrm{SHE}}^{*} \rho_{xx}}_{=\theta_{\mathrm{SHE}}^{*}} \quad \text{with} \quad \sigma_{xx} = \frac{1}{\rho_{xx}} = en\mu \tag{EA12.4}$$

A13 Ultrafast X-ray diffraction on NiO/Pt bilayers.

We develop in this part the ultrafast X-ray diffraction method performed by our collaborators M. Mattern, M. Bargheer (Potsdam University), to extract the strain induced by ultrafast laser heating in NiO/Pt bilayers as shown in our study in Chap. V.

A13.1 Extraction of the out-of-plane transient strain in NiO/Pt bilayers.

Experimental setup. Ultrafast X-ray diffraction (UXRD) and subsequent ultrafast reciprocal space mapping (URSM) are conducted with hard X-ray probe pulses at 8 keV, which are derived from a laser-driven X-ray plasma source and have a duration of approximately 200 fs and a footprint of about 300 µm [355, 356]. A more than three times larger area of the Pt layer is excited by p-polarized pump pulses with a duration of 100 fs at a central wavelength of 800 nm, which are incident under 25° relative to the surface normal with a fluence of 10 $\mathrm{mJ.cm}^{-2}$. The strain $\varepsilon_{zz} = \Delta q_z/q_z$ is the relative change of the Bragg peak position in reciprocal space.

Link with the out-of-plane strain. The time-resolved out-of-plane strain of the NiO layer is given by the relative change of the Bragg peak position in reciprocal space with the time delay t:

$$\varepsilon_{zz}^{\mathrm{NiO}}(t) = \frac{(q_z(t < 0\ \mathrm{ps}) - q_z(t))}{q_z(t < 0\ \mathrm{ps})} \tag{EA13.1}$$

Fig. A13.1 shows the reciprocal space around the (004) reflection of NiO as measured during the time-resolved experiment. The projection on the respective directions of the reciprocal space q_z and q_x (gray circles) consists of a background from the MgO substrate and the NiO Bragg peak. The determination of the position of the NiO Bragg peak along q_z and the corresponding expansion require the substration of the MgO background. We model the background from the diffraction of the substrate truncation rod by a Lorentzian fitted the intensity below 5.93 Å and above 5.98 Å. The difference between the total intensity and the modelled substrate background (black dashed line) determines the NiO Bragg peak (blue circles). Its time-dependent position along q_z (vertical gray dashed line) is determined by a center-of-mass analysis of the reciprocal-space maps recorded at each pump-probe delay.

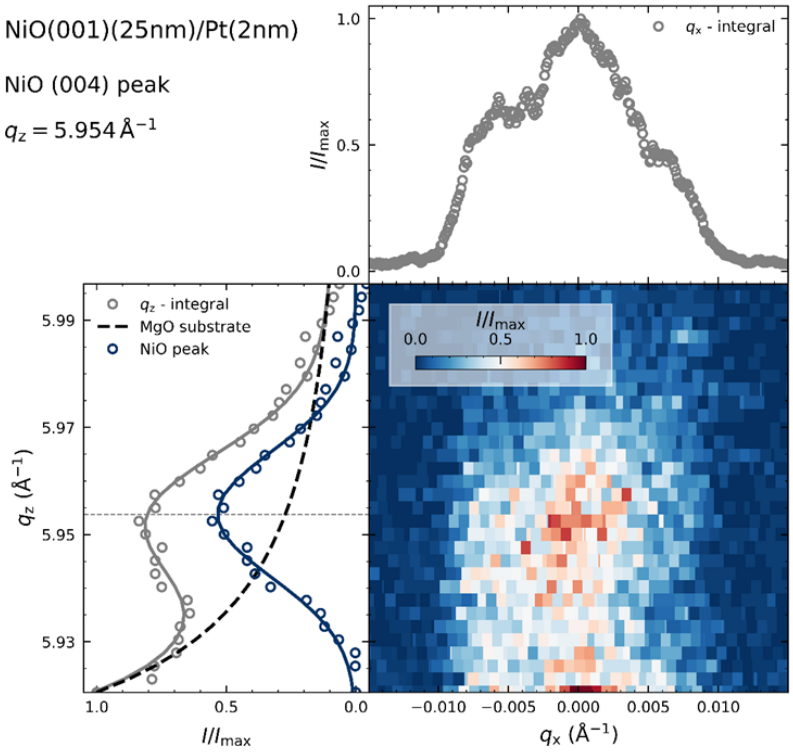

Figure A13.1: Reciprocal space mapping (RSM) around the (004) reflection of a 25 nm-thick NiO thin film on MgO substrate covered with Pt(2nm). The rising intensity at the small angle side of the RSM originates from the MgO substrate Bragg peak, which is cut from the figure due to its $\times 100$ higher intensity. The left panel displays the extraction of the NiO Bragg peak (blue circles) by integrating the intensity along the q_x-direction in reciprocal space (grey circles) and subtracting the modelled background provided by the MgO substrate (black dashed line). The blue and grey solid lines describe the fitted NiO Bragg peak and its superposition with the background, respectively. The vertical dashed grey line denotes the determined position of the NiO Bragg peak along q_z which determines the out-of-plane strain of the NiO layer $\varepsilon_{zz}^{\mathrm{NiO}}$.

A13.2 Simulation of the phonon propagation: coherent strain wave and incoherent heat.

To simulate the ultrafast strain response, we used the 1D module *udkm1Dsim* Python toolbox [358] which allows to compute, for a given heterostructure described by the material parameters given in Table A13.1 for NiO, MgO and Pt, the wave-equation of the displacement $u(z,t)$ under excitation by a source term $\sigma_{\mathrm{ext}}(z,t)$ which represents here the pump-induced stress:

$$\frac{\partial^2 u}{\partial t^2} - v_s^2 \frac{\partial^2 u}{\partial z^2} = -\frac{\partial \sigma_{\mathrm{ext}}}{\partial t} \tag{EA13.2}$$

where v_s represents the sound velocity in the material in the i-th layer. The module is able to

consider the electronic and phononic subsystems temperatures. In a first approximation, only the electronic subsystem is relevant in metallic Pt capping and the heat transport is made through phonon interactions in NiO, therefore we only account for one temperature in each layer denoted $\Delta T(z,t)$ (the so-called one temperature model). The two temperatures model will be further developed in NiO/Pt by M. Mattern (Potsdam University) in the scope of his thesis work. The stress induced by the pump on the Pt capping can be written as:

$$\sigma_{\text{ext}}^{\text{Pt}} = \rho_{\text{Pt}}^{Q}(z,t)\Gamma_{\text{p}}\left[1 - \frac{\Gamma_{\text{e}}}{\Gamma_{\text{p}}}\exp\left(-\frac{t}{\tau_{\text{ep}}}\right)\right] \tag{EA13.3}$$

where Γ_{e} and Γ_{p} are respectively the electronic and phononic Grüneisen constant, τ_{ep} is the electron-phonon coupling time and $\rho_{\text{Pt}}^{Q}(z,t) = C\Delta T$ accounts for the energy density deposited by the laser-induced stress where C is the heat capacity.

We present in Fig. A13.2 the simulated out-of-plane strain $\varepsilon_{zz}(z,t)$ and the temperature $\Delta T(z,t)$ for NiO(25nm)/Pt(2nm) on MgO substrate. From this information, we could *i*) identify that the coherent (strain wave) and incoherent (heat) phonon propagation contributes both to the mediated strain. Moreover, *ii*) the information of the strain and heat as a function of time and position will be valuable for computing the Néel vector dynamics (Section V.3.3.2).

Material	Pt	NiO	MgO
C (J.m^{-3}.K^{-1})	2.85 [422]	4.2 [423]	3.32 [424]
κ (W.m^{-1}.K^{-1})	71 [425]	31 [423]	50 [382]
ρ (g.cm^{-3})	21.45	6.79	3.58
v_s (nm.ps^{-1})	4.2 [426, 427]	6.99 [428]	9.12 [429]
Γ_{e}	1.6 [430]	-	-
Γ_{p}	2.6 [430]	0.9 [431, 432]	1.6 [433]
τ_{ep} (fs)	500 [434]	-	-

Table A13.1: Used thermo-elastic constants for Pt, NiO and MgO. C is the phonon heat capacity, κ is the heat conductivity, ρ is the mass density, v_s is the sound velocity, Γ_{e} and Γ_{p} are respectively the electronic (phononic) Grüneisen constant and τ_{ep} is the electron-phonon coupling time.

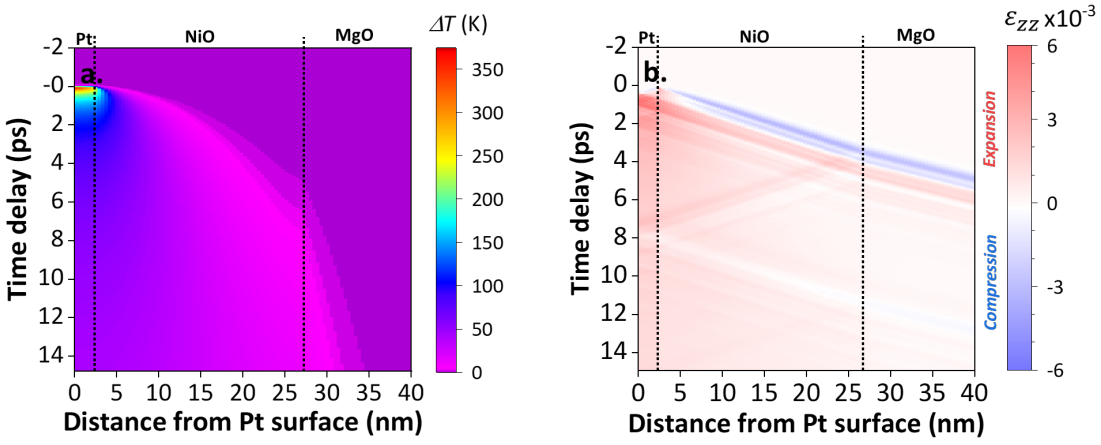

Figure A13.2: Simulated propagation of the phonon contribution. (a) Temperature map $\Delta T(z,t)$ and (b) strain map $\varepsilon_{zz}(z,t)$ as a function of the position z and time t in MgO//NiO(001)(25nm)/Pt(2nm).

A14 THz emission in canted rare-earth antiferromagnet $TmFeO_3$/Pt.

This is an Annex to Chap. V.

$TmFeO_3$: a weak ferromagnet with antiferromagnetic ordering. Thulium orthoferrite ($TmFeO_3$) is a particularly interesting and singular antiferromagnet, of space group *Pbnm* and having a Néel temperature of $T_N = 635$ K. Indeed, the magnetic moments carried by the Fe atoms are antiferromagnetic coupled in a G-type structure but are however, slightly canted due to the presence of Dzyaloshinskii-Moriya interactions (DMI). Therefore, $TmFeO_3$ owns a very small net magnetization and is envisioned as an interesting system to probe both ferromagnetic and antiferromagnetic excitation modes. Besides the Néel transition, $TmFeO_3$ antiferromagnet has a second transition temperature T_{SR} between 80 K and 90 K accounting for the spin reorientation (SR) of the magnetic moment due to a change of the magneto-crystalline anisotropy term. Above the spin reorientation transition, the magnetization lies along the a axis (easy-axis antiferromagnet). This transition thus leads to a spin reorientation inducing a tilt of the magnetization by 90°from the a axis to the b axis. The literature reported in details the transition of the spin-reorientation near 70-90 K in the transition region by optically-induced Faraday rotation [435, 436] and vector network analyzer measurements of the antiferromagnetic resonance [437]. Besides, the bandgap of $TmFeO_3$ of 1.6 eV is very close to the pump energy.

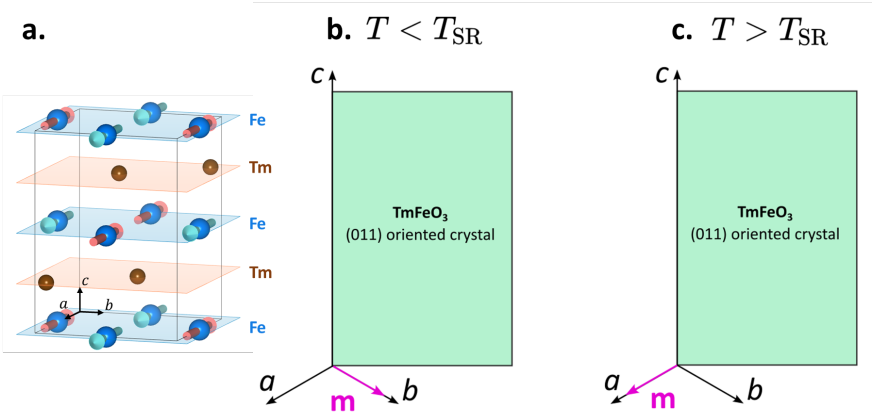

Figure A14.1: Spin configuration in $TmFeO_3$. (a) Crystallographic arrangement of $TmFeO_3$ overprinted with the antiferromagnetic spin texture above the spin reorientation transition. (b) Magnetization orientation (b) below and (c) above the spin-reorientation transition (SR).

Dzyaloshinskii-Moriya interactions.

The Dzyaloshinskii-Moriya interactions (DMI), or asymmetric exchange, tunes the exchange interaction between two neighbouring spins $\mathbf{s}_i$ and $\mathbf{s}_j$ as firstly discovered in hematite. This provokes a tilt of the neighbouring spins, also called canting, which creates a non-zero magnetization in canted antiferromagnets. DMI is a central interaction in spintronic materials, for instance with the nucleation of skyrmions, *etc.*

$$\mathcal{H}_{\text{DMI}} = \mathbf{D}_{ij} \cdot (\mathbf{s}_i \times \mathbf{s}_j) \tag{EA14.1}$$

THz emission spectroscopy of $TmFeO_3$/Pt. We studied a bilayer composed of a $TmFeO_3$(500µm) single crystal capped by Pt(2nm), especially in two crystalline orientations $\phi = \{0°, 90°\}$ to probe the magnetic arrangement. By convention, we choose $\phi = 0°$ as the direction collinear to the c axis and $\phi = 90°$ the direction perpendicular to the c axis. We report in Fig. A14.2a a THz emission from $TmFeO_3$/Pt obtained at room temperature, with an amplitude similar to the THz signal obtained in NiO/Pt bilayer. Noticeably, we report the THz emission only in the configuration where $\phi = 90°$ thus demonstrating a net spin-injection in Pt for spin-charge conversion. The spin-charge conversion via ISHE is indicated by the reversal of the THz polarization while reversing the applied magnetic field, proving at the same time that

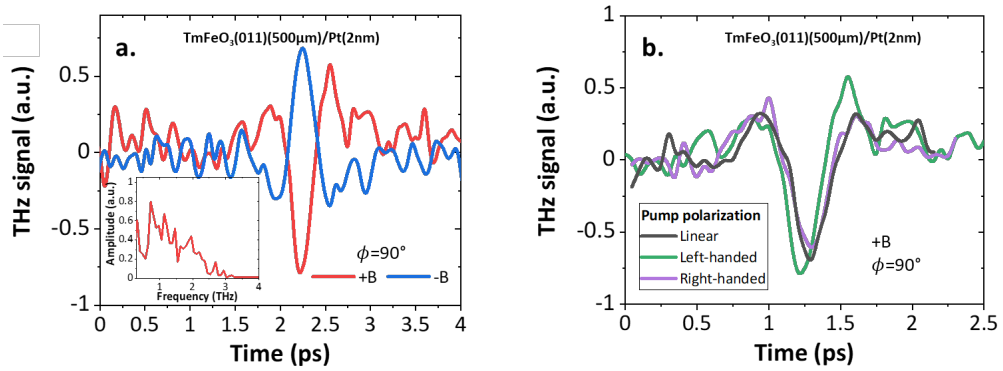

Figure A14.2: THz emission from $TmFeO_3$/Pt bilayer. (a) Reversal of the THz emission as a function of the applied magnetic field. The inset presents the Fourier transform of the THz signal. (b) Pump polarization dependence (linear *vs.* circular) of the THz signal.

the spin-injection arises from the dynamics of the weak ferromagnetic moment of $TmFeO_3$. The absence of a measurable signal for the $\phi = 0°$ configuration can arise from: *i*) the pure absence of a net injected spin current or *ii*) a presence of a net in-plane projection of a magnetic moment, however weaker than in the $\phi = 90°$ situation that would be undetectable by our setup due to the weakness of the signal.

We have tried to perform a temperature dependence of the THz signal in the $\phi = 90°$ configuration to follow the spin reorientation transition near $T_{SR} \simeq 70 - 80$ K reported in the literature, a dependence which is however inconclusive due to the difficulty to map a very weak signal in the cryostat (absorption by the cryostat optical windows).

We also measured the THz emission as a function of the pump polarization from $TmFeO_3$/Pt in the $\phi = 90°$ configuration as displayed in Fig. A14.2b. We observe a polarization-independent signal in favor of thermally-mediated process, a symmetry which would be followed by the ultrafast demagnetization of the small magnetic moment of $TmFeO_3$, to oppose to pure inverse Faraday magneto-optical effects also reported previously by Kimel *et al.* [436]. However on this point, one should carefully compare this study to the study proposed by Kimel *et al.* where non-thermal and thermal contributions are separated as a function of temperature. The non-thermal contributions are dominating at low temperatures with $T < T_{SR}$ compared to the thermal contributions dominating near the spin-reorientation transition. Besides, the mode frequency at low temperature is reduced down to 100-120 GHz (and of 400 GHz at room temperature), which could potentially explain why we have not been able to measure such THz signal from $TmFeO_3$/Pt near the transition due to the low-frequency cutoff of our detection. Still, this work thus opens interesting perspectives for controlling the small net magnetic moment of the weak $TmFeO_3$ antiferromagnet while possible benefit from the THz antiferromagnet modes to be explored in future studies.

A15 Finite elements methods to simulate the structure response.

This is an Annex to Chap. VI.

To simulate the engineered spintronic THz emitters (cavity-based and anti-reflective coatings, see Chap. VI), we performed finite elements method simulations using Comsol Multiphysics [371]. In details, we use the *Wave Optics* Module with the electromagnetic waves (frequency domain) physics interface.

A geometry is set following the design of the spintronic THz emitter, with a substrate of hundreds of microns (thickness t_s) and the spintronic emitter (typically 6 nm-thick). The materials are after set with the THz refractive index $n_{\mathrm{THz}} + i\kappa_{\mathrm{THz}}$. In particular, the spintronic THz emitter is modelled with by a unique metallic layer (*i.e.* no interface are included inside the 6 nm-thick layer). A particular attention is paid to the boundary conditions: the geometry is encapsulated in a circular region setting the simulation region (air). The borders are set with *Scattering Boundary Conditions*. The meshing is given by the physics-determined parameters (layer thickness, THz wavelength in the material, *etc.*). An example is shown in Fig. A15.1. A THz charge current $j_c(\omega)$ oscillating at the frequency ω is set at the surface of the spintronic THz emitter (via *Surface Current Density*). The frequency are ranging from 0.3 to 3 THz in general. An hemispherical line is placed far above the sample and serves as a detector by integrating the electric field on its contour. This sets the emission figure of merit as a function of frequency via $\zeta(\omega) \equiv \int E_{\mathrm{THz}}(\omega) dl$ and is given in V via a *Global Variable Probe*.

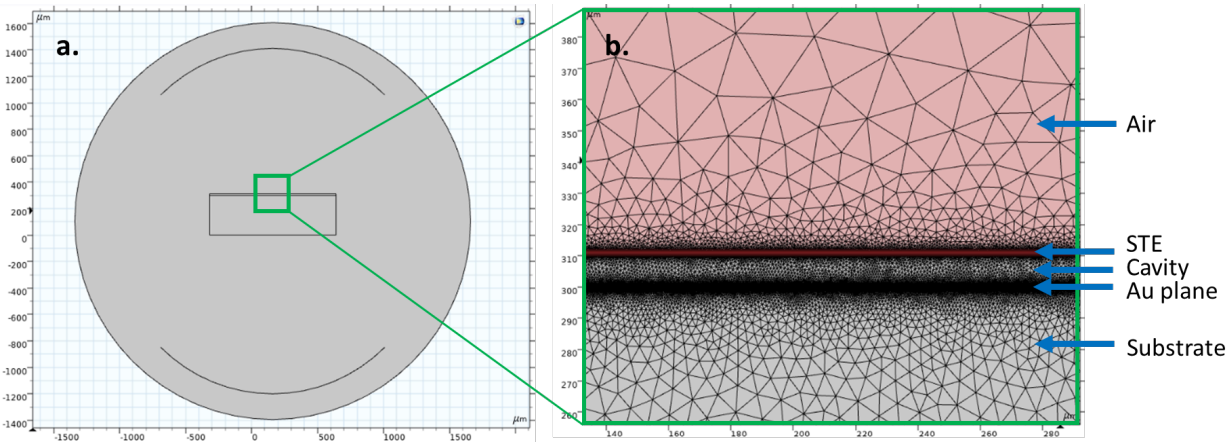

Figure A15.1: Structure configuration with Comsol Multiphysics. (a) Geometry of the structure, with the circular limits delimiting the simulations, and the hemispherical detection line. (b) Meshing of the layers composing the structure.

A16 THz reflector by buried metallic plane.

This is an Annex to Chap. VI.

At last, we open perspectives towards the harvesting of the radiation power lost in the substrate for the emitters in the reflection geometry. Indeed, as mentioned before and shown in the simulations, a non-negligible part of the radiation is lost in the substrate due to the better THz characteristic impedance matching. To counter this drawback of native STE, we imagine to realize a buried THz reflection composed of a metallic plane like Au. We have studied the impact of a buried Au plane below the STE, at a distance d, to reflect the generated THz wave. The Au plane is physically separated from the STE by using an insulating barrier (here Al_2O_3) deposited by atomic layer deposition (ALD) to prevent electric shunting of the generated THz current as displayed in Fig. A16.1a. Our preliminary results shown in Fig. A16.1b from our sapphire//Au(100nm)/Al_2O_3(10nm)/Co(2nm)/Pt(4nm) multilayer presents a reduced THz signal of a factor -75%, which can be explained by several hypothesis. The first hypothesis is that we may have a too thin insulating barrier (d =10 nm in this case). For that, we can estimate the potential electrical shunting due to the presence of a planar capacitance (two metallic planes charged with the THz electric field and separated by an insulating barrier). We can write the impedance of the insulating barrier as $Z(\omega) = 1/i\omega C = e/(i\omega\epsilon_0\epsilon_r S)$ where ω is the frequency of the field induced current, ϵ_0 is the vacuum permittivity, ϵ_r is the relative permittivity and S is the surface

of the planes, typically 5 mm^2. Secondly, we may have a high interface roughness between the Au plane and the deposited Al_2O_3 which would result in a low interface quality and thus a low sticking rate of the ALD deposited Al_2O_3 leading to the presence of parasitic conduction channels on a full sample sheet. In all cases, this would result in electrical current shunting. Lastly, the role of the THz impedance is to be highlighted in the THz absorption due to the additional metallic Au layer. Future studies will therefore focus on selecting a thicker insulating barrier (up to 50-100 nm) and to isolate lateral structures to avoid all potential current leaking from the top STE to the bottom thick Au plane.

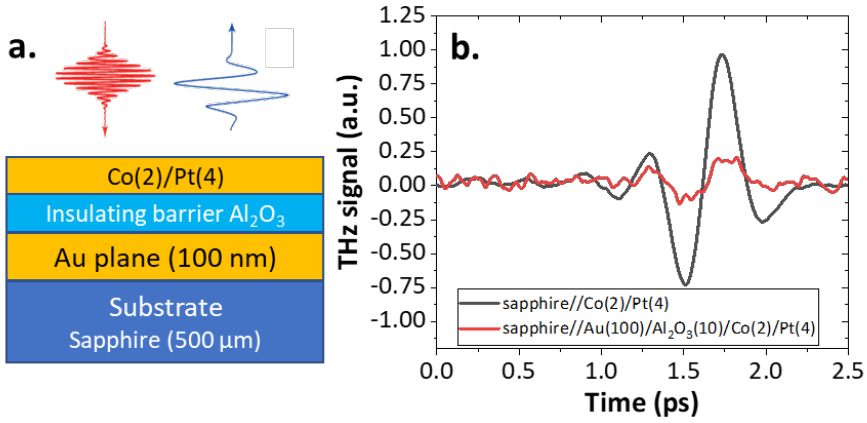

Figure A16.1: THz reflector using an insulating barrier and a metallic plane. (a) Schematics of the structure delimited by a Al_2O_3(10nm) insulating barrier and a Au(100nm) plane. (b) THz emission from sapphire//Au(100nm)/Al_2O_3(10nm)/Co(2nm)/Pt(4nm) reflector compared to reference sapphire//Co(2nm)/Pt(4nm)

université PARIS-SACLAY

ÉCOLE DOCTORALE
Physique en Île-de-France (PIF)

Titre: Courants de spin ultra-rapides assistés par interactions spin-orbite : vers de nouveaux concepts pour les émetteurs THz

Mots clés: terahertz, spintronique, isolants topologiques, antiferromagnétisme, interconversion spin-charge, dynamique ultra-rapide

Résumé: Le domaine terahertz (THz) est une partie importante du spectre électromagnétique, avec des applications pour l'imagerie médicale, le contrôle non-destructif ou encore les télécommunications ultra-rapides. Comparé aux autres régions du spectre, le domaine THz a été historiquement difficile d'accès à cause du manque de sources efficaces comptant sur des approches électroniques ou photoniques. Une récente percée a été la réalisation d'émetteurs THz spintroniques (STE) : des structures nanométriques, excitées optiquement et composées d'une couche ferromagnétique en contact avec un métal lourd à fort couplage spin-orbite (*e.g.* Co/Pt). Sous excitation ultra-rapide (femtoseconde), un courant de spin ultra-rapide est lancé à partir du matériau ferromagnétique vers le matériau adjacent. Par effet du couplage spin-orbite, le courant de spin subit un mécanisme de conversion spin-charge (SCC), comme l'effet Hall de spin inverse (ISHE), qui donne lieu à la génération transverse d'un courant de charge et à l'émission résultante d'un pulse THz en espace libre. La bande passante THz obtenue peut être large (de 300 GHz à 30 THz) et continue à cause de l'absence d'absorption par des phonons. Les performances des STE sont comparables à celles des cristaux non-linéaires et plusieurs variables d'ajustement peuvent être explorées pour une optimisation plus poussée.

Dans ce travail, nous présentons une étude fondamentale de l'opération des STE dans le régime subpicoseconde pour fournir des éléments de compréhension sur la SCC ultra-rapide. Nous illustrons le rôle des interfaces de spin, des longueurs de relaxation et des temps de renversement de spin sur l'émission THz. La première approche consiste à changer les propriétés de SCC dans les métaux lourds par des alliages de spin-Hall (*e.g.* Au:W, Au:Ta) pour augmenter la contribution extrinsèque de l'ISHE, ainsi que l'ingénierie d'interfaces atomiques pour optimiser l'injection de spin. Nous démontrons la manipulation des courants de spin en utilisant des drains de spin (*e.g.* Au:W) pour éviter les réflexions de spin indésirables. Le rôle de semi-métaux de Weyl (*e.g.* Co_2MnGa), qui possèdent une plus grande polarisation de spin au niveau de Fermi, est également discuté. Dans une seconde partie, nous investiguons un nouveau mécanisme SCC d'interface avec des isolants topologiques issus de la famille du Bi (*e.g.* $Bi_{1-x}Sb_x$, $SnBi_2Te_4$, Bi_2Se_2, Bi_2Te_3), pour lesquels une forte émission THz est reportée lorsque ces matériaux sont couplés avec des couches ferromagnétiques. Les isolants topologiques présentent des états de surface conducteurs alors que le matériau massif reste isolant, ce qui permet une plus faible absorption THz. Nous reportons une SCC plus forte aux interfaces, potentiellement par l'effet Rashba-Edelstein inverse via des états de surface hybridés de type Rashba, contrairement à l'ISHE dans les métaux lourds. Une troisième approche est de changer les propriétés de l'injecteur de spin. À la place de matériaux ferromagnétiques, nous présentons une architecture innovante basée sur des matériaux antiferromagnétiques (*e.g.* NiO/Pt), dont les modes propres résident naturellement dans le domaine THz. Nous montrons pour la première fois une contribution THz étroite en fréquence à 1 THz, qui est liée au vecteur de Néel. Nous prouvons que le rôle des interactions spin-phonon ultra-rapides est central. L'usage de matériaux antiferromagnétiques isolants offre donc une plateforme de choix pour l'émission cohérente et accordable dans le domaine THz. Pour finir, nous offrons des optimisations photoniques des STE, avec l'usage de couches anti-reflets ou de cavités THz, et nous démontrons théoriquement le photo-mélange THz spintronique. Ce travail représente une avancée significative dans la compréhension des STE et offre un aperçu de la nouvelle génération de sources spintroniques, qui se dirige vers la spintronique THz topologique ou encore vers l'émission THz à bande étroite.

université PARIS-SACLAY

ÉCOLE DOCTORALE
Physique en Île-de-France (PIF)

Title: Ultrafast spin-currents mediated by spin-orbit coupling: towards new concepts for THz emitters
Keywords: terahertz, spintronics, topological insulators, antiferromagnets, spin-charge conversion, ultrafast dynamics

Abstract: The terahertz (THz) domain represents an important part of the electromagnetic spectrum, with potential applications stretching from medical imaging, non-destructive testing to high-speed telecommunications. Compared to other spectral regions, the THz range has been historically challenging to access owing to the lack of efficient and compact sources using electronic or photonic approaches. A recent breakthrough has been the realization of spintronic THz emitters, nanometer-thin optically excited heterostructures that are composed of a ferromagnetic layer in contact with a high spin-orbit coupling material (*e.g.* Co/Pt). Upon ultrashort (femtosecond) excitation, an ultrafast spin current is launched from the ferromagnetic layer into the adjacent layer. Owing to the strong spin-orbit coupling, the injected spin-current undergoes a spin-charge conversion (SCC) mechanism, such as the inverse spin Hall effect (ISHE), which leads to the generation of transverse transient charge current and subsequent free-space single-cycle THz pulses. Importantly, the obtained THz bandwidth can be broad (from 300 GHz to 30 THz) and gapless owing to the ultrashort pump profile and the absence of phonon absorptions. The performances of such spintronic THz emitters are already comparable to those of non-linear crystals and considerable parameter space is possible for further optimization and implementation of additional functionalities.

In this work, we present an in-depth and fundamental study of the sub-picosecond operation of spintronic THz emitters, with an aim to provide insights into ultrafast SCC. We illustrate the key role of spintronic interfaces, effective spin relaxation lengths and spin-flip scattering times on the THz emission. The first approach here is to carefully tune the SCC properties in heavy metal systems through spin Hall alloys (*e.g.* Au:Ta, Au:W) to increase the extrinsic contribution to the ISHE, and the engineering of atomic interfaces to optimize the spin-injection. We show the manipulation of transient spin currents via the use of spin-sinks (*e.g.* Au:W) to avoid undesirable spin reflection. The role of Weyl semi-metals (*e.g.* Co_2MnGa) of high spin-polarization at the Fermi level, instead of standard ferromagnets, is also discussed. In the second part, we investigate a novel interfacial SCC mechanism in topological insulators from the Bi-based family (*e.g.* $Bi_{1-x}Sb_x$, $SnBi_2Te_4$, Bi_2Se_3, Bi_2Te_3), for which a strong THz emission is reported when coupled to ferromagnetic layers. Topological insulators present conductive surface states while the bulk remains insulating, allowing a lowered THz absorption as well as a possible enhancement of the SCC efficiency. We report that the SCC is larger at interfaces, potentially via the inverse Rashba-Edelstein effect on hybridized Rashba-like surface states, in contrast to the ISHE in the bulk of heavy metals. A third approach is then to change the properties of the spin-injector. Instead of ferromagnets, we show a cutting-edge architecture based on antiferromagnetic materials (*e.g.* NiO/Pt), as the intrinsic modes of such materials lies naturally in the THz range. We report for the first time a narrowband contribution to the THz emission centred at 1 THz that is linked to the antiferromagnetic Néel vector and where we evidence the central role of ultrafast spin-phonon interactions. The use of insulating antiferromagnetic materials offers thus an interesting platform for coherent emission and tunability over the THz range. Finally, we provide perspectives on the future photonic optimization of spintronic THz emitters through, for instance, the use of THz anti-reflective coatings or cavities and we demonstrate theoretically the spintronic THz photomixing operation to envision narrowband emitters. This work represents a significant step further in the understanding of spintronic THz emitters and provide insights on the novel generation of spintronic sources, going towards topological THz spintronics or narrowband THz emission.